A Study of Air Flow Through Saturated Porous Media and its Applications to In-Situ Air Sparging

by

Catalina Marulanda

Bachelor of Science in Civil Engineering
Lehigh University, Lehigh, Pennsylvania
(1994)

Master of Science in Civil and Environmental Engineering
Syracuse University, Syracuse, New York
(1996)

Submitted to the
Department of Civil and Environmental Engineering
in partial fulfillment of the requirements for the degree of

Doctor of Philosophy in Civil and Environmental Engineering

at the

MASSACHUSETTS INSTITUTE OF TECHNOLOGY

September 2001

© 2001 Massachusetts Institute of Technology
All rights reserved

Signature of author: _____
Department of Civil and Environmental Engineering
August 17, 2001

Certified by: _____
Professor Patricia J. Culligan, Thesis Co-Supervisor
Department of Civil and Environmental Engineering

Certified by: _____
Dr. John T. Germaine, Thesis Co-Supervisor
Department of Civil and Environmental Engineering

Accepted by: _____
Oral Buyukozturk
Chairman, Departmental Committee on Graduate Studies

ENG

MASSACHUSETTS INSTITUTE OF TECHNOLOGY
SEP 20 2001
LIBRARIES

V.1

A Study of Air Flow Through Saturated Porous Media and its Applications to In-Situ Air Sparging

by

Catalina Marulanda

Submitted to the Department of Civil and Environmental Engineering
on August 17, 2001 in Partial Fulfillment of the Requirements for the Degree of
Doctor of Philosophy in Civil and Environmental Engineering

ABSTRACT

The efficiency of an in situ air sparging system is controlled by the extent of contact between injected air and contaminated soil and pore fluid. Characterizing the mechanisms governing air propagation through saturated porous media is therefore critical to the design of an effective cleanup treatment. The objectives of this investigation were thus to identify and to quantify the parameters that affect the advancement of an air front through saturated soils. To this end, an experimental program was conducted in order to assess the impact of: 1) operational parameters, specifically the differences in air propagation as a result of injection under constant pressures and constant flow rate conditions, as well as the impact of injector geometry; and 2) medium properties, namely hydraulic conductivity and pore fluid characteristics. Experiments were conducted in a geotechnical centrifuge, which made it possible to test under a wide range of injection pressures while maintaining both realistic fluid and soil pressures, and sample stability.

Experimental results show that air propagation characteristics through saturated soils are primarily controlled by two factors, the pressure in the air phase and the hydraulic conductivity of the medium. Under constant pressure injection, the magnitude of the pressure gradient between air and pore fluid dictates the final shape of the air plumes. Under constant flow rate injection, the relationship between the rate of air inflow and of pore fluid outflow determines the volume available for air invasion, and consequently, the pressure in the air phase. Both the hydraulic conductivity of the medium and the compressibility of the air are crucial in the determination of the final plume volume.

Experimental findings were used in the development of a simplified model of air flow through porous media, which predicts the shape of plumes under constant flow rate injection conditions. The model is based on the premise that since the use of IAS systems is restricted to coarse, granular materials, the magnitude of capillary pressures is negligible relative to that of hydrostatic pressures. Air propagation can therefore be modeled as the advancement of a uniform front driven by an evolving pressure gradient.

Thesis Co-Supervisor: Professor Patricia J. Culligan
Title: Associate Professor of Civil and Environmental Engineering

Thesis Co-Supervisor: Dr. John T. Germaine
Title: Principal Research Associate in Civil and Environmental Engineering

Acknowledgements

The investigation presented in this dissertation was sponsored by the National Institutes of Health under Grant No. P42-ES04675. The support of the NIH and that of the Center for Environmental Health Sciences at MIT is gratefully acknowledged.

It is in all sincerity I say, that without the help and encouragement of the people included on these two pages I would have not been able complete this work. Their support came at different stages of the past five years, and in many different ways. It is with my deepest gratitude that I write these comments.

I would first like to thank *Professor Culligan* for having supported me during my time at MIT. This support not only consisted in academic and financial ties, but extended to her becoming involved with my interests and concerns. Her encouragement during Generals and throughout these difficult last months really made all the difference.... Lastly, it is to her insight that I owe my connection to the "sustainable underworld", an involvement that has changed my future plans and for which I am extremely grateful.

I feel very fortunate to have had the opportunity to work with Dr. Germaine, whose understanding of the basic principles behind... everything (!) and his highly trained intuition have never ceased to amaze me. Thank you for all of your help Dr. G.!!!

Many thanks to *Professor Nadim* for serving as the third member of my thesis committee, for his input, and especially for the time he spent with us in the midst of his frantic schedule.

I would like to especially recognize the kindness shown by *Professor Einstein* since the first weeks of my arrival. His perceptiveness and his interest in all of us were really amazing...

I am going to miss my daily hug from *Carolyn Jundzilo*, whose smiles, stories, and paintings lit up the daily walk up the hall. Thank you so much Carolyn for being so unbelievably special...

To *Alise Kalemkiarian* I owe, above all, the discovery of the pool. On top of that (!!!) she was always a great time during my escapades to the other side of the building... thanks Alise for taking such good care of all of us!

A special hug for *Mary Elliff*, my ultimate supporter, who really went out of her way to make us feel at home....

Yet another very heartfelt thank you to *Cynthia Stewart* and *Jessie Williamson* for taking care of all the administrative details of five years, in such a wonderfully nice way...

One final thanks to *Steven Rudolph*, amazing builder of everything, for patiently sitting with me while watching my box spin in the centrifuge...

Many many thanks to *Ana Borjas* and *Jennifer Manthos,* who added a touch of home to my early mornings and late evenings, respectively... Ana's coffee and Jenny's hugs started and ended my days on a kind, happy note.

The most gigantic thank you in the world is for *Don Schad*, the best friend one can possibly ask for... I am hereby officially opening up a spot on the tower for him. He has put up with me longer and with more tenacity than anyone else I know. As if that was not a formidable task in and by itself, without his help during the initial months of the modeling saga, **`bubbles.bas`** would have never made it to the surface....

The spotlight now sets on *Kurt Sjoblom*, whose friendship and company have been one of the greatest things of the past five years... thank you babe for.... *everything*!!!!

The warmest of hugs is for *Thomas Meyer*. To this day I miss his laughter and his presence in the office. Simply put, he is one of my all time favorite people, and his tacit support was felt all the way from vitzerland....*zank you sunshine*...

Surviving the first year of my Ph.D. and my General Exams, was in great part thanks to the care and company of *Grace Hwang,* my first friend at MIT. *Amazing Grace* will forever stick as the perfect nickname... the woman has never truly "stopped" since the first day I met her! She always managed however, to be around at the happiest and most heartfelt moments of the past five years

Ltnt. Laurent Levy, Spin Master, co-star in the soon-to-be-released **Tales from the 'Fuge**. From the Alumni pool to the temples of Nara, a little bit of a bumpy ride *Lorenzo* but gosh...so many great stories!

Jorge Gonzalez, el Rey, also known as *Papachin y su gran banda*, kept me laughing for two years and spiced up the late nights spent in the lab. *Gracias chico, la pasé delicioso*...

Guoping Zhang, my Chinese brother, residual soils guru and provider of lychee gummies, kept me company during countless nights spent at the office. *Xie, xie very much José*....

Marika Santagata-Sinfield, now mother of royalty, was simply a lot of fun to have around! I have really really missed her company...

Dinner discussions with *Salal Humair* did not only become weekly gastronomic treats, but allowed rare glimpses of reality outside the confines of MIT... I have really missed those talks...

Albert Essiam, partner in the thesis writing battle, shared with me until the last hour the agony of finishing... the last couple of months would have been even more difficult without his company.

Volker Hoffman, fantastic pen pal and virtual-he-muse, kept me entertained and distracted throughout months of lateral... propagation. *Danke sehr, Pinkerton*!

The final curtain call and the bouquet of red roses are for *Greg Da Re.* Although it may have seemed at times like the proverbial North-South divide went right through the 5-330B, the tropical people were always amazed by the northerners.... I loved almost every day spent in that office... Thank you *Jim* for keeping me sane for three years and for making me so incredibly happy this past year...

And then there is *Guga*, who for the sake of "posterity" will actually be referred to as *Maria Victoria Copello.* No one else with the exception of my family has been around me for as long as she has, and twenty six years of friendship qualifies someone for the **HONORARY RELATIVE** title... She, and of course Carlos, have been my family away from home for the past five years, and I have no way of expressing, effusively enough, how much having them around has meant. *Se les graduó la niña... por fin!*

Having come to the end of the acknowledgements, it is now time to recognize the support of my family... I cannot imagine having made it through this experience without my parents and my brother. This page is now being written because they were here with me every day, providing confidence and encouragement during the hardest of times. This degree is as much theirs as it is mine... *mushas gracias*...

A mi mami y a mi papi

Table of Contents

Page

Abstract **3**

Acknowledgements **5**

Foreword **7**

Table of Contents **9**

List of Figures **17**

List of Tables **27**

CHAPTER 1 INTRODUCTION **29**

1.1. PROBLEM STATEMENT 29

1.2. RESEARCH OBJECTIVES 30

1.3. ORGANIZATION OF THESIS 32

CHAPTER 2 BACKGROUND **35**

2.1. INTRODUCTION 35

2.2. AIR SPARGING 36

2.2.1. Overview *36*

2.2.2. System Parameters *38*

2.3. TWO-PHASE FLOW THROUGH POROUS MEDIA 40

2.3.1. General Background *40*

2.3.1.1.Interfacial tension and wettability 40

2.3.1.2.Capillary pressure 42

2.3.1.3.Pore entry pressure and residual saturation 43

2.3.1.4.Darcy's equation for multi-phase flow 45

2.3.2. Dimensionless Numbers *46*

2.3.3. Fingering *48*

2.3.3.1.Homogeneous porous media 48

2.3.3.2.Heterogeneous porous media 51

2.4. GAS-LIQUID FLOW 52

2.4.1. Unrestricted Movement of Air Bubbles in Liquids *53*

2.4.1.1.Constant pressure and constant flow rate conditions 53
2.4.1.2.The formation of bubbles 56
2.4.1.3.Bubble velocity 57
2.4.2. Restricted Movement of Air Bubbles in Liquids 61
2.4.2.1.Gas-liquid flow in vertical tubes 61
2.4.2.2.Gas-liquid flow in fluidized and packed beds 62
2.4.3. Prototype Representations of Gas-Liquid Flow in Porous Media 64
2.4.3.1.Flow through straight capillaries 65
2.4.3.2.Flow through constricted capillaries and capillaries of non-circular cross sections 67
2.4.3.3.Foams in Porous Media 68
2.5. AIR INJECTION IN SATURATED POROUS MEDIA 69
2.5.1. Driving Forces 69
2.5.1.1.Buoyancy and pressure gradients 69
2.5.1.2.Capillary pressure and hydrostatic pressure 72
2.5.2. Patterns of Air Flow 74
2.5.3. Zone of Influence 76
2.5.4. Conceptual Models of Air Flow Through Porous Media 78
2.5.5. Air Sparging Modeling 81
2.5.5.1.van Dijke et al. model (1995) - Overview and main assumptions 82
2.5.5.2.van Dijke et al. model (1995) 82
2.5.5.3.van Genuchten parameters 86
CHAPTER 3 CENTRIFUGE MODELING OF AIR SPARGING 89
3.1. INTRODUCTION 89
3.2. GEOTECHNICAL CENTRIFUGE TESTING 89
3.2.1. Overview 89
3.2.2. Scaling Laws 91
3.2.3. Variation of gradient with g-level 94
3.2.3.1.Darcy's law 95
3.2.4. Particle Size Effects 95
3.2.5. Stress Variations in Centrifuge Models 96

3.2.6. Modeling of Models *97*
3.3. CENTRIFUGE STUDY OF GOVERNING MECHANISMS 98
3.3.1. Experimental Injection Pressures *98*
3.3.2. Dimensionless Numbers *100*
CHAPTER 4 EXPERIMENTAL METHODS 103
4.1. INTRODUCTION 103
4.2. MIT GEOTECHNICAL CENTRIFUGE LABORATORY 103
4.2.1. Balanced Arm Centrifuge *103*
4.2.2. Centrifuge Controller *105*
4.2.3. Data Acquisition System *106*
4.2.4. Instrumentation *107*
4.3. EXPERIMENTAL SETUP 108
4.3.1. Sample Box *108*
4.3.1.1.Air sparging injectors 110
4.3.1.2.Wire mesh screens 111
4.3.2. Preparation of Centrifuge Experiments *112*
4.3.2.1.Setup of platform 112
4.3.2.2.Centrifuge setup 114
4.4. PROCEDURE FOR CONSTANT PRESSURE EXPERIMENTS 115
4.4.1. Experimental Setup *115*
4.4.2. Testing Procedures *116*
4.5. PROCEDURE FOR CONSTANT FLOW RATE EXPERIMENTS 117
4.5.1. Experimental Setup *117*
4.5.1.1.Tests with Pressure Volume Controller 118
4.5.1.2.Tests with flow meter 120
4.5.2. Testing Procedures *123*
4.5.2.1.Tests at 1-g 123
4.5.2.2.Tests at higher g-levels 124
CHAPTER 5 EXPERIMENTAL MATERIALS 127
5.1. INTRODUCTION 127

5.2. POROUS MEDIA 127
5.2.1. Transparent Medium *127*
5.2.2. Characterization of Porous Media *129*
5.2.2.1.Grain-size distribution 129
5.2.2.2.Hydraulic conductivity 130
5.3. PORE FLUID 130
5.4. SAMPLE PREPARATION 132
5.4.1. Samples in Immersion Liquid *133*
5.4.1.1.New samples 133
5.4.1.2.Reworked samples 137
5.4.2. Samples in Glycerol *139*
CHAPTER 6 DATA TYPES AND ANALYSIS 141
6.1. INTRODUCTION 141
6.2. DATA ANALYSIS 141
6.2.1. Video Capture Equipment *141*
6.2.2. Distortion Corrections *142*
6.3. AIR DISPLACEMENT AND VELOCITY DATA 144
6.4. QUANTIFICATION OF IMAGE DATA 147
6.4.1. Plume Outlines *147*
6.4.2. Plume Areas *150*
6.4.3. Plume Volumes *151*
6.4.4. Relative Zone of Influence *151*
CHAPTER 7 OVERVIEW OF EXPERIMENTAL RESEARCH PROGRAM 153
7.1. INTRODUCTION 153
7.2. VARIABLES CONSIDERED 153
7.2.1. Operational Parameters *154*
7.2.1.1.g-level 154
7.2.1.2.Pressure 154
7.2.1.3.Flow rate 155
7.2.1.4.Injector geometry 156

7.2.2. Porous Medium Parameters *156*
7.2.2.1.Grain-size and permeability 156
7.2.2.2.Pore fluid 157
7.3. SUMMARY OF EXPERIMENTAL PROGRAM 158
7.3.1. Free Field Experiments *158*
7.3.2. Constant Pressure Experiments *158*
7.3.3. Constant Flow Rate Experiments *161*
CHAPTER 8 EXPERIMENTAL RESULTS 165
8.1. INTRODUCTION 165
8.2. CONSTANT PRESSURE EXPERIMENTS 166
8.2.1. Free Field *166*
8.2.1.1.Flow patterns 166
8.2.1.2.Breakthrough velocities 172
8.2.2. Wire Mesh Screens *174*
8.2.3. Summary of Experimental Observations in the Free Field *176*
8.2.4. Air Injection in Porous Media *177*
8.2.4.1.Influence of g-level on air propagation 177
8.2.4.2.Influence of injector 188
8.2.4.3.Influence of porous medium 189
8.2.4.4.Breakthrough velocities 189
8.3. CONSTANT FLOW RATE EXPERIMENTS 193
8.3.1. Air Injection in Immersion Liquid *193*
8.3.1.1.Influence of injection flow rate on air propagation 193
8.3.1.2.Influence of injector type 203
8.3.1.3.Breakthrough velocities 205
8.3.1.4.Influence of g-level on air propagation 208
8.3.2. Air Injection in Glycerol *211*
8.4. SUMMARY OF PROPAGATION MECHANISMS 213
CHAPTER 9 INTERPRETATION OF EXPERIMENTAL RESULTS 217
9.1. INTRODUCTION 217

9.2. GENERAL RESULTS 217
9.2.1. Influence of Increasing g-Level *217*
9.2.2. Influence of Velocity of Propagation *219*
9.2.3. Influence of Injection Flow Rate and Injector Geometry *223*
9.2.4. Influence of Pressure Gradient *226*
9.2.5. Summary of experimental results and observations *229*
9.3. AIR PROPAGATION 232
9.3.1. Effects of g-Level on Constant Pressure Injection Experiments *232*
9.3.2. Effects of g-Level on Constant Flow Rate Injection Experiments *235*
9.3.3. Air Flow Patterns *238*
9.3.3.1.Flow regimes 238
9.3.3.2.Zones of influence 239
9.4. IMPLICATIONS TO AIR SPARGING OPERATIONS 241

CHAPTER 10 MODELING OF AIR SPARGING 243

10.1. INTRODUCTION 243
10.2. OBJECTIVE OF THE MODEL 243
10.3. PRINCIPLES OF PROPOSED MODEL 244
10.4. PROPOSED AIR SPARGING MODEL 247
10.4.1. General Equations *247*
10.4.2. Air Pressure Calculations *249*
10.4.3. Air and Water Flow *252*
10.4.4. Volume Balance *256*
10.4.5. Initial and Boundary Conditions and Input Parameters *259*
10.4.6. Modeling at High g-Levels *260*
10.5. RESULTS OF MODELING 260
10.5.1. Model Performance *261*
10.5.1.1. Injection pressure 261
10.5.1.2. Injection flow rate 263
10.5.1.3. Importance of radial boundary 264
10.5.1.4. Importance of pressure gradient 266
10.5.2. Comparison With Experimental Results *268*

10.5.3. Comparisons with van Dijke et al. (1995) Model *275*
10.5.4. Modeling of Models *278*
10.5.5. Heterogeneous Porous Media *285*

CHAPTER 11 CONCLUSIONS AND RECOMMENDATIONS 291

11.1. OVERVIEW OF RESEARCH STUDY 291
11.2. OVERVIEW OF EXPERIMENTAL RESULTS 292
11.2.1. Influence of Operational Parameters on Zone of Influence of IAS Plumes 292
11.2.1.1. g-level, buoyancy, and pressure gradients 292
11.2.1.2. Pressure 294
11.2.1.3. Flow rate 295
11.2.1.4. Injector geometry 296
11.2.2. Influence of Porous Medium Parameters on Zone of Influence of Plumes 296
11.2.2.1. Grain size, capillarity, and permeability 296
11.2.2.2. Pore fluid 297
11.2.3. Patterns of Air Flow *298*
11.3. OVERVIEW OF MODELING RESULTS 299
11.3.1. Principles of the Model *299*
11.3.2. Modeling results *300*
11.4. RECOMMENDATIONS FOR FUTURE RESEARCH 302
11.4.1. Equipment Development *302*
11.4.2. Suggestions for Further Research *303*

CHAPTER 12 REFERENCES 305

APPENDIX A DATA ACQUISITION PROGRAM 313

APPENDIX B CALIBRATION DATA 321

B.1. PRESSURE TRANSDUCERS 321
B.1.1. DI 2194 ..... *321*
B.1.2. DI 2394 ..... *322*
B.1.3. DI A500 ..... *323*
B.2. PRESSURE VOLUME CONTROLLERS 324

B.2.1.Low g-levels *324*
B.2.2 High g-levels *325*
B.3.FLOW METER 3216
APPENDIX C TESTING RECORDS 327
APPENDIX D ADDITIONAL EXPERIMENTAL RESULTS 339
APPENDIX E SUMMARY OF EXPERIMENTAL RESULTS 353
APPENDIX F AIR SPARGING PROGRAM 383
APPENDIX G MODEL EQUATIONS 399
G.1.CELL VOLUMES 399
G.2.FLOW IN THE X-DIRECTION 400
G.2.1. Area of Flow *400*
G.2.2. Width of Fluid in Cell *401*
G.3.FLOW IN THE Z-DIRECTION 402
G.3.1. Area of flow *402*
G.3.2. Height of Air in Cell *403*

List of Figures

Page

Figure 2-1 Schematic diagram of In-situ Air Sparging - Soil Vapor Extraction (IAS-SVE) setup 38

Figure 2-2 Definition of wetting based on contact angle: a) reference liquid is wetting; b) reference liquid is nonwetting (after Demond and Roberts, 1987) 41

Figure 2-3 Interface in a capillary tube and capillary pressure (after Demond and Roberts, 1987) 43

Figure 2-4 Typical capillary pressure-saturation curve illustrating hysteresis (after Bear, 1972) 44

Figure 2-5 Typical relative permeability curves (after Bear, 1972) 45

Figure 2-6 Two-phase immiscible fluid flow interface during upward flow (after Hill, 1952) 49

Figure 2-7 Variation of a) air pressure and b) flow rate with time during constant pressure and constant flow rate of injection conditions. 53

Figure 2-8 Flow through a sharp-edged orifice (after Roberson and Crowe, 1990) 55

Figure 2-9 Terminal rise velocity of air bubbles in water as a function of bubble size (after Haberman and Morton, 1956). 60

Figure 2-10 Flow patterns of gas-liquid flow in tubes (after Taitel, 1980) 62

Figure 2-11 Schematic of freely suspended drop in tube flow (after Olbricht, 1996) 65

Figure 2-12 General correlation for the rise velocity of slug flow bubbles (White and Beardmore, 1962) 66

Figure 2-13 Buoyancy forces acting on a submerged bubble: a) internal force approach; b) boundary stress approach. 70

Figure 2-14 Conceptual illustration of the differences in extent of initial air invasion 71

Figure 2-15 Relative impact of capillary pressure on air entry pressure at varying depths of injection. 73

Figure 2-16 Air flow patterns through heterogeneous porous media (after Ji et al., 1993) 76

Figure 2-17 Schematic of current models of air flow through saturated porous media: a) macroscopic channeling model with areas separated by areas of fully water saturated soil; b) continuum model with zones of uniform saturation; c) pore-scale fingering and macroscopic channeling (after Clayton, 1998). ...80

Figure 2-18 Schematic of the modeled space (after van Dijke et al., 1995) 84

Figure 2-19 Schematic of the relative significance of the van Genuchten parameters. a) variation of the α-parameter; b) variation of the m-parameter. 86

Figure 2-20 Variation in van Genuchten parameters for Sands (USDA classification) for Swedish soils compiled by Jonasson (1991). 88

Figure 3-1 Inertial stresses in centrifuge model (a) induced by rotation around fixed axis correspond to gravitational stresses in the corresponding prototype(b) (after Taylor, 1995) 90

Figure 3-2 Variation of pressure difference with elevation at increasing g-levels ($\Delta P = P_{inj} - P_{entry}$). Symbols illustrate air entry pressures at different elevations while lines represent injection pressures. 94

Figure 3-3 Stress variation with depth in centrifuge model and its corresponding prototype (after Schofield, 1980). 97

Figure 3-4 Principle of modeling of models (after Ko, 1988) 98

Figure 4-1 MIT Geotechnical centrifuge 104

Figure 4-2 Centrifuge strong box 109

Figure 4-3 Schematic of air sparging injectors: a) Multiple Port Injector (MPI); b) Single Port Injector (SPI). Injectors were 2 cm in height by 0.8 cm in diameter. 111

Figure 4-4 Wire mesh screen and Lexan rack 112

Figure 4-5 Setup of the centrifuge platform 113

Figure 4-6 Calibration of Pressure Volume Control unit 119

Figure 4-7 Setup for experiments at constant flow rate with flow meter 122

Figure 5-1 Grain size distributions of crushed glass samples (USCS) 129

Figure 5-2 Schematic of setup for sample preparation 135

Figure 6-1 *a) Illustration of "fish bowl effect" caused by wide angle camera. Distorted and undistorted grids are centered on the diamond, which indicates the point of no distortion; b) undistorted grid coordinates as a function of distorted coordinates.* 143

Figure 6-2 *Progression of air sparging front through a porous medium saturated with immersion liquid. Test shown was conducted at 1-g, under a constant flow rate q = 1.58 cm^3/s.* 146

Figure 6-3 *Vertical displacement of air front from injection point to phreatic surface as a function of time.* 147

Figure 6-4 *Air plume boundary obtained from subtraction background from image of moving air front (frame 5 – frame 1 on Figure 6.1)* 148

Figure 6-5 *Digitized boundary of the plume shown in Figure 6-4* 149

Figure 6-6 *Plume volume approximated by cylindrical surface elements (after* 150

Figure 6-7 *Schematic definition of relative zone of influence of air sparging plume (RZI)* 152

Figure 8-1 *Free field injection experiments in immersion liquid using injector MPI #2, at increasing g-levels: a) 10-g; b) 20-g; c) 30-g; d) 50-g; e) 70-g; and f) 90-g.* 167

Figure 8-2 *Free field injection experiments in immersion liquid using injector SPI #2, at increasing g-levels: a) 10-g; b) 20-g; c) 30-g; d) 50-g; e) 70-g; and f) 90-g.* 168

Figure 8-3 *Free field injection experiments in glycerol using injector MPI #2, at increasing g-levels: a) 10-g; b) 20-g; c) 30-g; d) 50-g; e) 70-g; and f) 90-g.* 169

Figure 8-4 *Free field injection experiments in glycerol using injector SPI #2, at increasing g-levels: a) 10-g; b) 20-g; c) 30-g; d) 50-g; e) 70-g; and f) 90-g.* 170

Figure 8-5 *Free field velocities of air under constant pressure injection, at increasing g-level in: a) immersion liquid; and b) glycerol.* 173

Figure 8-6 *Deformation of air bubble patterns in glycerol at varying g-levels due to flow though steel mesh screens - Injector SPI #1: a) 10-g; b) 20-g; c) 10-g; d) 20-g; e) 50-g.* 175

Figure 8-7 Injector MPI #1 – Propagation of injected air at 1-g through porous media saturated with immersion liquid. 178

Figure 8-8 Injector MPI #1 – Propagation of injected air at 10-g through porous media saturated with immersion liquid. 179

Figure 8-9 Injector MPI #1 – Propagation of injected air at 40-g through porous media saturated with immersion liquid. 180

Figure 8-10 Steady-state air plumes obtained at increasing g-levels following injection of air into porous media saturated with immersion liquid - Injector MPI #1: a) 1-g; b) 3-g; c) 10-g; d) 30-g; e) 40-g; f) 60-g. 181

Figure 8-11 Injector MPI #1 – Propagation of injected air at 5-g through porous media saturated with glycerol. 184

Figure 8-12 Injector MPI #1 – Propagation of injected air at 10-g through porous media saturated with glycerol 185

Figure 8-13 Injector MPI #1 – Propagation of injected air at 30-g through porous media saturated with glycerol 186

Figure 8-14 Steady-state air plumes obtained at increasing g-levels following injection of air into porous media saturated with glycerol - Injector MPI #1: a) 5-g; b) 10-g; c) 20-g; d) 30-g; e) 40-g; f) 50-g. 187

Figure 8-15 Displacement of the leading front of air sparging plumes versus time of entry, prior to breakthrough. Experiments conducted in crushed glass (SP) saturated with immersion liquid. Injections conducted under constant pressure conditions, under the indicated acceleration field. Injector type is included in each figure. 190

Figure 8-16 Displacement of the leading front of air sparging plumes versus time of entry, prior to breakthrough, through porous medium saturated with immersion liquid. Experiments conducted at constant pressure injection conditions under acceleration fields higher than 50-g. 192

Figure 8-17 Sequence of air propagation through SP sample saturated with immersion liquid, at 1-g. Injection conducted under constant flow rate conditions, with $q = 0.68\ cm^3/s$, using injector MPI #1. 194

Figure 8-18 Constant flow rate injection of air into porous medium saturated with immersion liquid. Test conducted at 1-g. Injector MPI #1: a) $0.26\ cm^3/s$; b) $0.68\ cm^3/s$; c) $1.15\ cm^3/s$; d) $1.58\ cm^3/s$; e) $2.26\ cm^3/s$; f) $2.66\ cm^3/s$. 196

Figure 8-19 Constant flow rate injection of air into porous medium saturated with immersion liquid. q = 10.83 cm^3/s - Test conducted at 1-g. Injector MPI #3. 198

Figure 8-20 Constant flow rate injection of air into porous medium saturated with immersion liquid. q = 15.14 cm^3/s - Test conducted at 1-g. Injector MPI #3. 199

Figure 8-21 Constant flow rate injection of air into porous medium saturated with immersion liquid. q = 19.44 cm^3/s - Test conducted at 1-g. Injector MPI #3. 201

Figure 8-22 Air plumes obtained at 1-g during injection at increasing, constant flow rates into porous media saturated with immersion liquid - Injector MPI #2: a) box prior to injection; b) q = 2.22 cm^3/s; c) q = 6.53 cm^3/s; d) q = 10.83 cm^3/s; e) q = 15.14 cm^3/s; f) q = 19.44 cm^3/s. 202

Figure 8-23 Displacement of the leading front of air sparging plumes versus time of entry, prior to breakthrough, through crushed glass saturated with immersion liquid. Injections conducted under constant rate of flow conditions, at 1-g, at the flow rates indicated. Full symbols are used to designate experiments conducted using multiple port injectors while open symbols indicate single port injectors. Some duplicate tests are included. 207

Figure 8-24 Steady state air plumes obtained at increasing g-levels following injection of air at constant flow rate into porous media saturated with immersion liquid – Injection flow rate q = 0.66 cm^3/s - Injector MPI #1: a) 1-g; b) 3-g; c) 6-g; d) 9-g; e) 12-g; f) 15-g. 209

Figure 8-25 Constant flow rate injection of air into porous medium saturated with glycerol. Test conducted at 1-g. Injector MPI #1: a) 0.26 cm^3/s; b) 0.68 cm^3/s; c) 1.15 cm^3/s; d) 1.58 cm^3/s; e) 2.26 cm^3/s; f) 2.66 cm^3/s. 212

Figure 8-26 Typical fingering pattern developing during propagation of air injected through saturated porous media. 214

Figure 8-27 Typical "fingering front" propagation, representing one type of uniform front propagation behavior for air injected in saturated porous media. 215

Figure 8-28 Uniform front propagation under increased acceleration levels 215

Figure 8-29 Fracturing as a result of injection of air through saturated porous media 216

Figure 9-1 Relationship between Bond and Capillary numbers for air sparging experiments conducted under Constant Pressure (CP) and Constant Flow

Rate (CFR) conditions. Results include tests done on samples saturated with Immersion Liquid (IL) and glycerol. 219

Figure 9-2 Influence of Capillary number on Relative Zone of Influence of air sparging plumes: a) under constant pressure injection; b) under constant flow rate injection. 221

Figure 9-3 Experimental results at 1-g plotted on phase diagram for immiscible displacements proposed by Lenormand et al. (1988). 223

Figure 9-4 Relative zone of influence as a function of injection flow rate: a) RZI at breakthrough; and b) RZI at steady state. Tests conducted at 1-g, under constant flow rate conditions, on samples of SP. 225

Figure 9-5 Relative Zone of Influence as function of injection pressure gradient; a) under constant pressure injection; and b) under constant flow rate injection. Pressure gradients calculated at the injection point. 228

Figure 9-6 Relative Zone of Influence as a function of the ratio between Bond and Capillary numbers. Includes results from all experiments successfully completed in this investigation. 230

Figure 9-7 Regions of air flow and air saturation index 231

Figure 10-1 Axisymmetric mesh for proposed air sparging model 247

Figure 10-2 Water outflows from mesh element 248

Figure 10-3 Iterative air pressure calculation procedure. 250

Figure 10-4 Volumes of pore fluid flow calculated for every element of the mesh 253

Figure 10-5 Calculation of gradients and volumes of flow 255

Figure 10-6 Schematic of volumes in axisymmetric mesh 256

Figure 10-7 Boundary conditions of finite difference model 259

Figure 10-8 Air propagation characteristics predicted under varying initial injection pressures. Plumes were obtained under constant pressure injection conditions. 262

Figure 10-9 Effect of increasing injection flow rate on the predicted shapes of air sparging plumes. 263

Figure 10-10 Influence of location of horizontal flow boundary on the shape of predicted air sparging plumes 265

Figure 10-11 Air and pore fluid pressure profile with elevation, under 1-g, 10-g and 20-g accelerations. Simulations conducted under constant flow rate of injection, with $q = 5x10^{-6}$ m^3/s *and* $k = 1x10^{-8}$ m^2. *Elevation of the air phase refers to the position of the leading edge of the plume as air advances upward.* 266

Figure 10-12 Experimental and modeling results of air sparging experiments conducted under constant flow rate of injection conditions at 1-g: a) $q = 0.26$ cm^3/s; *b)* $q = 2.7$ cm^3/s; *c) 28* cm^3/s. 269

Figure 10-13 Experimental and modeling results of air sparging experiments conducted under constant flow rate of injection conditions at varying g-levels: a) 1-g; b) 9-g; c) 30-g. Injection flow rate was maintained at a value of $q = 0.66$ cm^3/s. *Symbols show the outline of the experimental plumes while the solid lines plot the boundary of the modeled plumes.* 271

Figure 10-14 Relative zone of influence of air sparging plumes at breakthrough as function of ratio of Bond over Capillary numbers: a) observed air flow velocities; and b) estimated (theoretical) air flow velocities. 273

Figure 10-15 Illustration of inadequacy of Jonasson (1991) method to determine van Genuchten parameters from grain-size distribution curve. 276

Figure 10-16 Fitting of van Dijke et al. (1995) model to experimental air sparging plumes at q = 28 cm3/s. 277

Figure 10-17 Model simulations of air sparging plumes at: a) 1-g (prototype); b) 5-g; c) 10-g; and d) 20-g. The injection point is located at (0,0). 280

Figure 10-18 Results of computer simulations showing the influence of injection flow rate q, permeability k, and depth of injection, H on the volume air sparging plumes at breakthrough, V_p. 284

Figure 10-19 Variations of air flow patterns due to soil heterogeneity. a) layer of fine material (K2) in between two layers of coarse material (K1), such that K1/K2 = 100; b) layer of coarse material (K2) in between two layers of finer material (K1), such that K2/K1 = 100. 287

Figure 10-20 Air propagation through layered hydraulic conductivity sample. 289

Figure D-1 Air plumes obtained at increasing g-levels following injection of air into porous media saturated with immersion liquid - Injector MPI #2: a) 20-g; b) 30-g; c) 40-g; d) 60-g; e) 80-g; f) 100-g. 340

Figure D-2 Air plumes obtained at increasing g-levels following injection of air into porous media saturated with immersion liquid - Injector MPI #3: a) 20-g; b) 30-g; c) 40-g; d) 60-g; e) 80-g; f) 100-g. 341

Figure D-3 Air plumes obtained at increasing g-levels following injection of air into porous media saturated with immersion liquid - Injector SPI #1: a) 20-g; b) 30-g; c) 40-g; d) 60-g; e) 80-g; f) 100-g. 342

Figure D-4 Air plumes obtained at increasing g-levels following injection of air into porous media saturated with immersion liquid - Injector SPI #2: a) 10-g; b) 20-g; c) 30-g; d) 60-g; e) 80-g; f) 100-g. 343

Figure D-5 Air plumes obtained at increasing g-levels following injection of air into porous media saturated with immersion liquid - Injector SPI #3: a) 10-g; b) 20-g; c) 30-g; d) 60-g; e) 80-g; f) 100-g. 344

Figure D-6 Constant flow rate injection of air into porous medium saturated with immersion liquid. Test conducted at 1-g. Injector MPI #2: a) 0.26 cm^3/s; b) 0.68 cm^3/s; c) 1.15 cm^3/s; d) 1.58 cm^3/s; e) 2.26 cm^3/s; f) 2.66 cm^3/s. 345

Figure D-7 Constant flow rate injection of air into porous medium saturated with immersion liquid. Test conducted at 1-g. Injector MPI #3: a) 0.26 cm^3/s; b) 0.68 cm^3/s; c) 1.15 cm^3/s; d) 1.58 cm^3/s; e) 2.26 cm^3/s. 346

Figure D-8 Constant flow rate injection of air into porous medium saturated with immersion liquid. Test conducted at 1-g. Injector SPI #1: a) 0.26 cm^3/s; b) 0.68 cm^3/s; c) 1.15 cm^3/s; d) 1.58 cm^3/s; e) 2.26 cm^3/s; f) 2.66 cm^3/s. 347

Figure D-9 Constant flow rate injection of air into porous medium saturated with immersion liquid. Test conducted at 1-g. Injector SPI #2: a) 0.26 cm^3/s; b) 0.68 cm^3/s; c) 1.15 cm^3/s; d) 1.58 cm^3/s; e) 2.26 cm^3/s; f) 2.66 cm^3/s. 348

Figure D-10 Constant flow rate injection of air into porous medium saturated with immersion liquid. Test conducted at 1-g. Injector SPI #3: a) 0.26 cm^3/s; b) 0.68 cm^3/s; c) 1.15 cm^3/s; d) 1.58 cm^3/s; e) 2.26 cm^3/s; f) 2.66 cm^3/s. 349

Figure D-11 Air plumes obtained at increasing g-levels following injection of air at 350

Figure D-12 ..... Air plumes obtained at 1-g during injection at increasing, constant flow 351

Figure G-1 Schematic of one row of elements used in calculations of volume of voids available for flow 399

Figure G-2 Schematic of cross sectional area of pore fluid outflow in the x-direction . 400

Figure G-3 Volume of air propagating into adjacent cells 401

Figure G-4 Schematic of cross sectional area of pore fluid outflow in the z-direction 403

List of Tables

Page

Table 3-1 *Centrifuge scaling relationships* 91

Table 4-1 *Characteristics of Data Instruments pressure transducers* 108

Table 4-2 *Characteristics of air sparging injectors* 111

Table 5-1 *Characteristics of tested granular materials* 130

Table 5-2 *Hydraulic conductivity of tested materials* 130

Table 5-3 *Optical properties of glass and pore fluids (measured by R.P. Cargille Laboratories Inc.)* 132

Table 5-4 *Physical properties of pore fluids tested* 132

Table 7-1 *Summary of constant pressure injection experiments* 158

Table 7-2 *Summary of experiments conducted under constant rates of injection* 161

Table 7-3 *Summary of experiments conducted under gradually increasing constant rates of injection* 163

Table 8-1 *Summary of experimental observations* 213

Table 10-1 *Input parameters for finite difference air sparging model* 260

Table 10-2 *Scaling laws used in modeling of models* 279

Table 10-3 *Summary of input and output parameters from modeling of models simulations. Parameters corresponding to data presented in Figure 10-17 are highlighted.* 281

Table C-1 *Summary of Free field experiments (CP: Constant Pressure injection test; CFR: Constant Flow Rate injection test; FF: Free Field experiment; IL: Immersion Liquid; Gly.: Glycerol)* 328

Table C-2 *Constant pressure injection experiments (CP: Constant Pressure injection test; IL: Immersion Liquid; Gly.: Glycerol; Wat.: Water; MS: Medium Sand; MSF: Medium Sand with Fines)* 329

Table C-3 *Constant flow rate injection experiments (CFR: Constant Flow Rate injection test; IL: Immersion Liquid; Gly.: Glycerol; MS: Medium Sand; GB: Glass Beads)* 334

Table E-1 *Summary of characteristics of air sparging experiments conducted under a constant injection pressure* 355

Table E-2 *Summary of characteristics of air sparging experiments conducted under constant flow rates of injection* 373

CHAPTER 1

INTRODUCTION

1.1.PROBLEM STATEMENT

Over the past two decades, in-situ air sparging (IAS) has been used as a successful technique to remediate contaminated groundwater and saturated soil deposits (Lundegard and Anderson, 1993; Ahlfeld *et al.*, 1994; Brown, 1995). Air sparging consists of injecting pressurized gas into the ground, toward the aim of stripping volatile contaminants present below the ground water table as the gas flows upward through the soil column. The contaminated air is subsequently collected and treated at the ground surface, where disposal procedures are ultimately followed. When the characteristics of the contaminants and those of the subsurface deposits are favorable, IAS has been proven to be an effective, relatively economic, and fast groundwater cleanup technology (Brown, 1995; Reddy *et al.*, 1995).

If the volatility of the contaminants is not a limiting factor (*i.e.* the contaminants have high vapor pressures and high Henry's law constants), the effectiveness of an air sparging system is a function of the extent of the contact between the injected air and the contaminated deposit (Baehr *et al.*, 1989). Maximizing the volume of saturated soil that is reached by the injected air reduces volatilization time and therefore increases system efficiency (Baker and Benson, 1996).

In the last decade, laboratory and field studies of air sparging have focused on determining the variables that govern the flow of air through saturated soil deposits (Bohler *et al.*, 1990; Marley *et al.*, 1992; Reddy *et al.*, 1995). Visualization studies have been conducted, for example, that have described changes in patterns of air flow depending on soil properties and injection characteristics. (Ji *et al.*, 1993; Brooks *et al.*, 1999; Reddy and Adams, 2001). As a result of these studies, it is now well known that subsurface heterogeneity is the most critical factor in the development of air sparging plumes.

While these studies have provided useful qualitative information on the mechanisms of air propagation, they have failed to present recommendations that could be used to improve the efficiency of an air sparging system at a site of given characteristics. The relationship between operation characteristics, such as injection flow rate and pressure, and site characteristics, such as soil type and hydraulic conductivity is not well understood, and therefore no guidelines are available to optimize the operation of an air sparging system. The design and use of air sparging as a remediation technology is therefore restricted to experienced operators who, following pilot studies, determine the optimal operative characteristics of each specific system. It is clear that providing guidelines to increase system efficiency would greatly improve the usefulness of air sparging, converting it into a more widely applicable remediation technology.

1.2.RESEARCH OBJECTIVES

The specific research objectives of this study can be summarized as follows:

- to characterize the fundamental mechanisms that govern air flow through saturated porous media

- to quantify the parameters that control air propagation through saturated soils during air sparing

- to develop a simple model that predicts the extent of propagation of air during air sparging

- to provide recommendations for the design of efficient air sparging systems. Recommendations will focus on maximizing the zone of influence of IAS given a set of initial site and operational characteristics.

In order to meet these objectives, a research study was undertaken that aimed at identifying, and later understanding, the fundamental mechanisms governing the flow of injected air though saturated porous media.

The research study consisted of two separate parts, namely an extensive series of laboratory experiments and a computer modeling study. The experimental part of the investigation made use of two tools that made it possible to explore the behavior of air

injected into a porous medium under realistic field conditions that have, to date, been impossible to reproduce in the laboratory. The first of these tools was a geotechnical centrifuge. Through use of the geotechnical centrifuge, experiments were conducted under a wide range of acceleration fields and thus a large range of air injection pressures. The possibility of studying the behavior of air at increasingly high injection pressures, without compromising the stability of the soil specimen tested, was key to understanding specific air flow mechanisms. The second experimental tool employed was a transparent, saturated porous medium, which served as model soil, facilitating the observation of the patterns of air flow through the medium under the varying injection conditions.

The computer program used in the modeling study was generated during the course of this investigation, based on the proposed mechanisms of air flow put forth during the experimental phase of the study.

An important part of the research study stemmed from the basic mathematical definition of the minimum injection pressure for a given system. A pressure of injection can be calculated through a simple equation that adds the component of the hydrostatic head above the injection point to the component of capillary resistance. From the beginning of this study, one of the most fundamental questions concerned how the buoyancy forces and the capillary forces, as stated in the minimum pressure relationship, related to each other, and to what extent this relationship determined the characteristics of flow. It becomes evident, when looking at the system equation for air injection through porous media, that the magnitude of the two terms is different. Even in bench scale systems of very limited dimensions, the buoyancy term is significantly greater than the capillary term. The buoyancy term has, of course, no dependence on the characteristics of the medium, while the capillary term is solely dictated by these characteristics. The question then becomes that of evaluating exactly what is the effect of soil characteristics on the behavior of the injected air.

It is also clear when considering the equations of flow, that the movement of injected air through a porous medium saturated with a typical pore fluid, is inherently unstable. The effect of these microscopic instabilities on the behavior of the macroscopic flow as a whole was a question addressed during this investigation. Specifically, the issue of how relevant the instabilities are and the extent to which they should be

considered when designing an air sparging system was considered in the study of air flow characteristics.

Moreover, one of the biggest uncertainties that existed at the onset of the research concerned the identification and characterization of the patterns of air flow. There is still a certain degree of doubt over the types of flow regimes that develop as air flows through a porous medium. Specifically, whether bubbly, fingering, channeling, or uniform propagation conditions dominate. Previous experimental work has pointed out the fact that different flow regimes are observed depending on the type of soil used in the experiments. This investigation also aimed at finding out whether the differences in flow patterns are strictly related to the type of soil, or if the inter-relation between buoyant and capillary forces has an effect on the final characteristics of flow.

Having completed the experimental part of the investigation and having provided answers to the questions formulated above, the following challenge was that of predicting the size of the final air sparging plumes. Based on observations gathered during the experimental phase, a computer program was written that predicts the geometric characteristics of air sparging plumes at steady state. The program is based on a set of simplifying assumptions concerning the drivers of air flow through the saturated porous medium. These assumptions were based on observed phenomena, and ultimately reduced a quite complex multi-phase flow scenario to a simplified conservation of volume problem. The program provides a first estimate of the extent of the air sparging plume forming in a given soil deposit under a specified set of operating conditions. A minimum number of soil input parameters are required to provide the estimate of the final plume, all of which are routinely measured as part of subsoil explorations. The program was finally used to predict the impact of varying soil and injection characteristics on the final shapes of air sparging plumes.

1.3.ORGANIZATION OF THESIS

This thesis is divided into twelve separate chapters, which will be briefly summarized in this section.

Chapter 2 provides an overview of existing theoretical background. The information included in this chapter spans several fields of research, summarizing data from various disciplines concerning air-liquid flow. The chapter contains brief coverage of the concepts of multiphase flow through porous media and of gas-liquid flow, together with a review of the current state of knowledge in air sparging research.

Chapter 3 is a second, short, background chapter, that focuses specifically on centrifuge modeling. The principles of centrifuge research are discussed, covering the methods of interpretation of experimental data, and their specific applicability to air sparging research.

Chapter 4 presents a description of the experimental procedures used during laboratory air sparging testing. This includes procedures for sample preparation and for centrifuge operation. Experiments were conducted under constant pressure and constant flow rate injection conditions, and this section describes, in detail, the different procedures used during the two separate type of experiments.

Chapter 5 provides specifications concerning all the materials used in the experimental phase of the study, including grain size distributions of the porous materials used, and the chemical characteristics of the pore fluids employed.

Chapter 6 explicitly presents a description of the various forms in which data were collected during the experiments. The large majority of data gathered during the investigation was in the form of videotapes of the air sparging experiments. These images were captured, digitized, processed, and finally summarized before they were presented in their final form in the chapter covering experimental results. A detailed description of the data analysis is presented in this chapter, with the objective of providing a baseline for comparison of potential future results.

Chapter 7 summarizes the experimental program followed and outlines the variables investigated in the course of testing.

Chapter 8 presents results from all the experiments conducted. The chapter is divided into two major sections, the first one dealing with experiments conducted under constant pressure injection conditions. The second section focuses on results from experiments conducted under constant flow rate of injection conditions. The chapter

ends with a summary of observed mechanisms of air propagation through saturated porous media.

Chapter 9 consists of a discussion of the experimental results gathered during this study. Image data are converted into numerical parameters with which a more quantitative analysis of the mechanisms controlling air propagation through porous media is conducted. A conceptual model of air propagation is presented at the end of the chapter.

Based on results presented on Chapters 8 and 9, Chapter 10 introduces the computer program developed during the course of this investigation. A comparison of currently available models of air sparging opens the chapter. The central algorithm is then described in detail, followed by results of computer simulations. Simulations were done which verified results from some of the experiments conducted, and which reproduced results previously generated by other investigators using published models of air sparging. A discussion of the results presented is also included in this chapter.

Chapter 11 finally presents a summary of the conclusions generated during this investigation, and includes a list of recommendations for future research.

Chapter 12 closes the thesis including a list of all the references used throughout this document.

A series of appendices are also included for further clarification and completion of information presented in the body of the thesis. These appendices consist of Appendix A, which contains a printout of the data acquisition program used in the collection of experimental results. Appendix B contains pertinent information on calibration of instruments used in the laboratory. Appendix C provides summary tables of all experiments conducted during the testing phase of this investigation, and indicates the video tape number where a recording of the test can be located. Appendix D contains supplementary images collected during air sparging experiments that were not included in Chapter 8. Appendix E includes summary tables summarizing detailed characteristics of all the experiments conducted. Appendix F includes a copy of the air sparging program developed during this investigation, and finally Appendix G presents the derivation of some of the equations used in the model.

CHAPTER 2

BACKGROUND

2.1.INTRODUCTION

This chapter presents an overview of topics which are relevant to the study of air flow through porous media. Given the variety of topics summarized, the review is by no means complete. The amount of published research in any of the fields cited is very extensive. Thus, the intent of this overview is solely to bring attention to the various fields in which the topic of air flow has been investigated, and to present a number of key concepts and results that can be used in the interpretation of data from air sparging experiments.

The chapter is divided in four main sections. The first part, section 2.2, gives an overview of air sparging, including the basic principles and the controlling operational parameters. Section 2.3 provides a brief review of the basic concepts of multiphase flow though porous media, including fundamental principles and definitions. Within the context of two-phase flow, the concepts presented in this thesis are well known to Civil and Environmental Engineers, and a more extensive coverage of the topic was not believed necessary. Section 2.4 on the contrary, presents less familiar concepts and focuses on gas-liquid flow, primarily in pure liquids. The purpose of this section was to introduce the reader to the mechanisms controlling the behavior of air bubbles in liquids, from their formation and detachment, to their ascent, and to the factors affecting their rise velocity. This section also includes a discussion on restricted gas-liquid flow, namely flow through various models of porous media. Lastly, section 2.5 centers, once again, on air sparging, focusing more specifically on the flow characteristics of the injected air, as they have been documented in the literature. This last section describes the patterns of air flow that have been observed both in laboratory experiments and in field tests, together with the way in which zones of influence of air sparging wells are currently being estimated. This section then presents a review of the conceptual models that have been adopted by researchers, to date, when modeling air sparging. Finally, a more detailed

overview of the current models of air sparging is introduced, including a detailed summary of the most widely used analytical solution for predicting the zone of influence of an air sparging well.

2.2.AIR SPARGING

2.2.1. Overview

Organic chemicals are regularly introduced into the subsurface in various ways, such as leaking underground storage tanks and waste disposal facilities, mismanagement of industrial solvents, accidental surface spills, pipelines, and land application of wastes and pesticides. Because of the limited solubility and volatility of these substances under environmental conditions, organic contaminants commonly penetrate the ground surface as a liquid phase, immiscible with both air and water. A fraction of the contaminant is transported by the groundwater, creating contaminant plumes that rapidly migrate both vertically and horizontally. However, substantial portions of the contaminant source remain trapped in the soil by capillary forces, both above and below the water table depending on the physical properties of the contaminants (Baehr *et al.*, 1989).

Recovery of underground organic contaminants has been a source of study for over two decades, and a large number of in-situ technologies have been developed to remediate contaminated soils. It is clear that the characteristics of a given soil deposit (*i.e.* degree of heterogeneity, hydraulic conductivity, adsorption characteristics) as well as those of the contaminants (*i.e.* solubility, volatility), and of their distribution, ultimately determines the effectiveness of a given remediation scheme. Many remediation technologies have been used to treat contaminated sites, and abundant case studies can be found in the literature documenting successful treatments. The most commonly employed in-situ remediation techniques include: 1) *pump-and-treat systems*, that involve pumping of large volumes of groundwater, which have been used extensively in spite of their well known limitations. In fact, less than five percent of a hydrocarbon spill typically enters the dissolved phase, and therefore the concentrations that can be retrieved by a pumping technique are very low (Brown, 1995); 2) *bioremediation techniques*, which, while effective in treating hydrocarbons, are limited by several biological

parameters and require thorough mixing between the contaminated groundwater and the microorganisms injected into the subsurface (Reddy *et al.*, 1995); and 3) *in-situ chemical treatment or in-situ flushing,* which requires injection of chemicals into the subsurface in order to modify the properties of the existing contaminants, with the purpose of enhancing chemical removal from the ground. The delivery of the injected chemicals to the location of the contaminants poses significant practical difficulties (Reddy *et al.*, 1995)

It has been noted that the choice of a remediation technology strongly depends on the chemicals present in the ground. A group of organic substances of environmental interest that was singled out for a specific type of treatment due to its characteristic properties is the group of Volatile Organic Compounds (VOCs). These compounds have significant vapor concentrations relative to their aqueous solubilities. It is therefore reasonable to expect that VOCs would be recovered more effectively by enhancing air-phase transport rather than water-phase transport (Baehr *et al.*, 1989). This was in fact, the principle behind the development of in-situ air sparging.

In-situ air sparging (IAS) is a remediation technology which consists of injecting pressurized air into the saturated subsurface, with the objective of removing the contaminants present below ground. Air flows through the saturated soil deposit displacing the existing pore fluid and creating a transient state in which the pore spaces are filled with air. The contaminants trapped in the soil matrix volatilize when exposed to the injected air and can be subsequently transported out of the saturated zone by the advective air stream. The contaminants are then captured in the vadose zone and transported to the ground surface for final treatment. The use of IAS in conjunction with soil vapor extraction systems (SVE) has been proven an efficient, fast, and relatively economical procedure for the cleanup of saturated soil deposits, contaminated with VOCs (Leonard and Brown, 1992). Figure 2-1 presents a schematic diagram of an IAS-SVE system. Screened injection wells are located within the saturated zone, preferably to depths below the zone of contamination. Pressurized air is injected through these wells, under monitored flow rates and pressures, such that the zones of influence of the wells cover the entire area of contaminated soil. Air carrying volatilized contaminants flows upward and is subsequently captured in the unsaturated zone by vapor extraction wells,

which bring the contaminated air to the ground surface for final treatment. Air sparging has been extensively used in Germany since 1985 (Hiller and Gudemann, 1988) and was introduced in the United States in 1990 (Brown, 1995).

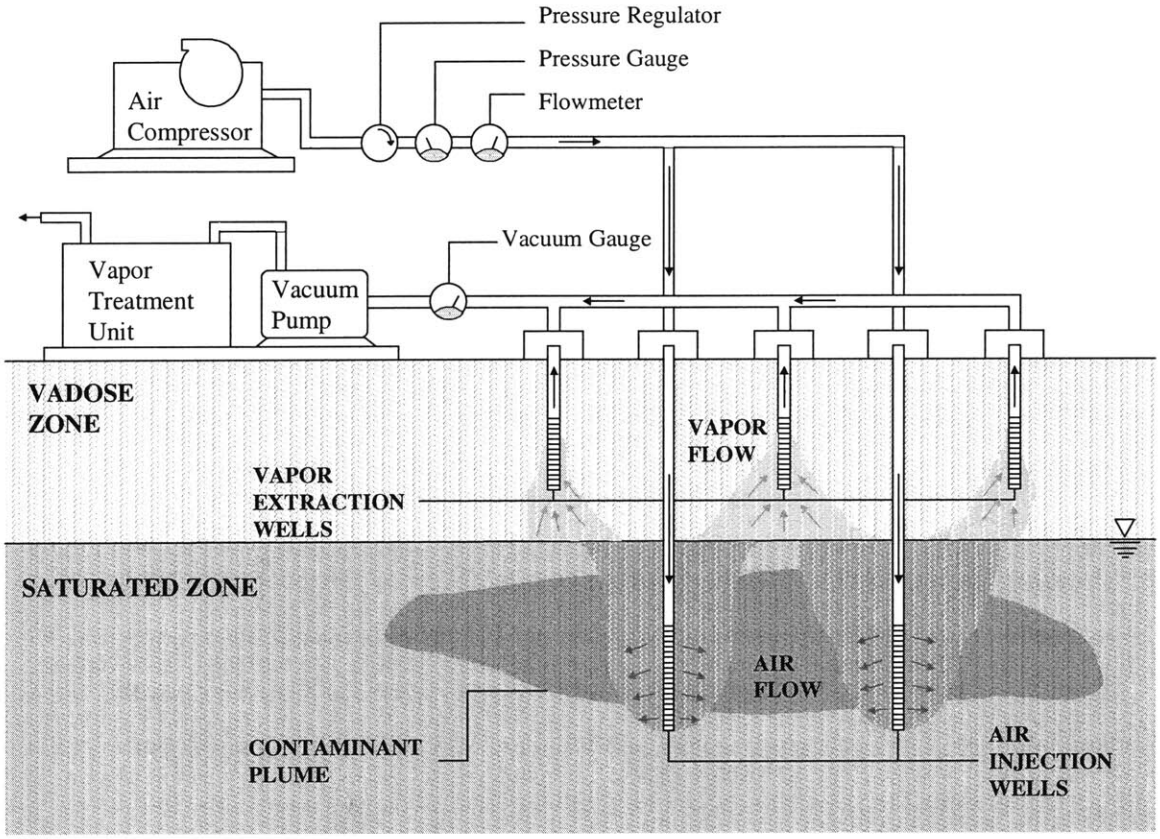

Figure 2-1 *Schematic diagram of In-situ Air Sparging - Soil Vapor Extraction (IAS-SVE) setup*

2.2.2. System Parameters

Flow of injected air through saturated soils only occurs when the air entry pressure of the porous medium at the injection point is exceeded. The minimum injection pressure needs to be sufficiently high to overcome the sum of the hydrostatic pressure, P_{hyd}, from the column of standing water located above the injection point and of the capillary pressure, P_{capil}, arising from the presence of the soil. The minimum injection pressure, $(P_{inj})_{min}$, is given by:

$$(P_{inj})_{min} = P_{hyd} + P_{capil} = \rho_{pf} * g * h_{wt} + \frac{4 * \sigma_{g/pf} * \cos\theta}{D} \qquad \text{Equation 2-1}$$

in which ρ_{pf} is the density of the pore fluid, h_{wt} is the height of the water table above the sparge point, $\sigma_{g/pf}$ is the interfacial tension between the gas phase and the pore fluid, θ is the contact angle, and D is the average pore size diameter.

In addition, air injection pressures must not exceed the in-situ effective stress of the soil σ', in order to avoid unwanted soil displacements at the sparge point (Widjaja *et al.*, 1984). For a granular material with no tensile strength under Rankine soil conditions, the upper bound to the sparging pressure is given by:

$$(P_{inj})_{\max} = \min(\sigma_{vertical}, \sigma_{horizontal})$$

$$\sigma'_{vertical} = \left(\rho_{sat} * h_s - \rho_{pf} * h_{wt}\right) * g \qquad \text{and} \qquad \text{Equation 2-2}$$

$$\sigma'_{horizontal} = K_0 * \sigma'_{vertical}$$

where ρ_{sat} is the saturated density of the soil and h_s is the height of the soil deposit above the sparge point. The coefficient of earth pressure at rest, K_0, can be estimated from the relationship $K_0 = 1 - \sin\phi'$ (Lambe and Whitman, 1969), where ϕ' is the angle of internal friction of the soil, which was an estimated 32° for the experiments reported here.

Once the static equilibrium condition has been overcome at the injection point, air invasion initiates, and water is displaced from the pore spaces by the pressurized air. A two-phase flow condition initiates through the medium, the characteristics of which were the focus of this research study.

The following section addresses a few issues related to multiphase flow through porous media. The section aims only at defining some of the terminology and at

highlighting a few aspects of *immiscible* flow through porous media, which will become relevant in following discussions concerning air sparging.

2.3.TWO-PHASE FLOW THROUGH POROUS MEDIA

2.3.1. General Background

Immiscible displacement of one fluid by another in a porous medium involves the movement of a fluid-fluid interface through the pore spaces of the medium. Whether the interface meets the pore wall such that the displacing fluid *wets* the solid, or whether the interface remains within the fluid leaving a film of displaced fluid on the walls of the medium, depends on interfacial tension relationships and on the hydrodynamic forces generated by the bulk flow (Wooding and Morel-Seytoux, 1976). These factors, and the resulting characteristics of the immiscible displacement, will be briefly summarized in the following sections.

2.3.1.1.Interfacial tension and wettability

When two immiscible fluids are in contact with each other at an interface, an interfacial energy arises from the difference between the inward attraction between the molecules in the interior of each phase and those at the contact surface (Bear, 1972). The *interfacial tension* between fluids i and j, noted σ_{ij}, is a constant for a given pair of fluids, and is defined as the amount of work necessary to separate a unit area of substance i from substance j (Bear, 1972).

When the interface between two immiscible fluids comes in contact with a solid surface, it does so at an angle with the surface. The *contact angle*, θ, is a measure of the *wettability* or the affinity of a given liquid for a given solid surface (Wooding and Morel-Seytoux, 1976). If a droplet is formed on a solid surface in the presence of a second liquid, then the angle formed by a tangent to that droplet passing through the point if the three-phase contact is referred to as the *contact angle* θ (Demond and Roberts, 1987). Figure 2-2 illustrates the definition of contact angle. If the contact angle through the reference liquid (*i.e.* the droplet liquid) is lower than 90° then the reference liquid

preferentially *wets* the solid. If conversely, θ is greater than 90° then the other liquid wets the solid (Demond and Roberts, 1987).

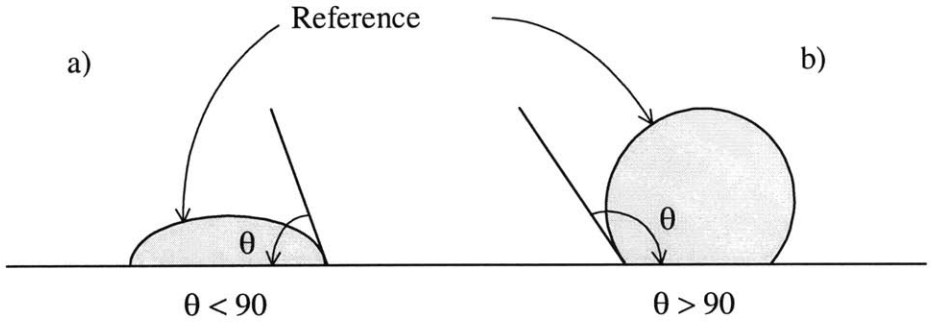

Figure 2-2 *Definition of wetting based on contact angle: a) reference liquid is wetting; b) reference liquid is nonwetting (after Demond and Roberts, 1987)*

Most descriptions of contact angle address situations in which the interface is static. The case of moving contact lines is significantly more complex, and there is a debate in the literature whether the definition of a dynamic contact angle is required. This angle would be affected among other parameters by the velocity of motion of the interface (Wooding and Morel-Seytoux, 1976; Adler and Brenner, 1988).

The subtle differences between static and dynamic contact angles are not so critical in the case of air sparging given the characteristics of the interface. In fact, if a three-phase interface consists of a liquid, a gas, and a solid, as is the case during air sparging, the liquid preferentially wets the solid surface. Wooding and Morel-Seytoux (1976) refer to various studies on liquid-gas displacement, and state that in such cases it is well established that a thin film of adsorbed liquid molecules separates the solid surface from the gas. Adsorption of liquid molecules from the vapor phase, or surface diffusion ahead of the contact line, builds up a film over which the bulk liquid spreads. Unless extraordinary measures are taken to ensure that solid surfaces are dry, the liquid phase is always the wetting fluid (Wooding and Morel-Seytoux, 1976).

2.3.1.2.Capillary pressure

When two immiscible fluids are in contact within the pores of a porous medium, a discontinuity in pressures exists across their interface. This pressure difference is referred to as the *capillary pressure*, P_{cap}, the magnitude of which depends on the curvature of the interface inside the void space (Bear, 1972). An expression for the capillary pressure is given by Equation 2-3 as:

$$P_{cap} = P_{nw} - P_w \qquad \text{Equation 2-3}$$

in which P_{nw} is the pressure in the nonwetting phase and P_w is the pressure in the wetting phase (Bear, 1972).

Several expressions exist in the literature that relate capillary pressure to 1) the properties of the medium, which take into account the influence of pore radius on the curvature of the interface; 2) the fluids present, which consider the influence of the interfacial tension on the characteristics of the interface; and 3) the degree of saturation of the given phases present in the medium, since saturation determines the volume of each fluid present in the void space. These expressions are based on idealized models of porous media, in which the curvature of the interface within a void space can be geometrically determined (Bear, 1972). Indeed, the definition of contact angle is less straightforward when the solid surfaces consist of the irregular grains of a porous medium. Pore spaces are typically modeled as capillary tubes of radii r as shown in Figure 2-3. If the radius of curvature of the interface is taken as R, then the expression for the capillary pressure used in Equation 2-1 is obtained.

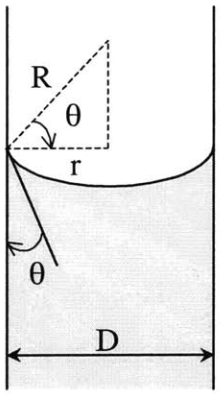

$P_{cap} = 4.\sigma.\cos\theta/D$

Figure 2-3 *Interface in a capillary tube and capillary pressure (after Demond and Roberts, 1987)*

2.3.1.3.Pore entry pressure and residual saturation

When a sample is initially saturated with a non-wetting fluid, the process by which a wetting fluid displaces the non-wetting one is called *imbibition*. In the reverse case, which is the fact during air sparging, a non-wetting phase displaces the wetting fluid, in a process referred to as *drainage* (Bear, 1972). Both drainage and imbibition are processes driven by capillary forces *alone*, and can be described by relationships of the form:

$$P_{cap} = P_{cap}(S_w) \quad \text{for the wetting phase}$$
$$P_{cap} = P_{cap}(S_{nw}) \quad \text{for the non-wetting phase} \qquad \text{Equation 2-4}$$

in which S_w and S_{nw} represent the wetting and the non-wetting saturations, respectively. In turn, the *degree of saturation* with respect to a particular fluid is defined as the fraction of the void volume of a medium occupied by that particular fluid (Bear, 1972).

The curves for imbibition and drainage are not represented by one unique function of saturation, due to the fact that capillary pressure is subject to hysteresis. Hysteresis is caused by a change in the angle of contact θ as a function of the direction of displacement of an interface, such that θ has different values for advancing or receding fronts (Bear, 1972). Figure 2-4 illustrates the phenomenon of hysteresis.

Starting from the right of Figure 2-4 (Point A) towards the left on the drainage path, the curve describes the capillary pressure associated with the wetting fluid as it is being displaced by the non-wetting phase. A certain volume of wetting fluid remains in the medium even at high capillary pressures, giving rise to the *irreducible saturation*, S_{w0}. Conversely, following the imbibition curve, a certain volume of fluid remains trapped in the medium even at zero capillary pressure. The saturation associated with this fluid volume is referred to as *residual saturation* of the non-wetting fluid, S_{nw0} (Bear, 1972).

Point A on the drainage curve shows that when a porous medium is initially saturated with wetting fluid, a minimum capillary pressure must be built at the interface with the non-wetting fluid before invasion can occur. The minimum pressure needed to initiate drainage is referred to the *pore entry pressure* of the non-wetting fluid (Bear, 1972).

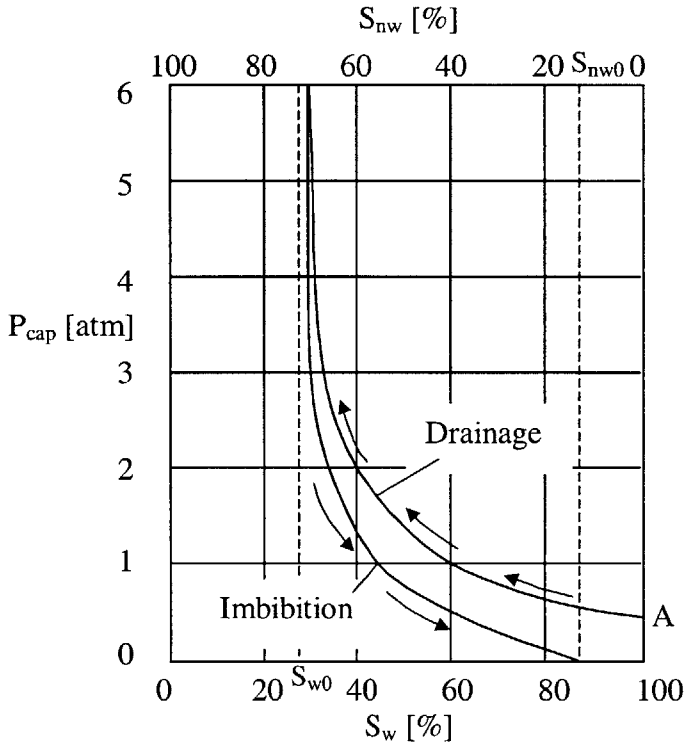

Figure 2-4 *Typical capillary pressure-saturation curve illustrating hysteresis (after Bear, 1972)*

2.3.1.4.Darcy's equation for multi-phase flow

The general form of Darcy's equation for multiphase flow can be written as:

$$q_i = -\frac{k \cdot k_{ri}}{\mu_i} \cdot (\nabla P_i - \rho_i \cdot g \cdot \nabla h) \qquad \text{Equation 2-5}$$

in which q_i represents the flow of the ith fluid per unit area of porous medium, k is the intrinsic permeability of the medium, k_{ri} is the relative permeability to the ith fluid, ρ_i and μ_i are the density and the viscosity of the ith fluid, respectively, P is pressure, and h is elevation (Demond and Roberts, 1987).

The concept of relative permeability accounts for the fact that immiscible fluids tend to interfere with one another as they flow through a porous medium. The presence of one fluid in a given pore through which a second fluid is flowing will reduce the permeability of the medium to the second fluid (Demond and Roberts, 1987). Relative permeability is therefore closely related to saturation, as illustrated by Figure 2-5.

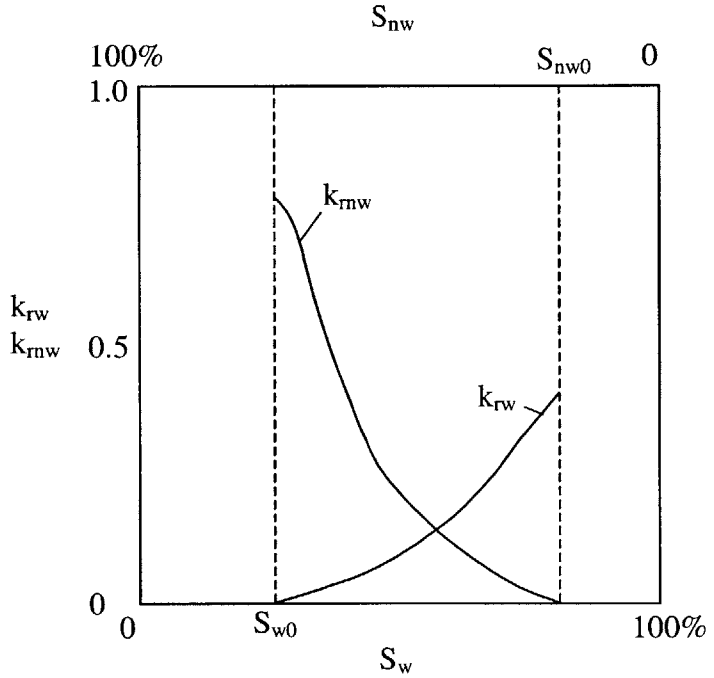

Figure 2-5 Typical relative permeability curves (after Bear, 1972)

As shown in the figure, the sum of the two permeabilities is typically smaller than one, implying that there are pores containing fluid that do not contribute to flow

(Demond and Roberts, 1987). The rapid decrease of k_{rw}, the relative permeability to the wetting phase, indicates that the larger pores (*i.e.* the greater volume of fluid) are occupied by the non-wetting phase first. As the S_{nw} increases, the average pore size saturated by the wetting phase becomes smaller, which also leads to an increase in k_{rnw}, the relative permeability to the non-wetting phase (Bear, 1972).

The combined effects of interfacial tension and wettability, capillarity, relative permeability, and grain size distribution on two-phase flow through a porous medium effectively cause the wetting fluid to be preferentially driven into the small pores of the medium, while the non-wetting fluid preferentially flows into the larger pores (Demond and Roberts, 1987). The implications of these effects to flow of air *injected under pressure* through the saturated pores of a medium will be evaluated in later sections.

2.3.2. Dimensionless Numbers

Flow regimes are generally described in terms of dimensionless numbers, which quantify the relative importance of the mechanisms driving and resisting flow. For the case of an interface between two immiscible fluids of interfacial tension σ, advancing with a superficial velocity U along a capillary of equivalent diameter d, the following dimensionless groups have been defined:

$$\mathrm{Re} = \frac{\rho U d}{\mu} \quad - \mathrm{Re}\ ynolds\ Number; \quad Ca = \frac{\mu U}{\sigma} \quad - Capillary\ Number$$

$$Bo = \frac{\Delta\rho\, g\, d^2}{\sigma} \quad - Bond\ Number; \quad We = \frac{\rho U^2 d}{\sigma} \quad - Weber\ Number$$

Equation 2-6

Re relates inertial forces to viscous forces, *Ca* relates viscous forces to capillary (surface tension) forces, *Bo* describes the ratio of gravitational and capillary forces, and *We* relates inertial forces and capillary forces (Wooding and Morel-Seytoux, 1976). Displacements of immiscible fluids through porous media are controlled by the relative magnitude of

buoyancy, viscous and capillary forces (Culligan and Barry, 1998). It has been shown, for example, that above a critical Capillary or Bond number, capillary trapping of a non-wetting fluid does not occur, whereas below a certain combination of *Ca* and *Bo*, trapping is dominated by capillary forces (Ratnam *et al.*, 1996).

The boundaries between linear and non-linear flow through porous media are determined by the magnitude of the Reynolds number. Wright (1968) conducted single-phase flow experiments to establish the correlation between turbulence and Reynolds number in the flow of water through granular media. Four flow regimes were identified, coinciding with an increase in the magnitude of the Reynolds number. At low Reynolds numbers, the flow transitions from a laminar regime in which Darcy's law applies, to a non-laminar regime where Darcy's theory is no longer valid and where the type of flow is described as "steady inertial". Further increases in flow rate, and hence in the Reynolds number, led to the onset of turbulence in what the author designated as a "turbulent transition" regime. At high values of the Reynolds number, the flow finally enters the last regime and becomes fully turbulent.

The boundaries between laminar and turbulent flow in the case of multiphase flow through porous media are not as clearly defined as in the case of single phase transport. Independent dimensionless numbers can be calculated for the various phases, as described by Wooding and Morel-Seytoux (1976). At high flow rates for example, gas-liquid flow through a porous medium can be defined as partially laminar in the gas phase, and fully turbulent in the liquid phase.

The mechanisms at play during air sparging can be described in terms of the parameters defined in this section. Injection of air into the saturated ground involves displacement of a wetting fluid, the interstitial groundwater, by a non-wetting fluid, the injected air. During injection, capillary forces tend to entrap the non-wetting phase and therefore to prevent the advancement of the air front. Conversely, buoyancy and viscous forces act to prevent entrapment.

In the context of multiphase flow, dimensionless numbers are conventionally defined in terms of the displacing fluid (Culligan and Barry, 1998). In studies of gas-

liquid flow however, unless specifically stated, it is general practice to ignore the effect of the gas phase (Grace *et al.*, 1976). The gas-liquid flow convention will be adopted in this study of air sparging, and liquid properties will be used when calculating dimensionless parameters.

2.3.3. Fingering

The previous two sections have described immiscible flow processes through porous media which occur under dynamically stable conditions. Stable displacements are characterized by a front of wetting or non-wetting fluid flowing through a medium an *uniformly* displacing the resident fluid. This section focuses on unstable flow propagation through porous media, known in the literature as *fingering*.

Fingers are instabilities that may develop at the point of contact between two fluids, miscible or immiscible, that flow through a porous medium. These instabilities originate due to the contrast in properties between the two fluids at the interface. If differences in density, viscosity and interfacial tension between the two fluids are significant, breakthrough of the displacing fluid will not occur in the form of a uniform invading front. Instead, fingers will develop in the direction of flow, forming branching patterns that bypass significant portions of the medium as they spread (Homsy, 1987).

2.3.3.1.Homogeneous porous media

The first scientist to provide an explanation for the phenomenon of viscous fingering was Hill (1952). He considered the displacement of a fluid of viscosity μ_1 and density ρ_1 by a fluid of viscosity μ_2 and density ρ_2. Figure 2-6 illustrates pressure conditions at the interface, as fluid 2 displaces fluid 1. The change in pressure across the interface, Δp, of a front moving upward with a superficial velocity U through a homogeneous porous medium of intrinsic permeability k, was derived from a one-dimensional form of Darcy's law. If driving forces are greater than stabilizing forces (*i.e.* $p_2 > p_1$), any small perturbation of the interface of height δx will be amplified and fingers will develop.

The condition for unstable *upward* flow is that $p_2 - p_1 > 0$, from which the following equation can be derived:

$$(\rho_1 - \rho_2)*g + (\mu_1 - \mu_2)*\frac{U}{k} > 0 \qquad \text{Equation 2-7}$$

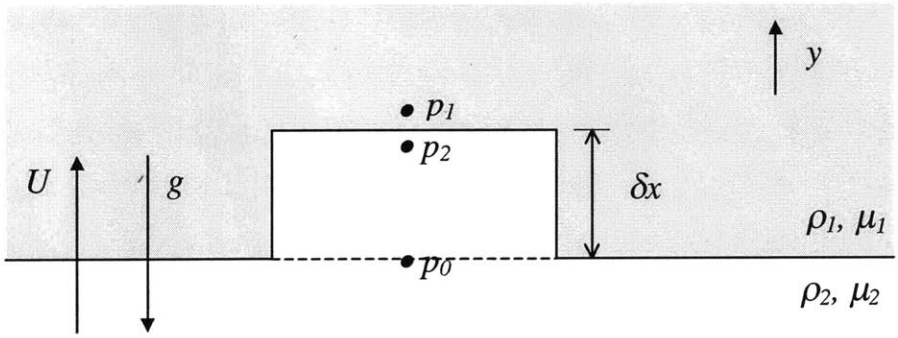

Figure 2-6 *Two-phase immiscible fluid flow interface during upward flow (after Hill, 1952).*

It is clear from Equation 2-7, that depending on the relative magnitude of $\Delta\mu$ and $\Delta\rho$, gravity and viscosity will act as either driving or stabilizing forces. For a given direction of flow a critical velocity U_c can be defined, above which instabilities will be amplified (Hill, 1952). For the *upward* flow condition described by Equation 2-7, this critical velocity is given by:

$$U_c = k*g*\frac{\rho_2 - \rho_1}{\mu_1 - \mu_2} \qquad \text{Equation 2-8}$$

Interfacial tension, although not explicitly present in the previous analysis also has an effect on the mechanisms of formation and propagation of fingers. These mechanisms have been explained in detail by Homsy (1987). It has been observed that after the onset of fingering, a few dominant fingers tend to develop and prevent other smaller, neighboring fingers from further growth. This process is commonly referred to

as *shielding* (Gupta and Greenkorn, 1974). The effect of surface tension is effectively to spread these dominant fingers to the extent that they become fronts, in turn susceptible to fingering. The mechanisms of splitting, shielding and spreading are repeated in the direction of the pressure gradient, until the characteristic fingering patterns are fully developed. Larger interfacial tensions result in wider tip-to-tip finger separations (Homsy, 1987 ; Kueper and Frind, 1988; Pavone, 1992).

Wettability also has a definite impact on the width of individual fingers. Experiments conducted by Stokes *et al.* (1986) demonstrated that if the displacing fluid preferentially wets the porous medium, then the width of a finger is significantly greater than the effective pore size of the medium, and finger properties can be scaled by the Capillary number, *Ca*. Finger width, specifically, was found to decrease with increasing value of *Ca*. Conversely, if the displaced fluid preferentially wets the medium, then finger widths were found to be in the same order as pore size, and independent of the Capillary number (Stokes *et al.*, 1986). In the case of non-wetting displacement, shielding tends to dominate over spreading, as fingers develop (Homsy, 1987).

A study of immiscible displacements through porous media was conducted by Lenormand *et al.* (1988) in which, following experimental and modeling studies, the various mechanisms controlling finger propagation were mapped on a dimensionless space. The authors conducted experiments using several combinations of resident and displacing fluids and subsequently described the different modes of fingering observed. Two dimensionless parameters were used to describe the observed phenomena, namely the capillary number *Ca* and the viscosity ratio *M*. The viscosity ratio was defined as the ratio of viscosities of the displacing fluid to that of the resident fluid. Three domains (combinations of *Ca-M*) were identified, inside which one type of displacement dominated, as follows: 1) *stable displacements* occurred at high *Ca*, when the driving force was the viscosity of the injected fluid. Capillary effects and pressure drops in the displaced fluid are negligible, and the displacement pattern presented a flat front with some minor irregularities at the scale of the pores; 2) *viscous fingering* occurred at intermediate *Ca,* and the principal force was due to the viscosity of the displaced fluid. In this case, capillary effects and pressure drops in the displacing fluid were negligible. The resulting fingers presented no loops and spread across the medium as they grew

towards the exit; and finally 3) *capillary fingering* was observed at low *Ca*, when the viscous forces in both fluids are negligible and the driving force is due to capillarity. In this case, the fingers grow in all directions and formed loops as they spread across the medium (Lenormand *et al.*, 1988).

The flow conditions that apply during air sparging, namely the upward immiscible displacement of a wetting liquid by a non-wetting gas, satisfy the condition postulated by Equation 2-7. Given the low density and the low viscosity of gases, especially relative to typical interstitial pore fluids found in-situ, the condition for instability will *always* be valid during air injection. Fingering should therefore always occur as air displaces pore fluid in a porous medium. Furthermore, given that air is non-wetting, it is expected that the scale of the resulting fingers should be of on the order of the pore size.

2.3.3.2.Heterogeneous porous media

The underlying assumption in the review of fingering phenomena presented in the previous section, is that the distribution of the hydraulic conductivity of the porous medium is uniform. This assumption is likely to be unrealistic for a natural soil deposit, at least at the scale of the zone of influence of the sparge well. It is possible in some situations, to sub-divide the porous medium into zones of relatively uniform hydraulic conductivity. The problem becomes that of determining to which extent each of these zones will control the flow patterns through the medium.

There is a certain degree of controversy in the literature concerning the validity of the term fingering in reference to a heterogeneous porous media. Kueper and Frind (1988) state that fingered-like fluid distributions across heterogeneous media are the result of channeling along preferential pathways, and that they are not "true" fingers as defined for the case of homogeneous media. In a heterogeneous medium, decreases in hydraulic conductivity correspond to decreasing pore size, and ultimately lead to increases in pore entry pressure. According to Kueper and Frind (1988), an advancing fluid front will tend to reduce its viscous losses and preferentially invade a layer of lower entry pressure, regardless of the differences between its properties and those of the resident fluid. An invading front will either pond when reaching a fine-grained layer

until entry pressure is overcome, or flow laterally until a higher conductivity layer is encountered. Kueper and Frind (1988) suggest that "fingered" fluid distributions result from this preferential channeling behavior and that they are not caused by instabilities of the flow.

Other investigators have extended the study of fingering phenomena to include flow through heterogeneous porous media, emphasizing that it is the combined action of the hydraulic conductivity differences and of fingering that determines invasion of a given formation (Brock and Orr, 1991; Tan and Homsy, 1992; Araktingi and Orr, 1993). When studying flow through a heterogeneous porous media, the scale of the heterogeneity and the degree of connectivity between the different conductivity units will determine the extent to which the flow regime is viscous-dominated or heterogeneity-dominated (Brock and Orr, 1991; Araktingi and Orr, 1993). When the scale of the heterogeneity is sufficiently large, hydraulic conductivity distributions will dictate flow patterns, regardless of the viscosity and density contrasts between the invading and the resident fluids in the unit. However, within a unit of higher hydraulic conductivity, the fingering mechanisms of spreading, splitting, and shielding take place, essentially as they would in an isolated homogeneous formation. The boundaries of the layer will limit spreading and splitting of the fingers if the range of pore size variations of the soils between layers is greater than the finger width (Brock and Orr, 1991; Araktingi and Orr, 1993; Moissis et *al.*, 1993).

2.4.GAS-LIQUID FLOW

As was stated in the introductory chapter of this thesis, the focus of this research study is to quantitatively describe the fundamental mechanisms controlling the flow of air through saturated porous media, in order to develop an experimental and theoretical framework for the practice of air sparging. Of particular interest is to determine how the presence of the porous medium affects air flow when compared to air flow in pure liquids. In order to understand the processes at play during gas injection into saturated soils, the literature was first reviewed for background on injection of gases into pure liquids. This section presents a brief summary of a number of studies on gas-liquid flow,

which have been found useful in understanding the mechanisms controlling bubbly flow in pure fluids.

2.4.1. Unrestricted Movement of Air Bubbles in Liquids

2.4.1.1.Constant pressure and constant flow rate conditions

The formation of bubbles by flow of gas through an upward-facing orifice can take place under constant pressure (CP) or under constant flow rate (CFR) conditions. These modes of injection represent the two ends of a range of flow control conditions that can take place during sparging. Figures 2-7 a) and b) show schematic representations of the variation of both pressure and flow rate, in time, during both types of injection modes. Focusing on air pressures first, by definition, the air pressure during a constant pressure injection experiment remains constant with time, as shown in Figure 2-7 a). In order to maintain a constant air pressure as the total volume injected is increasing, the flow rate during a CP test increases with time, and this is illustrated in Figure 2-7 b). Conversely, during CFR injection the flow rate remains constant with time as seen on Figure 2-7 b), while the air pressure decreases as the total volume injected increases as shown in Figure 2-7 a).

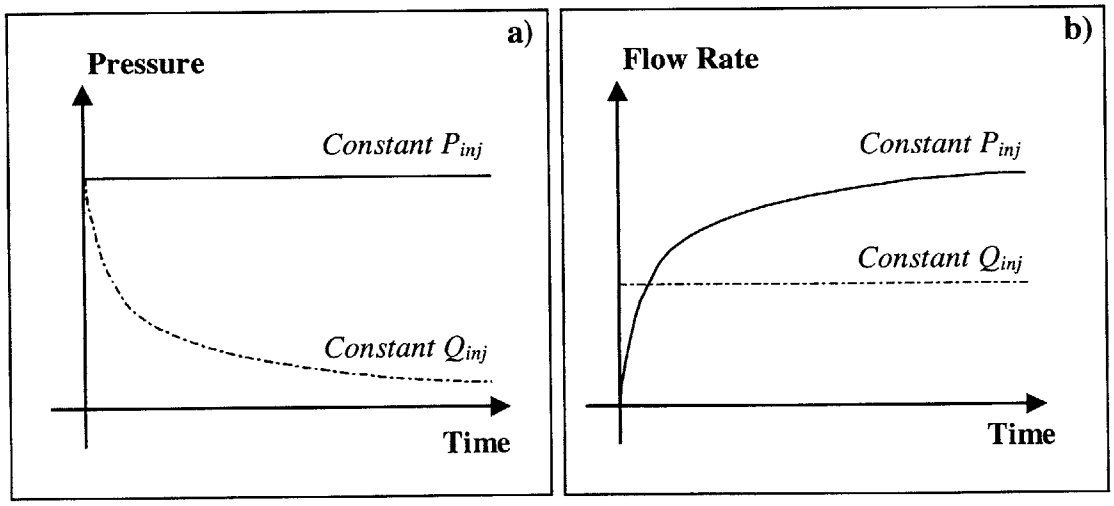

Figure 2-7 *Variation of a) air pressure and b) flow rate with time during constant pressure and constant flow rate of injection conditions.*

The flow rate and the pressure of air ultimately used during injection will represent a condition found within the two end modes illustrated on Figure 2-7. A CP injection experiment, for instance, can be visualized as CFR experiment conducted at very high flow rates.

Bubble size and consequently bubble velocity, are markedly influenced by air flow characteristics, and it is therefore critical to determine if constant pressure or constant flow rate conditions govern during bubble formation. The basic principles of fluid flow through an orifice will be briefly described, to illustrate the effect of CP and CFR conditions on bubble flow. A schematic of flow though a sharp-edged orifice is illustrated in Figure 2-8. As shown, the *vena contracta* or the area of minimum flow, A_2, is located downstream from the orifice, and it is smaller than the area of the orifice, A_0. The two areas can be related by the contraction coefficient, C_c, which for a circular orifice is defined by Equation 2-9 (Roberson and Crowe, 1990):

$$C_c = \frac{A_2}{A_0} = \left(\frac{d_2}{d_0}\right)^2 \qquad \text{Equation 2-9}$$

The contraction coefficient is a function of the Reynolds number at low values of *Re*, and a function of orifice geometry and the ratio *d/D* at high values of *Re* (Roberson and Crowe, 1990). By writing Bernoulli's equation between sections 1 and 2 and using the continuity equation, an expression for the discharge across the orifice can be obtained, in terms of the change in piezometric head across the orifice of its geometric characteristics. The final equation for viscous flow across an orifice can be expressed as follows:

$$Q = K A_0 \sqrt{2g\Delta h} \qquad \text{in which}$$

$$K = \frac{C_v C_c}{\sqrt{1 - C_c^2 A_0^2 / A_1^2}} \qquad \text{Equation 2-10}$$

Δh is the piezometric head difference between sections 1 and 2, and C_v is the coefficient of velocity, which is applied to account for viscous effects at increasing values of *Re* (Roberson and Crowe, 1990).

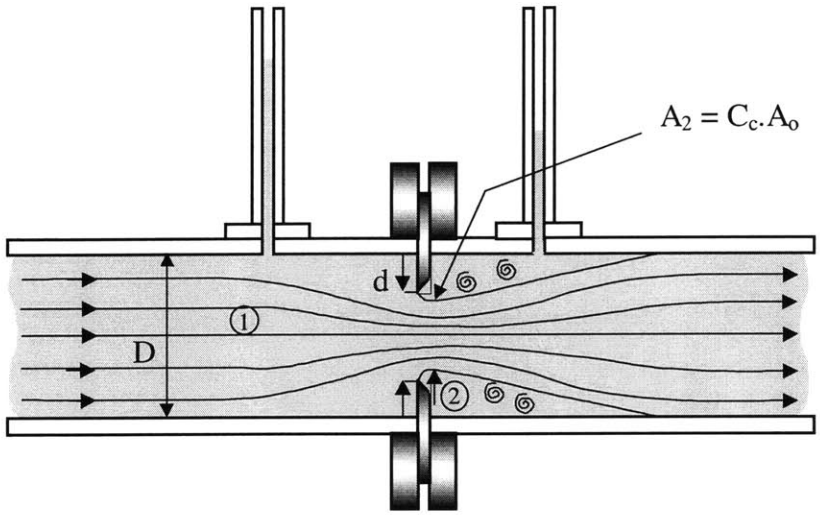

Figure 2-8 Flow through a sharp-edged orifice (after Roberson and Crowe, 1990)

Equation 2-10 becomes critical when describing bubble formation. As the bubble is forming, the pressure within decreases due to: 1) the upward displacement of its centroid; and 2) the decrease of the capillary pressure as its radius increases. Given that the flow rate through the orifice, *Q*, is proportional to the pressure difference across the orifice, the flow rate of air into the bubble may vary with time (Clift *et al.*, 1978). If there is a high pressure drop restriction (*i.e.* capillary) between the gas reservoir and the orifice, or a large pressure drop due to the orifice, then the pressure fluctuations due to the forming bubbles are much smaller than the pressure drop between the reservoir and the orifice. In this case, the gas flow rate can be taken as constant. Conversely, if the volume of the reservoir is very large in comparison with the volume of the bubbles being formed, then the varying gas outflow will not significantly change the pressure in the reservoir, and bubbles will be formed under constant pressure conditions (Davidson and Schüler, 1960b; Clift *et al.*, 1978).

If the gas flow rate is constant, then the volume of the bubble that detaches form an orifice is a function of the gas flow rate and kinematic viscosity of the liquid. The

dimensions of the orifice are of minor importance. For constant gas pressure however, the orifice dimensions become important, and the volume of the bubble is a function of the size and shape of the orifice, the density of the gas, the kinematic viscosity and surface tension of the liquid, and the pressure of the gas supply. In the case of a constant pressure supply, the gas flow rate through the orifice is proportional to its cross sectional area, and is therefore a dependent variable affected by all the factors that influence the volume of the bubble (Davidson and Schüler, 1960a).

2.4.1.2.The formation of bubbles

Many theoretical models exist which describe bubble formation in liquids, and a good reference for comparison is provided by Clift *et al.* (1978). All models depend on a force balance for predicting one or more stages of bubble growth. Upward motion of bubbles is determined by a balance between the upward buoyancy force and a combination of 1) drag forces of the Stokes kind; and 2) inertia forces due to the fact that the liquid surrounding the bubble accelerates with the bubble as it moves upward (Davidson and Schüler, 1960a). Almost all models approximate bubbles as spherical throughout the growth period. The simplest group of models is referred to as the "one-stage models", which assume that bubbles grow smoothly at the orifice until detachment. Detachment is believed to occur when the rear of a bubble passes the orifice, or when buoyancy exceeds the retarding forces. "Multiple-stage" models conversely, assume that a basic change in the mechanisms of bubble growth occurs at one or more points of the process (Clift *et al.*, 1978). Ramakrishnan *et al.* (1969) for example, describe the formation of a bubble as a two-stage process, namely an expansion stage and a detachment stage. During expansion the bubble grows while its base remains attached to the tip of the orifice. In the detachment stage, the base of the bubble moves away from the tip, while the bubble remains in contact with the orifice through a neck. When the flow rate Q is very small, "*vanishingly small*", the volume of the forming bubble can be directly obtained by equating the surface tension force with the buoyancy force. However, as Q increases the bubble expands, giving rise to inertial forces and viscous drag. Both of these forces add to the surface tension force (Ramakrishnan *et al.*, 1969).

Independent of the number of stages of the bubble formation process, the frequency of bubble emission depends on the flow rate of air injected in to the system, and three regimes have been identified accordingly. The first regime takes place under laminar flow conditions, during which the frequency of bubble emission is proportional to flow rate. Bubbles are relatively uniform, and their size is a function of orifice diameter, surface tension, and fluid density (van Krevelen and Hoftijzer, 1950; Hughes *et al.*, 1955; Davidson *et al.*, 1956, Leibson *et al.*, 1956). As a bubble forms, viscous drag forces accelerate the surrounding fluid. The bubble rises in the fluid due to buoyancy forces, and the portion of it left behind at the orifice becomes the nucleus for the next bubble. The second regime occurs as the flow rate is increased and turbulent flow conditions are reached. Bubble coalescence occurs very close to the orifice and the resultant bubble only rises a small distance before it shatters into many small bubbles. Finally, the third type of regime takes place as the flow rate is increased further. The large bubbles undergo a second coalescence during their ascent and the gas appears to come out of the orifice as one continuous jet. In reality, what is occurring is that irregular bubbles are rising with a very rapid swirling motion. Fluid circulates in a large eddy near the orifice, shattering the large bubbles and forming a large number of very fine bubbles (Davidson *et al.*,1956; Leibson *et al.*, 1956).

The occurrence of bubble coalescence has also been attributed to orifice characteristics. Small orifice diameters cause the neck of the bubble to be short at detachment, and therefore causes the bubble to be located close to the orifice during the formation and subsequent detachment of the following bubble. If the injection flow rate exceeds a critical value bubble coalescence occurs. The larger the orifice diameter, the greater the gas flow rate at which coalescence first occurs (Davidson and Schüler, 1960a).

2.4.1.3.Bubble velocity

The movement of a single bubble in an infinite fluid medium is not simple to establish because the properties of the bubble change continuously along its trajectory. The shape of the bubble and therefore its velocity, will be primarily determined by the interaction between buoyancy, viscosity, and interfacial tension.

Haberman and Morton (1956) conducted an extensive study on the motion of single bubbles in various fluids. Results showed that the shape of rising bubbles changes as their size increases. Bubbles are initially spherical, become ellipsoidal as they grow, and finally develop into large bubbles known as spherical caps, that have a mushroom-like shape. The specific bubble volume at which these transitions occur depends on the characteristic properties of the surrounding fluid. Observations also showed that the velocity of bubbles is dependent on their size. Larger bubbles rise at higher velocities than smaller ones, and their shape changes during ascent. Haberman and Morton (1956) evaluated the drag coefficients of rising bubbles, to try to interpret their changes in velocity. The authors found that the drag coefficients acting on these bubbles are predicted, at low velocities, by Stokes' law, while at higher velocities they are predicted by the Hadamard-Rybczynsky's law.

Stokes' law predicts the drag coefficient on a *rigid* spherical particle moving relative to a fluid of infinite extent. In the context of bubble flow, a rigid body designates a bubble in which no circulation of inner-gas occurs during ascent. Based on the assumption that creeping flow conditions apply, and thus that the fluid inertia is negligible, Stokes' law can be used to predict the velocity of a bubble, if the bubble can be treated as a rigid sphere. At low Reynolds numbers, the terminal rise velocity, v_∞, of small single bubbles predicted using Stokes' law is given by:

$$v_\infty = \frac{1}{18}\frac{d^2 * g * (\rho_f - \rho_g)}{\mu_f} \qquad \text{Equation 2-11}$$

in which d is the diameter of the bubble, ρ_f and ρ_g are the densities of the fluid and the gas, respectively, and μ_f is the viscosity of the fluid (Wallis, 1969).

Analogously, the Hadamard-Rybczynski's law estimates the drag coefficient of a fluid sphere. A fluid sphere designates, in this case, a bubble within which inner-gas is circulating during ascent. For cases in which $\mu_g << \mu_f$, the terminal rise velocity of a such a sphere predicted by this law is given by (Wallis, 1969; Clift *et al.*, 1978):

$$v_\infty = \frac{d^2 * g * (\rho_f - \rho_g)}{12\mu_f}$$ Equation 2-12

As noted, Haberman and Morton (1956) found that below a certain bubble size the terminal rise velocity of bubbles in liquids is well predicted by Stokes' law. However, above a critical diameter, bubble velocity is better described by the Hadamard-Rybczynski law. The latter gives velocities approximately 50% higher than those estimated by Stokes' law. The value of this critical diameter is also dependent on the properties of the fluid. Based on their observations, Haberman and Morton suggested that small bubbles rising in liquids behave as rigid bodies. As the size of the bubbles increases, the onset of internal circulation leads to a decrease in the drag coefficient, which ultimately results in an increase in the rise velocity. Larger bubbles therefore behave as fluid bodies.

The topic of bubble velocity in pure liquids has been further investigated, and it is now known that in an ideal system, *i.e.* one exempt of all contamination, the rise velocity of all bubbles, regardless of their size, is described by the Hadamard-Rybczynski law (Clift *et al.*, 1978). However, unless extreme precautions are taken, surface-active contaminants are typically present in any system. These contaminants tend to accumulate at the interface between two fluids, resulting in a reduction of the interfacial tension (Clift *et al.*, 1978). As bubbles rise in liquids, surface-active contaminants tend to be swept to the rear, causing gradients in interfacial tension across the surface of the bubble. These gradients result in tangential stresses, which ultimately lead to decreases in bubble velocity. Smaller bubbles are more susceptible to these gradients than larger bubbles, and therefore their velocities are lower than those of larger bubbles (Levich, 1962). The motion of small bubbles in contaminated systems is thus described by Stokes' law rather than Hadamard-Rybczynski's law.

As mentioned previously, three types of bubble shapes exist: small bubbles are spherical, larger bubbles are flattened and have a predominantly ellipsoidal shape, and the largest bubbles are referred to as spherical caps (mushroom cap shape). The motion of these bubbles changes according to their size, alternating from rectilinear, to helical path, to rectilinear with rocking (Haberman and Morton, 1956). Figure 2-9, taken from Haberman and Morton's study, shows the evolution of bubble velocity and shape as a function of their diameter.

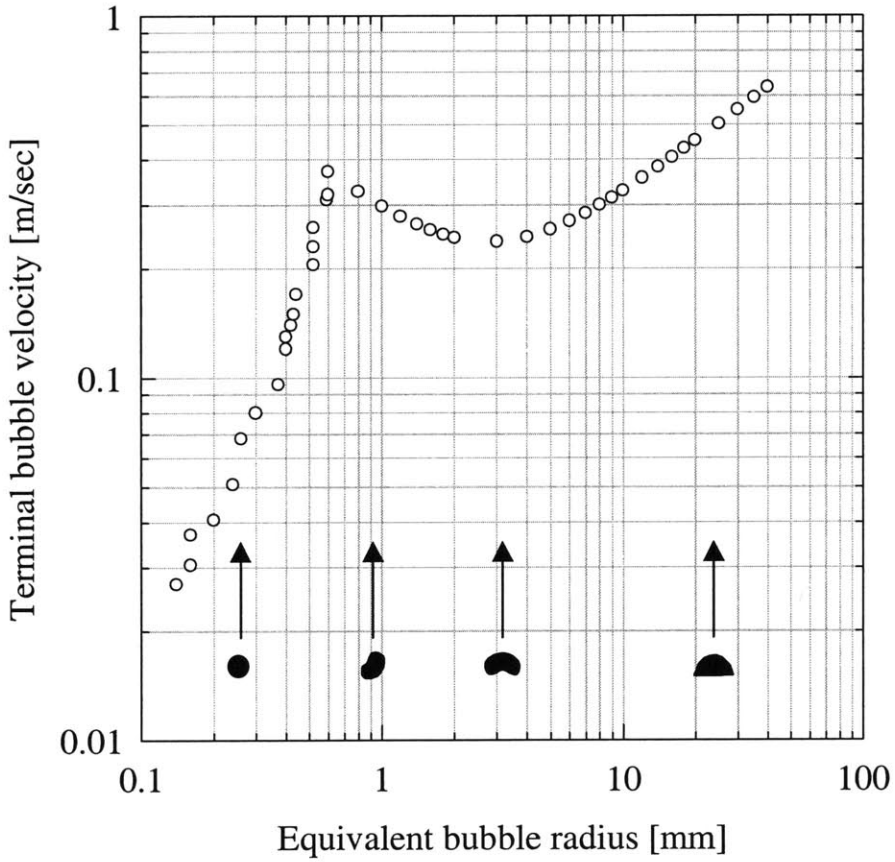

Figure 2-9 *Terminal rise velocity of air bubbles in water as a function of bubble size (after Haberman and Morton, 1956).*

The work of Haberman and Morton (1956) has been greatly extended. A large data base exists in the literature of bubbles sizes and their corresponding velocities in a variety of fluids. The work of Grace *et al.* (1976), for example, provides a graphical method of estimating terminal velocities of bubbles for all types of flow regimes.

Analytical expressions have also been derived for various types of bubble sizes and fluid properties. The reader is referred to Wegener and Parlange (1973), Wallis (1974), and Comolet (1979a, 1979b) for a complete treatment of the subject.

2.4.2. Restricted Movement of Air Bubbles in Liquids

The previous section on bubble velocity considered the movement of individual bubbles in infinite fluid media. The effect of containing walls is that of changing the boundary conditions acting on the bubble and consequently that of changing the characteristics of the gas liquid flow. This section provides and overview of the effects of lateral boundaries on the motion of bubbles.

2.4.2.1.Gas-liquid flow in vertical tubes

Taitel *et al.* (1980) studied gas-liquid flow in vertical tubes and described conditions in which transitions between flow patterns occur with varying gas flow rates. Four distinct modes of flow are identified: 1) bubble flow, where discrete bubbles are distributed in a liquid phase; 2) slug flow, in which large bullet-shaped bubbles of diameters similar to those of the tube move uniformly, separated by slugs of liquid; 3) churn flow, in which the large bubbles become distorted and the liquid slugs collapse due to a high gas concentration; and 4) annular flow, where the gas phase is continuous along the tube. Annular flow is characterized by a liquid film flowing adjacent to the wall and a gas core which carries entrained gas droplets. Figure 2-10 shows a schematic of the various patterns of gas flow through a pipe. These same patterns of flow were also observed by Mishima and Hibiki (1996) in their study of gas-liquid flow through vertical capillary tubes.

As the gas rate flowing into a tube is increased, bubble density increases, and coalescence occurs. With increasing flow rates the rate of coalescence increases but, as explained in the study of bubble flow in free liquids, with the onset of turbulence bubbles start to shatter, leading to a large number of smaller bubbles. If the coalescence rate is higher than the rate at which bubbles break up, a transition to slug flow takes place. As the flow rate is further increased transitions to churn and annular flow occur (Taitel *et al.*, 1980). In a study of gas-liquid flow through artificially fabricated fractures, Fourar and

Bories (1995) observed patterns of flow consistent with those observed by Taitel *et al.*(1980). However, at relatively low values of flow rate, Fourar and Bories (1995) observed what was referred to as fingering bubble flow. The flow patterns obtained showed more similarity to those observed in tubes than those expected in porous media.

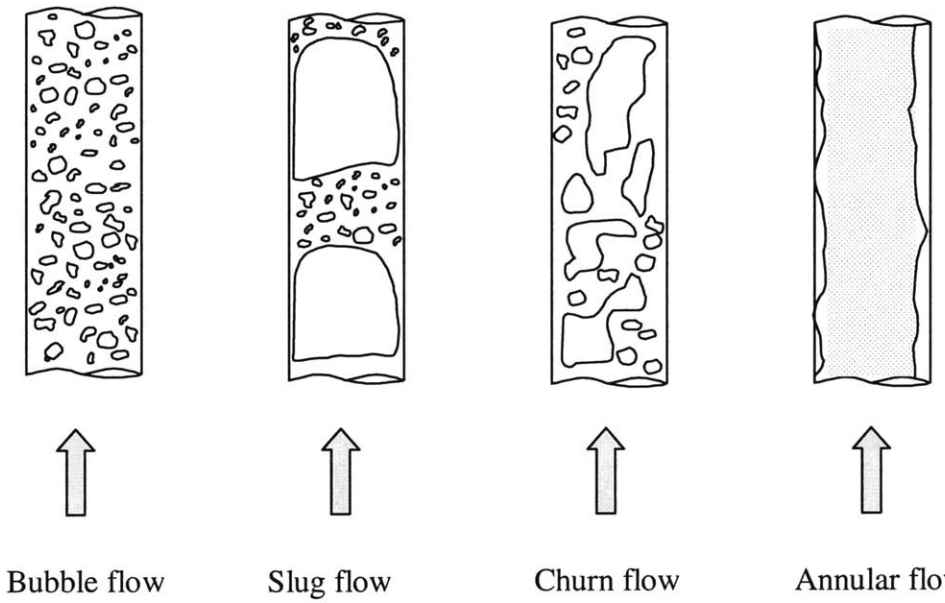

Figure 2-10 Flow patterns of gas-liquid flow in tubes (after Taitel, 1980)

2.4.2.2.Gas-liquid flow in fluidized and packed beds

Even though gas flow in tubes is a highly idealized and simplified model for air flow through porous media, it provides valuable information on how restrictions affect the general patterns of air flow, relative to the flow in pure liquids. The network of void spaces in a porous medium however, is significantly more complex than that in a tube, and therefore variations in the flow patterns described by Taitel *et al.* (1980) are to be expected. One step closer to the study of air flow through porous media can be taken by reviewing the work conducted on gas-liquid flow through fluidized and packed beds.

A fluidized bed is a bed of particles that can be partly or fully supported by an upward flow of fluid through its void spaces (Davidson *et al.*, 1977). When air is injected into a fluidized bed, bubbles are formed in the same manner as when air is

injected into a pure liquid. Bubbles formed in fluidized beds are similar to spherical caps rising in pure liquids, but their shape depends on the nature of the particles in the bed (Davidson *et al.,* 1977). Experimental results show that the rise velocity of bubbles in fluidized beds is lower than that in pure liquids, and that it decreases with increasing soil particle density. However, a point is reached at which, for a given bubble diameter and a given solid concentration, the soil particles have no effect on the rise velocity of the bubbles (Tsuchiya *et al.,* 1990; Bly and Worden, 1992; Tsuchiya and Furumoto, 1995). Experiments conducted by Tsuchiya and Furumoto (1995) evaluated the influence of particle density, particle shape, and bubble size on the resulting velocity and degree of tortuosity of rising bubbles. The authors found that high particle densities in fluidized beds account for a "general" reduction in the observed velocity of bubbles of all sizes, independently of the shape of the particles in the bed. This effect was found to be more pronounced for smaller bubbles. However, according to Tsuchiya and Furumoto (1995), there is a "peculiar" reduction in observed bubble rise velocities (for moderate and high solid densities) that depends strongly on both bubble size and particle shape. This latter effect is also particularly evident in the rise velocity and degree of tortuosity of small bubbles rising in beds of irregular sand particles. Velocities of small bubbles through the sand bed decreased greatly when compared to those in a pure fluid or through a bed of spherical glass beads. Rising paths of small bubbles through the sand bed were also highly tortuous. Rise velocities of larger bubbles was less affected by particle shape, and their rising paths were less tortuous.

It is important to emphasize that injection flow rates in fluidized beds are kept relatively low in order to maintain bubble flow conditions during operation, since the objective of the system is to enhance exchange between the solid and the fluid phases. High flow rates would lead to bubble coalescence and ultimately to the formation of air jets, therefore decreasing the efficiency of the system. Even though restrictions to air flow exist in fluidized beds relative to pure fluid systems, the boundaries restricting air flow are not as fixed as in the case of a porous media. Therefore, it is reasonable to assume that the presence of solid particles in fluidized beds is less disruptive to the rising motion of large bubbles. Large bubbles exert greater buoyancy and inertial forces than

small bubbles, and therefore can potentially displace suspended solid particles encountered in their trajectory.

The study of air flow through packed beds has also provided some insight in the study of gas flow through porous media. As opposed to fluidized beds, packed beds usually consist of columns of small diameters packed with a given porous material, through which the flow is heavily restricted. Continuous gas and liquid flow take place simultaneously through the columns. Observations of gas flow regimes in tubes made by Taitel *et al.* (1980) are remarkably similar to those made in packed beds by Turpin and Huntingdon (1967). The authors identify three separate regimes of gas flow, starting with bubbly flow at low gas flow rates. As the gas flow rate is increased at a constant liquid flow rate, the onset of slug flow is observed. Slug flow is defined as a non-homogeneous flow regime characterized by alternate portions of gas and liquid passing through the column. With further increases in flow rate "spray flow" begins, described as a continuous gas flow regime in which the liquid is suspended as a mist in the gas stream. Weekman and Myers (1964) had conducted similar experiments, and also identified three regimes of flow depending on input gas flow rate. Although not totally consistent with observations of Turpin and Huntingdon (1967), Weekman and Myers (1964) described a transgression of flow regimes with increasing flow rate from a continuous gas flow, to rippling flow, to pulsing flow.

2.4.3. Prototype Representations of Gas-Liquid Flow in Porous Media

As was noted earlier, the presence of gas-liquid interfaces strongly influences the flow of multiple phases through a porous medium. The challenges of relating pore-scale mechanisms to large-scale fluid movement, inherent to flow through porous media, become particularly difficult when describing flow which involves changes in fluid conformation within the matrix. In the particular case of gas-liquid flow, changes in fluid conformation include for instance breakup and coalescence of bubbles, two phenomena that are not completely described by the equations of motion (Olbricht, 1996). A number

of prototype porous media are reviewed in this section, which illustrate some important characteristics of gas-liquid flow through models of porous media.

2.4.3.1.Flow through straight capillaries

The simplest representation of gas-liquid flow in a small pore is the pressure-driven flow of a liquid containing a freely suspended, deformable, nonwetting bubble through a channel, as illustrated in Figure 2-11.

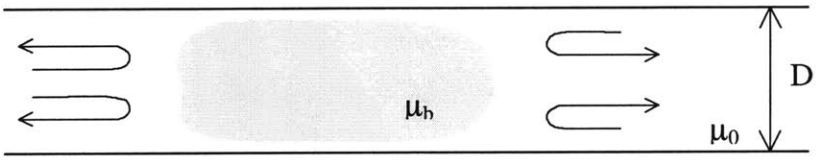

Figure 2-11 Schematic of freely suspended drop in tube flow (after Olbricht, 1996)

Discussions of wall effects on bubble flow found in the literature are divided according to the relative size of the bubble and the tube. The parameter λ is defined as the ratio between the diameter of the undeformed bubble and that of the tube. For values of λ lower than 0.6 the walls cause little additional deformation from what the bubble would be subjected to in an infinite medium. For values of λ greater than 0.6, the container walls have a definite effect on the shape of the bubble, and the flow should be treated as slug flow (Clift *et al.*, 1978).

For low values of λ ($\lambda < 0.3$), at low Reynolds numbers, bubble flow is governed by the viscosity ratio between the bubble fluid μ_b and the bulk fluid μ_o, and the Capillary number *Ca* (Olbricht, 1996). Bubble velocities can be estimated by the relationships defined previously for unbound rigid spheres (Clift *et al.*, 1978). For intermediate values of λ, the containing walls cause elongation of fluid particles in the longitudinal direction, and a decrease in their terminal velocity. The amount of deformation increases with *Ca* (Clift *et al.*, 1978; Olbricht, 1996).

The more interesting case in relation to air sparging is that of bubbles with ratios of λ greater than 0.6. In this case, the tube diameter, *D*, becomes the controlling length governing the velocity and the frontal shape of the bubble. Bubbles are then called slugs

or Taylor bubbles, and tend to be bullet shaped. The slug is composed of two parts, a rounded nose region whose shape and dimensions are independent of the overall slug length, and a cylindrical section surrounded by an annular film of the continuous fluid (Clift *et al.*, 1978). Provided that the length of the slug exceeds the tube diameter, slug length is found to be an unimportant variable, and the dynamics of the nose and the tail of the bubble govern the motion entirely. Usually the gas viscosity and density are much lower than the liquid viscosity and density, and therefore the gas in the bubble is effectively at constant pressure (Wallis, 1969).

The terminal velocity of slugs may be estimated through a graphical representation presented by White and Beardmore (1962) reproduced in Figure 2-12. This is a dimensionless plot that relates the three mechanisms governing slug rise, namely inertia, viscosity, and surface tension. The Eötvös number shown on the x-axis is equivalent to the Bond number. M is known as the Morton number, defined as $g\mu^4\Delta\rho/\rho\sigma^3$, where the fluid properties in question are those of the pore fluid.

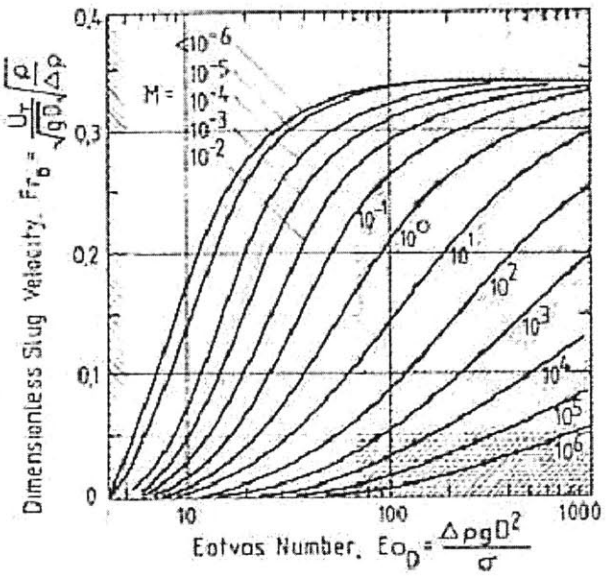

Figure 2-12 General correlation for the rise velocity of slug flow bubbles (White and Beardmore, 1962)

2.4.3.2.Flow through constricted capillaries and capillaries of non-circular cross sections

The individual pores or channels of a porous medium are tortuous, and of varying cross-sectional area. In order to model these irregularities in channel geometry investigators have employed channels containing one or more constrictions in the capillary diameter.

The size of a bubble relative to the size of the capillary, as described by λ, plays a critical role in the overall movement of the bubbles through constricted capillaries. As expected, increasing the bubble size leads to larger deformations. Whereas small drops are characterized by uniform deformations over the length of a corrugation, the deformations of larger bubbles vary as a function of axial position along the bubble. A large bubble ($\lambda > 0.7$) reaches a constriction, its leading end follows the capillary wall contour and squeezes through the throat. Once the leading meniscus clears the throat, its rise speed increases as it enters the diverging cross-section, while the trailing end of the bubble remains trapped behind the throat. This results in a substantial extension of the bubble in the axial direction. As the leading edge advances beyond the throat the curvature of the trailing end increases significantly, while that of the leading meniscus remains nearly unchanged. The resulting capillary difference between the trailing and the leading edges of the bubble leads to the acceleration of the fluid in the tail section as the trailing end leaves the constriction. Increasing bubble sizes eventually leads to breakup of the bubbles through *a tail-pinching* mechanism. This occurs as the bubble moves through the constriction, the trailing edge remains within the throat long enough to cause thinning of the midsection of the bubble, followed by eventual pinch-off and the formation of a satellite drop (Olbricht and Leal, 1983; Hemmat and Borhan, 1996).

Hemmat and Borhan (1996) found that bubble shapes are sensitive to the Bond number, *Bo*. Increasing *Bo* produces more elongated bubble shapes as the bubble passes through the constriction, particularly for larger bubble shapes. The bubbles are more deformable at higher values of *Bo*, which allows them to squeeze through the pores more easily. Air bubbles in particular, were found to follow the wall contour closely as they passed through corrugations, forming a liquid film of nearly uniform thickness between the interface and the tube wall. The thickness of this fluid film increases with increasing

Bo, resulting in less drag on the bubble. The rise velocity of the bubbles therefore increases, as the influence of capillary effects on their movement decreases (Hemmat and Borhan, 1996).

In capillaries of circular cross section, the film between the bubble and the tube wall is uniform owing to the axisymmetry of the flow. In capillaries of non-circular cross section, there are alternate paths for fluid flow in the axial direction. The corners of a capillary of square cross section, for instance, offer less resistance to flow than the thin film between the bubble and the capillary wall. The time scale for processes such as snap-off, which depend on such flows, can be considerably less in noncircular capillaries than in circular ones (Olbricht, 1996).

2.4.3.3.Foams in Porous Media

Only a very brief note on the influence of porous media on the characteristics of foam is presented in this section. The generation of foam within the void space of a porous medium is believed to provide insight in the mechanisms of bubble formation.

Formation of foam bubbles in packs of granular soils by simultaneous circulation of aqueous surfactant solutions and gas has shown that the average size of foam bubbles exiting a porous medium is independent of the bubble size of the foam injected into the medium. When the size of injected bubbles is greater than pore size, bubbles are subjected to splitting at branch points in the pore structure. Breakup of bubbles and dispersion of fluids continues along the bed until a "limiting" size is reached. Conversely, if the size of the foam bubbles injected into the porous media is smaller than the particle size of the medium, bubble coalescence occurs, ultimately yielding to larger foam bubbles (Gido *et al.*, 1989; Nutt *et al.*, 1992). Nutt *et al.* (1992) further suggest that the size of the foam bubbles exiting a given porous medium is approximately equal to the average pore size of the medium.

The previous sections have illustrated a series of characteristic properties and behavior of gas-liquid flow that will be of use in the study of air flow through porous media. It is clear that the mechanisms controlling air flow through soils will be more

complex than the ones presented. In particular, and most critical, is the interaction between bubbles, if indeed air remains in the form of bubbles as it flows through confined passages. The extent of these interactions will effectively determine the characteristics of the flow through the pores of the medium. Interactions between bubbles will be affected by the tortuosity of the medium and by the number of potential flow paths for the air to circulate, two factors that are inherent to the flow of air through porous media. The following section focuses specifically on the study of air flow through soils, where the influence of these two factors becomes evident.

2.5.AIR INJECTION IN SATURATED POROUS MEDIA

2.5.1. Driving Forces

2.5.1.1.Buoyancy and pressure gradients

The mechanism driving the upward movement of an air bubble in a fluid is buoyancy. Buoyancy is defined as a force acting upward, which exists in order to revert a submerged body to a state of equilibrium. Equilibrium is lost when a body of a given volume, with density different than that of the surrounding fluid, is submerged and displaces the fluid. The weight of the body is different than that of the equivalent volume of water displaced. Equilibrium is maintained by the presence of the buoyancy force, which is described by the expression ρ_w x g x *Volume*. Due to the sharp contrast between the densities of air and pore fluid, an air bubble in the free field will then rise due to the difference between the magnitudes of the upward buoyancy force F_b and the downward gravity force F_g as shown in Figure 2-13 a).

The buoyancy force can also be evaluated from a consideration of the fluid stresses (*i.e.* pressures) acting along the boundaries of a submerged body, as is shown in Figure 2-13 b). In the horizontal direction, the pressures in both the positive and negative x-direction cancel out. In the vertical direction, the pressure resulting from the column of water acting both above and below the bubble are different. On top of the bubble, the fluid pressure acts downwards, and it is equal to the hydrostatic pressure acting on the top surface of the bubble, in the simplifying case of a hydrostatic condition. The pressure

acting on the bottom surface of the bubble must be equal to that which would exist if the bubble was replaced by an equal volume of fluid having the same properties of the surrounding fluid. The difference in the pressure acting on the top and bottom sides, integrated along the surface area of the bubble is also equal to the buoyant force acting on the bubble.

Evaluating buoyancy in terms of boundary pressures offers the advantage of providing a direct method of incorporating buoyancy into pressure gradient calculations for the air sparging experiments conducted. Indeed, the pressure gradient driving the injected air, calculated as the difference between injection pressure and fluid pressure at the boundaries of the injected volume, is essentially a buoyancy calculation.

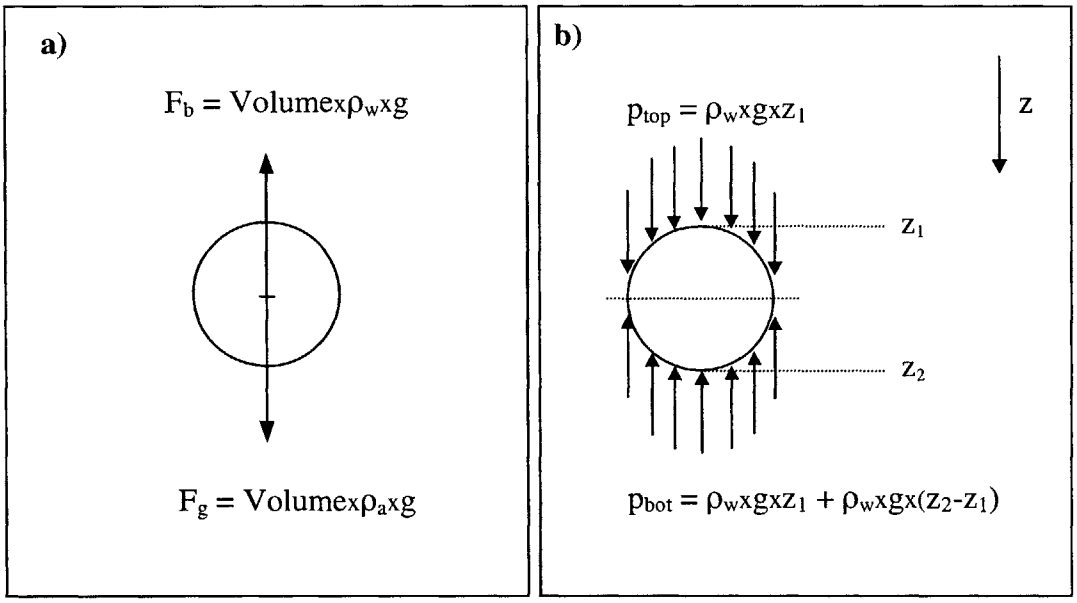

Figure 2-13 Buoyancy forces acting on a submerged bubble: a) internal force approach; b) boundary stress approach.

Buoyancy forces exist regardless of the type of submerged body, *i.e.* rigid or fluid, but are directly related to its volume, and therefore will vary with varying sizes. Changing volumes are inherent to the behavior of bubbles, thus leading to varying magnitudes of buoyancy forces. The case of an air bubble clearly illustrates this interaction. As the air bubble rises in a column of static water for example, the surrounding hydrostatic fluid pressure decreases with decreasing distance to the phreatic

surface. In order to balance the changes in external pressure, the pressure inside the bubble needs to decrease, and this leads to an expansion of its volume. Buoyancy forces consequently increase, and the bubble accelerates.

This investigation concentrated on evaluating the effects of pressure gradients/buoyancy on the movement of injected air through porous media. The use of the geotechnical centrifuge made it possible to evaluate flow characteristics under varying magnitudes of the pressure gradients. Clayton (1998) had for instance speculated on the effects of buoyancy on the initial patterns of expansion during air sparging. Figure 2-14 reproduces the qualitative description presented by Clayton (1998).

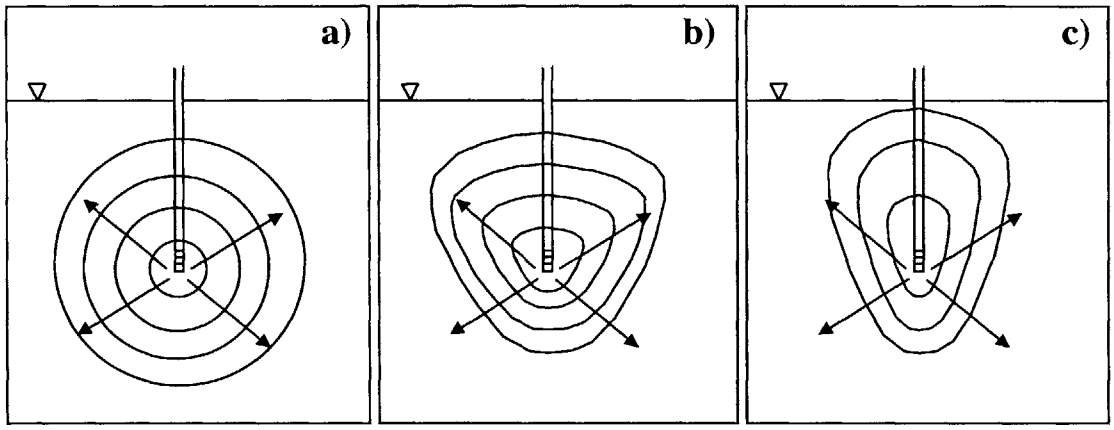

Figure 2-14 Conceptual illustration of the differences in extent of initial air invasion under conditions of: a) no buoyancy; b) moderate buoyancy; and c) strong buoyancy (after Clayton, 1998).

In a medium of homogeneous, isotropic hydraulic conductivity, if the fluid injected has the same density as the pore fluid, then buoyancy forces are equal to zero, and the injected fluid propagates spherically from the injection point, as depicted in Figure 2-14 a). This interpretation disregards pressure gradients existing within the injected phase. As the density contrast between the two fluids becomes larger, buoyancy forces are increasingly important, and air propagation tends to occur in a more vertical direction as shown in Figures 2-14 b) and c) (Clayton, 1998).

2.5.1.2.Capillary pressure and hydrostatic pressure

The discussion in this section concerns the relative magnitude of the components of the entry pressure. At the beginning of an air sparging experiment, the injection pressure is set equal to the sum of the hydrostatic and the capillary pressures at the injection point. If these two components of the pressure are compared, for depths of injection and for soil types representative of field conditions, the magnitude of the hydrostatic pressure is significantly larger than that of the capillary pressure. In fact, Figure 2-15 shows the variation of the ratio of these two pressures with depth of injection, for four different soil types. The variation is described by varying effective grain sizes, D_{10}, ranging from a value characteristic of a very coarse sand to one typical of a very fine sand. The x-axis shows the distance from the injection point to the phreatic surface, while the y-axis plots the relative magnitude of the two pressures. The magnitude of the capillary pressure was estimated from Equation 2-1, using a contact angle of 0°, which leads to an upper bound estimate of the pressure. It is clearly seen on the figure that the value of the capillary pressure is effectively marginal for the two coarser soils, at any depth of injection. The depth of injection becomes a factor for the finer soil, since at shallow depths the ratio of the pressures exceeds 20%. The relative importance of the capillary pressure therefore depends on the magnitude of the hydrostatic pressure (*i.e.* depth of injection), as well as the characteristic grain size.

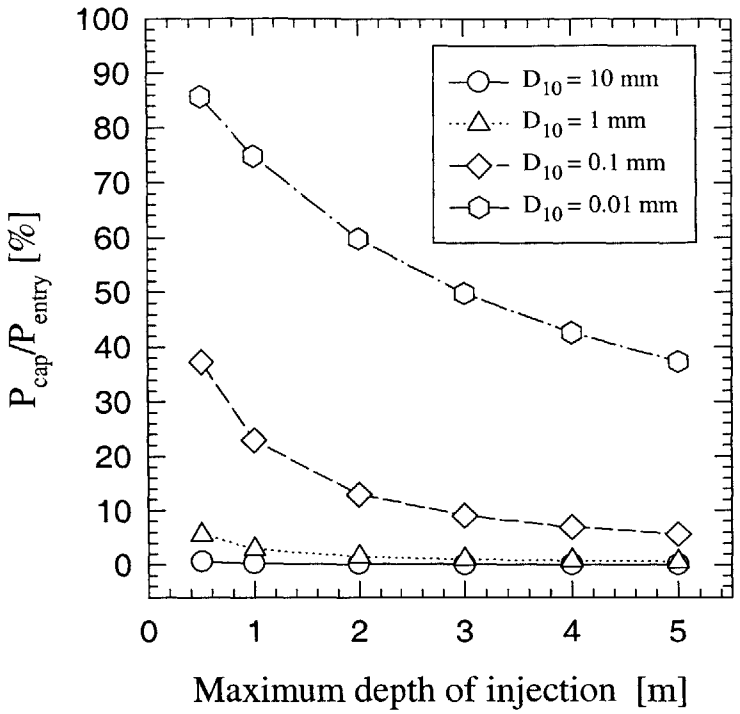

Figure 2-15 Relative impact of capillary pressure on air entry pressure at varying depths of injection.

The relevance of capillary pressure considerations in the study of air sparging *in coarse materials* is therefore questionable for all situations. Indeed, if air sparging is being conducted under constant pressure conditions, the importance of capillary pressures, at a field scale, is negligible when compared to the hydrostatic pressure component of the injection pressure. If constant flow rate conditions apply, then it is possible that the pressure in the air phase drops to such extent that capillary pressures become relevant, and in this type of situation they should be taken into account in the analysis.

In the specific case of this investigation, the importance of capillary pressure at high acceleration levels is even lower. Capillary pressures do not change with *g*-level since they only relate to the microscopic length of the porous medium and to intrinsic properties of the pore fluid. As a result, when hydrostatic pressures are increased at higher accelerations, the magnitude of the ratio P_{cap}/P_{entry} is further reduced.

The effective diameters of the materials tested in this study were 0.35 mm (MSF) and 0.79 mm (MS). The impact of capillary pressure on the behavior of injected air, if

significant, might be visible on results from experiments conducted on MSF samples, at low g-levels. The value of the ratio P_{cap}/P_{entry} is included in the tables on Appendix E, Summary of Experimental Results.

2.5.2. Patterns of Air Flow

The study of flow patterns of air injected through saturated soils during air sparging has been the focus of a number of research projects. The first series of visualization tests available were conducted by Ji *et al.* (1993) in their study of air flow patterns through water saturated glass beads. Beads of various sizes were used in their experiments, in which the influence of porous media characteristics on air plume behavior and shape was evaluated. Their experimental results showed that under steady applied pressures, the air flow regime depended on soil grain size. Bubbly flow was found to develop through the coarse-grained packs of beads (4mm in diameter), while channeling flow was observed through the finer-grained material (0.75 mm in diameter). Brooks *et al.* (1999) also conducted air sparging experiments in glass bead columns and concluded that channel flow generally occurs in porous media with an average grain size diameter equal to or less than 1 to 2 mm. Bubble flow in the form of bubbles, slugs, or mixed flow, occurs in media with a larger average pore size diameter. Observations from studies conducted by Wehrle (1990) and Semer *et al.* (1998) on air flow through granular soils were consistent with results presented by Ji *et al.* (1993) and Brooks *et al.* (1999). Both studies reported bubbly flow conditions taking place in gravel formations following air injection. Wehrle (1990) indicated that injected air rose through the gravel in the form of "groups of pulsating bubbles", and that no flow occurred through the sand. Semer *et al.* (1998) reported bubbly flow through the gravel, while injected air flowed along preferential pathways through the sand. Peterson *et al.* (1999) studied the influence of natural sediments on the pathways of the injected air. The authors stated that air-flow geometry is likely to be different in natural sediments when compared to glass beads, given that sorting, grain boundary irregularities, and packing may have significant effects on pore entry pressures and air migration pathways. Results indicated that air flow through soils with an average diameter of less than 1.3 mm occurs in discrete meandering

channels with areas of no flow occurring between individual channels. Air flow through soils with an average diameter greater than 1.84 mm was described as "*pervasive*", which indicated air flow throughout the entire sediment column, within certain lateral boundary limits (Peterson *et al.,* 1999). Results from their experiments were therefore also consistent with those presented by Ji *et al.* (1993). Elder and Benson (1999) conducted air sparging experiments at constant pressure on mixtures of beads ranging in sizes from fine, to coarse-medium, to coarse sand. Results indicated that at injection pressures slightly higher than air entry pressure air tended to move through the beads in discontinuous channels or slugs. Smaller slugs were seen to pause intermittently, until they coalesced with others and overcame air entry pressure. At higher pressures the slugs formed continuous air channels. These channels were found to be wider and spaced further apart in the fine beads than in the two other media, but they were more tortuous in the coarser beads (Elder and Benson, 1999).

Laboratory simulations of air sparging have shown that the presence of large-scale heterogeneities completely disrupts the air flow pathways through the soil. Results presented by Ji *et al.* (1993) and Baker and Benson (1996) show that the advancement of vertical air flow is prevented by layers of low hydraulic conductivity, which force the flow to spread horizontally until the layer of finer material is bypassed. A schematic of air flow patterns through heterogeneous porous media is shown on Figure 2-16. Results from field tests are also consistent with this behavior, as indicated for example by Reddy *et al.* (1995), Bohler *et al.* (1990), and Marley *et al.* (1992). A recent study on the effects of soil heterogeneity on air flow patterns during air sparging was conducted by Reddy and Adams (2001). The authors conducted experiments in two-dimensional tanks, in which varying configurations of four granular materials were used (coarse and fine sand and gravel). Bubbly flow was observed through the gravelly soils, while channeled flow took place through the sands. Experiments showed that when air flowing through a layer of a given permeability and tortuosity penetrates a second layer of slightly lower permeability, the size of the zone of influence increases but the air channel density decreases. If the permeability contrast between two layers is greater than an order of magnitude, air will not penetrate the less permeable layer and entire areas of the soil profile are bypassed by the flowing air (Reddy and Adams, 2001).

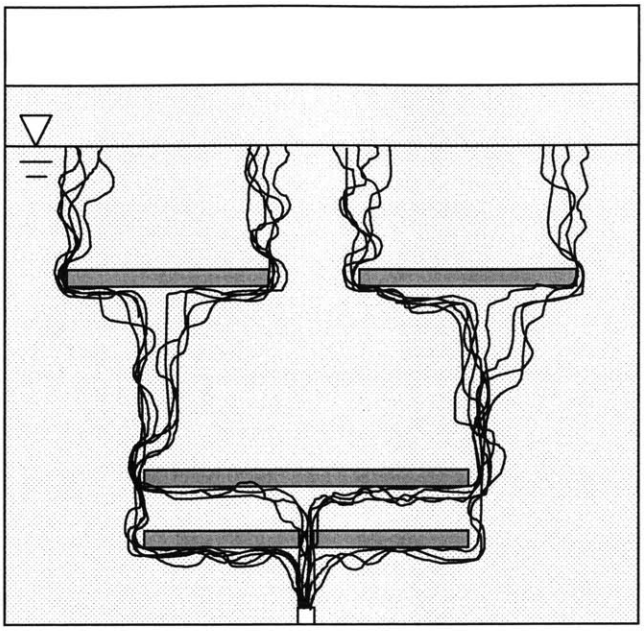

Figure 2-16 Air flow patterns through heterogeneous porous media (after Ji et al., 1993)

2.5.3. Zone of Influence

Given that the primary mechanism of contaminant removal in IAS systems is volatilization, the effectiveness of air sparging is controlled by the degree of contact between the injected air and the contaminants. More specifically, the rate of mass removal depends on the ease with which contaminants come into contact with the air stream. Contaminants located close to air-filled pores will be rapidly carried out of the system by the air stream, while those located away from the air flow will have to diffuse to these pores in order to be removed (Baker and Benson, 1996).

The extent of contact between air and contaminants is in turn a function of two factors: 1) the size of the plume, given by the total volume of soil contained within the boundaries of the air saturated medium; and 2) the degree of air saturation of the soil between the boundaries of the plume. The effectiveness of a system will depend on the relationship between these two factors: wide plumes with many water saturated pockets may not be as effective in terms of the amount of contamination removed as narrower plumes with a higher air channel density. The two factors have to be considered

simultaneously however, when determining the applicability of IAS as a cleanup technology for a given site.

The shape of the zone of influence is usually approximated by either a cone-shaped zone (Nyer and Sutherson, 1993) or a by a parabolic shaped zone (Reddy *et al.*, 1995; Chen *et al.*, 1996). Nyer and Sutherson (1993) report that the angle of inclination of the sides of the cone ranges from 15° for coarse gravel to 60° for silty sands. The dimensions of the zone of influence are believed to depend on soil characteristics, injection rate, and depth of injection (Reddy *et al.*, 1995). Elder and Benson (1999) reported that air plumes tended to be V-shaped at low injection pressures and U-shaped at higher pressures. The authors suggested that the change in plume shape at higher pressures indicates that air plumes broaden as air is driven outward near the well tip because the ratio of pneumatic to buoyant forces increases. Reddy and Adams (2001) reported parabolic plumes through uniform sands. The size of the zone of influence was found to increase with decreasing air permeability and increasing tortuosity. Narrower plumes were observed through gravels, similarly due to higher permeabilities and lower resistances to air flow (Reddy and Adams, 2001).

Lundegard and Andersen (1993) found that the zone of influence of an air sparging well varied during the course of injection. Three phases were identified: 1) an expansion phase, characterized by an initial transient period of growth of air pathways in both vertical and horizontal directions; 2) a collapse phase, also transient, during which a reduction of the lateral spread of air pathways occurs; and 3) a steady-state phase, through which the system remains static, provided air injection parameters are kept unchanged. According to the authors, water mounding develops during the expansion phase, and the zone of influence at this stage is bell-shaped. The zone of influence subsequently decreases and becomes conical as the air reaches the phreatic surface. During the collapse phase, some of the air pathways are re-saturated by ground water and the zone of influence decreases even further.

2.5.4. Conceptual Models of Air Flow Through Porous Media

The first widely used model of air sparging was developed by Sellers and Schreiber in 1992, to estimate the cleanup rate of an air sparging well. The model was based on the assumption that air flowed within the porous medium in the form of discrete bubbles, distributed evenly in the volume of influence around the air sparger. Complete-mixing conditions were assumed to take place within the zone of influence, the boundaries of which were defined by the extent to which sparging bubbles penetrated the contaminated aquifer. Based on relationships developed for gas-liquid flow, the model used fluid properties and injector characteristics in order to determine bubble sizes and bubble velocities. The loss of dissolved contaminant from the groundwater was subsequently balanced by the rate of contaminant mass transfer diffusing into the sparging bubbles (Sellers and Schreiber, 1992).

Increasing experimental and field observations collected in the past decade have effectively resulted in the elimination of the use of the bubble flow formulation. Modeling of air flow via discontinuous air bubbles is currently limited to flow through coarse grained materials (Ahlfeld *et al*, 1994). In its place, three conceptual models have been proposed in the literature, to date, to describe the flow of air through saturated porous materials. The various conceptual models are at the origin of the computer models currently existing to predict the performance of air sparging systems. Figure 2-17 presents a schematic representation of the characteristics air flow patterns resulting from the models that will be described below.

The first model was proposed by Ahlfeld *et al.* (1994), based on the experimental results by Ji *et al* (1993), in which air was found to flow through the porous medium in channels of continuous air phase rather than as free bubbles. The model proposed that pockets of pressurized air would invade the medium seeking the path of least resistance, that being the larger pore sizes. It was further suggested that air flow could be correlated with pathways of high permeability, and that the overall flow would be governed by heterogeneities in permeability. Ahlfeld *et al.* (1994) suggested that air flow would take place through widely spaced, macroscopic air flow channels, separated by regions fully

saturated by water. This conceptual representation is the one that has been adopted for example in the series of models proposed by Wilson *et al.* (1992-1996)

An alternate model of air flow is based on the assumption that air flow through saturated soils can be simulated as a continuum, with regions of uniform saturation distributed around the well. This view assumes that within the boundaries of the plume channel density is sufficiently uniform that contours of saturation can be defined (Clayton, 1998). This approach has been used in a number of numerical and theoretical models currently available in the literature, such as those of McCray and Falta (1997, 2000) and Van Dijke *et al.* (1995).

The third and last model of air flow through saturated soils was proposed by Clayton (1998). The author states that there is no evidence to support the channeling model for all coarse-grained materials, and suggests a model that accounts for both pore-scale air fingering and macroscopic air channeling during air invasion. Theoretical and experimental data are reported which show that pore-scale fingering is ubiquitous but does not imply that macroscopic channeling develops for all coarse-grained soils. The author proposes that channeling occurs extensively in coarser materials, where capillarity forces are small and buoyancy forces dominate. Air saturations in these soils are low, and the lateral extent of air flow is restricted. In finer materials conversely, capillary forces are high and air channeling does not tend to occur, which leads to higher air saturations and increasing extent of lateral air flow (Clayton, 1998).

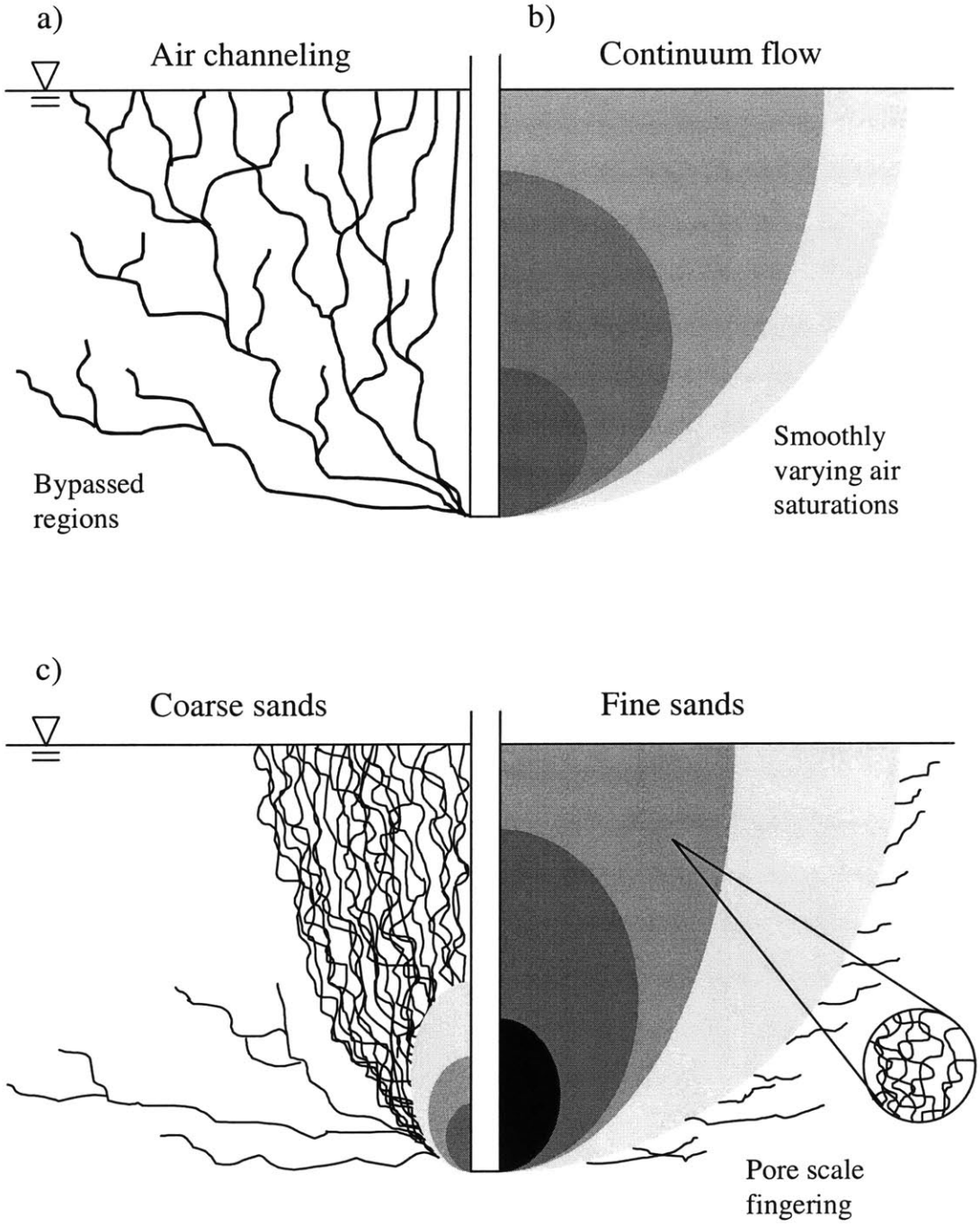

Figure 2-17 Schematic of current models of air flow through saturated porous media: a) macroscopic channeling model with areas separated by areas of fully water saturated soil; b) continuum model with zones of uniform saturation; c) pore-scale fingering and macroscopic channeling (after Clayton, 1998).

2.5.5. Air Sparging Modeling

There are currently two types of models of air sparging available in the literature: 1) lump-parameter models; and 2) multi-phase fluid flow models. The former type of models simulate the various mass transfer processes by lumping them into compartments and bulk parameters. In a two-compartment model of air sparging, for example, the compartments would represent the aqueous phase and the air phase. Equilibrium conditions are usually assumed between the phases such that lumped mass transfer coefficients can be determined for the different interfacial areas involved in the processes. The mechanics of the problem are therefore greatly simplified by separating processes that, in reality, are occurring simultaneously. Models are written to solve systems of equations that describe the behavior of the separate compartments, and the level of complexity of the models increases with the number of compartments defined (McCray, 2000).

Multiphase fluid flow models on the other hand, consider the interaction between the different phases flowing simultaneously through the medium. In the case of air sparging, this type of models involve the effects of capillary pressures between air and water, and the mutual impedance (relative permeability) of the two phases (McCray, 2000). These types of models are highly non-linear and therefore few analytical solutions are currently available.

In a recent state-of-the-art publication, McCray (2000) presents a comprehensive overview of the two types of modeling techniques, provides examples of currently available models, and compares the performance of the different methodologies. Experimental results from this study will be compared to predictions from one of the currently available analytical solutions of a multi-phase model of air sparging, developed by van Dijke *et al.* (1995). This model is widely used, partly because it makes it possible to predict the shape of an air sparging plume from a closed-form analytical solution. The following section gives a detailed description of its formulation.

2.5.5.1.van Dijke et al. model (1995) - Overview and main assumptions

van Dijke *et al.* (1995) developed a model that predicts the flow of air during air sparging applications, and consequently, the shape of the zone of influence of an air sparging well. The model explicitly incorporates soil, pore fluid, and injection parameters, and is therefore a useful resource in the validation of the experimental and numerical results presented in this thesis. The main principles, assumptions and equations discussed in their paper are presented in the following paragraphs.

In the formulation of their model, van Dijke *et al.* (1995) assumed that under natural subsurface conditions, air flow through saturated soils is most likely to occur in small continuous channels. With the assumption that a high air channel density is likely to exist in the main region of flow, air flow was modeled macroscopically as a continuum. The problem was solved by defining an axially symmetric space, in which air was injected through a vertically positioned well, in an initially saturated region below the vadose zone.

The model treats air and pore fluid as two immiscible, incompressible, continuous phases. The interaction between the two fluid phases and the porous medium is described by relative permeability and capillary pressure relationships, both of which are dependent on the medium saturation.

2.5.5.2.van Dijke et al. model (1995)

The flow of air during air sparging is treated as a two-phase flow problem. The model is based on Darcy's law for both air, a, and water, w, as defined by the following equation:

$$\vec{U}_j = -\frac{K_{abs}\, k_{rj}}{\mu_j}\nabla(P_j + \rho_j g Z) \qquad j = w,a \qquad \text{Equation 2-13}$$

and by the mass balance equations:

$$\phi \frac{\partial S_j}{\partial t} + \nabla \cdot \vec{U}_j = 0 \qquad j = w, a$$ Equation 2-14

in which K_{abs} is the absolute permeability of the soil, k_{rj} is the relative permeability of the fluid j, S_j is the fluid saturation, U_j is the Darcy velocity of fluid j, μ_j is the fluid viscosity, P_j is fluid pressure, ρ_j is fluid density, ϕ is the soil porosity, and g is gravity. The soil is assumed to be homogeneous and isotropic.

Equations 2-13 and 2-14 are combined with the constitutive relation:

$$S_w + S_a = 1$$ Equation 2-15

in which S_w is the water saturation and S_a is the air saturation.

The capillary pressure P_c is defined as the difference between the pressures in the two fluid phases:

$$P_c = P_a - P_w$$ Equation 2-16

Finally, the dependence of capillary pressure and relative permeability on the saturations is given by the following equations, based on van Genuchten equations (1980):

$$P_c(S_w) = \frac{\rho_w g}{\alpha}(S_w^{-1/m} - 1)^{1-m}$$ Equation 2-17

$$k_{rw}(S_w) = S_w^{1/2}(1 - (1 - S_w^{1/m})^m)^2$$ Equation 2-18

$$k_{ra}(S_a) = S_a^{1/2}(1 - (1 - S_a)^{1/m})^{2m}$$ Equation 2-19

where m and α are van Genuchten parameters of the soil.

Equations 2-13 and 2-14 are solved in the two-dimensional, axially symmetric space shown in Figure 2-18. The height $Z = 0$ corresponds to the position of the water table, along which $P_w = 0$. Along the top boundary of the domain, where $Z = H_t$, the air pressure $P_a = 0$. Air is injected into the system with a velocity U_{in}, through a well of radius E and length H_l - H_u such that the injection rate is defined by $Q = 2\pi E(H_l - H_u)U_{in}$.

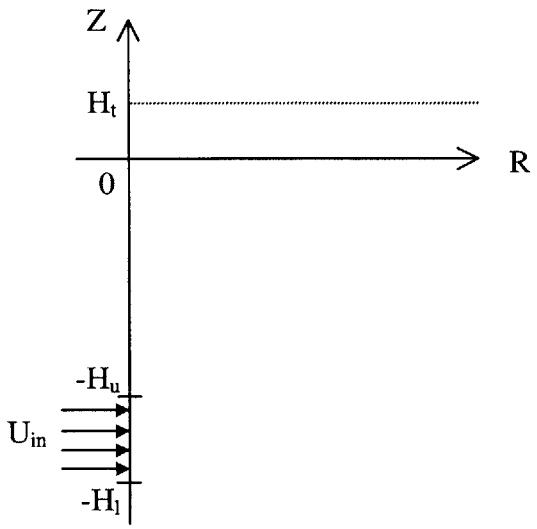

Figure 2-18 Schematic of the modeled space (after van Dijke et al., 1995)

The problem is solved for one of the phase saturations and one of the phase pressures. In general, however, it cannot be solved explicitly due to the non-linearity of the equation. In their paper, the authors present solutions to the set of equations in question, obtained using a numerical flow model. Solutions consist of air saturation contour plots, as a function of time, for a given set of input parameters.

The solution of the general case as it was presented in the paper by van Dijke *et al.* paper is complex and requires finite element programs. The authors, however, simplify the problem and its solution by solving it for the case of steady-flow conditions. Two key assumptions are made in the solution of the steady-case problem, which are based on results from the numerical simulations: 1) water pressure is approximately hydrostatic at large times, implying that water velocity can be disregarded with respect to air velocity; and 2) given the large density contrast between the two fluids, flow in the *z*-

direction is dominated by advection. A final, closed-form, expression is provided for the interface that separates the region where air saturation is positive, to that where $S_a = 0$, in other words, the boundary of the air plume. The equation for the boundary of the plume, $f(z)$ is defined in terms of several dimensionless parameters and presented as a function of the depth z from the water table, as follows:

$$f(z) = f_0 \cdot (z+1)^{1/(2(p_D+1))} \qquad \text{for } z \geq -1$$

$$f_0 = \left(\frac{4 n_D}{N_1} N_2^{p_D} \right)^{1/(2(p_D+1))} \left(\frac{p_D + 1}{p_D} \right)^{1/2} \qquad \text{Equation 2-20}$$

in which the dimensionless numbers N_1 and N_2 are defined by the expressions:

$$N_1 = \frac{(\rho_w - \rho_a) \cdot H \cdot \alpha}{\rho_w} \qquad \text{and} \qquad N_2 = \frac{2 \cdot \mu_a \cdot U_{in} \cdot E \cdot (H_l - H_u)}{K_{abs} \cdot (\rho_w - \rho_a) \cdot g \cdot H^2} \qquad \text{Equation 2-21}$$

and the parameters n_D and p_D are given by the following equations:

$$n_D = \frac{2(1-m)}{4m+1} \cdot m^{(m-1)/(4m+1)} \qquad \text{and} \qquad p_D = \frac{2(1-m)}{4m+1} \qquad \text{Equation 2-22}$$

Results from the van Dijke *et al.* (1995) model are directly related to the flow rate of injection, and also strongly dependent on the values of the van Genuchten parameters assigned to the porous medium. The general shape of the radius of influence predicted is a parabola, the characteristic dimensions of which vary significantly with the chosen values α and m. In contrast, the influence of the permeability of the medium on the final solution is not as significant. The permeability of the soil is a parameter that appears explicitly stated in the definition of N_2, but its effect, relative to that of the van Genuchten parameters, is limited.

2.5.5.3.van Genuchten parameters

Given the importance of the van Genuchten parameters, not only to the van Dijke *et al.* model, but also to the other two models that are presented in the following sections, a very brief overview of the significance of α and m and some typical values for a group of soils of interest to air sparging will be provided here.

van Genuchten (1980) presented a closed-form analytical equation that provides an adequate fit for measured soil water retention curves. The equation provides means of describing the relationship between the capillary pressure, P_c, and the saturation, S, of a given soil based on two fitting parameters, α and m. Due to its simplicity, the van Genuchten equation has been widely used in the modeling of unsaturated flow.

The parameter α normalizes all soils to one same relative level. The larger the value of α, the lower the plateau of the soil on the *Pc-S* relationship, and therefore the coarser the soil. Figure 2-19 is a schematic showing the significance of the variations of the van Genuchten parameters, and Figure 2-19 a) illustrates the shifts in the water retention curve with varying values of α. The α-parameter has dimensions of $length^{-1}$.

The parameter m governs the symmetry of the water retention curve, as illustrated by Figure 2-19 b). The m-parameter is dimensionless and its value varies from 0 to 1. The lower the value of m, the higher the tendency of the soil to retain fluids by capillarity (Jonasson, 1991).

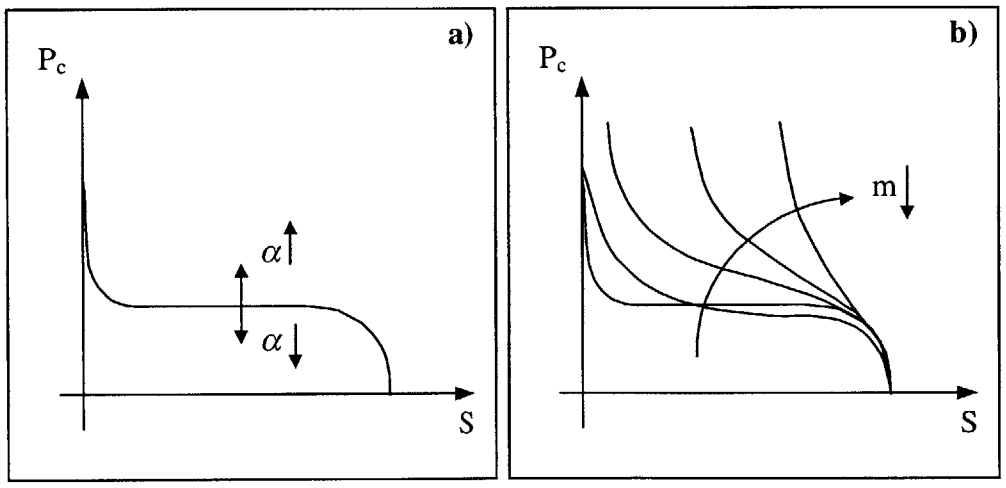

Figure 2-19 Schematic of the relative significance of the van Genuchten parameters. a) variation of the α-parameter; b) variation of the m-parameter.

The relationship between the hydraulic conductivity of a soil and the values of α and m is not straightforward, and wide variations in values are estimated for soils of comparable grain size distributions and therefore comparable permeabilities. In order to compare the predictions of the models that will be later presented in this thesis with the experimental results in Chapter 8, it was necessary to determine the van Genuchten parameters of the crushed glass used in laboratory testing. Jonasson (1991) developed a procedure to determine van Genuchten parameters from grain size distribution curves, and compiled a data base of α and m parameters of Swedish soils according to soil type. This procedure was followed on the grain size distribution curve of the MS material, and the following values of the van Genuchten parameters were obtained:

$$\alpha = 3.56 \text{ m}^{-1} \text{ and } m = 0.79$$

Figure 2-20 is a plot of α and m values for soils compiled on Jonasson's (1991) database. The soils plotted on the figure were chosen from the database because they had similar grain size distributions as the crushed glass tested in the laboratory. These soils consisted of Sands of grain sizes ranging from 0.05 mm to 2.0 mm according to the USDA textural classification. The soils had a non detectable clay content, and their porosity ranged from 0.35 to 0.45. The hydraulic conductivities of the soils plotted on the figure however, ranged from a minimum value of 3.89×10^{-4} cm/s to a maximum value of 5.19×10^{-2} cm/s.

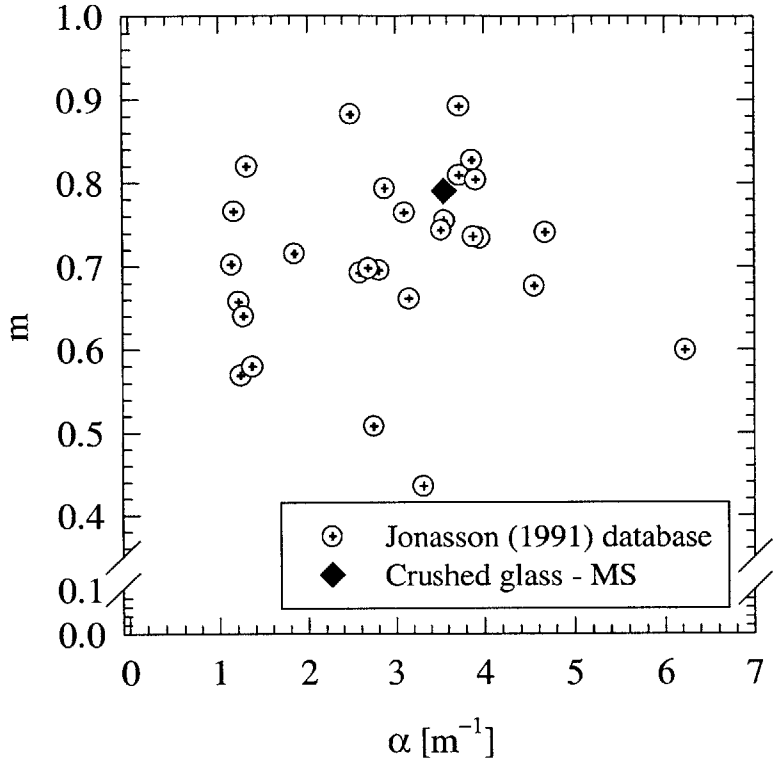

Figure 2-20 Variation in van Genuchten parameters for Sands (USDA classification) for Swedish soils compiled by Jonasson (1991).

The values of the van Genuchten parameters determined for the crushed glass are reasonable when compared to granular materials of similar characteristics. The range of α and m values presented in the Figure 2-20 however, would lead to drastically different estimates of air sparging plume sizes, if the van Dijke *et al.* (1995) model was used to predict the zone of influence of the steady-state plumes.

CHAPTER 3

CENTRIFUGE MODELING OF AIR SPARGING

3.1.INTRODUCTION

This chapter presents an overview of centrifuge testing, the experimental technique used to conduct the majority of the testing performed during this research study. The chapter is divided into two main sections, the first of which focuses on general aspects of centrifuge modeling. This initial section presents the basic principles of testing and modeling, and describes some of the problems resulting from testing at higher accelerations. Section 3.2 focuses on centrifuge modeling of air sparging specifically, presenting an evaluation of the experimental advantages that the technique offers in the study of the fundamental principles controlling the behavior of air flow through porous media.

3.2.GEOTECHNICAL CENTRIFUGE TESTING

3.2.1. Overview

In a field such as geotechnical engineering, in which both the mechanical and the hydraulic properties of soils are controlled by the state of stress of the material, the ability to replicate field conditions during testing is critical. A geotechnical centrifuge offers unique modeling possibilities in this respect, since it makes it possible to test, in the laboratory, the same material encountered in the field under the exact same stress and fluid pressure conditions that exist in-situ. This is done by subjecting a scaled model of the prototype to an inertial radial acceleration, such that the model in the centrifuge is effectively under a gravitational field many times stronger than the prototype under the Earth's gravity. The top surface of the soil model is therefore subjected to zero stress, while the magnitude of the stresses increases with depth as a function of the unit weight of the soil, as is the case in the prototype (Taylor 1995).

The principle behind centrifuge testing is illustrated in Figure 3-1. The behavior of a prototype subjected to the earth's gravity g, can be reproduced in the laboratory by a scaled model subjected to a centrifugal acceleration field of magnitude $n.g$. A centrifugal field $\omega.r^2$ is generated by rotating the model with an angular velocity of ω, at a distance r from the axis of the centrifuge. Stress distributions throughout the model and the prototype are the same, as long as the products of depth times acceleration for model and prototype are identical (Schofield, 1980).

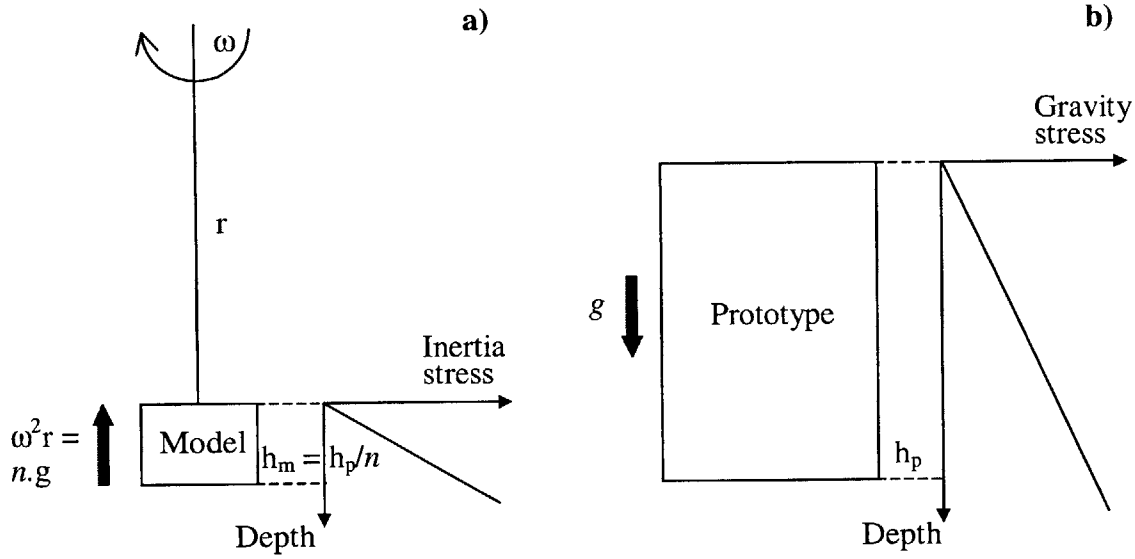

Figure 3-1 *Inertial stresses in centrifuge model (a) induced by rotation around fixed axis correspond to gravitational stresses in the corresponding prototype(b) (after Taylor, 1995)*

The expression *g-level* will be used in the remainder of this thesis to refer to the acceleration field that is applied to a centrifuge sample, as the gravitational field is increased by the factor n. For instance, a g-level of 100, or a 100-g field refers to an acceleration 100 times greater than the Earth's gravity, and to an n factor equal to 100.

3.2.2. Scaling Laws

Centrifuge modeling requires that scaling laws be derived in order to ensure similarity between the model and prototype. These laws relate the variables measured in the model (*i.e.* velocities, time for breakthrough) to the actual processes occurring in the prototype. The fundamental scaling law is obtained from the condition of *stress similarity*, which requires that stresses in the model and the prototype be equal. Hence, if an acceleration of n times the Earth's gravity g is applied to a material of density ρ, then the total vertical stress σ_m, at a depth h_m in the model is given by Equation 3-1 (Taylor, 1995):

$$\sigma_m = \rho \cdot n \cdot g \cdot h_m \qquad \text{Equation 3-1}$$

In the prototype, the total vertical stress σ_p is given by Equation 3-2:

$$\sigma_p = \rho \cdot g \cdot h_p \qquad \text{Equation 3-2}$$

As a result, for σ_m to be equal to σ_p, h_m needs to be equal to h_p/n, which leads to a $1/n$ scaling ratio model-to-prototype for linear dimensions (Taylor, 1995). Table 3.1 presents a summary of the scaling relationships that apply to centrifuge modeling of flow problems, adapted from work by Culligan and Barry (1998).

Table 3-1 Centrifuge scaling relationships

Variable	**Model/prototype ratio**
Gravity, g	n
Macroscopic length, z	$1/n$
Microscopic length, d, and porosity, ϕ	1
Fluid pressure, p	1
Fluid velocity, u	n
Fluid density, ρ, viscosity, μ, and interfacial tension, σ	1

Special attention needs to be given to the scaling of time in centrifuge modeling. The scaling factor for time derived from similitude analysis of problems not influenced by inertia is $1{:}n^2$, such that $t_m = t_p/n^2$ where t_p is the time in the prototype and t_m is the time in the model (Arulanandan *et al.*, 1988). This scaling factor implies that an event that occurs in the prototype in the course of one day, can be reproduced in the centrifuge by subjecting the scaled model to an acceleration of 100-g for 8.64 seconds.

Time scaling has significant implications to seepage processes, and as noted by Taylor (1995), the interpretation of its impact on centrifuge modeling practices has created a certain amount of controversy. Two opinions exist currently concerning the effect of time scaling on the definition of hydraulic gradients and hydraulic conductivities. The discussion presented by Taylor (1995) is summarized in this section.

The one-dimensional expression for Darcy's seepage velocity is given by the equation:

$$v = K \,.\, i \qquad \text{Equation 3-3}$$

in which v is the superficial velocity of seepage flow, K is the hydraulic conductivity of the soil, and i is the hydraulic gradient. It has been already noted that the velocity of flow in a centrifuge model is n times that of the prototype, such that $v_m = n.\ v_p$. To satisfy this scaling relationship, according to Equation 3-3, either the hydraulic conductivity or the hydraulic gradient need to be scaled. The controversy on the velocity scaling hinges of which of these two parameters is dependent on the acceleration field.

The first camp of opinion states that the hydraulic gradient is a dimensionless ratio between two lengths that are themselves scaled, and that therefore it is independent of g-level. If the hydraulic conductivity of the material is expressed in terms of its intrinsic permeability, the following expression exists:

$$K = \frac{k \cdot k_r \cdot \rho \cdot n \cdot g}{\mu} \qquad \text{Equation 3-4}$$

in which k is the intrinsic permeability of the soil, k_r is the relative permeability and μ is the viscosity of the pore fluid. Equation 3-4 states that if the same pore fluid is used in the model and the prototype, the hydraulic conductivity of a material is a function of acceleration field, such that $K_m = n.\ K_p$ This interpretation implies that the intrinsic permeability k is the fundamental parameter characterizing a soil, whereas K needs to be scaled with g-level.

The second camp in the debate states that the K is indeed a fundamental material property which does not depend on the acceleration field. The hydraulic gradient however, is treated as a ratio of pressure drop over distance, and interpreted as a parameter representative of a pressure gradient through a soil. From the original principle of similitude, since pressures are the same in the model and the prototype whereas distances are reduced by n, then this definition of hydraulic gradient clearly implies that i scales with g-level, and that $i_m = n.\ i_p$ (Taylor, 1995).

The end result of both interpretations is that seepage velocity increases in the model relative to that in the prototype. The two approaches however, may lead to different ways of interpreting results from centrifuge modeling experiments, as will be shown in later chapters of this thesis.

Having presented all the scaling relationships it must be noted that the centrifuge experiments conducted as part of this research study did not fully comply with the scaling laws presented in Table 3-1. Given the dimensions of the centrifuge platform and of the box, conforming with the linear dimension scaling law at high g-levels would have involved injections through samples with very small phreatic surface elevations. At these minimal elevations it would have not been possible to observe the propagation of air plumes. As a result, experiments were conducted on samples with approximately constant phreatic surface elevations, under increasingly high g-levels. The magnitude of the stresses and fluid pressures was therefore increasing with g-level, as was the injection pressure necessary for entry. Since the actual dimensions of the model were not being scaled, interpretation of experimental results will have to be performed with care, such that comparisons between results corresponds to equivalent prototypes.

3.2.3. Variation of gradient with g-level

As the acceleration field increases in the centrifuge, the magnitude of the pressure gradients driving fluid flow is significantly altered, and buoyancy forces acting on a submerged body increase in direct proportion to g-level. For the specific case of air sparging experiments conducted at high g-levels, the pressure difference between entry pressure and the pressure at the phreatic surface also increases with g, as is illustrated in Figure 3-2. The figure shows the variation of entry pressure P_{entry}, with elevation at three different g-levels, namely n = 1, 10 and 50. Elevation 0.0 corresponds to the top of the injection point while El. 1.0 represents the phreatic surface. Also included in the figure are the values of the injection pressures P_{inj} corresponding to the different g-levels.

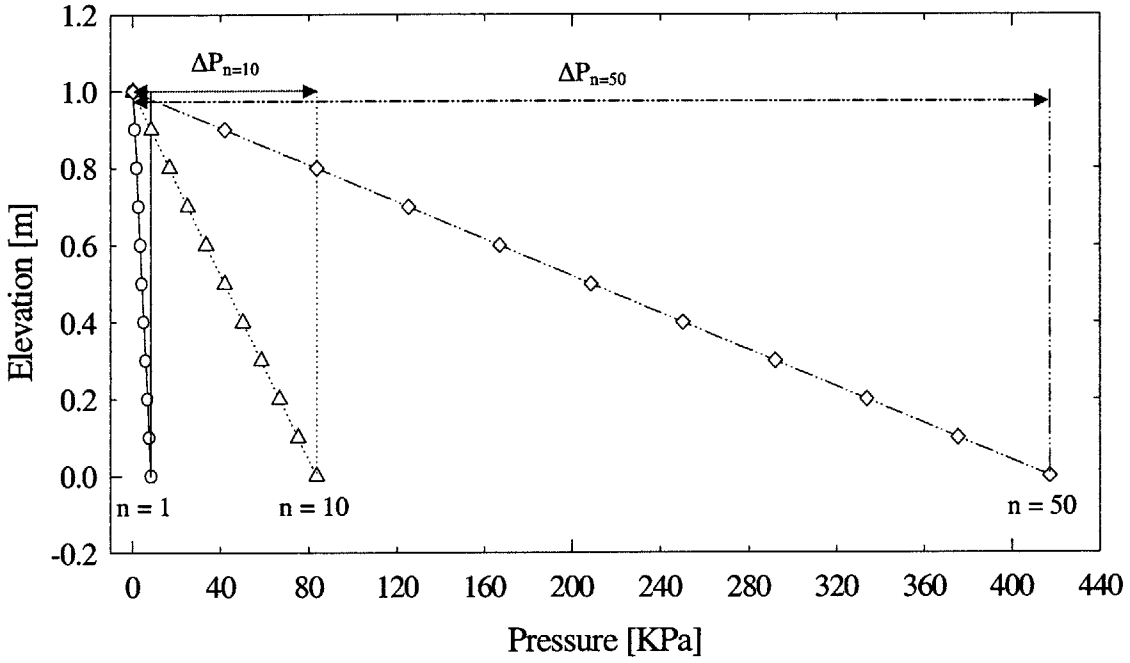

Figure 3-2 *Variation of pressure difference with elevation at increasing g-levels ($\Delta P = P_{inj} - P_{entry}$). Symbols illustrate air entry pressures at different elevations while lines represent injection pressures.*

At this point of the discussion it is assumed that pressure in the air phase remains constant with elevation, and equal to that at the injection point, P_{inj}. It is quite clear from the figure that the difference between entry pressure and pressure in the air phase, ΔP, increases drastically with g-level as the phreatic surface is approached. Pressure

gradients will therefore be very large at increasing *g*-level, and will further increase with decreasing elevation.

3.2.3.1.Darcy's law

In addition to the similarity condition imposed on stresses, when centrifuge modeling involves problems associated with flow through porous media, it is necessary to maintain the validity of Darcy's law. This condition can be satisfied if the Reynolds number *Re* is maintained below a value of 1 (Arulanandan *et al.*, 1988). This condition will be checked for all the experiments presented in this research study.

3.2.4. Particle Size Effects

As is shown in Table 3-1, microscopic lengths, namely the grain-size and pore dimensions of the material tested in the centrifuge, are not scaled with *n*. The same material is therefore tested at increasing gravitational accelerations, assuming that the size of the particles is unaffected by *g*-level.

The influence of soil particle size during centrifuge testing is a topic which has received considerable attention from the centrifuge modeling community. The relative sizes of soil grains and structural elements or boundaries, and specifically the need to reduce the size of soil particles by a factor *n*, has been considered by a number of investigators (Bolton and Lau, 1988; Goodings and Gilette, 1996). One of the assumptions behind centrifuge testing is that a soil with grains sufficiently small that it behaves as a continuum at the scale of the prototype will also behave as a continuum in the model (Goodings and Gilette, 1996). Results of slope stability, bearing capacity, and pile behavior for example, have shown that minimum model dimensions exist under which grain size begins to influence model behavior (Bolton and Lau, 1988; Goodings and Gilette, 1996). However, it has also been noted that since the behavior of soil particles is not exclusively dictated by their size but is also influenced by their mechanical and surface properties (*i.e.* stress-strain behavior, chemical interactions between particle surfaces and pore fluids), the effects of particle size are not critical in all cases (Taylor, 1995).

In the case of air sparging, surface particle effects are in most cases not relevant. Surface effects are for the most part observed in clays and air sparging would ordinarily not be used for cleanup of clayey deposits. However, particle size effects could, indeed, be significant during centrifuge modeling if, as discussed by Taylor (1995), the operation of an air sparging well on a very coarse granular soil was being modeled at high centrifugal accelerations. In such a situation, soil particle size could be significant relative to model dimensions, and considerations would need to be made with regards to the relative size of the injection well for example.

3.2.5. Stress Variations in Centrifuge Models

The Earth's gravitational acceleration acting on a prototype is effectively uniform with depth. When a model is subjected to an acceleration field in the centrifuge on the other hand, a slight increase in acceleration occurs with depth. This increase originates from the fact that the acceleration in the centrifuge varies radially, and therefore increases with depth of the model (Schofield, 1980). Figure 3-3 illustrates the magnitude of the difference between the stresses computed for a centrifuge model and those for its corresponding prototype.

The non-linear variation of the stresses in the model can be estimated, and an exact correspondence in stresses exists between model and prototype at two-thirds of the model depth. Furthermore, if the radius from the centrifuge axis to the top of the model is R, then the vertical stress at depth z in the model can be determined from Equation 3-4 (Taylor, 1995):

$$\sigma_m = \int_0^z \rho \cdot \omega^2 \, (R + z) \, dz = \rho \cdot \omega^2 \cdot z \left(R + \frac{z}{2} \right) \qquad \text{Equation 3-5}$$

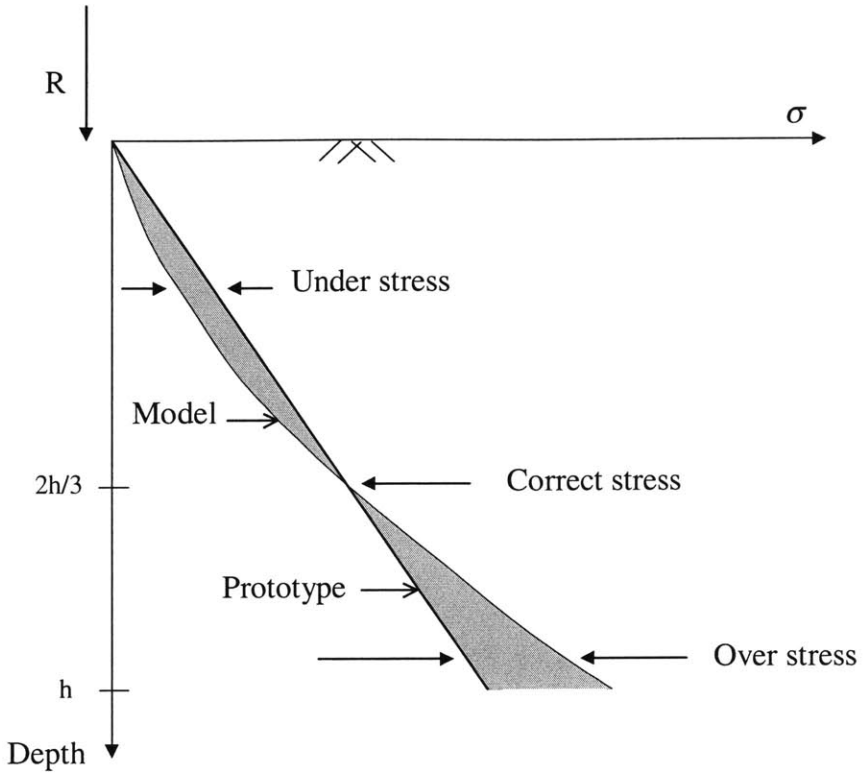

Figure 3-3 *Stress variation with depth in centrifuge model and its corresponding prototype (after Schofield, 1980).*

3.2.6. Modeling of Models

Comparisons between centrifuge tests conducted under different *g*-levels is done through the principle of *modeling of models*. Experiments are conducted using models at different scales subjected to different *g*-levels. If the product of length times acceleration for the different models is the same, then experimental results are expected to be repeated in the various models (Schofield, 1980). Ko (1988) illustrated the modeling of models technique using Figure 3-4. Modeling of a 10 m-high prototype could be done 1) at full scale under the Earth's gravitational acceleration (point A_1); 2) at $1/10^{th}$ scale in a centrifuge spinning at 10-*g* (point A_2); 3) at $1/100^{th}$ scale in a centrifuge at 100-*g* (point A_3); or at any other combination of size and acceleration provided that boundary conditions and size effects do not interfere with the behavior of the model as discussed in section 3.2.2.1 (Ko, 1988).

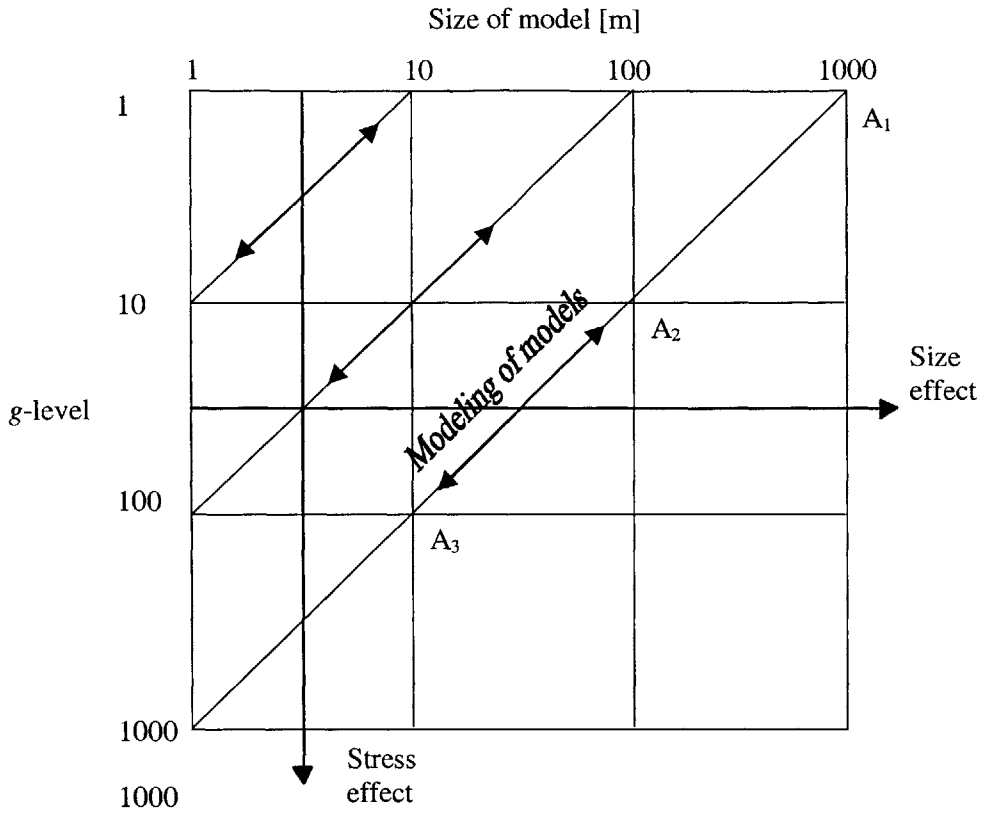

Figure 3-4 Principle of modeling of models (after Ko, 1988)

3.3.CENTRIFUGE STUDY OF GOVERNING MECHANISMS

3.3.1. Experimental Injection Pressures

The study of air sparging in the centrifuge offers unique advantages. Testing in the centrifuge makes it possible to reproduce in-situ stress and fluid pressure distributions, ensuring that the modeled values of air entry pressure, hydrostatic pressure, and hydraulic conductivity are representative of the prototype problem. No other experimental method, outside full-scale testing, offers the same advantages as centrifuge testing in this respect.

When the governing equations for air sparging, 2-1 and 2-2, which refer to prototype conditions, are rewritten for the centrifuge model, they become:

$$(P_{inj})_{min}\Big|_{model} = P_{hyd} + P_{capil} = \rho_{pf} * ng * \frac{h_{wt}}{n} + \frac{4*\sigma_{g/pf} * \cos\theta}{D} \qquad \text{Equation 3-6}$$

and

$$(P_{inj})_{max}\Big|_{model} = K_0 * \left(\rho_{sat} * \frac{h_s}{n} - \rho_{pf} * \frac{h_{wt}}{n} \right) * ng \qquad \text{Equation 3-7}$$

Experiments under increasingly higher injection pressures can be conducted while maintaining the overall stability of the system. As shown by Equation 3-6, the value of the minimum injection pressure increases as a function of *g*-level. Air flow patterns under a wide range of injection pressures and air flow rates can be investigated directly, without exceeding the maximum pressure requirements imposed by Equation 3-7. A number of investigators have suggested that increasing air injection pressure increases air channel density and air saturation (Marley *et al.*, 1992; Ahfeld *et al.*, 1994; Brown, 1995). Others have maintained that after an initial increase in air saturation, increasing injection pressure does not result in significantly higher saturations (Baker and Benson, 1996). It is likely that the laboratory experiments, in which the effect of higher injection pressures on air flow patterns has been investigated, have caused fracturing of soil samples, as the injection pressures exceed in-situ effective stresses. Ji *et al.* (1993) for example, report "fluidization" of their porous media as air injection pressure is increased beyond the critical value. If an injection pressure gradient (ΔP) is defined as:

$$\Delta P = P_{inj} - \rho_{pf} * ng * \frac{h_{wt}}{n} \qquad \text{Equation 3-8}$$

then the effect of increasing injection pressure can also be evaluated over a wider range than what would be possible in reduced-scale experiments conducted at 1-*g* in the

laboratory. It is very likely that air flow regimes vary as air pressures through the soil increase, as was the case for flow of air in pure liquids.

3.3.2. Dimensionless Numbers

Centrifuge testing provides an additional tool to investigate the fundamental mechanisms that control the flow of air through porous media. Air injected into the ground rises upward under the effect of buoyancy forces. The density contrast between injected air and pore fluid is considerably large, and therefore buoyancy forces play a very significant role in the development of air flow patterns though saturated soils. Conversely, capillary forces are inversely proportional to the pore size diameter of the porous media, and will act to entrap the injected air, opposing the action of buoyancy forces. Viscous forces effectively act in conjunction with capillary forces to increase the extent of the area affected by a sparging well. Of particular interest to this research study will be to determine whether the relative importance of these three types of forces determines the characteristics of air flow through a saturated porous material.

Experiments in the centrifuge can be designed such that a wide range of buoyancy-capillary-viscous conditions are considered, while maintaining conditions that are realistic of field situations. Indeed, buoyancy forces can easily be increased during by increasing the gravitational acceleration imposed on the model. The equation for the Bond number can be rewritten for the centrifuge model as:

$$Bo|_{model} = \frac{\Delta\rho * ng * d^2}{\sigma} \qquad \text{Equation 3-9}$$

Capillary forces remain unchanged at higher *g*-levels, since microscopic lengths do not scale with gravity. Viscous forces can also be increased by centrifuge testing, either by increasing the injection flow rate or the injection pressure applied to the sample, without compromising the overall stability of the model.

The effect of increasing buoyancy on flow patterns of air through soils at constant capillary pressures can be therefore investigated during centrifuge testing, by observing

the behavior of a given centrifuge model subjected to a range of centrifugal accelerations. The relationship between displacing and entrapping forces in the medium, and their effect on observed flow regimes can thus be established using this technique.

CHAPTER 4

EXPERIMENTAL METHODS

4.1.INTRODUCTION

This chapter presents a description of the centrifuge facilities at MIT, along with an overview of the equipment and the procedures used in the experimental phase of this thesis. Section 4.2 describes the general characteristics of the MIT geotechnical centrifuge, the instrumentation used during testing, and the data acquisition system. Section 4.3 focuses on the centrifuge platform, where the sample box and the video camera were located during air sparging experiments. Sections 4.4 and 4.5 present both the equipment and the procedures followed during the two forms of experiments that were conducted, namely constant pressure and constant flow rate tests, respectively.

4.2.MIT GEOTECHNICAL CENTRIFUGE LABORATORY

4.2.1. Balanced Arm Centrifuge

Air sparging experiments were conducted using the balanced arm geotechnical centrifuge facility in the Department of Civil and Environmental Engineering, located in room 1-079. The MIT centrifuge, a Genisco Model 1231 G-Accelerator, can accelerate a 200-lb [91 Kg] package to an acceleration of 150-*g*, or a 150-lb [68 Kg] package to an acceleration of 200-*g* (Pahwa, 1985).

The centrifuge consists of an arm A on which two swinging platforms B and C are mounted, diametrically opposed to each other, as shown in Figure 4-1. The axle of the electric motor driving the centrifuge, D, is perpendicular to the arm of the centrifuge and located at its center as indicated by E. The arm is equipped with a pivot point at the center of rotation that facilitates static balance. As the arm rotates, platform B swings up about a trunnion F, such that the centrifugal force acts perpendicular to the platform at its center. The sample box is placed on platform B and a counterweight G is located on

platform C. The radius of the arm from the shaft to the trunnion is 42 inches [106.7 cm], and the base of the platform is 9.25 inches [23.5 cm] below the axis of the trunnion. The centrifuge is enclosed in a cylindrical shell H, made of a ¼-inch [0.64 cm] boiler plate (Pahwa, 1985).

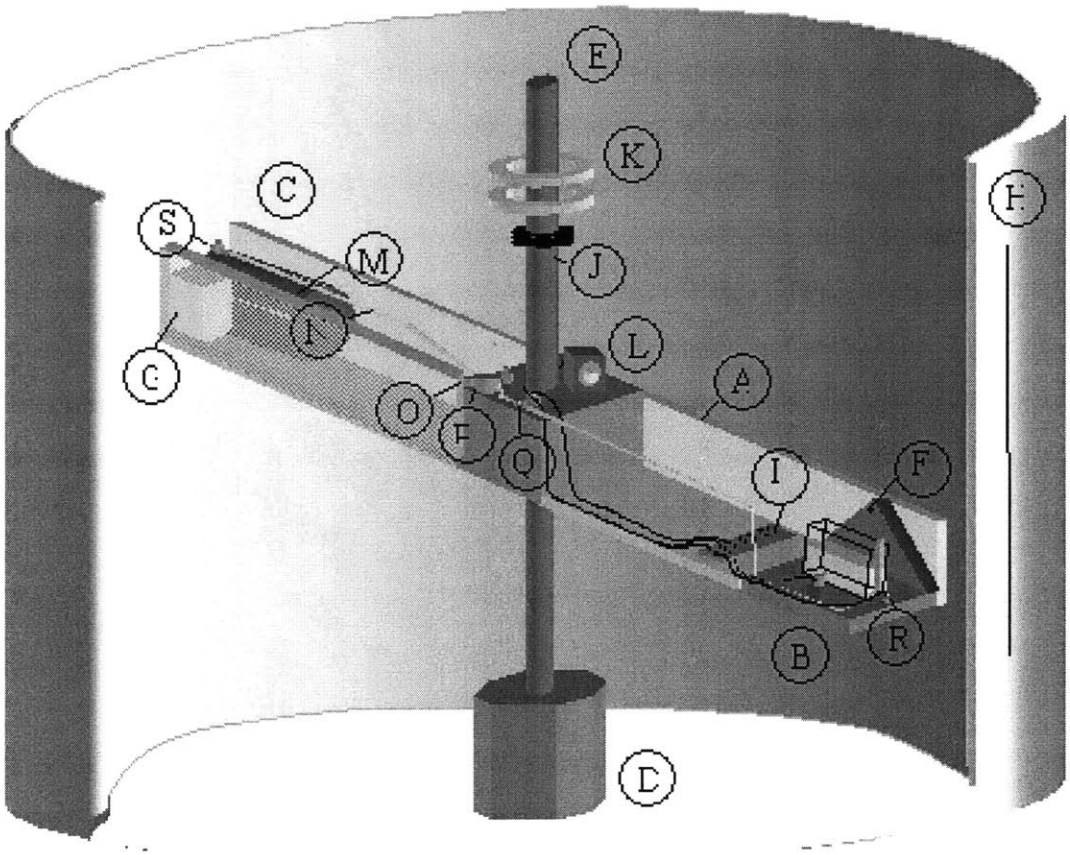

Figure 4-1 MIT Geotechnical centrifuge

Electrical connections needed for instrumentation, I, are made through a set of 24 slip rings, J, mounted on the shaft directly below the central lights K. All electrical cables are tightly bound by cable ties and held in place through a series of plastic supports glued onto the centrifuge arm. Testing can be monitored from the control room through a central camera L, also mounted on the arm, which spins as the arm rotates (Pahwa, 1985). The camera is an RCA TV Camera, model TC 2000, modified for

operation at high *g*-levels (Ratnam, 1996). Details of the sample box and all other equipment and instruments located along the arm will be provided in the following sections of this chapter.

Monitoring of experiments during centrifuge tests was done from the control room through an RCA monitor. All tests were recorded using a Quasar VCR. A summary of the contents of the 20 tapes containing records of all tests performed during this research is included in Appendix C. The VCR was connected to a time-date generator unit made by Panasonic (Model WJ-810). This unit made it possible to superimpose time, date, a stopwatch, and typed text on the images being recorded. All recordings are then labeled with the name of the experiment, the date and time when it was conducted, and a chronometer. Readings from this chronometer were used in computations of air flow velocity through the sample.

4.2.2. Centrifuge Controller

The operation of the centrifuge is computer controlled from the neighboring control room. The controller is run by a multipurpose microprocessor, through a controlling program written in FOURTH. The program makes it possible for the operator of the centrifuge to chose from three operating modes: 1) a MANUAL mode, which operates the centrifuge at operator specified parameters until directed to stop by a keyboard command; 2) a PROGRAM mode, in which the operator programs form one to fifteen "run sets" each containing its own defined set of operating parameters. The controller subsequently executes the sequence of "run sets" during centrifuge operation; and 3) a REMOTE mode, similar to the PROGRAM mode except that data are entered through a remote port (Genisco Operating Manual, 1985).

All the centrifuge experiments presented in this thesis were conducted under the PROGRAM mode. While in this mode, the controller operates the centrifuge using three variables:

1. Velocity, in rpm, states the target velocity of each "run set". All entries must be in the range of 0 to 410 rpm.

2. Time, in seconds, determines the duration of spin for each "run set". Entries must be in the range of 0 to 300 s.

3 Ramp, in seconds, determines the duration of the ramp time for each "run set". Entries must also be in the range of 0 to 300 s. This parameter can act as both an acceleration or a deceleration variable, and is only limited by the mechanical limits of the centrifuge (*i.e.* programmed ramps cannot be faster than the capabilities of the centrifuge itself).

Once the "run sets" have been programmed, the controller linearly ramps from one set to the following, according to the ramp time specified for that set. Once the new set is reached, the spin velocity is maintained constant until the run time for that set is exceeded. During a set, the spin velocity of the centrifuge and the remaining time in the set are displayed on the screen. At the end of the last "run set" in the program, the controller decelerates to zero velocity (Genisco Operating Manual, 1985). For additional details on the operation sequence or on the controlling program, the reader is referred to the operating manual of the centrifuge.

In reality, the spin velocity was not constant during a given set, and fluctuations in the order of +/- 1 rpm occurred. These were not judged to be significant to the overall progression of the experiment, and were ignored in the analysis. There was however, a discrepancy between the value of the target spin velocity entered by the operator and that reached by the centrifuge. The controller systematically "over-spun" the centrifuge relative to the target velocity specified. The difference between actual and programmed spin velocities was in the order of 5 to 8 rpm in excess. This difference decreased with time of operation, but remained significant regardless of time. With experience, the differences in spin velocity were predictable, and were accounted for in the values programmed into the controlling program.

4.2.3. Data Acquisition System

The data acquisition system used for centrifuge tests consisted of a 486 microprocessor personal computer outfitted with two data acquisition cards. The cards

held an analog to digital converter chip AD1170, manufactured by Analog Devices in Norwood, Massachusetts. The first card was set to a gain of 100, and was used to sample data from the pressure transducers. Since all the channels on the chip are gained simultaneously and since the output range of the chip is ±5 Volts, this card could only be used to sample the low voltage output instruments. The second card was then used without a gain, to sample input voltages and data from the tachometer.

The data acquisition program used was written by Dr. Kurt Sjoblom, and was adapted to be run in the centrifuge computer. The program is written in QBASIC, and a complete printout is included in Appendix A, Data Acquisition System. For additional details on the program, the reader is referred to Sjoblom (2000). The program sampled all channels every second, and data was computed to a 18-bit resolution with an integration time of 300 ms.

4.2.4. Instrumentation

In order to determine the injection air pressure at different points along the pressure line, two pressure transducers were used during air sparging experiments. The location of the transducers is indicated in Figure 4-1, as shown by Q and R. The first transducer provided a reading of the pressure of the air on the centrifuge arm, outside the pressure source. The second transducer recorded the injection pressure on the platform, at the entrance of the sample box. Both transducers were calibrated in the centrifuge, using the same electrical wiring that was used during testing.

The transducers used during the experimental series were manufactured by Data Instruments, and their specific characteristics are summarized in Table 4-1. Calibration curves are included in Appendix B, Calibration Data.

Table 4-1 Characteristics of Data Instruments pressure transducers

Model	Range	Excitation	Span	Calibration Factor	Location of transducer
DI A500	50 psi	5.0 V	100 mV ± 1mV	-2518.89 psi/V/V_{in}	Centrifuge arm
DI 2194	25 psi	5.0 V	100 mV ± 1mV	-1254.71 psi/V/V_{in}	Centrifuge platform
DI 2394	25 psi	5.0 V	100 mV ± 1mV	1264.22 psi/V/V_{in}	Centrifuge platform

A tachometer was mounted on the centrifuge shaft, which provided a continuous record of the centrifugal acceleration during tests at high *g*-levels. The tachometer essentially consisted of a frequency-to-voltage converter. Every rotation of the centrifuge sent 600 pulses through the circuit, which converted them into a DC voltage output. This voltage was subsequently calibrated and used to determine angular velocity of the centrifuge arm, in rpm. The tachometer was connected to the data acquisition system through the slip rings, which made it possible to store values of the angular with time of testing. The tachometer was built by doctoral candidate Laurent Levy, and a detailed description of its design will be included in his dissertation.

4.3.EXPERIMENTAL SETUP

4.3.1. Sample Box

The fluid pressures and soil stresses acting on the walls of a centrifuge sample box can become substantial as the *g*-level increases during a centrifuge experiment, and therefore resistant sample containers, referred to as strong boxes, are used for testing.

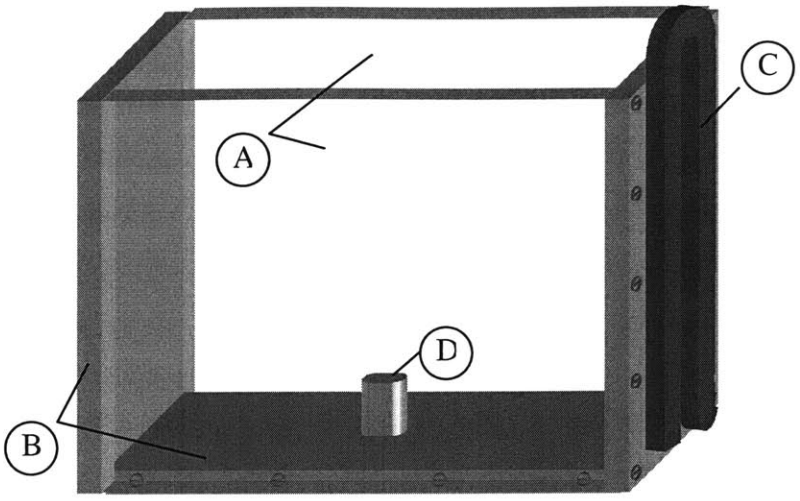

Figure 4-2 Centrifuge strong box

All air sparging experiments were conducted in a strong box of internal dimensions 30 x 28 x 10 cm. The front and back panels of the box were made of ¼ inch-thick pieces of transparent Lexan A, while the sides and the base of the box were made of ¼ inch-thick pieces of aluminum B, as shown in Figure 4-2.

Air was injected into the box through a cavity drilled into the base plate. As shown in Figure 4-2, the cavity connected the external tubing C, through which air was supplied to the box, to the injection port located at the center of the base of the box D. The outside tubing consisted of an inverted u-shaped aluminum tube, which curved above the top edge of the box in order to keep fluids from draining out during sample preparation. Injection ports consisted of 2 cm-high replaceable brass fittings that were screwed on to the base of the box. An o-ring was used between the injector and the base plate to maintain a tight seal, and to avoid air leaking out from the connection into the saturated medium. The strong box was filled with granular material and subsequently saturated following sample preparation procedures described in detail in Chapter 5.

4.3.1.1.Air sparging injectors

The influence of injection port geometry on the characteristics of air flow through the saturated medium was one of variables investigated in this study. Six different injection port geometries were tested under constant pressure and constant flow rate conditions, and the characteristics of the resulting air plumes were compared. An additional injection port was obtained by modifying one of the injectors' geometry, as explained below.

Two types of geometries were tested, as depicted in Figure 4-3: 1) three multiple port injectors, *MPI*s, which consisted of 2 cm-high brass fittings with four rows of 12 equally-spaced circular orifices around the sides; and 2) three single port injectors, *SPI*s, consisting of brass fittings with only one circular orifice on the top face.

The geometric characteristics of the injectors were selected in order to better understand the behavior of injected air through soils. Single port injectors for instance, are not representative of those that would be found in actual IAS applications. However, as was discussed in Chapter 2, bubble flow from single orifices in pure fluids and in fluidized beds has been studied extensively, and a number of correlations exist for these systems that predict bubble velocities as a function of injector orifice. The idea behind the design of the SPIs was therefore that of simplifying, as much as possible, the entry characteristics of air in porous media, such that comparisons between flow through pure liquids and flow through saturated porous media could be made. If bubbly flow conditions through porous media did indeed take place, injecting air through SPIs would make it possible to follow the trajectory of individual bubbles released from a localized orifice into a porous medium. Additionally, using SPIs made it feasible to evaluate the relative importance of orifice opening and pore size diameter to the overall characteristics of air flow in soils. By varying the diameter of the injection orifice, the diameter of the bubbles released into the medium was varied in such a way that bubbles both greater and smaller than the average pore size diameter of the soil were formed. The effect of exit diameter of the injected air on the resulting plume shapes could therefore be evaluated.

Conversely, MPIs were designed as a simplified version of injection screens typically used in field applications. Although tracking of individual bubbles was not

possible with these injectors, they provided a more uniform and realistic air flow field. The characteristics of the injectors used in the air sparging experiments are summarized in Table 4-2. Three different orifice diameters were used for each injector, namely 2 mm, 1 mm and 0.5 mm. A seventh injector, Injector 2b, is included in Table 4-2. This injector was obtained by blocking three rows of orifices on Injector 2, in order to obtain the same area of injection as that of Injector 3. This was done by covering the orifices with aluminum foil and sealing it in place with a coat of epoxy.

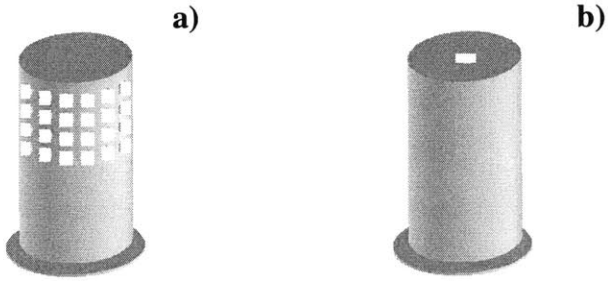

Figure 4-3 *Schematic of air sparging injectors: a) Multiple Port Injector (MPI); b) Single Port Injector (SPI). Injectors were 2 cm in height by 0.8 cm in diameter.*

Table 4-2 *Characteristics of air sparging injectors*

Injector Type	Injector Name	Number of Orifices	Orifice Diameter [mm]	Total area of injection [mm^2]
MPI	MPI #1	48	2.0	150.8
MPI	MPI #2	48	1.0	37.7
MPI	MPI #3	48	0.5	9.4
MPI	MPI #4	12	1.0	9.4
SPI	SPI #1	1	2.0	3.1
SPI	SPI #2	1	1.0	0.8
SPI	SPI #3	1	0.5	0.2

4.3.1.2.Wire mesh screens

As will be explained in Chapter 8, air sparging tests were initially conducted in pure liquids in order to study the characteristics of gas-liquid flow in the experimental

setup. In addition to these tests, a second series of experiments was conducted in pure liquids, in which air was injected into the box and was then forced to flow through wire mesh screens of varying apertures. Figure 4-4 shows a sketch of the screen rack that was built to fit into the strong box. The rack A was designed to support rectangular screens at adjustable elevations from the base of the box. The walls of the rack were made with transparent Lexan, which made it possible to see through the front of the box and observe the bubbling patterns. The screens consisted of an aluminum frame B and an interchangeable strip of wire mesh C. The objective of the screens was to provide a uniform restriction of known dimensions to the vertical air flow. The screens were therefore the first approach at characterizing the flow of air bubbles through constrained passages.

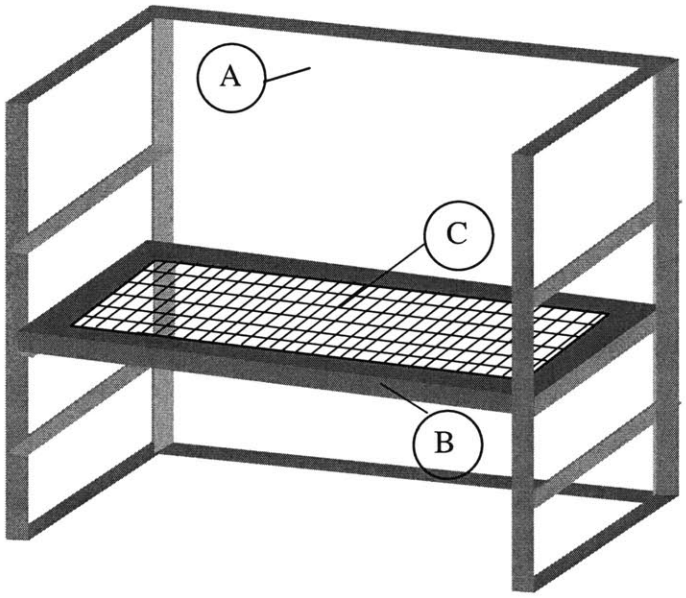

Figure 4-4 Wire mesh screen and Lexan rack

4.3.2. Preparation of Centrifuge Experiments

4.3.2.1.Setup of platform

Figure 4-5 illustrates the characteristics of the centrifuge platform. The strong box A was bolted onto a one-inch aluminum plate B, which was in turn bolted onto the

centrifuge's swinging platform. The details of the sample box have been included in Figure 4-2. A T-connector located on the side of the box connected its external tubing system E to the pressure line F and to a pressure transducer G. The pressure line ultimately led to the pressure source as was shown in Figure 4-1, while the pressure transducer provided readings of injection air pressures as air entered the box. A fluorescent light source C was located behind the strong box, making it possible to observe the flow of air through the sample while in flight. A wide-angle CCD micro-camera D, manufactured by Panasonic (Model GP-KS162), was also bolted onto the platform directly in front of the box, with which a continuous record of all experiments was obtained. The control unit for the camera was located on the centrifuge arm. The camera was powered by a 12 Volt DC voltage that was also supplied through the slip rings. The output from the control unit was brought into the centrifuge control room, were it was both displayed on a TV monitor and recorded on a VCR. The progression of the air front as is flowed through the saturated medium was then followed and a continuous record was taped, as the experiment progressed.

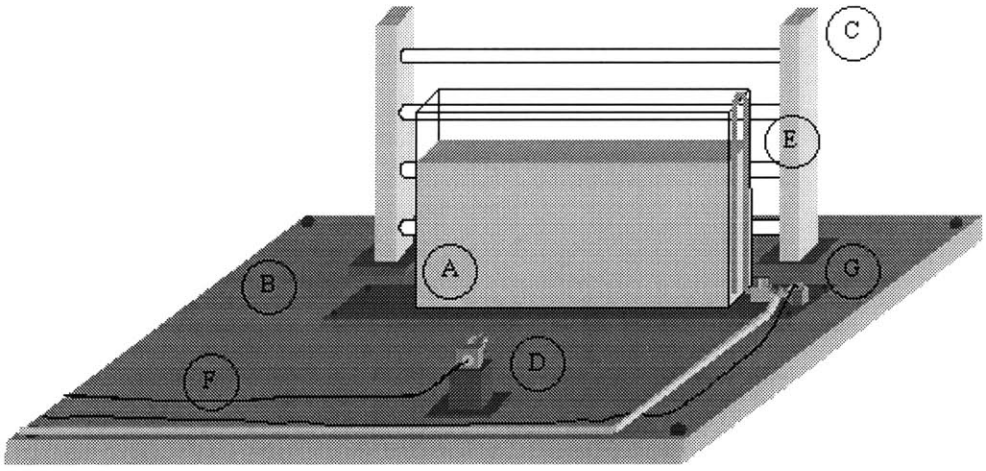

Figure 4-5 Setup of the centrifuge platform

4.3.2.2.Centrifuge setup

The specific procedure for testing, depending on whether the experiment was conducted under constant pressure or constant flow rate conditions will be explained, in detail, in the following two sections. Independent of the type of test conducted however, once the platform was loaded and all of the pressure connections were made, the centrifuge balance had to be checked. This was done by releasing the safety lever on the centrifuge arm and letting the arm equilibrate on its pivot point. The counterweight was adjusted until the weight of the two platforms was the same. At this point the safety lever was re-engaged, and the centrifuge was ready for testing.

Depending on the specific experiment to be conducted, an acceleration sequence was programmed into the centrifuge controller. Given the discussion presented in Chapter 3, the angular velocity of the centrifuge, ω, for a desired g-level, was calculated using Equation 4.1:

$$\omega = \sqrt{\frac{n \cdot g}{R}} \qquad \text{Equation 4-1}$$

in which ω is given in rad/s, n is the target gravity level (*i.e.* for a target acceleration of 10-g, n = 10) , and R is the radius of rotation. The units of ω had to be converted to rpm before being entered in the controller program (2π rad = 1 revolution), and an average value of R had to be selected. A value of R of 1.2 m (47 inches) has been used in the past (Ratnam, 1994), and a tabulated correlation between n and ω for this value of R exists. This was the value used in the initial calculations, but stress and fluid pressure calculations were later adjusted for variations of g-level with depth in the model.

Ramping intervals were carefully chosen to allow sufficient time for the centrifuge to reach the desired spin velocity. The help of Stephen Rudolph, an experienced centrifuge operator, was crucial in gaining experience with the choice of ramping intervals at the beginning of the experimental phase.

4.4.PROCEDURE FOR CONSTANT PRESSURE EXPERIMENTS

4.4.1. Experimental Setup

The first type of air sparging tests conducted were constant pressure experiments. With the knowledge of the position of the phreatic surface of the prepared sample and the *g*-level at which the experiment was to be conducted, injection pressures were calculated and set be fractionally higher than the air entry pressure at the injection port, as given by Equation 2-1.

Gas at constant pressure was supplied to the sample box from the compressed cylinder M located on platform C, as shown in Figure 4-1. Compressed nitrogen was used as the injection gas. The tank was refilled after one or two experiments depending on the duration of sparging, to ensure that injection pressures could be maintained throughout the entire experiment. The pressure line N carrying air from the cylinder to the sample box was made of rigid plastic tubing and strongly secured to the rotating arm by cable ties. This line connected the cylinder to an electronic solenoid valve O which could be operated from the centrifuge control room. The solenoid valve operates with an input voltage of 12 Volts, and only opens when a pressure front is detected at its entrance port. The valve would be opened in flight, allowing air to flow into the strong box. A pressure regulator P and a 50 psi pressure transducer Q were located immediately following the valve along the line, which were used to set exit pressures from the cylinder to the calculated injection pressures. The transducer also provided continuous measurements of the source pressure throughout the test. The pressure line continued along the other half of the rotating arm until it reached a second pressure transducer R (25 psi), located immediately outside the strong box on the swinging platform. This transducer provided a continuous reading of the air injection pressure. This transducer was connected directly onto the outer u-shaped metal tubing that lead to the injection port inside the sample box. Details of these connections are also illustrated in Figure 4-5.

Spinning of the box under would begin once the data acquisition system, the video recording unit, and the digital chronometer had been started.

4.4.2. Testing Procedures

Given the small vertical dimension of the sample box, the required entry pressure at 1-*g* was very low, and therefore most constant pressure tests were conducted at *g*-levels higher than 1-*g*. As was mentioned in section 4.2.2, the centrifuge tended to over-accelerate relative to the target value set in the acceleration sequence. With experience, the over acceleration could be predicted relatively well and target values were set accounting for a predicted excess in *g*-level. However, injection pressures were set prior to initializing the centrifugal motion and could not be adjusted during experiments. If the injection pressures were set too high for the *g*-level at which the test was ultimately conducted, then air entry would occur at an excessive pressure. Since samples could only be used once, the centrifuge was programmed to reach an acceleration slightly higher than that at which sparging (at the set injection pressure) was to initiate. The centrifuge was then programmed to decelerate at a very slow rate, maintaining long holding periods in between constant acceleration ramps. The electronic valve was opened once deceleration started, such that the exact acceleration and pressure at which breakthrough occurred could be recorded. The valve was maintained open until steady-state conditions were reached, defined here as the point at which the shape of the plume ceased to change.

A step by step procedure of constant pressure injection tests can be summarized as follows:

1. The sample box was bolted onto the platform, all cables were fastened, and the arm was balanced.
2. The nitrogen cylinder was refilled. This was done by wheeling a standing nitrogen cylinder into the centrifuge room and transferring gas into the centrifuge tank.
3. The injection pressure (source pressure) was set corresponding to the *g*-level at which testing would take place. This was achieved by closing the entrance valve on the sample box (H on Figure 4-5), opening the exit valve on the centrifuge pressure tank (S on Figure 4-1), and opening the solenoid valve O. The pressure would be adjusted through regulator P according to readings given by transducer Q. Since adjustment of the pressure had to be done from the center of the arm, a voltmeter was temporarily connected to the electrical ports on the centrifuge arm, through which the transducer readings could be monitored. Once the target injection pressure was reached the solenoid

valve was shut off, the pressure line was vented to relieve any excess pressure, and the entrance valve on the sample box was opened. It is clear that the valve on the centrifuge tank also remained open throughout the test.

4. The centrifuge door was closed, the computers and video recorder were turned on, and acceleration started.

5. As was explained above, once the target acceleration level was reached, very slow deceleration steps initiated. This made it possible to reach the accurate *g*-level at which sparging was meant to occur. The solenoid valve was opened once these ramping down steps started.

6. Breakthrough would typically occur within seconds after air was first observed at the injection point. The experiment would continue until no further changes in plume geometry were observed. If *g*-level remained approximately constant (within the range of the fluctuations previously cited), plume geometry would not change at all after the first few seconds of injection.

7. The solenoid valve was then shut off, the data acquisition system and the recording devices were stopped, and the centrifuge was brought to a halt.

8. The sample box was then dismounted and saturation procedures, as will be described in Chapter 5, were initiated.

4.5.PROCEDURE FOR CONSTANT FLOW RATE EXPERIMENTS

4.5.1. Experimental Setup

Air sparging experiments at constant injection flow rate were also performed in the centrifuge, using a different injection apparatus. Tests were conducted at flow rates which ranged from very low to intermediate, and the equipment used varied accordingly. Only low flow rate tests were conducted at increased *g*-levels mainly due to constraints securing the equipment at high accelerations.

Two types of experiments were conducted at 1-*g*: 1) tests at very low flow rates, ranging from 0.26 cm^3/s to 2.6 cm^3/s; and 2) tests at intermediate flow rates, ranging from 3 cm^3/s to 28 cm^3/s. The first type of tests were performed using a pressure volume controller (PVC) similar to the ones used throughout the geotechnical laboratories. The

second type of tests was conducted using a flow meter and a metering valve directly connected to the nitrogen cylinder. The characteristics of each setup are described in the following sections.

4.5.1.1.Tests with Pressure Volume Controller

As mentioned before, Pressure Volume Controllers (PVCs) are used throughout the geotechnical laboratories for a number of triaxial testing applications. A PVC unit consists of a piston housed in a stainless steel cylinder driven at a constant rate by a DC motor. An electronic control unit is used to control the voltage supplied to the motor, such that the flow rate pushed by the piston out of the housing cylinder can be adjusted as a function of the voltage supplied. A complete description of the PVC unit is provided by Sinfield (1997).

Two different PVC units were used during the course of testing. The first one was a standard unit used in the laboratories, consisting of parts made of brass. This unit was large and considerably heavy, and was used for constant rate of flow tests at 1-*g*. When higher *g*-level experiments at constant rate of flow were started, it became clear that it would not be feasible to mount that specific PVC on the centrifuge. The dimensions of the unit exceeded the available space on the arm, and its weight was a concern. As a result a second unit was used, which was that used by Sinfield (1997). This second unit was made of stainless steel parts, it was smaller, and lighter.

The PVC was mounted on the centrifuge arm and used to supply a constant rate of air flow to the sample. A new figure is not necessary to illustrate this setup, since it was virtually identical to the one used in constant pressure tests. Referring back to Figure 4.1, the PVC unit was bolted onto the center of the arm, at the location where the central camera L had previously resided. A three-way valve was located at the exit port of the unit, one side connected to the line which went through the pressure tank, the solenoid valve, the regulator, and the pressure transducer. The other side of the valve was directly connected to the pressure line that carried air to the sample box.

The motor driving the PVC was connected to the control box in the control room through the slip rings. Continuous readings could therefore be obtained of the voltage supplied to the motor, from which the resulting flow rate could be estimated. Calibration

of the PVC required a particular setup, which would allowed to measure a volume of air pushed by the piston per unit of time, for a given input voltage. This calibration was performed by measuring the volume of water displaced in a cylinder of known volume, per time. Figure 4-6 illustrates the setup used for this calibration. The calibration procedure was the same for both PVC units used in our experiments.

A 1000 mL glass graduated cylinder A was submerged, inverted, into a large container full of water, B. A piece of plastic tubing C was connected on one end to the exit valve E of the PVC unit D, while its other end was located inside the inverted glass cylinder. The motor driving the PVC was switched on, the piston was fully retracted, and a given input voltage was selected. The glass cylinder was held in place either manually or with a small weight. At the beginning of the calibration, the level of water in the cylinder was marked. As the piston started advancing and air started flowing through the tube, water in the cylinder was displaced by air and the water level decreased. The total change of water level in the cylinder was measured in a given interval of time, and from this value, a volume of air flowing into the cylinder was computed.

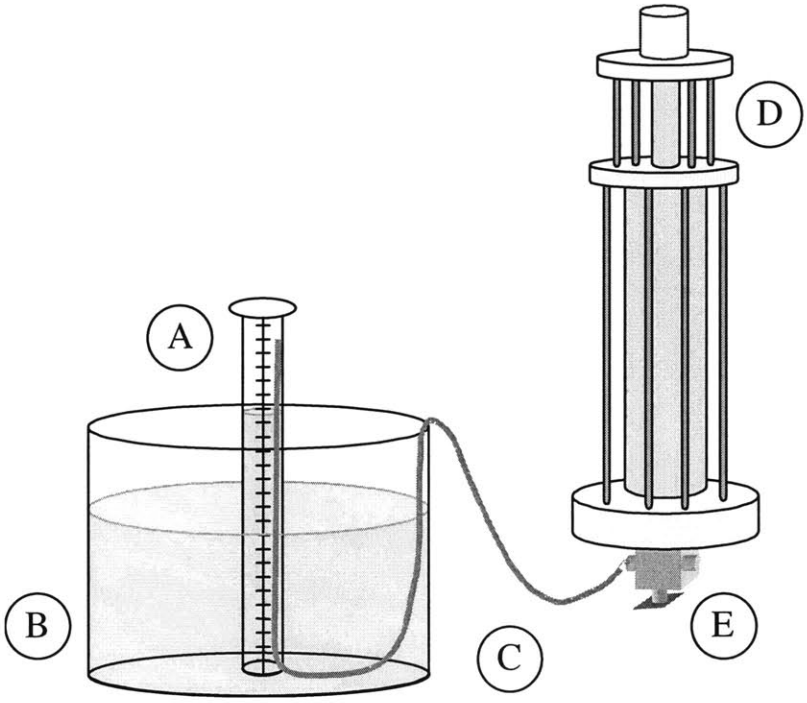

Figure 4-6 Calibration of Pressure Volume Control unit

This procedure was repeated a number of times for each input voltage, since readings of water levels down the cylinder varied considerably in some cases. A calibration curve was finally obtained which spanned the entire range of input voltages (20 Volts). The following two equations were fit through the calibration curves for the two Pressure Volume Control units used in this thesis. Equation 4-2 is valid for the first PVC used in experiments conducted a 1-*g*. Equation 4-3 is valid for the second unit, which was used at higher accelerations. Calibration curves for both PVC units are included in Appendix B, Calibration Data.

$$Q_{1-g} = 0.1317 \cdot V_{in} - 0.0013 \qquad \text{Equation 4-2}$$

$$Q_{high\,g} = 0.0654 \cdot V_{in} - 0.0146 \qquad \text{Equation 4-3}$$

in which Q is the flow rate of air out of the PVC *in* cm^3/s for a given input voltage *Vin, in Volts.*

The flow rates obtained from the two units were comparable, but as was mentioned at the beginning of this section, their magnitude was very low, with a maximum value of approximately 3.0 cm^3/s. The advantage of using the PVC was that they could be used in experiments under increasing *g*-levels, as opposed to the alternate apparatus, which will be described next.

4.5.1.2.Tests with flow meter

Constant rate of flow tests at flow rates ranging from 3 cm^3/s to 28 cm^3/s were conducted at 1-*g* only. The setup for these experiments is illustrated in Figure 4-7. Tests were conducted using a flow meter E in series with a metering valve A. The flow meter was manufactured by Meterate GPE, in the United Kingdom. The valve was also connected to a regulator C, immediately followed by the compressed nitrogen cylinder (not shown in the figure). The knob B on the metering valve made it possible to adjust the aperture of the orifice on the valve. By choosing a very small orifice diameter, the pressure drop through the valve was very large, and as a result, the exit flow rate was

approximately constant. Air then flowed through the flow meter, through a pressure transducer, and finally was injected into the sample.

The detailed procedure followed when running experiments using this setup will be addressed in the following section. Prior to conducting experiments however, the flow meter was calibrated. The calibration procedure that was followed was similar to that described for the PVC, in that the volume of water displaced from a cylinder was measured per unit time (see Figure 4-6). For increasing values of the pressure supplied to the metering valve and thus for increasing readings on the flow meter, the total volume of water displaced from a submerged cylinder was measured. The only additional step taken while calibrating the flow meter was that different curves of flow rate versus flow meter reading were plotted for different apertures of the valve. Calibrations curves are included in Appendix B. It was found that variations in orifice openings within the range allowed by the valve knob were not significant, and that the pressure drop through the orifice, for all openings, was sufficient to lead to approximately constant readings of flow rate. A linear regression through all the data resulted in the following calibration equation for the flow meter:

$$Q = 2.153 \cdot x - 4.239 \qquad \text{Equation 4-4}$$

in which Q is the flow rate *in units of* cm^3/s and x is the reading on the flow meter scale. The value of x ranges from 0 to 16 on the scale, and it is dimensionless. Inspection of Equation 4-4 would suggest a negative reading at zero flow rate. In reality, it was impossible to obtain a stable reading on the flow meter for values of x smaller than 3. Oscillations of the small ball in the inner tube were in the order of +/- one division, and it was ultimately decided not to run any experiments at such low range of flows. Experiments previously conducted using the PVC had in any case already covered the range of very small flow rates.

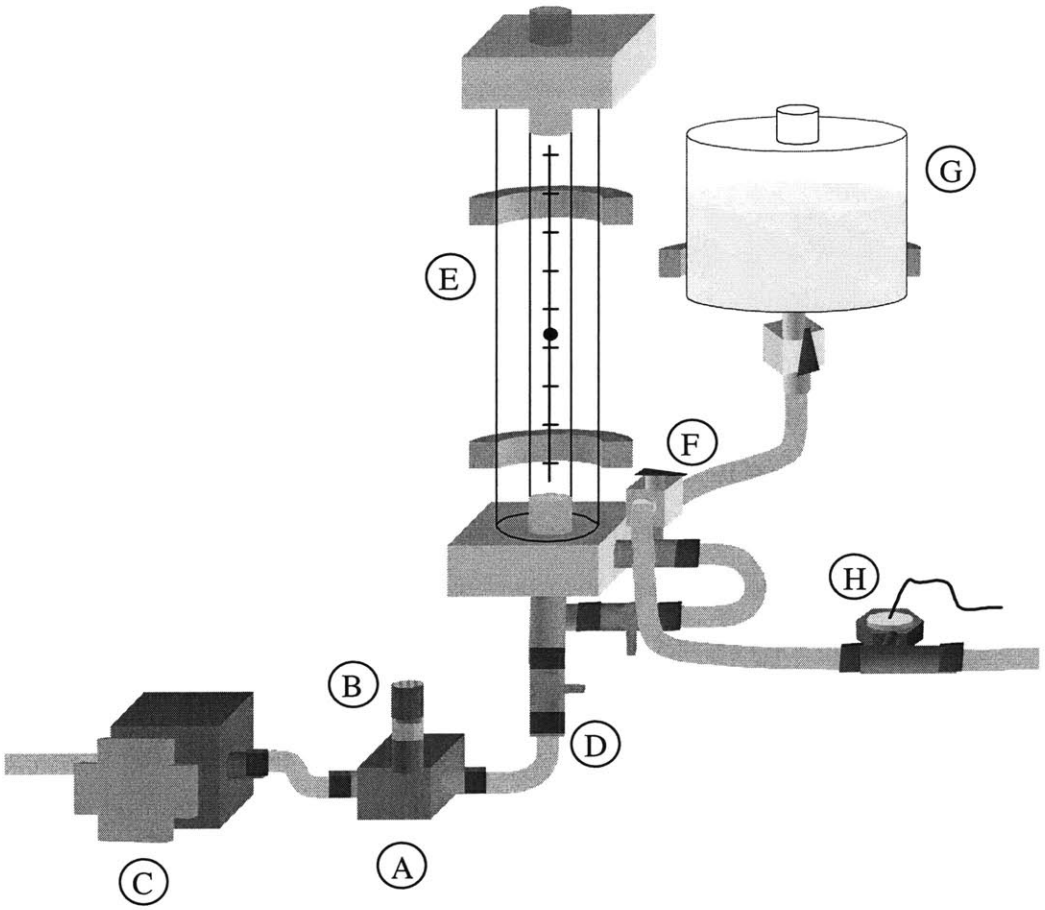

Figure 4-7 Setup for experiments at constant flow rate with flow meter

Given the number of different components of this setup, and their size, it was not feasible to secure it on the centrifuge platform at high *g*-levels. All tests for which injection took place at intermediate flow rates were therefore conducted at 1-*g*. The apparatus was nevertheless located on the centrifuge platform, in order to ensure uniformity in the quality of the images taken during air injection.

4.5.2. Testing Procedures

4.5.2.1.Tests at 1-g

Experiments performed using the PVC system were done according to the following procedure:

1. The sample box was prepared and mounted on the centrifuge platform as previously described. Even tests conducted at 1-*g* were performed on the centrifuge platform, in order to obtain consistent video images (*i.e.* lightning, camera settings) and to maintain a consistent injection setup characteristics (*i.e.* transducer settings, length of pressure lines).
2. The data acquisition system was started and the video recording equipment were switched on.
3. The input voltage for the PVC corresponding to the desired injection flow rate was selected.
4. The experiment started by turning the 3-way valve on the PVC towards the sample box, and by turning the motor on in order to start pressurizing the line leading to the box. Pressurization took place by compressing the air in the PVC's main reservoir and in the line until entry pressure in the sample was reached, and air started to invade the system. Air continued to be pushed at a constant rate until steady-state conditions were reached, or until the end of the travel length of the piston.
5. The motor was turned off at this point, along with the recording equipment and the data acquisition system.

The procedure followed to conduct experiments using the flow meter setup was different. Refer to Figure 4-7 for illustration.

1. The sample box was bolted to the platform. The data acquisition system and recording equipment were subsequently started.
2. The valve on the compressed nitrogen cylinder was opened, and regulator C was adjusted in order to get air flowing through the valve. Experiments were started at the lowest possible flow rate, and therefore regulator C was completely open at the beginning of a test.

3. Valve D was opened to let air into the flow meter E. As air flowed in the ball inside the inner cylinder moved up. Once the ball stopped oscillating, the regulator pressure was adjusted until the desired reading on the flow meter was obtained.

4. When the ball was stable at the target flow rate, the three-way-valve F was opened towards the water reservoir G. The purpose of the reservoir was to release any excess pressure in the tubing system, before it went into the sample box. The reservoir was equipped with an exit port on the top, which released excess pressure out of the system. After a couple of seconds observing steady bubbling in the reservoir, valve F was turned in the direction of the sample box (not shown in the figure).

5. Pressure readings were taken by transducer H immediately before the injection air went into the box.

6. For tests in which the flow rate was gradually increased, the source pressure was increased at regulator C after one minute of injection, such that readings on the flow meter increased by two units, or approximately 4.3 cm^3/s.

4.5.2.2.Tests at higher g-levels

Constant flow rate experiments conducted at *g*-levels higher than 1-*g* were all performed using the PVC method of injection. The procedure followed in conducting these experiments was the following:

1. The platform was loaded and all of the systems were initialized.

2 The PVC was mounted on the centrifuge and the piston was fully retracted.

3. Pressure connections were changed slightly from what is shown in Figure 4-1. One side of the three-way-valve on the PVC was temporarily connected to the standing nitrogen cylinder. The other side of the valve was connected to the solenoid valve O on Figure 4-1. The pressure regulator P was bypassed, such that the solenoid valve was directly connected to the pressure transducer Q. The rest of the setup presented in the figure remained unchanged.

4. The PVC reservoir was filled with compressed nitrogen. The pressure was set to the entry pressure of the sample at the *g*-level at which the test was to be conducted. Starting experiments with the reservoir full of pressurized gas reduced the line

pressurization time and made it possible to observe the growth of the plume at high *g*-levels before the piston ran out of stroke.

5. The PVC was disconnected from the nitrogen cylinder and the three-way-valve was opened towards the solenoid valve. The solenoid valve was closed at this point.

6. The valve at the entrance of the external tubing on the strong box was opened and the centrifuge door was closed.

7. The centrifuge was started and when the target *g*-level was reached, the solenoid valve was opened.

8. The PVC motor was then turned on, and the input voltage was adjusted to the desired injection flow rate. The pressure in the PVC reservoir would decrease during spin up, and therefore some time was needed to pressurize the line to the level of the sample entry pressure. Air was injected into the sample at a constant rate until steady-state conditions were reached, or until the piston ran out of stroke.

9. The centrifuge was then stopped and all systems were turned off.

CHAPTER 5

EXPERIMENTAL MATERIALS

5.1.INTRODUCTION

This chapter describes the materials that were used in the experimental phase of this research study. Section 5.2 presents an overview of the method that was employed to obtain a transparent porous medium, and provides the characterization of the three different types of granular materials tested. Section 5.3 describes, and gives, the properties of the two types of pore fluids used. Section 5.4 presents a detailed description of the sample preparation procedure.

5.2.POROUS MEDIA

5.2.1. Transparent Medium

One of the central objectives of this research study was to observe and characterize air flow patterns during air sparging experiments. In order to visualize the flow of air through a porous medium, a transparent substitute for soil was developed. The *immersion method,* developed by Wakabayashi (1950), was the visualization technique chosen for this study. According to this method, a solid particle submerged in a fluid of the same refractive index becomes transparent when exposed to a light source within a certain range of wavelengths. This principle has been used by a number of investigators over the years (Dantu 1957, Rangelow *et al.* 1992, Konagai *et al.* 1992, Montemagno and Gray 1995), in studies where the motion of individual particles is of importance. In the case of the specific experiments conducted for this study, the use of a transparent porous medium made it possible to observe the type of flow regime that was taking place during a given air sparging experiment (*i.e.* bubbling, channeling, etc), and to determine the scale of flow (*i.e.* channeling versus fingering). Experiments were performed by placing the strong box, full with the transparent medium, against a light

source. The injected air was then visible as a black plume propagating through a white background.

Preliminary experiments suggested that borosilicate glass (Pyrex) had refractive properties that could be matched by commercially available fluids, and therefore it was chosen as a substitute for soil particles. Pyrex beads of various diameters are commercially available, but they did not appear transparent when submerged in fluids of matching indices of refraction. Konagai *et al.* (1992) noted that glass beads are made from dripping melted glass onto cold water, and that air bubbles are commonly trapped in such beads. This type of manufacturing defects affect the optical properties of the beads and as a result, the index of refraction might change from one bead to the next. The authors recommended the technique of crushing glass blocks as the most reliable way of obtaining high quality particles. They suggested that high crushing power reduces both scratching of the surface of the grains and cracking of the interior, two mechanisms that greatly decrease the optical purity of the glass particles (Konagai *et al.*, 1992).

Pyrex was thus purchased in bulk from ACE Glass as glass rods, 2 mm in diameter. The rods were brought to the laboratory and manually crushed in a compaction mold with a compaction hammer. Only a few blows of the hammer were needed to crush the glass, which pulverizes easily, hence the use of the mold to contain all the glass particles. The crushed material was subsequently washed with soap, dried, and sieved in order to separate it into adequate grain-sizes. Thorough washing of the crushed glass was essential in order to maximize visibility through the medium once it was immersed in the liquid of matching refractive properties.

It is worth noting that, as the material was being sieved, the brass sieves were permanently scratched by the glass particles. It was therefore necessary to wash the crushed material thoroughly after sieving, since it appeared yellowish when extracted from the sieves.

5.2.2. Characterization of Porous Media

5.2.2.1.Grain-size distribution

Three different porous media were used in this research study. Two of the materials consisted of crushed particles of a various sizes, classified as poorly graded sands (SP) by the Unified Soil Classification System (USCS). Figure 5-1 shows the grain size distributions of both materials. The soils were relatively uniform, with one of the materials having a greater percentage of fines. Both materials were highly angular, and, as was noted in the previous section, had sharp edges. The specific gravity of the glass, G_s, was measured in the laboratory according to ASTM Standard D854-58, and found to be equal to 2.24.

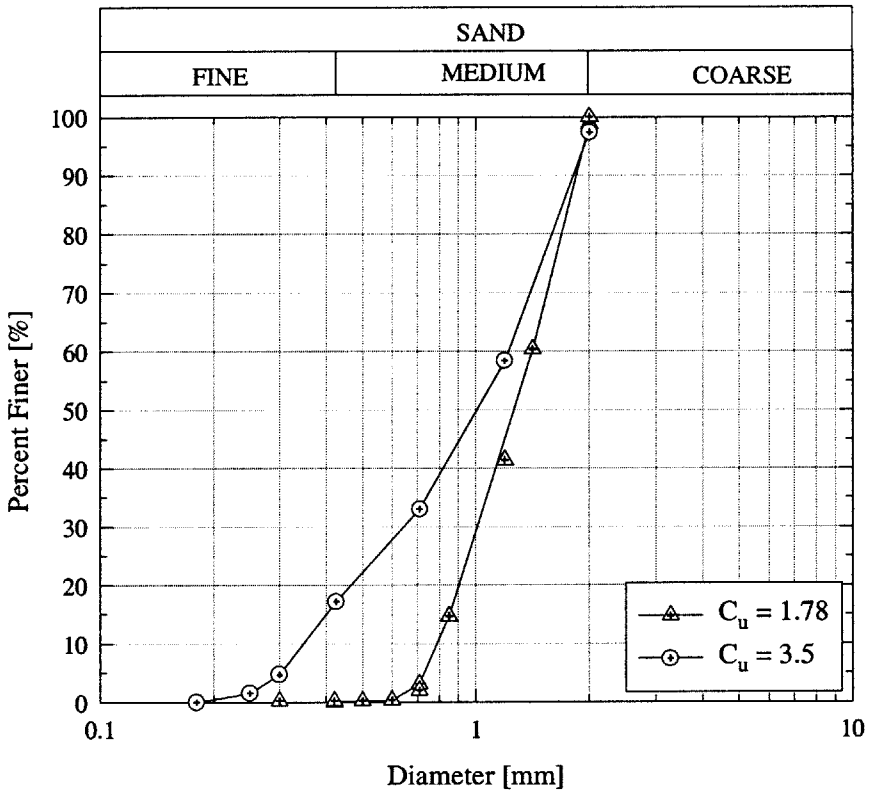

Figure 5-1 Grain size distributions of crushed glass samples (USCS)

The third material tested consisted of uniform glass beads, 4 mm in diameter, which were used in a limited number of experiments. Table 5-1 summarizes the characteristics of the granular materials used in the experiments.

Table 5-1 Characteristics of tested granular materials

	$C_u = D_{60}/D_{10}$	$C_c = D^2_{30}/D_{10}.D_{60}$	D_{10}, [mm]
SP	1.78	1.29	0.79
SP with fines	3.5	0.97	0.35
Glass Beads	---	---	Uniform size D = 4

5.2.2.2.Hydraulic conductivity

Flexible wall hydraulic conductivity tests were performed on the three materials, under constant head conditions, using water as the pore fluid. Experiments were performed over a range of hydraulic gradients and the pertinent data is included in Appendix D. A summary of the results obtained is presented in Table 5-2

Table 5-2 Hydraulic conductivity of tested materials

Material	**Hydraulic conductivity [cm/s]**	**Intrinsic permeability [cm^2]**
SP	0.611	1.31×10^{-4}
SP with fines (SPF)	0.148	3.17×10^{-5}
Glass Beads	9.00	1.93×10^{-3}

5.3.PORE FLUID

The choice of the liquid to use as pore fluid in air sparging experiments was dictated by both optical and physical constraints. The optical limitations were that the liquid needed to be colorless, transparent and, above all, match the index of refraction of the crushed glass. The physical requirements were that the liquid was non-reactive (*i.e.* low volatility, low flashing point) and non-toxic.

The first liquid found that complied with all of the above requirements was glycerol. Crushed glass submerged in glycerol is completely invisible, and from an optical point of view is thus an ideal pore fluid. Glycerol with 99.5% purity was purchased from Mallinckrodt (at VWR), in 4L bottles. Although initial experiments were conducted exclusively in glycerol, its physical properties, and particularly its very high viscosity (approximately 550 times that of water), made it necessary to find an alternate fluid.

A sample of the crushed glass was sent to R.P. Cargille Laboratories, Inc. for measurement of the index of refraction, n. Cargille Labs specializes in manufacturing "custom-made" fluids of specific optical properties. Their services were commissioned to 1) measure the optical properties of the crushed glass, and 2) to produce a fluid of matching optical properties. The fluid received was referred to as *Immersion Liquid Code 5040*, a mixture of aliphatic/alicyclic hydrocarbons and hydrogenated terphenyl. The liquid was designed to match the index of refraction of the glass under a light with a wavelength of 5893 angstroms, at which its optical compatibility is optimum. The match of indices of refraction is still adequate under a regular white light source, and given the space constraints in the centrifuge, a more sophisticated light source was not used. The immersion liquid is insoluble in water, partly soluble in acetone and ethanol, and soluble in carbon tetrachloride, ethyl ether, freon TF, heptane, methylene, chloride, naphtha, toluene, turpentine, and xylene

The optical match between glycerol and Pyrex was still better than that between the immersion liquid and the glass. In the latter case, the edges of the particles are detectable as a slight "rainbow" effect was observed. This effect is caused by a mismatch in the *dispersion*, which is the change in refractive index with wavelength (Montemagno and Gray, 1995). Table 5-3 lists the optical properties of the crushed glass and the two pore fluids used, and demonstrates the reason behind the quality of the match between Pyrex and glycerol. Nonetheless, the discrepancy in dispersion of the immersion liquid was acceptable, and thus it was selected as the second fluid to be used in the experiments.

Table 5-3 *Optical properties of glass and pore fluids (measured by R.P. Cargille Laboratories Inc.)*

Material	Refractive index, n	Dispersion [Abbe υ]
Pyrex (crushed sample)	1.4716	67.6
Glycerol (99.5% purity)	1.4714	58.1
Immersion Liquid code 5040	1.4716	50.3

The physical properties of the two liquids chosen as substitute pore fluids are considerably different that those of water, the pore fluid typically found in-situ. Table 5-4 summarizes their properties and provides those of water for comparison. The viscosity and the density of both liquids, and primarily of those for glycerol are clearly different. However, the use of dimensionless numbers in the evaluation of air flow through porous media makes it possible to compare fluids of widely different properties. The relative magnitude of viscous, buoyant, and capillary forces in the different liquids can be determined and evaluated in a dimensionless space, where fluid properties are factored out, and only the interactions between the forces are expressed.

Table 5-4 *Physical properties of pore fluids tested*

Liquid	Dynamic viscosity, μ [Pa.s]	Density, ρ [g/cm^3]	Interfacial tension, σ [N/m]
Glycerol	0.620	1260	6.3×10^{-2}
Immersion liquid	1.79×10^{-2}	850	3.0×10^{-2}
Water	1.00×10^{-3}	1000	7.3×10^{-2}

5.4.SAMPLE PREPARATION

It was necessary to adapt sample preparation procedures depending on the pore fluid used. Preparing samples in glycerol was much more complicated and time

consuming than in the immersion liquid, given the high viscosity of glycerol. The following two sections describe the procedures followed during saturation of the crushed glass samples.

The crushed glass was thoroughly washed, oven-dried, and cooled before the beginning of a series of tests. The importance of carefully washing the glass has already been stressed, for visibility purposes. Complete drying of the material and cooling prior to saturation were also critical. The immersion liquid is not soluble in water, therefore traces of moisture on the glass drastically reduced the visibility of the medium, in addition to changing the properties of the liquid.

The most critical factor in sample preparation was to ensure that all air had been evacuated before the strong box was filled with the pore fluid. Residual air bubbles trapped in the glass could create preferential flow pathways through the soil, and could limit visibility through the medium once air injection started.

5.4.1. Samples in Immersion Liquid

Two different sets of procedures are included in this section, namely the preparation of new samples and that of reworked samples. New samples were those which were started with an empty box and clean, dry glass. These were prepared every time injectors were switched, or every time the pore fluid was changed. Reworked samples were those prepared after an air sparging experiment had been conducted, when the box was already full of glass and liquid and needed only to be saturated.

5.4.1.1.New samples

The procedure followed during preparation of new samples submerged in optical fluid consisted of the following steps:

1. The strong box was thoroughly washed and dried, and the injector to be used in the experiment was screwed on to the base of the box. The mass of the empty box was recorded. Valve F, shown on Figure 5.2, was closed prior to the start of filling. This figure will be used to illustrate several points of the saturation procedure.

2. The box was clamped to a shaking table and filled to approximately one quarter of its height with pure immersion liquid. A record was kept of the mass of liquid being transferred into the box. The immersion liquid could be reused a number of times, without any evident changes in its appearance. However, with exposure to light and with use, the liquid turned from colorless to yellowish, at which point it was necessary to discard it. The frequency of changes of pore fluid was variable, and depended on the level of visibility through the sample.

3. The shaking table was then turned on and crushed glass was manually deposited in the box. This was done by gradually raining dry material from the top of the box, by layers. Shaking was maintained throughout the filling process. A record was kept of the mass of dry glass that was poured in the box.

4. Additional liquid was added, if needed, as glass was rained into the box. The position of the phreatic surface was always visible during filling, in spite of air bubbles present in the sample. The location of the phreatic surface was monitored such that approximately five centimeters of dry material remained above its final position at the end of filling.

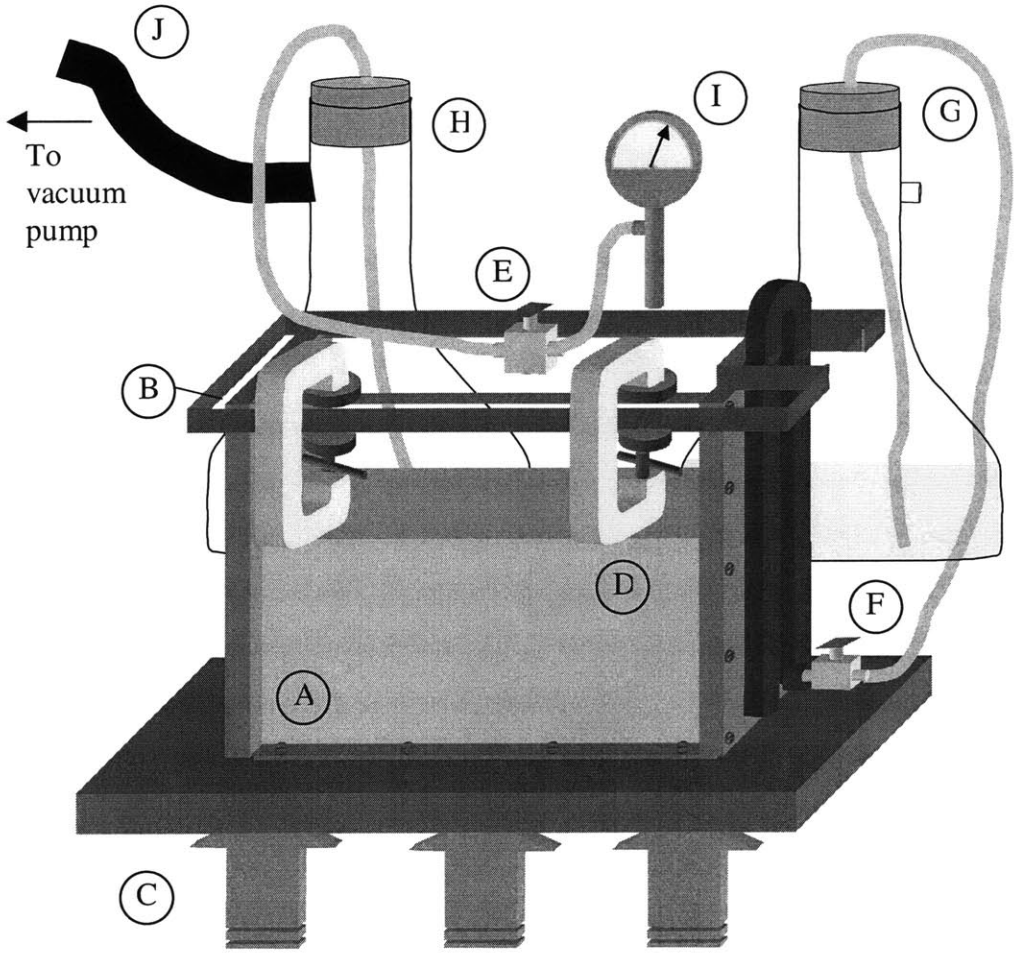

Figure 5-2 Schematic of setup for sample preparation

5. The shaking table was turned off and the box was sealed. A piece of Lexan was used to cover the top of the box, as shown by B in Figure 5-2. A notch was cut out of the lid in order to accommodate the outside tubing of the box. A tight seal between the box and the lid was obtained by using a rubber gasket (not shown in the figure). The gasket consisted of a rectangular piece of rubber (2 mm-thick) of dimensions slightly larger than the edges of the box, which was draped over the box. A hole was also cut out of the gasket, which was aligned with valve E. The lid was held in place by ten clamps located around the box, of which only two are shown on the figure for clarity.

6. Connections to the vacuum pump were then made, as shown in the figure. Tubing was taken from valve E into an empty volumetric flask H. The flask was itself connected to the vacuum pump with vacuum-tubing J. The other port on valve E was connected to a

vacuum gage I, which made it possible to check the tightness of the seal between the box and the lid.

7. The vacuum pump was then started, valve E was opened, and the shaking table was turned on. A vacuum in excess of 29 inches of mercury was maintained on the box for two hours. It is important to note that saturation, as used in the context of these procedures, is a state defined purely based upon visual standards. A saturated sample was one in which no trapped air bubbles were visible either from the front or from the back window of the box.

8. The shaking table remained on for half an hour after the vacuum pump had been turned off. Within this time the vacuum in the box slowly decreased to approximately 15 inches of mercury. The height of the phreatic line in the sample fell as the tension in the liquid decreased. After half an hour the shaking table was turned off, the clamps were released, and the box was opened. If, on the other hand, the vacuum was released soon after the pump was turned off, air would finger downwards through the sample as the liquid level dropped, and the saturation procedure had to be re-started.

9. The mass of the full box was then recorded, and the final heights of the phreatic surface and of the surface of the sample were measured. Mass and height measurements were later used for calculations of sample porosity.

10. Finally, a clear grid was placed over the front face of the box, which was used to track the movement of the air plume during sparging.

A modification to the box was introduced after the first series of samples was prepared on the shaking table. Similarly to the process which occurred during sieving of the glass, strong shaking of the box caused scratching of the aluminum side panels, which in turn led to staining of the pore fluid. "Swirls" of gray-colored fluid propagated from the sides of the box towards the center, making it impossible to see through the sample. A strip of stainless steel shim was then cut with length equal to the length of the two side panels plus the base panel of the box. A hole was cut in the center of the strip through which the injector was attached to the base of the box. The strip was glued to the box with epoxy and allowed to dry overnight. The box was subsequently refilled and saturated as previously described and no additional problems with staining of the pore

fluid occurred. The shim strip was changed periodically, usually corresponding with changes of the pore fluid, since it tended to rip at the edges and corners as glass grains were trapped underneath.

5.4.1.2.Reworked samples

This section summarizes the procedures followed when saturating that had been used in previous air sparging tests. It was not necessary to empty the box and re-start the sample preparation procedure after every experiment. The preparation of reworked samples is summarized in the following steps:

1. After an air sparging experiment was conducted, the sample box was removed from the centrifuge platform and placed on the shaking table. Valve F was closed and the sample was thoroughly reworked using a metallic rod. This consisted in essentially destroying any possible air pathway remaining in the sample. Since the soil was wet it was relatively simple to stir it around the box, making sure no material was left undisturbed. It was also important not to spill any material or fluid, since the masses of the pore fluid and the glass could not be independently obtained and previous mass measurements were to be used in calculations of porosity.
2. The box was then covered with the rubber gasket and the Lexan lid and subsequently sealed with clamps. Valve E was closed and the box was drained from the bottom, through valve F. This was done by connecting the vacuum pump to the side port of volumetric flask G, while the tubing coming through the flask's rubber stopper was connected to F.
3. The vacuum pump was turned on, valve F was opened, and the pore fluid drained from the sample was collected in G. Once all the pore fluid had been collected, valve F was closed and the connection to the vacuum pump was transferred to flask H. A rubber stopper was used to seal the side port on flask G.
4. The vacuum in the box was released by temporarily disconnecting the vacuum gage and opening valve E to the atmosphere. The valve was then closed and the connections remade. The vacuum pump and the shaking table were turned on at this

point, E was opened towards the flask, and a vacuum of 29 inches of mercury was applied to the box for half an hour.

5. Wetting was then performed by opening F towards flask G and by allowing pore fluid to flow upward through the sample. Valve F was closed after all the fluid flowed out from flask G.

6. Vacuum and shaking were continued for a minimum of two hours. The choice of the time interval was somewhat variable, depending on the conditions of the sample. As was previously described, if air pockets were visible after two hours of saturation time, the procedure would be extended.

7. The shaking table remained on for half an hour after the vacuum pump had been turned off, at which point the clamps were released and the box was opened.

8. The mass of the full box was then obtained, and the final heights of the phreatic surface and of the surface of the sample were measured. Any differences in mass between two saturation procedures were attributed to loss of pore fluid, and adjustments of volume of fluids estimates were made accordingly.

10. The clear grid was placed over the front face of the box.

At the end of a series of experiments in immersion liquid and prior to saturation with glycerol, the glass needed to be completely washed. Washing the immersion liquid off the glass is a long procedure and the use of a solvent is required. The fluid is only partially soluble in acetone, but given the level of hazard of the alternate solvents and the solubility of acetone in water, it was selected as the solvent to use. The glass was placed in a plastic funnel plugged with glass wool, and acetone was re-circulated as the glass was stirred. After several cycles the crushed glass was placed in evaporating dishes with soap water and heated with Bunsen burners. The water was allowed to boil and was replaced with fresh soap water until "oil beads" were no longer visible. The soap was subsequently rinsed off and the glass was oven-dried.

5.4.2. Samples in Glycerol

Saturating samples of crushed glass in glycerol was significantly more difficult and time consuming than in immersion liquid. Approximately a full day was spent preparing one sample in glycerol, given the difficulties in evacuating all the trapped air.

Saturating *clean* glass with glycerol could be done without major difficulties following the same procedure described above for saturation of new samples in immersion liquid. However, if the glass had been previously submerged in glycerol, draining it and evacuating the air as explained in the procedure for saturation of reworked samples was not practical given the amount of time it required. Therefore, the preparation of reworked samples was done according to the following steps:

1. The box was emptied out and weighed. The wet glass was carefully placed in a container, trying to avoid any loss of material.
2. The empty box (unwashed) was then clamped to the shaking table, and the table was turned on.
3. Samples were then prepared by manually raining the glycerol-wet glass, in layers, into the empty box. Shaking was maintained as the material was being deposited.
4. After a layer of approximately 4 cm was rained in, the sample was covered, sealed, and subjected to a vacuum in excess of 29 inches of mercury. Vacuum was applied through valve E, as described in the saturation procedures for the immersion liquid. The vacuum was maintained on the layer of glass until all visible air bubbles had migrated to the surface of the free liquid. Mobilization of entrapped bubbles under vacuum and shaking was possible as long as the height of the layer (*i.e.* the distance to the free surface) was maintained below 5 cm. Bubbles trapped within layers thicker than 5 cm of glass would not be mobilized by this procedure, regardless of the time left under vacuum. It was therefore critical to ensure full saturation of every layer before proceeding to the following one.
5. The vacuum was then stopped and shaking was maintained for half an hour on the sealed box.
6. The clamps were then released, the box was opened, and the raining procedure was be repeated for the next layer (steps 3 through 5) until the whole box was filled.
7. The mass of the full box, as well as the height of liquid and glass were recorded.

8. One of the most critical parts of this procedure is that independent measurements of the mass of glass and liquid could not be made. It was therefore of extreme importance to thoroughly clean every container used during transfer of the wet material with a spatula, in order to recover as much material as possible. It was also critical to keep track of the masses of every container, such that final mass estimates could be made as accurately as possible.

Cleaning the glass after the series of experiments in glycerol was completed was simple, as glycerol is soluble in water. It was only necessary to circulate water through the glass for a short period of time and it was ready to be oven-dried.

CHAPTER 6

DATA TYPES AND ANALYSIS

6.1.INTRODUCTION

The data collected during this study consisted primarily of video tapes of experiments. Since the study of patterns of air flow was done by inspection of images, the critical issue was that of quantifying, in a consistent manner, the image data obtained throughout the experimental phase. Analysis of the images generated during air sparging experiments was therefore an integral part of the data reduction process, and will be explained, in detail, in this chapter.

The chapter is divided into three main sections. Section 6.2 focuses on data collection and analysis, and includes a description of the video recording and capturing equipment. This section also describes the procedure used to correct captured images for the distortion caused by the wide-angle lens of the camera. Next, section 6.3 illustrates the method used in the determination of the velocity of propagation of the injected air front through the medium. Finally, section 6.4 describes the image processing program used to digitize the plumes obtained from experiments, together with the method used to calculate plume volumes. Details of the procedure used to determine the zone of influence of an injector are also illustrated in this section.

6.2.DATA ANALYSIS

6.2.1. Video Capture Equipment

Images were captured from videotapes of air sparging experiments using the video capturing device *Snappy 2.0*, manufactured by PLAY Inc., Rancho Cordoba, CA. This device consists of a high resolution video capturing chip that is simultaneously connected to one of the serial ports of the PC, to the video player, and to the TV monitor. *Snappy 2.0* made it possible to watch the tape of the experiment, to pause it at any

specific point in time, and to capture the frame of interest. The captured frames were then saved as black and white bitmap files.

6.2.2. Distortion Corrections

The distortion caused by using a wide-angle lens camera is obvious when looking at images recorded during air sparging tests. A marked "fish bowl effect" made it necessary to correct the images for distortion when calculations involving length and dimensions were performed. Corrections for camera distortion were made by superimposing a distorted picture of the grid used during experiments over that of an undistorted grid. This was done by taking a picture of the distorted grid, digitizing it, and plotting the coordinates of its nodes, together with those of an undistorted grid of known dimensions. Figure 6-1 a) shows a diagram of the distorted and undistorted grid coordinates. This figure illustrates, very clearly, the extent of the distortion, *i.e.* the "fish bowl effect". The origin of the coordinate system has been set to correspond with the injection port, at the top of the injector. This location of the origin will be maintained for the remainder of this thesis, such that air enters the porous media at point (0,0) and its trajectory is tracked along the positive x and y directions.

The relative location of the grids was set with respect to the point indicated by a diamond on Figure 6-1 a), on which the two grids were centered. When the strong box and the camera were bolted onto the platform, this point was located directly in front of the center of the camera lens. The grid was always centered at this point as it was superimposed on the sample box. It is assumed that there is no distortion at this point, and therefore that the coordinates of this node, $x = 0$ and $y = 6.35$, on both the distorted an undistorted grids are the same.

Digitization of all images was done using the public domain program *Scion Image* (version Beta 3b), based on the Macintosh program *NIH Image* written by Wayne Rasband at the US National Institutes of Health. The original program was modified for Windows by the Scion Corporation, and is available from the Internet by anonymous FTP from *www.scioncorp.com.*

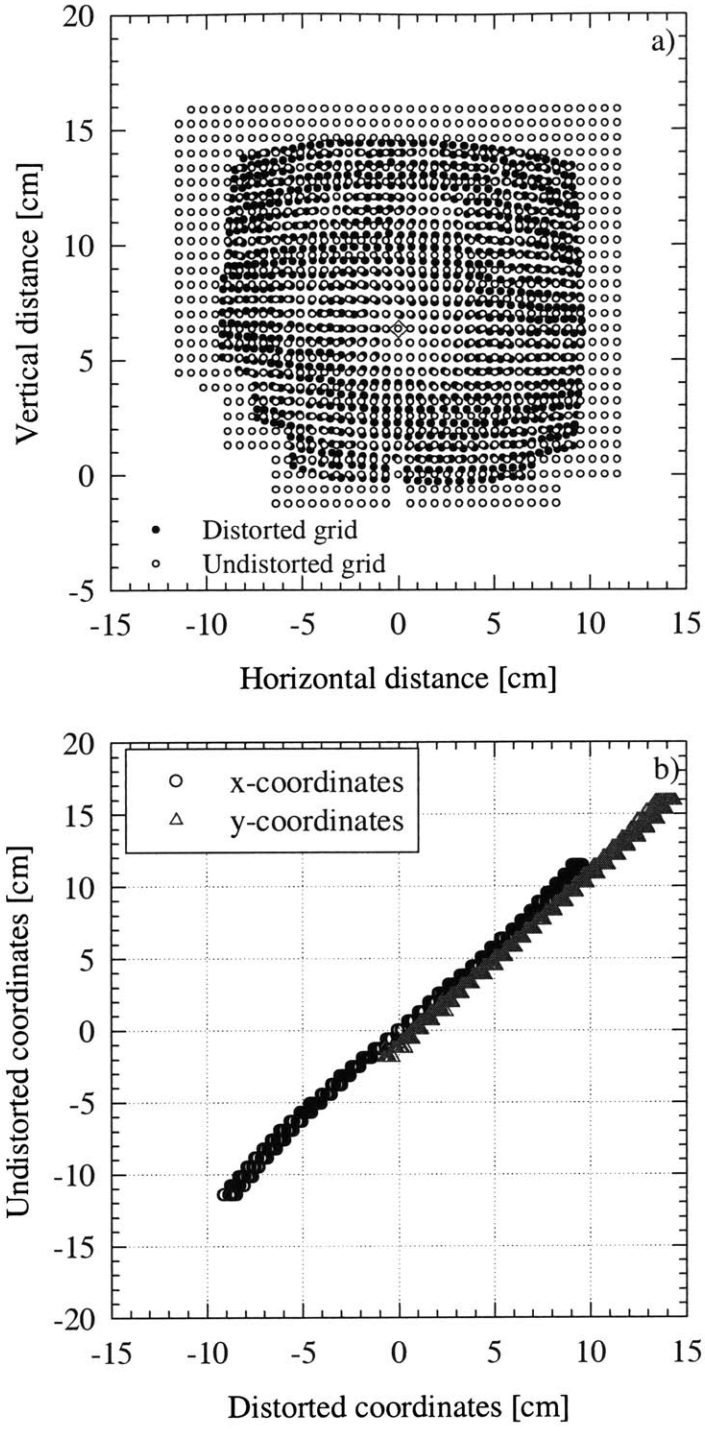

Figure 6-1 *a) Illustration of "fish bowl effect" caused by wide angle camera. Distorted and undistorted grids are centered on the diamond, which indicates the point of no distortion; b) undistorted grid coordinates as a function of distorted coordinates.*

The distorted grid was used to calibrate the extent of distortion at every point around the box. The x and y coordinates of the distorted node points were obtained and plotted versus the undistorted x and y coordinates, as shown in Figure 6.3b. The circles show the relationship between the undistorted x-coordinate on the ordinate axis versus the distorted x-coordinate on the abscissa axis. The triangles show the same relationship for the y-coordinates. The purpose of these plots was to determine a relationship that could be used to calculate the undistorted coordinates of a point from its distorted coordinates. It is clear from the plots that the further away a point is located from the point of no distortion (0, 6.5), the greater the amount of distortion. Polynomial regressions were fitted through the data points, which resulted in the following two relationships:

$$x' = 0.002x^3 - 0.0033x^2 + 1.0784x - 0.0696 \qquad r^2 = 0.9988$$

$$y' = 0.0012y^3 - 0.0209y^2 + 1.2485y - 1.0202 \qquad r^2 = 0.9974 \qquad \text{Equation 6-1}$$

where x' and y' are the new coordinates of points x and y, corrected for distortion.

Plots of plume boundaries and calculations of area and surface revolution of plumes will be presented in the following chapters. All the coordinates of the digitized plumes were first translated to the system of coordinates with origin at the injection point, and then corrected for distortion using Equation 6-1.

It should be noted that no correction was made for the effects of distortion into the box. The distortion caused by the fact that images of the plume are taken through the Lexan window and into the strong box was not accounted for data corrections.

6.3.AIR DISPLACEMENT AND VELOCITY DATA

Videotapes of the experiments were played frame by frame in order to track the displacement of the leading edge of the advancing air front as a function of time. The grid superimposed on the front panel of the strong box was of known dimensions, and therefore provided a means of measuring air displacement without correcting for camera distortion. The data obtained from video tapes were measurements of the vertical

displacement of the breakthrough front per increment of time, up to the phreatic surface. Changes in time were tracked using the digital chronometer that had been superimposed on the images during taping. This device measured time with an accuracy of milliseconds. Air flow velocities were then obtained by calculating the slopes of the plots of vertical displacement versus time.

Figure 6-2 shows typical images from an air sparging experiment, that were used to calculate displacement times of the air front. The pictures shown are from an experiment conducted at 1-*g*, at a constant rate of injection of 1.58 cm^3/s, in a sample saturated with immersion liquid, using MPI #3 (orifice diameter = 0.5 mm). The pictures show the strong box full of saturated porous media, and the air front advancing vertically from the injection point, which is located at the mid point of the base of the image. Figure 6-3 shows the plot of vertical displacement as a function of time, obtained from a sequence of images similar to that shown in Figure 6-2, but showing additional pictures of air propagation. Frames B, C, and D on Figure 6-2 for instance, correspond to points B, C, and D on Figure 6-3. The velocity of the breakthrough front as it propagates through the soil is taken as the slope of the regression line shown in the figure, namely 1.84 cm/sec.

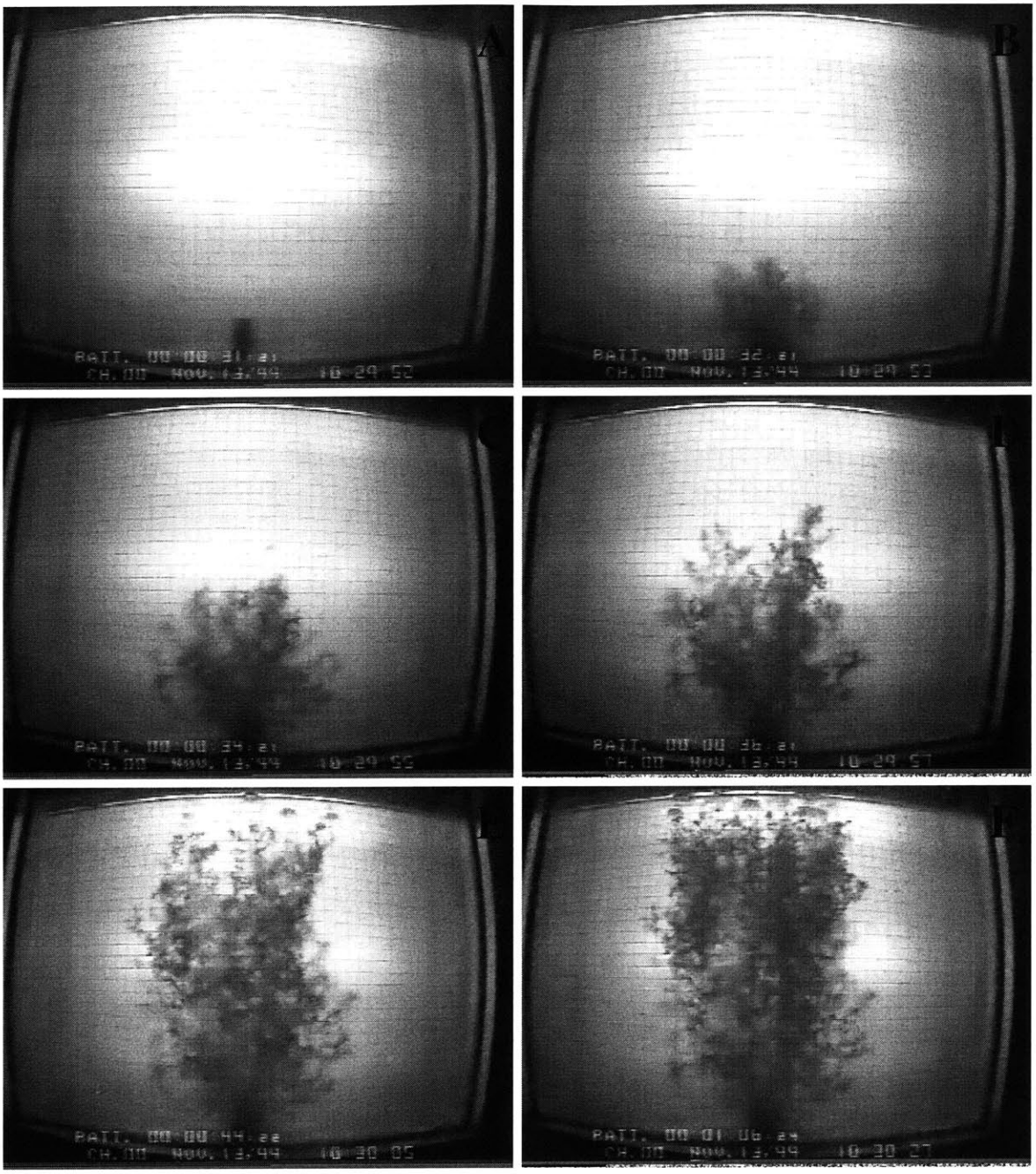

Figure 6-2 *Progression of air sparging front through a porous medium saturated with immersion liquid. Test shown was conducted at 1-g, under a constant flow rate q = 1.58 cm^3/s.*

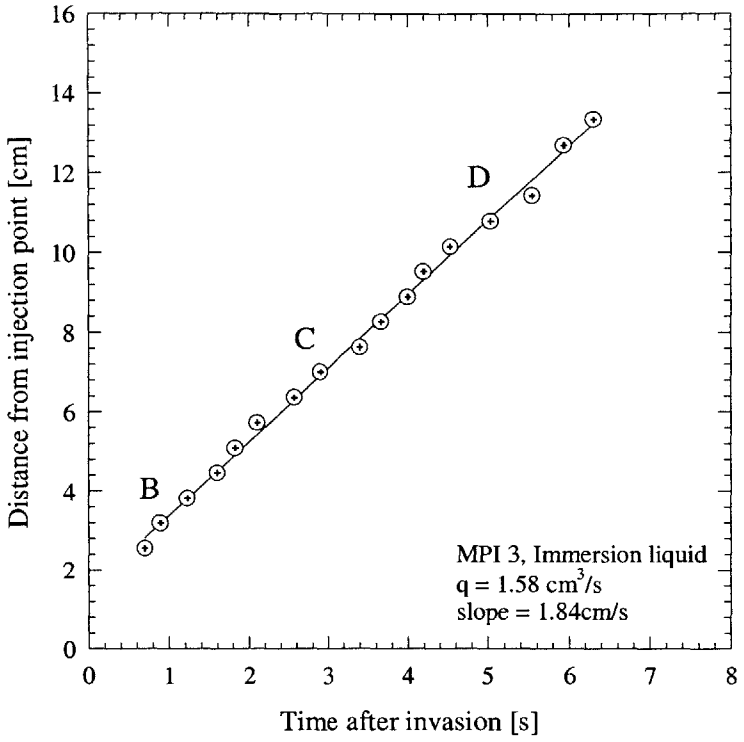

Figure 6-3 *Vertical displacement of air front from injection point to phreatic surface as a function of time.*

6.4.QUANTIFICATION OF IMAGE DATA

6.4.1. Plume Outlines

Calculations of plume volumes and in-plane areas (plane *x*-*z*) were performed on all of the images collected during experiments. These calculations required knowledge of the coordinates of the boundary of the plumes corrected for distortion. Plume boundaries were first manually digitized using *Scion Image*. Given that air does not always propagate as a uniform front, determining the boundaries of the plumes was not a simple process and therefore a number of steps were taken to ensure that a consistent digitizing procedure was followed throughout this work.

Scion Image includes a function called Image Math, which is used to perform basic mathematical operations, such as additions and subtractions with images. Because lighting conditions could change from test to test, and because imperfections of the sample limited the amount of contrast between the invading air and the porous medium, the background was always subtracted from the image showing the invading air. An image of the sample box before invasion was therefore always captured, to be used as the background frame. When the background was subtracted from the image of the plume, the difference between the two images was the air in the sample box. A typical result from this procedure is illustrated in Figure 6-4, which shows the image obtained after subtracting frame A (in Figure 6-1) from frame E.

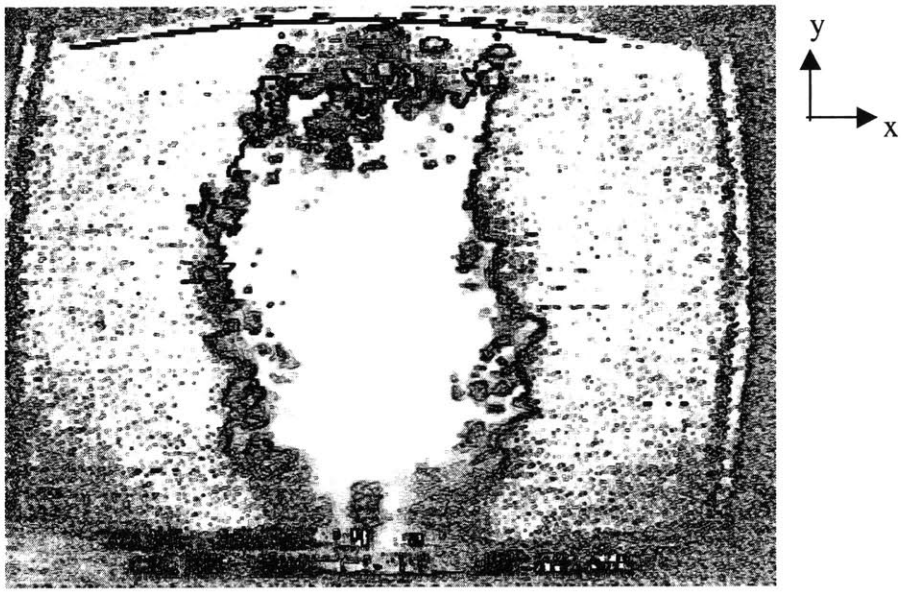

Figure 6-4 *Air plume boundary obtained from subtraction background from image of moving air front (frame 5 – frame 1 on Figure 6.1)*

It is clear from Figure 6-4, that digitizing the boundary of the plume involves a certain level of interpretation, and that areas of partial air saturation or areas of zero air saturation inside plume boundaries may be counted as part of the plume. The more

irregular the air propagation, the greater the error associated with the approximation that all the zone within the boundary was saturated with air.

The two rules used when digitizing plume boundaries can be summarized as follows:

1. Dead-end channels or fingers were not included as part of the final plume boundary. It is easy to see how including a lateral spreading channel which never reaches the phreatic surface can lead to very large over-estimations of the surface of revolution of a given plume.

2. Areas of water saturated media within the boundaries of the plume (*i.e.* holes) were generally counted as saturated zones, unless the dimensions of the zone were visibly significant, *i.e.* greater than 5% of the total in-plane area of the plume.

Digitalization was performed by manually tracing the boundary of the plumes, following the criteria established above for determining the location of the boundary. Figure 6-5 shows the boundaries of the plume shown in Figure 6-4, after digitization and translation to the system of coordinates presented in Figure 6-3.

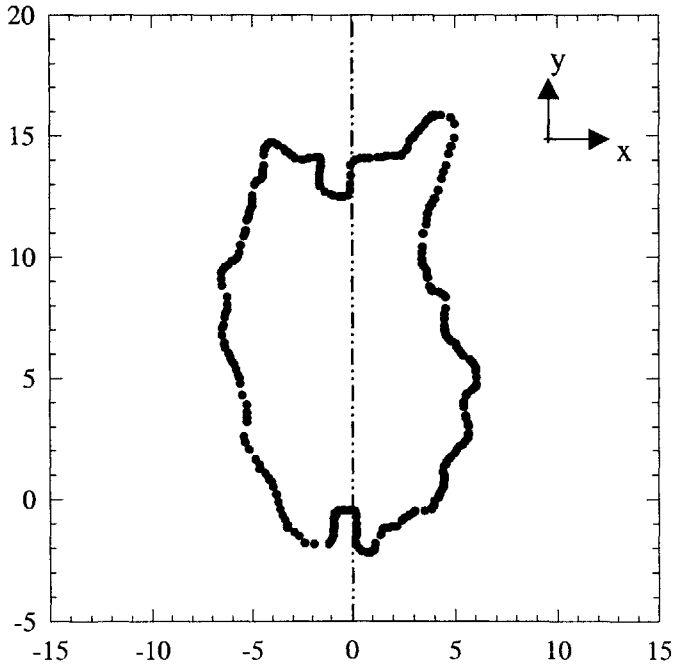

Figure 6-5 Digitized boundary of the plume shown in Figure 6-4

The coordinates of all the points along the boundary of the plume are the final form of the data that will be used for calculations of in-plane areas and volumes of the plumes.

6.4.2. Plume Areas

Computations of in-plane areas of the plume within the digitized boundaries were done using the program MATLAB (The MathWorks Inc., Natick MA). The function *polyarea(x,y)* computes the area of the polygon defined by vectors [x] and [y], which contained the coordinates of the points on the boundary of the plume. The planar area of the plume was normalized by the height of the water table, and this value was subsequently used in comparisons of zones of influence resulting from different injection conditions.

Plume volumes were calculated by revolving plume boundaries around the axis of the injector, and then approximating the total volume by the sum of the volumes of individual cylinders, as shown in Figure 6-6.

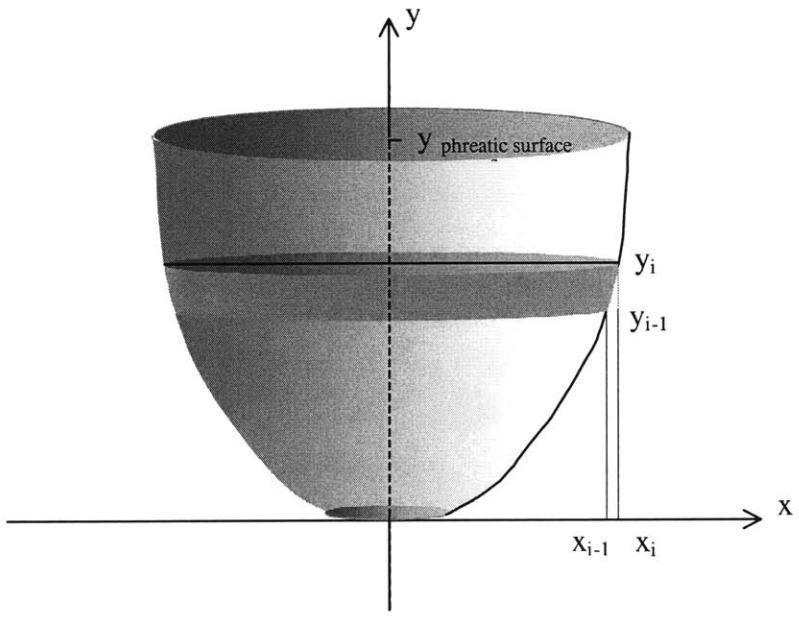

Figure 6-6 *Plume volume approximated by cylindrical surface elements (after Boyce and DiPrima, 1988).*

6.4.3. Plume Volumes

The total volume of an air sparging plume, V, was calculated using the following expression:

$$V = \sum_{i=1}^{n} \pi . x_i^2 . (y_i - y_{i-1}). \qquad \text{Equation 6-2}$$

Experimental plumes were not always perfectly symmetric with respect to the y-axis. For that reason, independent calculations of plume volumes were performed using the coordinates of both the left and right sides of the digitized plumes. The final values of V that will be presented in chapter 9 are the averages of the values calculated from these two sides.

6.4.4. Relative Zone of Influence

A new parameter was defined to quantify the size of the zone of influence of the injectors, namely the relative zone of influence, *RZI*. Defining this new variable was necessary because the elevation of the phreatic surface was not constant for all the experiments reported. Comparisons of the different zones of influence therefore required these to be normalized by the available volume of saturated material for a given experiment. In order to make the *RZI* dimensionless, the calculated volume of the plume was normalized by the volume of the largest plume that could be obtained for a given phreatic surface elevation, as shown in Figure 6-7. The largest plume for a given sample geometry was assumed to be cylinder-shaped, and of radius equal to the depth of the injection point below the phreatic surface. The relative zone of influence of an injector is then given by the following expression:

$$RZI = \frac{Plume\ volume}{2\pi z_{wt}^3} \times 100 \qquad \text{Equation 6-3}$$

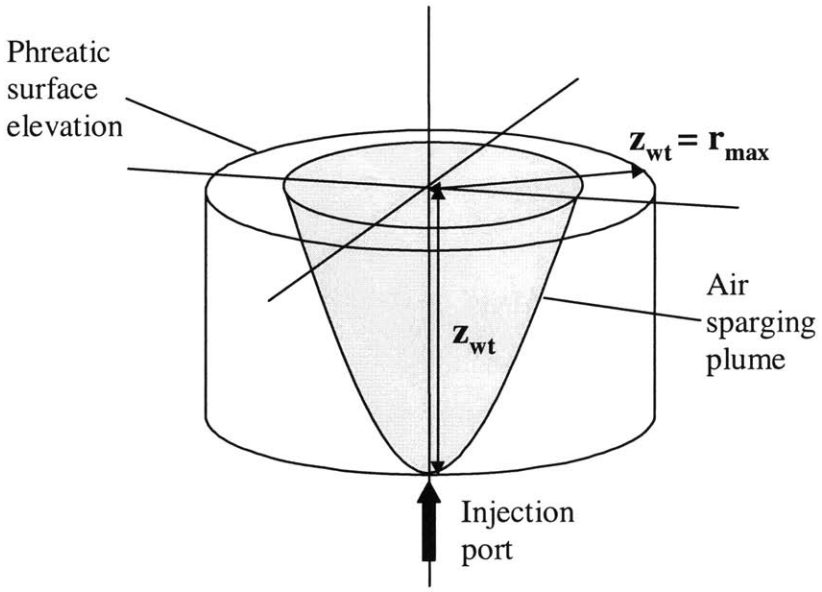

Figure 6-7 *Schematic definition of relative zone of influence of air sparging plume (RZI)*

CHAPTER 7

OVERVIEW OF EXPERIMENTAL RESEARCH PROGRAM

7.1.INTRODUCTION

This chapter describes the methodology followed in the completion of this research study. The objective of this chapter is to present a summary of the approach followed in advancing understanding of the mechanisms that control the flow of injected air through saturated porous media. This approach consisted: first, in isolating a number of parameters which were believed to have a significant effect on the behavior of the injected air, and next, establishing, through an extensive experimental investigation, the specific role of these parameters in the resulting patterns of air flow.

Section 7.2 discusses all of the variables investigated in this research program, and elaborates on the reasons why each specific variable was singled out for further study. Section 7.3 poses the various questions that were addressed by the research, concerning the factors controlling the flow of air through porous media. Finally, section 7.4 presents a summary of the experiments that were successfully completed during the course of this investigation.

7.2.VARIABLES CONSIDERED

Chapter 2 presented background information both on the fundamental aspects of gas-liquid flow, and on the parameters known to affect the performance of air sparging systems. The information presented in that chapter formed the basis of the experimental study. The variables of interest were separated into two groups, namely those encompassing operational parameters (*i.e.* injection pressures and flow rates), and those characterizing the properties of the saturated porous medium. These two groups were addressed independently, as will be described below.

7.2.1. Operational Parameters

7.2.1.1.g-level

The use of the geotechnical centrifuge made it possible to conduct experiments at increasing *g*-levels. The following experimental features were possible, given the fact that testing was performed under higher acceleration fields:

1. Realistic fluid pressure distributions of the pore fluid were always maintained.
2. Testing was conducted at increasing air injection pressures without compromising the overall stability of the model
3. On a more fundamental level, the influence of buoyancy forces on the flow of air through a saturated medium was investigated. Given the density contrast between injected and resident fluids, the influence of buoyancy on the movement of air was expected to be large. More specifically, the relative magnitude of driving buoyancy forces and retaining capillary forces was thought to have a major impact on the characteristics of flow. By increasing the acceleration field acting on a sample, it was possible to increase the magnitude of the buoyancy forces while maintaining the capillary forces constant, which enabled an investigation into the extent of the influence of buoyancy on air flow.

As was described in Chapter 4, experiments at constant injection pressure and flow rate were conducted under *g*-levels increasing from 1-*g* to 100-*g*.

7.2.1.2.Pressure

Injection pressure is one of the parameters governing the behavior of air injected into porous media. It has been suggested that increasing air injection pressure above the air entry pressure, P_{entry}, leads to an increase in air channel density, and consequently to an increase in air saturation within the boundaries of an air sparging plume (Marley *et al.*, 1992; Ahfeld *et al.*, 1994; Brown, 1995). This presumed influence has not been adequately quantified, and a systematic study of the effects of increasing injection air pressures does not exist in the literature. The influence of injection pressures on the characteristics of air flow was therefore one of the major foci of this research.

The majority of the experiments conducted in the centrifuge were performed by increasing injection pressures. These higher pressures however, reflect the fact that as the g-level increases, hydrostatic pressures at the injection point also increase, therefore leading to higher values of P_{entry} with g-level. In order to adequately evaluate the influence of injection pressures, the value of the increment of injection pressures, ΔP, as expressed by Equation 3-8 needs to be increased. Because of the difficulties in setting the target g-level, and therefore the corresponding injection pressure at the beginning of the experiments, the variation in ΔP values for the experiments conducted was not uniform. A value of ΔP was obtained for every test performed, however, and these will be used in the evaluation of the influence of increasing pressures on air flow characteristics.

7.2.1.3.Flow rate

Air sparging can also be conducted under constant injection flow rate conditions, where the magnitude of the flow rate has a critical impact on the propagation characteristics of air in saturated soils. Increasing injection flow rates has been suggested as a means of improving the efficiency of air sparging systems by increasing air saturation in the soil (Ahfeld *et al.*, 1994; Brown, 1995). In fact, the size of the plumes predicted by the most widely cited model of air sparging is directly dependent on the injection flow rate (van Dijke *et al.*, 1996).

A few studies available in the literature have considered the influence of ranges of flow rates on air sparging plumes (Ji *et. al*, 1993; Elder and Benson, 1999). Injection pressures corresponding to the experimental flow rates are rarely provided, which makes it difficult to isolate the effects of increasing the rate of air flow on plume characteristics.

Experiments conducted for this research were performed under constant injection flow rates that varied from 0.26 cm^3/s to 30 cm^3/s. The purpose of these experiments was to verify, and subsequently quantify, the relationship between plume growth and injection flow rate. Tests were performed to investigate whether plume growth increased proportionally to flow rate until boundary effects prevented further air propagation, or whether the growth of the plume reached a maximum value, independent of flow rate.

Injection pressures were measured, along with flow rates, so that a more complete picture of air entry characteristics could be used in the interpretation phase of this investigation.

7.2.1.4.Injector geometry

As was discussed in Chapter 2, the dimensions of the orifice from which an air bubble is emitted are important in the case of constant pressure injection into pure liquids. On the other hand, if the orifice is sufficiently small, its influence on the resultant bubble dimensions under constant flow rate injection conditions is not significant. Air sparging experiments were conducted to determine if injector geometry, in the presence of a porous medium, still played a significant role in the development of airflow patterns. By comparing air patterns emitted from different injectors under both constant pressure and constant flow rate injection conditions, the impact of injector geometry on air flow characteristics was evaluated.

More specifically, the influence of orifice dimensions on the propagation characteristics of air through porous media was investigated using seven different injector geometries. Injector openings varied not only in their size, which straddled the average pore size diameter of the soils tested, but also in their number, and in their position around the injection port. Orifice dimensions could potentially have an impact on the movement of injected air through soils, if the size of the bubbles being emitted is smaller than the pore diameter of the soils. Although it is probably not realistic to expect flow of individual bubbles through the pores of a medium, regardless of the grain-size of the material, it is conceivable that the amount of coalescence would be limited in the case of small bubbles injected into a coarse medium. This type of flow would have a substantial impact on the size of the zone affected by the treatment. Therefore, it is of interest to determine if bubbly flow does indeed take place.

7.2.2. Porous Medium Parameters

7.2.2.1.Grain-size and permeability

The influence of the grain and pore size of a porous medium on flow considerations is well known. The permeability of the medium, and therefore its

hydraulic conductivity, are tied to the grain size distribution of a soil, and control the flow characteristics though the material. The study of air sparging involves the flow of pore fluid out of a porous medium and the flow of air into that medium, both of which are strongly dependent on the hydraulic conductivity of the soil. The extent to which propagation characteristics of the injected air are governed by the hydraulic conductivity of the medium was investigated in this study.

Visibility considerations imposed constraints on the grain size distributions of the materials used. Very fine grains did not appear transparent when submerged in the selected pore fluids. Therefore, the media tested were predominantly medium to coarse grained with few fines. Three different materials with different hydraulic conductivities were tested under similar injection conditions. Comparison of the resultant plumes provided information on the effect of material properties on flow behavior of air through saturated soils. Most of the samples tested were homogeneous, although a number of experiments were conducted on samples with layers of finer material, in order to see their effects on the final air patterns.

7.2.2.2.Pore fluid

The reason for conducting air sparging experiments on porous media saturated with fluids other than water, was to obtain a transparent medium through which air propagation could be clearly observed. Having obtained a transparent saturated porous medium, the use of different pore fluids also provided some additional advantages. Although variability of the properties of pore fluids in field situations is not usually a matter of concern in air sparging applications, varying the properties of the experimental pore fluids made it possible to investigate, further, the effects of different hydraulic conductivities of the porous material. As indicated by Equation 3-3, the hydraulic conductivity of a soil varies as a function of the viscosity of the interstitial fluid. Experiments were conducted using three different pore fluids, namely water, glycerol, and an optical fluid, allowing the influence of the liquids on the resulting air plumes to be investigated.

7.3.SUMMARY OF EXPERIMENTAL PROGRAM

Summary tables of the air sparging experiments successfully completed are included in this section. These tables are intended to give an overview of the experiments conducted, and only include some descriptive information about the tests. For a complete description of all the relevant parameters of each experiment completed refer to Appendix E, Summary of Experimental Results, in which the tables below are considerably expanded. The following abbreviations are used in the tables:

SP: Crushed glass, poorly graded sand (USCS)

SPF: Crushed glass, poorly graded sand with fines

GB: Glass Beads

IL: Optical fluid - Immersion Liquid

Glyc.: Glycerol

Δq: Step-increment of injection flow rate, in cm^3/s

7.3.1. Free Field Experiments

Air injections into pure liquids were conducted both under constant pressure and constant flow of injection conditions, for every injector, at *g*-levels ranging from 1-*g* to 100-*g*. Summary tables for these experiments are also included in Appendix E.

7.3.2. Constant Pressure Experiments

Table 7-1 Summary of constant pressure injection experiments

Test Name	Injector	Pore fluid	Soil type	Actual *g*-level	P_{inj} [KPa]	ΔP [KPa]
LL01i1	MPI #1	IL	SP	1.0	11.7	10.0
LL10i1	MPI #1	IL	SP	10.7	38.5	4.1
LL20i1	MPI #1	IL	SP	19.8	39.7	0.5
LL30i1	MPI #1	IL	SP	28.4	103.3	2.2
LL40i1	MPI #1	IL	SP	39.9	109.2	3.8
LL50i1	MPI #1	IL	SP	46.0	74.8	2.6
LL60i1	MPI #1	IL	SP	58.8	82.2	0.2
LL70i1	MPI #1	IL	SP	67.9	101.5	2.9
LL80i1	MPI #1	IL	SP	79.6	119.1	2.8
LL90i1	MPI #1	IL	SP	83.5	127.6	3.6

Test Name	Injector	Pore fluid	Soil type	Actual *g*-level	P_{inj} [KPa]	ΔP [KPa]
LL100i1	MPI #1	IL	SP	98.9	148.8	3.5
LL110i1	MPI #1	IL	SP	111.2	160.4	2.5
LL130i1	MPI #1	IL	SP	135.7	210.1	0.6
LL150i1	MPI #1	IL	SP	152.1	235.9	3.6
2LL1i1	MPI #1	IL	SPF	1.0	12.7	11.1
2LL10i1	MPI #1	IL	SPF	11.1	17.7	0.8
2LL20i1	MPI #1	IL	SPF	18.9	29.8	0.8
3LL20i1	MPI #1	IL	SPF	18.6	31.6	0.4
2LL30i1	MPI #1	IL	SPF	28.2	49.9	1.0
2LL40i1	MPI #1	IL	SPF	37.3	64.5	2.2
2LL50i1	MPI #1	IL	SPF	48.6	88.6	1.8
2LL60i1	MPI #1	IL	SPF	57.2	98.2	2.6
2LL70i1	MPI #1	IL	SPF	67.8	120.9	1.5
2LL80i1	MPI #1	IL	SPF	78.2	136.3	1.2
2LL90i1	MPI #1	IL	SPF	87.9	148.0	1.9
2LL100i1	MPI #1	IL	SPF	98.7	171.5	1.8
LL1i2	MPI #2	IL	SP	1.0	9.2	7.5
LL10i2	MPI #2	IL	SP	10.9	15.0	0.4
LL20i2	MPI #2	IL	SP	18.9	28.5	0.6
LL30i2	MPI #2	IL	SP	28.4	46.4	0.1
LL40i2	MPI #2	IL	SP	38.1	60.6	0.7
LL50i2	MPI #2	IL	SP	48.1	79.3	3.1
LL60i2	MPI #2	IL	SP	57.9	97.2	0.1
LL70i2	MPI #2	IL	SP	67.7	107.1	3.8
LL80i2	MPI #2	IL	SP	78.0	129.5	3.4
LL90i2	MPI #2	IL	SP	88.1	139.4	1.0
2LL1i2	MPI #2	IL	SPF	1.0	10.5	8.9
2LL10i2	MPI #2	IL	SPF	10.7	19.0	1.3
2LL20i2	MPI #2	IL	SPF	18.7	32.9	2.4
2LL30i2	MPI #2	IL	SPF	27.6	50.0	4.2
2LL40i2	MPI #2	IL	SPF	36.6	65.7	6.1
2LL50i2	MPI #2	IL	SPF	47.1	83.4	5.9
2LL60i2	MPI #2	IL	SPF	57.6	100.8	5.2
2LL70i2	MPI #2	IL	SPF	66.8	112.1	4.4
2LL80i2	MPI #2	IL	SPF	77.3	134.5	1.5
2LL90i2	MPI #2	IL	SPF	87.4	167.9	4.6
2LL100i2	MPI #2	IL	SPF	98.3	169.8	2.4
LL01i3	MPI #3	IL	SP	1.0	10.3	8.7
LL20i3	MPI #3	IL	SP	18.7	34.7	1.9
LL30i3	MPI #3	IL	SP	28.9	54.5	1.3
LL40i3	MPI #3	IL	SP	39.4	73.5	0.7
LL50i3	MPI #3	IL	SP	48.0	84.0	1.9
LL60i3	MPI #3	IL	SP	58.7	100.9	0.5
LL80i3	MPI #3	IL	SP	78.1	130.3	1.3
LL90i3	MPI #3	IL	SP	87.7	142.5	1.9
LL100i3	MPI #3	IL	SP	98.0	159.9	2.1
2LL1i3	MPI #3	IL	MSF	1.0	11.3	9.5
2LL10i3	MPI #3	IL	MSF	11.0	19.8	0.9

Test Name	Injector	Pore fluid	Soil type	Actual *g*-level	P_{inj} [KPa]	ΔP [KPa]
2LL20i3	MPI #3	IL	MSF	19.0	32.9	0.6
2LL30i3	MPI #3	IL	MSF	27.9	48.3	1.6
2LL40i3	MPI #3	IL	MSF	37.4	65.5	2.1
2LL50i3	MPI #3	IL	MSF	47.7	81.6	1.9
2LL60i3	MPI #3	IL	MSF	56.9	97.1	1.2
2LL70i3	MPI #3	IL	MSF	67.0	112.9	2.7
2LL80i3	MPI #3	IL	MSF	78.0	133.7	2.2
2LL90i3	MPI #3	IL	MSF	87.7	148.6	2.9
2LL100i3	MPI #3	IL	MSF	98.0	168.2	3.0
LL1i4	SPI #1	IL	SP	1.0	11.58	9.8
LL10i4	SPI #1	IL	SP	10.2	20.2	4.1
LL20i4	SPI #1	IL	SP	18.8	31.0	0.7
LL30i4	SPI #1	IL	SP	28.2	51.8	1.6
LL40i4	SPI #1	IL	SP	37.7	65.7	2.0
LL50i4	SPI #1	IL	SP	49.2	89.1	2.8
LL60i4	SPI #1	IL	SP	57.3	98.5	2.7
LL70i4	SPI #1	IL	SP	67.4	111.6	1.4
LL80i4	SPI #1	IL	SP	77.4	135.5	2.3
LL90i4	SPI #1	IL	SP	88.2	150.3	1.6
LL100i4	SPI #1	IL	SP	101.0	176.9	1.5
LL1i5	SPI #2	IL	SP	1.0	9.8	8.0
LL10i5	SPI #2	IL	SP	10.6	17.7	0.1
LL20i5	SPI #2	IL	SP	18.8	32.3	1.0
LL30i5	SPI #2	IL	SP	28.0	49.1	1.6
LL40i5	SPI #2	IL	SP	37.5	65.2	2.3
LL50i5	SPI #2	IL	SP	47.3	82.6	2.8
LL60i5	SPI #2	IL	SP	56.8	99.5	3.7
LL70i5	SPI #2	IL	SP	67.5	116.4	2.6
LL80i5	SPI #2	IL	SP	77.3	134.1	3.1
LL90i5	SPI #2	IL	SP	87.3	150.5	4.8
LL100i5	SPI #2	IL	SP	98.7	168.4	3.6
LL1i6	SPI #3	IL	SP	1.0	9.4	7.5
LL10i6	SPI #3	IL	SP	7.9	16.4	2.9
LL20i6	SPI #3	IL	SP	18.4	32.6	1.6
LL30i6	SPI #3	IL	SP	27.6	48.8	2.2
LL40i6	SPI #3	IL	SP	37.5	65.7	2.4
LL50i6	SPI #3	IL	SP	47.3	82.9	2.7
LL60i6	SPI #3	IL	SP	57.8	99.5	2.0
LL70i6	SPI #3	IL	SP	67.7	118.1	2.3
LL80i6	SPI #3	IL	SP	77.2	133.7	2.9
LL90i6	SPI #3	IL	SP	88.9	152.0	0.6
LL100i6	SPI #3	IL	SP	98.7	154.7	1.4
LL1i7	MPI #4	IL	SP	1.0	10.2	8.4
LL10i7	MPI #4	IL	SP	9.9	18.1	1.8
LL20i7	MPI #4	IL	SP	18.9	31.6	0.7
LL30i7	MPI #4	IL	SP	28.2	47.9	1.4
LL40i7	MPI #4	IL	SP	37.1	61.9	0.8
LL50i7	MPI #4	IL	SP	47.3	80.5	2.7

Test Name	Injector	Pore fluid	Soil type	Actual *g*-level	P_{inj} [KPa]	ΔP [KPa]
LL60i7	MPI #4	IL	SP	56.2	96.7	4.2
LL70i7	MPI #4	IL	SP	67.0	114.0	3.2
LL80i7	MPI #4	IL	SP	76.4	128.7	3.8
LL90i7	MPI #4	IL	SP	87.0	147.2	4.1
LL100i7	MPI #4	IL	SP	97.4	153.0	3.1
GLY05i1	MPI #1	Glyc.	SP	5.2	22.1	9.2
GLY10i1	MPI #1	Glyc.	SP	8.5	25.5	2.8
GLY20i1	MPI #1	Glyc.	SP	18.7	51.8	1.1
GLY30i1	MPI #1	Glyc.	SP	28.6	78.2	3.7
GLY40i1	MPI #1	Glyc.	SP	37.9	93.9	1.9
GLY45i1	MPI #1	Glyc.	SP	42.9	104.3	1.7
GLY50i1	MPI #1	Glyc.	SP	49.0	124.7	0.8
GLY60i1	MPI #1	Glyc.	SP	58.9	143.2	0.3
GLY70i1	MPI #1	Glyc.	SP	70.2	182.5	4.3
GLY80i1	MPI #1	Glyc.	SP	81.2	206.0	1.9
GLY90i1	MPI #1	Glyc.	SP	92.9	240.8	0.6
WAT10i1	MPI #1	Water	GB	10.0	NA	NA
WAT20i1	MPI #1	Water	GB	20.4	NA	NA
WAT30i1	MPI #1	Water	GB	30.7	NA	NA
WAT40i1	MPI #1	Water	GB	41.0	NA	NA
WAT50i1	MPI #1	Water	GB	52.0	NA	NA
WAT60i1	MPI #1	Water	GB	62.7	NA	NA
WAT70i1	MPI #1	Water	GB	73.6	NA	NA
WAT80i1	MPI #1	Water	GB	83.5	NA	NA
WAT90i1	MPI #1	Water	GB	94.3	NA	NA
WAT100i1	MPI #1	Water	GB	105.2	NA	NA

7.3.3. Constant Flow Rate Experiments

Table 7-2 Summary of experiments conducted under constant rates of injection

Test Name	Injector	Pore fluid	Soil type	Actual *g*-level	Flow Rate [cm^3/s]	P_{inj} [KPa]	ΔP [KPa]
LLsl2i1	MPI #1	IL	SP	1.0	0.26	8.27	6.9
LLslwi1	MPI #1	IL	SP	1.0	0.66	8.34	7.0
LLmd3i1	MPI #1	IL	SP	1.0	1.05	7.45	6.1
LLmedi1	MPI #1	IL	SP	1.0	1.58	9.03	7.7
LLmd2i1	MPI #1	IL	SP	1.0	2.11	10.96	9.6
LLfasi1	MPI #1	IL	SP	1.0	2.63	9.31	7.9
LL1slwi1	MPI #1	IL	SP	1.0	0.67	NA	NA

Test Name	Injector	Pore fluid	Soil type	Actual *g*-level	Flow Rate [cm^3/s]	P_{inj} [KPa]	ΔP [KPa]
LL3slwi1	MPI #1	IL	SP	2.9	0.67	8.83	5.1
LL6slwi1	MPI #1	IL	SP	6.7	0.67	12.27	3.8
LL9slwi1	MPI #1	IL	SP	10.4	0.67	19.86	7.1
LL12slwi1	MPI #1	IL	SP	12.5	0.67	23.1	7.5
LL15slwi1	MPI #1	IL	SP	17.1	0.67	32.34	11.1
LL30slwi1	MPI #1	IL	SP	31.3	0.67	47.64	9.2
LL70slwi1	MPI #1	IL	SP	71.4	0.67	94.39	5.5
LL100slwi1	MPI #1	IL	SP	101.4	0.67	133.76	8.5
LL30md2i1	MPI #1	IL	SP	46.54	1.29	60.3	7.8
LL70md2i1	MPI #1	IL	SP	93.5	1.29	134.9	4.4
LL100md2i1	MPI #1	IL	SP	133.07	1.29	188.2	9.2
LL1gslwh2i1	MPI #1	IL	SP	1.0	0.67	4.1	3.0
LL6gslwh2i1	MPI #1	IL	SP	6.6	0.67	NA	NA
LL12gslwh2i1	MPI #1	IL	SP	11.1	0.67	15.0	3.6
LL15gskwh2i1	MPI #1	IL	SP	14.2	0.67	20.3	4.5
LL20gslwh2i1	MPI #1	IL	SP	19.7	0.67	27.7	5.4
LL30gslwh2i1	MPI #1	IL	SP	29.0	0.67	40.1	5.8
LL70gslwh2i1	MPI #1	IL	SP	69.8	0.67	109.8	4.5
LLsl2i2	MPI #2	IL	SP	1.0	0.26	8.89	7.5
LLslwi2	MPI #2	IL	SP	1.0	0.66	8.83	7.5
LLmd3i2	MPI #2	IL	SP	1.0	1.05	8.34	7.0
LLmedi2	MPI #2	IL	SP	1.0	1.58	8.27	6.9
LLmd2i2	MPI #2	IL	SP	1.0	2.11	8.69	7.3
LLfasi2	MPI #2	IL	SP	1.0	2.63	8.83	7.4
LLsl2i3	MPI #3	IL	SP	1.0	0.26	NA	NA
LLslwi3	MPI #3	IL	SP	1.0	0.66	NA	NA
LLmd3i3	MPI #3	IL	SP	1.0	1.05	NA	NA
LLmedi3	MPI #3	IL	SP	1.0	1.58	8.62	7.2
LLmd2i3	MPI #3	IL	SP	1.0	2.11	9.03	7.7
LL10gslwi3	MPI #3	IL	SP	11.7	0.67	NA	NA
LL20gslwi3	MPI #3	IL	SP	21.7	0.67	28.75	1.8
LL30gslwi3	MPI #3	IL	SP	32.9	0.67	41.58	1.1
LL70gslwi3	MPI #3	IL	SP	73.9	0.67	93.98	2.0
LL100gslwi3	MPI #3	IL	SP	101.0	0.67	135.69	10.9
LL30gmd3i3	MPI #3	IL	SP	31.6	1.05	42.4	3.0
LL70gmd3i3	MPI #3	IL	SP	73.7	1.05	96.74	5.0
LL100gmd3i3	MPI #3	IL	SP	104.5	1.05	NA	NA
LL20gmd2i3	MPI #3	IL	SP	21.1	1.29	36.06	10
LL30gmd2i3	MPI #3	IL	SP	31.3	1.29	61.6	9.00
LLsl2i4	SPI #1	IL	SP	1.0	0.26	8.34	6.9
LLslwi4	SPI #1	IL	SP	1.0	0.66	8.55	7.1
LLmd3i4	SPI #1	IL	SP	1.0	1.05	8.83	7.4
LLmedi4	SPI #1	IL	SP	1.0	1.58	8.76	7.3
LLmd2i4	SPI #1	IL	SP	1.0	2.11	8.55	7.1
LLfasi4	SPI #1	IL	SP	1.0	2.63	8.69	7.2
LLsl2i5	SPI #2	IL	SP	1.0	0.26	NA	NA
LLslwi5	SPI #2	IL	SP	1.0	0.66	NA	NA

Test Name	Injector	Pore fluid	Soil type	Actual *g*-level	Flow Rate [cm^3/s]	P_{inj} [KPa]	ΔP [KPa]
LLmd3i5	SPI #2	IL	SP	1.0	1.05	NA	NA
LLmedi5	SPI #2	IL	SP	1.0	1.58	9.52	8.1
LLmd2i5	SPI #2	IL	SP	1.0	2.11	8.21	6.8
LLfasi5	SPI #2	IL	SP	1.0	2.63	10.27	8.9
LLsl2i6	SPI #3	IL	SP	1.0	0.26	8.48	7.1
LLslwi6	SPI #3	IL	SP	1.0	0.66	9.17	7.8
LLmd3i6	SPI #3	IL	SP	1.0	1.05	9.38	8
LLmedi6	SPI #3	IL	SP	1.0	1.58	8.89	7.5
LLmd2i6	SPI #3	IL	SP	1.0	2.11	8.89	7.5
LLfasi6	SPI #3	IL	SP	1.0	2.63	10.76	9.4
LL1gBDi1s	MPI #1	IL	GB	1.0	0.67	8.55	6.9
LL3gBDi1s	MPI #1	IL	GB	2.6	0.67	11.58	7.6
LL6gBDi1s	MPI #1	IL	GB	6.1	0.67	9.58	0.3
LL12gBDi1s	MPI #1	IL	GB	11.6	0.67	20.89	4.1
LL20gBDi1s	MPI #1	IL	GB	18.8	0.67	36.3	9.2
LL1gBDi1f	MPI #1	IL	GB	1.0	1.29	8.89	7.3
LL3gBDi1f	MPI #1	IL	GB	2.8	1.29	11.72	7.4
LL1gBDi3s	MPI #3	IL	GB	1.0	0.67	9.1	7.4
LL3gBDi3s	MPI #3	IL	GB	3.1	0.67	12.27	7.4
LL12gBDi3s	MPI #3	IL	GB	11.9	0.67	22.0	3.8
LL20gBDi3s	MPI #3	IL	GB	20.3	0.67	NA	NA
LL1gBDi3f	MPI #3	IL	GB	1.0	1.29	8.62	7.0
LL3gBDi3f	MPI #3	IL	GB	3.1	1.29	11.93	7.0

Table 7-3 *Summary of experiments conducted under gradually increasing constant rates of injection*

Test Name	Injector	Pore fluid	Soil type	*g*-level	Flow Rate [cm^3/s]	$(P_{inj})_{max}$ [KPa]	ΔP [KPa]
LLi3fw1	MPI #3	IL	SP	1.0	4.4	7.1	5.7
LLi3fw2	MPI #3	IL	SP	1.0	8.7	10.9	9.5
LLi3fw3	MPI #3	IL	SP	1.0	13.0	11.5	10.1
LLi3fw4	MPI #3	IL	SP	1.0	17.3	16.1	14.7
LLi3fw5	MPI #3	IL	SP	1.0	Increase to 28.1	6.6	5.3
LLi3fw6	MPI #3	IL	SP	1.0	Increase to 28.1	4.5	3.1
LLi3fw7	MPI #3	IL	SP	1.0	Increase to 28.1	2.8	1.4
LLi11gfw1	MPI #1	IL	SP	1.0	3 to 28.1 - Δq 4.3	11.9	10.5
LLi11gfw2	MPI #1	IL	SP	1.0	3 to 28.1 - Δq 4.3	12.9	11.5
LLi21gfw1	MPI #2	IL	SP	1.0	3 to 28.1 - Δq 4.3	4.3	3.0
LLi21gfw2	MPI #2	IL	SP	1.0	3 to 28.1 - Δq 4.3	7.5	6.1
LLi31gfw1	MPI #3	IL	SP	1.0	3 to 28.1 - Δq 4.3	4.5	3.1

Test Name	Injector	Pore fluid	Soil type	*g*-level	Flow Rate [cm^3/s]	$(P_{inj})_{max}$ [KPa]	ΔP [KPa]
LLi31gfw2	MPI #3	IL	SP	1.0	3 to 28.1 - Δq 4.3	4.2	2.8
LLi41gfw1	SPI #1	IL	SP	1.0	3 to 28.1 - Δq 4.3	4.9	3.5
LLi41gfw2	SPI #1	IL	SP	1.0	3 to 28.1 - Δq 4.3	3.7	2.3
LLi61gfw4	SPI #3	IL	SP	1.0	3 to 28.1 - Δq 4.3	22.8	21.4
LLi61gfw2	SPI #3	IL	SP	1.0	3 to 28.1 - Δq 4.3	22.4	21.0

CHAPTER 8

EXPERIMENTAL RESULTS

8.1.INTRODUCTION

This chapter presents results of experiments conducted to study the mechanisms controlling air propagation through saturated porous media. Most of the data included in this chapter are in the form of images, since the differences in air propagation observed during the experiments are best described by pictures taken during injection. These image data will be subsequently summarized and converted into numerical results, which will be used later in the characterization of the flow mechanisms themselves.

The chapter is divided into three major sections, starting with section 8.2, which covers air sparging experiments conducted under a constant pressure injection conditions. Next, section 8.3 presents results of tests conducted under constant flow rate of injection. Within each of these two sections, the characteristics of the flow of air in pure liquids are presented, followed by results showing the progression of propagation behavior through saturated porous media under varying experimental conditions. These experimental conditions include increasing *g*-levels and increasing injection flow rates. In addition, the effect of two different pore fluids and two different porous media on the characteristics of air propagation are evaluated. The impact of varying injector geometries is discussed, and experimental air velocities through the porous media are presented. Finally, section 8.4 presents a summary of the experimental observations presented throughout the chapter, and highlights the various patterns of propagation of air injected into saturated porous media.

Only a selected group of images is included in the chapter, which illustrate the points of importance in the discussion. A complete set of images is included in Appendix D, which further completes the data presented.

8.2.CONSTANT PRESSURE EXPERIMENTS

8.2.1. Free Field

Most of the discussion about gas-liquid flow presented in Chapter 2 referred to flow of single bubbles in pure liquids. It is clear that once the porous medium is incorporated into the analysis, together with high injection pressures, increases in buoyancy forces, and varying injector geometries, the bubble features discussed in the background section will need to be significantly modified in order to describe the new flow characteristics. For these reasons, prior to conducting air sparging experiments through the saturated glass, centrifuge air injections were performed in the free field (*i.e.* fluid only). Tests were conducted at the same *g*-levels and under the same injection conditions that would later be used for injections in porous media. The series of experiments in the free field provided insight into the impact of increasing buoyancy and of changing injector characteristics on the gas-liquid flow conditions.

8.2.1.1.Flow patterns

Air flow patterns observed in the free field varied substantially as *g*-level increased. Figures 8-1 through 8-4 show images captured during experiments conducted at increasing *g*-levels in the immersion liquid and glycerol, respectively. The figures include results from experiments conducted using injectors MPI #2 and SPI #2 only. Experiments conducted using the other four injectors followed similar trends.

The impact of the fluid on bubble geometry is evident from the figures, as seen by comparing bubbles which formed in immersion liquid to those in glycerol. Using the bubble flow terminology, bubbles formed in the immersion liquid are for the most part small, and would be referred to as spherical, ellipsoidal, or wobbling bubbles. Bubbles that formed in glycerol are considerably larger and would be designated as ellipsoidal-caps or spherical caps (Wegener and Parlange, 1973; Clift *et. al,* 1978). Differences in bubble characteristics were anticipated, since bubble types in a given liquid vary depending on the relative magnitude of interfacial, viscous, and inertial forces at the varying *g*-levels. Given the drastic differences in bubble characteristics, air flow patterns are likely to be highly dependent on the pore fluid, if, once injected into the porous media, air travels in the form of discrete bubbles.

Flow characteristics of bubbles in the immersion liquid will be described first.

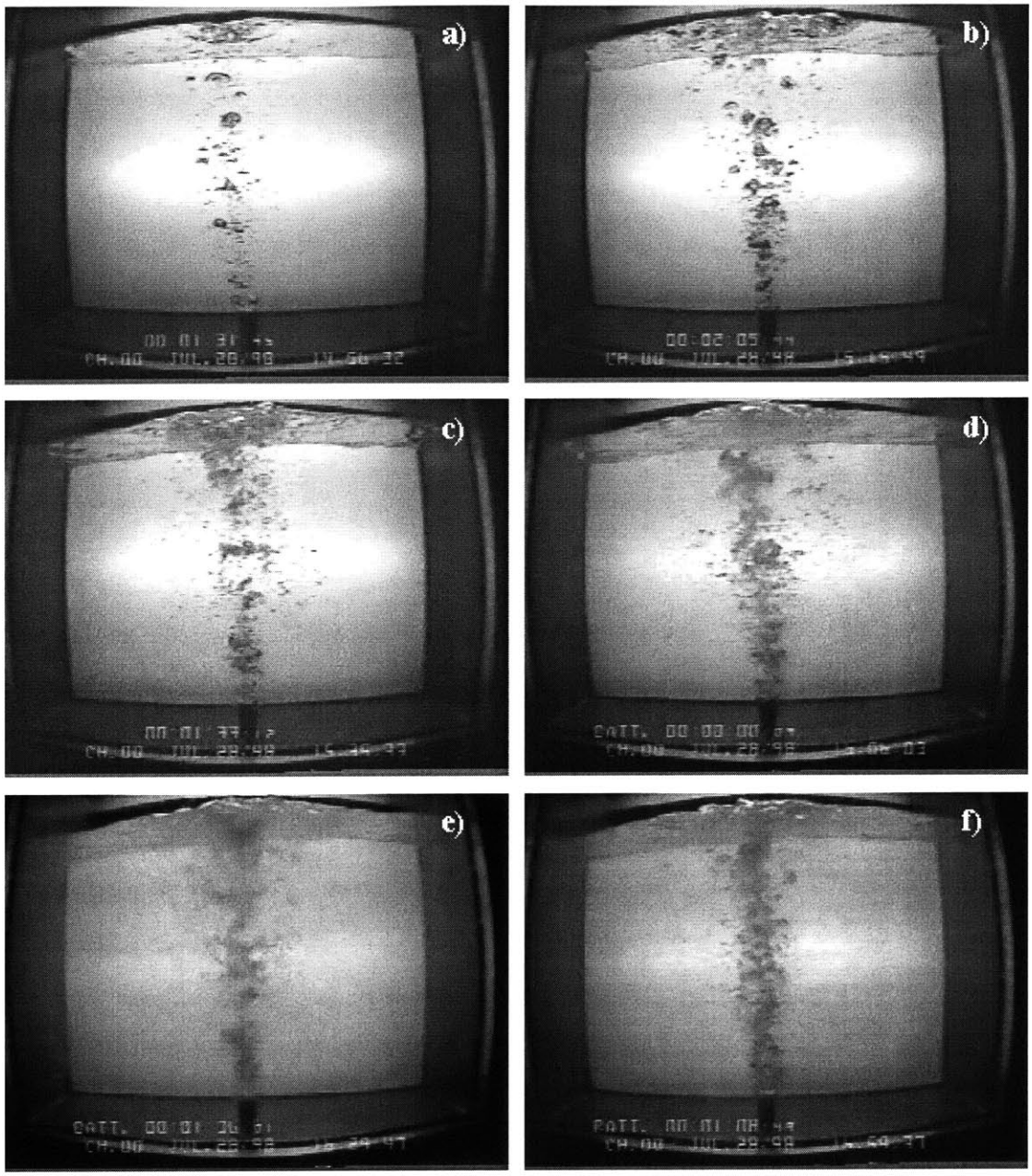

Figure 8-1 *Free field injection experiments in immersion liquid using injector MPI #2, at increasing g-levels: a) 10-g; b) 20-g; c) 30-g; d) 50-g; e) 70-g; and f) 90-g.*

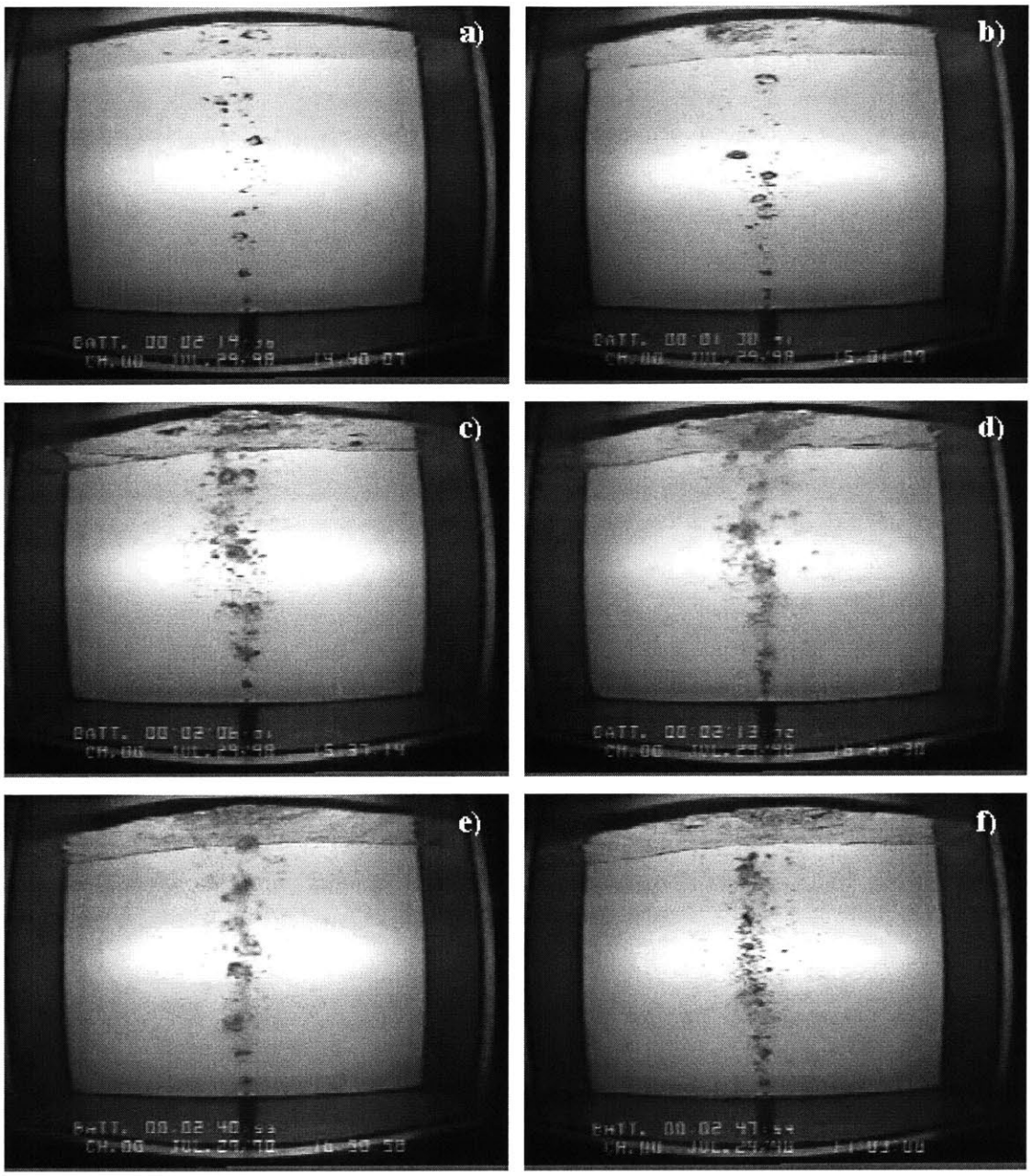

Figure 8-2 *Free field injection experiments in immersion liquid using injector SPI #2, at increasing g-levels: a) 10-g; b) 20-g; c) 30-g; d) 50-g; e) 70-g; and f) 90-g.*

In the case of the free field experiments conducted in this study, air injection was continuous, and thus the frequency of bubble emission was significantly higher than those used in the studies previously reviewed. As a result, interaction between bubbles

was predominant, since bubbles injected at the same time made their ascent simultaneously.

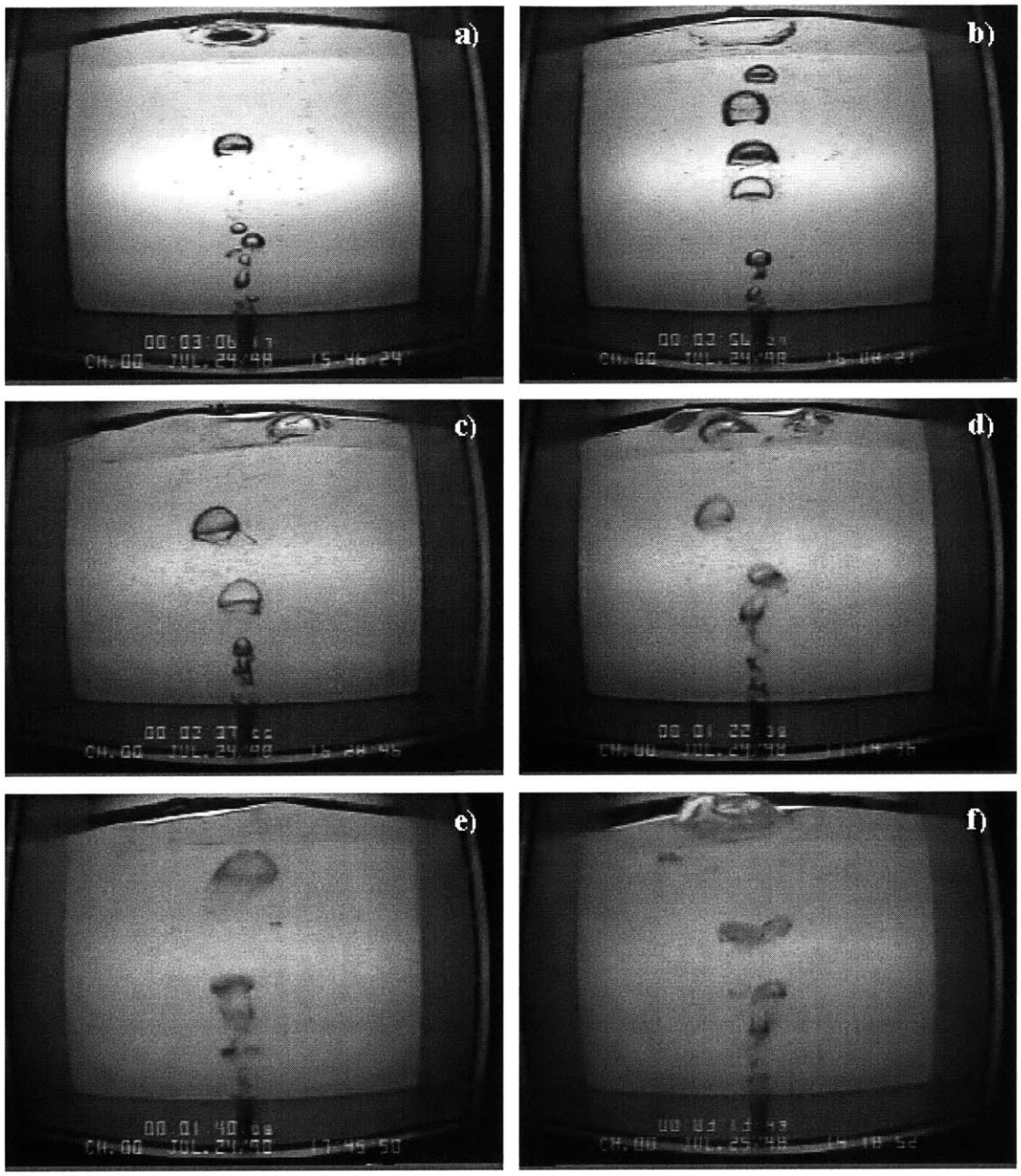

Figure 8-3 *Free field injection experiments in glycerol using injector MPI #2, at increasing g-levels: a) 10-g; b) 20-g; c) 30-g; d) 50-g; e) 70-g; and f) 90-g.*

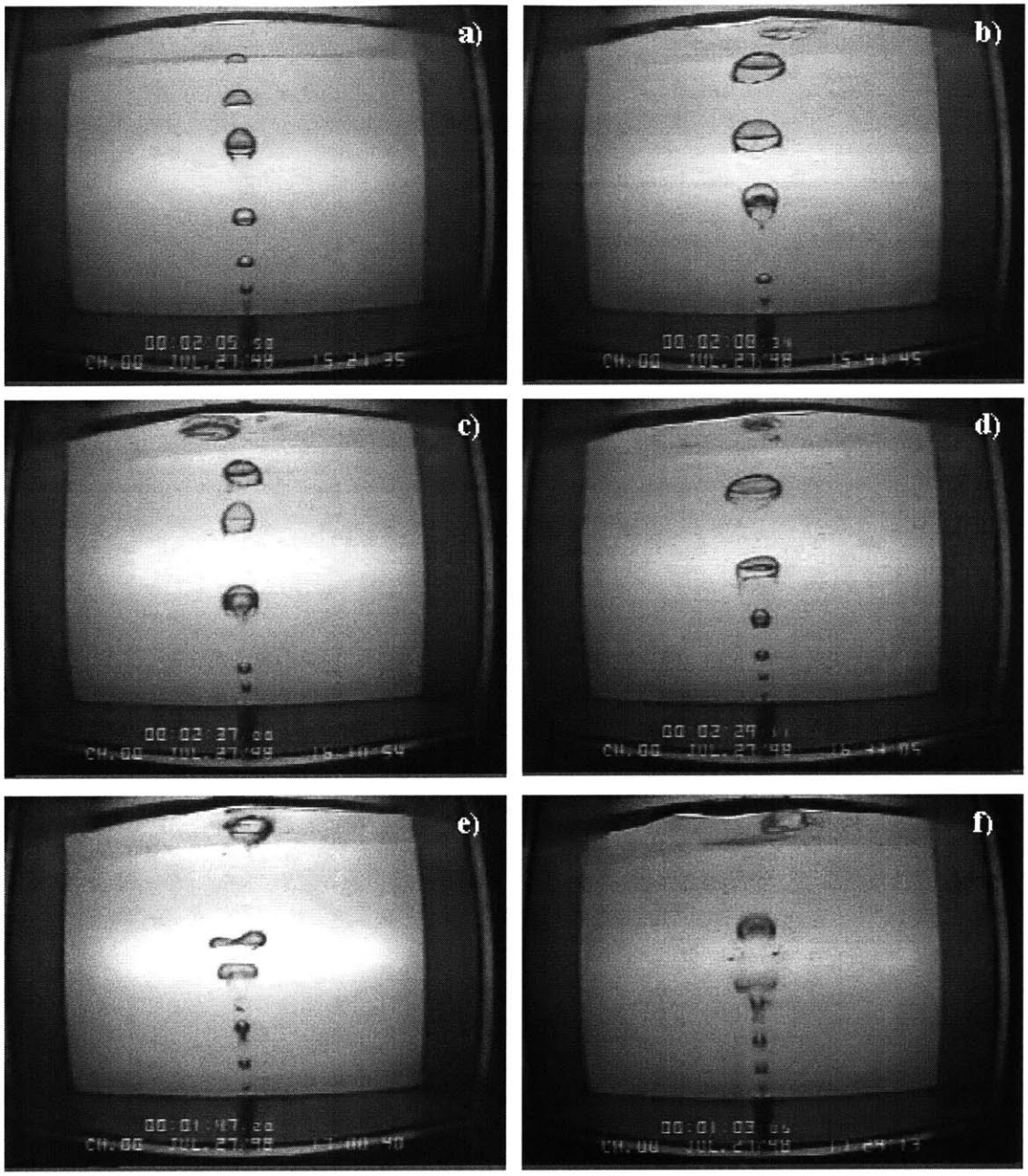

Figure 8-4 *Free field injection experiments in glycerol using injector SPI #2, at increasing g-levels: a) 10-g; b) 20-g; c) 30-g; d) 50-g; e) 70-g; and f) 90-g.*

At *g*-levels lower than 10-*g*, bubbles injected from single port injectors rose mostly independent of each other, in primarily rectilinear trajectories. The bubbles had clearly differentiable irregular shapes, and their size increased slightly as the phreatic

surface was approached. Increases of g-level up to an acceleration of approximately 30-g, resulted in larger bubble sizes immediately outside of the injector, and to more irregular bubble shapes. The trajectory of the bubbles continued to be primarily rectilinear, but lateral deviations from the vertical path were observed. Bubble velocities increased at higher g-levels. As g-level increased to approximately 50-g, bubble coalescence became widespread. Coalescence lead to the formation of considerably larger bubbles and to a high number of very fine bubbles. At accelerations higher than 50-g, bubbles rose in what appeared to be a continuous jet of air, where individual bubbles could not be identified. The velocity of propagation of the jet was very high, and the phreatic surface was reached within only a few frames of the video camera. As g-levels exceeded 70-g, liquid recirculation patterns became evident as "slushing" occurred against the sides of the box. As a result, after breakthrough, the injection jet did not flow vertically from the injector to the phreatic surface, but oscillated from one side to the other of the injection point.

The behavior of bubbles injected from multiple port injectors was slightly different, mainly due to the fact that conditions in the box became turbulent soon after breakthrough. Since multiple bubbles entered the box at the same time, a liquid circulation pattern was established close to the injector. Bubbles rose with a swirling motion and collided with each other, therefore creating more turbulent conditions at lower g-levels than those observed for single opening ports. Bubble coalescence occurred at every g-level, at a short distance from the top of the injectors.

The trends described for bubbly flow in the immersion liquid were also observed in glycerol. The conditions described above were accentuated, since the size of the injected air bubbles was significantly greater in glycerol than in immersion liquid as shown by Figures 8-3 and 8-4. Due to the large size of the bubbles formed at the injector, interactions between bubbles were frequent, and bubble coalescence occurred very close to the injection point. Flow characteristics therefore became turbulent soon after entry of air occurred, at every g-level tested. Collisions between bubbles resulted in highly deformed ellipsoidal caps of random trajectories and an increasing number of very fine

bubbles. These patterns were further accentuated in the case of the multiple port injectors.

8.2.1.2.Breakthrough velocities

The free field velocity of the initial bubble front both in glycerol and in immersion liquid, due to injection from single and multiple port injectors, was determined by taking the slope of displacement versus time plots (see section 6.2.2). It must be noted, however, that once breakthrough occurred and the air front reached the phreatic surface, turbulence in the box increased significantly even at the lower *g*-levels, with the following two consequences: 1) the bubbles were accelerated by the circulating fluid; and 2) bubble collisions promoted bubble coalescence and hence further increases in velocity. Velocities at this point could no longer be determined accurately.

Velocities in the free field from tests conducted using the six different injectors are presented in Figure 8-5. The velocities shown in the figure are those of the first front of bubbles that was injected, as the column of fluid located above the injector was being displaced, and air reached the phreatic surface.

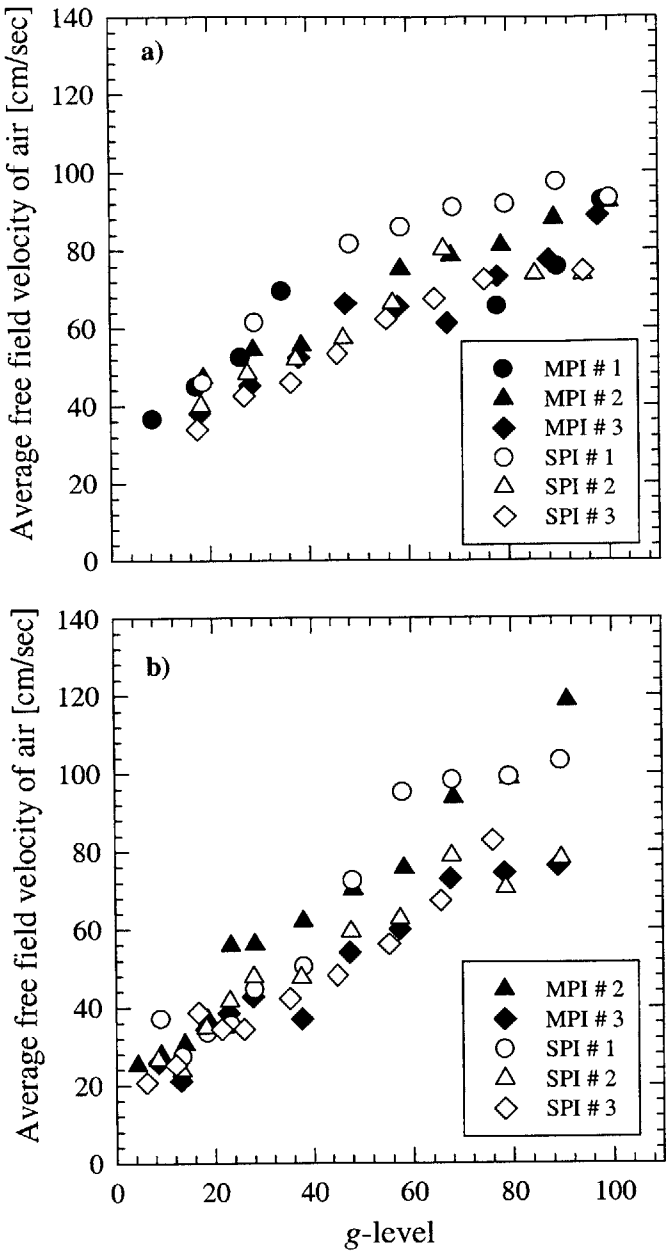

Figure 8-5 *Free field velocities of air under constant pressure injection, at increasing g-level in: a) immersion liquid; and b) glycerol.*

Free field velocities in glycerol were found to be on average 25% higher than those in immersion liquid. Velocities in the box increased with increasing *g*-level.

Increases in bubble velocity with *g*-level are attributable to two factors. First, as bubbles rise, the surrounding fluid pressure acting along their boundaries decreases. The decrease in confinement leads to a volume increase, and therefore bubbles expand as they

flow upward. Buoyancy forces increase with increasing bubble volume and as a result, bubbles accelerate during their ascent. Second, as the *g*-level increases, injection pressures also increase in order to overcome the static head above the injection point. As the pressure of injection increases, the frequency of bubble emission becomes greater, and therefore bubble coalescence occurs closer to the injection point. Bigger bubbles are then formed shortly after entry, and for the same reason discussed above, their free field velocities increase with *g*-level.

8.2.2. Wire Mesh Screens

Mesh screens were used to investigate the manner in which a flow restriction affected the size of ascending bubbles as well as the overall bubbly flow pattern. The objective of using the screens was that of simulating, and manipulating, entry characteristics of air flow into porous media, by varying the opening size of the mesh screen. This constituted an idealized way of varying pore space diameter and initial bubble diameter, respectively. The screens were positioned at varying distances from the top of the injection port using the rack described in section 4.3.1.2, and experiments were conducted using the single port injectors at increasing *g*-levels. Experiments were conducted both in glycerol and in the immersion liquid.

Only a moderate amount of information, mainly qualitative in nature, was collected from this series of experiments. Experiments conducted in glycerol are more adequate for illustration purposes, and a selection of images are shown in Figure 8-6. This figure includes images collected during experiments conducted in glycerol, using injector SPI #1, at *g*-levels equal to 10-*g*, 20-*g*, and 50-*g*. The cross sectional area of the screen openings shown in the figure is 1 mm^2. The screen is located 3 cm above the top of the injector in Figures 8-6 a) and b), and 8 cm above in Figures 8-6 c), d), and e).

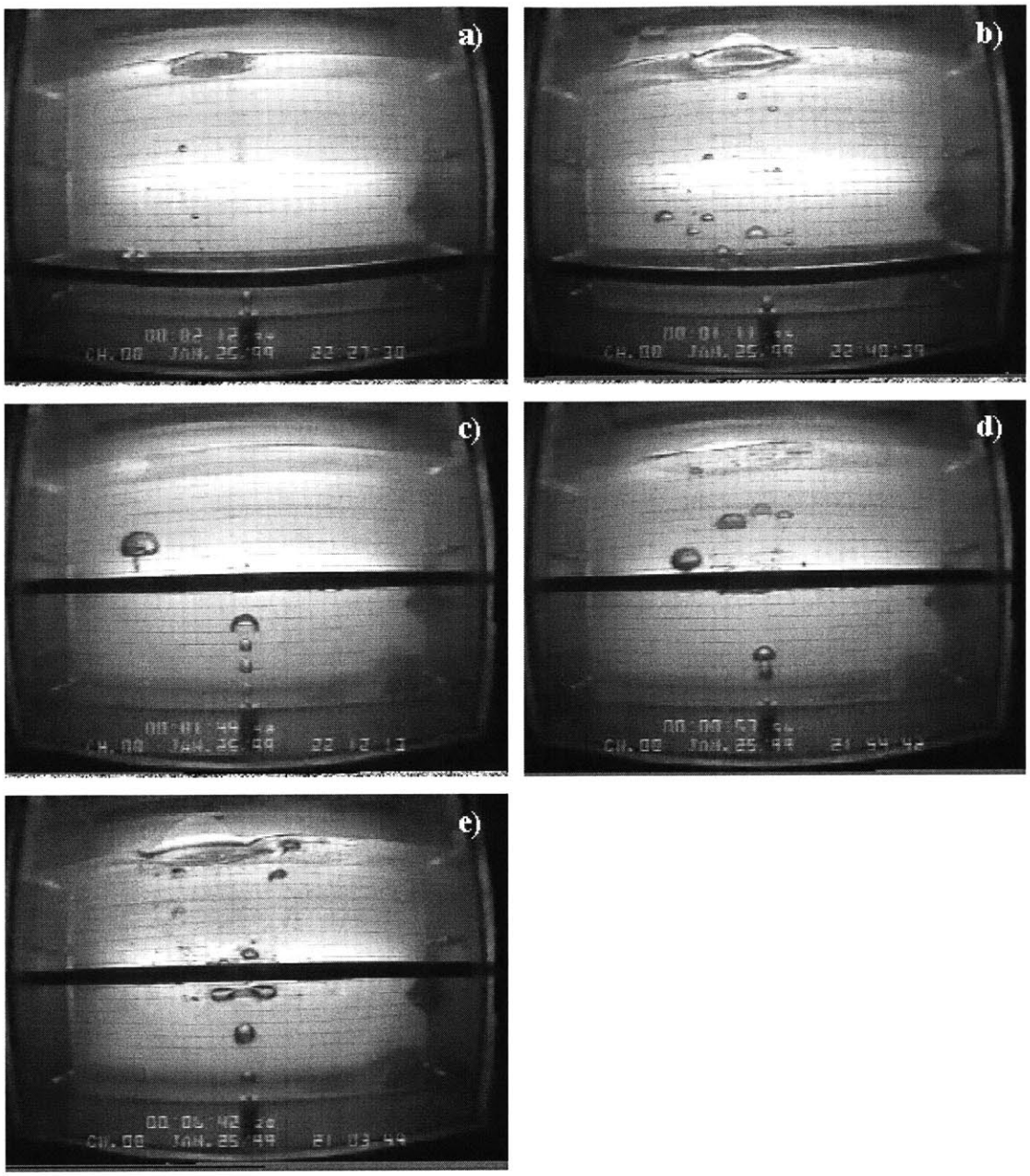

Figure 8-6 *Deformation of air bubble patterns in glycerol at varying g-levels due to flow though steel mesh screens - Injector SPI #1: a) 10-g; b) 20-g; c) 10-g; d) 20-g; e) 50-g.*

At low *g*-levels, individual bubbles reaching the lower side of the screen were not able to penetrate the mesh opening and break through to the upper side. Bubbles then accumulated underneath the screen and subsequently coalesced forming a larger bubble.

This bubble would, in turn, remain stationary until a critical volume was reached, at which point buoyancy was sufficient to drive the bubble through the mesh openings. It was unfortunately not possible to establish the size of the big bubble that formed underneath the screen, since only its edges were visible through the wide-angle camera. However, as the test progressed, the large bubble would either 1) deform and flow through the mesh, remaining large throughout the remaining distance of ascent, as illustrated in Figures 8-6 a) and c); or 2) break into smaller bubbles as it flowed across the mesh, at higher *g*-levels, as shown in Figures 8-6 b) and d). The difficulty with increasing the *g*-level in these tests was that fast rising bubbles collided against the screen breaking up upon impact and passing through. This further contributed to turbulence in the box, and as a result, bubbles were deformed, forced through the screen, and broke up into many very fine bubbles as shown in Figure 8-6 d).

8.2.3. Summary of Experimental Observations in the Free Field

Examples of bubbly flow due to continuous injection of air into pure liquids clearly showed that bubble interaction is a major characteristic of the flow at all *g*-levels and for all types of injectors. The frequency of bubble emission under constant pressure conditions is such that even in the free field, upward flow of single bubbles did not occur. Images presented showed that even in the absence of any flow restriction, as bubble frequency increased a jet formed, and air flowed upward essentially as one channel. Furthermore, in the presence of a restriction in the form of a screen, bubbles coalesced at the entry side while driving forces overcame restricting forces. At this point entry pressures were overcome and bubble flow resumed on the other side of the screen.

It is therefore not realistic to assume that air will flow through a porous medium, a medium of successive restrictions, in the form of bubbles if a continuous flow is established through the medium. Under constant pressure conditions the frequency of bubble emission is sufficiently high that bubble coalescence is pervasive, even if the pores of the medium are very large relative to the entry diameter of injected air bubbles.

8.2.4. Air Injection in Porous Media

This section presents a summary of results obtained from air sparging experiments conducted, at constant injection pressure, through the transparent porous medium. Under these testing conditions the pressure in the air phase is set at the source, behind the injection point. The flow rate through the soil is determined by the resistance of the saturated medium to the advancement of the air front under the applied pressure.

8.2.4.1.Influence of g-level on air propagation

Increasing acceleration fields during constant pressure injection experiments had a drastic effect on the characteristics of air propagation through porous media. Figures 8-7, 8-8, and 8-9 illustrate the advancement of the air front through the sample from the moment air enters the sample box until steady state conditions are reached, at increasing *g*-levels. These images make it possible to observe the impact of increasing *g*-level not only on final plume shapes, but also during the various stages of plume formation. Two terms need to be defined in order to describe the plumes. The term *steady-state* is used to designate the state after which no further change in plume geometry was observed. The term a*ir saturation* is used loosely to describe the air density within the boundaries of the plume, estimated from relative intensity of the gray scale.

Figure 8-7 for example, shows sequential images taken during injection of air through a sample submerged in immersion liquid, at 1-*g*. Lateral spreading occurs from the initial stages of entry, and continues until steady-state is reached (shown in the last image of the sequence). As a result, a large zone of influence is obtained at the end of the experiment. It is important to observe that significant plume growth occurs at the base, close to the injector, which will be referred to as *basal spreading*. Air does not propagate as a stable front, but rather advances as a cluster of channels, with individual channels moving upward at essentially the same velocity. Within the channels, a smaller form of propagation is noticeable, of the scale of the pore spaces, in the characteristic branching pattern of fingers. The final air saturation within the boundaries of the plume is high on average, but liquid-saturated areas, left over from gaps between the fingers are still visible at steady-state.

Figures 8-8 and 8-9 show similar sequences of air propagation in immersion liquid, but under acceleration fields of 10-*g* and 40-*g*, respectively. As shown on the images, the difference in air flow patterns and plume shape with increasing *g*-level is pronounced.

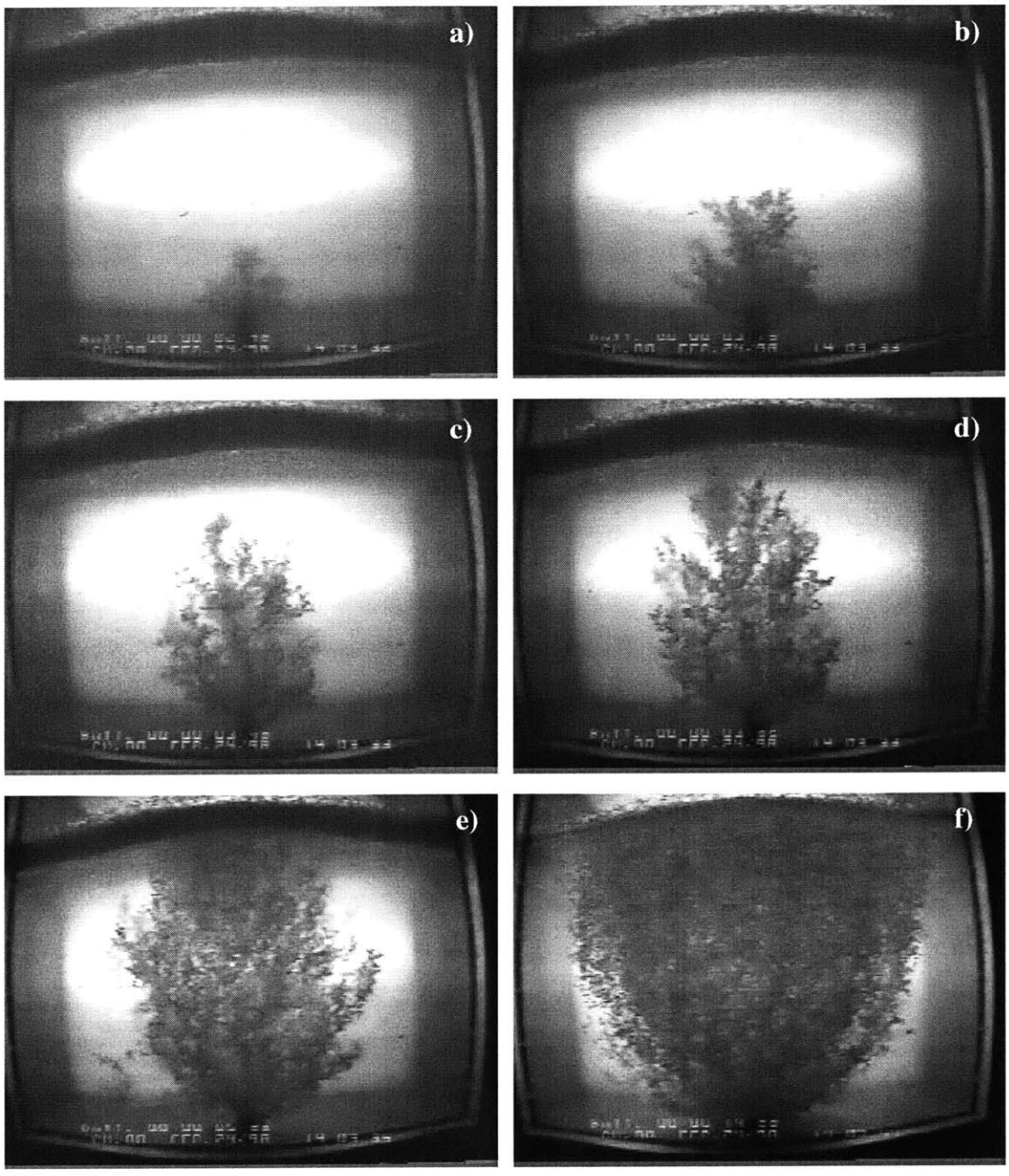

Figure 8-7 *Injector MPI #1 – Propagation of injected air at 1-g through porous media saturated with immersion liquid.*

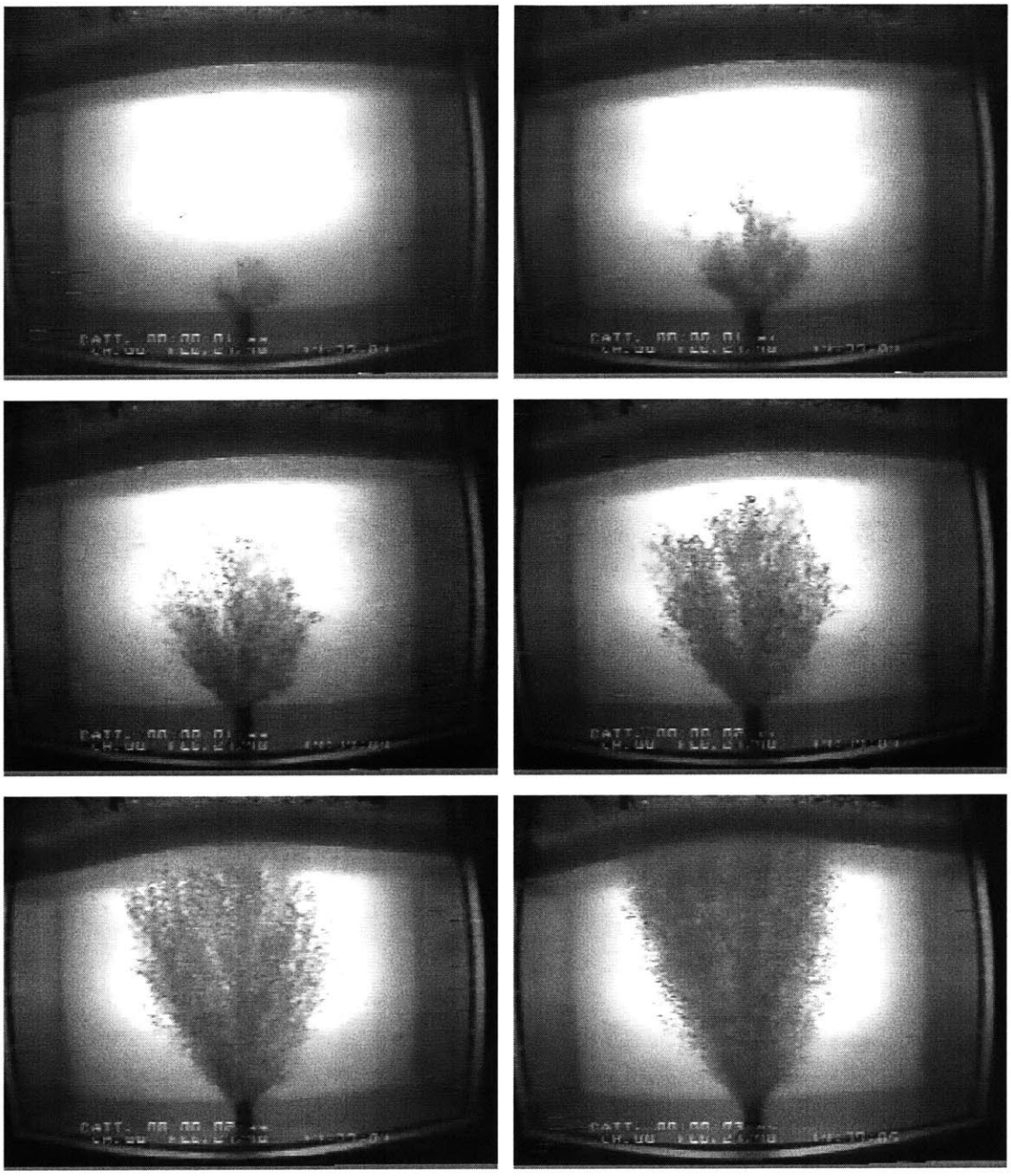

Figure 8-8 *Injector MPI #1 – Propagation of injected air at 10-g through porous media saturated with immersion liquid.*

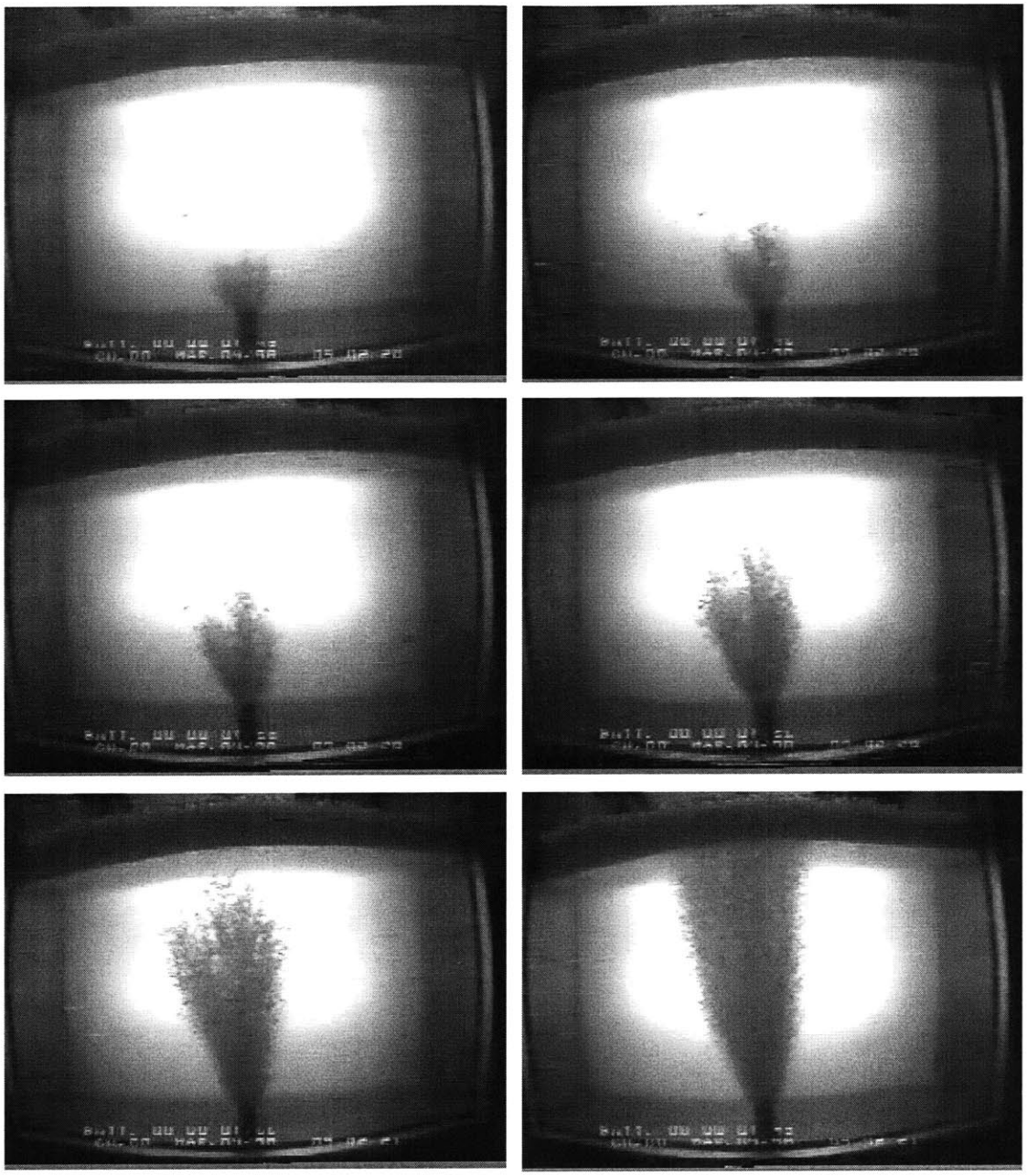

Figure 8-9 *Injector MPI #1 – Propagation of injected air at 40-g through porous media saturated with immersion liquid.*

Lateral air propagation decreases rapidly with increasing acceleration level, leading to a drop in the zone of influence of a given injector. The decrease in the zone of influence of the plume at 10-*g* relative to that at 1-*g* for example, is of approximately 50%. At 10-*g*

propagation is still taking place as a finger front, although individual fingers are not so clearly differentiated. By the time at which accelerations have reached 40-*g*, propagation takes place as a more uniform front.

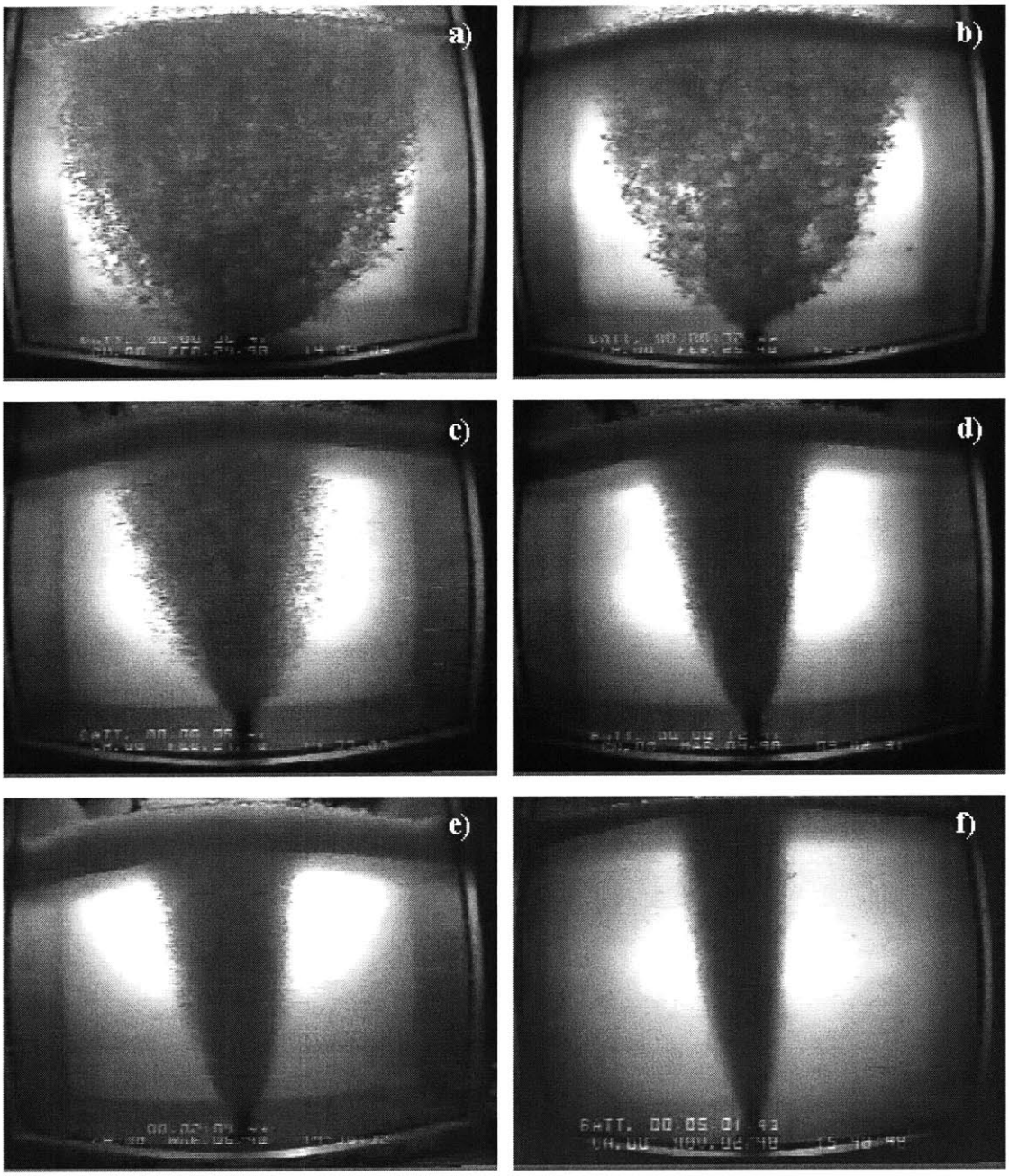

Figure 8-10 *Steady-state air plumes obtained at increasing g-levels following injection of air into porous media saturated with immersion liquid - Injector MPI #1: a) 1-g; b) 3-g; c) 10-g; d) 30-g; e) 40-g; f) 60-g.*

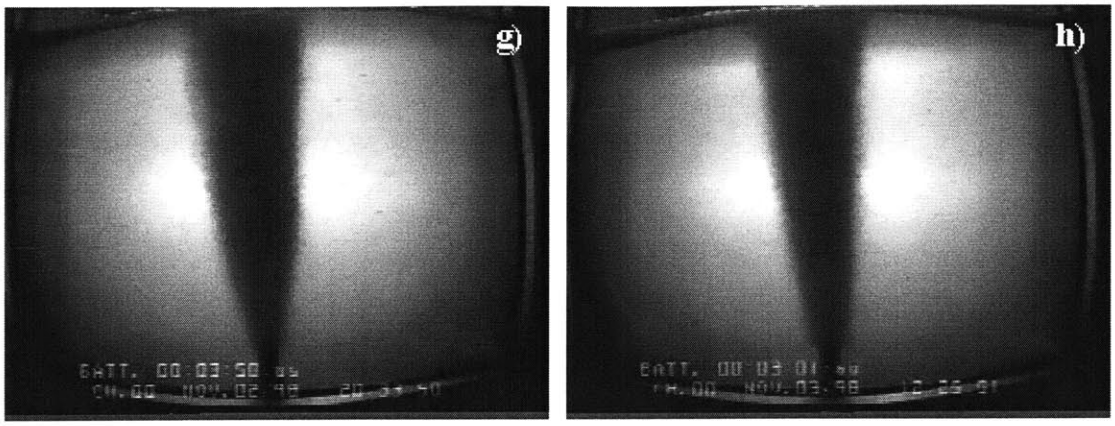

Figure 8-10 (ctd.) *Air plumes obtained at increasing g-levels following injection of air into porous media saturated with immersion liquid - Injector MPI #1: g) 80-g; h) 100-g.*

The effects of increasing acceleration levels on final plume shapes in media saturated with immersion liquid are summarized in Figure 8-10. This figure shows steady-state plumes obtained under accelerations ranging from 1-*g* to 100-*g*. Several features are noticeable when comparing the progression of plume shapes with increasing *g*-level. For instance, the decrease in plume width is sharp with small increases in *g*-level until approximately 40-*g*, at which point further increases in *g*-level cause a less pronounced reduction in plume size. The extent of basal lateral spreading is the first characteristic to noticeably decrease with slight increases in *g*-level, leading to much steeper inclination of the sides of the plume. Further increases in *g*-level consistently reduced the size of the resulting plume, until very narrow jets were obtained under accelerations ranging from 70-*g* to 100-*g*. It is also interesting to see that the boundary between air-saturated and immersion-liquid-saturated regions is not sharp for acceleration fields lower than 30-*g*. In contrast, plumes are fully saturated up to their boundaries at *g*-levels ranging from 30-*g* to 100-*g*, clearly delineating the boundary between the two saturation regions.

The feature that characterized air propagation at 1-*g*, and to a certain extent was still occurring at accelerations below 10-*g*, was the fact that the plume continued to grow laterally after breakthrough had occurred. The cluster of channels initially flowed

vertically, with a substantial amount of lateral propagation. However, after the initial front had reached the phreatic surface, plume growth continued horizontally, as new channels formed outside the boundaries of the breakthrough plume. The fact that plume expansion continued after breakthrough accounted for the large amount of basal spreading, and more generally for the very large size of the final plumes at 1-*g*. With increasing acceleration the amount of plume growth after breakthrough decreased, such that the breakthrough plume was essentially the same as the steady-state plume.

Figures 8-11 through 8-13 illustrate air propagation characteristics in porous media saturated with glycerol under accelerations of 5-*g*, 10-*g*, and 20-*g*, respectively. The plume at 1-*g* is not presented because boundary effects interfered with plume formation. At 1-*g*, air propagation was such that air hit the front of the box before steady-state conditions were reached. The plume expanded in the horizontal direction from the injection point, at a slower rate than vertical propagation, but the front of the box was hit before breakthrough occurred. An increase in *g*-level to 5-*g* significantly decreased the extent of lateral flow, and no boundary interference was observed for the rest of the experiments.

As was observed in samples saturated with immersion liquid, air propagation at 5-*g* clearly shows the occurrence of fingers. Air flow is unstable, and consequently, air saturation within plume boundaries at steady-state is relatively low, with visible areas of total liquid saturation. A fingering pattern of propagation is still observed at 10-*g* as shown in Figure 8-12, but the branching pattern has effectively disappeared at 30-*g*. Basal propagation, and more generally all lateral propagation, decreases rapidly with increasing *g*-levels, and the vertical direction is visibly the preferred direction of flow.

The evolution of steady state plumes with *g*-level is summarized in Figure 8-14, which shows the progressive trend of decreasing zone of influence under increasing acceleration fields.

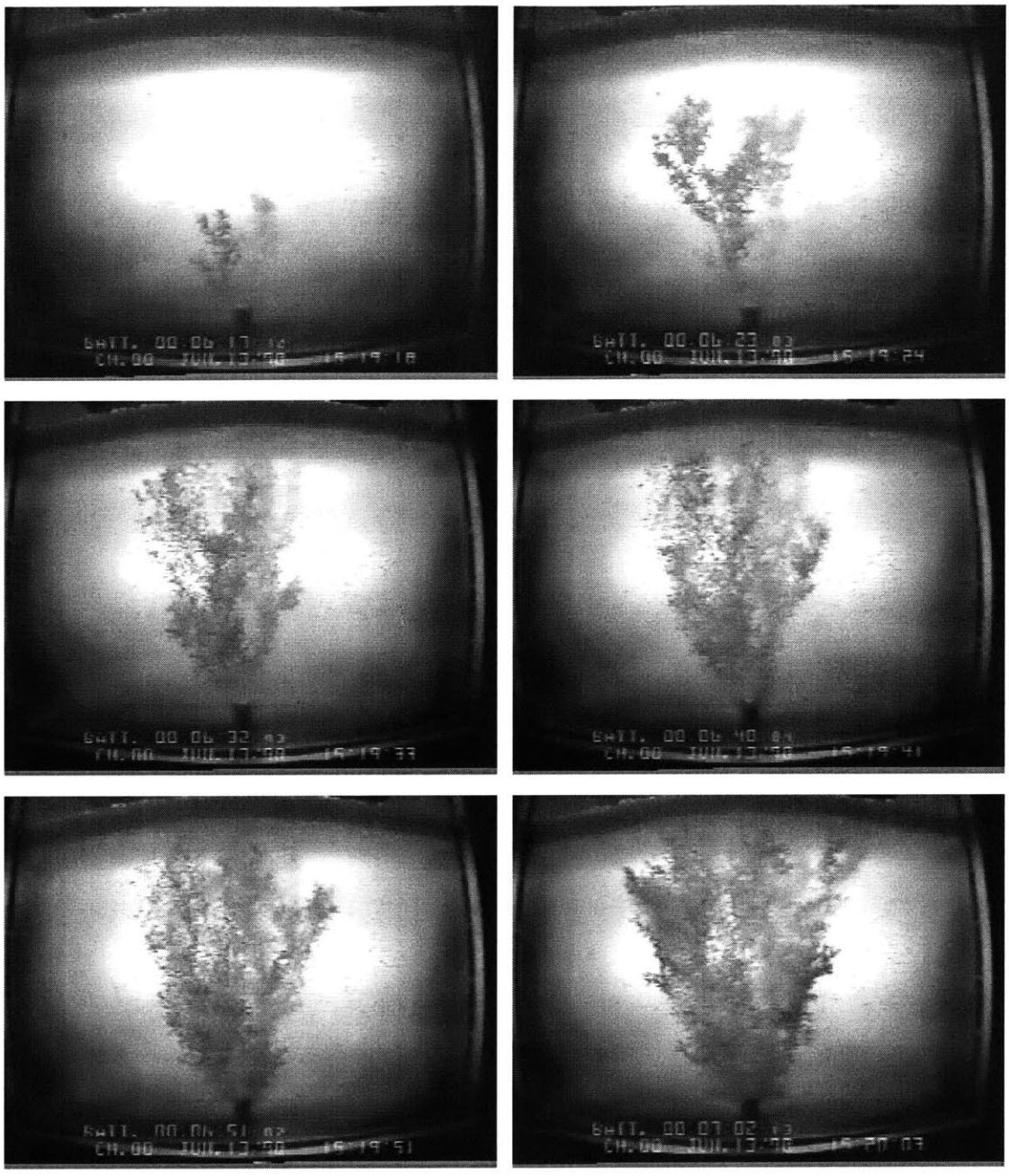

Figure 8-11 Injector MPI #1 – Propagation of injected air at 5-g through porous media saturated with glycerol.

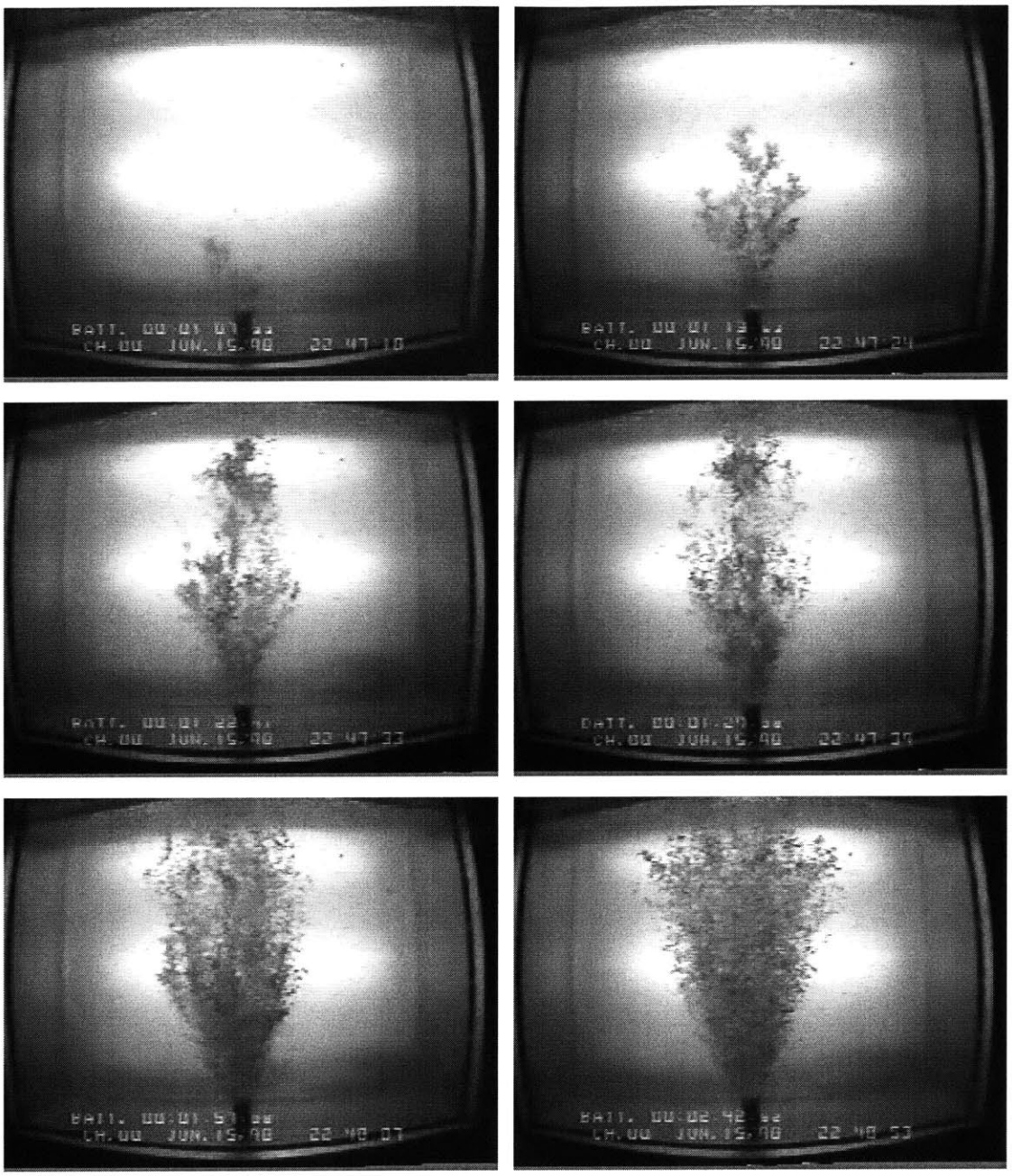

Figure 8-12 Injector MPI #1 – Propagation of injected air at 10-g through porous media saturated with glycerol

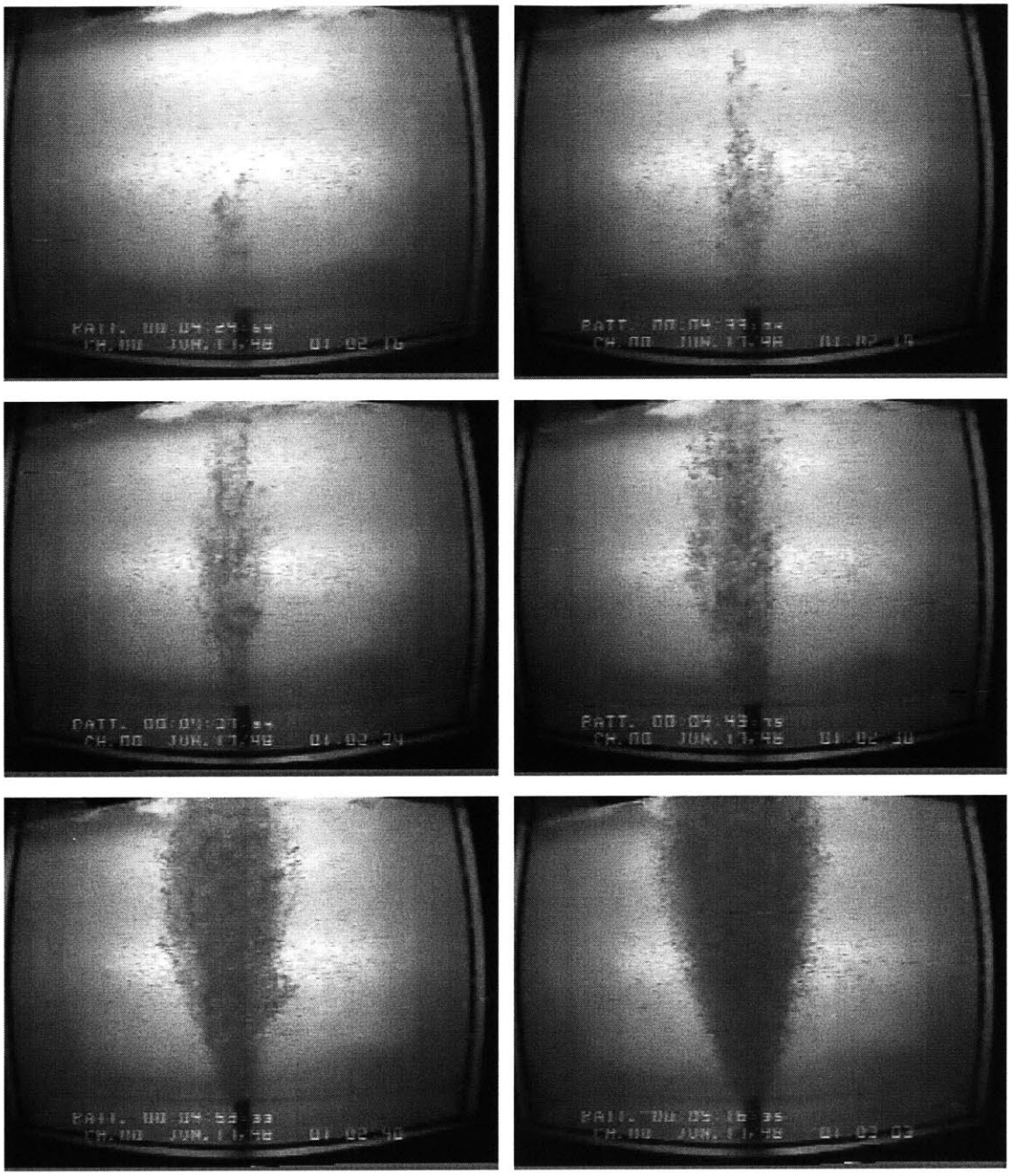

Figure 8-13 Injector MPI #1 – Propagation of injected air at 30-g through porous media saturated with glycerol

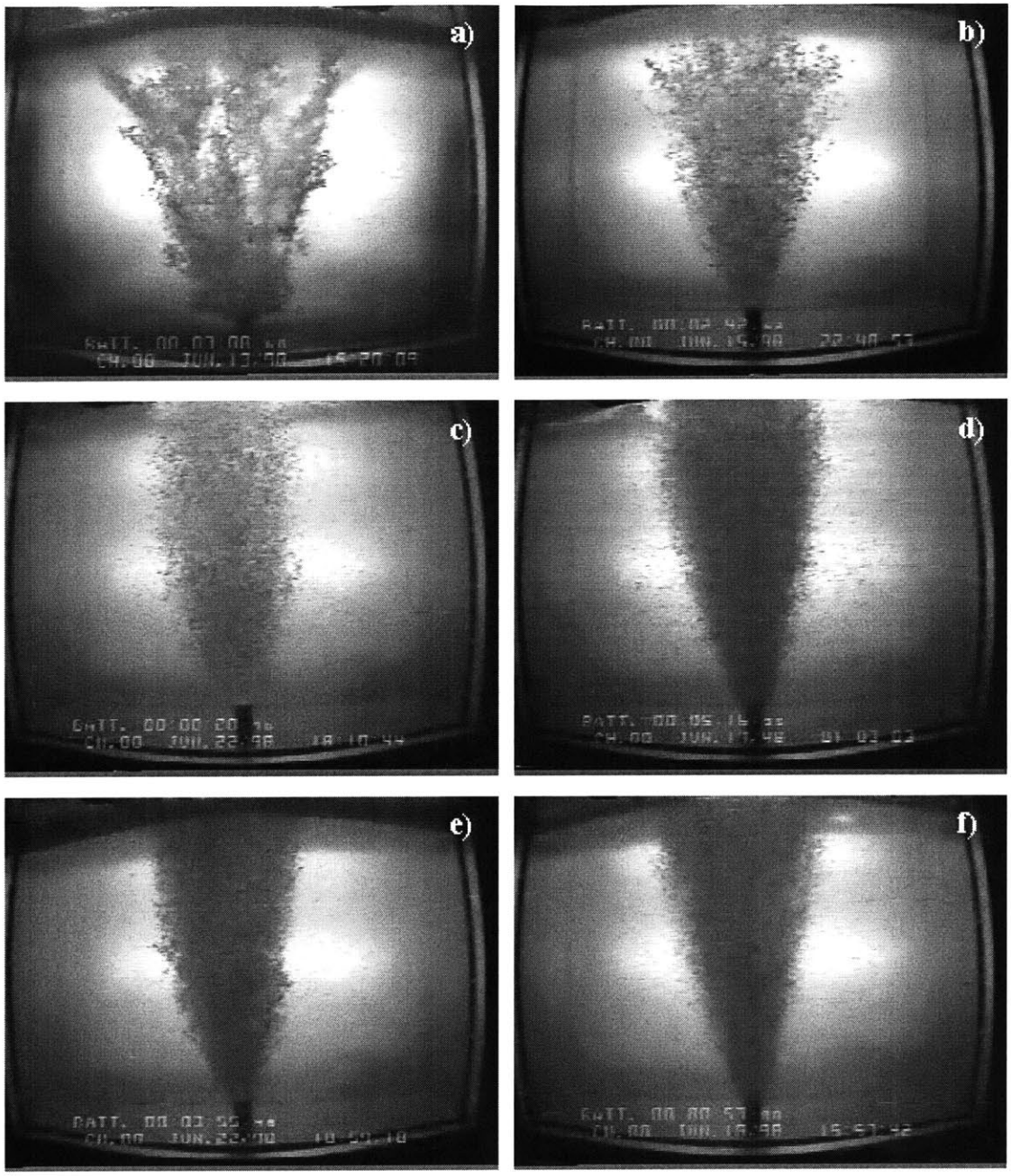

Figure 8-14 *Steady-state air plumes obtained at increasing g-levels following injection of air into porous media saturated with glycerol - Injector MPI #1: a) 5-g; b) 10-g; c) 20-g; d) 30-g; e) 40-g; f) 50-g.*

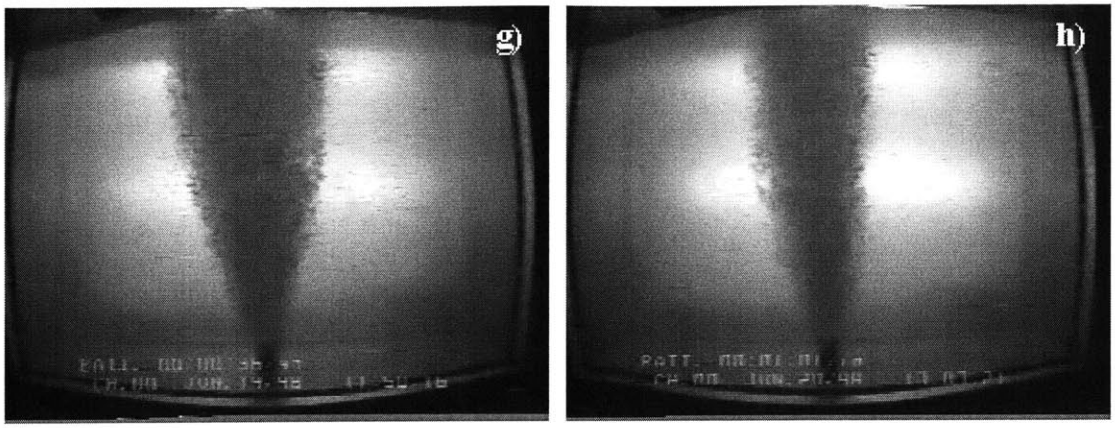

Figure 8-14 (ctd.) *Steady-state air plumes obtained at increasing g-levels following injection of air into porous media saturated with glycerol - Injector MPI #1: g) 70-g; h) 90-g.*

Plumes obtained at *g*-levels ranging from 5-*g* to 20-*g* were characterized by relatively low air saturations, with areas through which air clearly did not flow. Low *g*-level plumes are not as well delineated, and the interface between the liquid-saturated and the air-saturated regions is not as sharp as that of plumes obtained at higher *g*-levels. Plumes obtained at *g*-levels higher than 30-*g* were completely saturated with air within their boundaries. The movement of the front interface progressively became more stable, and air saturations within the plume boundaries were very high.

8.2.4.2.Influence of injector

The variation of plume characteristics formed under constant injection pressure, at increasing *g*-levels, for varying injector geometries are included in Appendix D, Additional Experimental Results. Figures D-1 through D-5 summarize steady state plumes through samples of MS submerged in immersion liquid. As shown in the figures, at a given *g*-level, there was no significant difference between the steady-state plumes obtained using the three multiple port injectors. The zone of influence of the plumes decreased with increasing *g*-level, but the impact of injector geometry was not noticeable. There was a small difference in plume size when comparing steady-state plumes obtained from *SPI*s to those from *MPI*s. The zone of influence of single port injectors was

smaller, and there was a decreasing trend in plume size with decreasing orifice diameter. The most visible difference in the plumes occurred at the injection point. The injector orifice is visible in most of the images, clearly showing that the plume was formed from a point source. The inclination of the sides of the air plumes were therefore very steep, and minimal lateral propagation was observed, even at the lower *g*-levels. The plumes obtained using injector *SPI*#3 were consistently smaller than all other plumes, and at high *g*-levels they were limited to a very thin line.

8.2.4.3.Influence of porous medium

Experiments conducted at varying *g*-levels, under constant pressure conditions, and using multiple port injectors were repeated in samples of SP with fines. Images of these experiments will not be presented, but results from these experiments are included in later sections of this chapter. No consistent difference was observed between the plumes obtained in SP samples and those in SPF samples.

Resulting zones of influence were comparable to the ones previously described, therefore suggesting that the difference in hydraulic conductivity between the two materials used was not sufficient to generate a noticeable change in propagation patterns.

8.2.4.4.Breakthrough velocities

The velocity of the breakthrough front was estimated from videotapes of centrifuge experiments. Figures 8-15 a) through f) present a summary of experimental results obtained from tests on SP samples saturated with immersion liquid. The vertical distance from the top of the injector to the leading edge of the advancing plume is plotted as a function of the time at which breakthrough starts. In essence, these graphs show the advancement of the breakthrough front from the moment it enters the porous medium to the moment it leaves the field of vision of the mini-camera. The slope of these plots is the velocity of the injected air.

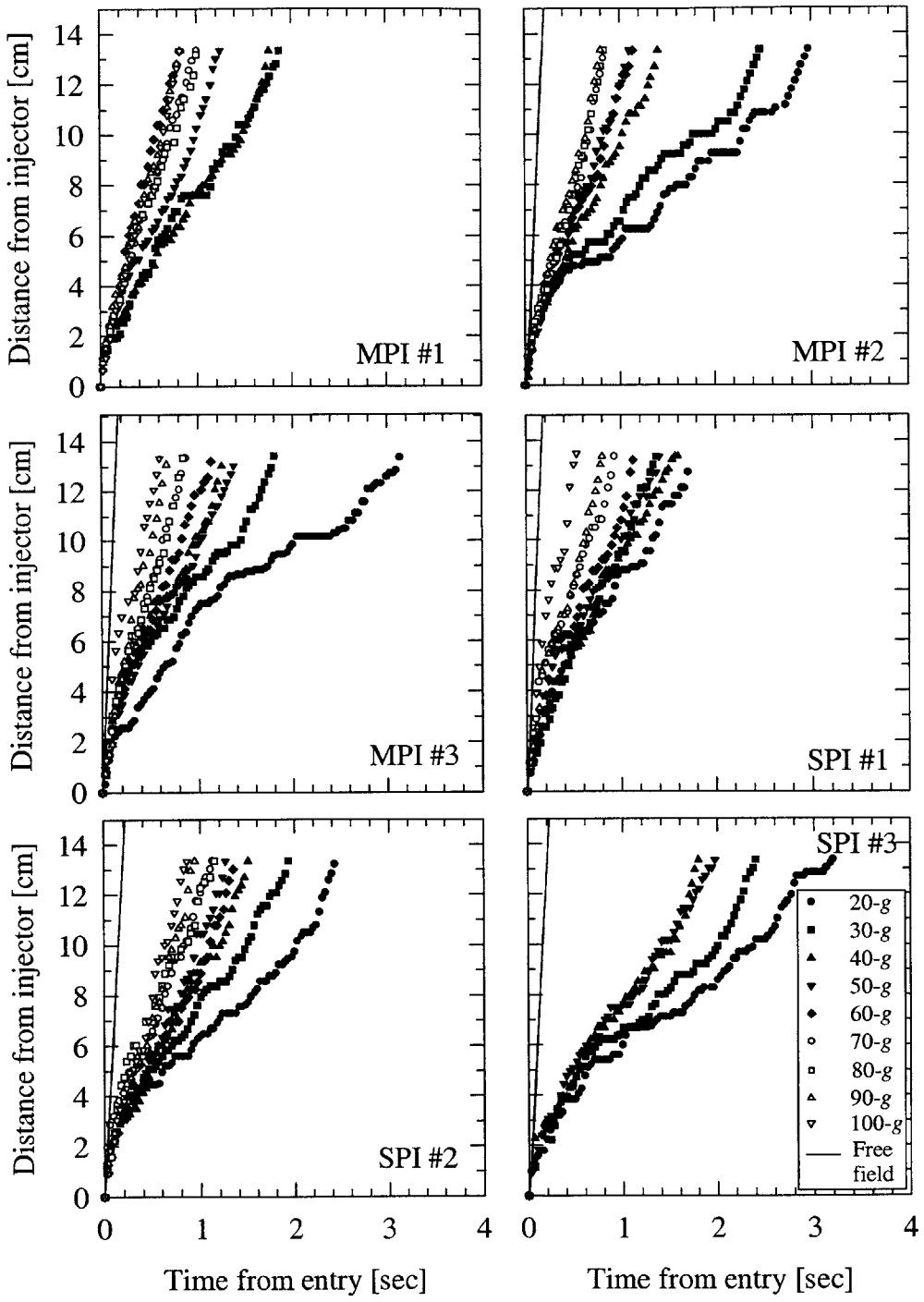

Figure 8-15 *Displacement of the leading front of air sparging plumes versus time of entry, prior to breakthrough. Experiments conducted in crushed glass (SP) saturated with immersion liquid. Injections conducted under constant pressure conditions, under the indicated acceleration field. Injector type is included in each figure.*

Six graphs are included on the figure, each summarizing results obtained from one specific injector. Within each plot, each curve shows results from one test conducted at a specific g-level. Included for reference in the graphs are also plots of the displacement versus time relationship obtained in the free field. In the scale of Figure 8-15, variations in the displacement of the breakthrough front during free field propagation, at varying g-levels, cannot be appreciated. Results of injection conducted at 30-g were therefore selected as representative of all the free field data, for each injector.

As shown in Figure 8-15 breakthrough velocities of air plumes increased with increasing g-level, for all injectors. This result was expected, since $(P_{inj})_{min}$ increases with g-level. Propagation velocities at g-levels lower than 40-g were non-uniform, for all injectors, as indicated by changes in the slope of the displacement versus time relationship. Non-uniformities in the propagation behavior were more prevalent for plumes formed with the smallest opening sizes, and especially for plumes formed with *SPI*s. At acceleration lower than 40-g, the advancement of the air was at times arrested after a certain distance from the injection point, and this distance decreased with decreasing g-level. The plume stopped moving forward and it either spread laterally or remained of constant size, resulting in a step-like displacement-time plot. When propagation stopped, the distance from the injection port to the leading air front determined the behavior of the plume. If the front was stopped close to the injector, marginal lateral growth of the plume took place, most likely due to the fact that the hydrostatic pressure remained high at the given depth. As the distance from the front edge of the plume to the injector increased, and therefore as the hydrostatic pressure at the top of the plume decreased, lateral spreading of the plume became more pronounced.

Breakthrough velocities for experiments conducted at accelerations equal to 50-g and higher increased uniformly for all injectors. Results from experiments conducted at accelerations higher than 50-g, from all injectors, were grouped by g-level as shown in Figure 8-16 a) through f). It is clear from the plots that at accelerations higher than 50-g neither the opening size of the injector nor its geometry has any effect on the propagation behavior of the air at breakthrough. Furthermore, if an average value of the velocities measured for the different injectors is computed at g-levels higher than 50-g and this value is then normalized by the average free field velocity at the corresponding g-level,

then it is found that velocities of the air through the porous medium are approximately six times smaller than those in pure liquid. Thus, the retarding effect of the porous medium is constant at high accelerations, once the pattern of air flow has effectively become a straight jet of air through the medium.

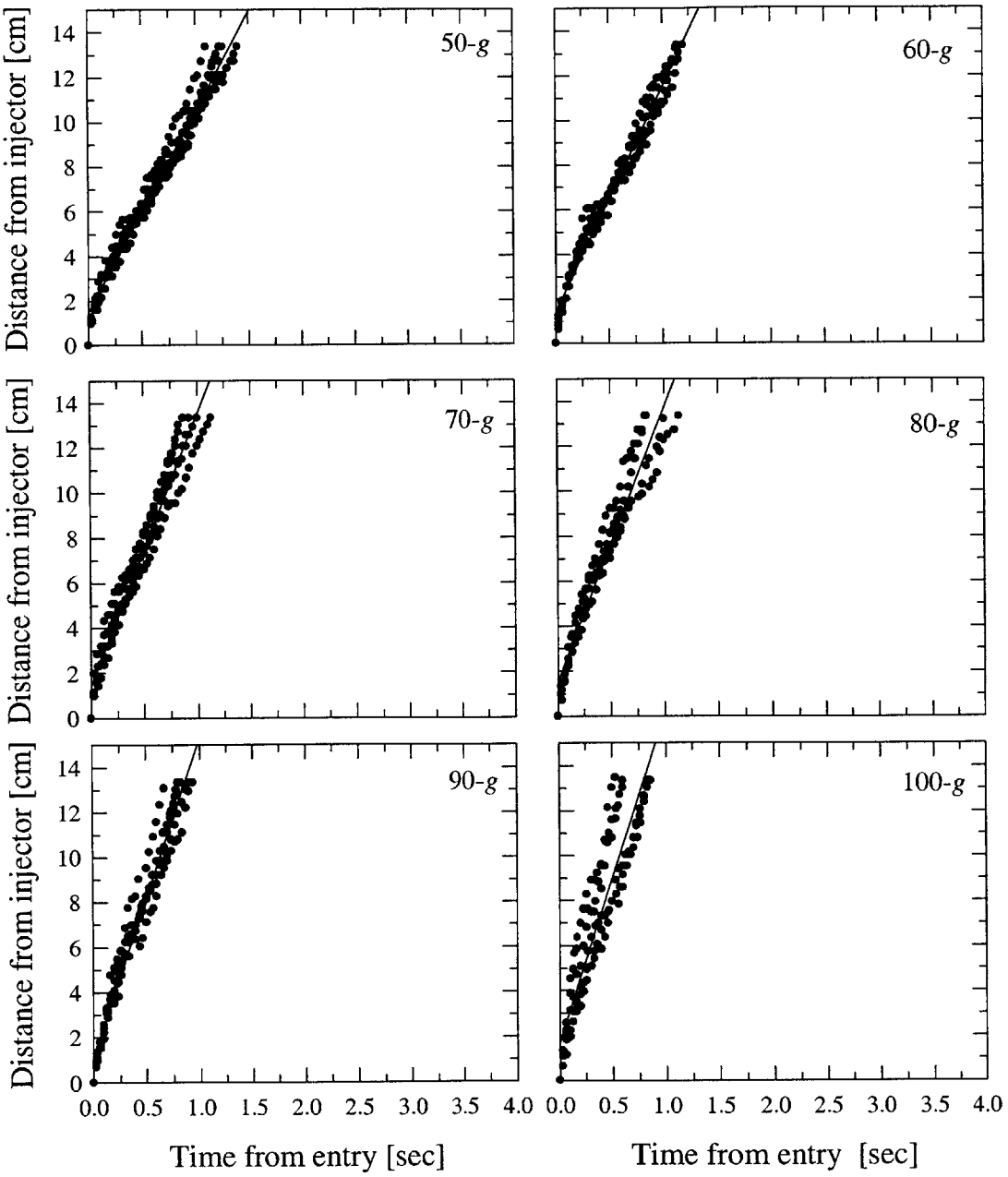

Figure 8-16 *Displacement of the leading front of air sparging plumes versus time of entry, prior to breakthrough, through porous medium saturated with immersion liquid. Experiments conducted at constant pressure injection conditions under acceleration fields higher than 50-g.*

It should be noted that the air velocities measured during experiments are approximately one order of magnitude higher than those what would be estimated from relationships presented in Chapter 2, including those predicting velocities of air slugs. The effective pore size diameter of the porous medium is therefore not an adequate predictive parameter to use as the characteristic length of the bubbles or slugs in these relationships.

8.3.CONSTANT FLOW RATE EXPERIMENTS

8.3.1. Air Injection in Immersion Liquid

8.3.1.1.Influence of injection flow rate on air propagation

The effect of increasing injection flow rates under constant rate of flow conditions was believed to be the most critical parameter affecting the characteristics of air sparging plumes. Thus, the impact of flow rate, q, on the characteristics of air propagation was then studied over a range of flow rates varying from 0.26 cm^3/s to 28.0 cm^3/s. In order to better describe the effect of increasing values of q on air flow patterns, this section presents results of experiments conducted under 1-g conditions only. Section 8.3.1.2 will expand the presentation to include the effects of increasing q and increasing acceleration levels, ranging from 1-g to 100-g.

Figure 8-17 shows a sequence of images of air propagating through an MS sample saturated in immersion liquid, at 1-g, at a low injection rate of 0.68 cm^3/s, using injector MPI #1. The same type of pore-scale fingering behavior observed during constant pressure experiments was visible during plume formation. Under a low flow rate of injection however, fingers propagate independently. The predominant direction of propagation is vertical, but a significant amount of tortuosity is evident as air advances through the sample. A limited amount of lateral spreading takes place as the breakthrough fingers advance, caused primarily by the erratic path of advancement. However, the feature that is peculiar to the formation of the plume under the low flow rate injection conditions, is that additional fingers continue to form after the leading front has reached the phreatic surface. Plume growth therefore continues after breakthrough,

such that the steady-state shape of the plumes is relatively large, given the low magnitude of q. Air saturation within plume boundaries however, is moderate, and definite regions of liquid saturated medium are visible at steady-state.

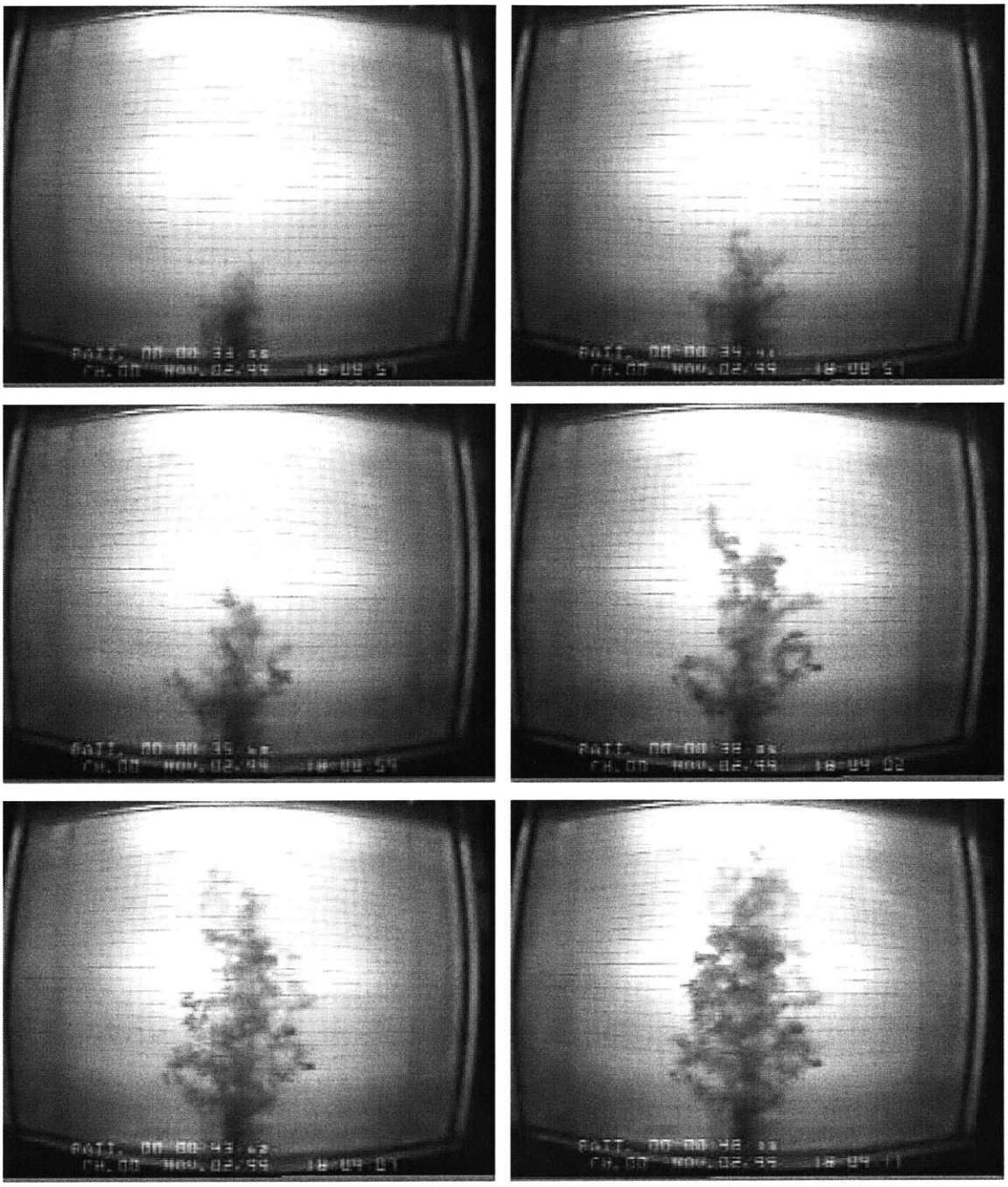

Figure 8-17 *Sequence of air propagation through SP sample saturated with immersion liquid, at 1-g. Injection conducted under constant flow rate conditions, with q = 0.68 cm^3/s, using injector MPI #1.*

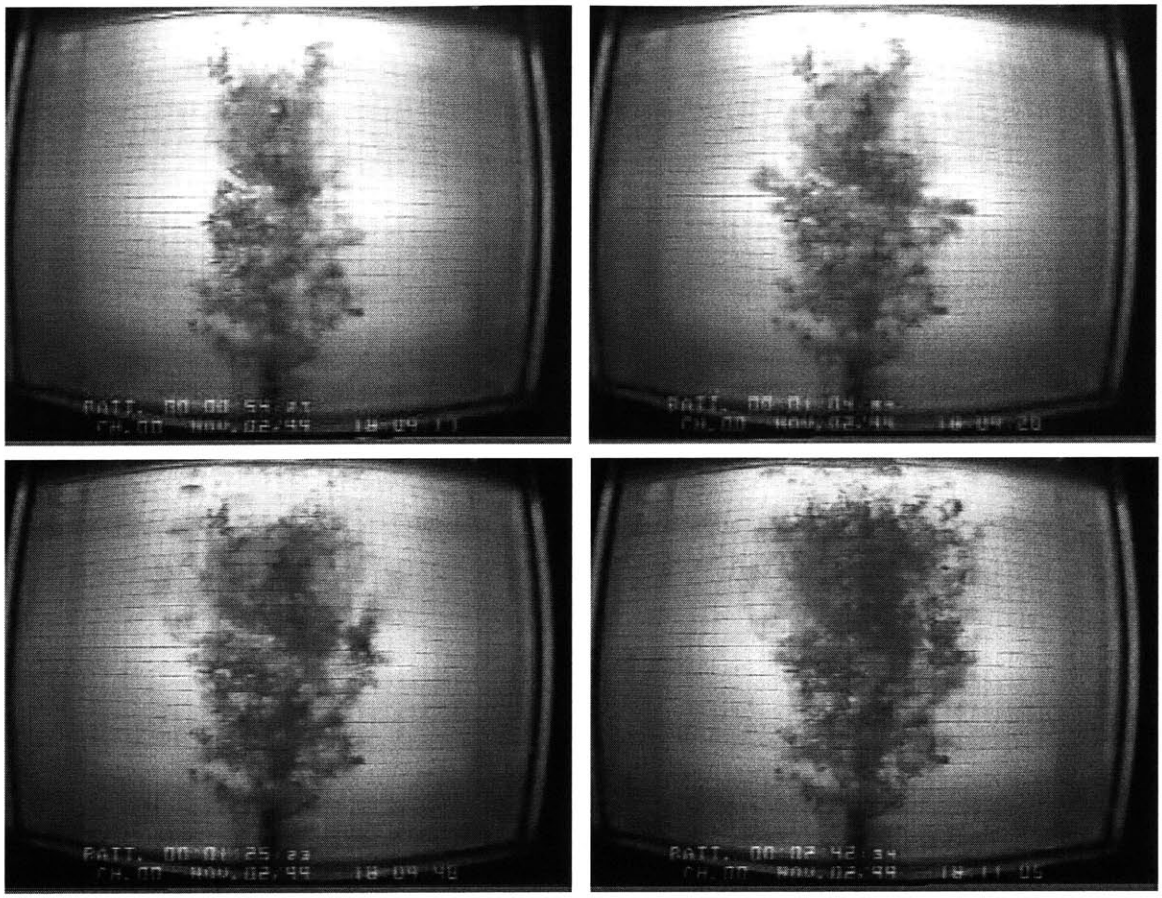

Figure 8-17 (ctd.) *Sequence of air propagation through SP sample saturated with immersion liquid, at 1-g. Injection conducted under constant flow rate conditions, with q = 0.68 cm^3/s, using injector MPI #1.*

The effect of increasing flow rates of injection on the zone of influence of injectors is illustrated in Figure 8-18. This figure shows steady-state plumes obtained using injector MPI #1, at constant injection flow rates ranging from 0.26 cm^3/s to 2.66 cm^3/s, under a gravitational acceleration field of 1-*g*. Appendix D also includes Figures D-6 through D-10 which summarize results from experiments conducted using the remaining five injection ports, at the same injection flow rates. The differences between the plumes included in Figure 8-18, and those obtained from constant pressure injection tests *at 1-g*, (Figure 8.7) is drastic. The zones of influence of the plumes obtained at low flow rates,

in all cases, were noticeably smaller than those obtained at 1-g under constant pressure conditions, with a consistent trend of increasing *ZOI* with q.

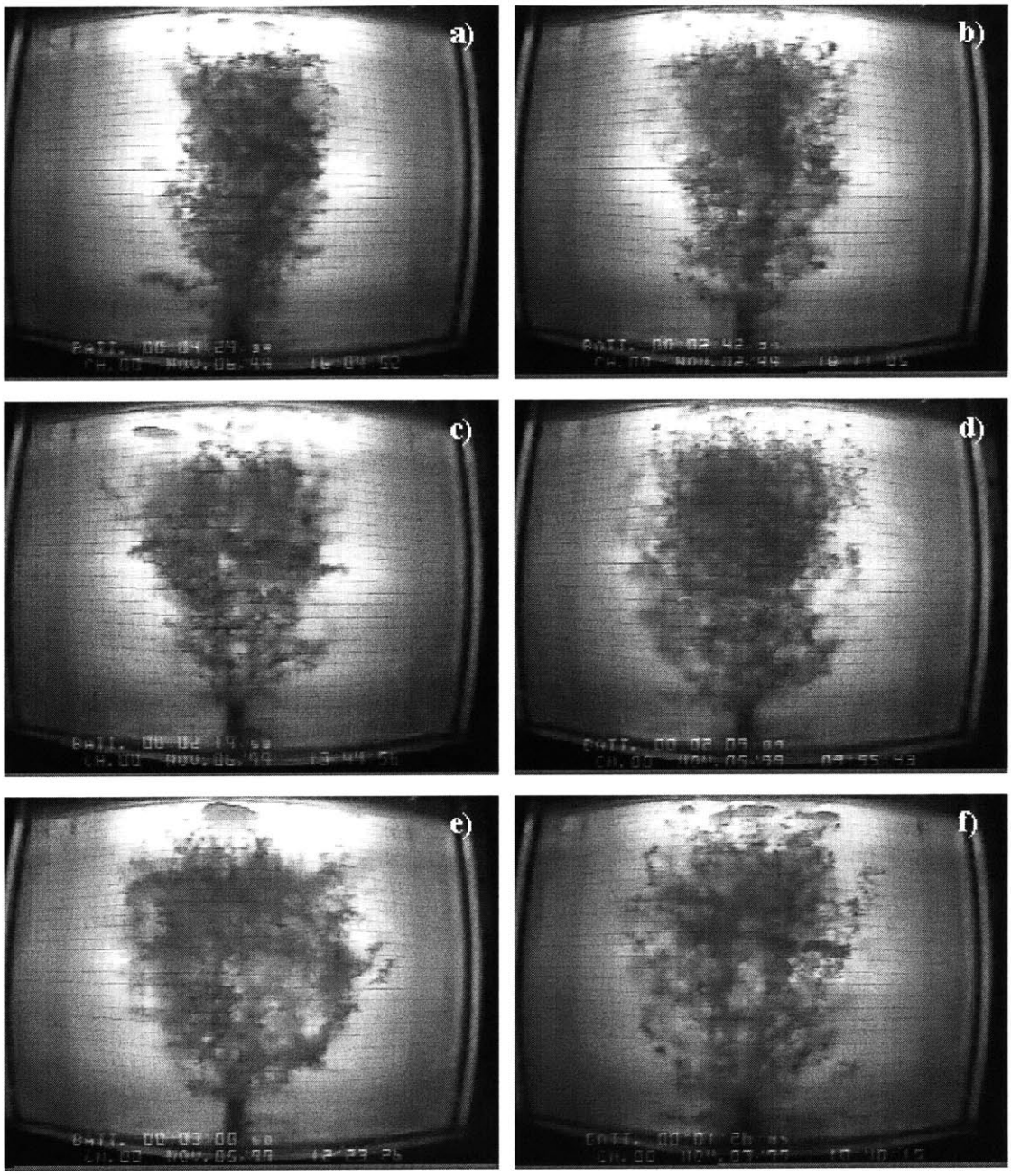

Figure 8-18 *Constant flow rate injection of air into porous medium saturated with immersion liquid. Test conducted at 1-g. Injector MPI #1: a) 0.26 cm^3/s; b) 0.68 cm^3/s; c) 1.15 cm^3/s; d) 1.58 cm^3/s; e) 2.26 cm^3/s; f) 2.66 cm^3/s.*

As was noted in Chapter 2, a constant pressure injection test can be conceptually envisioned as a test at a very high injection flow rate, sufficiently high to maintain a constant pressure condition as the air plume grows. In this framework, large increases in the injection flow rate result in increases in the zone of influence of the plume. Figure 8-18 also shows that saturation values were consistently lower than in constant pressure experiments. It is clear that air flow occurred in the form of channels, some of which can still be seen in the pictures, since the region within plume boundaries was in most cases not saturated by the end of the experiment.

The impact of increasing injection flow rates on air propagation and plume shapes was also evaluated at a higher range of flow rates ranging from 10.83 cm^3/s to 28.0 cm^3/s. These experiments were all conducted at 1-*g*,using a metering valve and a flow meter to regulate and measure, respectively, the volume of flow injected per unit time.

Figures 8-19 through 8-21 show sequences of air propagation recorded during experiments in this higher range of flow rates. Injection flow rate for these particular tests was set to a fixed value at the start of injection. Figure 8-19, for example, shows the plume obtained when entry occurred at an injection rate of 10.83 cm^3/s using injector MPI #3. The resulting plume propagated in a very unstable manner, through wide channels separated by considerable volumes of liquid-saturated material. Air flow velocity was high in the channels, which essentially propagated vertically until the phreatic surface was reached. The plume at steady-state was very narrow at the base, indicating very little lateral propagation at the beginning of plume formation. Final air saturation values were very low. Figures 8-20 and 8-21 similarly illustrate propagation which occurred when the injection flow rate was "instantaneously" set to 15.14 cm^3/s and 19.44 cm^3/s, respectively. No propagation front was ever established, and air advanced through a few channels which accommodated the entire volume of air being injected. Limited lateral propagation occurred after breakthrough, but the final zones of influence for these experiments were small and of very low air saturation. The zone of influence of these plumes is smaller than that of plumes formed at flow rates one order of magnitude lower, going against the expected behavior of the injected air.

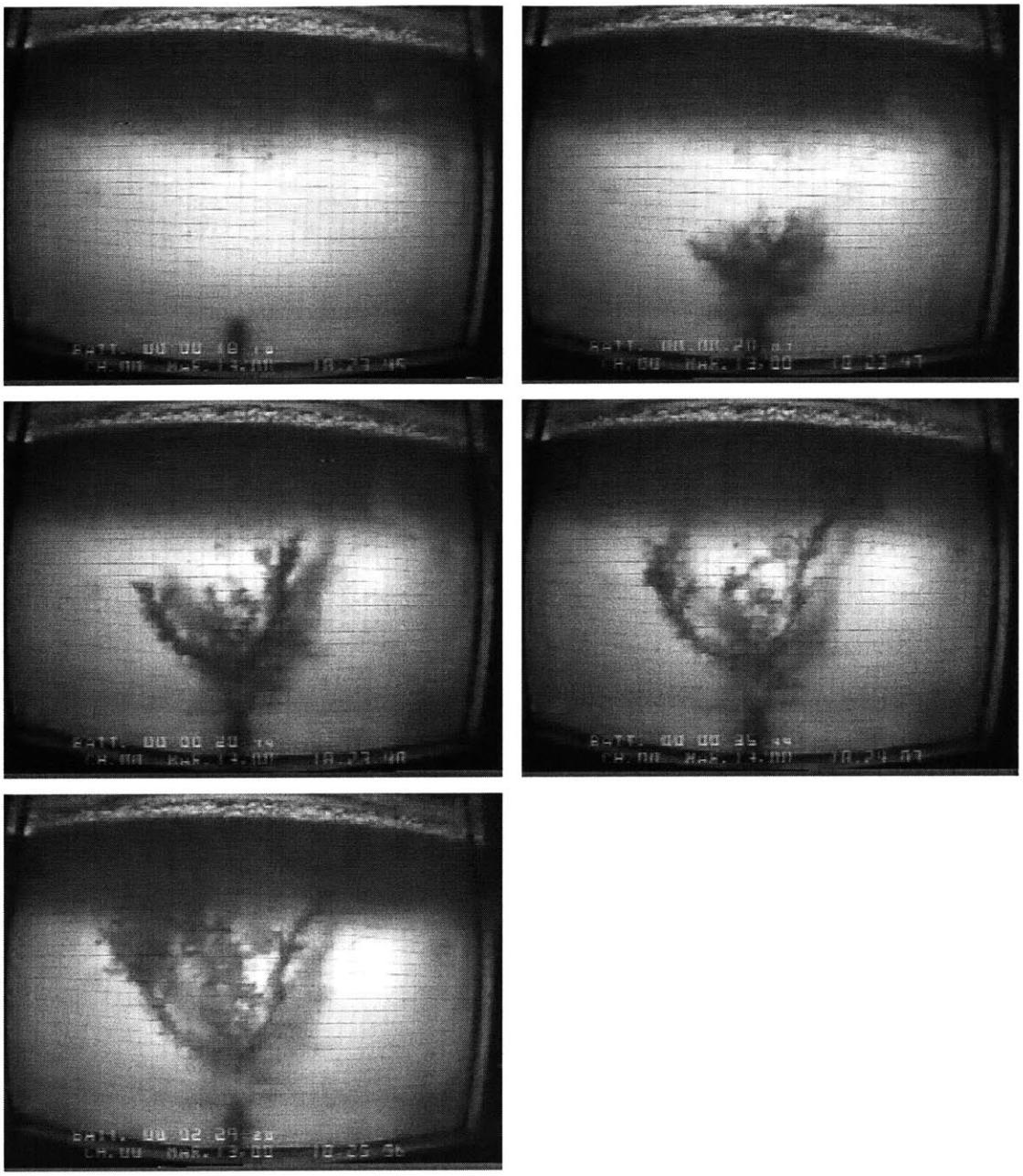

Figure 8-19 *Constant flow rate injection of air into porous medium saturated with immersion liquid. $q = 10.83\ cm^3/s$ - Test conducted at 1-g. Injector MPI #3.*

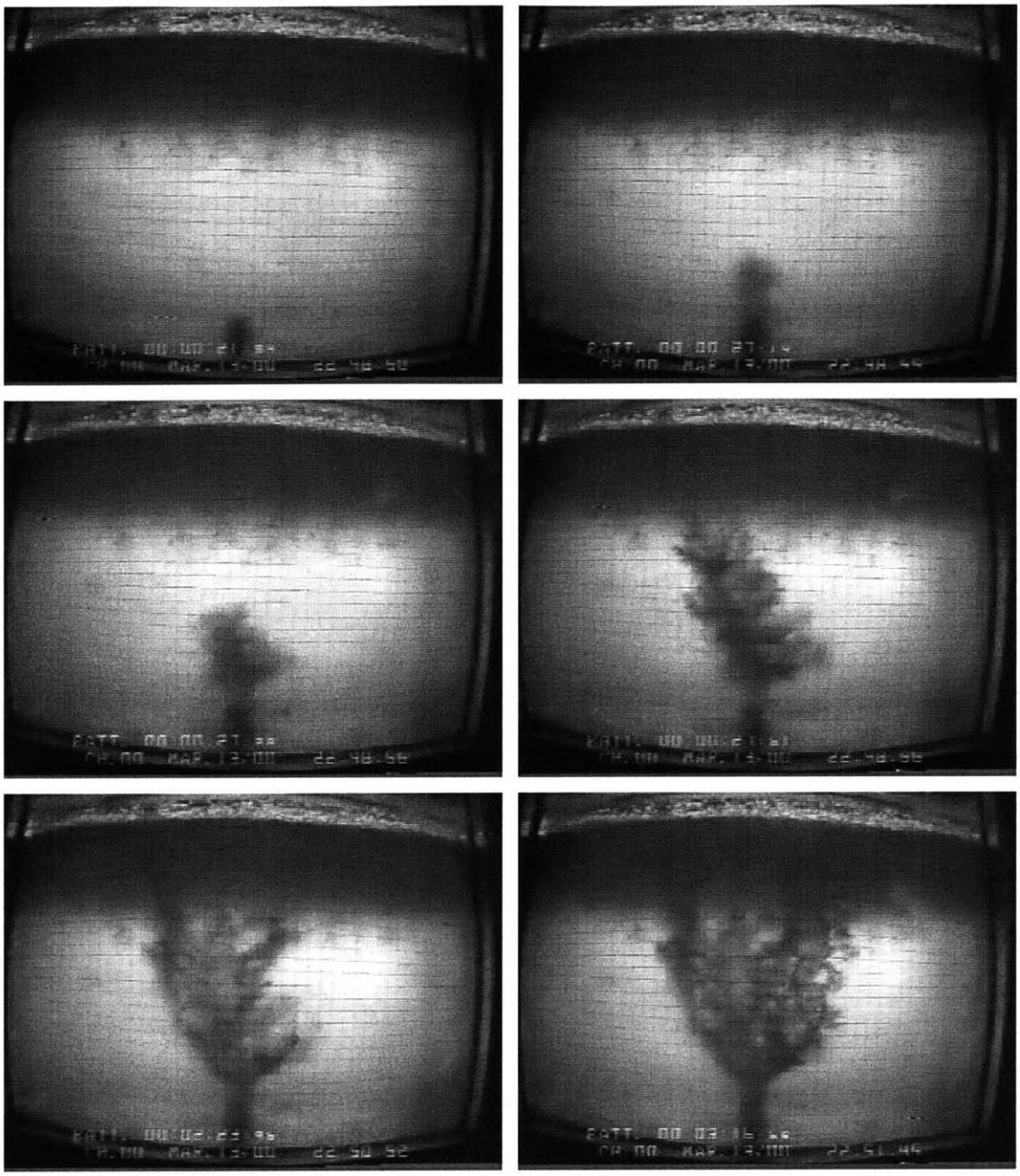

Figure 8-20 *Constant flow rate injection of air into porous medium saturated with immersion liquid. q = 15.14 cm^3/s - Test conducted at 1-g. Injector MPI #3.*

The propagation characteristics of the plumes formed in the higher range of injection flow rates, and of those obtained at flow rates ten times lower, were completely different. The major difference between them is that at low injection flow rates, before breakthrough, several channels flow upward simultaneously, and thus the air being injected is distributed among the various flow paths as propagation takes place. When the flow rate increases, the velocity of air flow through the soil also increases, and the number of channels advancing at the same time is significantly reduced. In the sequences shown on Figures 8-19 through 8-21 one or two channels at the most are formed before breakthrough, and this number increases only slightly after the phreatic surface has been reached.

These observations suggested that the rate at which air was being injected was possibly too fast, and that the material was being fractured during injection. Conceptually, if the volume of air being injected is greater than the volume of water that can be displaced out of the pores in a given interval of time, then air accumulates at the interface between air and water and the pressure begins to increase. The over-pressurized air is driven out of the system through a preferential flow path, *i.e.* a fracture, and lateral propagation is reduced to a minimum.

At this point of the experimental program, it was therefore decided to conduct experiments in which the injection flow rate was gradually increased. Tests were performed starting from a low initial value of the flow rate and the increase was ramped such that enough time was allotted for the water to flow out while air was being injected. Figure 8-22 shows a sequence of plume growth observed during experiments in which injection flow rate were gradually increased from 3 cm^3/s to 28 cm^3/s, at 1-*g*, and using injector MPI #2. Appendix D includes Figure D-11, which shows a similar sequence of propagation obtained using injector MPI #3.

The differences in the resulting plume geometries when compared to those shown in Figures 8-19 through 8-21 are drastic, for all injectors used. The initial stages of plume formation are consistent with what was observed during experiments at very low flow rates. After the plumes reached steady-state under a given flow rate however, the injection flow rate was slightly increased, and the resulting effect was that new flow

pathways were formed. Increasing the flow rate forced a certain volume of air to flow through established channels, while the remaining volume of air expanded the plume radially.

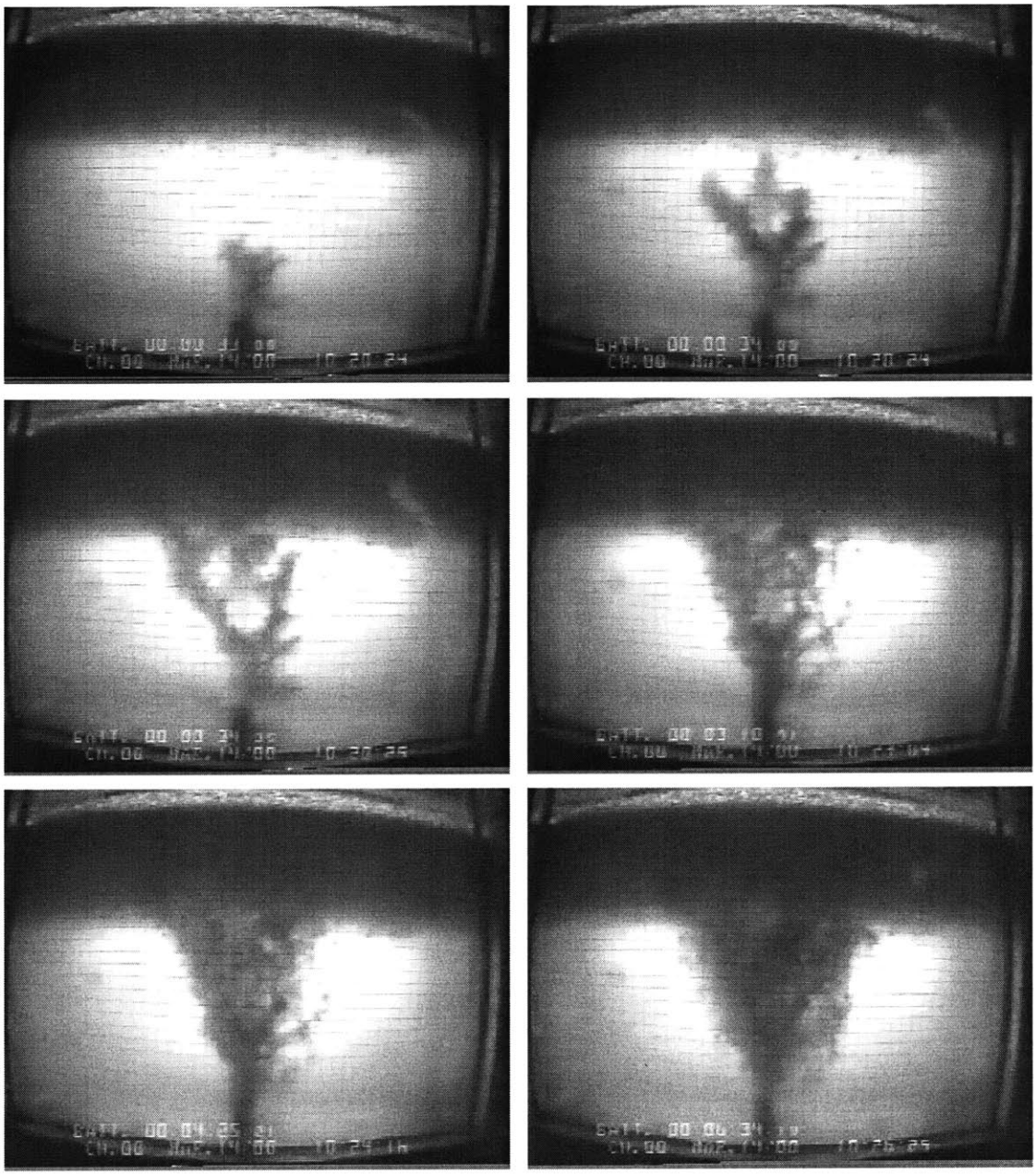

Figure 8-21 *Constant flow rate injection of air into porous medium saturated with immersion liquid. q = 19.44 cm^3/s - Test conducted at 1-g. Injector MPI #3.*

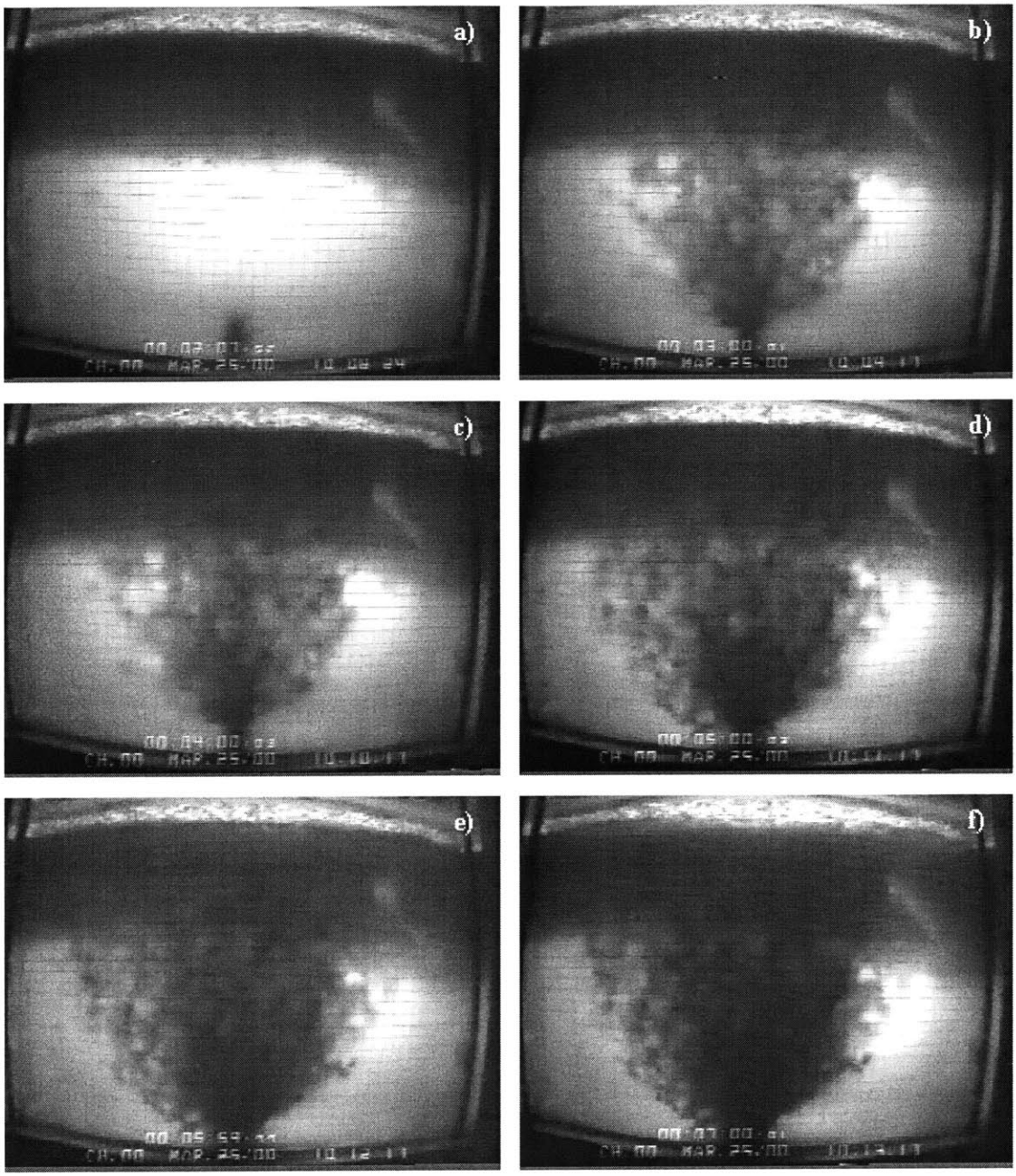

Figure 8-22 *Air plumes obtained at 1-g during injection at increasing, constant flow rates into porous media saturated with immersion liquid - Injector MPI #2: a) box prior to injection; b) q = 2.22 cm^3/s; c) q = 6.53 cm^3/s; d) q = 10.83 cm^3/s; e) q = 15.14 cm^3/s; f) q = 19.44 cm^3/s.*

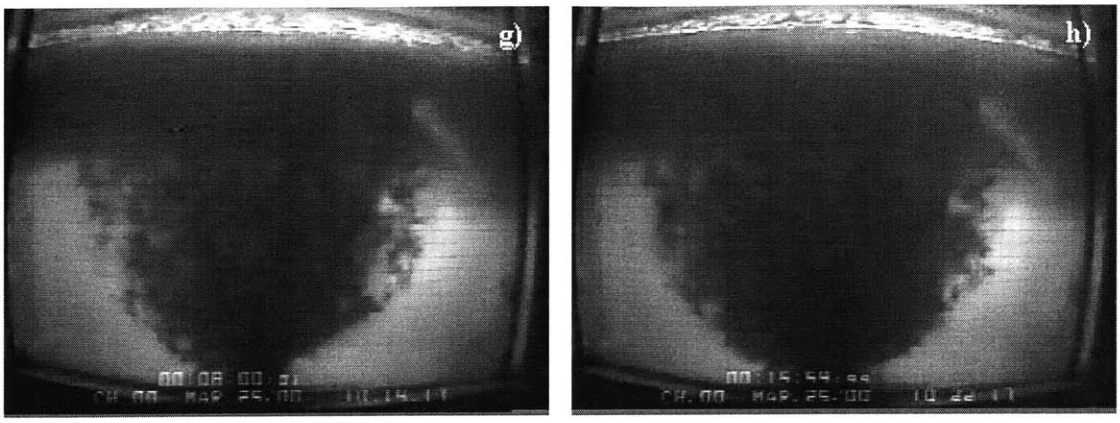

Figure 8-22 (ctd.) *Air plumes obtained at 1-g during injection at increasing, constant flow rates into porous media saturated with immersion liquid - Injector MPI #2: g) q = 23.75 cm^3/s; h) q = 28.06 cm^3/s.*

The manner in which these plumes became wider at higher *q's* was by opening new channels along the existing plume boundaries, as if a layer of air was superimposed along the plume outline with each increase in flow rate. The final plumes were very wide, regardless of the injection port used, and air saturation within the boundaries was high.

It is at this point useful to note that, given the way in which air propagation takes place in these experiments, no air velocity data were collected. Because breakthrough occurred at low injection velocities, the velocity of the air in a channel at a later time cannot be tracked through the darkened transparent medium. Only results for area of revolution of the plume will be presented for these experiments, included in summary tables in Appendix E.

8.3.1.2.Influence of injector type

As was observed under constant pressure injection conditions, injector geometry has a distinctive effect on the resulting plume shapes, if the plumes obtained using single port injectors are compared to those from multiple port injectors. In fact, the plumes obtained while using the three *MPI*s are essentially identical, while in the case of the *SPI*s the plumes obtained with the three injectors are all different from each other.

The zone of influence of the plumes was expected to grow as a function of the injection flow rate, even in the low range of injection flow rates. Although this effect was indeed captured by volume calculations of the digitized plumes, as will be shown in chapter 9, the increase of plume size with flow rate was only distinctly observed in images of plumes obtained using injector *MPI* #1. It must be noted however, that in the case of *MPI* #1, air saturation within the boundaries of the plumes decreased as the area of influence increased. Plumes formed with the two remaining multiple port injectors only showed a slight difference in size with increasing flow rate, as can be seen in Figures D-6 and D-7. Air saturations within the plumes did not appear to be affected by the increasing flow rates.

The characteristics of plumes obtained with *MPI*s are relatively uniform along the boundaries of the plume, meaning that the majority of the air channels that leave the injector reach the phreatic surface by the end of the test. Dead-end channels are indeed visible in some of the pictures, but the plumes still present a clearly delineated boundary. Plumes are practically cylindrical and symmetric about the axis of the injector. The extent of lateral air propagation is significantly lower than in the case of constant pressure injection plumes, where the air plumes were wide parabolas spreading from the top of the injection point. A limited amount of lateral spreading takes place at the base of the plume, but after this basal horizontal spreading is arrested, air flow is primarily vertical. The sides of the plume are thus very steep, *i.e.* vertical, regardless of the injection flow rate.

In the case of plumes formed using *SPI*s, with a few exceptions, air flow through the sample became increasingly erratic at higher q's, which meant that the number of dead-end fingers increased with q. The plumes then appeared to have spread laterally, but in reality the boundaries were not well defined and air saturations were low.

The general features observed in the case of the *MPI* plumes do not apply to a large number of the plumes obtained while using *SPI*s. The most striking characteristic of the single port injector plumes is the widespread presence of dead-end fingers. As a result, the boundaries of the plumes are difficult to define and the plumes are not symmetric with respect to the axis of injection. In some extreme cases, for instance that of the plumes formed while using *SPI* #3 (as shown in Figure D-10), lateral air propagation was

so limited that the entire plumes consisted of a few disconnected channels extending from the injection point to the phreatic surface. After breakthrough occurred, air flow was limited to the established channels with no further propagation in the lateral direction.

In summary, given the background information presented in Chapter 2 concerning the effects of constant flow rate conditions on bubble characteristics, and more specifically that the effects of orifice diameter are of minor importance to bubble geometry under constant rate of flow injection, different injector types were not expected to have a major impact on the characteristics of the air sparging plumes. This supposition however was not confirmed experimentally, and it was found, that at flow rates up to 2.7 cm^3/s, the type of injector does have a significant effect on plume characteristics. Even at these low flow rates, the limited area available for flow when using *SPI*s appears to cause a pressure build-up at the outlet, which is sufficient to cause local fracturing of the medium. Given that the injection flow rates are low, once excess pressures are relieved, no additional build-up occurs, and subsequent air flow takes place through a limited number of independent channels, *i.e.* fractures, bypassing entire areas of what would presumably be the zone of influence of the injector. Once breakthrough occurs no new pathways for air flow are established, and plume growth is completely arrested.

8.3.1.3.Breakthrough velocities

The velocity of the breakthrough front, at 1-*g*, through SP samples saturated in immersion liquid, was determined for all the injectors at all flow rates, and plots of displacement of the air front versus time are shown in Figure 8-23.

The graphs presented are based on the position of the leading channel of each plume. These velocities are therefore not indicative of the time to reach steady-state conditions, since considerable additional air propagation occurred after the leading front reached the phreatic surface. It is evident that air flow velocities at such low injection are significantly lower than those observed in the case of constant pressure tests, as was expected. The differences in propagation behavior of air injected through single versus multiple port injectors which was observed in the images is clearly illustrated in these figures. *SPI* velocities are higher, and show a higher level of non-uniformity, especially

at the lowest injection flow rates (*i.e.* 0.26 cm^3/s to 1.15 cm^3/s). In fact, increasing flow rates has a much greater impact on *SPI*s that it does on *MPI*s. Propagation velocities for the latter seem relatively unaffected by the increase in flow rate for q ranging from 0.26 cm^3/s to 2.8 cm^3/s.

The final velocity estimates made from these plots have been tabulated and are presented in Appendix E, Summary of Experimental Results.

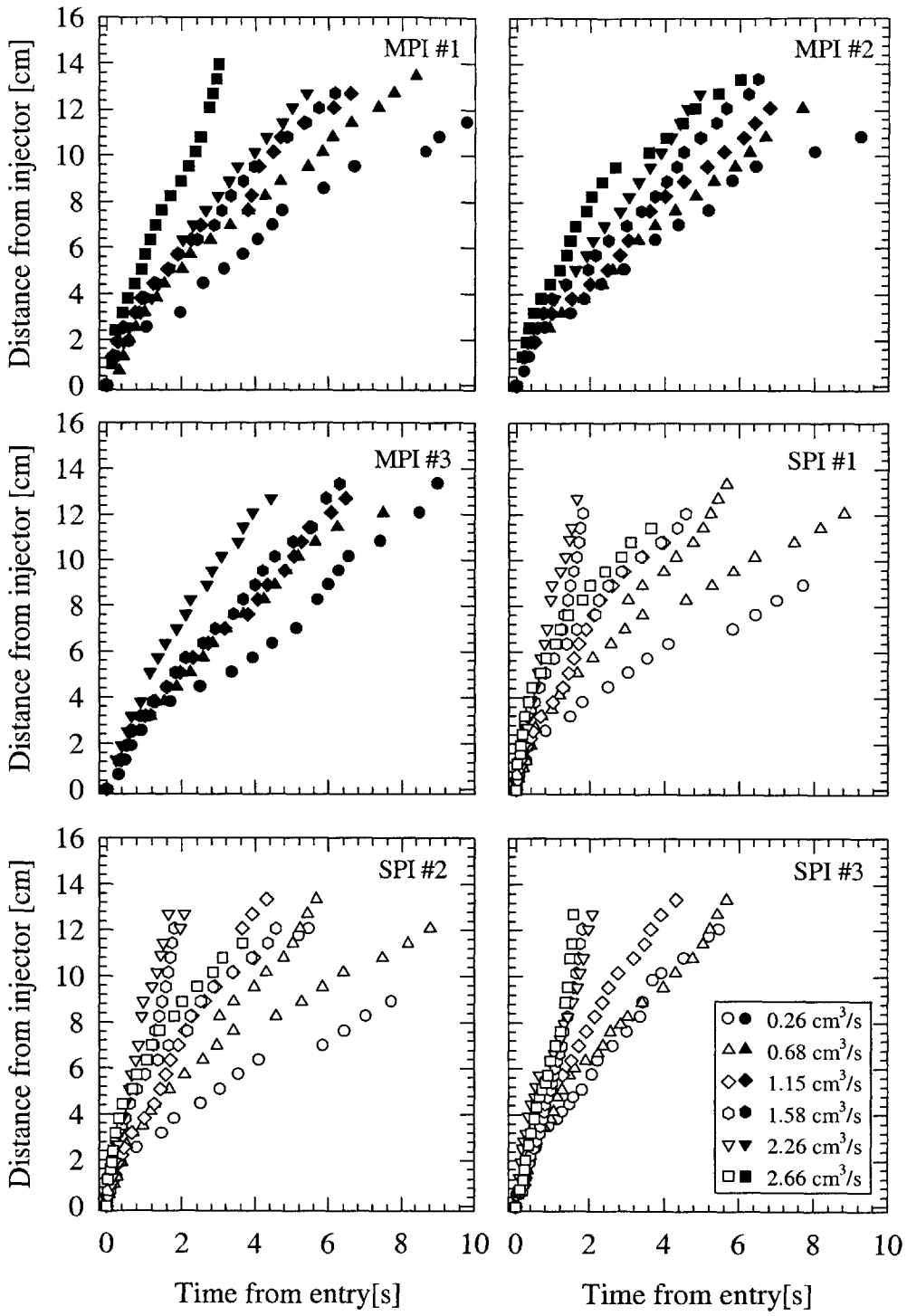

Figure 8-23 Displacement of the leading front of air sparging plumes versus time of entry, prior to breakthrough, through crushed glass saturated with immersion liquid. Injections conducted under constant rate of flow conditions, at 1-g, at the flow rates indicated. Full symbols are used to designate experiments conducted using multiple port injectors while open symbols indicate single port injectors. Some duplicate tests are included.

8.3.1.4.Influence of g-level on air propagation

Results illustrating the influence of increasing acceleration levels on the propagation of air injected at constant flow rate, through soils saturated in immersion liquid, will be presented in this section. The range of injection flow rates used in this first series of experiments ranged from 0.26 cm^3/s to 2.66 cm^3/s, while accelerations ranged from 1-*g* to 100-*g*.

The impact of an increasing acceleration field on the plumes obtained using injector *MPI* #1 is shown on Figure 8-24. Figure D-11 in Appendix D shows an equivalent sequence of plumes obtained at increasing *g*-levels using injector MPI #3. The injection flow rate in all these experiments was maintained at 0.66 cm^3/s. The figure clearly shows the drastic variations in plume characteristics as injection is conducted under increasing acceleration fields.

Air flow characteristics at 1-*g* were dominated by the presence of channels, leading to relatively low air saturations within the plume boundaries. Increasing the *g*-level slightly, from 1-*g* to 3-*g* (Figure 8-24 a to b), has the immediate effect of increasing air saturation within the plume. The zone of influence decreases only marginally, but the air flow patterns within plume boundaries are significantly different. Air flow velocity increases, which is to be expected since air pressures gradients are increasing, causing the air to propagate more as a front than as individual channels. As a result, air saturation within the plume becomes higher. As the *g*-level is gradually increased the width of the plume progressively decreases. For increases in *g*-level up to 15-*g*, plume boundaries still show signs of air flow through relatively tortuous channels, indicated by the fact that the fluid interface is not uniform. At acceleration levels of 30-*g* plume boundaries have become uniform and the zone of influence has decreased by more than 50%. With further increases in *g*-level the width of the plume decreases to such extent, that at 100-*g* it becomes equal to the diameter of the injection port.

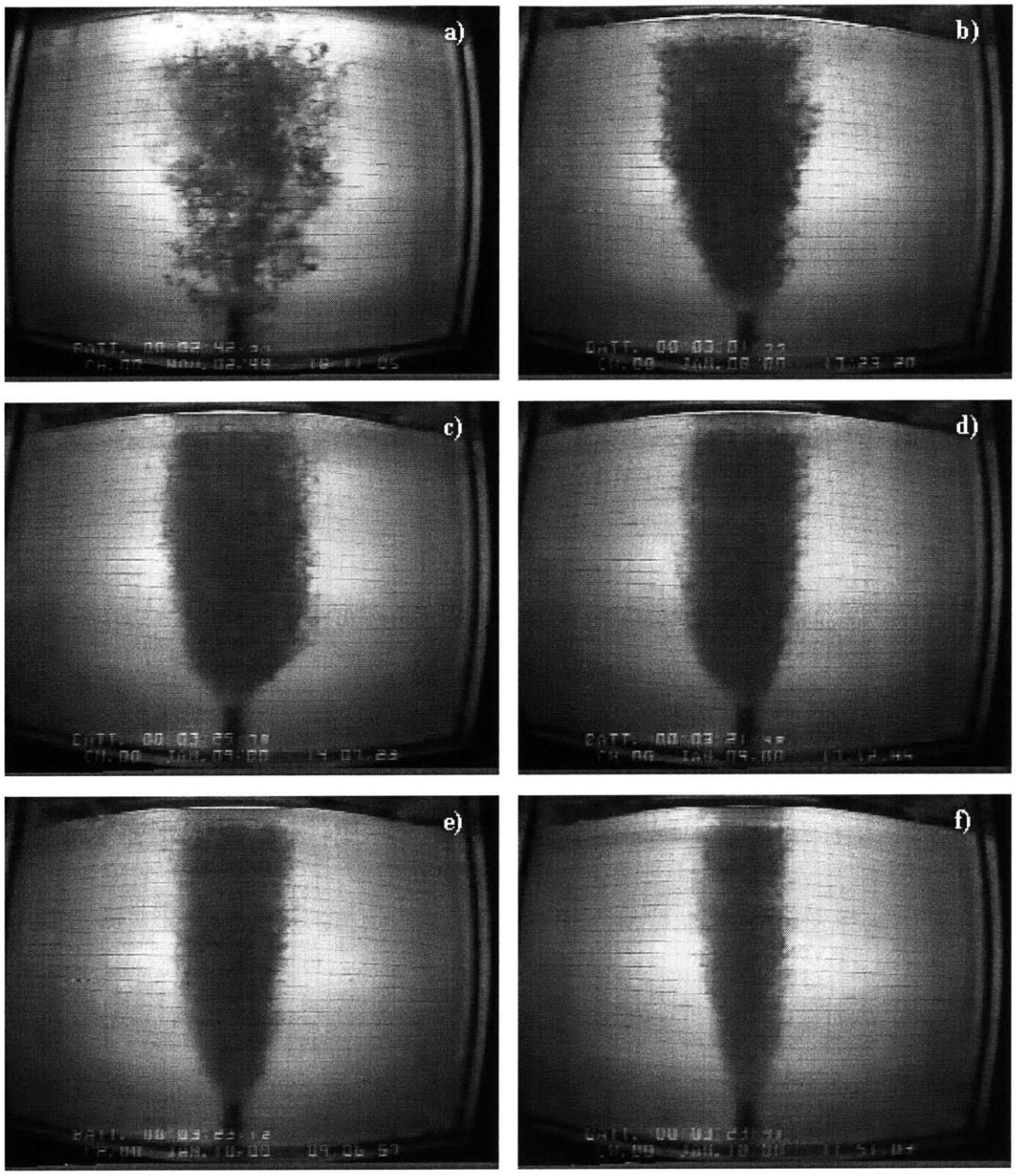

Figure 8-24 *Steady-state air plumes obtained at increasing g-levels following injection of air at constant flow rate into porous media saturated with immersion liquid – Injection flow rate q = 0.66 cm^3/s - Injector MPI #1: a) 1-g; b) 3-g; c) 6-g; d) 9-g; e) 12-g; f) 15-g.*

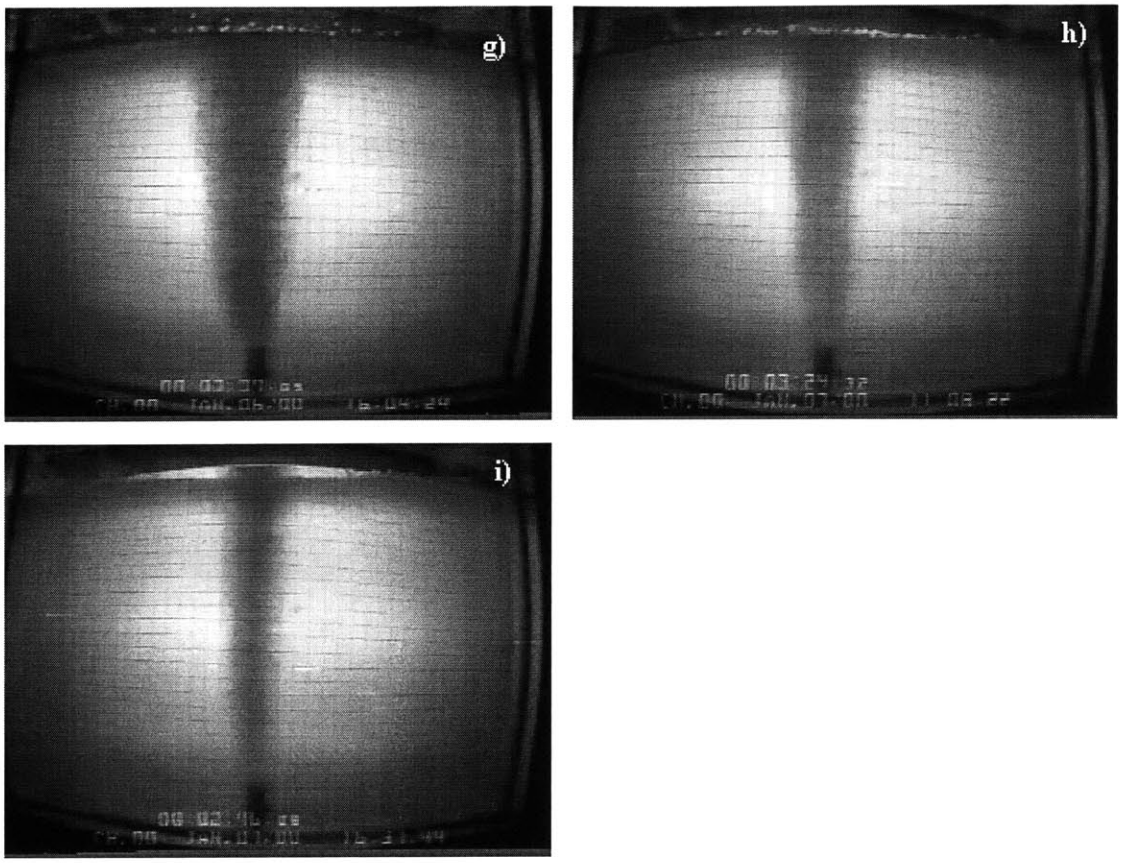

Figure 8-24 (ctd.) *Steady-state air plumes obtained at increasing g-levels following injection of air at constant flow rate into porous media saturated with immersion liquid – Injection flow rate q = 0.66 cm^3/s - Injector MPI #1: g) 30-g; h) 70-g; i) 100-g.*

No figures will be presented showing plumes obtained under injection flow rates higher than 0.66 cm^3/s, at varying *g*-levels, because the differences in zones of influence and air flow pattern characteristics, at the range of flow levels investigated, was not significant from the ones already presented in Figure 8-24. The zone of influence rapidly decreased under increasing acceleration fields, for every flow rate tested, and the propagation characteristics evolved from a slow fingering/channeling mode to a rapidly propagating, uniform front.

No significant differences were observed in the geometry of the plumes or in their propagation characteristics with the different types of injectors used in when injection was performed at high *g*-levels. It should be emphasized however, that experiments using single port injectors were not conducted, and that these were the injectors for which noticeable differences in plume characteristics had been observed at 1-*g*.

8.3.2. Air Injection in Glycerol

The same type of experiments presented in section 8.3.1 were conducted using glycerol instead of immersion liquid as the pore fluid. Air was injected into glycerol-saturated MS samples at constant flow rates ranging from 0.26 cm^3/s to 2.66 cm^3/s.

Figure 8-25 shows pictures taken during air sparging experiments in glycerol performed using injector *MPI* #1. A completely different form of air propagation was observed through these samples, at every flow rate tested. Distinct preferential channels developed at the injection point, forming an angle of approximately 45° with the horizontal plane. These channels eventually hit the sides of the box, at which point air flow continued along the boundaries. These channels, which resembled failure surfaces originating at the injection point, developed during every experiment conducted in samples saturated with glycerol, regardless of the injector type or of the injection flow rate. No breakthrough velocities or evaluation of zones of influence will therefore be presented for constant flow rate experiments in glycerol.

The characteristics of air propagation in glycerol are consistent with the properties of the liquid. The ratio of the viscosity of glycerol to that of the immersion liquid is approximately equal to 25. This contrast in viscosity combined with the difference in density between the two fluids, effectively makes the hydraulic conductivity of the medium saturated with glycerol approximately 23 times lower than that of the medium saturated with immersion liquid. The rate at which glycerol can be displaced from the pores of the medium under a given injection flow rate is therefore considerably lower than if injection was performed in immersion liquid, and fracturing pressures were probably reached during experiments such as the one illustrated in Figure 8-25. The mechanisms of pressure buildup will be extensively presented in Chapter 9.

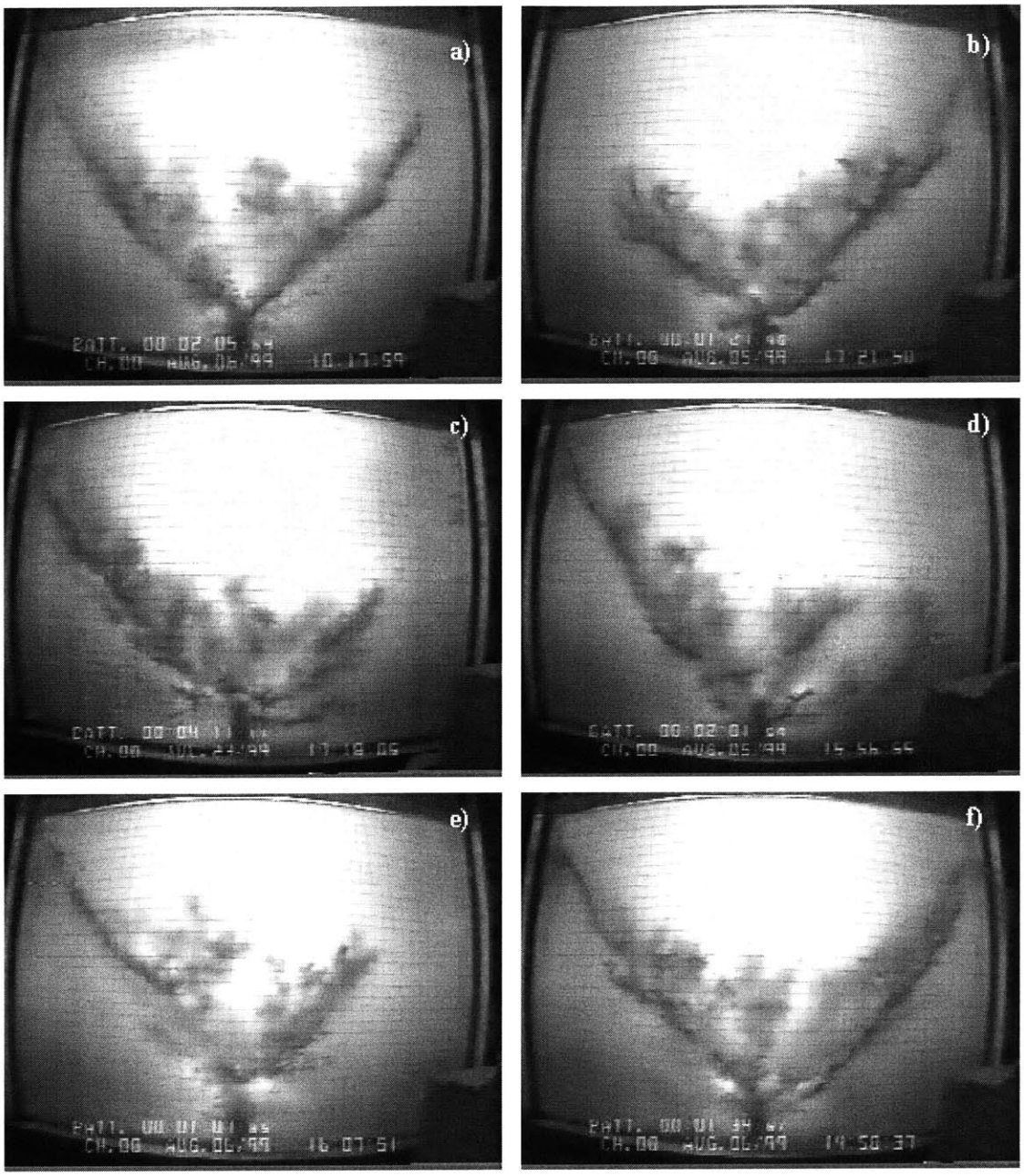

Figure 8-25 Constant flow rate injection of air into porous medium saturated with glycerol. Test conducted at 1-g. Injector MPI #1: a) 0.26 cm^3/s; b) 0.68 cm^3/s; c) 1.15 cm^3/s; d) 1.58 cm^3/s; e) 2.26 cm^3/s; f) 2.66 cm^3/s.

8.4.SUMMARY OF PROPAGATION MECHANISMS

The general characteristics of air propagation and plume formation in porous media observed during the experiments presented in this chapter have been summarized in Table 8-1.

Table 8-1 Summary of experimental observations

***g*-level**	**Constant pressure injection**	**Constant flow rate injection**
1-*g*	- Very wide plumes with high saturations - Significant basal propagation - Propagation as uniform finger front	- ZOI increases with increasing q - Rapid increase in q causes local soil failure - Gradual increase in q results in very large ZOI - Very low air saturations at lowest q since individual fingers propagate - Saturations increase with q as uniform front develops
g > 1 to 100-*g*	- Systematic reduction in ZOI of plumes - High saturations within plume boundaries - Air propagates as uniform front – no evidence of fingers	

For all the experiments conducted, air flow patterns during injection can be described by one of the three following modes of propagation:

1. Fingering
2. Uniform propagation:
   - as fingering front, or
   - as uniform front
3. Fracturing

Fingering was observed at low injection flow rates, q < 3 cm^3/s or under low acceleration fields, *g*-level < *15-g*. During fingering, air propagates through the medium in an unstable manner, along individual channels, from the injection point to the phreatic surface. The tortuosity of the paths followed by the fingers decreases with velocity of propagation. Steady-state plumes resulting from fingering propagation are typically not very wide, and air saturation within plume boundaries is low. Figure 8-26 illustrates a typical example of fingering propagation.

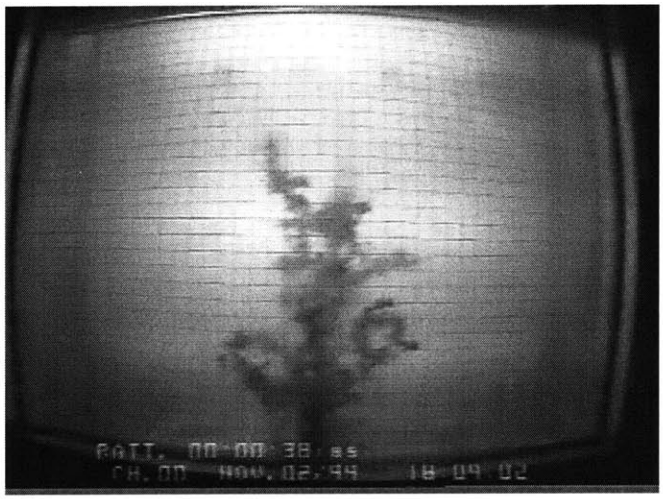

Figure 8-26 Typical fingering pattern developing during propagation of air injected through saturated porous media.

The second form of propagation observed during the experimental phase of this research was referred to as *uniform front propagation*. This type of air flow pattern was observed at: 1) higher flow rates of injection ($q < 28\ cm^3/s$) ; and 2) under higher acceleration levels (*g*-level < 40-*g*). In the first case, the propagating front can be described as a cluster of channels advancing at comparable velocities, forming a "fingering front". The zone of influence of plumes propagating in this manner is typically large, with significant lateral spreading. Saturation within plume boundaries is also relatively high. Figure 8-27 illustrates this form of propagation.

Figure 8-27 Typical "fingering front" propagation, representing one type of uniform front propagation behavior for air injected in saturated porous media.

As *g*-levels increase in excess of 50-*g*, a different type of *uniform propagation* was observed. Under these conditions, a uniform front develops as air flows through the sample. The velocity of propagation is typically high, plume width decreases with increasing acceleration level, and air saturations are high within plume boundaries. Figure 8-28 shows an example of this second type of uniform propagation.

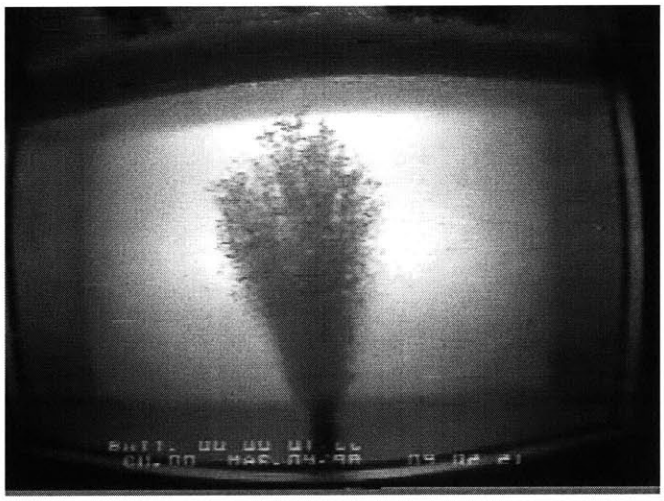

Figure 8-28 Uniform front propagation under increased acceleration levels

The final mode of propagation consists of *fracturing* behavior, in which the injection flow rate is too high relative to the rate at which pore fluid can be displaced from the porous medium. As a result, pressures in the air build up and reach the critical fracturing pressure of the medium. Fracture planes become preferential flow channels along which all air flow takes place. Figure 8-29 illustrates a clear case of fracturing behavior.

Figure 8-29 Fracturing as a result of injection of air through saturated porous media

CHAPTER 9

INTERPRETATION OF EXPERIMENTAL RESULTS

9.1.INTRODUCTION

This chapter presents the interpretation of experimental results presented in Chapter 8. All image data were converted into numeric results, with which a quantitative analysis of the flow of injected air through saturated porous media was conducted.

The chapter is divided in three major parts. Section 9.2 presents a series of relationships showing the influence of the various operational and soil parameters on the final size of air sparging plumes. The impact of increasing injection flow rates, pressure gradients, and *g*-level on the size of the resulting plumes is discussed. Section 9.3 presents a conceptual model of air propagation though soils under both constant pressure and constant flow rate injection conditions. The model describes propagation behavior, plume sizes, and air flow patterns. This conceptual model of air flow is based entirely on experimental observations, and will constitute the basis of the numerical model that will be presented in Chapter 10. Section 9.4 summarizes the key points stressed by the conceptual model and places them in the context of air sparging operations.

9.2.GENERAL RESULTS

9.2.1. Influence of Increasing *g*-Level

An objective of this study was to describe air propagation in terms of dimensionless parameters, which quantify the relationship between the forces driving and those resisting flow. An initial look at the relationship between the Bond and the Capillary numbers calculated from results of all of the experiments conducted provides insight into the mechanisms at play during air sparging. In particular, the effect of increasing *g*-level on the velocity of propagation of the air front can be evaluated. One of the hypothesis put forth at the beginning of this study, which was inspired by bubble flow

considerations, was that buoyancy forces play a major role in the mechanism of air propagation. In an idealized depiction of air flow through a porous medium, air flowing out of an injector would do so in the form of bubbles, which would quickly coalesce upon "entry" into the medium. Under high *g*-level conditions, the diameter of the bubbles forming at the injection point is reduced and bubble deformation as they flow through capillary restrictions, according to Hemmat and Borhan (1996), is enhanced. Even though the model of individual bubbles flowing through the porous medium has been rejected, at increasing *Bo* air flow is expected to take place at higher velocities and with less interference from the porous medium.

The relationship between *Bo* and *Ca* for all the experiments conducted is presented in Figure 9-1. Full symbols represent results from constant rate of injection tests while open symbols were used for plotting results from constant pressure injections. The effective grain size of the various materials tested (D_{10}) was used as the characteristic length in the expression for the Bond number. Average velocities used in calculations of the Capillary number were obtained from displacement versus time plots of the moving air front, as described in Chapter 6.

It is clear from Figure 9-1 that *Bo* and *Ca* are directly related, and that *Ca* increases with increasing *Bo*. However, the relationship shown on the figure is not necessarily illustrating the effect of a less restricted form of air propagation, as speculated, whereas it is certainly showing the effect of increasing pressure gradients at increasing *g*-levels. Indeed, as the *g*-level increases air entry pressures increase, and consequently injection pressures are also higher. Larger injection pressures lead to an increase in pressure gradients and ultimately to higher air velocities, thus increasing the value of *Ca*. This increase in *Ca* cannot be attributed to a different mode of air propagation at higher *g*-levels, and for this reason, Figure 9-1 is not an adequate indicator of the potential effects of buoyancy on air flow behavior through porous media. The figure does, however, show differences in the *Bo-Ca* relationship for the two pore fluids used, as seen on the steep slope of the relationship for experiments conducted in glycerol. In the case of the immersion liquid, the slope is constant, regardless of the type of porous material used in the experiments. Given that the dimensionless parameters account for

the variability in the properties of the fluids, the difference in the slopes of the plots in Figure 9-1 alludes to differences in the mode of propagation related to the fluid.

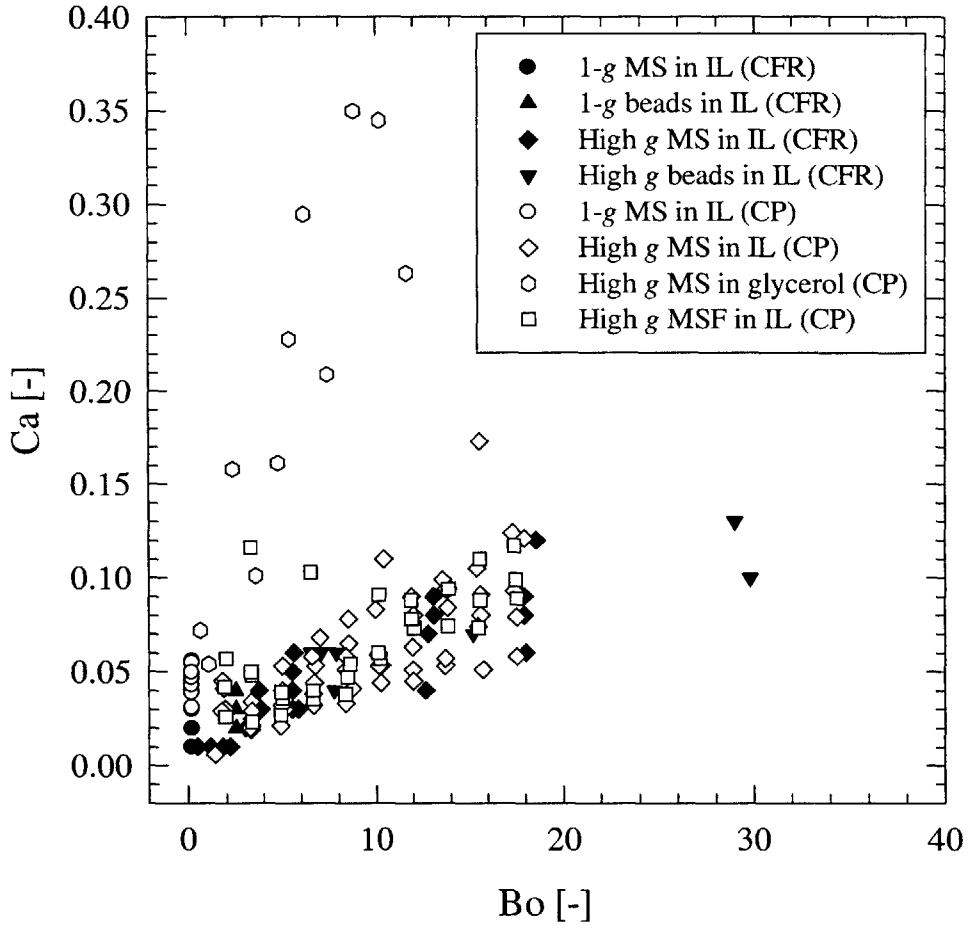

Figure 9-1 *Relationship between Bond and Capillary numbers for air sparging experiments conducted under Constant Pressure (CP) and Constant Flow Rate (CFR) conditions. Results include tests done on samples saturated with Immersion Liquid (IL) and glycerol.*

9.2.2. Influence of Velocity of Propagation

The velocity of air propagation and its effect on plume dimensions can be initially evaluated by studying the relationship between plume size, expressed in terms of relative zone of influence (*RZI*), and the Capillary number. This relationship is shown in Figures 9-2 a) and b) for experiments conducted under constant pressure and constant flow rate

injection conditions, respectively. All *RZI* values were calculated for steady state plumes. The figures summarize results from experiments conducted at *g*-levels ranging from 1-*g* to 100-*g*. Values of *Ca* increase with increasing *g*-level.

Several comments can be made when comparing these two figures, the most apparent of which is the drastic decrease in the size of the plumes, under both injection conditions, as *Ca* increases. The drop of *RZI* with increasing *Ca* occurs rapidly, and takes place as *g*-levels start to increase. The size of plumes obtained under constant pressure injection drops by approximately 95% as the acceleration field increases from 1-*g* to 20-*g*. *RZI*s of constant flow rate plumes drop by approximately 85% for an equivalent increase in *g*-level. After the initial drop in *RZI*, increasing capillary numbers lead to marginal decreases in plume sizes for all of the materials tested and both of the pore fluids used. The data therefore suggests that the velocity of flow of air through the porous medium alone, is not controlling the size of the plumes. Furthermore, the hypothesis of less interference from the porous medium on air propagation at high *g*-levels does not seem to be valid. The size of the plumes collapses rapidly and permanently as *g*-levels start to increase, and the role of the porous medium does not appear to be significant after this point.

The fact that propagation velocity alone is not controlling plume size is also noticeable when comparing the size of plumes formed under constant flow rate and constant pressure injection. The plumes obtained during constant pressure injection, at the low range of *g*-levels, are approximately two times larger than those under constant flow rate injection. However, the breakthrough fronts of the largest constant pressure plumes moved at velocities comparable to those of the largest constant flow rate plumes. It should also be noted that the saturations of the constant pressure plumes were significantly higher than those of the constant flow rate plumes, as was shown in images of captured plumes presented in Chapter 8.

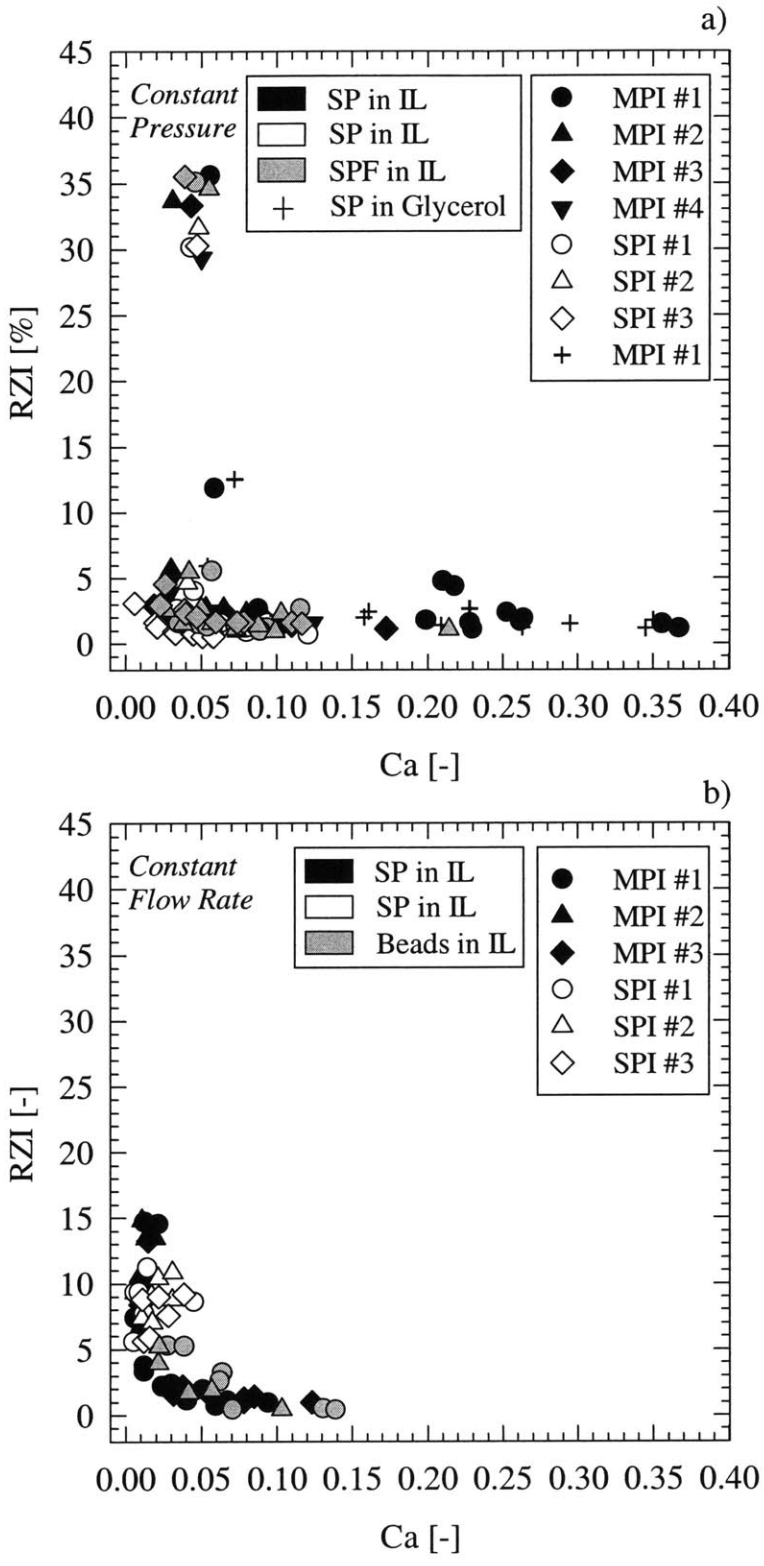

Figure 9-2 *Influence of Capillary number on Relative Zone of Influence of air sparging plumes: a) under constant pressure injection; b) under constant flow rate injection.*

A particular grouping of data points on Figure 9-2 b) behaves in a distinct fashion. The data points in question correspond to steady state plumes obtained at 1-*g* using single port injectors. Values of *Ca* corresponding to these tests are erratic, and tend to be higher than those for tests under comparable injection conditions but using multiple port injectors. Air propagation characteristics for these experiments had been noted to be different, in previous discussions presented in Chapter 8. During these experiments, independent and unstable fingers breakthrough and reach the phreatic surface at relatively high velocities. Additional fingers form subsequently, leading to wider plumes of low saturation. The particular behavior of this group of data points will be addressed in a later section.

In order to see how the air sparging plumes obtained in this study compared with other immiscible flow results available in the literature, data were plotted on the phase diagram developed by Lenormand *et al.* (1988). As was discussed in Chapter 2, Lenormand *et al.* were able to describe the characteristics of immiscible displacements through porous media in terms of two dimensionless parameters, the capillary number *Ca* and the mobility ratio *M*, where *M* is the ratio of the displacing to the resident fluid viscosities. Figure 9-3 shows experimental data from tests performed under 1-*g* conditions plotted on their phase diagram. Only results at 1-*g* were plotted, since the authors limited their study to experiments of horizontal propagation, specifically to minimize the effects of gravity forces. In their experiments, injection was performed under constant flow rate conditions.

Included on the figure are the various boundaries of flow domains proposed by the authors, which were defined experimentally, based on differences of propagation patterns at varying values of *Ca* and *M*. Data collected during this investigation fall within Region I, a zone characterized by a low viscosity ratio, where the viscous forces in the injected fluid are negligible in comparison with viscous forces in the displaced fluid. Furthermore, all of the data points plot in the low capillary range. According to Lenormand *et al.* (1988), the low *Ca* group corresponds to the domain of capillary fingering, where the viscous forces are negligible in both fluids and the principal force is due to capillarity.

This described behavior clearly does not correspond to that which was observed during experiments conducted in this study, since capillary forces do not appear to be controlling the behavior of air propagation. The phase diagram proposed by Lenormand *et al.* (1988) therefore appears to have limitations, and may not be applicable for cases of vertical flow, or for cases were capillary pressures are so much lower than other pressures affecting the flow.

As discussed in Chapter 2, at high *g*-levels, the influence of capillary pressure on air propagation characteristics is even less noticeable. The effect of increasing pressure gradients with increasing acceleration levels has obvious impacts on the patterns of air flow. Pictures taken during air sparging experiments have shown the drastic decrease in the zone of influence of the injectors, when testing is conducted under increasing *g*-levels.

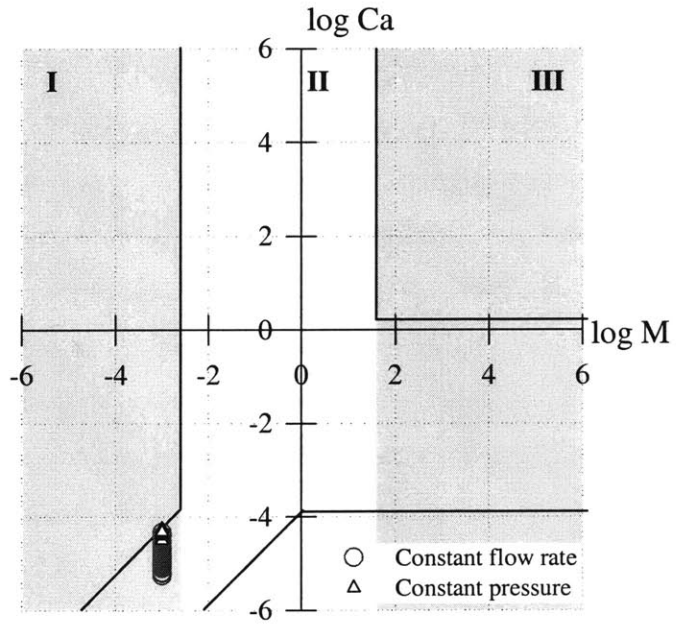

Figure 9-3 *Experimental results at 1-g plotted on phase diagram for immiscible displacements proposed by Lenormand et al. (1988).*

9.2.3. Influence of Injection Flow Rate and Injector Geometry

The role of capillarity at low *g*-levels, where the magnitude of the hydrostatic pressure is not so high relative to the capillary pressure, needs to be further investigated.

Air propagation characteristics at 1-*g* were noticeably different that at higher *g*-levels, when injection was conducted under constant flow rate conditions and at low injection rates. Propagation took place along tortuous channels/fingers, and this meandering ultimately resulted in relatively large plumes. Additionally, plume growth continued after the first air front reached the phreatic surface, such that breakthrough plumes were different than steady-state plumes. The distinctive cluster of data points noted on Figure 9-2 b) corresponds to steady state plumes which propagated in this manner. Figures 9-4 a) and b) focus specifically on this group of plumes, and present *RZI* results at breakthrough and at steady state, as a function of injection flow rate for the various injectors tested. The figure shows that steady state plumes in crushed glass at 1-*g*, for injection flow rates ranging from 0.26 cm^3/s to 2.6 cm^3/s, are on average 1.5 to 2 times larger than those at breakthrough. *RZI*s increase with increasing injection flow rate. Differences in propagation depending on the geometry of the injectors that had been noted in Chapter 8 are evident on Figure 9-4 b). Specifically, steady state plumes formed using single port injectors are, in general, smaller than those obtained using multiple port injectors. Propagation characteristics of *SPI*s are very irregular, and "fully developed" plumes were not always obtained by the end of the experiments conducted. It is interesting to notice that steady state and breakthrough plumes obtained in glass beads under the same injection conditions were equivalent, and no tortuous propagation was observed.

With increasing *g*-levels, the distinction between breakthrough and steady state plumes disappears, as well as the effect of injector geometry on final plume size. Under 1-*g* conditions and at very low injection flow rates however, given the experimental depth of injection and the pore size characteristics of the porous medium, capillary forces may be sufficiently high to cause a change in air propagation behavior. Indeed, the ratio of P_{cap}/P_{hydro} for the crushed glass, in a typical experimental setup was approximately 13%. The same ratio for the glass beads was approximately 3.5%. Results suggest thus that in cases in which capillarity becomes significant relative to hydrostatic pressure, and in which injection flow rates are maintained low, a fingering mechanism governs air propagation. This mechanism introduces tortuosity in the advancement of the air front, and therefore results in relatively wide plumes with low air saturations.

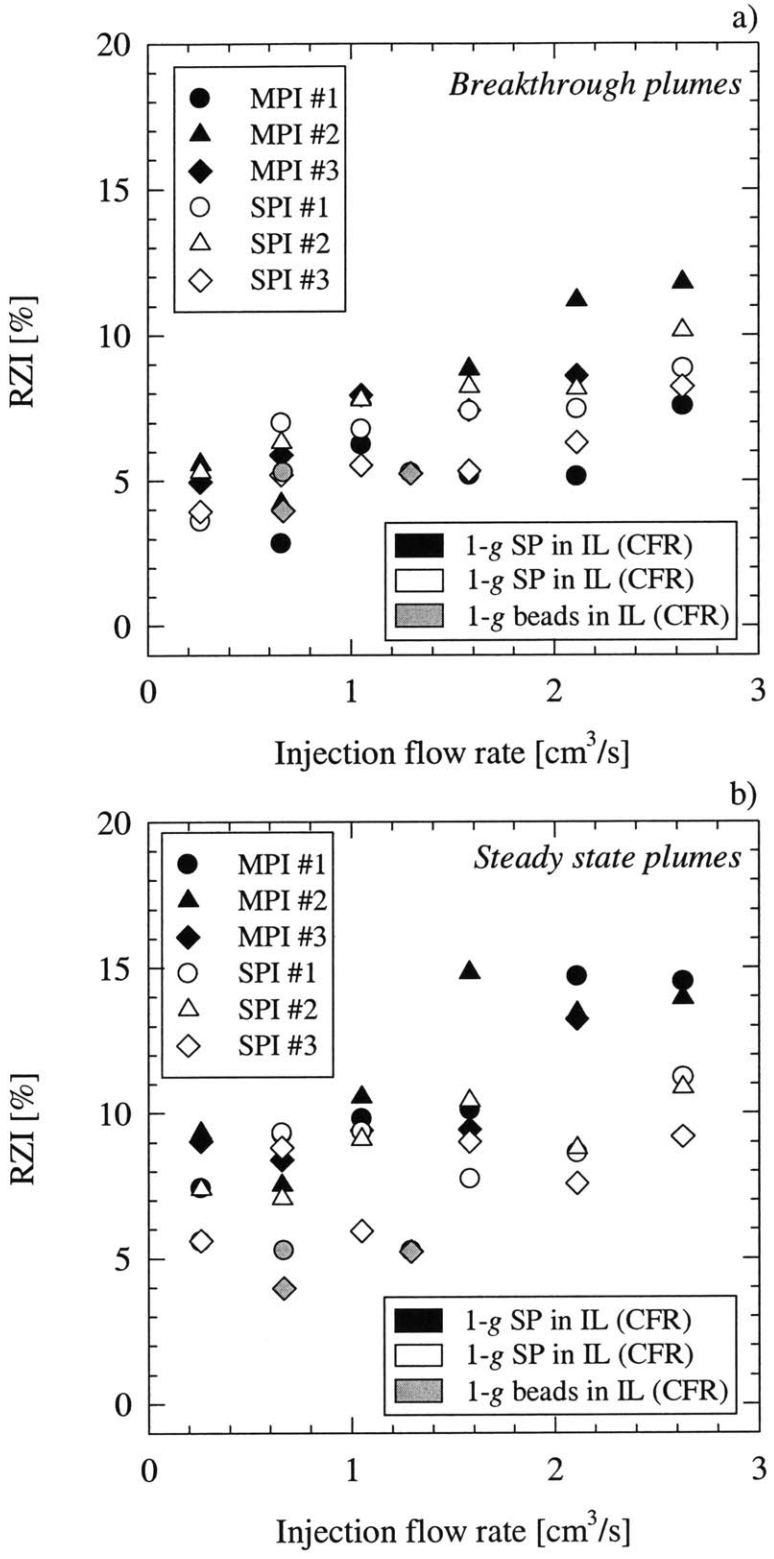

Figure 9-4 *Relative zone of influence as a function of injection flow rate: a) RZI at breakthrough; and b) RZI at steady state. Tests conducted at 1-g, under constant flow rate conditions, on samples of SP.*

Flow rates must remain low for this mode of flow to be maintained. In fact, if the flow rate is increased such that pressure in the air phase builds up, fracturing is likely to occur, terminating the advancement of the fingers.

9.2.4. Influence of Pressure Gradient

The relative size of the plumes was then plotted as a function of initial pressure gradient. The definition of initial pressure gradient should be explicitly stated, since the figures presented may be misleading without clarification. The pressure in the air phase as the plume advanced through the medium during experiments was not measured. The only pressure measurement available was that of the pressure of the air as it was injected into the box. The values of the pressure gradient plotted in the figures were then calculated as the difference between the piezometric head in the injected air and that in the pore fluid (calculated from the value of the entry pressure the injection point), over the saturated height of the sample.

Assuming at this point of the discussion that the pressure in the air phase remained constant during constant pressure experiments, pressure gradients have increased as propagation was taking place, since, for a constant value of the pressure in the air phase, the distance to the flow boundaries was decreasing. For constant flow rate tests, changes in pressure gradients must have occurred as propagation took place, as the pressure in the air phase, was likely not constant throughout the experiment. The magnitude of injection flow rates was obviously critical to the manner in which the gradient evolved during plume propagation. Indeed, depending on the relative magnitudes of the volume of air injected to that of the volume of pore fluid displaced, the pressure in the air phase either increased or decreased. Pressure gradients were, of course, a function of this relationship.

The relationship shown in Figures 9-5 a) and b), between the relative zone of influence and the measured initial pressure gradient is very similar to that observed with *Ca*, as expected, since pressure gradients drive the flow. Under constant injection pressure conditions, a 85% drop of in the value of *RZI* occurs immediately after pressure

gradients increased above 10 (g-levels increased above 10-g). A 95% reduction in the size of the plumes has occurred when accelerations reach 20-g, and the value of *RZI* remains relatively constant for further increases in gradient. The same behavior is observed for all injector geometries, and for all porous media tested. As shown in Figure 9-5 b), comparable reductions in *RZI*s for constant flow rate conditions occur, although initial plumes were approximately half the size of the constant pressure plumes. The drop in *RZI* at increasing gradients is even more marked in the case of the glass beads, through which the plume is practically vertical as g-levels start to increase.

The drastic differences in plume size when comparing results from constant pressure to those from constant flow rate conditions at low g-levels are again evident in this figure. The fact that, at low g-levels, comparable initial gradients between constant pressure and constant flow rate experiments lead to considerably different plume sizes, suggests that gradients during constant flow rate injection indeed decrease as propagation occurs. The pressure in the air phase must therefore be decreasing significantly as air flow takes place, in order to account for lower gradients even when the travel flow path is also becoming smaller. The fact that capillary numbers for these same constant flow rate tests are not drastically smaller than those under constant pressure conditions would seem to contradict the statement of decreasing gradients, since it is, after all, the pressure gradients that drive flow. However, it must be reemphasized that the velocities used in calculations of *Ca* are those of the breakthrough front, and that although, in most of the constant flow rate cases they are lower than those under constant pressure conditions, the decrease in pressure gradient at that stage of plume formation might not be so severe. The plumes under 1-g accelerations fields continue to spread after breakthrough, and at later stages of the experiment, the decrease in gradient might be much more significant.

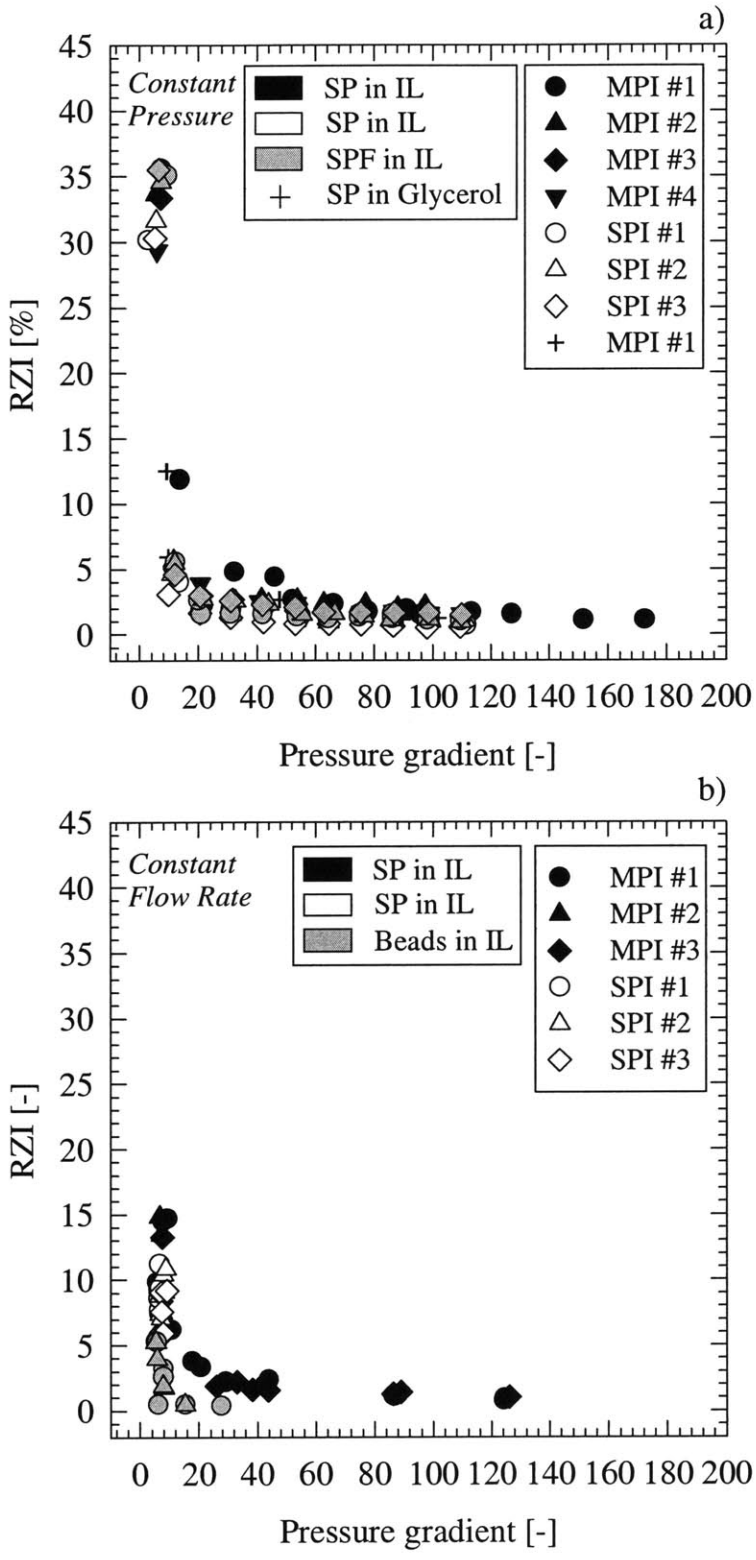

Figure 9-5 *Relative Zone of Influence as function of injection pressure gradient; a) under constant pressure injection; and b) under constant flow rate injection. Pressure gradients calculated at the injection point.*

9.2.5. Summary of experimental results and observations

The images presented in Chapter 8 and the figures presented in this chapter have shown that the effect of increasing pressure gradients, at high *g*-levels, is to cause a drastic decrease in the size of the zone of influence of an injector. As the pressure gradient between the injected air and the surrounding fluid increases, for every fractional displacement of the air front in the vertical direction, the vertical gradient increases in relation to the horizontal gradient. As a result, flow preferentially occurs upward, increasing the vertical propagation trend, thus leading the observed plume geometry.

In this context, experimental data results are summarized in Figure 9-6. The figure plots *RZI* as a function of the ratio of *Bo* to *Ca*. This ratio was selected as the final parameter characterizing plume propagation, since it relates the effects of buoyancy and of propagation velocity to the properties of both the medium and the pore fluid. This accounts for differences in air propagation in the two pore fluids tested, and in the different porous media considered.

The figure normalizes all of the experimental results, and shows the drastic reduction of the *RZI* with increasing values of *Bo/Ca*. Experimental data define two zones of distinct flow characteristics: 1) at low *g*-levels, a zone characterized by fingering patterns, in which macroscopic air flow takes place through distinct channels; and 2) at increasing acceleration fields, a zone in which air propagation occurs as a narrow uniform front flowing at relatively high velocities.

Data presented in Figure 9-6 can be explained in two different ways depending on whether the constant hydraulic gradient or the constant hydraulic conductivity interpretation is chosen to explain the physical mechanisms taking place during centrifuge modeling. If it is argued that pressure gradients do not scale with *g*-level, such that experiments conducted at 1-*g* and at 100-*g* are subjected to the same pressure gradient, then the hydraulic conductivity of the material must be scaled. In the context of the data presented in Figure 9-6, this would imply that as accelerations are increasing, experiments are effectively modeling coarser and coarser materials. The observed reduction in plume size with pore size (and hence grain size) increase is drastic, and therefore the effectiveness of air sparging as a treatment method in very coarse soils becomes questionable.

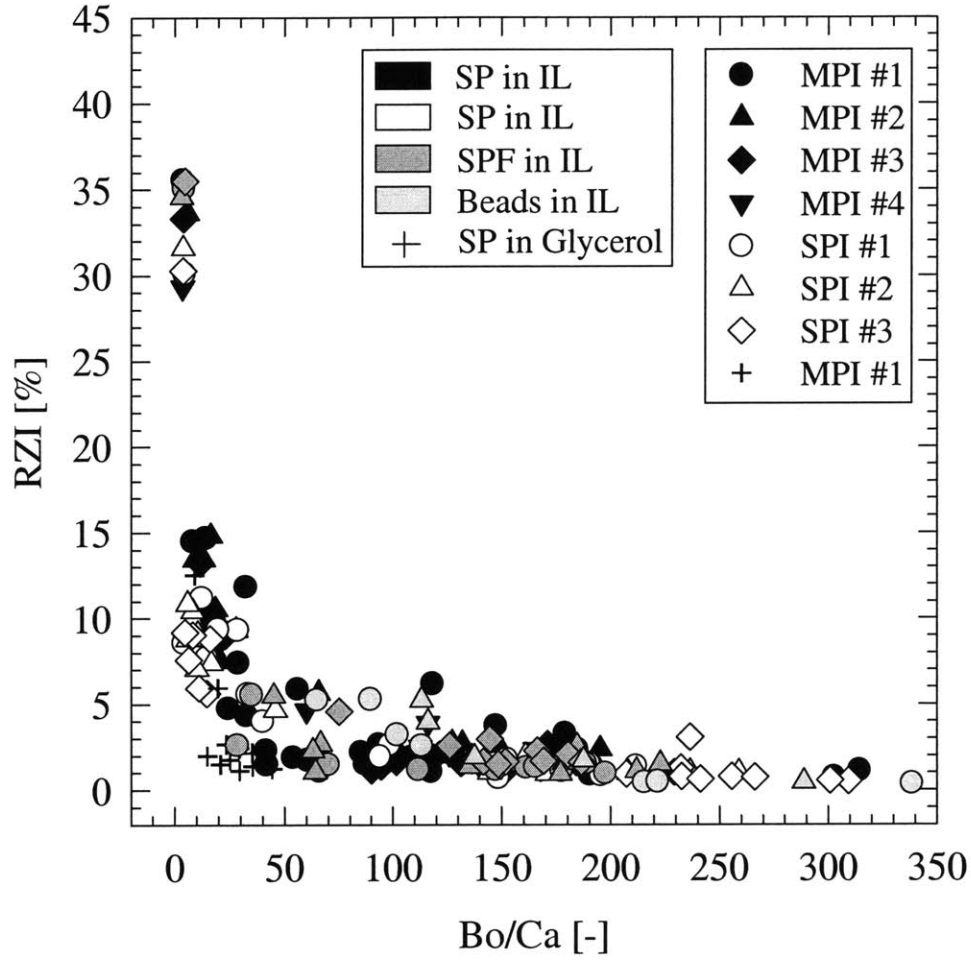

Figure 9-6 *Relative Zone of Influence as a function of the ratio between Bond and Capillary numbers. Includes results from all experiments successfully completed in this investigation.*

If , conversely, it is argued that the hydraulic conductivity of the material does not change at increasing accelerations, then pressure gradients must increase with *g*-level. Figure 9-6 therefore suggests that plume size drops as the soil is subjected to increasing pressure gradients. This implies that injecting air at increasing pressures, *even while maintaining the stability of the soil*, will result in drastic decreases of the zone of influence of an air sparging well.

Data included in Figure 9-6 are plotted again on Figure 9-7, where the two zones of flow have been distinguished by linear regressions. Data plotting in R*egion 1* are essentially all the results from experiments conducted at 1-*g*. An additional grouping of the data is included in the figure, to account for difference in saturation of the steady-state plumes. The zone of influence of an injector provides a measurement of the extent of the volume of soil that is reached by the injected air, but does not describe the degree of air saturation of the soil within the boundaries of the plume. Depending on the specific purpose and design of an air sparging well, the degree of air saturation of the soil plays a critical role. If diffusion of volatile contaminants from a liquid saturated region to the neighboring air channels is likely within a reasonable amount of time, then a partially air saturated plume may be all that is necessary to clean-up the soil deposit. If however, diffusion is not a feasible alternative, then a smaller zone of influence where air saturation is high will be more adequate than a larger area of low saturations.

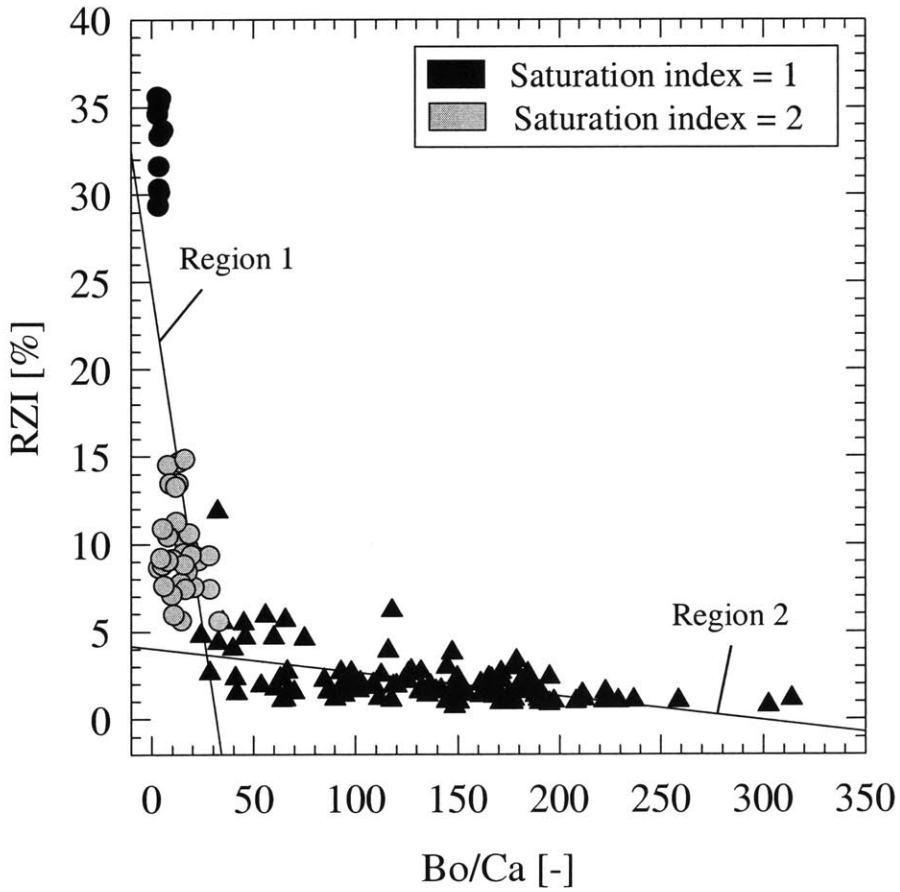

Figure 9-7 Regions of air flow and air saturation index

In order to quantify the degree of saturation of the different plumes, the images of steady-state plumes were analyzed, and an air saturation index was assigned to each one of them. After comparing all the plumes it became evident that a wide range of saturation indices was unnecessary. The plumes were either completely saturated between their boundaries, or showed signs of channeling and fingering, in which case pockets of pore-fluid-saturated material were visible at the end of the experiments. The variability in plume geometry, and the level of resolution of the images collected would not have made a more detailed breakdown of the saturations meaningful. The criterion used to classify the plumes was therefore straightforward: a value of 1 was assigned to fully saturated plumes, while a value of 2 was given those that were partially saturated. As shown in Figure 9-7 only a cluster of data points were classified as having an saturation index of 2, which correspond to the low constant rate of injection experiments conducted at 1-*g*.

9.3.AIR PROPAGATION

Based on observations of all the experiments conducted, on the analysis of the data collected, and on the background information presented in earlier chapters, a conceptual model of air propagation through saturated porous media is presented in this section.

9.3.1. Effects of *g*-Level on Constant Pressure Injection Experiments

The main assumption that will be made in the description of injection under constant pressure conditions is that the pressure in the air phase as air flows through the soil and *until the phreatic surface is reached* is constant and equal to the source pressure. This statement therefore suggests that, as long as breakthrough has not taken place, the entire plume can be effectively treated as a big bubble that is still attached to the injection orifice. This assumption was initially taken as valid in the case of the experimental setup used in this investigation, and it was presumed that the volume of the source pressure would remain constant during an air sparging experiment. The assumption seemed reasonable provided that the volume of air in the plume remained small relative to the volume of the source and the line, but its validity, in the context of the experimental work

conducted, will be evaluated in following sections. In a more realistic field scenario however, where the volume of the source pressure is not limited, the assumption that the pressure in the plume is maintained constant is reasonable, and only requires additional air to be introduced in the system in order to maintain a constant pressure.

Furthermore, experimental results showed that regardless of the mechanism of propagation, whether air is flowing through the soil as fingers, through channels, or as a front, the mode of propagation is continuous (*i.e.* is not in the form of discrete bubbles). The pressure at any point within the air phase must therefore be continuous and equal to the pressure at the injection point, that being the source pressure.

The source pressure (*i.e.* injection pressure) in a constant pressure injection experiment is set such that static equilibrium conditions at the injection point are overcome, and thus the pressure is sufficient to cause entry at every point of the soil column. In fact, the smaller the distance to the phreatic surface the higher the air pressure is relative to the air entry pressure at that given elevation. From a pressure point of view then, air propagation will occur at any elevation during a constant pressure experiment, as long as entry pressures at the injection point have been exceeded and as long as air flow is maintained at the injection point.

If flow velocities are maintained low enough that laminar flow conditions are satisfied, water and air flow through the medium are governed by Darcy's law. Flow through a homogenous soil of constant hydraulic conductivity, in any direction, is therefore dictated by the hydraulic gradient imposed on the two fluids. The hydraulic gradient, in turn, is a function of: 1) the difference between the piezometric heads in the air phase and that in the water phase at the elevation of the interface between air and water; and 2) the length of the flow pathway. The conditions under which vertical flow occurs will be considered first, followed by horizontal flow conditions.

The pressure in the water phase, in the vertical direction, decreases with distance to the phreatic surface as the hydrostatic pressure decreases. Conversely, under constant pressure injection conditions, the air pressure remains at the same value independent of elevation. As a result, as the interface between air and water moves vertically during air sparging the pressure gradient driving the flow increases. At the same time, as the phreatic surface is approached, the length of the flow pathways decrease. Both of these

factors result in increasing hydraulic gradients in the vertical direction as flow propagation takes place.

Flow conditions are considerably different in the horizontal direction. First, the pressure gradient between the air and water phases at a given elevation remains constant as the flow advances laterally, since neither the hydrostatic pressure nor the pressure in the air phase change at a constant depth. The second factor in the determination of the hydraulic gradient, namely the length of the flow pathway, is not as straightforward to determine as it is in the vertical direction. How far from the injection point does the air travel, or at what distance from the injector can we assume that the water is at hydrostatic conditions? The location of this lateral boundary has important implications to the lateral spread of the air plume, because it controls the magnitude of the hydraulic gradient in the x-direction. If the boundary is located close to the injection well, then the length of the longest flow pathway will be small, the hydraulic gradient in the x-direction will be large, and significant lateral spreading may occur. If, on the other hand, the boundary is located far away from the injection point the horizontal gradient will be small, and air flow will preferentially occur in the vertical direction. At this point of the discussion however, in order to illustrate the mechanisms of flow, it will be assumed that the location of the horizontal boundary is known at a fixed radial distance from the injection point. This distance is taken as the distance from the phreatic surface to the injection point, such that the length of the flow paths are initially equal in both directions, and therefore such that no preferential propagation takes place due to boundary effects.

Once air is injected at constant pressure into the ground it migrates both in the vertical and horizontal directions. With every length unit the air travels in the vertical direction the gradient increases due to both the increase in the pressure difference and the decrease in the flow length, while the increase in the horizontal gradient is exclusively due to the decrease of the flow length. The tendency for vertical flow to occur is therefore further increased as the front of the plume moves closer and closer to the phreatic surface.

Experimental results at constant injection pressure obtained under high acceleration fields showed a dramatic decrease in lateral spreading of the air sparging

plume with increasing g-level. The mechanisms by which these narrow plumes were obtained can also be explained through hydraulic gradient considerations.

Injection pressure must to be increased at increasing g-levels in order to match the increase of the hydrostatic component of the air entry pressure. As was illustrated in Figure 3-2, the value of ΔP, the pressure difference between entry pressure and air pressure, increases as the phreatic surface is approached for tests conducted at high g-levels. Increases in ΔP lead to higher hydraulic gradients in both the radial and the vertical directions. Vertical gradients are higher than radial gradients and therefore flow is preferentially driven vertically. The lateral spreading of the plumes is consequently reduced, since there is not sufficient time for increasing flow to occur in the radial direction before breakthrough occurs.

9.3.2. Effects of g-Level on Constant Flow Rate Injection Experiments

Air propagation through saturated porous media under constant rate of flow injection conditions is dictated by more parameters than propagation under constant pressure injection. The fact that more variables are involved in the flow process makes the study of air flow through the porous medium slightly more complex, but also adds possibilities of controlling the characteristics of propagation.

In the following analysis, treatment of two phase-flow has been done by assuming that one phase is completely displaced by the second one as flow is occurring. The conceptual model proposed therefore assumes that flow characteristics correspond to a type of plug-flow at the level of the pores, *i.e.* complete air saturation.

The key difference between air propagation during constant flow rate injection is that the pressure in the air phase cannot be assumed to be constant as air propagates through the soil. At the beginning of injection the pressure is, as a minimum, set equal to the air entry pressure of the material. After entry has occurred however, the pressure in the air phase within the porous medium depends on the relationship between the volume of air that is being injected per unit time, and the volume of pore fluid that can be displaced in that same time interval. The former is an operational parameter that can be

controlled and monitored, while the latter is dictated by the hydraulic conductivity of the soil and by the hydraulic gradient driving the flow.

Depending on the injection flow rate being used and on the properties of the material, one of the two following scenarios may develop: 1) if a given volume of air is injected into a soil at a faster rate than that at which the pore fluid can be displaced, pressure build up occurs. The air occupies the pore volume available and compresses, leading to an increase in pressure in the air phase. If the injection flow rate is very high compared to the rate of flow through the medium, then the pressure buildup occurs rapidly and the risk of fracturing the soil is high. If the injection flow rate is moderate, increasing pressures will result in increases in hydraulic gradient, leading to higher volumes of pore fluid flow being displaced from the medium, and thus to less risks of failing the soil. As the plume propagates and the volume occupied by the air phase expands the air pressure decreases, and more air is required before pressure build up starts again. 2) If the injection flow rate is too slow, air propagation cannot proceed continuously and advancement of the air front is interrupted. The plume propagates until the air pressure is not sufficient to displace additional pore fluid at a given elevation. Pressure eventually builds up again as more air is injected into the system, at which point advancement of the plume continues.

The two types of propagation described above result in drastically different plumes. In cases in which pressure build-up occurs and hydraulic fracturing is not induced, lateral propagation is likely to decrease as the pressure builds up. Indeed, as is the case during constant pressure injection, the position of the flow boundaries relative to the location of the air-water interface dictate the preferential directions of flow. If the gradient in one direction becomes fractionally larger than in the other, flow will preferentially take place in that direction. This effect rapidly causes a drastic reduction in the propagation along the other direction of flow. Given the density contrast between air and pore fluid, the preferential direction is inherently vertical. Unless the build-up in pressure occurs early enough in the propagation that a pressure bulb is formed at the injection point, vertical propagation overrides lateral plume growth and the resulting plumes are narrow. If, on the other hand, a pressure bulb is created, the injection source is effectively enlarged around the injector, and both vertical and lateral propagation will

take place at the same rate provided that the flow boundaries are located at the same distance from the injection point.

In cases in which very low injection flow rates are used, only a few channels develop given that the pressure in the air phase is insufficient for displacement of pore fluid. The occurrence of dead-end fingers is pervasive, as the volume of air tends to be channeled through a minimum number of pathways if critical entry pressure conditions are approached. The development of the plume is very slow, and air saturations are very low. Once breakthrough occurs all air flow takes place through one or two channels, and no further growth of the plume is observed.

The mechanisms outlined apply only to a certain extent when injection at constant flow rate is conducted under increased accelerations. Given that entry pressure conditions must be satisfied at the beginning of injection independently of the injection flow rate, and that pressure gradients increase so significantly at high g-levels, constant flow rate injection conditions at high g-levels are very similar to constant pressure conditions. Indeed, in cases in which the injection flow rate is low the initial over-pressurization is sufficient to drive the air flow up through the soil column, in spite of the low volume of air being supplied. Lateral propagation is limited, but no dead-end fingers occur. If, on the contrary, the flow rate is high, the same conditions observed during constant pressure injection are observed.

It is clear that the formation of a plume under constant rate of flow conditions is much more dependent on the hydraulic conductivity of the material than that of a plume forming under constant pressure injection. In the case of the former, the ease of pore fluid displacement dictates the extent of lateral propagation of the plume. If the hydraulic conductivity of the material is high enough that only marginal pressures are required to displace the pore fluid, air propagation occurs without significant pressure buildup, and consequently, lateral propagation is small. In fact, if the hydraulic gradients needed to displace the pore fluid at the injection point are relatively small, given that air pressure is being dissipated with plume growth and that vertical gradients are higher than horizontal gradients, flow preferentially occurs in the vertical direction with minimal lateral flow. If, conversely, the hydraulic conductivity is low, significant pressure buildup will be

needed to maintain sufficiently high hydraulic gradients that displace the pore fluid, and consequently, lateral propagation close to the injection point has a higher likelihood of occurring. However, if the hydraulic conductivity of the material is too low, pressure buildup is such that fracturing of the soil will likely occur before any significant propagation takes place.

In the case of plumes formed under constant pressure conditions, the impact of the hydraulic conductivity of the material on the final size of the plume is relatively smaller, since pressure buildup does not occur as injection proceeds. If K is too high the same effect described in the case of constant flow rate conditions occurs, since lateral propagation is not favored. If the hydraulic conductivity is low however and pore fluid is not being displaced, pressure buildup does not occur, and propagation eventually takes place along a path of least resistance, for instance a lower conductivity cluster.

9.3.3. Air Flow Patterns

9.3.3.1.Flow regimes

Results from the experimental investigation conducted have clearly demonstrated that bubbly flow does not occur following injection of air through saturated porous media. Bubbly flow conditions through the sample were never observed during testing of any of the granular materials used in this study. Bubbles were only visible if the sample was observed from above, at 1-g, as air channels reached the phreatic surface. During propagation through the porous medium however, even in the case of the coarse glass beads, bubble coalescence was predominant.

Air flow patterns observed during the experimental program can be classified as channeling, uniform front propagation, or fracturing, with varying levels of intermediate patterns between the extremes. Channeling always occurred under 1-g conditions, for both pore fluids used, and through all the samples of crushed glass tested. Visibility through the glass beads was not adequate enough to see if air was flowing through individual channels or as a front.

Channels can be described as wide fingers that propagate either individually or in clusters, depending on the injection conditions. At 1-g, smaller scale finger propagation

occurs around the boundary of the large channels, such that pore scale propagation and macroscopic propagation are occurring simultaneously as the air migrates upward. Areas of low air saturation remain in between the channels, but the number and the size of pore fluid pockets also varies with injection characteristics.

As g-level increases, and consequently as buoyancy/pressure gradients increase, the velocity of the air channels increases, individual channels start to group together in clusters advancing at a relatively uniform velocity, and the channeling pattern progressively becomes a uniform front propagation. It is worth noting that according to Equation 2-7 which describes the onset of fingering, the type of displacement that occurs during air sparging is always expected to be unstable, and increases in velocity of propagation do not have a theoretical stabilizing effect. The distance between channels reduces with very slight increases in g-level, leading to an increase in the saturation values within the boundaries of the plume. This increase in saturation however, is accompanied by a drastic reduction of the width of the air plume, and therefore by a drop in the zone of influence of a given injection well. When the injection flow rate becomes too large relative to the hydraulic conductivity of the medium, or when the injection pressure is too high, fracturing conditions are reached. Failure planes develop following fracturing, along which preferential flow paths are established, and additional plume growth is minimal.

The progression in air flow patterns described above was observed for flow through samples of the two materials tested, saturated with the two pore fluids considered. The detailed characteristics of the propagation varied slightly depending on the pore fluid used, such as the rate of reduction of plume width with increasing g-level for example, which was lower in the case of glycerol-saturated samples. The end result was the same in both fluids however, at high values of g.

9.3.3.2.Zones of influence

The impact of increasing g-level and consequently of increasing injection gradients on the zone of influence of an air sparging well has been extensively discussed

in previous sections, and will not be described any further. Air propagation occurs as a uniform front, and the zone of influence of the plumes are drastically reduced.

At 1-*g* however, under injection pressure conditions which do not cause fracturing of the soil above the injection point, the characteristics of injection have a significant effect on the resulting volume of soil affected by a given well. Propagation, as discussed, occurs in the form of channels, but depending on whether injection is performed under constant flow rate or constant pressure conditions, the area of influence can change drastically.

Injection under constant pressure conditions will be discussed first. Injection at constant pressure leads to the largest zones of influence for a given injection port. Because the pressure in the air phase is the same at all points until the point at which breakthrough occurs, the initial stages of plume formation are critical to the development of a wide plume. If the injection pressures are maintained within a range that does not cause the formation of a fracture, the injected air initially propagates uniformly in all directions and the injection source effectively changes from a point source to an expanding source. Indeed, if the injection point is sufficiently deep that vertical gradients do not immediately become greater than horizontal gradients, the plume itself becomes the source of pressure during the initial stages. As a result, the plume expands laterally at its base, and establishes flow patterns for the air to flow through before breakthrough occurs. If this basal expansion does not occur at the beginning of plume formation, once the air reaches the phreatic surface flow preferentially occurs in the vertical direction and final lateral expansion is limited. It is therefore beneficial to maintain the injection pressures marginally above the minimum injection pressure such that pressure gradients are as low as possible at the base, to allow for the initial expansion of the pressure bulge. For a given value of the hydraulic conductivity, the widest plumes are obtained for the case of the deepest injection points, where the time during which the pressure bulge expands is the longest.

In the case of constant flow rate injection conditions, given the high dependency of propagation mechanisms on the hydraulic conductivity of the porous medium, the characteristics of the final plume heavily depend on the type of injection. If the injection

flow rate is low relative to the hydraulic conductivity of the material the final plume is very narrow and of very low air saturation. If the volume of air injected is not sufficient to maintain the pressure necessary for propagation in multiple channels, then only a few channels propagate at any given point. The channels are independent, and each one forms as a separate plume, with practically no lateral propagation. If, conversely, the flow rate is too high relative to the value of K, then the volume injected per unit time cannot be accommodated sufficiently fast, and as was shown in earlier sections, fracturing of the medium occurs: flow breaks through a single channel, limiting the final extent of lateral extension.

If however, the flow rate is increased as plume propagation is taking place, the rate of plume advancement is compensated by the rate at which air is being injected. The decrease in the pressure of the air phase as the plume expands is compensated by the rate at which air is being injected, and as a result, lateral propagation takes place. The final plumes are wide, and of sizes equivalent to those obtained under constant injection pressure conditions, as was demonstrated during laboratory experiments.

9.4.IMPLICATIONS TO AIR SPARGING OPERATIONS

This section summarizes the conclusions that have been made throughout this chapter concerning the mechanisms of air propagation through saturated porous media.

1. The extent of expansion of an air sparging plume is primarily controlled by the pressure of the air phase, and therefore by the pressure gradients that result as air propagates through the porous medium. If the pressure is too high fracturing will occur. Conversely, if the pressure is too low, a very narrow plume will develop given that lateral propagation will not have an opportunity to occur relative to vertical propagation. The optimal operation of a system must therefore ensure that the pressure at the injection point as large as possible given soil stability constraints, in order to allow, as much basal expansion of the plume as possible.

2. The second variable that controls the extent of propagation of an air sparging plume is the hydraulic conductivity of the porous medium. In the case of constant rate of flow conditions especially, the amount of expansion is directly related to the relationship between the flow rate and the conductivity. For maximum expansion of a plume, the rate of air injection must be balanced by the rate of advancement of the air front through the soil, and therefore by the rate of flow of pore fluid out of the medium.

3. For constant flow rate of conditions, it is advantageous to maintain, if possible, a pressure higher than the entry pressure of the porous medium such that, independently of the amount of pressure lost in the air phase as the plume expands, the entry pressure conditions are met both in the lateral and horizontal directions. It is clear however, that injecting at very high pressures will cause fracturing of the soil. In cases in which this would be a feasible option, one solution to the fracturing problem would be that of increasing the overburden over the injection point, (*i.e.* dry material contributing to total stress calculations) in order to increase the overall stability of the problem..

4. Capillary pressures for coarse materials are negligible relative to hydrostatic pressures, and flow calculations can be made only considering the advancement of the advective front.

5. Injector geometry does not have a significant impact on the characteristics of an air sparging plume as long as flow is injected uniformly over a significant area of flow.

6. Bubbly flow conditions do not occur as air flows through porous media. Air displacement occurs in the form of channels, and as pressure gradients increase, in the form of a uniform front.

CHAPTER 10

MODELING OF AIR SPARGING

10.1. INTRODUCTION

Having completed the experimental phase of the investigation, the remaining objective of this study was to write a computer model that could be used to predict the size of air sparging plumes. The idea was to develop a tool that would provide, in a simple manner and with a limited number of input parameters, an estimate of the zone affected by the sparging well. This chapter presents the air sparging model that was developed during the course of this research study. The model is based on experimental results and observations. It requires only a minimum number of input parameters, and based solely on a conservation of volume approach, provides an approximation of the area of soil affected by an air sparging well.

This chapter is divided in the following manner: section 10.2 describes the general objectives of the computer model. Section 10.3 provides a description of the principles and of the main assumptions that were used in the development of the model, while section 10.4 describes the main parts of the central algorithm. The complete computer code is included in Appendix F, and the reader is referred to it for detailed reference. Section 10.6 starts with an evaluation of the general performance of the model, which consists of an evaluation of the effects of varying injection pressures, flow rates, location of flow boundaries, and pressure gradients. Results from model simulations are then compared with experimental findings presented in Chapter 8, as well as with results from other currently available models of air sparging.

10.2. OBJECTIVE OF THE MODEL

The motivation for developing a new model for air sparging originated in the difficulty to use models currently available in the literature. As was described in the background chapter, the most widely used models of air sparging (Van Dijke *et al.*, 1995;

McCray and Falta, 1997) are based on saturation-capillary behavior relationships for flow of immiscible fluids through porous media. Both of these models require input parameters that, in a non-intuitive manner, describe the microscopic behavior of the injected air in the pore spaces of the soil, rather its macroscopic behavior. Input parameters such as the Van Genuchten parameters, on which these two models are strongly dependent, are difficult to estimate, can vary widely within a given soil type, and may not be feasible to measure. Therefore, the difficulties using the existing models limits their applicability and their use as indicators of the potential effectiveness of air sparging as a remedial technology for a given site.

The model of air flow through porous media presented in this chapter was developed from the observation that patterns of air flow could be described very simply, in a qualitative manner, by using only two parameters, namely the hydraulic conductivity of the porous medium, K, and the flow rate of the injected air, Q. A computer program was then written to determine, quantitatively, if the model predictions did indeed result in plume shapes that matched experimental results.

The model presented in this chapter was not developed to determine air saturation contours or air pressure contours within the boundaries of an air sparging plume. Given the assumptions made in the development of the model, which will be reviewed in the following two sections, once the model reaches steady-state, the volume of soil contained within the boundaries of the plume is assumed to be completely saturated with air. Results of model simulations therefore provide an estimate of the best case scenario that would.

10.3. PRINCIPLES OF PROPOSED MODEL

The air sparging model was developed based primarily on the premise that air flow through a fully saturated porous medium will only occur after the existing pore fluid has been displaced. The rate of air flow into the soil will consequently depend on the rate of pore fluid out, since pore liquids are more viscous than air. The flow of pore fluid out of the porous medium under an applied hydraulic gradient is controlled by the hydraulic

conductivity K of the medium, and therefore, the rate at which air can invade pore spaces will also be dictated by K.

The model computes the advancement of air through the soil assuming stable flow conditions. This assumption of course was not supported by the results of experiments conducted at 1-g presented in chapter 8, which show that fingering/channeling is the controlling mechanism of flow propagation. The model however, aims at estimating the extent of the zone affected by an air sparging well, which in the best case scenarios (as seen in the experimental results) is a fully air saturated region, in spite of the occurrence of fingering. Furthermore, the model can be used to estimate air propagation characteristics at high g-levels, under which, the assumption of a uniform propagation front is valid.

All calculations are performed before the front of the air plume has reached the water table, and program execution stops once breakthrough has occurred. The injected air is effectively modeled as a large bubble, assuming that all the air present in the system is interconnected. The following assumptions are used in the execution of the model:

1. *Single-phase Darcy's law applies in the x and z-directions and is used for calculations of water flow.* It is reasonable to assume that Darcy's conditions apply during model execution given the velocity of the water flow. In order to ensure the stability of the soil deposit during injection, hydraulic gradients, i, are checked at every time step and are maintained below critical gradient conditions. Within the range of stable gradients, fluid velocities are sufficiently low to maintain laminar flow conditions, and therefore to meet Darcy's criteria.

2. *The distribution of fluid pressures in the liquid phase is assumed to be hydrostatic.* This assumption implies that the water displaced by the injected air dissipates in the surrounding cells, and that no excess pressure results from water flow or from water table mounding. At the same time however, water flow is modeled by imposing a high pressure at the air-water interface.

3. *Air pressures everywhere inside the boundaries of the plume are assumed to be equal.* The model accounts for air compressibility by adjusting the pressure inside the plume according toto the volume of air injected and the volume of the advancing plume.

Flow losses in the air are assumed to be negligible as pressure redistributes inside the plume boundaries, and thus the pressure at every point is assumed to be the same.

4. *Reverse flow conditions in the x and z-directions do not occur at any point during the simulation.* Reverse flow refers to flow in the direction opposite to that of the injected air, in the z-direction, or opposite to that of the lateral spread in the x-direction. Reverse flow would occur for example in cases of insufficient air pressure, in which water would have a tendency to flow back into the element and displace air. These cases are not considered by the model, and flow only takes place in the positive x and z-directions. Given the pressure at which the air is present in the system while being injected this assumption is reasonable, and water will only flow back into the voids after the flow of air has been discontinued.

5. *The soil is assumed to be homogeneous, isotropic, and initially fully saturated with pore fluid.*

The program calculates water flow in two dimensions, along the x and z directions, but calculations are integrated over the depth dimension making the results of the computations axisymmetric. Figure 10-1 shows a schematic of the mesh used in the algorithm to make the flow calculations. The two-dimensional mesh consists of i columns and j rows, where each element has dimensions dx and dz specified as input parameters of the model. Additionally, the angle α, also specified as an input parameter, constitutes the depth dimension over which the 2-D elements are integrated. Elements located on the first column are therefore wedge-shaped, while the reminder of the elements of the mesh are portions of annuli.

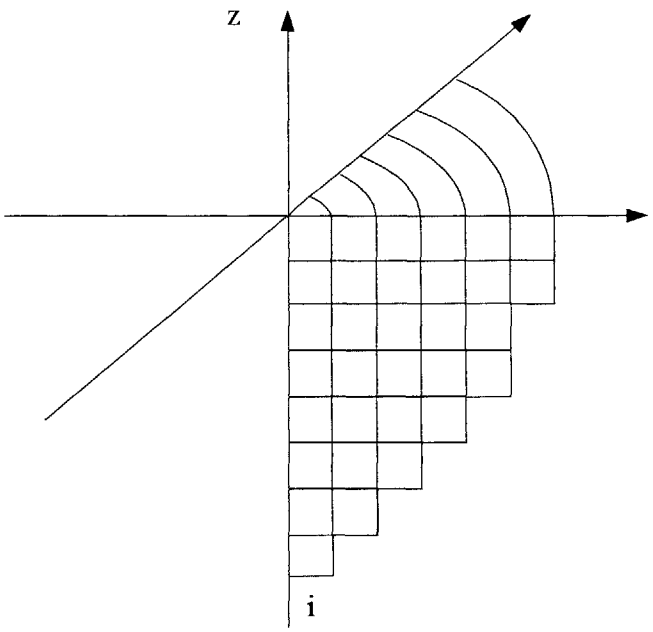

Figure 10-1 Axisymmetric mesh for proposed air sparging model

10.4. PROPOSED AIR SPARGING MODEL

10.4.1. General Equations

A final difference approach was used in the development of the air sparging model. Flow calculations are based on the premise that the flow of pore fluid out of the pore spaces of the medium limits the flow of air through the medium. The limiting parameter is therefore the total volume of water that flows out of the mesh elements during a time step. Given the low viscosity of air and its volume change properties, the flow of air into a given pore is never a limiting factor, and all pore spaces left without water during a time step are invaded by air.

Since the volume of air in the system is conservative, the computer program keeps track of the volume injected in time, of the volume of pore fluid displaced (*i.e.* the volume of the plume) , and consequently, of the pressure in the air phase. Air pressure becomes the driving force for pore fluid outflow. The program computes fluid outputs

for cells at every time step, and flow through the system is modeled with a series of conservation of volume equations.

Every element of the mesh is initially assumed to be fully saturated with water. Calculations of volume of water displaced are performed by independently estimating the volume of water flowing out of a cell in the x and in the z-as illustrated in Figure 10-2. The porosity of the porous medium, θ, is an input parameter for the model and V_T is the total volume of a mesh element. V_{wox} and V_{woz} correspond to the volumes of water out of the cell in the x and z directions, respectively.

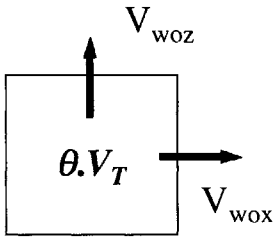

Figure 10-2 Water outflows from mesh element

As shown in the figure, no inputs of water from adjacent cells are computed by the program. It is assumed that once displaced from the pores of an element, excess water dissipates in the surrounding space, and no further account of that water volume is maintained. Equation 10-1 is the simple equation solved iteratively, for every element of the mesh. V_w^{t+1} represents the volume of water in a given element at time $t = t+1$, calculated from the volume of water existing at time t minus the sum of the outputs in the x and z directions:

$$V_w^{t+1} = V_w^t - \left(V_{wox}^t + V_{woz}^t\right) \qquad \text{Equation 10-1}$$

Additionally, conservation of volume imposes constraints in both directions, such that the total flow out of an element does not exceed the initial volume of water in the element. The flow of water in the x and z directions is calculated from Darcy's law according to Equation 10-2, where K is the hydraulic conductivity of the material, $i_{x,z}(z)$ is

the hydraulic gradient in either the x or z directions, which is a function of depth z, A is the cross sectional area of a mesh element, and t is the duration of a time step:

$$V_{wox}^{t} = \min\left(K.i_x(z).A.t, V_w^t \right)$$
$$V_{woz}^{t} = \min\left(K.i_z(z).A.t, V_w^t \right)$$

Equation 10-2

10.4.2. Air Pressure Calculations

The air sparging model developed estimates air plumes under constant flow rate conditions. The pressure in the air phase is therefore an unknown which needs to be determined at the beginning of each time step. Air pressures range between air entry pressure and hydraulic fracturing pressure, and they decrease with expansion of the air plume. This section presents the iterative procedure used to calculate the pressure of the injected air, and illustrates some of the difficulties associated with this calculation. Figure 10-2 shows a schematic of the steps followed in the calculation of the air pressure, P_{air}.

During a time step, a given volume of air is injected into the system, according to the chosen injection flow rate. The pressure of the injected air is calculated using the Ideal Gas Law (IGL), and is a function of the number of moles of air injected and of the volume of pore space available in the plume. This pore volume is in turn a function of the volume of water that has been displaced under the given injection pressure. At the beginning of a time step the pressure of the air is unknown, and therefore the volume of water flow and the resulting volume of available pore spaces are also unknown. The program assumes an initial volume of pore space available, and for the known number of moles injected, the pressure of the air into the assumed volume of pores is determined. This is represented in Figure 10-3 under the label ITERATION #1. This pressure is subsequently used to calculate the volume of water flow in the x and z directions, labeled as q_x and q_z in the central box of the figure. A detailed explanation of flow calculations will be presented in following sections, but once determined, the calculated volume of water is compared to the assumed volume of available pore space, designated as V_{pores}.

ITERATION #1

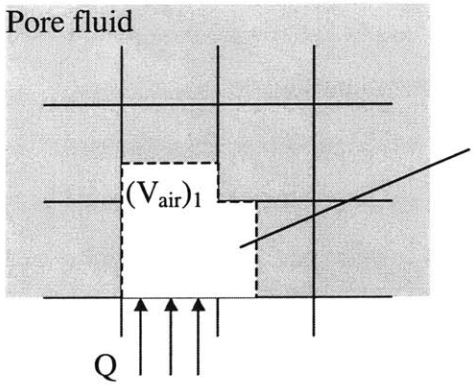

$(V_{air})_1$ = Assumed air volume

n = Moles of air injected
= (Q . Δt)/ Molecular weight of air

$(P_{air})_1$ = (n . R. T)/$(V_{air})_1$
(Ideal Gas Law)

$(P_{air})_1$ → $i_x \Rightarrow (q_{water})_x$ → V_{pores}

$(P_{air})_1$ → $i_z \Rightarrow (q_{water})_z$ → V_{pores}

$$\left| (V_{air})_1 - V_{pores} \right| = \varepsilon$$

IF $\varepsilon \leq 1\%$ THEN
- $(V_{air})_1 = V_{pores}$
- $P_{air} = (P_{air})_1$

IF $\varepsilon > 1\%$ THEN
- Assume $(V_{air})_2$ and $(P_{air})_2$
- Start iteration #2

ITERATION #2

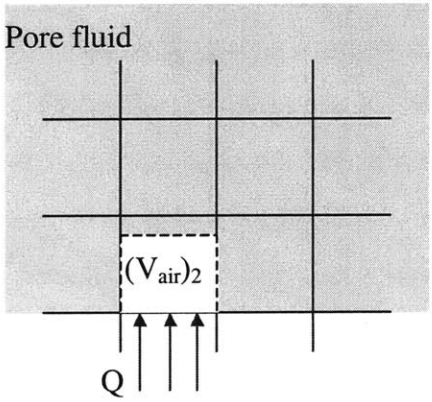

Figure 10-3 Iterative air pressure calculation procedure.

If the difference between assumed and calculated pore space is lower than a constant ε ($\varepsilon < 1\%$), then the estimated air pressure is correct and flow calculations for the following mesh element continue. If, however, the two volumes do not match, the process is repeated by assuming a new volume of available pore air, as is shown under the label ITERATION #2 on Figure 10-3.

The greatest difficulty associated with the iteration procedure results from the use of the Ideal Gas Law (IGL) and the enormous pressures that it estimates at the early stages of the model execution. Indeed, at the beginning of the execution, the volume of available pores is minimal, since all mesh elements are fully saturated with water. In order to begin air propagation, the model assumes that the pore volume of one cell will be filled with air at the onset of air injection. The magnitude of this available volume for air flow varies as a function of the size of the mesh elements, but it will be in the order of pore volumes. In contrast, the number of moles of air injected per second for a typical injection flow rate is large, and when compressed into a volume on the order of a pore space, it leads to enormous pressures. These pressures are easily greater than fracturing pressures and are of course, not realistic but an artifact of the calculation process. In order to "attenuate" the pressures computed by the IGL, constant pressure conditions in the air phase are forced during the initial execution steps.

The principle behind this measure can be explained as follows. In order to maintain a constant pressure while the plume is propagating, the number of moles of air injected per time step needs to be increased. At the beginning of program execution, the rate of plume growth is low, and therefore the number of moles that need to be injected per time step to maintain the pressure is small. On the other hand, under constant flow rate conditions, the number of moles injected is always the same, and therefore at the beginning of propagation, over-pressuring occurs. The program independently calculates the number of moles that would be injected into the system under constant pressure and under constant flow rate conditions. While the rate of increase of the number of moles under constant flow rate conditions is higher than that under constant pressure then the latter type of injection is maintained. When the two types of injection conditions lead to the same number of moles injected per time step, then the program switches to a constant

flow rate injection condition and remains in that mode until the end of program execution.

An additional difficulty introduced with the use of the IGL comes from the fact that pressures are expressed in terms of *absolute pressures*. If the estimated number of available cells at the beginning of the iteration process is too low, the resulting pressures of the air phase will be negative when they are converted into units of gage pressure. The iterative loop may never converge once negative pressures are introduced. In order to avoid this problem, the estimated available volume for air to flow into is assumed to be a fraction of the current volume of air at a given iteration. The variable **guessCells** is the estimated volume of pore space that the air will occupy at the end of the iteration, calculated as 5% of the current volume of air at the given iteration. In other words, as a first estimate, the plume is assumed to grow by 5% every time step.

```
guessCells = airCells + .05 * airCells
pAir = ((molesInj * R * T) / (guessCells * volPores)) - Patm
```

10.4.3. Air and Water Flow

This section describes the procedure used to compute flow of pore fluid and subsequently of air, out of the elements of the mesh. Three volumes of water are computed separately for every element, at every time step, in order to account for all the mechanisms driving flow in the x and z directions. These volumes are ultimately combined when incorporated in the conservation of volume equations, leading to the final estimates of total volume of fluid flow.

Figure 10-4 illustrates the various volumes of pore fluid that are computed for as the air plume propagates. For clarity purposes, the volumes will be first shown and explained in a two-dimensional figure and will be redrawn in the mesh used by the program. Given cell (i, j) *full of air,* pore fluid will be driven out of the surrounding cells due to the following mechanisms:

1. **volZ(i,j+1)** is the volume of pore fluid flowing in the z-direction from cell (i, j+1), driven by the pressure gradient from cell (i, j).

2. **volX(i+1,j)** is the volume of pore fluid flowing in the *x*-direction from cell (i+1, j), driven by the pressure gradient from cell (i, j).

3. The height of air in cell (i, j+1) is multiplied by the width of air in cell (i+1, j) to determine the volume of air that flows into cell (i+1, j+1), which is designated as **volXZ(i+1,j+1)**. This type of flow is two-dimensional, and referred to as *cross flow*.

Two different arrays are defined in directions X, Z, and XZ, to store the volumes of air and water that are being displaced or that exist in a cell at a given time. In the *x*-direction for example, these arrays are designated as **volAirX(i,j)**, **volWaterX(i,j)**, **volAirXZ(i,j)**, and **volWaterXZ(i,j)**. The program first computes the volumes of water that can flow out in both directions under the given pressure gradients. It sets that volume equal to the new volume occupied by air, and subsequently determines the air pressure in the new volume of pores available. This final volume is ultimately compared to that estimated at the beginning of the iteration, and calculations either proceeds if $\varepsilon < 1\%$ or a new iteration starts if the values of ε is greater than 1%.

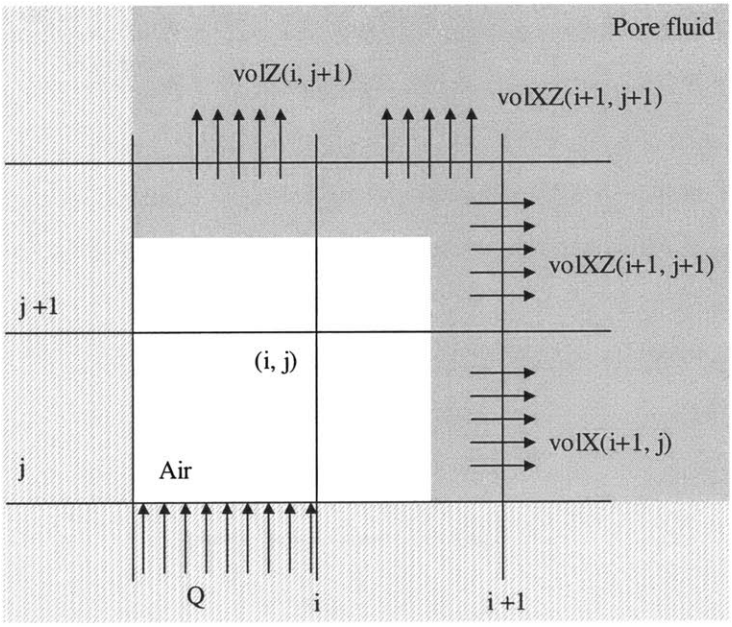

Figure 10-4 Volumes of pore fluid flow calculated for every element of the mesh

A restriction is imposed in the model to the way that flow is modeled, such that computations of **volX(i+1, j)** and **volZ(i, j+1)** are not performed unless element **(i,j)** is full of air. This is necessary to avoid situations in which a very small volume of air flows upward, reaches the phreatic surface, and ends program execution before any significant plume growth has occurred. As a result, not every element of the mesh needs to be evaluated for flow calculations during a given iteration, and computations only involve mesh elements that are full of air and their surrounding elements. At the end of every time step, the mesh is scanned for elements full of air, and all elements which meet the criterion are marked. The array **marker(i,j)** stores values of 1 for mesh elements (i,j) that are involved in flow calculations and values of 0 for all remaining elements.

The actual calculation of the volumes of pore fluid flowing in the various directions proceeds as follows. Please refer to figure 10-5 for illustration purposes.

1. Having assumed a volume of available pores for air flow, the pressure in the air phase, P_{air}, is calculated.
2. The mesh is scanned for cells full of air. Once a cell (i,j) has been identified as contributing to flow calculations (*i.e.* **marker(i,j) = 1**), the positions of air-liquid interfaces in its surrounding cells are located.
3. Values of the entry pressure, P_{entry}, at the various interfaces around (i,j) are calculated, according to Equation 2-1.
4. If the pressure in the air is greater than or equal to P_{entry} then flow calculations proceed. If, conversely, entry pressure conditions are not satisfied, the next marked cell in the mesh is analyzed.
5. Values of head at the various air-liquid interfaces and the resulting hydraulic gradients are determined. Gradients are calculated from the head difference between the air phase and the water phase at a given interface, divided by the distance to the flow boundary. The boundary for flow in the z-direction is the phreatic surface, while the boundary in the x-direction is located at a predetermined distance from the axis of the well. The pressure of the water phase

is set equal to the hydrostatic pressure everywhere in the domain. A discussion on the location of the horizontal flow boundary and its influence on the lateral spread of the air plumes is included in later sections.

6. Darcy's law is then used to calculate the volume of pore fluid flowing in each particular direction per time step under the applied gradients.

7. The time step chosen for execution of the model was constrained by the total amount of water that could flow out of one cell. The maximum volume of liquid per time step flowing from a cell was equal to the total volume of the pores of that cell. If at any point during program execution the volume of flow exceeded that maximum volume, the program would stop and an error message would appear on the screen.

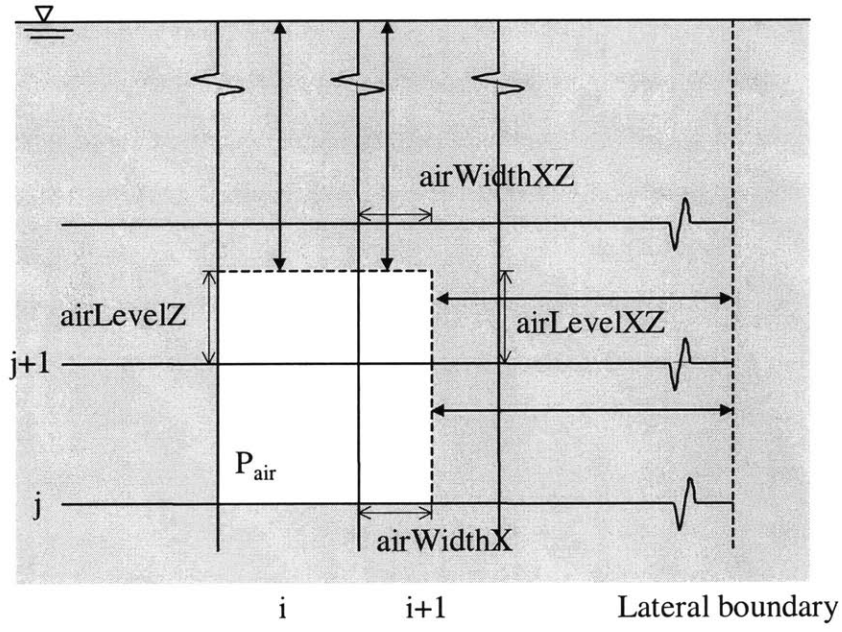

Figure 10-5 Calculation of gradients and volumes of flow

In actuality the mesh is not two dimensional, and given that the geometry of the cells changes from column to column, calculations to determine the width and the height of air in a partially saturated cell are slightly more involved. Figure 10-6 shows an accurate representation of two rows of elements, and the dimensions involved in the

calculation of volumes. The complete equations are not presented in the body of this chapter, but are included in detail in Appendix G.

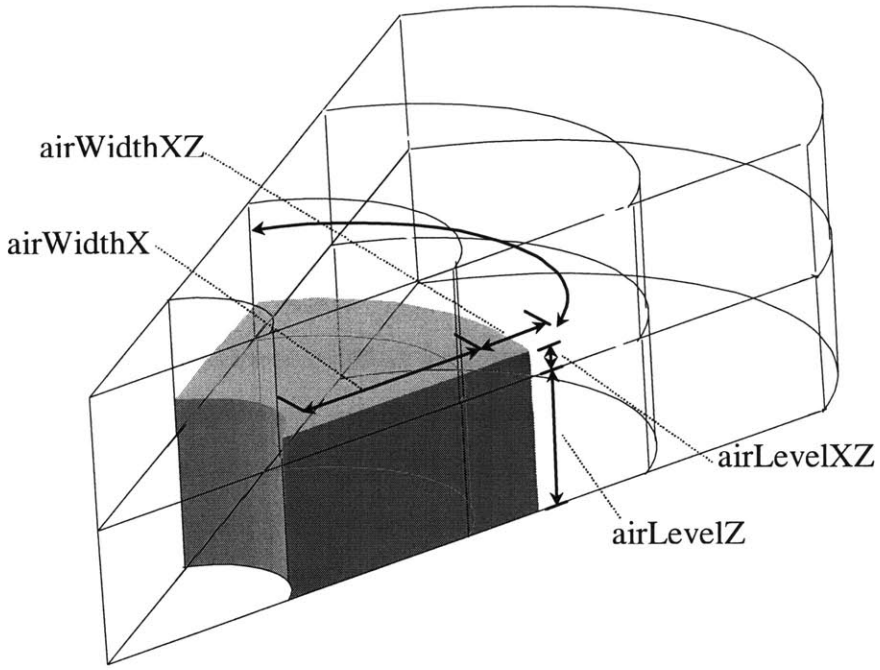

Figure 10-6 Schematic of volumes in axisymmetric mesh

10.4.4. Volume Balance

After computing the various volumes of pore fluid that would be displaced under the given air pressure, pore fluid was replaced by air in the designated cells. Once the volume of pore fluid exiting a given cell was determined, that volume was not accounted for any longer. As discussed above, pore fluid was assumed to dissipate in the system, and only the total volume of air was tracked.

The following portion of computer code was taken from the program, and it illustrates the procedure that was followed to distribute air and pore fluid in a given cell. This particular fragment of code determines the amount of air that flows in the vertical direction, from a cell (i,j) into a cell (i, j+1). If the volume of pore fluid that may flow out of a cell (i, j+1) under the estimated pressure is greater than the volume of pore fluid that is currently in the cell (*i.e.* **`volWater(i,j+1)`**), then all the liquid flows out of the

cell and the total volume of the pores is replaced by air. If on the other hand, **volZ(i,j+1)** is smaller than the volume of pore fluid currently in cell (i, j+1), then the volume of fluid remaining is the difference between the two quantities. The volume of air left in the cell, **volAir(i, j + 1)**, is then computed as the difference between the volume of pores and the volume of liquid remaining in the cell. This procedure is repeated exactly for calculations of flow in the horizontal direction.

```
' Vertical flow
IF volAir(i, j + 1) = volPores(i, j + 1) THEN GOTO 396

     IF volZ(i, j + 1) > volPores(i, j + 1) THEN
        PRINT "Gradient too high -z"
        GOTO 1550
     ELSEIF volZ(i, j + 1) >= volWater(i, j + 1) THEN
        volWater(i, j + 1) = 0
        volAir(i, j + 1) = volPores(i, j + 1)
     ELSE
        volWater(i, j + 1) = volWater(i, j + 1) - volZ(i, j + 1)
        volAir(i, j + 1) = volPores(i, j + 1) - volWater(i, j + 1)

     END IF
```

Calculations of cross flow volumes are different from those of horizontal and vertical volumes. The volume of air flowing into the diagonal cell (i+1, j+1) is computed as the product of the height of air in cell (i, j+1) multiplied by the width of air in cell (i+1, j) IF the volume of pore fluid flowing out of the cell under the given gradients is greater than or equal to that calculated volume of air. In order to avoid counting the same volume of air multiple times, the variable **deltaXZ** is defined as the difference between the air in the cell at step $t - 1$, stored as **tempVolXZ(i + 1, j + 1),** and the volume of air calculated at step t. For cases in which the calculated volume of air is smaller than the total volume of liquid in the cell, the volume ultimately flowing into the cell becomes the difference between the volume of pores and the volume of water left in the cell. The portion of computer code shown below illustrates the procedure used in the calculation of the volume of cross flow.

```
' CROSS FLOW
IF (volAir(i + 1, j) = volPores(i + 1, j) OR volAir(i, j + 1) =
                       volPores(i, j + 1)) THEN GOTO 1280

 IF pAir > Pentry(((j + 1) + actualLevelZ(i, j + 1) / dz) / 2) THEN
```

```
    volXZ(i + 1, j + 1) = porosity * (pi / (2 * angle)) * ((i +
                          actualWidthX(i + 1, j) / dx) ^ 2 - i ^ 2)
                          * dx ^ 2 * actualLevelZ(i, j + 1)

    IF volXZ(i + 1, j + 1) > volPores(i + 1, j + 1) THEN
      PRINT "Gradient too high -XZ"
      GOTO 1550
    ELSE
      deltaXZ = volXZ(i + 1, j + 1) - tempVolXZ(i + 1, j + 1)
      volWater(i + 1, j + 1) = volWater(i + 1, j + 1) - deltaXZ
      volAir(i + 1, j + 1) = volPores(i + 1, j + 1) -
                             volWater(i + 1, j + 1)
      tempVolXZ(i + 1, j + 1) = volXZ(i + 1, j + 1)
    END IF

ELSE
    volXZ(i + 1, j + 1) = volXZ(i + 1, j + 1)
END IF
```

When all the volume calculations have been completed the total volume of air in the system is determined and compared to the initial estimate. If the two volumes match the program advances to the following time step. If the volumes are not the same, a new volume of air is assumed equal to the average between the estimated and the calculated volumes. The volumes of air and pore fluid in every element of the mesh are reset to their initial values at the beginning of the time step, and iterations are repeated until a match between the estimated and calculated volumes of air is obtained.

10.4.5. Initial and Boundary Conditions and Input Parameters

As mentioned previously, given the symmetry of air sparging systems, the program only calculates the advancement of half of the air plume. The origin of the coordinate system is placed at the injection point, at a depth H below the level of the phreatic surface. Figure 10-7 shows a schematic of the layout of the mesh in two dimensions which includes the boundary conditions.

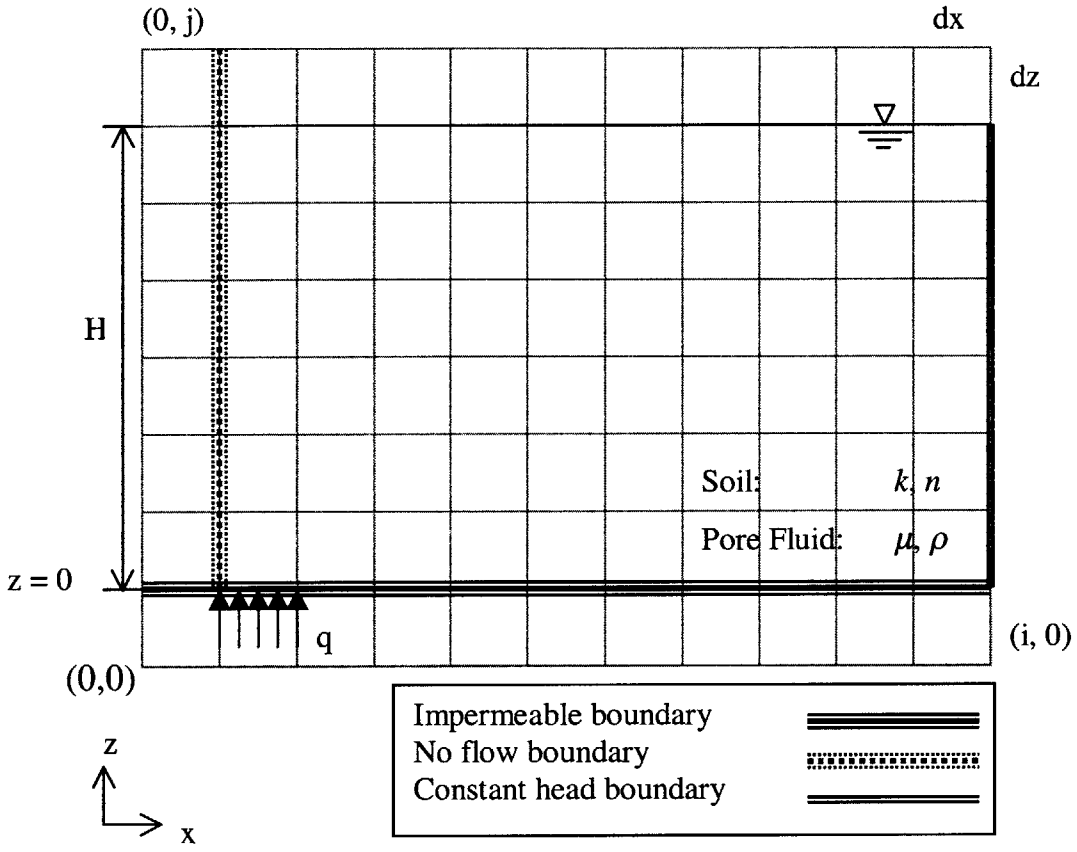

Figure 10-7 Boundary conditions of finite difference model

The first row ($i = 0$) and the first column ($j = 0$) are used to specify boundary conditions, such that the actual porous medium starts at $i = 1$ and $j = 1$. The axis of symmetry of the system ($i = 1$) is defined as a no-flow boundary, and therefore all horizontal inputs to the cells along this boundary are set to zero. Likewise, the line representing the ground level at $j = 1$ is defined as an impermeable boundary, and

therefore vertical inputs V_{iz} to all the cells along this boundary *with the exception* of the injection cell are set to zero.

A number of input parameters need to be specified by the user at the beginning of the program. These input values are summarized in Table 10-1:

Table 10-1 Input parameters for finite difference air sparging model

Modeling Parameters	Porous Medium Parameters	Operational Parameters
• Cell dimensions: dx & dy • Duration of time step: dt • Gravity, g	• Soil properties: D_{10}, porosity, k (intrinsic permeability) • Pore fluid properties: μ, ρ, σ • Air properties: ρ	• Injection flow rate, q • Depth of injection: H • Tolerance

10.4.6. Modeling at High g-Levels

The computer program was written such that simulations of propagation at high g-levels could be conducted. For modeling of flow characteristics under the Earth's gravitational acceleration the factor n is set equal to 1, or it can be adjusted to account for increasing acceleration fields. As was described in Chapter 3, two approaches exist when scaling flow processes at high g-levels: 1) the hydraulic gradient is assumed to remain constant at increasing accelerations, and therefore the scaling of the Darcy velocities is achieved by scaling the hydraulic conductivity of the material; and 2) the hydraulic conductivity of the material is maintained constant and the hydraulic gradients are scaled with g-level. Simulations were conducted using both approaches in order to verify that results from the two methods were consistent.

10.5. RESULTS OF MODELING

This section presents results from a series of computer simulations that were conducted with the following objectives: 1) to test the adequacy of the model in capturing the shape of the air sparging plumes that were observed in the laboratory at all g-levels;

and 2) to make predictions of the size of plumes that would be obtained under varying operational conditions and on porous media of varying hydraulic conductivities.

10.5.1. Model Performance

The following sections provide an overview of the basic performance of the model under varying input parameters.

10.5.1.1. Injection pressure

Model simulations of air sparging start under constant pressure injection conditions. The value of the injection pressure, P_{inj}, is set by default to that of the entry pressure, P_{entry}. It is possible, however, to increase the initial value of the injection pressure, as long as it is maintained below fracturing pressure. The effects of varying injection pressures have been illustrated in Figure 10-8. Results from computer simulations are shown as boundaries, within which the soil is fully air saturated. They were plotted using a contouring program, which interpolated between output air saturation values at every node in the mesh as a way of determining the boundaries of the air plume. In order to avoid problems misreading contour interpolations, it was decided that only those cells that were 100% full of air would be counted as being part of the air sparging plume. As a result, some of the cells located outside the plume boundaries included in the figures are partially full of air, and these are not accounted for in later calculations of plume volume.

Figure 10-8 plots results from four model simulations conducted under *constant pressure conditions*, with P_{inj} ranging from entry pressure to one that is 40% higher. Only half of the plumes are shown in the figure, the other half being symmetrical to the axis of injection located at (0,0). Constant pressure rather than constant flow rate plumes are shown in the figure, in order to independently illustrate the effect of increasing P_{inj} on the size of air sparging plumes, without having to modify injection flow rates. In order to obtain comparable air pressures under constant flow rate conditions, increasingly higher injection flow rates would have been necessary. Instead, air pressure in the plume was set to a constant value, and the resulting effects on plume growth were evaluated.

As shown in Figure 10-8 the effect of increasing injection pressure is that of increasing basal plume propagation, and consequently, the overall size of the final plumes. The reason for the increase in lateral spreading is that with higher air pressures the preference for vertical flow relative to horizontal flow decreases. If P_{inj} is greater than P_{entry} at the injection point, given that vertical and horizontal gradients are comparable at that depth, air flow is equally likely to occur in either direction. The plume initially spreads radially from the injection point, effectively becoming a circular uniform source as opposed to a point source, further promoting plume growth. Depending on the location of the horizontal flow boundary, a certain depth is reached at which point vertical gradients become higher than horizontal, and preferential vertical flow starts to occur. Once this point has been crossed, vertical gradients gradually become more dominant, and lateral plume expansion stops. The smaller the difference P_{inj} - P_{entry} the less horizontal propagation, since the depth at which vertical gradients become more significant than horizontal gradients decreases. This point is treated in more detail in section 10.5.1.3, where the importance of pressure gradients on plume shapes is discussed.

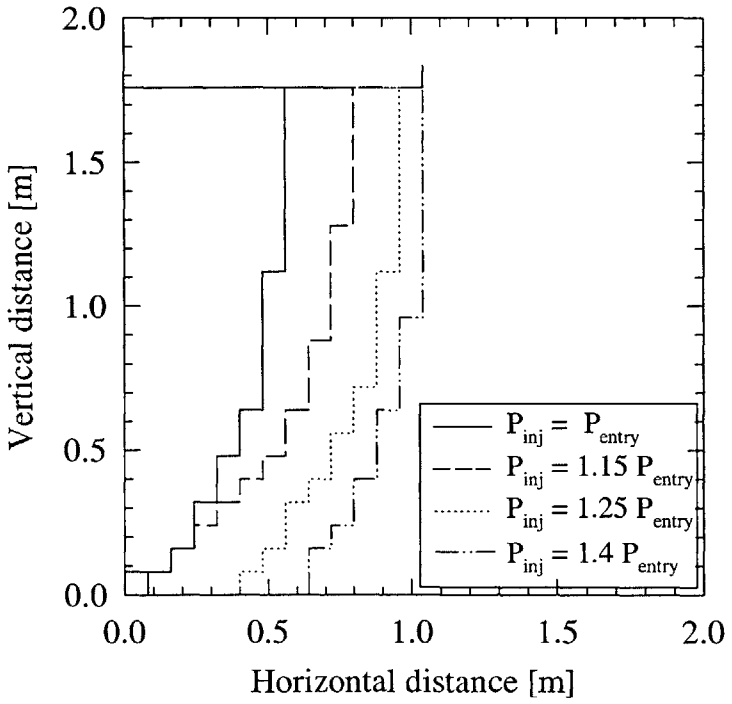

Figure 10-8 Air propagation characteristics predicted under varying initial injection pressures. Plumes were obtained under constant pressure injection conditions.

10.5.1.2. Injection flow rate

The model presented predicts the shape of air sparging plumes resulting from constant flow rate of injection. Figure 10-9 illustrates the effects of increasing the value of q on the shape of the predicted plume. Injection under 1-g conditions, at three increasing values of q was simulated, namely $q_1 = 5x10^{-7}$ m^3/s, $q_2 = 5x10^{-6}$ m^3/s, $q_3 = 5x10^{-5}$ m^3/s. These flow rates are slightly higher than those used during laboratory experiments, which ranged from $2x10^{-7}$ m^3/s to $2.8x10^{-5}$ m^3/s. The permeability of the soil used in the set of simulations was $k = 1x10^{-8}$ m^2, and the pore fluid had the properties of the immersion liquid. This value of the permeability is slightly lower than that of the crushed glass used during the experimental phase of this investigation ($k_{glass} = 1.3\ x10^{-8}$ m^2). Flow boundaries in both the x and z directions were located at a distance of 1 m from the injection point, and the distance from the air-water interface to the x-boundary was allowed to decrease as propagation took place. The influence of the location of radial boundaries on the shape of the predicted plumes will be discussed in the following section.

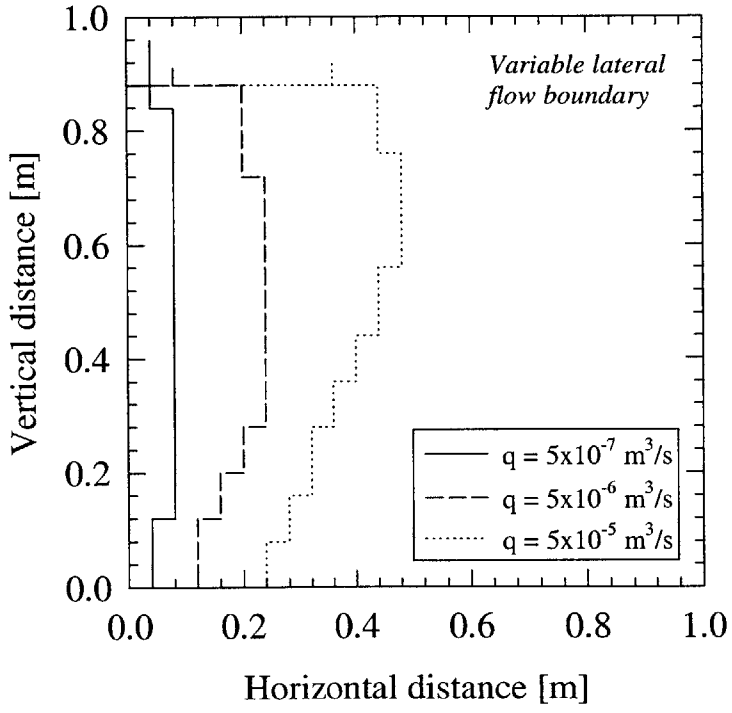

Figure 10-9 Effect of increasing injection flow rate on the predicted shapes of air sparging plumes.

Increasing injection flow rates results in a noticeable increase in the volume of the plumes. A one order of magnitude increase in the flow rate, from q_1 to q_2, resulted in a plume 4.7 times larger, while increasing q_2 to q_3 caused a 2.9-time increase in plume volume. The shape of the plumes changes considerably under the different flow rates. The extent of lateral expansion during injection at q_1 is minimal, and air migrates upward along a very narrow vertical plume. Basal propagation, and consequently lateral plume growth increases with increasing flow rates, and the shape of the plume becomes characteristically conical.

Model predictions of plume growth under increasing flow rates illustrate the mechanisms of air propagation proposed in Chapter 9. Specifically, the fact that lateral spreading of plumes is arrested as air pressure decreases is well captured by the model. In the case of injection at q_3, air pressures reached entry pressures soon after invasion, no significant lateral growth occurred, and propagation takes place primarily in the vertical direction. As injection flow rates increase, the pressures inside the boundaries of the plume remain higher than entry pressure for a longer time of propagation, and as a result, steady-state volumes of the plumes increase significantly.

10.5.1.3. Importance of radial boundary

One parameter that needs careful evaluation the distance from the injection point to the flow boundaries. The location of the vertical flow boundary is straightforward, and is given by the elevation of the phreatic surface. However, accurately setting the location of the horizontal boundary is critical, since it determines, to a large extent, the amount of lateral propagation of the air plumes. The value of the horizontal pressure gradient is calculated using the distance to the flow boundary, so the driving force for the plume in the horizontal direction is inversely proportional to the distance to the boundary.

Only one experimental setup was investigated during this study, and therefore all of the results available were obtained from injection performed at a constant distance to the horizontal boundary, that being the side of the sample box (15 cm from the injection point). Although the elevation of the phreatic surface varied slightly from test to test,

typical distances from the injection point to the vertical boundary, as listed in tables presented in Appendix E, were in the same range as those to the horizontal boundary. In order to maintain consistency between the results of all simulations, horizontal flow boundaries were located at the same distance from the injector as vertical boundaries. Furthermore, the distance from the air-water interface to the horizontal boundary was maintained constant as propagation took place. This measure effectively located the horizontal boundary far away from the injection point, and therefore, horizontal gradients did not increase significantly relative to the vertical gradients. This reduction in the potential for lateral plume spreading was consistent for all depths, and at all g-levels however, allowing to study the parameters governing plume propagation consistently.

Figure 10-10 illustrates the effects of the use of a constant flow boundary in model simulations. This figure plots steady-state plumes obtained under the same conditions as those in Figure 10-9 (*i.e.* q, k and g), but the distance from the air-pore fluid interface to the radial boundary is maintained constant during propagation.

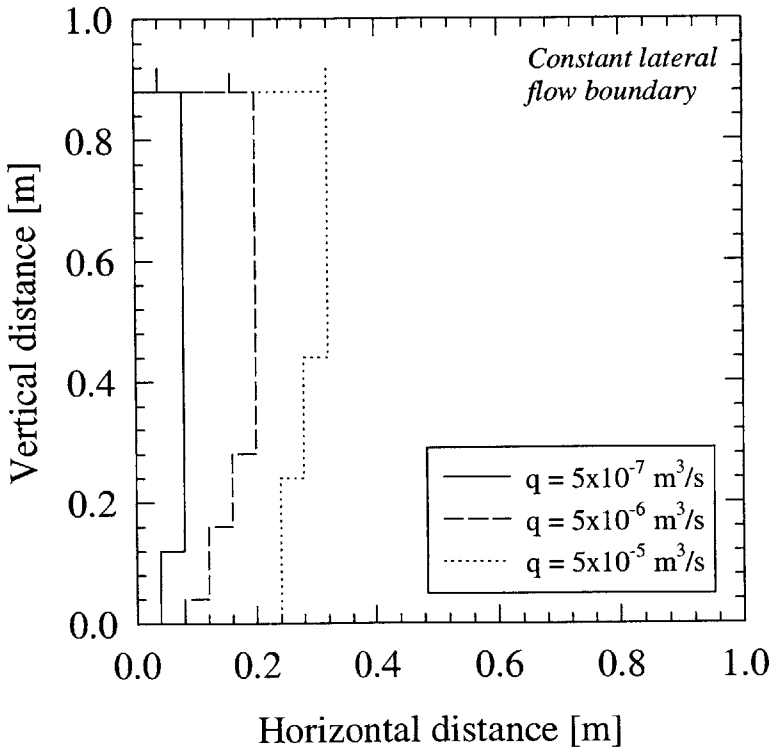

Figure 10-10 Influence of location of horizontal flow boundary on the shape of predicted air sparging plumes

As a result, horizontal gradients remain low in spite of the increase in injection flow rate, since air pressures are still decreasing as the plume advances vertically. Reductions in plume growth take place for injections at q_2 and q_3, but the location of the flow boundary has no effect in the propagation characteristics at the lowest flow rate. The value of q_1 is so low that air pressures drop below entry pressures immediately after invasion occurs, and only vertical propagation is possible, regardless of the location of the radial boundary.

10.5.1.4. Importance of pressure gradient

Figure 10-11 is a plot showing the evolution of the air pressure as a function of depth. The depth of the leading edge of the plume is plotted at1-*g*, 10-*g*, and 20-*g*. The figure also includes, for reference, the value of the hydrostatic pressure profile with depth.

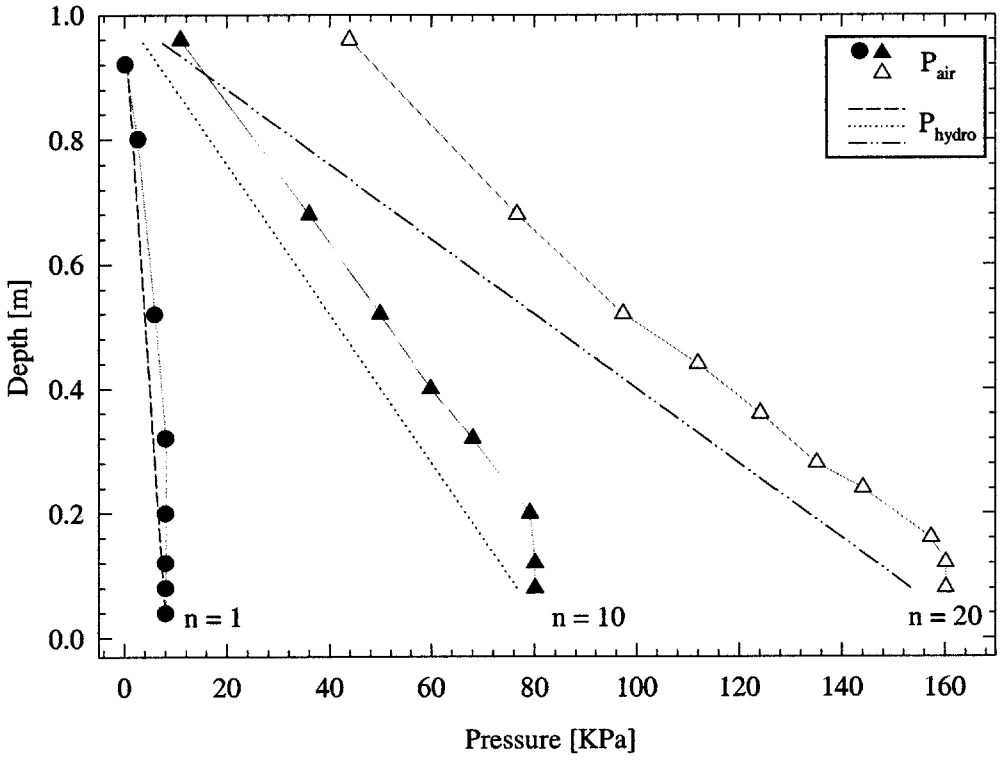

Figure 10-11 Air and pore fluid pressure profile with elevation, under 1-g, 10-g and 20-g accelerations. Simulations conducted under constant flow rate of injection, with q = 5x10^{-6} m^3/s and k = 1x10^{-8} m^2. Elevation of the air phase refers to the position of the leading edge of the plume as air advances upward.

Zero depth represents the injection point, while a depth of 1.0 m represents the phreatic surface. All simulations were conducted under constant flow conditions, *with* $q = 5\ cm^3/s$.

Figure 10-11 shows that during the initial steps of plume propagation the pressure in the air is maintained constant, as indicated by a vertical air profile. Constant flow rate conditions are invoked when the rate of increase of the number of moles that would be injected under constant flow rate conditions is lower than that under constant pressure conditions. Since the number of moles being injected per unit time becomes constant and plume volume continues to increase, the pressure in the air starts to decrease. Under constant flow rate injection air pressures track the profile of the pore fluid pressure, which further justifies the mechanism of air propagation observed at high *g*-levels. Indeed, lateral and vertical plume propagation occur concurrently as long as the pressure in the air is higher than pore entry pressure. Because fluid pressures in the vertical direction decrease as the plume propagates upward *and* remain constant in the horizontal direction as the plumes spread laterally, the difference between air pressure and fluid pressure is greater in the vertical than in the horizontal direction. Once constant flow rate injection takes effect and air pressure in the plume begins to drop, assuming that the distance to the flow boundary is equal in both directions, vertical gradients become higher than horizontal gradients. Vertical propagation thus gradually becomes more significant than lateral propagation as air pressures decreases, until horizontal spreading effectively stops. The extent of lateral propagation of the plume is therefore dependent the distance the plume is allowed to advance before pressures begin to drop and horizontal growth is arrested.

Referring to Figure 10-11, the distance that the plume advances under constant pressure conditions is greater at low *g*-levels. In fact, as acceleration increases, hydrostatic pressures become higher, and the number of moles that needs to be injected per unit time to maintain a constant injection pressure, which is at least equal to air entry pressure, also increases. The rate-limiting condition that switches from constant pressure to constant flow rate conditions is invoked earlier during program execution, and therefore the plume advances a smaller distance under constant pressure conditions. Because air pressures in the plume start decreasing when the air water interface is closer

to the injector, lateral plume growth at high g-levels stops further away from the phreatic surface. As a result, air sparging plumes become gradually narrower with increasing g-level.

10.5.2. Comparison With Experimental Results

During the experimental phase of this study, air sparging plumes were generated under constant flow rate conditions which spanned three orders of magnitude, ranging from very low rates of 0.26 cm^3/s to intermediate rates of 28 cm^3/s. The adequacy of the proposed model at predicting the shape and the size of air sparging plumes was determined using results from these experiments. Input parameters were the properties of the SP material used in experiments, and the properties of the immersion liquid. The acceleration level was set to 1-g.

Figures 10-12 a), b) and c) show comparisons between experimental results and model simulations for the three values of the flow rate considered. Experimental results for the three multiple port injectors are included in the figures, represented by full symbols. As shown in Figure 10-12, agreement between experimental and modeled plumes is very good. The essential shape of the air sparging plumes is well captured by the program, particularly the fact that the plumes are not parabolic. It is interesting to see that the proposed model captures very well the near vertical propagation of the air after the distance to the phreatic surface decreases below approximately half of the total depth. This feature was clearly observed during the experimental part of this study.

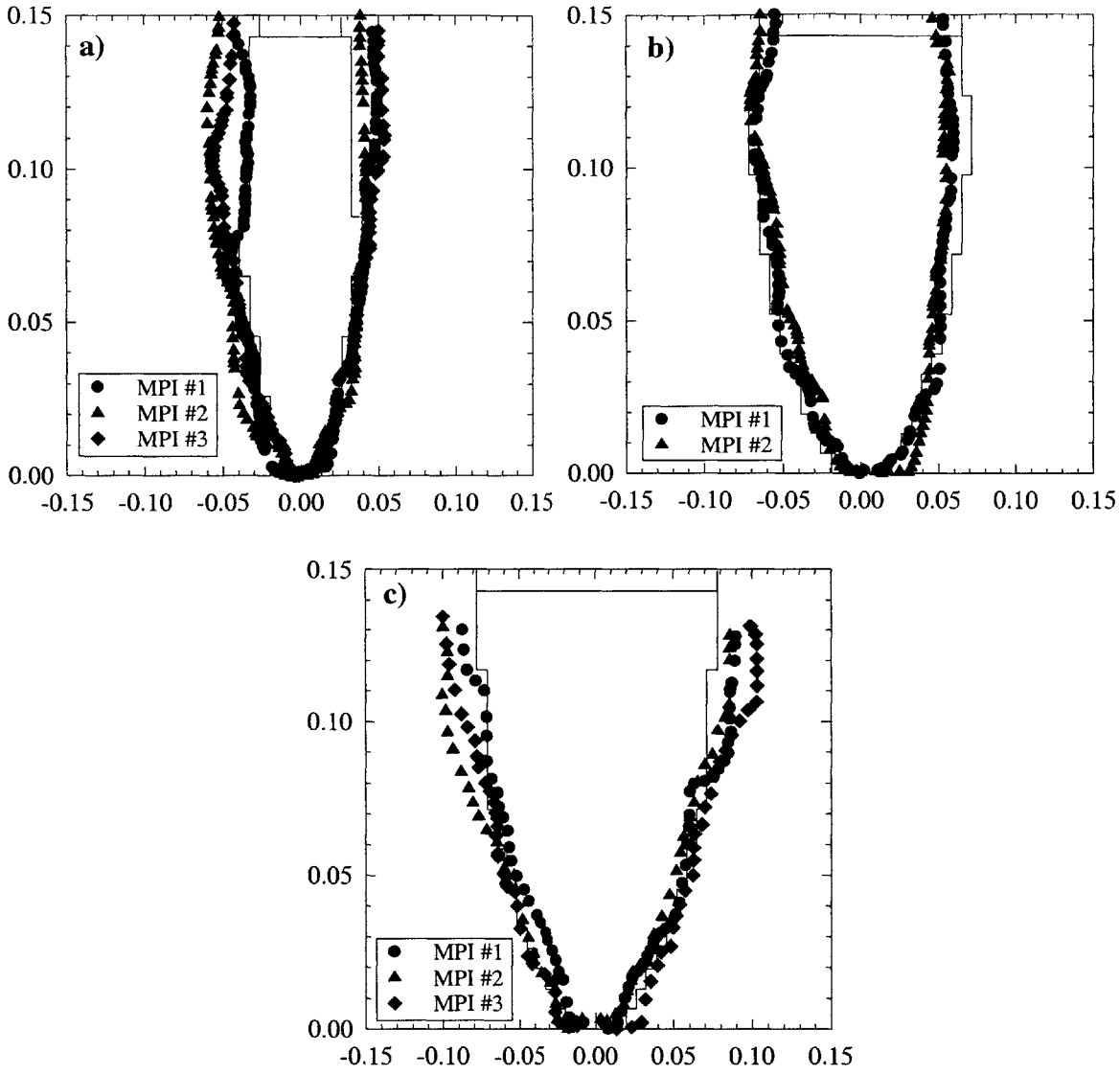

Figure 10-12 Experimental and modeling results of air sparging experiments conducted under constant flow rate of injection conditions at 1-g: a) q = 0.26 cm^3/s; b) q = 2.7 cm^3/s; c) 28 cm^3/s.

Results from model simulations under high accelerations were also compared to experimental observations. Simulations were conducted in which the scaling that had been performed during laboratory experiments was reproduced, exactly. In other words, only gravity, and consequently hydrostatic and entry pressures, were multiplied by the factor *n*. The dimensions of the sample box were entered as boundary input parameters, and the properties of the SP material and those of the immersion liquid were used to characterize the saturated porous medium. Figure 10-13 presents experimental and

modeling results from tests conducted at 1-*g*, 9-*g*, and 30-*g*, under a constant flow rate of injection of 0.66 cm^3/s

The behavior observed during laboratory experiments under increasing accelerations is well captured by results from the simulations, namely the sharp reduction of the zone of influence of the plume. The nearly vertical propagation of the air plume is a consequence of the relative magnitude of the horizontal and vertical gradients, which becomes accentuated at high *g*-levels.

As acceleration increases, as is shown on Figure 10-13 c), the program slightly underestimates the size of the resulting plume. If simulations are conducted at *g*-levels higher than 30-*g*, the modeled plume ultimately becomes a vertical line extending from the injector to the phreatic surface. It is clear that such narrow plumes were never observed in the laboratory, and that there was a minimum zone of influence associated with the diameter of the injectors that was independent of *g*-level. The existence of this minimum plume was noticeable on the pictures presented in Chapter 8, and is due to the fact that the injector has a physical size. During the initial stages of injection, air is injected around the surface area of the injector. As the *g*-level increases, the cross sectional area of the plumes never expands past this initial injection value, which becomes the minimum width of the plume. Limitations concerning the size of the mesh elements of the model however did not allow to accurately reproduce the dimensions of the injectors used in the experiments. Injection points were modeled as one cell, and therefore, at high *g*-levels, the width of the plume converges to one cell.

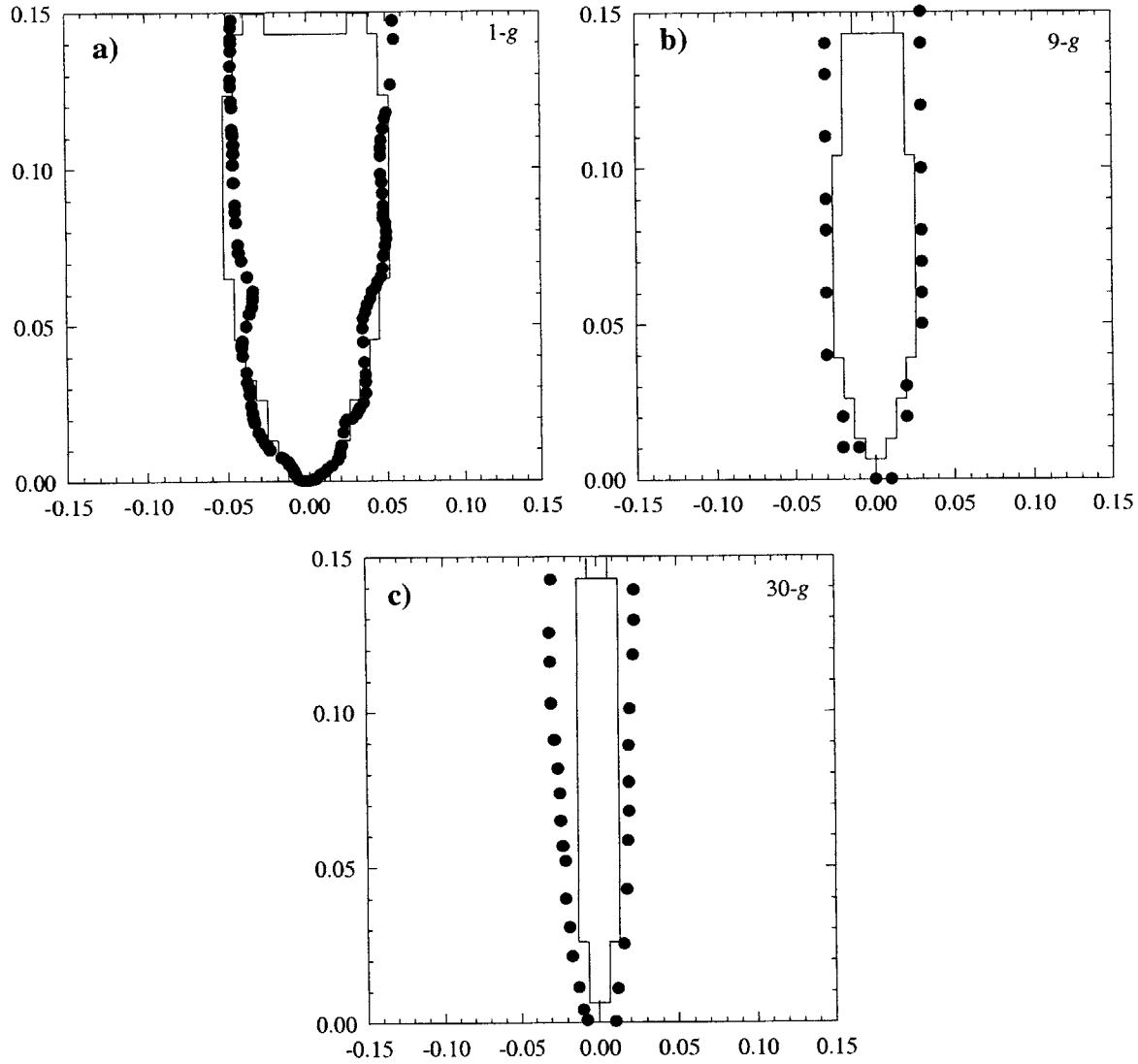

Figure 10-13 Experimental and modeling results of air sparging experiments conducted under constant flow rate of injection conditions at varying g-levels: a) 1-g; b) 9-g; c) 30-g. Injection flow rate was maintained at a value of q = 0.66 cm³/s. Symbols show the outline of the experimental plumes while the solid lines plot the boundary of the modeled plumes.

The model was subsequently used to predict experimental observations shown in Figure 9-6, which described the relationship between the relative zone of influence and the ratio *Bo/Ca*. Simulations were conducted to reproduce results from constant flow rate injection tests. Most of the data included in Figure 9-6 has been re-plotted in Figures 10-

14 a) and b), along with model predictions. Two major changes have been introduced to the data presented. The first one concerns the manner in which the ratio *Bo/Ca* was calculated. Figure 10-14 a) presents values which were computed using air *observed* air propagation velocities (*i.e.* those presented in Figure 8-23). The values of *Bo/Ca* presented in Figure 10-14 b) on the other hand, are based *theoretical* velocities. These velocities were estimated from Darcy's law, using injection pressures measured during experiments. The reason for presenting two sets of data is that observed velocities were up to five times smaller than theoretical velocities, especially those measured at high *g*-levels, when pressure gradients were large. Given that the model is based on Darcy's law, the fit between predicted and observed values is not good as *g*-levels increase, as shown in Figure 10-14 a). Experimental values of *Bo/Ca* are up to one order of magnitude higher than their corresponding predictions, since the observed velocities used in the calculation of *Ca* were significantly lower. Two reasons are proposed to account for the differences in velocities. First, the frame speed of the camera used in recording experimental data was too low, and therefore the time resolution was not sufficient to capture the actual velocity of the air front. The second reason for the discrepancy is that as *g*-levels flow conditions cease to be laminar, and therefore Darcy's law is no longer valid to predict velocities through porous media. An evaluation of the Reynolds number calculated based on theoretical velocity values for all the experiments conducted (presented in Appendix E) supports this explanation.

The second difference between data presented in Figure 10-14 and that included in Figure 9-6 concerns the group of *RZI* of plumes obtained at flow rates ranging from 0.28 cm^3/s to 2.6 cm^3/s. Propagation of these plumes continued after breakthrough, resulting in steady state *RZI* values that were higher than those predicted by the model. However, the model is based on the assumption that breakthrough and steady state plumes are equivalent, and therefore propagation after the air front has reached the phreatic surface is not considered. The *RZI* of the group of plumes in question was therefore re-calculated, *at breakthrough*, and these are the values included in Figure 10-14. *RZI*s at breakthrough are approximately half the size of those at steady-state.

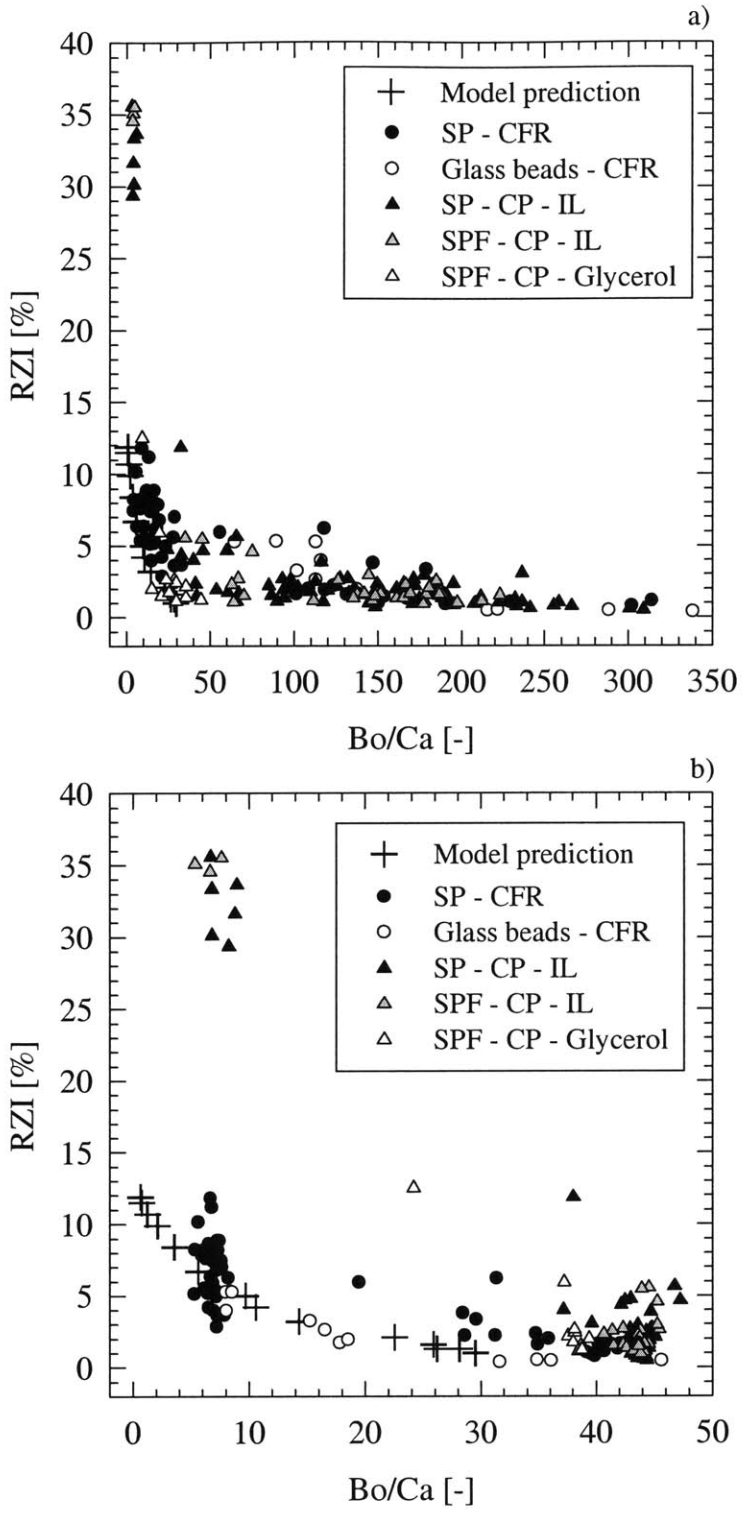

Figure 10-14 Relative zone of influence of air sparging plumes at breakthrough as function of ratio of Bond over Capillary numbers: a) observed air flow velocities; and b) estimated (theoretical) air flow velocities.

Having taken of all these considerations into account, model predictions presented in Figure 10-14 b) can be compared to experimental results. Model simulations give a lower bound estimate of the experimental data, particularly at increasing *g*-levels. The extent of lateral propagation predicted by the model reduces to practically zero as g-levels increase given the current way of defining the injection point. It is therefore reasonable to expect that the predicted plumes will gradually become smaller than those observed in the laboratory.

At the low range of *g*-levels, model predictions give an adequate estimate of the size of the plumes obtained, *at breakthrough*, under constant flow rate conditions, although it is clear that a different mode of propagation is taking place. It has been postulated that these experimental data points reflect the effect of capillarity, and since this mechanism is not accounted for in the model, predicted plumes will not be totally accurate.

It is interesting to see that *RZI*s of experimental plumes obtained at low g-levels under constant pressure injection conditions are not at all predicted by the model. Although no measurements of injection flow rates are available for these experiments, in order to maintain constant pressure conditions, these tests must have been conducted at very high flow rates relative to those plotted on the predicted curve. The model would predict fracturing conditions at under such range of flow rates. It is therefore possible that the data corresponding to constant pressure tests is showing the occurrence of soil fracturing during air injection. No fracture planes (*i.e.* preferential flow pathways) were observed during the experiments, but localized failures may have taken place. This type of failure may have effectively widened the area available for flow, not causing a complete failure of the sample but instead resulting in the spreading of the air sparging plume. This proposed partial failure mechanism was not observed at increasing *g*-levels, where the shape of experimental constant pressure plumes is predicted by the model.

10.5.3. Comparisons with van Dijke *et al.* (1995) Model

Results obtained from the model presented by van Dijke *et al.* (1995) will be compared to predictions from the air sparging model developed in this study. The model was described in detail in Chapter 2, and the input parameters needed for its use, namely van Genuchten's α and m, were derived based on Jonasson (1991) method.

Figure 10-15 shows a comparison between experimental results obtained at a flow rate q of $28\ cm^3/s$ and predictions from the van Dijke *et al.* (1995) model. Results included in the figure were obtained from simulations conducted using the following input parameters: $q = 2.8x10^{-5}\ m^3/s$ (28 cm^3/s), pore fluid properties of the immersion liquid, namely $\rho = 850\ kg/m^3$, $\mu = 0.01785\ Pa.s$, and the material properties of the crushed glass $k = 1.3x10^{-8}\ m^2$, $\alpha = 3.56\ m^{-1}$, and $m = 0.79$. van Genuchten parameters for the crushed glass were derived based on Jonasson (1991) method.

It is evident from Figure 10-15 that the Jonasson (1991) method, which would be typically used if only a grain-size distribution of the material was available, does not lead to an accurate set of van Genuchten parameters. The plumes predicted by the van Dijke *et al.* model using these parameters greatly overestimate experimental results. The predicted parabola is very wide, and completely misses all of the features of the experimental plume, at every depth. The method proposed by Jonasson (1991) should therefore be used with great care if it is the only source of characteristic properties of a porous medium.

If a moisture characteristic curve of the material in which air sparging is to be conducted is not available, input parameters for the van Dijke *et al.* model need to be obtained from published data. The greatest difficulty in using this approach however, is that the governing equations are extremely dependent on the values of α and m, and that therefore the number of parameter combinations that fit a given set of data may be large. Since these parameters are not intuitively descriptive of soil behavior, and furthermore are not necessarily related to hydraulic conductivity, predictions of the zone of influence of a well may be very inadequate.

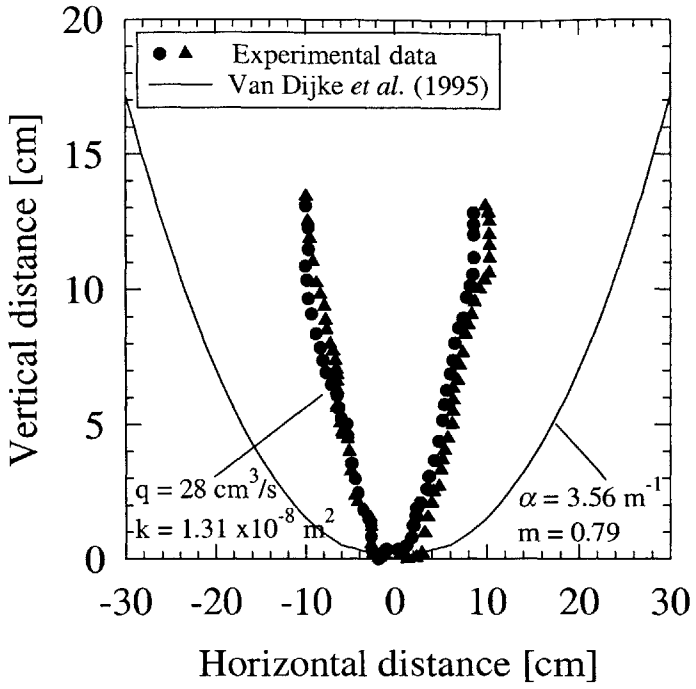

Figure 10-15 Illustration of inadequacy of Jonasson (1991) method to determine van Genuchten parameters from grain-size distribution curve.

To illustrate this point, the van Dijke *et al.* (1995) model was calibrated using experimental results, as shown in Figure 10-16. The outlines of experimental plumes obtained in the laboratory under constant flow rate of injection conditions, at $q = 28$ cm^3/s, are shown as solid symbols. Also included in the figure, are the predictions of the van Dijke model, fitted to two different set of parameters α and m. Values of $m = 0.41$ and $\alpha = 3.0\ m^{-1}$ were obtained by trial and error, by matching model predictions to the experimental outlines. Also shown in the figure with a dotted line are the outlines predicted using a set of van Genuchten parameters found in the literature, for medium uniform sand, of values $\alpha = 5\ m^{-1}$ and $m = 0.45$ (Cheng, 1998).

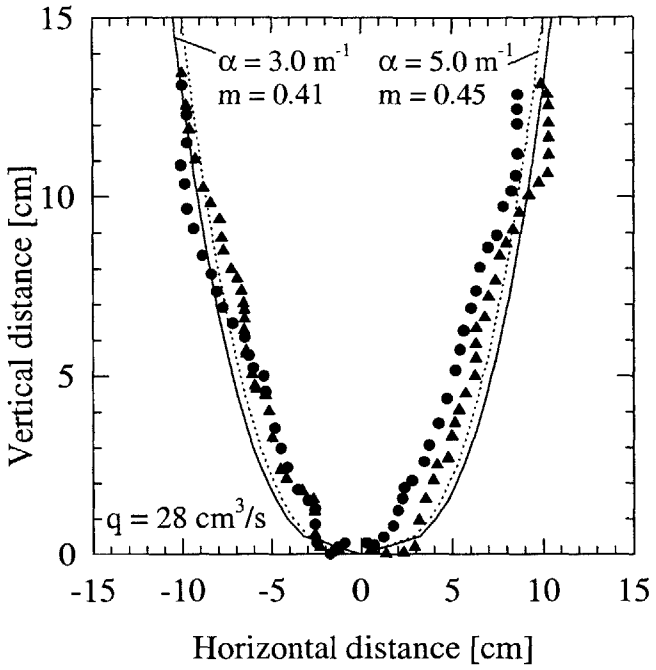

Figure 10-16 Fitting of van Dijke et al. (1995) model to experimental air sparging plumes at q = 28 cm3/s.

It is clear from Figure 10-16, that sets of van Genuchten parameters exist with which accurate predictions of air sparging plumes can be made. Obtaining characteristic soil parameters without prior knowledge of the shape of the plumes however, may be difficult. This is particularly evident when comparing the two predicted plumes presented in Figure 10-16, which are almost identical to each other, in spite of a significant difference in the value of the van Genuchten parameter α. Predictions from the van Dijke *et al.* model are extremely dependent on the value of *m,* but not so sensitive to that of α. Increasing or decreasing the value of α can thus be done to correct for the high sensitivity of the model to *m,* and adequate predictions result. One of the major problems associated with such a fitting procedure is thus that a range of combinations of input parameters exits which will fit calibration data, but do not account for soil behavior characteristics.

However, while differences in input parameters may partly explain the discrepancy in predictions between the model developed during this investigation and the

van *Dijke et al.* model, they are not the fundamental distinction, and will therefore not account for the most significant distinctions between the results. Two major conceptual differences are included in the model developed during this study, the first of which is the fact that capillary pressure-saturation relationships are not used to predict pressure distributions within the boundaries of the plume. Predictions of air propagation are controlled solely by hydraulic considerations, and more specifically by the rate of pore fluid flow through the medium under the applied air pressure gradients. Hydraulic conductivity, an intrinsic soil property, becomes the only medium parameter that dictates the advancement of the air front.

The second major difference between this model and the van Dijke *et al.* model lies in the fact that the latter does not consider the effects of gas compressibility. Volume changes that occur as the plume propagates through the soil and the resulting pressure variations are critical to the final shape of air sparging plumes. The extent of lateral propagation in particular, strongly depends on the pressure inside the plume relative to the pore fluid pressure. An accurate prediction of the evolution of air pressures as the volume of the plume expands is therefore necessary in determining its final shape.

10.5.4. Modeling of Models

Given that, in the model, scaling of the length dimension was no longer a limitation, the applicability of the principle of modeling of models to the study of air sparging was investigated. By using the model it was possible to decrease all the dimensions involved in the propagation of air through porous media in order to account for increasing values of the acceleration field.

This section presents results of simulations which were conducted at four different accelerations, namely 1-g, 5-g, 10-g and 20-g. When conducting computer simulations of modeling of models, the scaling of the gravity term, of the length dimensions, and of the hydraulic conductivity/hydraulic gradient was straightforward. The scaling of the injection flow rate however, had to be investigated. As the linear dimensions of the model are decreased by n, the volume of pore space available for flow as the pore fluid is displaced is decreased by n^3. It is clear therefore, that unless the

volume of air injected per unit time is also scaled, the resulting pressure in the air phase during the initial stages of propagation would drastically increase, to account for the disparity between the volume of air in and the volume of pore fluid out. The discussion presented in Chapter 9 showed that the pressure in the air phase is the parameter governing the extent of propagation of the air prior to breakthrough. Thus, the scaling law for the injection flow rate was derived based on the premise that in order to obtain equivalent plumes at varying g-levels, the pressures in the plumes had to be the same. Given the decrease in volume of the plumes at increasing g-level, the injection flow rate needs to be scaled by a factor of $1/n$. Table 10-2 summarizes the scaling laws were used by the program at increasing g-levels:

Table 10-2 Scaling laws used in modeling of models

Prototype	**Model**
Acceleration, g	$n.g$
Macroscopic lengths, L	L/n
Hydraulic conductivity, K	$K.n$
Injection flow rate, q	q/n

As shown in Table 10-2 results presented in this section were obtained by scaling the hydraulic conductivity and by maintaining a constant hydraulic gradient at increasing g-levels. Equivalent results would have been obtained by maintaining a constant value of the hydraulic conductivity while scaling the hydraulic gradient.

Figure 10-17 shows breakthrough plumes at the four g-levels indicated, for an injection flow rate, at 1-g, of $q = 1x10^{-6}\ m^3/s$ and an intrinsic permeability $k = 1x10^{-9}\ m^2$. The properties of the pore fluid used in the computations correspond to those of immersion liquid, and therefore at 1-g, the corresponding value of the hydraulic conductivity is $K = 0.12\ cm/s$. Figure 10-17 a) corresponds to simulations for the prototype (1-g) of dimensions 1 m by 1 m. All relevant information concerning the input parameters and the results of the simulations is included in Table 10-3, where it has been highlighted for clarity. Note that Figures 10-17 b), c), and d) show the breakthrough plumes *at the model scale*, and therefore the dimensions of these plumes decrease as a function of g-level.

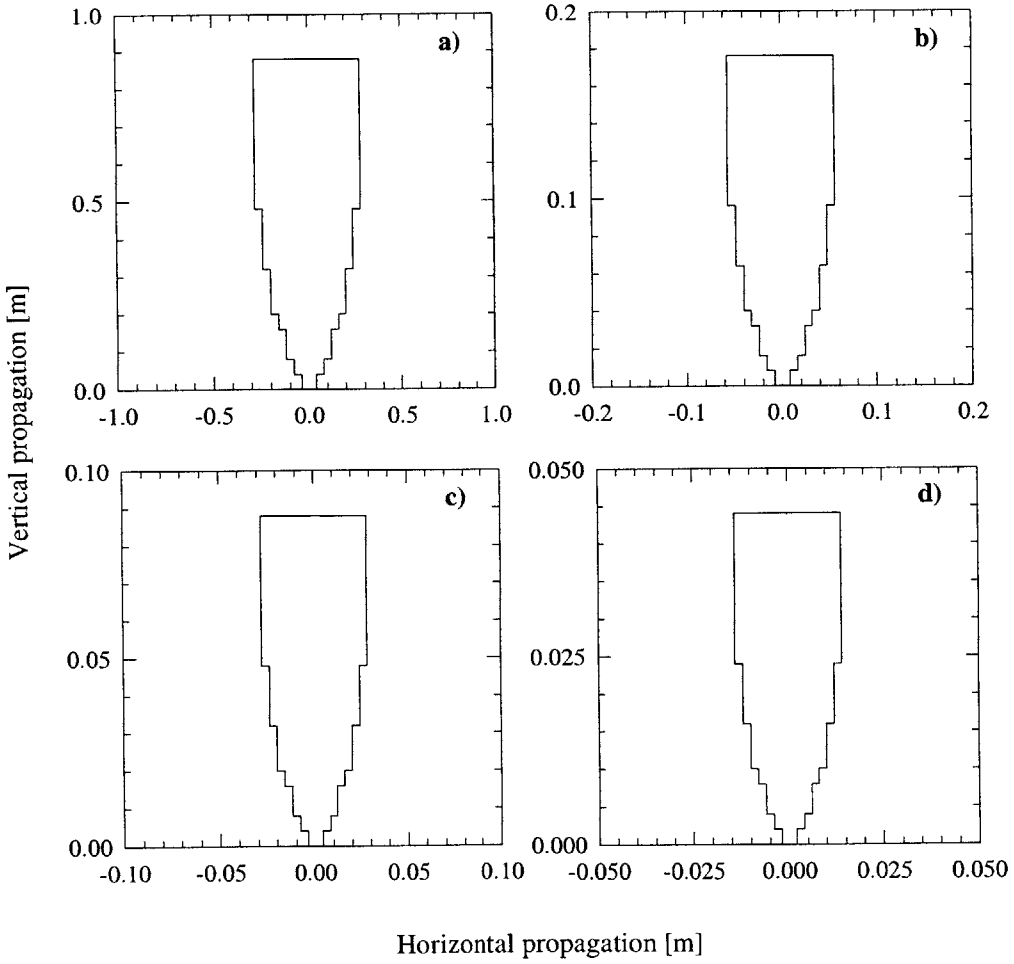

Figure 10-17 Model simulations of air sparging plumes at: a) 1-g (prototype); b) 5-g; c) 10-g; and d) 20-g. The injection point is located at (0,0).

The purpose of showing the plumes at different scales and not converted to prototype dimensions was that of demonstrating that the breakthrough shape of the plumes is the same at all *g*-levels. Comparison of the plots shown in the figure suggests that propagation characteristics are independent of *g*-level, when all dimensions are being scaled, since the relative extent of the lateral spread is the same for all the plumes. The total volume of the plumes clearly decreases with increasing *g*-level due to scaling, but their aspect ratio is constant. If the pressure in the air phase is maintained constant at varying *g*-levels, in accordance with the principles of similitude outlined in Chapter 3, the propagation characteristics of air injected into saturated porous media are the same at all *g*-levels.

Table 10-3 *Summary of input and output parameters from modeling of models simulations. Parameters corresponding to data presented in Figure 10-17 are highlighted.*

n	q [m^3/s]	k [m^2]	dx, dz [m]	Total height [m]	t_{actual} [s]	$t_{expected} = t_{actual}/n^2$ [s]	Total volume [m^3]
1	1.00E-05	1.00E-09	0.04	1	633.34	633.34	1.02E-01
5	2.00E-06	1.00E-09	0.008	0.2	25.33	25.33	8.09E-04
10	1.00E-06	1.00E-09	0.004	0.1	6.33	6.33	1.02E-04
20	5.00E-07	1.00E-09	0.002	0.05	1.58	1.58	1.26E-05
1	1.00E-06	1.00E-09	0.04	1	739.06	739.06	7.02E-02
5	2.00E-07	1.00E-09	0.008	0.2	29.51	29.56	5.57E-04
10	1.00E-07	1.00E-09	0.004	0.1	7.33	7.39	6.84E-05
20	5.00E-08	1.00E-09	0.002	0.05	1.84	1.85	8.62E-06
1	1.00E-07	1.00E-09	0.04	1	1140.60	1140.60	2.27E-02
5	2.00E-08	1.00E-09	0.008	0.2	45.44	45.62	1.81E-04
10	1.00E-08	1.00E-09	0.004	0.1	11.35	11.41	2.26E-05
20	5.00E-09	1.00E-09	0.002	0.05	2.90	2.85	2.91E-06

Table 10-3 summarizes the scaling results for three sets of modeling of models simulations, where expected scaled values can be compared to the actual results provided by the program. Comparison between values of expected and actual time show the perfect agreement between the model results those predicted with the scaling laws. The case presented in Figure 10-17 will be used as an illustrative example. At 1-*g*, the time for the air front to reach the phreatic surface for values of the flow rate and the permeability of $q = 1x10^{-6}\ m^3/s$ and $k = 1x10^{-9}\ m^2$, respectively, was $t_{break} = 633.34\ s$. At 10-*g*, the expected time for breakthrough of the plume is $(t_{break})_{prototype}/n^2 = 633.34/10^2 = 6.33\ s$, which corresponds exactly with the time calculated by the model. Results of computer simulations therefore suggest that the technique of modeling of models can in fact be used to accurately reproduce the propagation of air through saturated soil deposits during in situ air sparging. Given that the mechanism governing air propagation is pressure driven, the familiar laws of similitude apply to air sparging, and centrifuge modeling can be effective used, at all scales, to model the process.

Analysis of results from modeling of models simulations suggested that the ratio of the injection flow rate to the permeability of the material, q/k, was a parameter that could be used to predict the extent of propagation of a given plume. Indeed, model results showed that the shape of two air sparging plumes propagating at the same *g*-level was identical if the ratio q/k is the same. A much lower injection flow rate is necessary, when injecting into a medium of low permeability, in order to obtain a plume of equivalent shape as that which forms through a coarser medium. The term "shape" of an air sparging plume in this context designates the aspect ratio of the plume, or the amount of lateral propagation relative to the vertical propagation.

The fact that the ratio q/k is an indicator of propagation is not surprising, since it is the precisely the relationship between the amount of fluid injected into the medium and that displaced, which dictates the evolution of the pressures in the system, and ultimately therefore, the driving force of propagation. A "low" value of q/k would suggest an under-pressurized plume, a case in which the injection flow rate is too low, and the soil's conductivity is not being fully utilized. As a result, one would expect plumes to be

narrow, since no pressure buildup is taking place and therefore vertical propagation preferentially occurs. As the ratio of *q/k* increases, the pressure in the air phase also increases, and consequently the size of the plumes becomes larger. A point is reached after which the ratio becomes "too large" and injection is effectively taking place under constant pressure conditions. The volume of air being injected is too high, not enough pore fluid can be displaced per unit time, and the pressure does not dissipate. If the ratio continues to increase the soil eventually fails.

This was indeed the behavior that was observed when computer simulations were performed while varying *q/k*. It must be stressed at his point, and before results are presented, that this dependence of plume shape on *q/k* is <u>only</u> valid when capillary pressures can be neglected relative to hydrostatic pressures. If pore sizes of the porous media become sufficiently small, hydraulic conductivity considerations (*i.e.* relative velocity of flow displacement) will not be the only factor governing pressure in the air phase, and consequently, the value of *q/k* is no longer exclusively descriptive of plume propagation. For that reason, the values of the hydraulic conductivities used in the following simulations were maintained in the range of the very coarse soils, i.e. K values ranging from *1.0* to *0.01 cm/s*.

Figure 10-18 presents the summary plot of a number of computer simulations conducted, in which the ratio *q/k* was varied, and the volume of the resulting plume was computed. The figure shows the dependence of the plume volume V_p normalized by the height of injection H, on the value of *q/k*. Concentrating first on the general behavior of all the plots included in the figure, it can be seen that the overall volume of the plumes initially increases rapidly with *q/k*. This corresponds to the phase during which pressure buildup is occurring, lateral spreading of the plumes is enhanced, and therefore the zone of influence of air sparging increases. An over-pressurization phase follows, as shown by the flattening out of the plots, during which flow rates become too high for pressures to dissipate, and if the soil does not fracture, constant pressure conditions are reached. Vertical pressure gradients under these conditions become very high, and further pressurization of the system does not lead to increases in plume size. It must be noted that, in order to maintain the stability of the soil while performing the calculations shown in the figure, an increasingly high overburden pressure was specified, as the value of *q/k*

was increased. It is very likely however, that in a real system, the soil would fail under the given air pressures at values of *q/k* lower than those indicated in Figure 10-18.

The effect of injection depth has not yet been directly addressed in this thesis, although results have already been shown that allude to its significance. Figure 10-18 shows a family of curves, and it can be clearly seen that the volume of the air sparging plumes can drastically increase at higher depths of injection. The ratio *V/h* is not an ideal descriptor of plume size, because it does not provide any indication on the extent of the basal spread of the plume. As the depth of injection increases, plume growth can increase very significantly, if the system is maintained slightly over-pressurized.

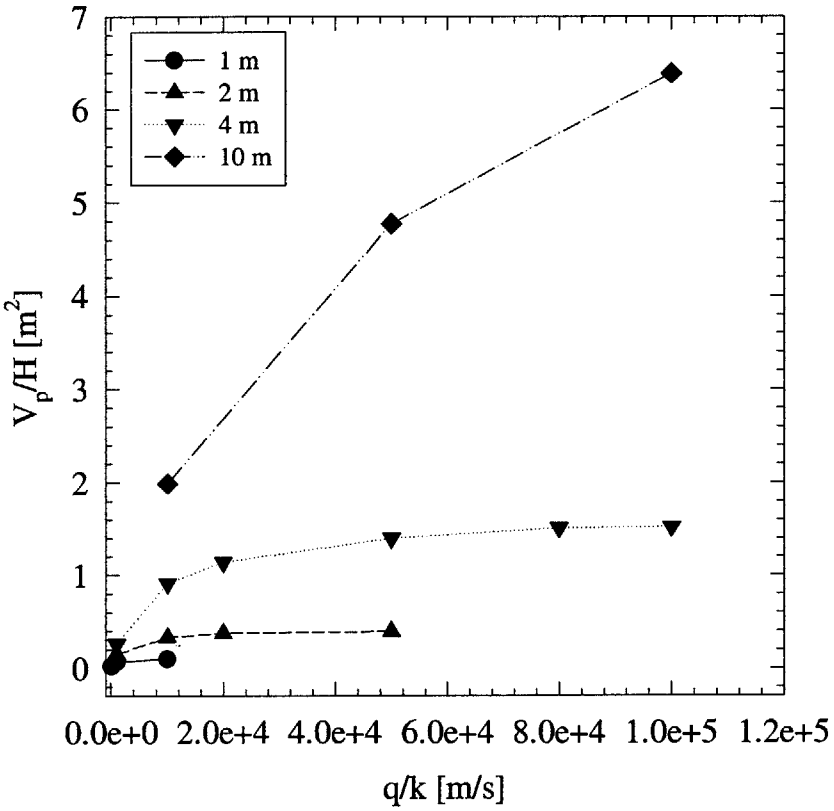

Figure 10-18 Results of computer simulations showing the influence of injection flow rate q, permeability k, and depth of injection, H on the volume air sparging plumes at breakthrough, V_p.

This statement is a direct consequence of the propagation characteristics of the air that have been described throughout the chapter. Considering first the case of a low

injection flow rate. If the system is under-pressurized, again meaning that the conductivity of the soil is sufficiently high that more pore fluid volume could be displaced per unit time, the resulting plumes will be narrow regardless of the depth of injection. Minimal lateral spreading occurs under these conditions, and the plumes propagate vertically. If however the air pressure in the system is maintained high, by injecting at a high flow rate, the entire base of the plume becomes the source of propagation. Increasing depths allow more time for the plume to spread at the base, and therefore to establish more propagation channels through which air can later migrate vertically. The wider the plume is at the base the larger the zone of influence of the well, and this feature is further enhanced at greater depths, since the time for breakthrough increases, for a given permeability. The influence of injection depth is clearly shown by the plots on Figure 10-18, which illustrate the drastic differences between plumes resulting from modeled injections at depths of 1 m, 2 m, 4 m and 10 m.

10.5.5. Heterogeneous Porous Media

A particularly useful feature of the computer program is that it offers the possibility of predicting the shape of plumes in soil systems of heterogeneous hydraulic conductivities. An array of permeabilities can be specified as an input file, such that a specific value of k is assigned to every node of the mesh. Flow calculations are performed in the same way that in the case of a homogeneous system except for the fact that varying permeabilities add complexity to the manner in which the air propagates. The direction of flow is not exclusively controlled by the magnitude of the pressure gradient, but by the combination of gradient and permeability.

Although no experimental data was available for comparison, a set of simulations were conducted on heterogeneous permeability fields with very marked non-uniformities. Two fields of 1 m by 1 m were defined, through which a layer of soil with a uniform permeability contrast of two orders of magnitude was specified. Such fields are shown in Figures 10-19 a) and b), where a layer of material is sandwiched between two layers of soil with permeabilities 100 times smaller and 100 times greater than that of the inner layer, respectively. The figures show the outline of the right hand side of the predicted

plumes. The left hand sides of the plumes are not included in the figure, but would be symmetric to the axis of the wells, at $x = 0$. The injection flow rate used in these simulations was $q = 1\text{x}10^{-5}$ m^3/s and the permeability k_l was set equal to $1\text{x}10^{-9}$ m^2. Therefore, in the absence of the layers the plumes would be equivalent to that presented as the prototype plume in Figure 10-19.

The effect of the discontinuity in permeabilities is clear. In the case of the fine layer of material, the plume propagates upward, reaches the lower permeability layer and then propagation stops. Pressure in the air phase begins to build up since air continues to be injected at a constant rate into a constant volume, and therefore lateral propagation is favored.

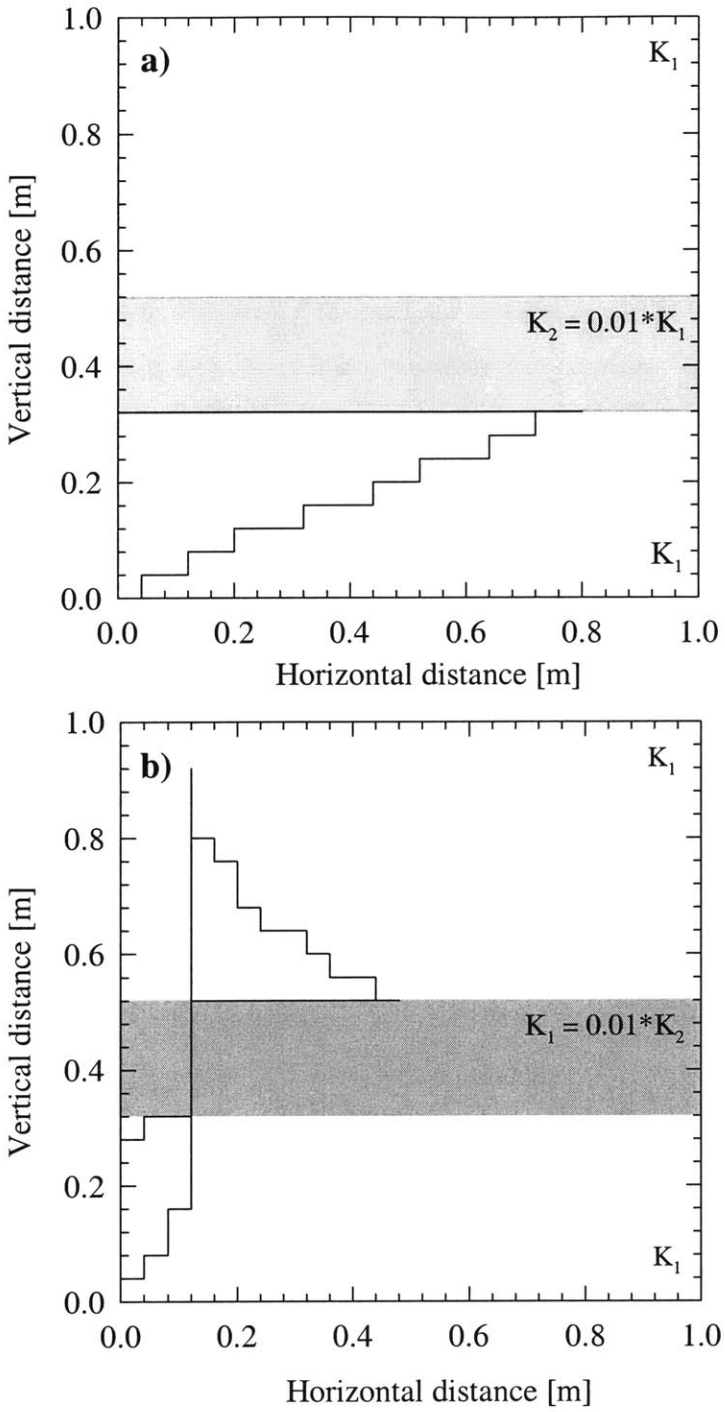

Figure 10-19 Variations of air flow patterns due to soil heterogeneity. a) layer of fine material (K2) in between two layers of coarse material (K1), such that K1/K2 = 100; b) layer of coarse material (K2) in between two layers of finer material (K1), such that K2/K1 = 100.

The simulation ended when the lateral spread reached the horizontal flow boundary at the right. Given that the contrast in permeabilities is sufficiently high, the gradient necessary to break through the finer layer is not reached before significant lateral propagation takes place, after which, horizontal gradients become large and preferential flow takes place in the horizontal direction.

In the case of the coarse layer of material in between the finer layers, air propagation has different characteristics. The initial stages of air flow are the same as those presented in Figure 10-19 a), and the plume propagates as described previously until air flow reaches the coarser layer. Since the permeability of this layer is significantly higher than that in the lower layer, air flow takes place vertically, immediately after the layer is reached. It is interesting to see that virtually no horizontal propagation occurs through the coarse material, since the gradients have already reached the critical point at which flow is preferentially vertical. As the flow reaches the upper finer layer of soil however, pressure buildup begins to occur again, and horizontal flow occurs along the interface of the two layers. Even though the flow propagates significantly in the horizontal direction, as vertical flow is initiated once again, and the flow advances faster upward.

Figure 10-20 illustrates another heterogeneous hydraulic conductivity field, one that was established following the sketch of the sample layering presented by Ji *et al.* (1993) presented in Chapter 2. Only the right hand side of the plume is shown, and the contrast between the values of K is of two orders of magnitude, the layers being more impermeable than the surrounding soil. In comparison with the two previous cases of heterogeneous media, Figure 10-20 illustrates the manner in which air flow circumvents the layers of lower hydraulic conductivity. The layering shown in this figure illustrates how lateral spreading is increased relative to the uniform hydraulic conductivity case as the air flow reaches the finer layers. As the front advancement is slowed down, air pressure builds up under the layers, which in turn promotes lateral propagation.

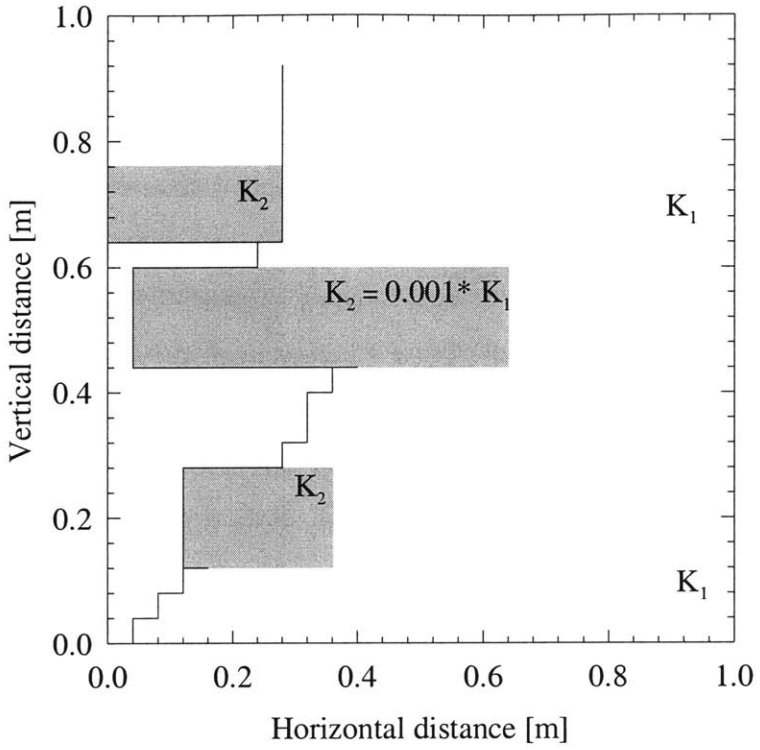

Figure 10-20 Air propagation through layered hydraulic conductivity sample.

CHAPTER 11

CONCLUSIONS AND RECOMMENDATIONS

11.1. OVERVIEW OF RESEARCH STUDY

The objective of the investigation presented in this thesis was that of determining and describing the mechanisms characterizing the flow of injected air through porous media during in situ air sparging operations. The work concentrated on studying the fundamental relationship between the mechanisms known to drive and resist the flow of air through soils, namely the buoyant and capillary forces, respectively.

The research study consisted in two main parts, the first of which concentrated on experimental modeling of air sparging process. An extensive experimental study was conducted that investigated the change in the patterns of air flow as the relative magnitude of these forces changed, as well as the change of the size and characteristics of the zone of influence of an air sparging well.

The testing program concentrated on: 1) intrinsic properties of the saturated porous medium, such as hydraulic conductivity of the soil and viscosity of the pore fluid; and 2) two critical IAS operational parameters, namely injection pressure and flow rate. Medium properties have been addressed in different contexts by prior studies of air sparging, but operational variables have not been explicitly considered. The differences in the shape and the mode of propagation of air plumes under constant flow rate and constant pressure injection conditions were thoroughly investigated.

In order to run laboratory experiments under stable conditions as pressurized air was being injected into the soil samples, testing was conducted in a geotechnical centrifuge. By increasing the acceleration field to which the porous medium was subjected, entry pressures, primarily dictated by the magnitude of the hydrostatic pressures, also increased. Injection pressures were thus increased to overcome larger entry pressures. The relationship between driving and retarding forces was therefore altered as acceleration levels were increased, with resulting consequences on the patterns of the air flow.

The study of air flow patterns through porous media would have not been possible if air propagation had not been visible. The use of a transparent porous medium allowed to track the movement of the air front in time, and to monitor changes in the patterns of flow under varying operational conditions.

The second part of this research focused on the mathematical modeling of air sparging. Experimental results and observations were used in the development of a conceptual model of air flow through saturated porous media. This model was subsequently used to develop a computer program that predicts the shape of the steady-state plume based on the hydraulic conductivity of the medium and on the air injection flow rate.

11.2. OVERVIEW OF EXPERIMENTAL RESULTS

11.2.1. Influence of Operational Parameters on Zone of Influence of IAS Plumes

11.2.1.1. g-level, buoyancy, and pressure gradients

A major part of the results and the conclusions obtained during this investigation were made possible by the fact that testing was being conducted in a geotechnical centrifuge, and therefore by the possibility of increasing the acceleration fields acting on the samples tested. This experimental capability made it possible to evaluate the impact of two parameters, namely fluid pressure distributions and air pressure gradients, on the characteristics of air flow through porous media, under injection conditions which would otherwise have not been realistically reproduced in the laboratory.

The effects of buoyancy and pressure gradient on air propagation through materials for which the capillarity component of the entry pressure is not significant relative to the hydrostatic component, will be summarized first. These were the type of media investigated throughout this work, for which it was found, that for values of the ratio P_{cap}/P_{entry} lower than 12%, capillarity effects did not affect propagation.

An important component of the manner in which air plumes propagate through these types of soils results from the pressure distribution in the pore fluid. The fact that the fluid pressure resisting the advancement of the air front decreases with the distance

from the air-water interface to the phreatic surface dictates, to a large extent, the shape of an air sparging plume. This is the case given that the difference between the air pressure and the pore entry pressure controls the magnitude of the pressure gradient that controls the advancement of the air front. The possibility of maintaining realistic pressure distributions pressures by increasing the g-level while evaluating the effects of varying injection pressures on plume shapes, was essential to obtaining the results presented in this thesis. Constant fluid pressure distributions, which have been used in prior experimental modeling of air sparging, are not representative of field conditions and will therefore not lead to adequate predictions of the shape of air sparging plumes.

Experiments showed that increasing g-levels, and therefore increasing buoyancy forces, results in the drastic increase of air pressure gradients at the injection point, which ultimately causes a significant reduction in the size of resulting air sparging plumes. The relationship between pressure gradients and plume size was clearly established by the experimental results. Pressure gradients drive air propagation, and therefore isolating the factors affecting their magnitude is useful in understanding their effect on plume shapes. Two components dictate the value of pressure gradients: 1) the difference between air pressure and pore entry pressure, ΔP; and 2) the distance from the air-water interface to the flow boundaries. The following scenarios can take place during injection, with their corresponding consequence on air propagation:

a) if ΔP is maintained constant and the distance from the air-water interface to both the lateral and the vertical fluid boundaries is the same, equal gradients develop in both horizontal and vertical directions, and the plume spreads uniformly in both directions. However, given that pore fluid pressures decrease in the positive z-direction while they remain constant in the x-direction, vertical flow is inherently favored. At some stage of the propagation vertical gradients become higher than horizontal gradients, and upward plume propagation preferentially occurs. If ΔP remains high, horizontal gradients remain significant relative to vertical gradients as the plume advances, and propagation takes place in both directions. The resulting plumes are wide at the base, and consequently, large zones of influence are generated.

b) if ΔP decreases as the plume advances, the difference between vertical and horizontal gradients becomes more crucial. At some distance from the injector, the air

pressure in the horizontal direction is not sufficient to overcome entry pressure, while it continues to be large enough to drive the plume upward. At this point vertical propagation takes over, and horizontal plume propagation is arrested. The resulting plumes are much narrower than in case a).

With increasing *g*-levels, the rate of increase of vertical gradients with decreasing distance from the interface to the phreatic surface increases considerably (see Figure 3-10), and thus vertical flow is further preferred. Resulting air sparging plumes become gradually more narrow, as the potential for horizontal propagation is eliminated.

The importance of pressure gradients on air propagation through saturated porous media described above was limited to those soils for which capillarity effects are not significant. If the effect of capillary forces is a concern, such that P_{cap}/P_{entry} at the injection point is greater than 10%, then additional mechanisms are involved in plume propagation. In particular, given that capillary resistance is unaffected by directional considerations, the relative preference for vertical propagation is not as marked as previously described. This is especially valid close to the injection point, where pore fluid pressures are comparably high at various depths along the air-water interface. The difference between air pressure and pore fluid pressure does not necessarily control propagation, particularly if heterogeneities in the distribution of capillary pressures exist along the interface. It is to be expected, therefore, that plumes propagating through soils which show capillary effects are wider at the base, and lead to significant zones of influence.

11.2.1.2. Pressure

The magnitude of the pressure gradient driving air propagation is of extreme importance to the size of the steady-state plume. Air pressures at the initial stages of invasion determine, to a large extent, the size of the zone of influence of a given air sparging well. Indeed, lateral propagation occurs until the pressure in the plume at a given elevation is higher than the pore entry pressure. Horizontal gradients become lower than vertical gradients after a certain amount of propagation has occurred, at which point horizontal plume spreading is drastically reduced and most of the plume

advancement is in the vertical direction. Once a preferential direction of flow is established, propagation in the other direction never matches the rate of advancement of the first direction, since the gradients increase at different rates. Thus, the longer the air pressure is maintained over P_{entry}, the wider the resulting plume will be. Moreover, if constant pressure injection conditions can be maintained, then injection pressures should be set as high above entry pressures as allowed by soil stability criteria in order to promote spreading at the injection point. If the amount of initial basal spreading is significant, then the cross sectional area of the plume from which vertical propagation occurs is large, and the zone of influence of the final plume is also large.

Monitoring of air pressures must be done, such that injection pressures do not reach fracturing pressures at the injection point. If the soil fails, a fracture plane develops, and flow preferentially occurs along the fracture. Plume growth is marginal once a failure plane has been created.

11.2.1.3. Flow rate

Air sparging plumes obtained under constant flow rate injection conditions may be as large as those obtained under constant pressure conditions, if the rate of injection is monitored carefully and adjusted to the flow requirements imposed by the soil. Indeed, given that during constant flow rate injection a fixed volume of gas is being introduced into a limited volume of void space, unless the volumes in and out of the system are monitored, two situations may take place: 1) the volume of air injected is too high relative to the volume of pore fluid being displaced. In this case, the air compresses in the soil pores, pressures increases rapidly causing failure of the medium, and a preferential flow path is established; or 2) the volume injected is not sufficient to maintain pressures greater than pore entry pressure at all elevations around the air-water interface. Under these conditions lateral plume propagation does not take place, and as a result, narrow plumes are obtained.

In order to obtain wide plumes during constant flow rate conditions, the injection flow rate needs to be progressively increased. Under these conditions, the volume of air injected at the beginning of propagation is not too high relative to the volume of pore space displaced and pressure buildup does not occur. As air advances through the soil the

flow rate must be increased, in order to maintain the pressure in the air phase at a high enough value to promote propagation in both vertical and lateral directions. The key to developing a large plume in constant flow rate injection conditions is that of maintaining the pressure in the air phase within an adequate range such that preferential directions of flow do not become established.

Under constant flow rate injection conditions, the properties of the porous medium will ultimately dictate the rate of increase of the injection flow rate. The more permeable the soil, the faster pore fluid will be displaced under the applied gradient, and therefore the faster the rate of increase of the injection flow rate may be.

11.2.1.4. Injector geometry

The geometry of the injection ports, *i.e.* the area available for flow, had a limited impact on the shape and size of the air sparging plumes obtained. Two injector configurations were tested, and for each configuration, ports with three different flow areas were used.

Results showed that when the injector flow area imposed a restriction to air flow, even before invasion of the porous medium occurred, the pressure in the air phase built up sufficiently to cause localized failure of the porous medium at the injection point. For low flow rates of injection, this localized failure mechanism observed during injection through the smallest ports contributed to larger plume spreading than that observed when using the larger injector sizes. The localized failure effectively opened up channels for air to flow, ultimately leading to relatively wide steady state plumes, even at the lowest flow rates. As injection flow rates increased, local fracturing became more pronounced, and steady-state plumes were more irregular, with prevalent channels though which most of the air flow occurred.

11.2.2. Influence of Porous Medium Parameters on Zone of Influence of Plumes

11.2.2.1. Grain size, capillarity, and permeability

The resisting effect of a saturated porous medium to the advancement of an injected air front is exerted in two forms: 1) by the hydraulic conductivity of the material,

through the intrinsic permeability of the porous medium and the viscosity of the pore fluid; and 2) by the capillary resistance of the porous medium, dictated primarily by the size of its pore spaces. The importance of the hydraulic conductivity of the material to the development of air sparging plumes has already been alluded to, in that it controls the rate at which pore fluid is displaced from the medium, and thus the rate at which the air front can advance. The types of soils in which IAS is typically conducted are medium to coarse sands, of relatively high hydraulic conductivity. Average grain sizes for these soils are large enough that capillary forces are not of concern, and therefore hydraulic conductivity of the medium is the property that dictates the rate of air flow through the soil.

However, experimental results have shown that the effect of capillary forces on air flow can in fact become significant enough to influence the mode of propagation of an injected air front, even through soils with relatively high pore diameters. The effect of capillary pressure on air flow cannot only be evaluated on the basis of a pore diameter, but it needs to be assessed relative to pore entry pressures. Even in coarse materials, the importance of capillary forces as a resisting mechanism to the advancement of air propagation increases with decreasing pore fluid pressures, in other words, with decreasing distance to the phreatic surface. The importance of pore fluid pressures to pore entry pressure decreases with decreasing depth, while capillary pressures remain constant. The value of the ratio P_{cap}/P_{entry} therefore increases as the leading front of the air plumes approaches the phreatic surface. A value of P_{cap}/P_{entry} greater than 12% at the injection point was observed to affect the propagation characteristics of air sparging plumes. It is therefore important, when assessing the relevance of capillary pressure restrictions to air flow during air sparging, to consider the depth at which injection is to be performed.

11.2.2.2. Pore fluid

The properties of the pore fluid have an important effect on the size of air sparging plumes, primarily because they alter the conductivity of the porous medium and thus affect the advancement of the air front. The hydraulic conductivity of a medium is inversely proportional to the viscosity of the pore fluid, and therefore, increasing the

viscosity of the interstitial fluid increases the resistance of the medium to air propagation. The development of air sparging plumes in two different pore fluids was investigated in this study: 1) glycerol, with a viscosity 500 times greater than that of water; and 2) an optical fluid, referred to as immersion liquid, with a viscosity 21 times greater than that of water.

The effects of varying viscosity between the two fluids were clearly visible on the air sparging plumes obtained. It was not possible to complete one single constant flow rate of injection experiment in glycerol, at any flow rate. The resistance to flow was so pronounced that pressure buildup, even at the lowest flow rate (*i.e.* $q = 0.26\ cm^3/s$) caused fracturing of the material. Fracturing under constant flow rate injection in samples saturated with immersion liquid was only observed under flow rates in excess of $10\ cm^3/s$.

Under constant pressure injection conditions, plumes developing in glycerol under accelerations lower than 40-*g* were wider than those developing in immersion liquid. Increasing medium resistance to air flow promoted basal plume spreading, and consequently resulted in wider steady-state plumes. Under accelerations of 50-*g* and greater, the decrease in plume size was drastic in the case of both pore fluids, and differences in plume sizes were not significant.

11.2.3. Patterns of Air Flow

Results from air sparging experiments conducted under constant pressure and constant flow rate of injection conditions, and under accelerations ranging from 1-*g* to 100-*g*, suggest that air flow patterns during injection through saturated porous media can be described by one of the following modes of propagation:

1. *Fingering* - Observed during injection at low flow rates ($q < 3\ cm^3/s$) or at the lowest range of acceleration fields tested (*g-level* < 15-*g*). During this form of propagation, air flow is unstable and occurs along individual channels. The tortuosity of finger flow paths decreases with increasing velocity of propagation. Steady-state plumes resulting from fingering propagation are typically narrow, and air saturation within plume boundaries is low.

2. *Uniform propagation* - Mode of propagation that occurs in two forms:

a) fingering fronts, characterized by clusters of air channels propagating at similar velocities. This type of propagation was observed under constant flow rate injection, at higher rates than those which caused fingering, *i.e.* $q < 28\ cm^3/s$, or under acceleration levels lower than 40-*g*. Zone of influence of plumes resulting from this type of propagation are large, with considerable lateral spreading. Air saturation within plume boundaries is high.

b) uniform front, observed during constant pressure injection at *g*-levels higher than 50-*g*. Propagation characterized by a fast moving air-pore fluid interface. Zones of influence of plumes decrease with increasing acceleration levels. High air saturations inside plumes.

3. *Fracturing* – Observed under in cases in which injection flow rate is too high relative to the rate at which pore fluid can be displaced from medium. Air pressure thus builds up, and reaches the critical fracturing pressure of the medium. Failure of the soil occurs, and characteristic fracture planes develop. No plume develops, and air flow takes place along failure planes.

11.3. OVERVIEW OF MODELING RESULTS

The experimental results obtained during this investigation were at the basis of a computer program that was written to simulate the propagation of air injected into saturated porous media under constant flow rate conditions. The program was envisioned as a tool to simplify the prediction of the zone of influence of an air sparging well, and therefore one of the objectives was to limit the amount of input parameters, while maintaining an accurate estimate of the extent of air propagation.

11.3.1. Principles of the Model

The program consists of an axisymmetric finite difference algorithm, which based on a conservation of volume approach computes the volumes of pore fluid displaced and

of air injected into the medium, per unit time. Two essential input parameters are needed to conduct air sparging simulations, namely the hydraulic conductivity of the porous medium and the injection flow rate. The final output of the program is the shape of the zone of influence of an air sparging well.

Two critical experimental observations were implemented in the algorithm of the program, which differentiate it from other currently available models:

1. The program is only to be used for modeling air propagation behavior through coarse, saturated, granular materials. The reason for this constraint is that capillary pressure considerations are not included in the formulation of the problem. In coarse materials, the entry pressure of air at a given depth below the phreatic surface is essentially controlled by the pore fluid pressure. Indeed, the magnitude of capillary pressures relative to hydrostatic pressures is negligible, and therefore a study of air flow based on capillary pressure-saturation relationships is not representative of the governing mechanisms. Air propagation can be more simply modeled as a uniform front displacement governed by Darcy's law, and therefore dependent on the hydraulic conductivity of the medium and on the driving hydraulic gradient.

2. Air propagation through saturated porous media is controlled by the magnitude of the pressure gradient and thus by the pressure in the air. The compressibility of the air phase, *i.e.* the pressure-volume relationship of the injected air into a surrounding pressurized medium is therefore an essential characteristic of the propagation, which must be incorporated in the problem solution.

11.3.2. Modeling results

Results from model simulations of all the types of experiments conducted in the laboratory, for which capillarity was indeed negligible, were in general agreement with the observed results. It is therefore possible to describe the propagation characteristics of air through porous media based solely on knowledge of the hydraulic conductivity of the material, and on the injection flow rate. The following types of experiments were successfully reproduced:

- Injection of air under constant flow rate and under constant pressure conditions at 1-*g*. It should be noted that while the program captures the shape of the air plumes, it does not model the flow patterns of the air, *i.e.* the fingering and channeling patterns observed in the laboratory. The model of air sparging presented assumes that propagation occurs as a uniform front, such that the volume of soil contained within the boundaries of the modeled plume is 100% saturated with air. As a result, the saturation values of the modeled plumes are different from that of some of the observed plumes, particularly those obtained under constant flow rate injection at 1-*g*.
- Injection under increasing acceleration fields were also accurately reproduced by computer simulations. The model captured the behavior observed in the laboratory, namely the drastic narrowing of the air sparging plumes as hydraulic gradients increased.

Additionally, it was verified that if scaling laws are accurately followed, modeling of models can be used to predict the propagation behavior of air during air sparging. Due to experimental limitations in the scaling of the length dimension, the applicability of centrifuge modeling as a predictive tool to determine the actual size of an air sparging plume had not been verified in the laboratory. Model simulations suggested that since plume propagation flow is controlled by the air pressure, the principles of similitude apply and typical scaling relationships can be used to replicate the behavior of air injected into a prototype. The injection flow rate must be scaled, and the scaling factor is given by $1/n$. If all scaling laws are applied it was found that the shapes of modeled air plumes stay constant at increasing *g*-levels, and that the scaling relationship for time is valid.

Results of computer simulations also showed that air propagation characteristics through saturated coarse soils can be described by the ratio q/k. The size of air sparging plumes forming in different soil deposits of the same depth is the same, if the value of q/k is constant between deposits. The depth of injection has an amplifying effect on air sparging plumes if the ratio q/k is sufficiently high, such that a certain amount of pressure buildup occurs in the air phase. If this is the case, the size of air sparging plumes increases with the thickness of the soil deposit.

One of the features of the model is that it allows for a hydraulic conductivity field to be entered as input for the calculations. If values of K can be defined at all the nodes in of the computation mesh, then the effect of hydraulic conductivity heterogeneities can be investigated. This was in fact demonstrated for a number of layered soil deposits, through which highly irregular plumes propagated, further demonstrating the critical role of K to air flow calculations through saturated porous media.

11.4. RECOMMENDATIONS FOR FUTURE RESEARCH

11.4.1. Equipment Development

- The importance of air pressure to the propagation characteristics of air through saturated porous media has been stressed at length throughout this thesis. During this investigation however, the only pressure measurement that was available was at the injection point. It has been implicitly assumed in the discussions presented in this thesis, that pressure losses as air flows through the soil are not likely to be significant given the low viscosity of the air. All pressure variations have therefore been attributed to the expansion/compression behavior of the air as if flows through the system, and have therefore been estimated by the ideal gas law.

Quantitative measurements of the actual pressure in the medium as propagation takes place would be of great value in the characterization of flow mechanisms. Measurements of pressure during air sparging experiments were unsuccessfully attempted during the first two years of this investigation. Manometers, miniature pressure transducers, differential pressure transducers, and needle probes were used to try to get readings of the air pressure. These readings however, are extremely difficult to obtain given that upon contact with the air, instruments are no longer saturated and pressure continuity is lost. The implementation of a method and a procedure to obtain pressure readings would be a most valuable way of advancing this research.

- The development of a method for measuring injection flow rates during constant pressure injection experiments would be very valuable to in the evaluation of the effects of operational mechanisms on the propagation characteristics of injected air.

- The equipment used to conduct constant flow rate of injection experiments could be optimized. More capacity is needed to inject air at higher flow rates both at 1-*g* and especially at higher *g*-levels. Although the experiments conducted at the very low range of flow rates were extremely helpful to the understanding of flow processes, their applicability as prediction tools for field applications is limited. Valuable knowledge would surely be obtained from experiments conducted under higher injection flow rates.

- A more quantitative set of saturation measurements could be generated if a camera of higher resolution was available. The current video equipment is adequate, but it does not allow for automation of data processing. A more sophisticated camera and image analysis software would lead to much more accurate quantification of patterns of air flow and of zones of influence of air sparging wells.

11.4.2. Suggestions for Further Research

- Much time was spent during this study characterizing the effects of buoyancy/gradients on the propagation of air. An extensive experimental database now exists that can be used to describe air flow through soils at high *g*-levels. More experiments can be conducted to fully characterize air flow at a lower range of *g*-levels, still higher than gravitational, but not so high that lateral propagation is completely prevented. Specifically, more experiments should be conducted under acceleration fields ranging from 1-*g* to 15-*g*.

- Very few experiments were conducted that investigated the effects of soil heterogeneities at higher *g*-levels. More testing could be done to establish if the effects of layering can be offset by injecting air at high gradients, and more specifically, if low permeability barriers can be bypassed at high injection gradients.

CHAPTER 12

REFERENCES

Adler, P. M., and Brenner, H. (1988). "Multiphase Flow in Porous Media." *Annual Review of Fluid Mechanics*, 20, 35-59.

Ahlfeld, D. P., Amine, D., and Wei, J. (1994). "A Conceptual Model of Field Behavior of Air Sparging and Its Implications for Application." *Ground Water Monitoring Review*, 14(4), 132-139.

Araktingi, U. G., and Orr, F. M. J. (1993). "Viscous Fingering in Heterogeneous Porous Media." *SPE Advanced Technology Series*, 1(1), 71-80.

Arulanandan, K., Thompson, P. Y., Kutter, B. L., Meegoda, N. J., Muraleetharan, K. K., and Yogachandran, C. (1988). "Centrifuge Modeling of Transport Processes for Pollutants in Soils." *Journal of Geotechnical Engineering*, 114(2), 185-205.

Baehr, A. L., Hoag, G. E., and Marley, M. C. (1989). "Removing Volatile Contaminants from the Unsaturated Zone by Inducing Advective Air-Phase Transport." *Journal of Contaminant Hydrology*, 4, 1-26.

Baker, D. M., and Benson, C. H. (1996). "Review of Factors Affecting In Situ Air Sparging." *Proceedings of the specialty conference on Non-Aqueous Phase Liquids (NAPLs) in Subsurface Environment - Assessment and Remediation, November 12-14, Washington, DC*, 292-310.

Bear, J. (1972). *Dynamics of Fluids in Porous Media*, Elsevier, New York.

Bly, M. J., and Worden, R. M. (1992). "The Effects of Solids Density and Void Fraction on the Bubble Rise Velocity in a Liquid-Solid Fluidized Bed." *Chemical Engineering Science*, 47(13/14), 3281-3288.

Bohler, U., Brauns, J., and Nahold, M. (1990). "Air Injection and Soil Air Extraction as a Combined Method for Cleaning Contaminated Sites - Observations from Test Sites in Sediments and Solid Rocks." *Contaminated Soil'90, Third International KfK/TNO Conference on Contaminated Soil, 10-14 December, Karlsruhe, Federal Republic of Germany*, 2, 1039-1044.

Bolton, M. D., and Lau, C. K. (1988). "Scale effects arising from particle size." Centrifuge 88, J. F. Corte, ed., Balkema, Rotterdam, The Netherlands, 127-131.

Boyce, W. E., and DiPrima, R. C. (1988). Calculus, John Wiley & Sons Inc.

Brock, D. C., and Orr, F. M. J. (1991). "Flow Visualization of Viscous Fingering in Heterogeneous porous Media." *66th SPE Annual Technical Conference and Exhibition - Dallas, TX.*, Gamma, 211-222.

Brooks, M. C., Wise, W. R., and Annable, M. D. (1999). "Fundamental Changes in In Situ Air Sparging Flow Patterns." *Ground Water Monitoring Review*(Spring), 105-113.

Brown, R. (1995). Handbook of Bioremediation, Lewis Publishers.

Chen, M. R., Hinkley, R. E., and Killough, J. E. (1996). "Computed tomography imaging of air sparging in porous media." *Water Resources Research*, 32(10), 3013-3024.

Cheng, Z. (1998). "Flow Problems in Air Venting and Air Sparging," M.S. Thesis, Massachusetts Institute of Technology.

Clayton, W. S. (1998). "A Field and Laboratory Investigation of Air Fingering During Air Sparging." *Ground Water Monitoring Review*(Summer), 134-145.

Clift, R., Grace, J. R., and Weber, M. E. (1978). Bubbles, Drops, and Particles, Academic Press.

Comolet, R. (1979a). "Sur le mouvement d'une bulle de gaz dans un liquide." *La Houille Blanche*, 34(1), 31-42.

Comolet, R. (1979b). "Vitesse d'ascension limite d'une bulle de gaz isolee dans un liquide peu visqueux." *Journal de Mecanique Appliquee*, 3(2), 145-171.

Culligan, P. J., and Barry, D. A. (1998). "Similitude requirements for modelling NAPL movement with a geotechnical centrifuge." *Proceedings of the Institution of Civil Engineers Geotechnical Engineering*, 131, 180-186.

Dantu, P. (1957). "Contribution a L'Etude Mecanique et Geometrique des Milieux Pulverulents." *Proceedings of the International Conference on Soil Mechanics and Foundation Engineering, London*, 1, 144-148.

Davidson, J. F., Harrison, D., and Guedes de Carvalho, J. R. F. (1977). "On the Liquidlike Behavior of Fluidized Beds." *Annual Review of Fluid Mechanics*, 9, 55-86.

Davidson, J. F., and Schuler, B. O. G. (1960a). "Bubble Formation at an Orifice in a Viscous Liquid." *Transactions of the Institution of Chemical Engineering*, 38, 144-154.

Davidson, J. F., and Schuler, B. O. G. (1960b). "Bubble Formation at an Orifice in an Inviscid Liquid." *Transactions of the Institution of Chemical Engineering*, 38, 335-342.

Davidson, L., and Amick, E. H. J. (1956). "Formation of Gas Bubbles at Horizontal Orifices." *AIChE Journal*, 2(3), 337-342.

Demond, A. H., and Roberts, P. V. (1987). "An Examination of the Relative Permeability Relations for Two-Phase Flow in Porous Media." *Water Resources Bulletin*, 23(4), 617-628.

Elder, C. R., and Benson, C. H. (1999). "Air Channel Formation, Size, Spacing, and Tortuosity During Air Sparging." *Ground Water Monitoring Review*(Summer), 171-181.

Fourar, M., and Bories, S. (1995). "Experimental Study Of Air-Water Two-Phase Flow Through A Fracture (Narrow Channel)." *International Journal of Multiphase Flow*, 21(4), 621-637.

Gido, S. P., Hirt, D. E., Montgomery, S. M., Prud'homme, R. K., and Rebenfeld, L. (1989). "Foam Bubble Size Measured Using Image Analysis Before and After Passage Through Porous Medium." *Journal of Dispersion Science and Technology*, 10(6), 785-793.

Goodings, D. J., and Gillette, D. R. (1996). "Model Size Effects in Centrifuge Models." *Geotechnical Testing Journal*, 19(3), 277-285.

Grace, J. R., Wairegi, T., and Nguyen, T. H. (1976). "Shapes and Velocities of Single Drops and Bubbles Moving Freely Through Immiscible Liquids." *Transactions of the Institution of Chemical Engineering*, 54, 167-173.

Gupta, S. P., and Greenkorn, R. A. (1974).). "An Experimental Study of Immiscible Displacement With an Unfavorable Mobility Ratio in Porous-Media." *Water Resources Research*, 10(2), 371-374.

Haberman, W. L., and Morton, R. K. (1956). "An Experimental Study of Bubbles Moving in Liquids." *Transactions of the American Society of Civil Engineers*, 121, 227-252.

Hemmat, M., and Borhan, A. (1996). "Buoyancy-Driven Motion of Drops and Bubbles in a Periodically Constricted Capillary." *Chemical Engineering Communications*, 148-150, 363-384.

Hill, S. (1952). "Channelling in packed columns." *Chemical Engineering Science*, 1(6), 247-253.

Hiller, D., and Gudemann, H. (1988). "In situ remediation of VOC contaminated soil and groundwater by vapor extraction and groundwater aeration". *Proceedings, Haztech '88 International.* Cleveland, Ohio. September 1988.

Homsy, G. M. (1987). "Viscous Fingering in Porous Media." *Annual Review of Fluid Mechanics*, 19, 271-311.

Hughes, R. R., Handlos, A. E., Evans, H. D., and Maycock, R. L. (1955). "The Formation of Bubbles at Simple Orifices." *Chemical Engineering Progress*, 51(12), 557-563.

Ji, W., Dahmani, A., Ahlfeld, D. P., Lin, J. D., and Hill, E. (1993). "Laboratory Study of Air Sparging: Air Flow Visualization." *Ground Water Monitoring Review*, 13(4), 115-126.

Jonasson, S. A. (1991). "Estimation of Soil Water Retention for Natural Sediments from Grain Size Distribution and Bulk Density," Ph.D. Dissertation, Chalmers University of Technology, Goteborg, Sweden.

Ko, H. Y. (1988). "Summary of the state-of-the-art in centrifuge modeling testing." Centrifuges in Soil Mechanics, W. H. Craig, R. G. James, and A. N. Schofield, eds., Balkema, Rotterdam, The Netherlands, 11-18.

Konagai, K., Tamura, C., Rangelow, P., and Matsushima, T. (1992). "Laser-Aided Tomography: A Tool for Visualization of Changes in the Fabric of Granular Assemblage." *Structural Engineering/Earthquake Engineering*, 9(3), 193s-201s.

Kueper, B. H., and Frind, E. O. (1988). "An Overview of Immiscible Fingering in Porous Media." *Journal of Contaminant Hydrology*, 2, 95-110.

Lambe, T. W. (1973). "Predictions in Soil Engineering." *Geotechnique*, 23(2), 149-202.

Leibson, I., Holcomb, E. G., Cacoso, A. G., and Jacmic, J. J. (1956). "Rate of Flow and Mechanics of Bubble Formation from Single Submerged Orifices." *AIChE Journal*, 2(3), 296-306.

Lenormand, R., Touboul, E., and Zarcone, C. (1988). "Numerical models and experiments on immiscible displacements in porous media." *Journal of Fluid Mechanics*, 189, 165-187.

Leonard, W. C., and Brown, R. A. (1992). "Air Sparging: An Optimal Solution." *Proceedings of the 1992 Petroleum Hydrocarbons and Organic Chemicals in Ground Water: Prevention, Detection, and Restoration, November 4-6, Houston, TX*, 349-363.

Levich, V. G. (1962). Physicochemical Hydrodynamics, Prentice Hall.

Levy, L. (2002). Ph.D. Dissertation, Massachusetts Institute of Technology.

Lundegard, P. D., and Andersen, G. (1993). "Numerical Simulation of Air Sparging Performance." *Proceedings of the 1993 Petroleum Hydrocarbons and Organic Chemicals in Ground Water: Prevention, Detection, and Restoration, November 10-12, Houston, TX*, 461-476.

Marley, M. C., Hazebrouck, D. J., and Walsh, M. T. (1992). "The Application of In Situ Air Sparging as an Innovative Soils and Ground Water Remediation Technology." *Ground Water Monitoring Review*, 12(2), 137-144.

McCray, J. E. (2000). "Mathematical modeling of air sparging for subsurface remediation: state of the art." *Journal of Hazardous Materials*, 72, 237-263.

McCray, J. E., and Falta, R. W. (1997). "Numerical Simulation of Air Sparging for Remediation of NAPL Contamination." *Ground Water*, 35(1), 99-110.

Mishima, K., and Hibiki, T. (1996). "Some Characteristics of Air-Water Two-Phase Flow in Small Diameter Vertical Tubes." *International Journal of Multiphase Flow*, 22(4), 703-712.

Moissis, D. E., Wheeler, M. F., and Miller, C. A. (1993). "Simulation of Miscible Viscous Fingering Using Modified Method of Characteristics: Effects of Gravity and Heterogeneity." *SPE Advanced Technology Series*, 1(1), 62-70.

Montemagno, C. D., and Gray, W. G. (1995). "Photoluminescent volumetric imaging: A technique for the exploration of multiphase flow and transport in porous media." *Geophysical Research Letters*, 22(4), 425-428.

Nutt, C. W., Burley, R. W., Anwer Rajah, D. M., and Polychronopolis, J. T. (1992). "Foam Generation in Porous Media." *International Journal of Engineering Fluid Mechanics*, 5(3), 373-390.

Nyer, E. K., and Sutherson, S. S. (1993). "Air Sparging: Savior of Ground Water Remediations or just Blowing Bubbles in the Bath Tub?" *Ground Water Monitoring Review*, 13(4), 87-91.

Olbricht, W. L. (1996). "Pore-Scale Prototypes of Multiphase Flow in Porous Media." *Annual Review of Fluid Mechanics*, 28, 187-213.

Olbricht, W. L., and Leal, G. (1983). "The creeping motion of immiscible drops through a converging/diverging tube." *Journal of Fluid Mechanics*, 134, 329-355.

Pahwa, A. (1987). "Quick Release Tests on Centrifuge of Wall Retaining Saturated Sand Backfill," M.S. Thesis, Massachusetts Institute of Technology, Cambridge, MA.

Pavone, D. (1992). "Observations and Correlations for Immiscible Viscous-Fingering Experiments." *SPE Reservoir Engineering*, 187-194.

Peterson, J. W., Lepczyk, P. A., and Lake, K. L. (1999). "Effect of sediment size on area of influence during groundwater remediation by air sparging: a laboratory approach." *Environmental Geology*, 38(1), 1-6.

Ramakrishnan, S., Kumar, R., and Kuloor, N. R. (1969). "Studies in bubble formation - I Bubble formation under constant flow conditions." *Chemical Engineering Science*, 24(4), 731-747.

Rangelow, P., Konagai, K., Matsushima, T., and Park, C. S. (1992). "Visualization of Granular Material Deformation Through Laser-Aided Tomography." *Bulletin, Earthquake Resistant Structure Research Center, University of Tokio*, 25, 61-67.

Ratnam, S. (1996). "Geotechnical Centrifuge Modeling of the Behavior of Light NonAqueous Phase Liquids (LNAPLS) in Sand Samples Under Hydraulic Flushing," M.S. Thesis, Massachusetts Institute of Technology, Cambridge, MA.

Ratnam, S., Culligan-Hensley, P. J., and Germaine, J. T. (1996). "The behavior of light nonaqueous phase liquids under hydraulic flushing." *Proceedings of the Second International Congress on Environmental Geotechnics - Osaka, Japan*, 1, 1061-1066.

Reddy, K. R., and Adams, J. A. (2001). "Effects of Soil Heterogeneity on Airflow Patterns and Hydrocarbon Removal During In Situ Air Sparging." *Journal of Geotechnical and Geoenvironmental Engineering*, 127(3), 234-247.

Reddy, K. R., Kosgi, S., and Zhou, J. (1995). "A Review of In-Situ Air Sparging for the Remediation of VOC-Contaminated Saturated Soils and Groundwater." *Hazardous Waste & Hazardous Materials*, 12(2), 97-118.

Roberson, J. A., and Crowe, C. T. (1990). Engineering Fluid Mechanics. Houghton Mifflin Company.

Schofield, A. N. (1980). "Cambridge Geotechnical Centrifuge Operations." *Geotechnique*, 30(3), 227-268.

Sellers, K. L., and Schreiber, R. P. (1992). "Air Sparging Model for Predicting Groundwater Cleanup Rate." *Proceedings of the 1992 Petroleum Hydrocarbons and Organic Chemicals in Ground Water: Prevention, Detection, and Restoration, November 4-6, Houston, TX*, 365-376.

Semer, R., Adams, J. A., and Reddy, K. R. (1998). "An experimental investigation of air flow patterns in saturated soils during air sparging." *Geotechnical and Geological Engineering*, 16, 59-75.

Sinfield, J. V. (1998). "Fluorescence of Contaminants in Soil and Groundwater Using a Time-Resolved Microchip Laser System," Ph.D. Dissertation, Massachusetts Institute of Technology, Cambridge, MA.

Sjoblom, K. J. (2000). "The Mechanisms Involved During the Desaturation Process of a Porous Matrix," Ph.D. Dissertation, Massachusetts Institute of Technology, Cambridge, MA.

Stokes, J. P., Weitz, D. A., Gollub, J. P., Dougherty, A., Robbins, M. O., Chaikin, P. M., and Lindsay, H. M. (1986). "Interfacial Stability of Immiscible Displacement in a Porous Medium." *Physical Review Letters*, 57(14), 1718-1721.

Taitel, Y., Bornea, D., and Dukler, A. E. (1980). "Modelling Flow Pattern Transitions for Steady Upward Gas-Liquid Flow in Vertical Tubes." *AIChE Journal*, 26(3), 345-354.

Tan, C. T., and Homsy, G. M. (1992). "Viscous fingering with permeability heterogeneity." *Physics of Fluids A*, 4(6), 1099-1101.

Taylor, R. N. (1995). Geotechnical Centrifuge Technology, Blackie Academic and Professional.

Tsuchiya, K., and Furumoto, A. (1995). "Tortuosity of Bubble Rise path in a Liquid-Solid Fluidized Bed: Effect of Particle Shape." *AIChE Journal*, 41(6), 1368-1374.

Tsuchiya, K., Song, G. H., and Fan, L. S. (1990). "Effects of particle properties on bubble rise and wake in two-dimensional liquid-solid fluidized bed." *Chemical Engineering Science*, 45(5), 1429-1434.

Turpin, J. L., and Huntington, R. L. (1967). "Prediction of Pressure Drop of Two-Phase, Two-Component Concurrent Flow in Packed Beds." *AIChE Journal*, 13(6), 1196-1202.

van Dijke, M. I. J., van der Zee, S. E. A. T. M., and van Duijn, C. J. (1995). "Multi-phase flow modeling of air sparging." *Advances in Water Resources*, 18(6), 319-333.

van Genuchten, M. T. (1980). "A Closed-form Equation for Predicting the Hydraulic Conductivity of Unsaturated Soils." *Soil Science Society of America Journal*, 44, 892-898.

van Krevelen, D. W., and Hoftijzer, P. J. (1950). "Studies of Gas-Bubble Formation - Calculation of Interfacial Area in Bubble Contactors." *Chemical Engineering Progress*, 46(1), 29-35.

Wakabayashi, T. (1950). "Photo-elastic Method for Determination of Stress in Powdered Mass." *Journal of the Physical Society of Japan*, 35(2), 383-385.

Wallis, G. B. (1969). One-dimensional Two-phase Flow, McGraw-Hill Book Company.

Wallis, G. B. (1974). "The Terminal Speed of Single Drops or Bubbles in an Infinite Medium." *International Journal of Multiphase Flow*, 1, 491-511.

Weekman, V. W. J., and Myers, J. E. (1964). "Fluid-Flow Characteristics of Concurrent Gas-Liquid Flow in Packed Beds." *AIChE Journal*, 10(6), 951-957.

Wegener, P. P., and Parlange, J. Y. (1973). "Spherical-Cap Bubbles." *Annual Review of Fluid Mechanics*, 5, 79-100.

Wehrle, K. (1990). "In-situ cleaning of CHC Contaminated Sites: Model-Scale Experiments Using the Air Injection (In-Situ Stripping) Method in Granular Soils." *Proceedings Contaminated Soil.* Eds. Hinsenveld and Brink. Kluwer Academic Publishers. 1061-1062.

White, E. T., and Beardmore, R. H. (1962). *Chemical Engineering Science*, 17, 351-361.

Widjaja, H., Duncan, J. M., and Seed, H. B. (1984). *Scale and Time Effects in Hydraulic Fracturing*, US Army Corps of Engineers. Miscellaneous Paper GL-84-10.

Wilson, D. J. (1992). "Groundwater Cleanup by in-situ Sparging. II. Modeling of Dissolved Volatile Organic Compound Removal." *Separation Science and Technology*, 27(13), 1675-1690.

Wilson, D. J., Gomez-Lahoz, C., and Rodriguez-Maroto, J. M. (1994). "Groundwater Cleanup by In-Situ Sparging. VIII. Effect of Air Channeling on Dissolved Volatile Organic Compounds Removal Efficiency." *Separation Science and Technology*, 29(18), 2387-2418.

Wilson, D. J., Kayano, S., Mutch, R. D., and Clarke, A. N. (1992). "Groundwater Cleanup by in-situ Sparging. I. Mathematical Modeling." *Separation Science and Technology*, 27(8&9), 1023-1041.

Wilson, D. J., Norris, R. D., and Clarke, A. N. (1996). "Groundwater Cleanup by In-Situ Sparging. IX. Air Channeling Model for Nonaqueous Phase Liquid Removal." *Separation Science and Technology*, 31(7), 915-939.

Wooding, R. A., and Morel-Seytoux, H. J. (1976). "Multiphase Fluid Flow Through Porous Media." *Annual Review of Fluid Mechanics*, 8, 233-274.

Wright, D. E. (1968). "Nonlinear Flow Through Granular Media." *Journal of the Hydraulics Division, Proceedings of the American Society of Civil Engineers*, 94(HY4), 851-872.

APPENDIX A

DATA ACQUISITION PROGRAM

The data acquisition program presented in this appendix is an adapted version of the program written by Dr. K.J. Sjoblom (2000). The original code was modified by L. Levy and C. Marulanda. The program is written in QBASIC.

```
DECLARE SUB Estimrpm ()
DECLARE SUB Estimglevel ()
DECLARE SUB Switch ()
DECLARE SUB ReadFile (File$)
DECLARE SUB SetUpDataFile ()
DECLARE SUB WriteToFile ()
DECLARE SUB GetVoltage ()
DECLARE SUB PrintEngData ()
DECLARE SUB Pause ()
DECLARE SUB SetUpScreen ()
DECLARE SUB SetUpDAQ (Card)
DECLARE SUB IntroScreen ()
DECLARE SUB Printmask (Row!, Column!, Number!, Places!)
DECLARE SUB CenterText (Column!, Text$)
DECLARE SUB PrintLabels (Row!, Column!, Text$)
DECLARE FUNCTION Voltage (Channel!, Gain!, Card!)
DECLARE FUNCTION Time ()
DECLARE FUNCTION Max (Numbera, Numberb)
DECLARE SUB Introparam ()
DECLARE SUB GetTime ()
DECLARE SUB CreateFile ()
DECLARE SUB Choice ()

DIM SHARED lv!
DIM SHARED hv!
DIM SHARED cf
DIM SHARED rpm
DIM SHARED glevel
DIM SHARED height
DIM SHARED AD1170(2)
DIM SHARED Multiplex(2)
DIM SHARED IntTime
DIM SHARED IntBit
```

```
DIM SHARED DAQFileName$
DIM SHARED InputFileName$
DIM SHARED TimeNext
DIM SHARED InitialTime
DIM SHARED DeltaTime
DIM SHARED TimeInterval
DIM SHARED StartDate$
DIM SHARED Clock

'Voltage reading from each channel
DIM SHARED LowVolt(6)
DIM SHARED Highvolt(6)


CLS
IntroScreen
Pause
Choice
Introparam
SetUpDataFile
Pause
SetUpScreen
InitialTime = TIMER
StartDate$ = DATE$
DO
 GetTime
 IF ((DeltaTime) / TimeInterval) > Clock THEN
  GetVoltage
  Estimrpm
  PrintEngData
  WriteToFile
  END IF
 LOOP WHILE INKEY$ <> CHR$(27)

 SUB Switch
 PRINT "Switch tachometer selector to position: ",
  SELECT CASE cf
  CASE IS = 16.2444
  PRINT "Up to 75 RPM"
  CASE IS = 46.0048
  PRINT "Up to 225 RPM"
 CASE IS = 72.7184
  PRINT "Up to 350 RPM"
 CASE IS = 119.682
 PRINT "Up to 400 RPM"
 END SELECT
```

```
 Pause
END SUB

SUB CenterText (Column, Text$)
 length = LEN(LTRIM$(RTRIM$(Text$)))
 start = (80 - length) / 2
 PrintLabels Column, start, Text$
END SUB

SUB Choice
 CLS
 PRINT
 PRINT
 INPUT "Do you want to create a parameter file (y/n)? ", a$
 IF a$ = "y" OR a$ = "Y" THEN
  CreateFile
  ELSE
   CLS
   PRINT
   PRINT
   INPUT "Enter parameter file name: ", InputFileName$
  END IF
END SUB

SUB CreateFile
 INPUT "Enter name of new parameter file: ", InputFileName$
 INPUT "Enter number of low voltage channels: ", a
 INPUT "Enter number of high voltage channels: ", b
 INPUT "Enter time interval between readings (sec): ", c
 PRINT "Integration time: "
 PRINT "  1. 1 ms"
 PRINT "  2. 10 ms"
 PRINT "  3. 16.67 ms"
 PRINT "  4. 20 ms"
 PRINT "  5. 100 ms"
 PRINT "  6. 166.7 ms"
 PRINT "  7. 300 ms"
 INPUT "Select integration time: ", selection
 d = 15 + selection
 cf = 100!
INPUT "Enter maximum RPM of your test: ", rp
IF rp <= 75 THEN
  cf = 16.2444
  ELSE
   IF rp > 75 AND rp <= 225 THEN
    cf = 46.0048
```

```
   ELSE
    IF rp > 225 AND rp <= 350 THEN
     cf = 72.7184
     ELSE
      cf = 119.682
     END IF
    END IF
  END IF
 INPUT "Do you wish to specify a particular radius to calculate the G-level (y/n)? ", a$
  IF a$ = "y" OR a$ = "Y" THEN
   INPUT "Enter height (in cm) from base of platform at which you want the G-level to be
calculated: ", height
   ELSE
    PRINT "The G-level will be calculated at the center of gravity of the platform."
    height = 8.255 'center of gravity
   END IF
  radin = 41.5 + 8.75 - height / 2.54
  radcm = 2.54 * radin
  PRINT "At high RPM, the radius at which the G-level will be calculated is: ", radin,
  PRINT " inches, or ",
  PRINT radcm,
  PRINT " cm"
 OPEN InputFileName$ FOR OUTPUT AS #1
 PRINT #1, a, b, c, d, cf
 CLOSE #1
  Pause
 END SUB

 SUB Estimrpm
  rpm = cf * Highvolt(1)
  glevel = (41.5 + 8.75 - height / 2.54) * rpm ^ 2
 END SUB

 SUB GetTime
  DeltaTime = Time - InitialTime
  TimeNext = -DeltaTime + Clock * TimeInterval
  IF TimeNext > 0 THEN
   Printmask 6, 63, TimeNext, 2
   ELSE Printmask 6, 63, 0, 2
   END IF
 END SUB

 SUB GetVoltage
  FOR i = 1 TO lv!
   LowVolt(i) = Voltage(i - 1, 10, 1)
   NEXT i
```

```
 FOR i = 1 TO hv!
  Highvolt(i) = Voltage(i - 1, 1, 2)
  NEXT i
END SUB

SUB Introparam
 CLS
 PRINT
 PRINT
 ReadFile InputFileName$
 IntBit = 15    'bit precision
 SetUpDAQ (1)
 SetUpDAQ (2)
 Switch
 CLS
 INPUT "Enter output data file name: ", DAQFileName$
 Clock = 0     'Initializes counter for data sampling
END SUB

SUB IntroScreen
 CLS
 CenterText 10, "Centrifuge Program"
 CenterText 11, "Version 2.0 - 3/20/98"
 CenterText 12, "Written by Kurt Sjoblom,"
 CenterText 13, "But Tremendously Improved by"
 CenterText 14, "Catalina Marulanda and Laurent Levy"
END SUB

FUNCTION Max (Numbera, Numberb)
 IF Numbera > Numberb THEN
  Max = Numbera
  ELSE Max = Numberb
  END IF
END FUNCTION

SUB Pause
 CenterText 24, "Press any key to continue..."
 DO
  LOOP UNTIL INKEY$ <> ""
END SUB

SUB PrintEngData
 FOR i = 1 TO lv!
  Printmask 2 + 2 * i, 12, LowVolt(i), 5
  NEXT i
 FOR i = 2 TO hv!
```

```
 Printmask 2 + 2 * i, 29, Highvolt(i), 5
 NEXT i
Printmask 18, 37, rpm, 4
Printmask 18, 40, glevel, 5
Printmask 4, 68, DeltaTime, 2   'prints elapsed time in seconds
'prints no. of readings written on data file
 LOCATE 2, 63
 PRINT Clock + 1
END SUB

SUB PrintLabels (Row, Column, Text$)
 LOCATE Row, Column
 PRINT Text$;
END SUB

SUB Printmask (Row, Column, Number, Places)
 Mask$ = "####."
 FOR i = 1 TO Places
  Mask$ = Mask$ + LTRIM$("#")
  NEXT i
 LOCATE Row, Column
 PRINT USING Mask$; Number;
END SUB

SUB ReadFile (File$)
 OPEN File$ FOR INPUT AS #1
 INPUT #1, lv!, hv!, TimeInterval, IntTime, cf
 'IntTime is the integration time of A/D converter
 'TimeInterval is the interval for data sampling in seconds
 CLOSE #1
END SUB

SUB SetUpDAQ (Card)
rountine to setup data aquisition card
routine to be run once
 768 = decimal I/O address of AD1170 A/D converter
 776(old), 772(new) = decimal I/O address of multiplexer channel selector
 15 = multiplexer connection to ground
'
 StrawberryTree = 6928
 Switch = StrawberryTree + 4
 Multiplex(Card) = 772 + (Card - 1) * 1024
 AD1170(Card) = Multiplex(Card) - 4
 'set default calibration time
 OUT AD1170(Card), 70: WAIT AD1170(Card), 1, 1
 'load data format into 2nd byte
```

```
 OUT AD1170(Card) + 1, IntBit
 'lock in the loaded data format
 OUT AD1170(Card), 48: WAIT AD1170(Card), 1, 1
 'begin background calibration
 OUT AD1170(Card), 176: WAIT AD1170(Card), 1, 1
END SUB

SUB SetUpDataFile
 OPEN DAQFileName$ FOR OUTPUT AS #1
 PRINT #1, "'Centrifuge Program'"
 PRINT #1, "'Version 2.00, 3/20/98'"
 PRINT #1, "'Written by Kurt Sjoblom'"
 PRINT #1, "'But Tremendously Improved by'"
 PRINT #1, "'Catalina Marulanda and Laurent Levy'"
 PRINT #1, DATE$, TIME$
 PRINT #1, "'Time'",
 FOR i = 1 TO lv!
  PRINT #1, "'LowCh " + LTRIM$(STR$(i - 1)) + "'",
  NEXT i
 FOR i = 1 TO hv!
  PRINT #1, "'HighCh " + LTRIM$(STR$(i - 1)) + "'",
  NEXT i
 PRINT #1,
 CLOSE #1
END SUB

SUB SetUpScreen
 SCREEN 10     '640x350 graphics
 CLS
 PrintLabels 2, 13, "Low Volt       High Volt"
 PrintLabels 3, 13, "--------       ---------"
 PrintLabels 4, 47, "Time at last reading:"
 PrintLabels 4, 76, "secs"
 PrintLabels 2, 47, "Last reading #:"
 PrintLabels 6, 47, "Next reading in:"
 PrintLabels 6, 71, "secs"
 FOR i = 1 TO Max(lv!, hv!)
  PrintLabels 2 + 2 * i, 5, "Ch " + (LTRIM$(STR$(i - 1)))
  NEXT i
 PrintLabels 18, 13, "RPM at last reading:"
 PrintLabels 20, 13, "G-level at last reading:"
END SUB

FUNCTION Time
 CurrentDate$ = DATE$
 IF StartDate$ = CurrentDate$ THEN
```

```
 Time = TIMER
 ELSE Time = 86400 + TIMER
 END IF
END FUNCTION

FUNCTION Voltage (Channel, Gain, Card)
 'Take regular readings
 OUT Multiplex(Card), Channel
 OUT AD1170(Card), IntTime: WAIT AD1170(Card), 1, 1
 'Convert to voltage
 LowByte = INP(AD1170(Card) + 1)
 MidByte = INP(AD1170(Card) + 2)
 HiByte = INP(AD1170(Card) + 3)
 Counts = LowByte + 256 * MidByte + 65536 * HiByte
 'reenable background calibration
 OUT AD1170(Card), 176: WAIT AD1170(Card), 1, 1
 Voltage = (Counts * 10 / 2 ^ (IntBit + 7) - 5) / Gain
END FUNCTION

SUB WriteToFile
 OPEN DAQFileName$ FOR APPEND AS #1
 PRINT #1, DeltaTime,
 FOR i = 1 TO lv!
  PRINT #1, LowVolt(i),
  NEXT i
 PRINT #1, rpm,
 FOR i = 2 TO hv!
  PRINT #1, Highvolt(i),
  NEXT i
 PRINT #1,
 CLOSE #1
 Clock = Clock + 1
END SUB
```

APPENDIX B

CALIBRATION DATA

B.1.PRESSURE TRANSDUCERS

B.1.1. DI 2194

Model: Data Instruments 2194

Capacity: 25 psi

Calibration Factor: -1254.71 psi/V/V_{in}

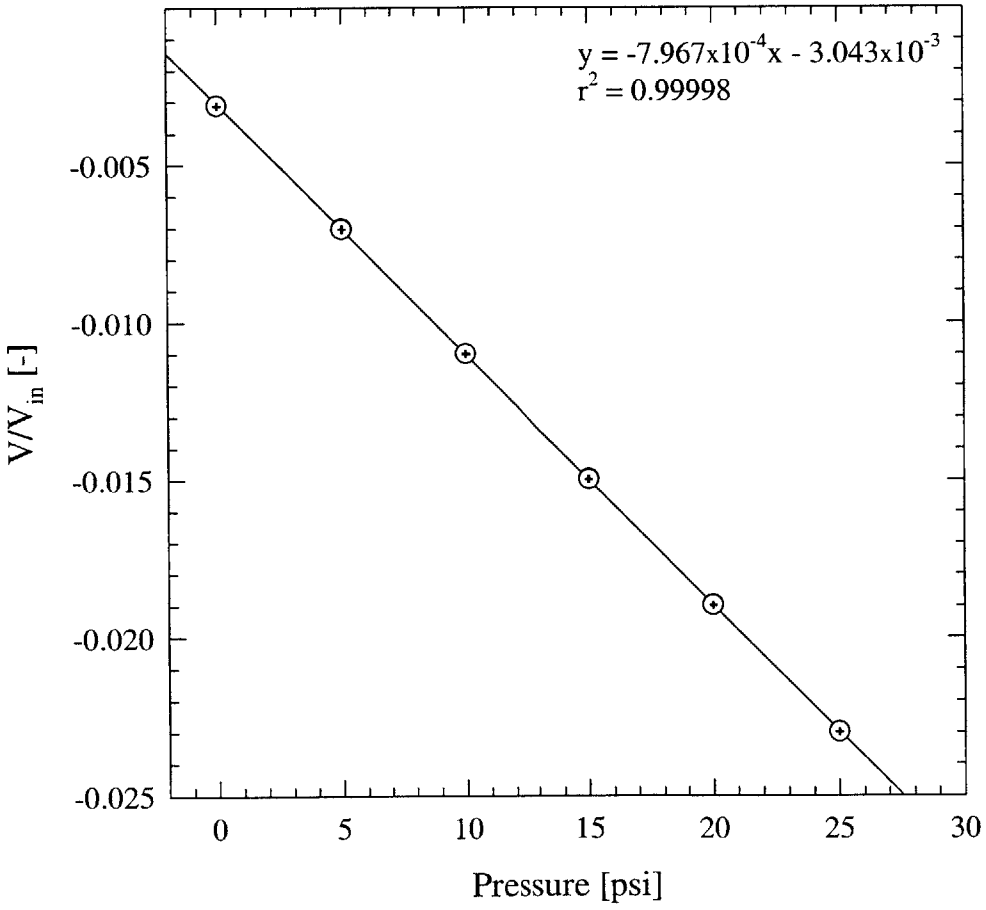

B.1.2. DI 2394

Model:	Data Instruments 2394
Capacity:	25 psi
Calibration Factor:	1264.22 psi/V/Vin

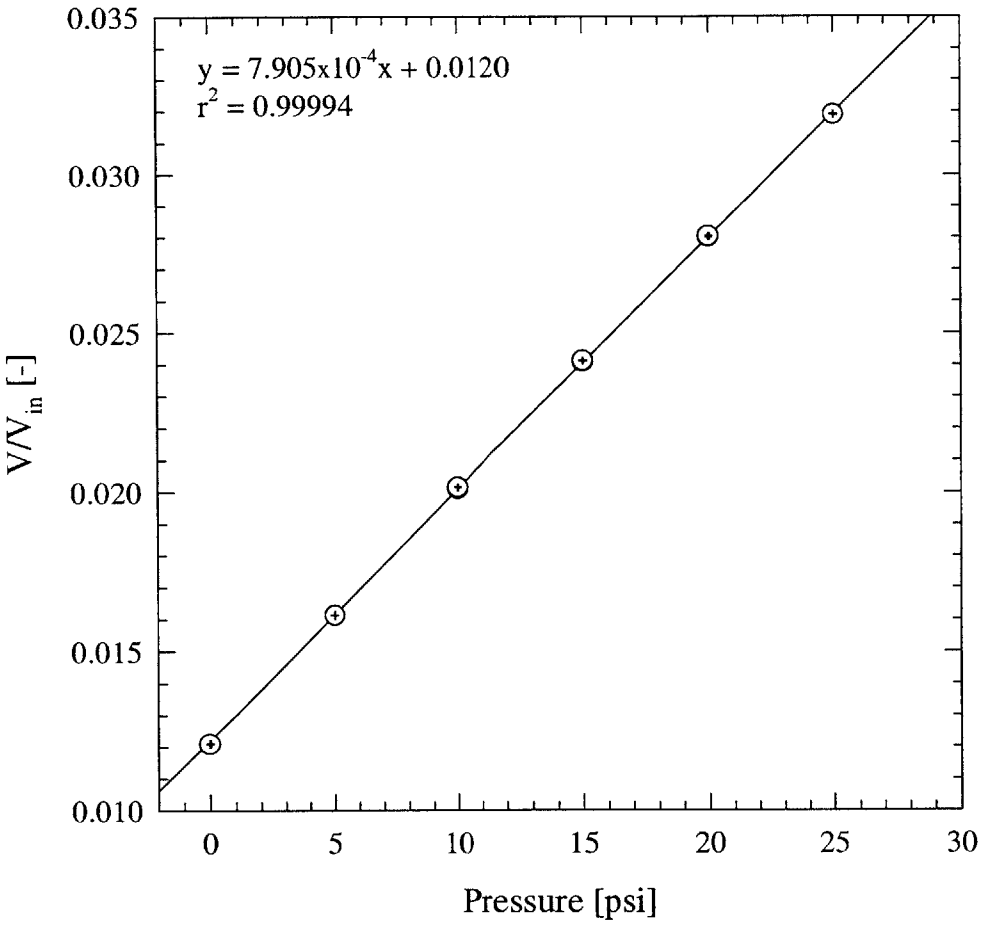

B.1.3. DI A500

Model:	Data Instruments A500
Capacity:	50 psi
Calibration Factor:	-2525.26 psi/V/V_{in}

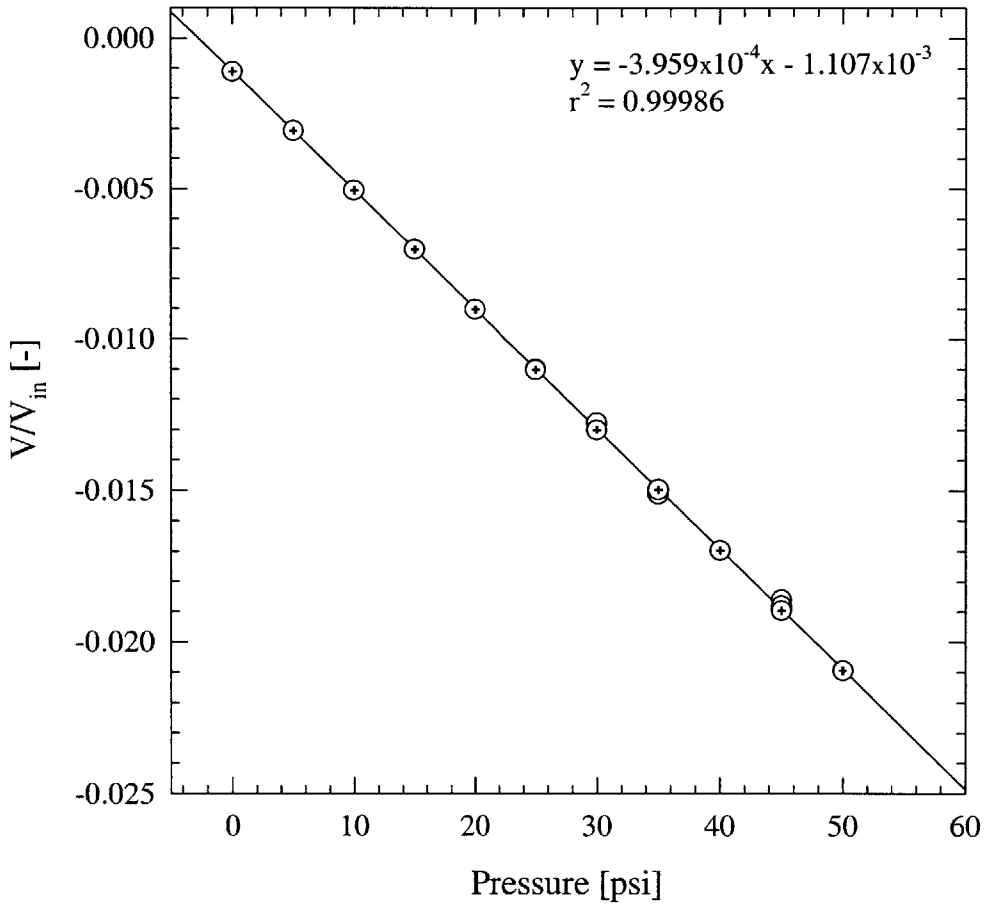

B.2. PRESSURE VOLUME CONTROLLERS

B.2.1.Low *g*-levels

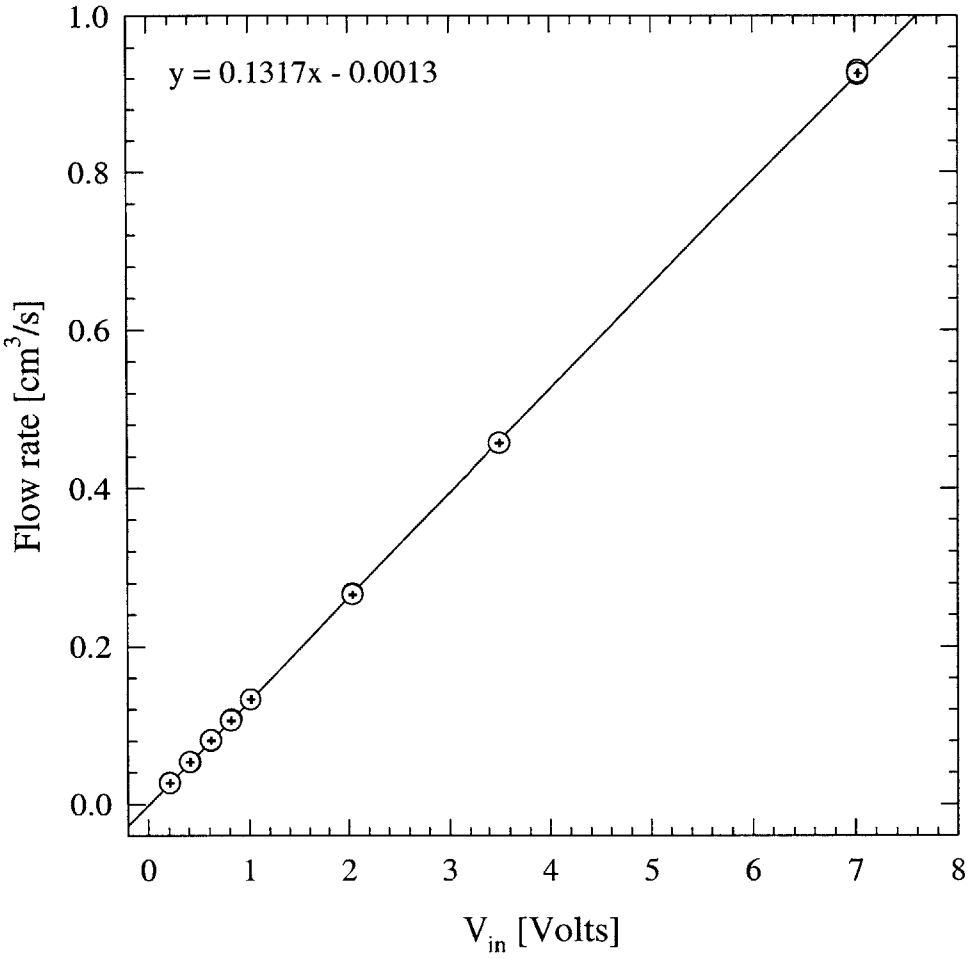

B.2.2 High *g*-levels

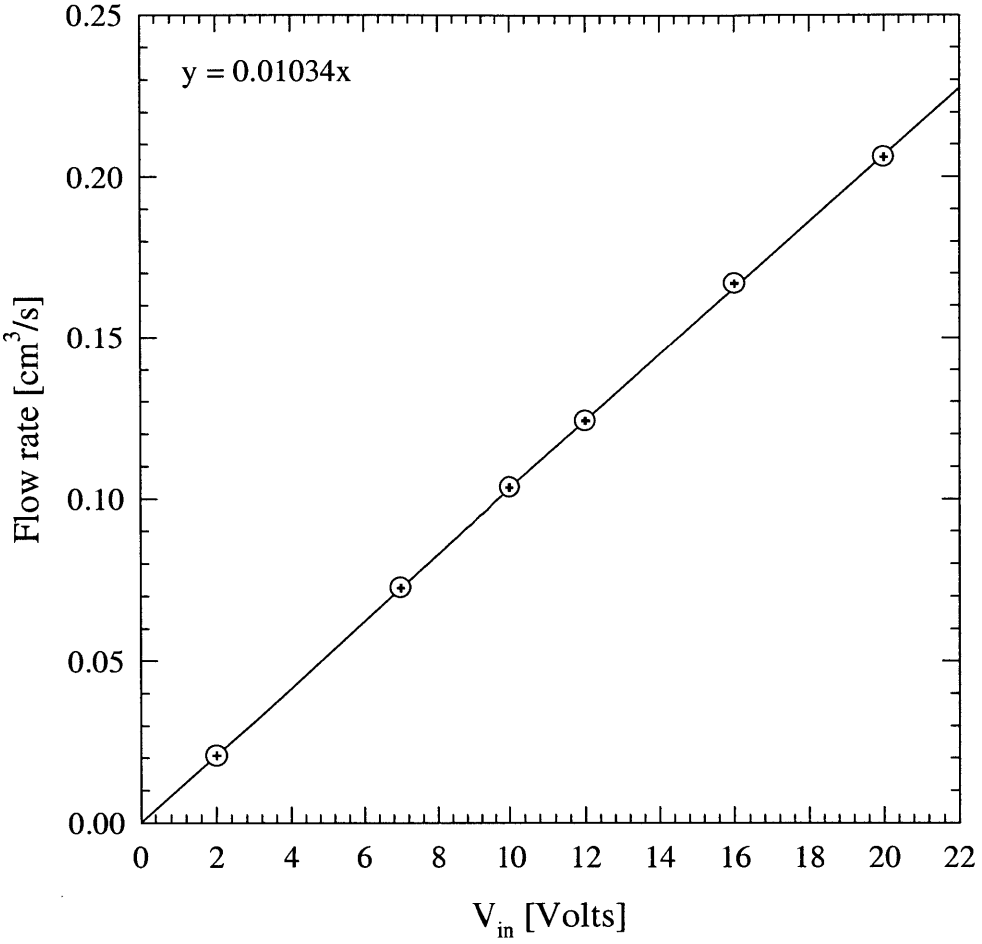

B.3. FLOW METER

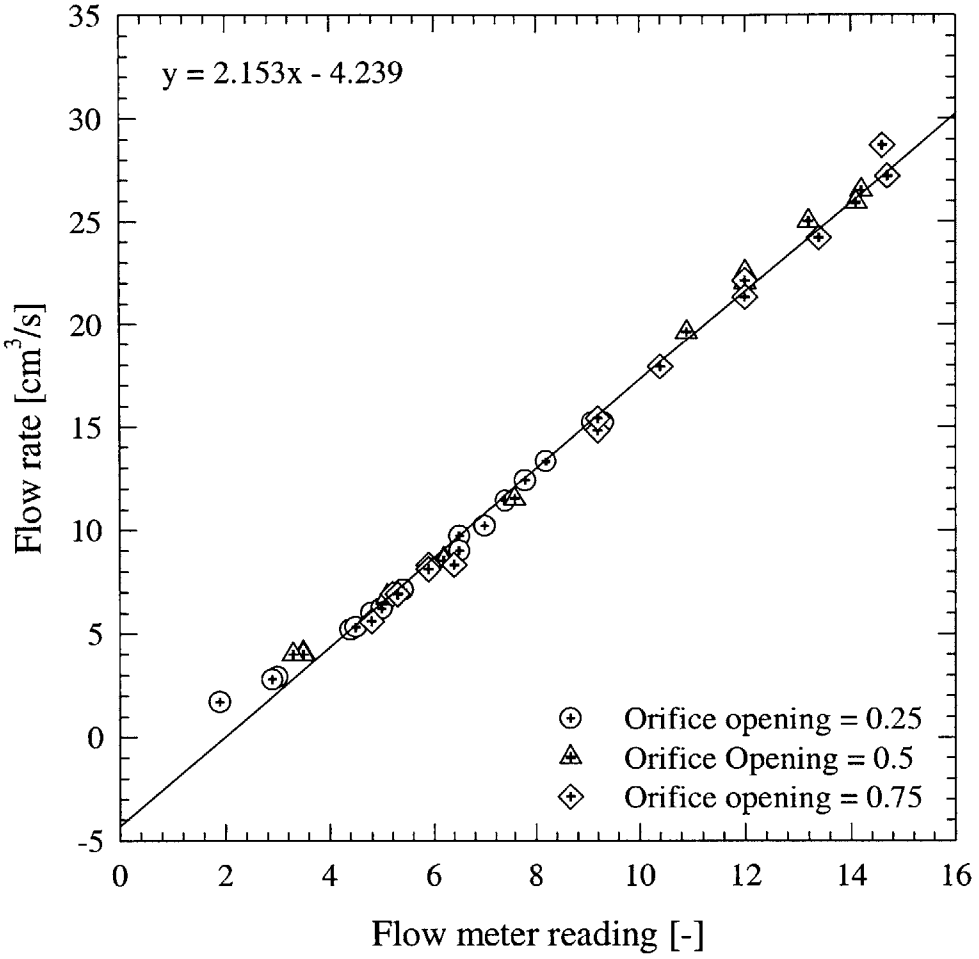

APPENDIX C

TESTING RECORDS

A large majority of the conclusions presented in this thesis resulted from observation of videotaped air sparging experiments. Although many summary pictures captured from those tapes were included in the body of the thesis, the work is not complete without the recorded experiments. Conclusions regarding propagation of the air front in particular, can only be fully put into context after watching the tapes.

Twenty VHS tapes contain the extent of the experiments conducted, many of which were not explicitly presented in the thesis. Experiments were individually labeled and dated on the tapes. The following tables list all the experiments conducted by type, provides a brief description of the general characteristics of each test, and includes the number of the tape where the experiment was recorded.

Table C-1 *Summary of Free field experiments (CP: Constant Pressure injection test; CFR: Constant Flow Rate injection test; FF: Free Field experiment; IL: Immersion Liquid; Gly.: Glycerol)*

Test Name	Injectn. type	Injector	Pore Fluid	Target *g*-level	Tape
FFL10i1, i2, i3, i4, i5, i6	CP	MPI #1, 2, 3 and SPI #1, 2, 3	IL	10	II, VI, and VII
FFL20i1, i2, i3, i4, i5, i6	CP	MPI #1, 2, 3 and SPI #1, 2, 3	IL	20	II, VI, and VII
FFL30i1, i2, i3, i4, i5, i6	CP	MPI #1, 2, 3 and SPI #1, 2, 3	IL	30	II, VI, and VII
FFL40i1, i2, i3, i4, i5, i6	CP	MPI #1, 2, 3 and SPI #1, 2, 3	IL	40	II, VI, and VII
FFL50i1, i2, i3, i4, i5, i6	CP	MPI #1, 2, 3 and SPI #1, 2, 3	IL	50	II, VI, and VII
FFL60i1, i2, i3, i4, i5, i6	CP	MPI #1, 2, 3 and SPI #1, 2, 3	IL	60	II, VI, and VII
FFL70i1, i2, i3, i4, i5, i6	CP	MPI #1, 2, 3 and SPI #1, 2, 3	IL	70	II, VI, and VII
FFL80i1, i2, i3, i4, i5, i6	CP	MPI #1, 2, 3 and SPI #1, 2, 3	IL	80	II, VI, and VII
FFL90i1, i2, i3, i4, i5, i6	CP	MPI #1, 2, 3 and SPI #1, 2, 3	IL	90	II, VI, and VII
FFL100i1, i2, i3, i4, i5, i6	CP	MPI #1, 2, 3 and SPI #1, 2, 3	IL	100	II, VI, and VII
FFL110i1, i2, i3, i4, i5, i6	CP	MPI #1, 2, 3 and SPI #1, 2, 3	IL	110	II, VI, and VII
FFL120i1, i2, i3, i4, i5, i6	CP	MPI #1, 2, 3 and SPI #1, 2, 3	IL	120	II, VI, and VII
FFL130i1, i2, i3, i4, i5, i6	CP	MPI #1, 2, 3 and SPI #1, 2, 3	IL	130	II, VI, and VII
FFL140i1, i2, i3, i4, i5, i6	CP	MPI #1, 2, 3 and SPI #1, 2, 3	IL	140	II, VI, and VII
FFG05i1, i2, i3, i4, i5, i6	CP	MPI #1, 2, 3 and SPI #1, 2, 3	Gly	5	III, V, and VI
FFG10i1, i2, i3, i4, i5, i6	CP	MPI #1, 2, 3 and SPI #1, 2, 3	Gly	10	III, V, and VI
FFG20i1, i2, i3, i4, i5, i6	CP	MPI #1, 2, 3 and SPI #1, 2, 3	Gly	20	III, V, and VI
FFG25i1, i2, i3, i4, i5, i6	CP	MPI #1, 2, 3 and SPI #1, 2, 3	Gly	25	III, V, and VI
FFG30i1, i2, i3, i4, i5, i6	CP	MPI #1, 2, 3 and SPI #1, 2, 3	Gly	30	III, V, and VI
FFG40i1, i2, i3, i4, i5, i6	CP	MPI #1, 2, 3 and SPI #1, 2, 3	Gly	40	III, V, and VI
FFG50i1, i2, i3, i4, i5, i6	CP	MPI #1, 2, 3 and SPI #1, 2, 3	Gly	50	III, V, and VI
FFG60i1, i2, i3, i4, i5, i6	CP	MPI #1, 2, 3 and SPI #1, 2, 3	Gly	60	III, V, and VI
FFG70i1, i2, i3, i4, i5, i6	CP	MPI #1, 2, 3 and SPI #1, 2, 3	Gly	70	III, V, and VI
FFG80i1, i2, i3, i4, i5, i6	CP	MPI #1, 2, 3 and SPI #1, 2, 3	Gly	80	III, V, and VI
FFG90i1, i2, i3, i4, i5, i6	CP	MPI #1, 2, 3 and SPI #1, 2, 3	Gly	90	III, V, and VI
FFG100i1, i2, i3, i4, i5, i6	CP	MPI #1, 2, 3 and SPI #1, 2, 3	Gly	100	III, V, and VI

Table C-2 *Constant pressure injection experiments (CP: Constant Pressure injection test; IL: Immersion Liquid; Gly.: Glycerol; Wat.: Water; MS: Medium Sand; MSF: Medium Sand with Fines)*

Test Name	Injection type	Injector	Pore Fluid	Soil type	Target *g*-level	Tape
LL01i1	CP	MPI #1	IL	MS	1	I
LL10i1	CP	MPI #1	IL	MS	10	I
LL20i1	CP	MPI #1	IL	MS	20	I
LL30i1	CP	MPI #1	IL	MS	30	I
LL40i1	CP	MPI #1	IL	MS	40	I
LL50i1	CP	MPI #1	IL	MS	50	I
LL60i1	CP	MPI #1	IL	MS	60	I
LL70i1	CP	MPI #1	IL	MS	70	I
LL80i1	CP	MPI #1	IL	MS	80	II
LL90i1	CP	MPI #1	IL	MS	90	I
LL100i1	CP	MPI #1	IL	MS	100	I
LL110i1	CP	MPI #1	IL	MS	110	I
LL130i1	CP	MPI #1	IL	MS	130	I
LL150i1	CP	MPI #1	IL	MS	150	I
2LL1i1	CP	MPI #1	IL	MSF	1	IX
2LL10i1	CP	MPI #1	IL	MSF	10	IX
2LL20i1	CP	MPI #1	IL	MSF	20	IX
2LL30i1	CP	MPI #1	IL	MSF	30	IX
2LL40i1	CP	MPI #1	IL	MSF	40	IX
2LL50i1	CP	MPI #1	IL	MSF	50	IX
2LL60i1	CP	MPI #1	IL	MSF	60	IX
2LL70i1	CP	MPI #1	IL	MSF	70	IX
2LL80i1	CP	MPI #1	IL	MSF	80	IX
2LL90i1	CP	MPI #1	IL	MSF	90	IX
2LL100i1	CP	MPI #1	IL	MSF	100	IX

Table C-2 (ctd.) *Constant pressure injection experiments (CP: Constant Pressure injection test; IL: Immersion Liquid; Gly.: Glycerol; Wat.: Water; MS: Medium Sand; MSF: Medium Sand with Fines)*

Test Name	Injection type	Injector	Pore Fluid	Soil type	Target *g*-level	Tape
LL1i2	CP	MPI #2	IL	MS	1	VIII
LL10i2	CP	MPI #2	IL	MS	10	VIII
LL20i2	CP	MPI #2	IL	MS	20	VIII
LL30i2	CP	MPI #2	IL	MS	30	VIII
LL40i2	CP	MPI #2	IL	MS	40	VIII
LL50i2	CP	MPI #2	IL	MS	50	VIII
LL60i2	CP	MPI #2	IL	MS	60	VIII
LL70i2	CP	MPI #2	IL	MS	70	VIII
LL80i2	CP	MPI #2	IL	MS	80	VIII
LL90i2	CP	MPI #2	IL	MS	90	VIII
LL100i2	CP	MPI #2	IL	MS	100	VIII
2LL1i2	CP	MPI #3	IL	MSF	1	X
2LL10i2	CP	MPI #3	IL	MSF	10	X
2LL20i2	CP	MPI #3	IL	MSF	20	X
2LL30i2	CP	MPI #3	IL	MSF	30	X
2LL40i2	CP	MPI #3	IL	MSF	40	X
2LL50i2	CP	MPI #3	IL	MSF	50	X
2LL60i2	CP	MPI #3	IL	MSF	60	X
2LL70i2	CP	MPI #3	IL	MSF	70	X
2LL80i2	CP	MPI #3	IL	MSF	80	X
2LL90i2	CP	MPI #3	IL	MSF	90	X
2LL100i2	CP	MPI #3	IL	MSF	100	X
2LL1i3	CP	MPI #3	IL	MS	1	X
2LL10i3	CP	MPI #3	IL	MS	10	X
2LL20i3	CP	MPI #3	IL	MS	20	X

Table C-2 (ctd.) *Constant pressure injection experiments (CP: Constant Pressure injection test; IL: Immersion Liquid; Gly.: Glycerol; Wat.: Water; MS: Medium Sand; MSF: Medium Sand with Fines)*

Test Name	Injection type	Injector	Pore Fluid	Soil type	Target *g*-level	Tape
2LL30i3	CP	MPI #3	IL	MS	30	X
2LL40i3	CP	MPI #3	IL	MS	40	X
2LL50i3	CP	MPI #3	IL	MS	50	X
2LL60i3	CP	MPI #3	IL	MS	60	X
2LL70i3	CP	MPI #3	IL	MS	70	X
2LL80i3	CP	MPI #3	IL	MS	80	X
2LL90i3	CP	MPI #3	IL	MS	90	X
2LL100i3	CP	MPI #3	IL	MS	100	X
LL1i4	CP	SPI #1	IL	MS	1	VIII
LL10i4	CP	SPI #1	IL	MS	10	VIII
LL20i4	CP	SPI #1	IL	MS	20	VIII
LL30i4	CP	SPI #1	IL	MS	30	VIII
LL40i4	CP	SPI #1	IL	MS	40	VIII
LL50i4	CP	SPI #1	IL	MS	50	VIII
LL60i4	CP	SPI #1	IL	MS	60	VIII
LL70i4	CP	SPI #1	IL	MS	70	VIII
LL80i4	CP	SPI #1	IL	MS	80	VIII
LL90i4	CP	SPI #1	IL	MS	90	VIII
LL100i4	CP	SPI #1	IL	MS	100	VIII
LL1i5	CP	SPI #2	IL	MS	1	IX
LL10i5	CP	SPI #2	IL	MS	10	IX
LL20i5	CP	SPI #2	IL	MS	20	IX
LL30i5	CP	SPI #2	IL	MS	30	IX
LL40i5	CP	SPI #2	IL	MS	40	IX
LL50i5	CP	SPI #2	IL	MS	50	IX

Table C-2 (ctd.) *Constant pressure injection experiments (CP: Constant Pressure injection test; IL: Immersion Liquid; Gly.: Glycerol; Wat.: Water; MS: Medium Sand; MSF: Medium Sand with Fines)*

Test Name	Injection type	Injector	Pore Fluid	Soil type	Target *g*-level	Tape
LL60i5	CP	SPI #2	IL	MS	60	IX
LL70i5	CP	SPI #2	IL	MS	70	IX
LL80i5	CP	SPI #2	IL	MS	80	IX
LL90i5	CP	SPI #2	IL	MS	90	IX
LL100i5	CP	SPI #2	IL	MS	100	IX
LL1i6	CP	SPI #3	IL	MS	1	VIII
LL10i6	CP	SPI #3	IL	MS	10	VIII
LL20i6	CP	SPI #3	IL	MS	20	VIII
LL30i6	CP	SPI #3	IL	MS	30	VIII
LL40i6	CP	SPI #3	IL	MS	40	VIII
LL50i6	CP	SPI #3	IL	MS	50	VIII
LL60i6	CP	SPI #3	IL	MS	60	VIII
LL70i6	CP	SPI #3	IL	MS	70	VIII
LL80i6	CP	SPI #3	IL	MS	80	VIII
LL90i6	CP	SPI #3	IL	MS	90	VIII
LL100i6	CP	SPI #3	IL	MS	100	VIII
GLY05i1	CP	MPI #1	Gly	MS	5	III
GLY10i1	CP	MPI #1	Gly	MS	10	III
GLY20i1	CP	MPI #1	Gly	MS	20	III
GLY30i1	CP	MPI #1	Gly	MS	30	III
GLY40i1	CP	MPI #1	Gly	MS	40	III
GLY45i1	CP	MPI #1	Gly	MS	45	III
GLY50i1	CP	MPI #1	Gly	MS	50	III
GLY55i1	CP	MPI #1	Gly	MS	55	III
GLY60i1	CP	MPI #1	Gly	MS	60	III

Table C-2 (ctd.) *Constant pressure injection experiments (CP: Constant Pressure injection test; IL: Immersion Liquid; Gly.: Glycerol; Wat.: Water; MS: Medium Sand; MSF: Medium Sand with Fines)*

Test Name	Injection type	Injector	Pore Fluid	Soil type	Target *g*-level	Tape
GLY70i1	CP	MPI #1	Gly	MS	70	III
GLY80i1	CP	MPI #1	Gly	MS	80	III
GLY90i1	CP	MPI #1	Gly	MS	90	III
WAT10i1	CP	MPI #1	Wat	GB	10	IV
WAT20i1	CP	MPI #1	Wat	GB	20	IV
WAT30i1	CP	MPI #1	Wat	GB	30	IV
WAT40i1	CP	MPI #1	Wat	GB	40	IV
WAT50i1	CP	MPI #1	Wat	GB	50	IV
WAT60i1	CP	MPI #1	Wat	GB	60	IV
WAT70i1	CP	MPI #1	Wat	GB	70	IV
WAT80i1	CP	MPI #1	Wat	GB	80	IV
WAT100i1	CP	MPI #1	Wat	GB	100	IV

Table C-3 *Constant flow rate injection experiments (CFR: Constant Flow Rate injection test; IL: Immersion Liquid; Gly.: Glycerol; MS: Medium Sand; GB: Glass Beads)*

Test Name	**Injection type**	**Injector**	**Pore Fluid**	**Soil type**	**Flow Rate [cm^3/s]**	**Target level**	***g*- Tape**
LLsl2i1	CFR	MPI #1	IL	MS	0.26	1	XVI
LLslwi1	CFR	MPI #1	IL	MS	0.66	1	XVI
LLmd3i1	CFR	MPI #1	IL	MS	1.05	1	XVI
LLmedi1	CFR	MPI #1	IL	MS	1.58	1	XVI
LLmd2i1	CFR	MPI #1	IL	MS	2.11	1	XVI
LLfasi1	CFR	MPI #1	IL	MS	2.63	1	XVI
LL1slwi1	CFR	MPI #1	IL	MS	0.67	1	XVII
LL3slwi1	CFR	MPI #1	IL	MS	0.67	3	XVII
LL6slwi1	CFR	MPI #1	IL	MS	0.67	6	XVII
LL9slwi1	CFR	MPI #1	IL	MS	0.67	9	XVII
LL12slwi1	CFR	MPI #1	IL	MS	0.67	12	XVII
LL15slwi1	CFR	MPI #1	IL	MS	0.67	15	XVII
LL30slwi1	CFR	MPI #1	IL	MS	0.67	30	XVII
LL30md2i1	CFR	MPI #1	IL	MS	1.29	30	XVII
LL70slwi1	CFR	MPI #1	IL	MS	0.67	70	XVII
LL70md2i1	CFR	MPI #1	IL	MS	1.29	70	XVII
LL100slwi1	CFR	MPI #1	IL	MS	0.67	100	XVII
LL100md2i1	CFR	MPI #1	IL	MS	1.29	100	XVII
LLsl2i2	CFR	MPI #2	IL	MS	0.26	1	XVI
LLslwi2	CFR	MPI #2	IL	MS	0.66	1	XVI
LLmd3i2	CFR	MPI #2	IL	MS	1.05	1	XVI
LLmedi2	CFR	MPI #2	IL	MS	1.58	1	XVI
LLmd2i2	CFR	MPI #2	IL	MS	2.11	1	XVI
LLfasi2	CFR	MPI #2	IL	MS	2.63	1	XVII

Table C-3 (ctd.) *Constant flow rate injection experiments (CFR: Constant Flow Rate injection test; IL: Immersion Liquid; Gly.: Glycerol; MS: Medium Sand; GB: Glass Beads)*

LLsl2i3	CFR	MPI #3	IL	MS	0.26	1	XVII
LLslwi3	CFR	MPI #3	IL	MS	0.66	1	XVII
LLmd3i3	CFR	MPI #3	IL	MS	1.05	1	XVII
LLmedi3	CFR	MPI #3	IL	MS	1.58	1	XVII
LLmd2i3	CFR	MPI #3	IL	MS	2.11	1	XVII
10gslwi3	CFR	MPI #3	IL	MS	0.67	10	XVII
20gslwi3	CFR	MPI #3	IL	MS	0.67	20	XVII
30gslwi3	CFR	MPI #3	IL	MS	0.67	30	XVII
70gslwi3	CFR	MPI #3	IL	MS	0.67	70	XVII
100gslwi3	CFR	MPI #3	IL	MS	0.67	100	XVII
30gmd3i3	CFR	MPI #3	IL	MS	1.05	30	XVII
70gmd3i3	CFR	MPI #3	IL	MS	1.05	70	XVII
100gmd3i3	CFR	MPI #3	IL	MS	1.05	100	XVII
20gmd2i3	CFR	MPI #3	IL	MS	1.29	20	XVII
30gmd2i3	CFR	MPI #3	IL	MS	1.29	30	XVII
LLsl2i4	CFR	SPI #1	IL	MS	0.26	1	XV
LLslwi4	CFR	SPI #1	IL	MS	0.66	1	XV
LLmd3i4	CFR	SPI #1	IL	MS	1.05	1	XV
LLmedi4	CFR	SPI #1	IL	MS	1.58	1	XV
LLmd2i4	CFR	SPI #1	IL	MS	2.11	1	XV
LLfasi4	CFR	SPI #1	IL	MS	2.63	1	XV
LLsl2i5	CFR	SPI #2	IL	MS	0.26	1	XV
LLslwi5	CFR	SPI #2	IL	MS	0.66	1	XV
LLmd3i5	CFR	SPI #2	IL	MS	1.05	1	XV

Table C-3 (ctd.) *Constant flow rate injection experiments (CFR: Constant Flow Rate injection test; IL: Immersion Liquid; Gly.: Glycerol; MS: Medium Sand; GB: Glass Beads)*

LLmedi5	CFR	SPI #2	IL	MS	1.58	1	XV
LLmd2i5	CFR	SPI #2	IL	MS	2.11	1	XV
LLfasi5	CFR	SPI #2	IL	MS	2.63	1	XV
LLsl2i6	CFR	SPI #3	IL	MS	0.26	1	XV
LLslwi6	CFR	SPI #3	IL	MS	0.66	1	XV
LLmd3i6	CFR	SPI #3	IL	MS	1.05	1	XV
LLmedi6	CFR	SPI #3	IL	MS	1.58	1	XV
LLmd2i6	CFR	SPI #3	IL	MS	2.11	1	XV
LLfasi6	CFR	SPI #3	IL	MS	2.63	1	XV
LL1gBDi3s	CFR	MPI #3	IL	GB	0.67	1	XVIII
LL1gBDi3f	CFR	MPI #3	IL	GB	1.29	1	XVIII
LL3gBDi3s	CFR	MPI #3	IL	GB	0.67	3	XVIII
LL3gBDi3f	CFR	MPI #3	IL	GB	1.29	3	XVIII
LL6gBDi3s	CFR	MPI #3	IL	GB	0.67	6	XVIII
LL12gBDi3s	CFR	MPI #3	IL	GB	0.67	12	XVIII
LL20gBDi3s	CFR	MPI #3	IL	GB	0.67	20	XVIII
Gsl2i1	CFR	MPI #1	Gly	MS	0.26	1	XIV
Gslwi1	CFR	MPI #1	Gly	MS	0.66	1	XIV
Gmed2i1	CFR	MPI #1	Gly	MS	1.05	1	XIV
Gmedi1	CFR	MPI #1	Gly	MS	1.58	1	XIV
Gfasi1	CFR	MPI #1	Gly	MS	2.63	1	XIV
Gsl2i2	CFR	MPI #2	Gly	MS	0.26	1	XIII
Gslwi2	CFR	MPI #2	Gly	MS	0.66	1	XIII
Gmed2i2	CFR	MPI #2	Gly	MS	1.05	1	XIII
Gmedi2	CFR	MPI #2	Gly	MS	1.58	1	XIII
Gfasi2	CFR	MPI #2	Gly	MS	2.63	1	XIII

Table C-3 (ctd.) *Constant flow rate injection experiments (CFR: Constant Flow Rate injection test; IL: Immersion Liquid; Gly.: Glycerol; MS: Medium Sand; GB: Glass Beads)*

Gslwi3	CFR	MPI #3	Gly	MS	0.66	1	XIII
Gmedi3	CFR	MPI #3	Gly	MS	1.58	1	XIII
Gfasi3	CFR	MPI #3	Gly	MS	2.63	1	XIII
Gsl2i5	CFR	SPI #2	Gly	MS	0.26	1	XIV
Gslwi5	CFR	SPI #2	Gly	MS	0.66	1	XIV
Gmed2i5	CFR	SPI #2	Gly	MS	1.05	1	XIV
Gmedi5	CFR	SPI #2	Gly	MS	1.58	1	XIV
Gfasi5	CFR	SPI #2	Gly	MS	2.63	1	XIV
Gsl2i6	CFR	SPI #3	Gly	MS	0.26	1	XIV
Gslwi6	CFR	SPI #3	Gly	MS	0.66	1	XIV
Gmed2i6	CFR	SPI #3	Gly	MS	1.05	1	XIV
Gmedi6	CFR	SPI #3	Gly	MS	1.58	1	XIV
Gfasi6	CFR	SPI #3	Gly	MS	2.63	1	XIV

APPENDIX D

ADDITIONAL EXPERIMENTAL RESULTS

This Appendix includes additional sequences of images of air propagation through saturated porous media, collected during the experimental phase of this investigation, which were not included in Chapter 8. They are included to provide additional documentation on the propagation behavior of injected air though soils.

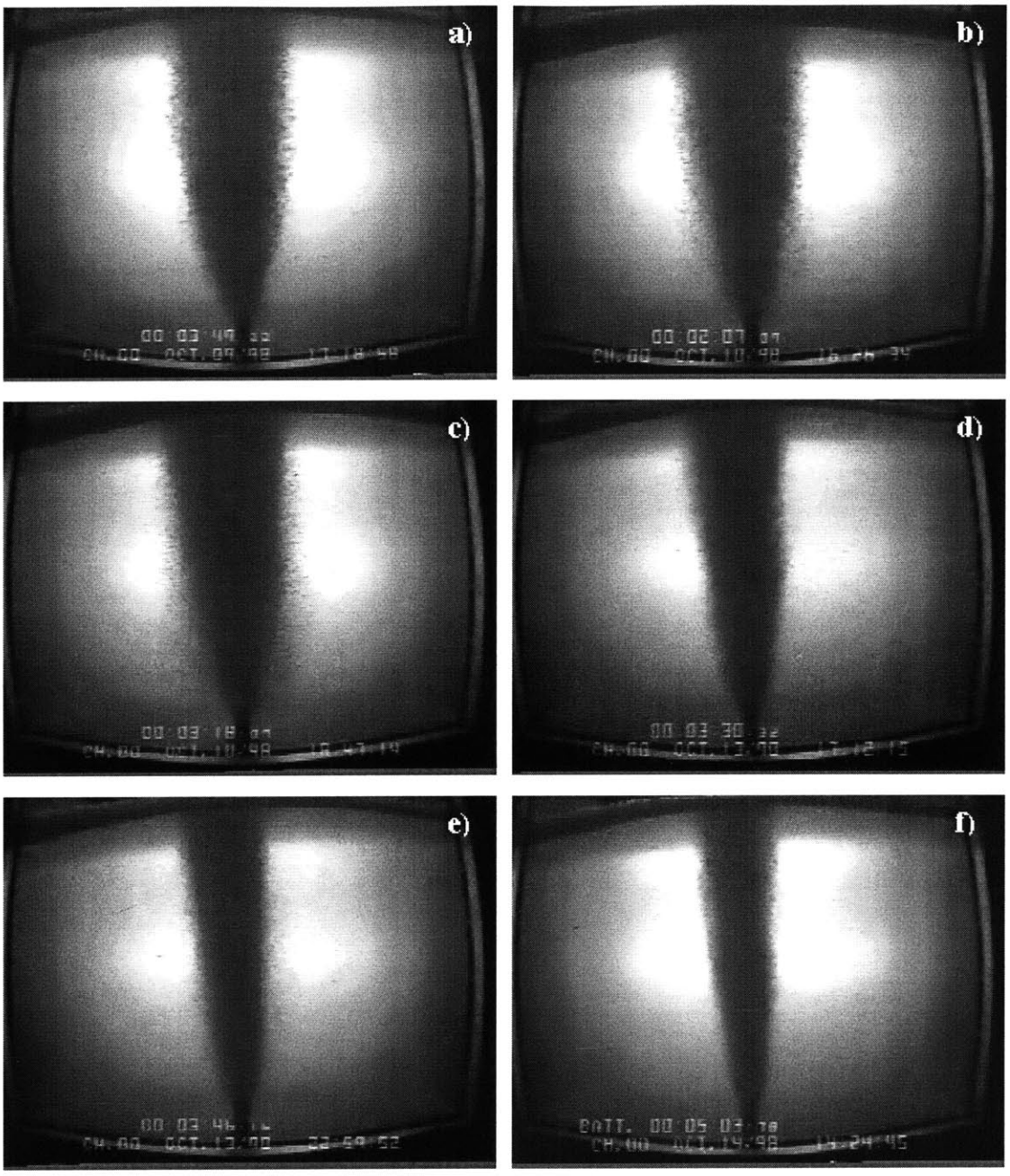

Figure D-1 *Air plumes obtained at increasing g-levels following injection of air into porous media saturated with immersion liquid - Injector MPI #2: a) 20-g; b) 30-g; c) 40-g; d) 60-g; e) 80-g; f) 100-g.*

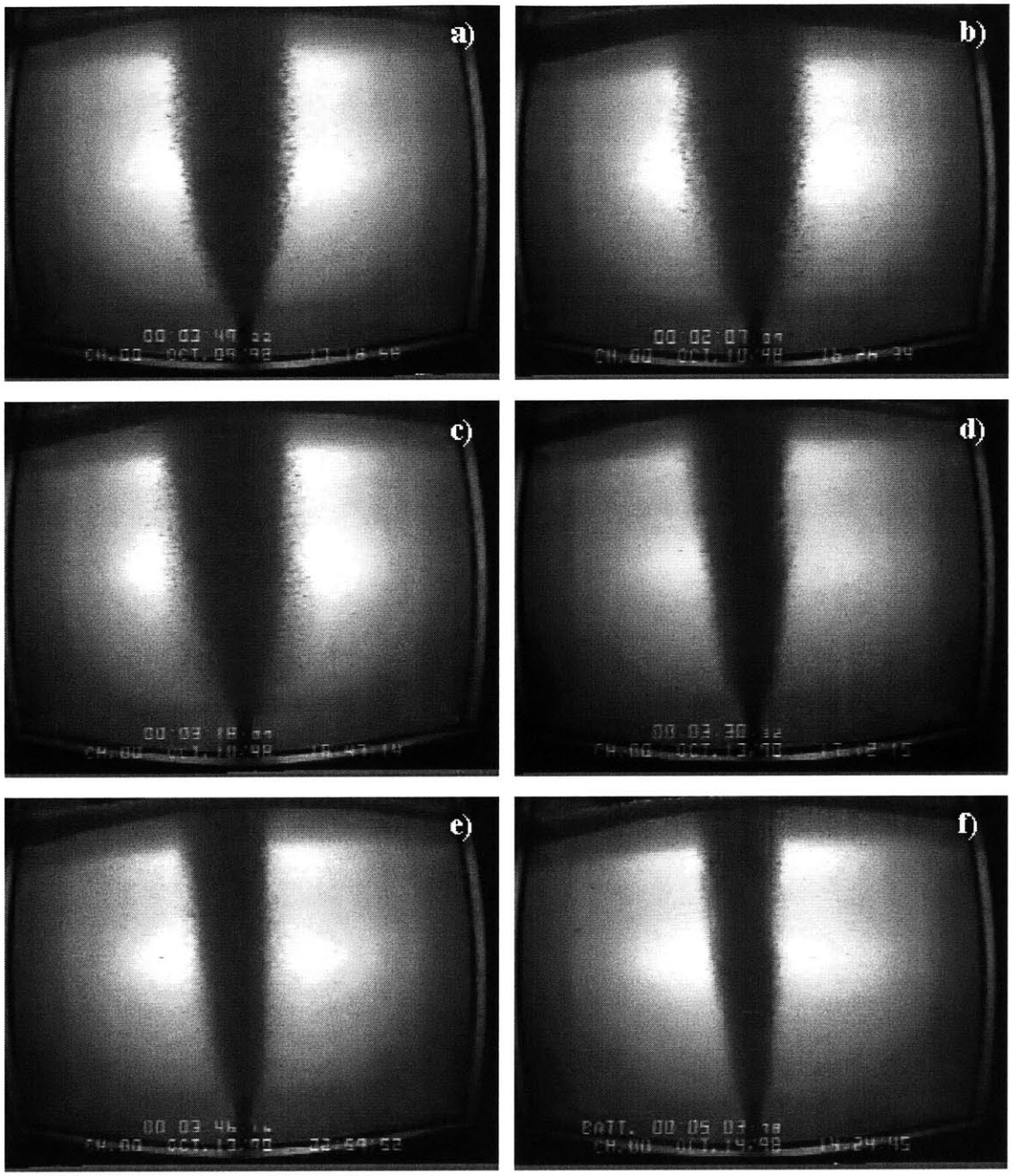

Figure D-2 *Air plumes obtained at increasing g-levels following injection of air into porous media saturated with immersion liquid - Injector MPI #3: a) 20-g; b) 30-g; c) 40-g; d) 60-g; e) 80-g; f) 100-g.*

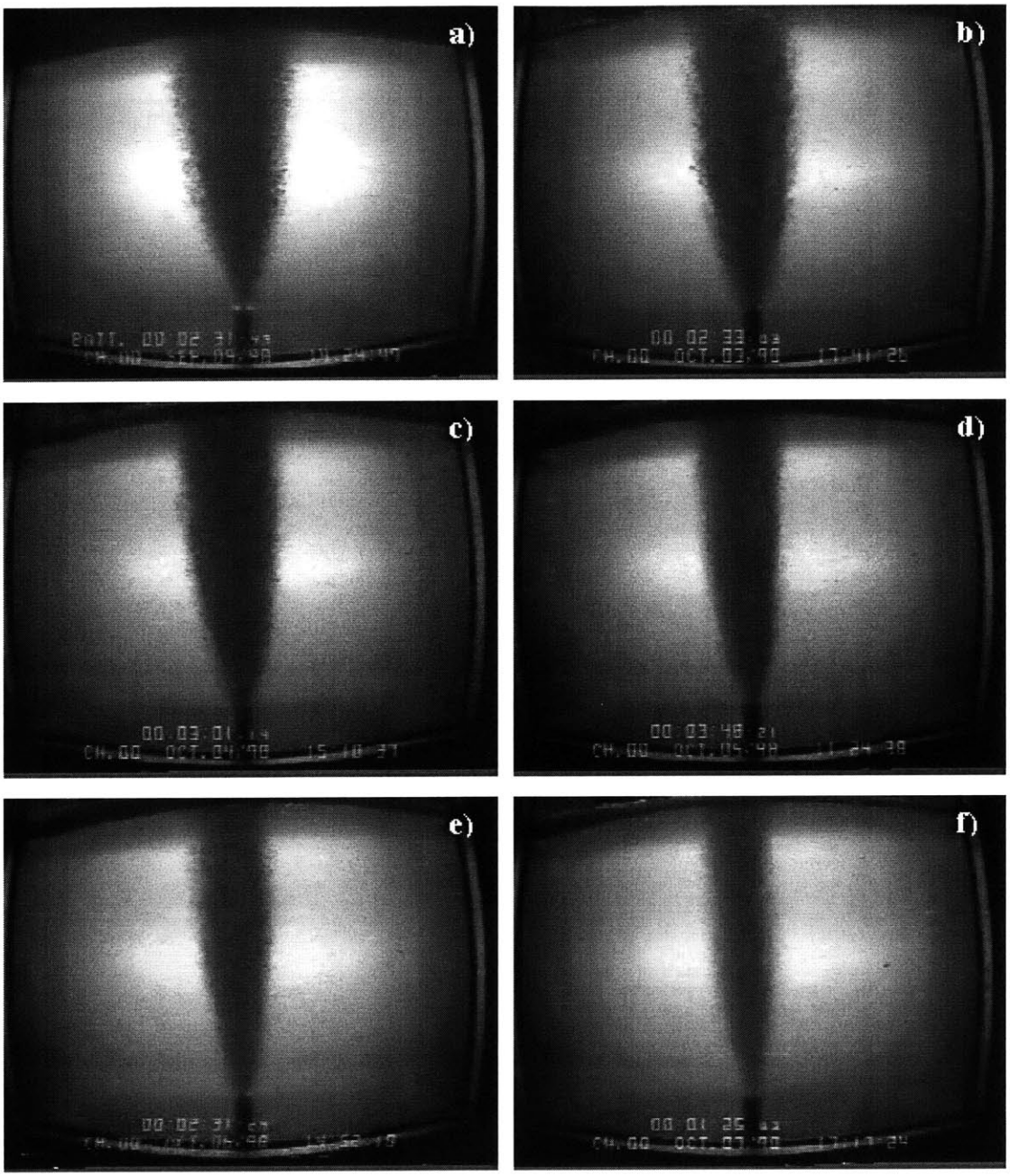

Figure D-3 *Air plumes obtained at increasing g-levels following injection of air into porous media saturated with immersion liquid - Injector SPI #1: a) 20-g; b) 30-g; c) 40-g; d) 60-g; e) 80-g; f) 100-g.*

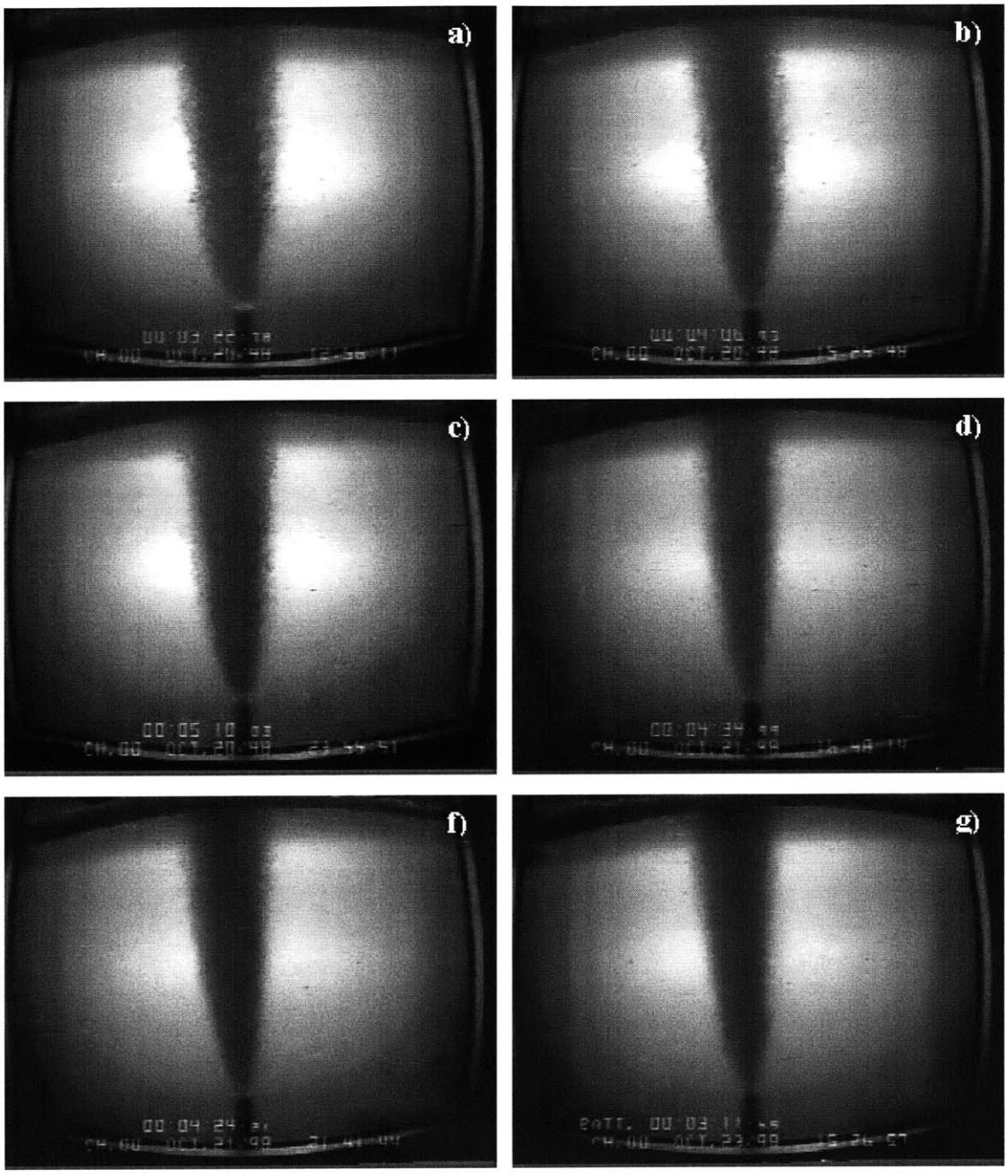

Figure D-4 *Air plumes obtained at increasing g-levels following injection of air into porous media saturated with immersion liquid - Injector SPI #2: a) 10-g; b) 20-g; c) 30-g; d) 60-g; e) 80-g; f) 100-g.*

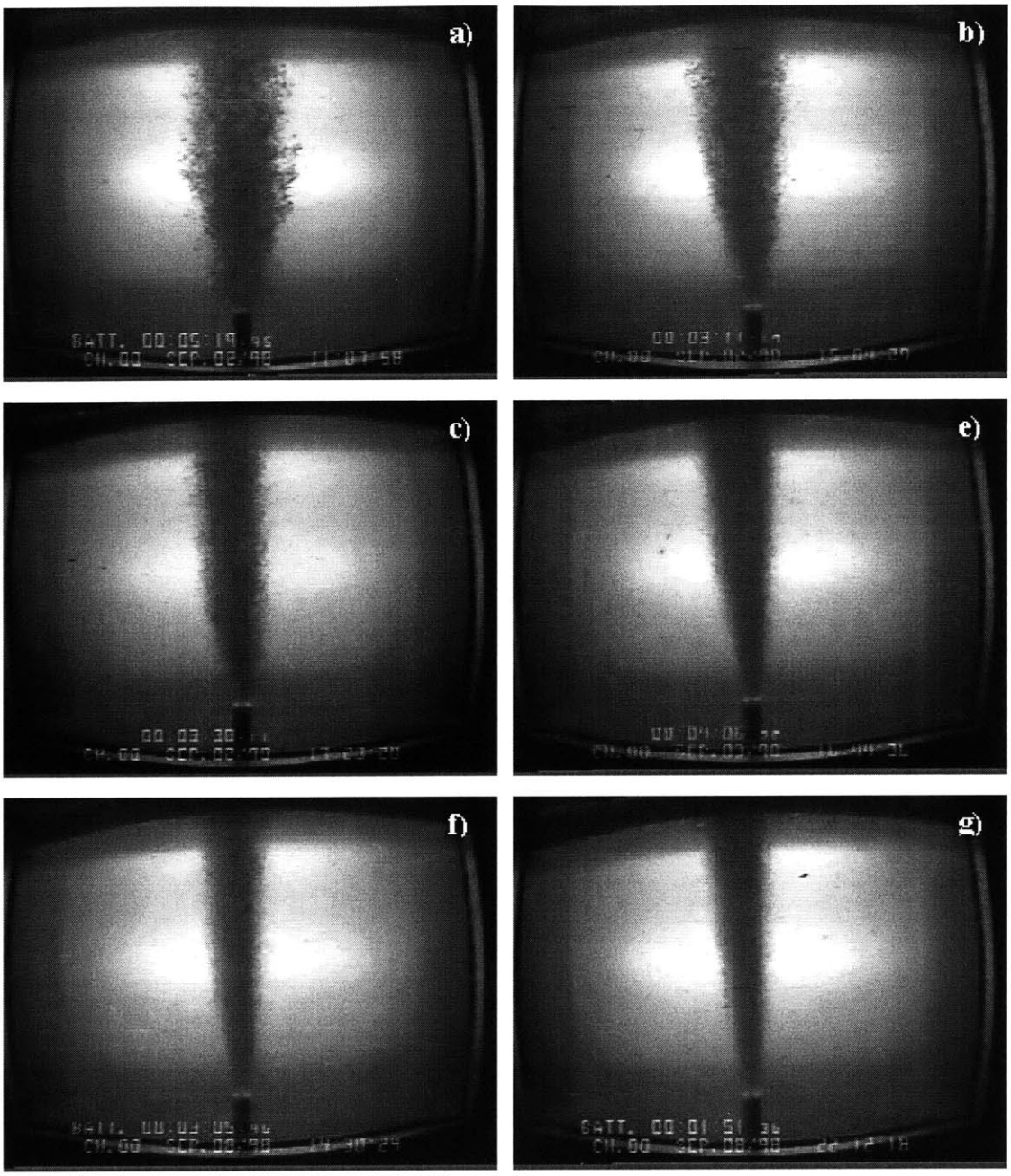

Figure D-5 *Air plumes obtained at increasing g-levels following injection of air into porous media saturated with immersion liquid - Injector SPI #3: a) 10-g; b) 20-g; c) 30-g; d) 60-g; e) 80-g; f) 100-g.*

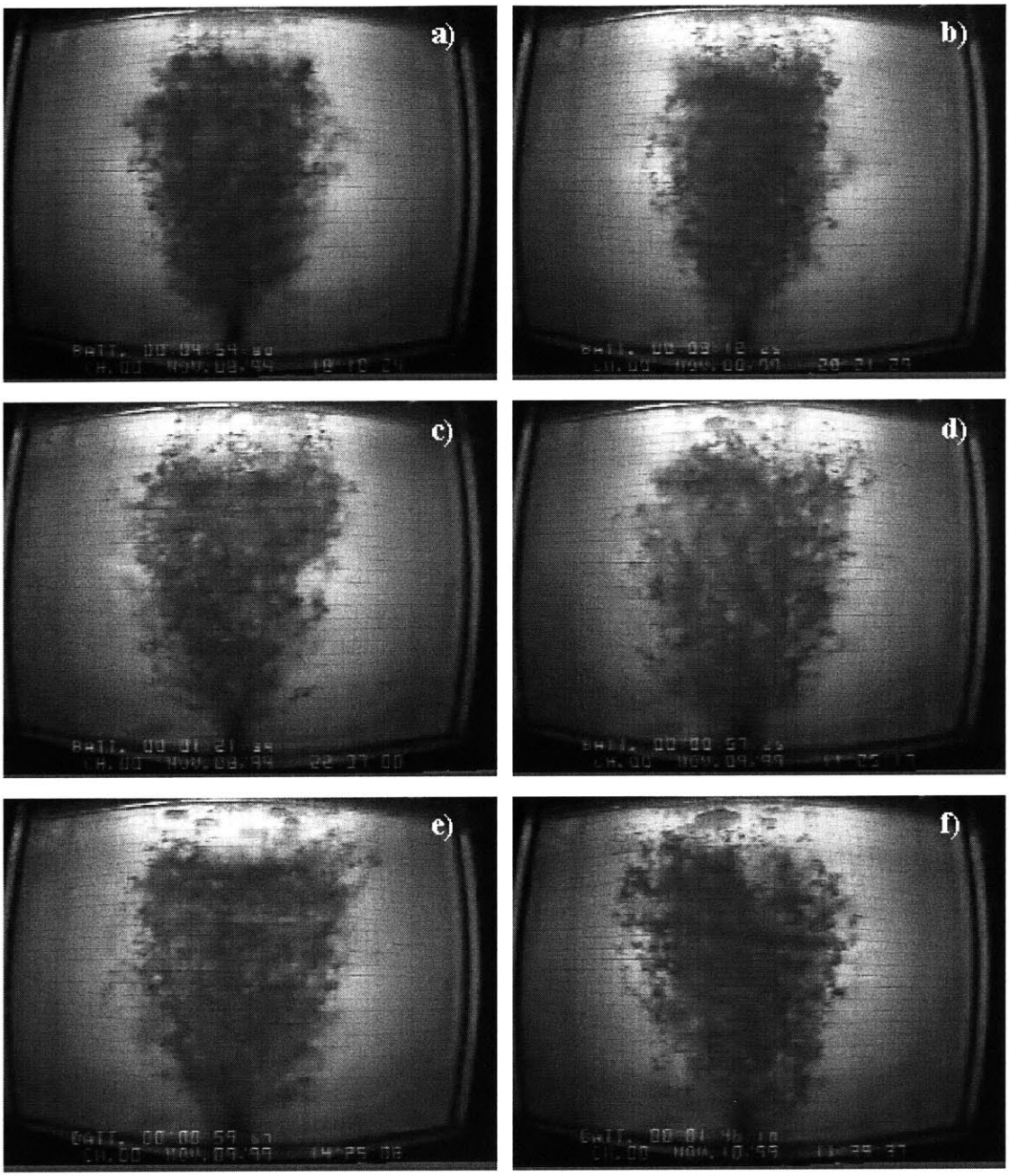

Figure D-6 *Constant flow rate injection of air into porous medium saturated with immersion liquid. Test conducted at 1-g. Injector MPI #2: a) 0.26 cm^3/s; b) 0.68 cm^3/s; c) 1.15 cm^3/s; d) 1.58 cm^3/s; e) 2.26 cm^3/s; f) 2.66 cm^3/s.*

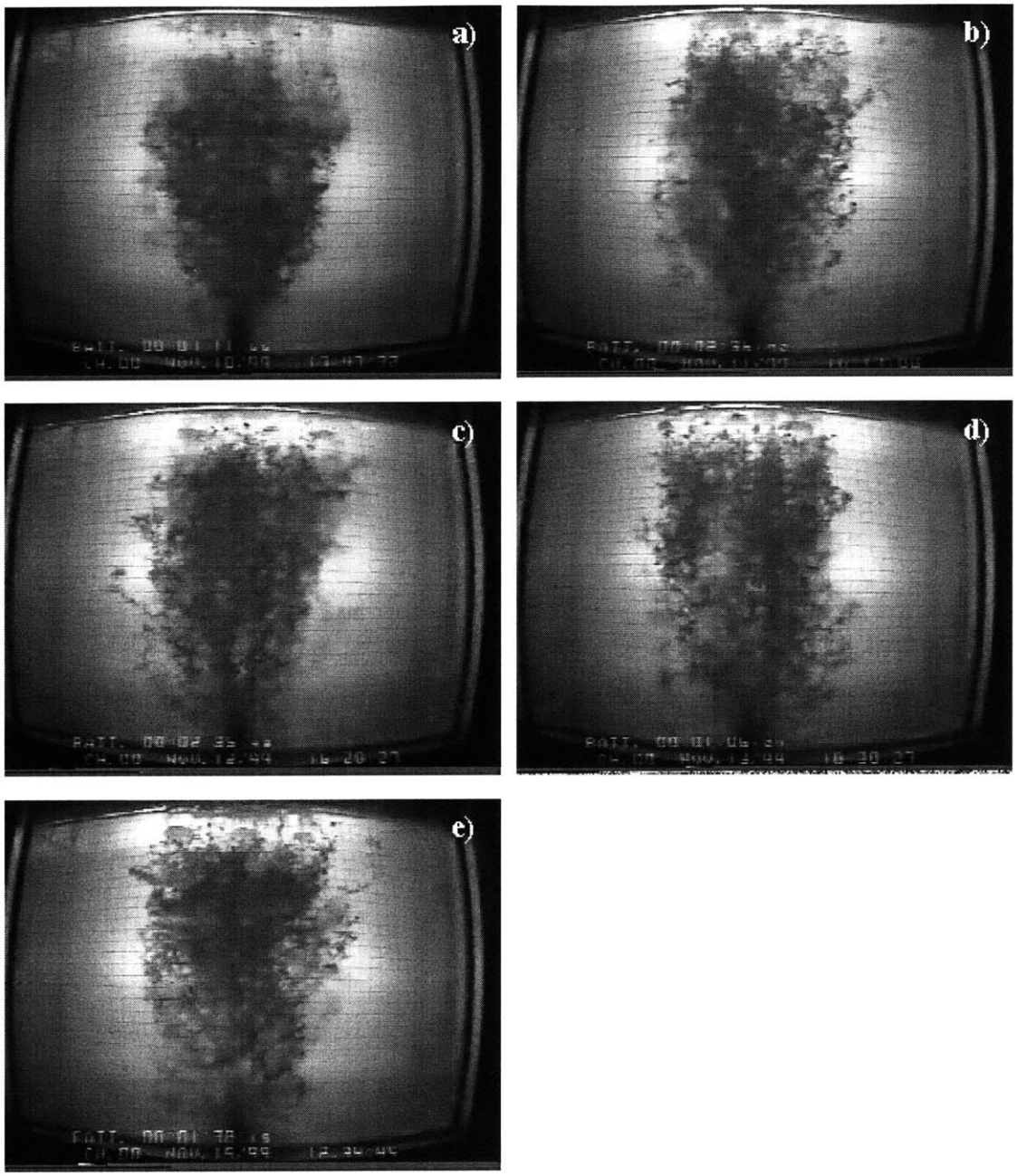

Figure D-7 *Constant flow rate injection of air into porous medium saturated with immersion liquid. Test conducted at 1-g. Injector MPI #3: a) 0.26 cm^3/s; b) 0.68 cm^3/s; c) 1.15 cm^3/s; d) 1.58 cm^3/s; e) 2.26 cm^3/s.*

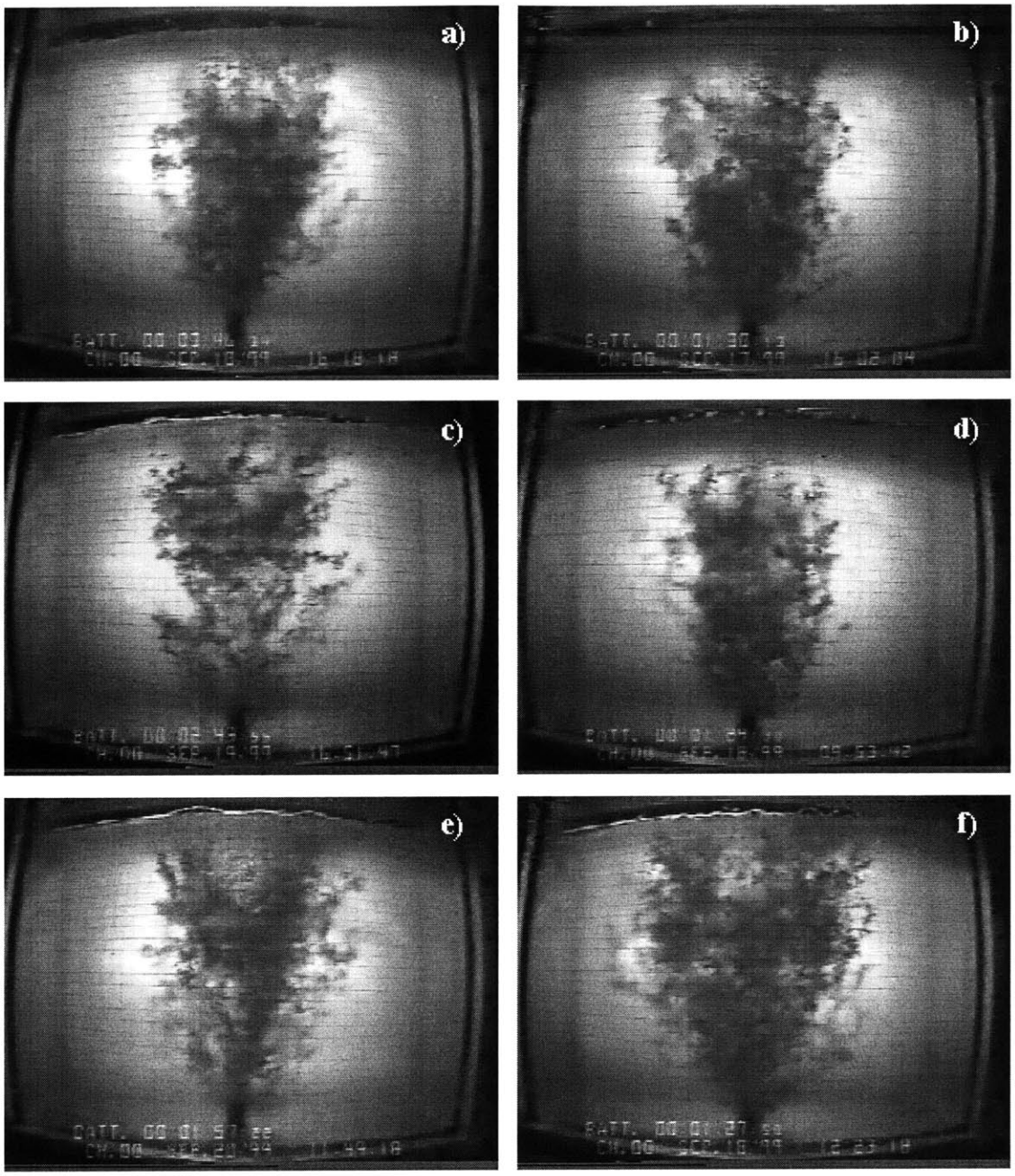

Figure D-8 *Constant flow rate injection of air into porous medium saturated with immersion liquid. Test conducted at 1-g. Injector SPI #1: a) 0.26 cm^3/s; b) 0.68 cm^3/s; c) 1.15 cm^3/s; d) 1.58 cm^3/s; e) 2.26 cm^3/s; f) 2.66 cm^3/s.*

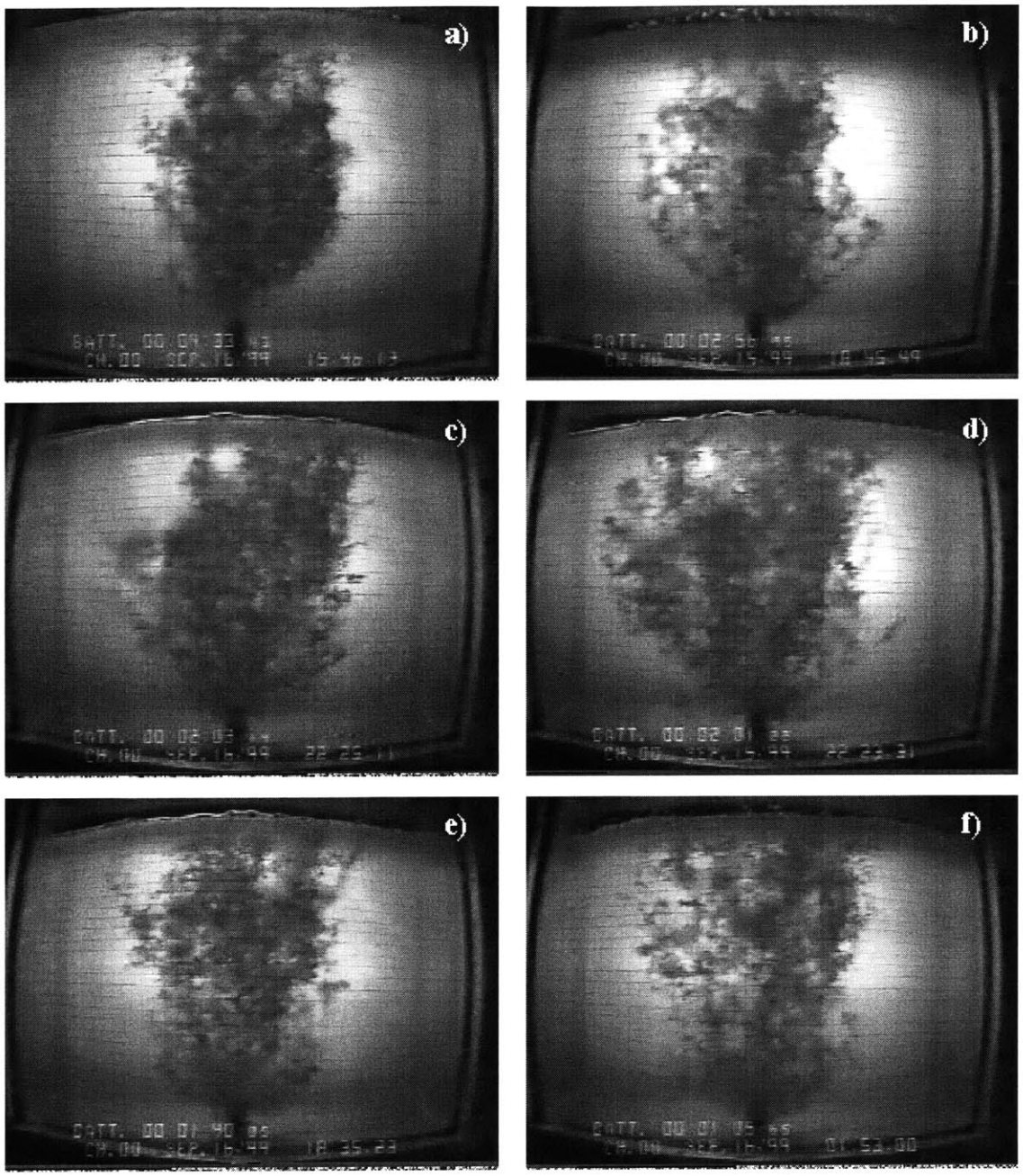

Figure D-9 *Constant flow rate injection of air into porous medium saturated with immersion liquid. Test conducted at 1-g. Injector SPI #2: a) 0.26 cm^3/s; b) 0.68 cm^3/s; c) 1.15 cm^3/s; d) 1.58 cm^3/s; e) 2.26 cm^3/s; f) 2.66 cm^3/s.*

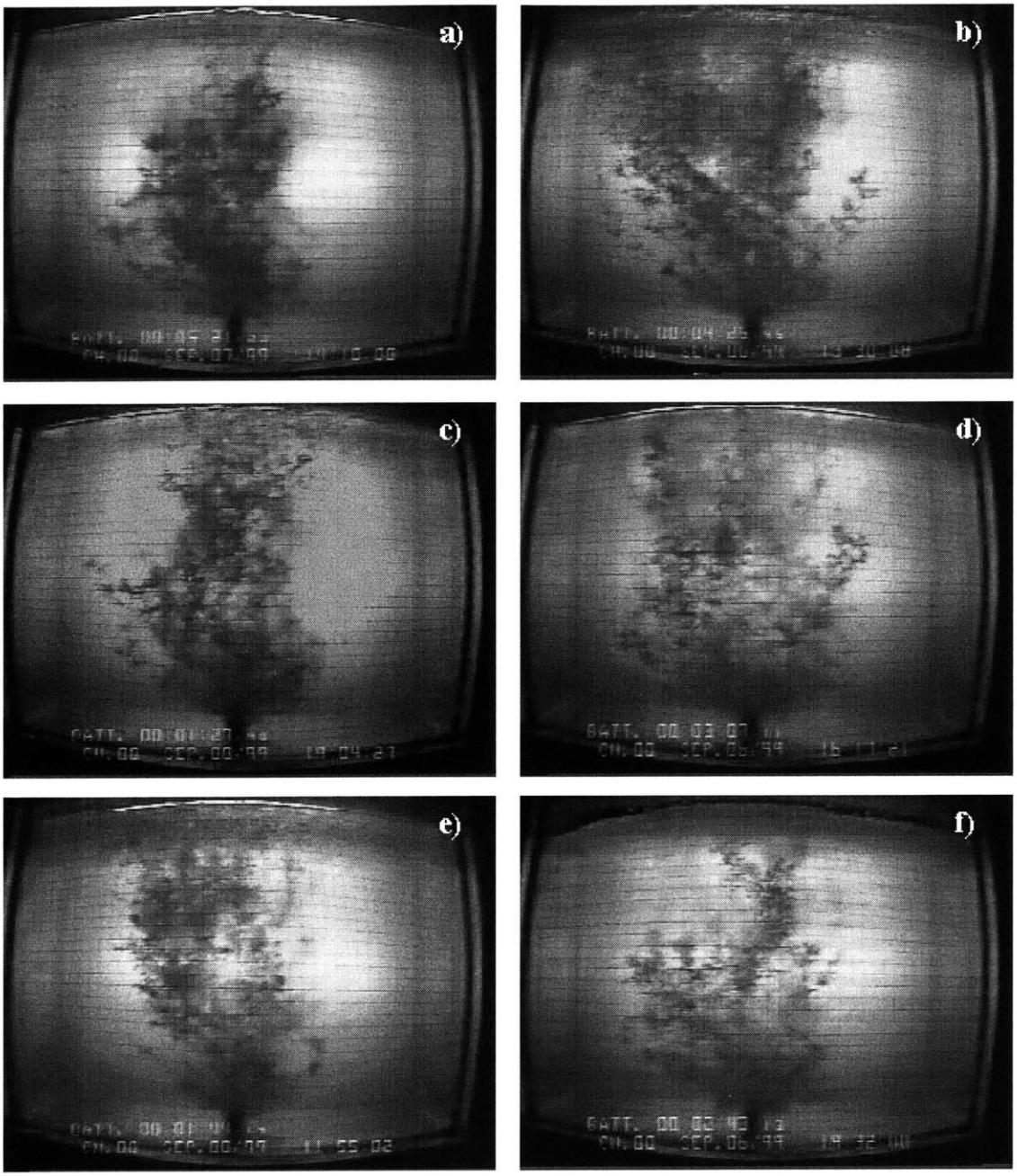

Figure D-10 Constant flow rate injection of air into porous medium saturated with immersion liquid. Test conducted at 1-g. Injector SPI #3: a) 0.26 cm^3/s; b) 0.68 cm^3/s; c) 1.15 cm^3/s; d) 1.58 cm^3/s; e) 2.26 cm^3/s; f) 2.66 cm^3/s.

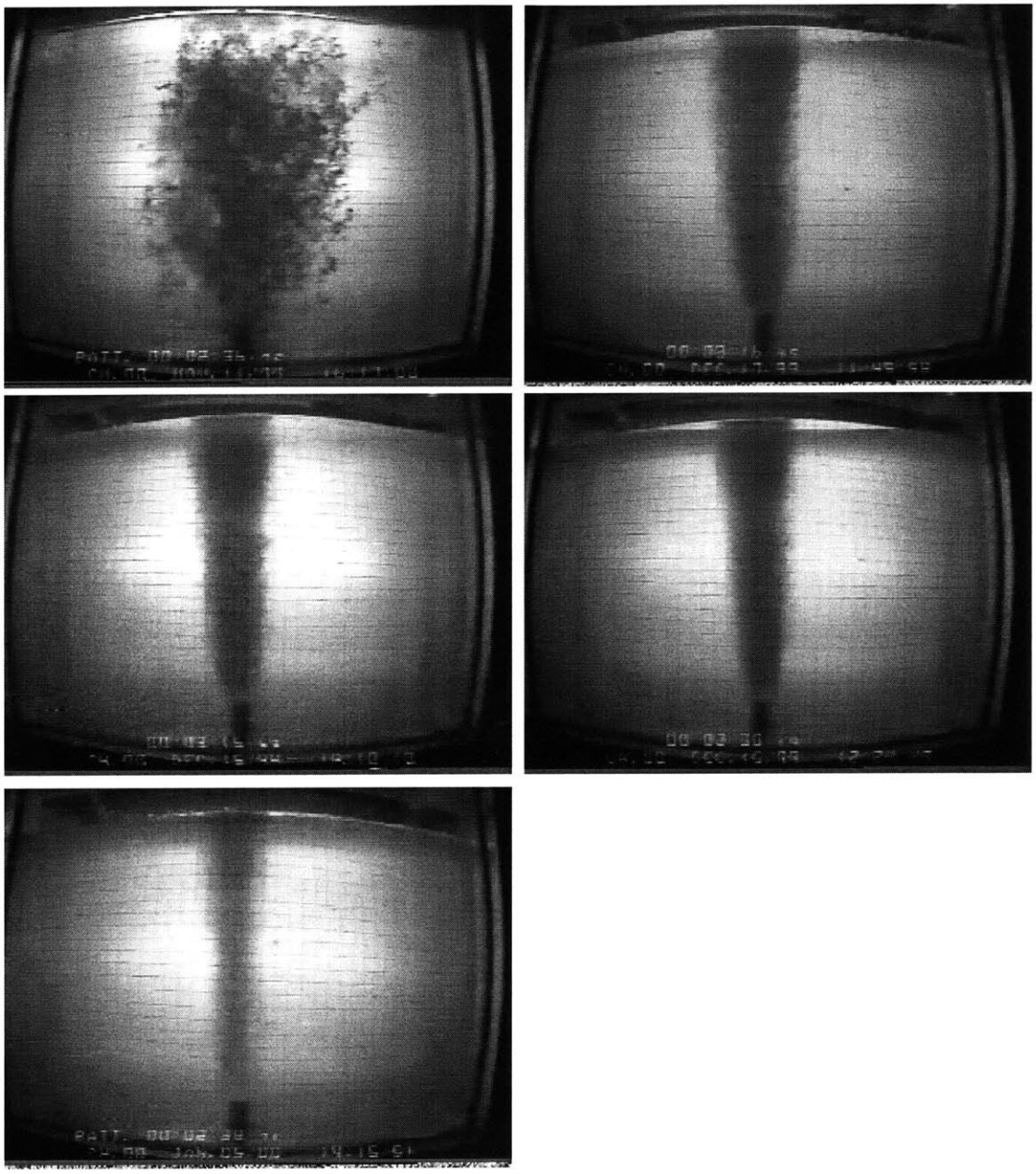

Figure D-11 Air plumes obtained at increasing g-levels following injection of air at constant flow rate into porous media saturated with immersion liquid – Injection flow rate q = 0.66 cm^3/s - Injector MPI #3: a) 1-g; b) 20-g; c) 30-g; d) 70-g; e) 100-g.

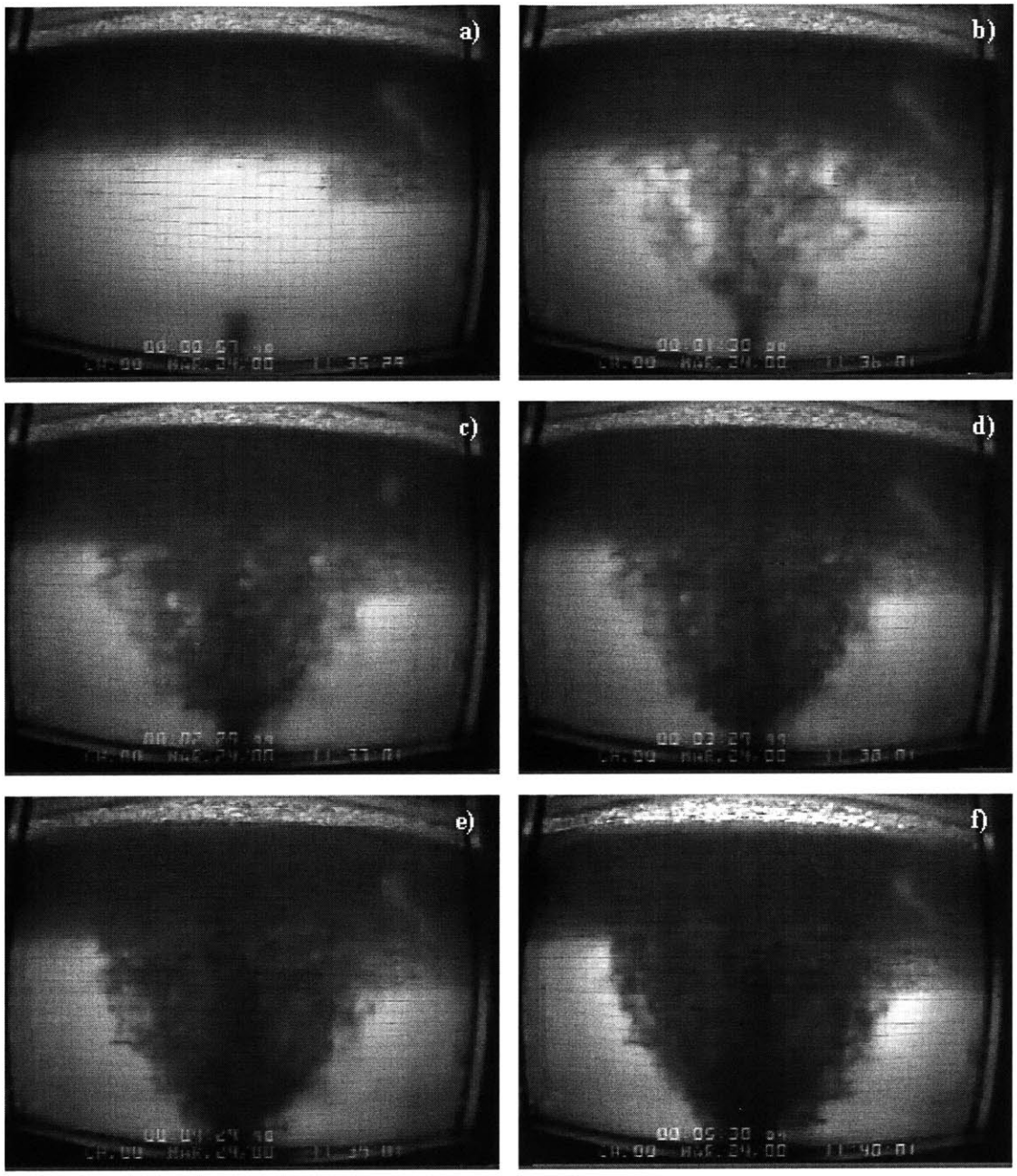

Figure D-12 *Air plumes obtained at1-g during injection at increasing, constant flow rates into porous media saturated with immersion liquid - Injector MPI #3: a) box prior to injection; b) q = 2.22 cm^3/s; c) q = 6.53 cm^3/s; d) q = 10.83 cm^3/s; e) q = 15.14 cm^3/s; f) q = 19.44 cm^3/s.*

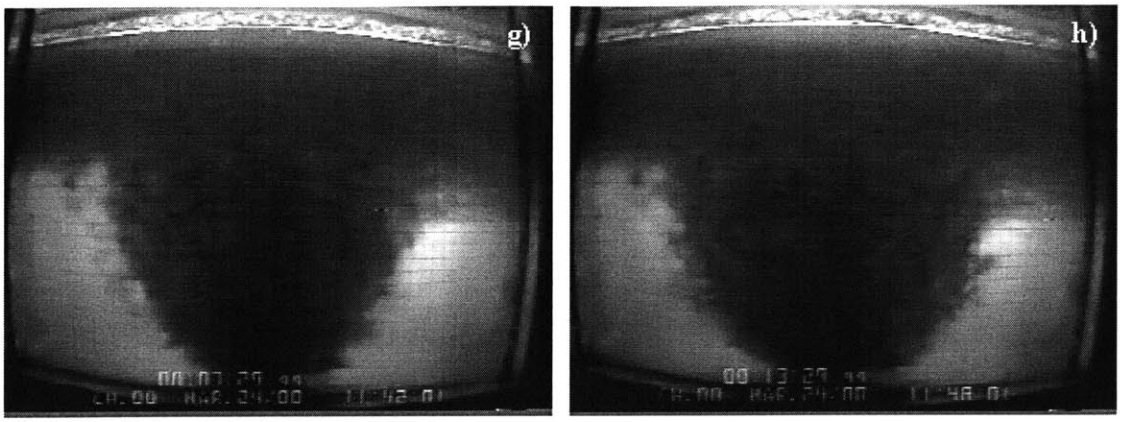

Figure D-12 (ctd.) *Air plumes obtained at1-g during injection at increasing, constant flow rates into porous media saturated with immersion liquid - Injector MPI #3: g) q = 23.75 cm^3/s; h) q = 28.06 cm^3/s.*

APPENDIX E

SUMMARY OF EXPERIMENTAL RESULTS

Two tables are included in this Appendix, which contain all the relevant information pertaining the experiments presented in this thesis. Table E-1 summarizes results from constant pressure tests, while Table E-2 contains information related to the experiments conducted under constant flow rate of injection. The following legend key provides an description of all the table headings.

Injector: Type of injector – Multiple Port Injectors (MPIs) or Single Port Injector (SPIs)

Pore fluid: Type of pore fluid – Immersion liquid (IL) or Glycerol (Glyc.)

Target g-level: *g*-level at which sparging was planned to take place

Actual ω: Angular velocity at which air invasion occurred

Actual g-level: *g*-level at which air invasion occurred

P_{inj}: Injection pressure, measured at the injection point

h_S: Height of crushed glass in the strong box

h_{LL}: Height of pore fluid in the strong box

σ: Total stress at the injection point

u: Fluid pressure at the injection point

σ': Effective stress at the injection point

P_{entry}: Entry pressure at the injection point

ΔP: $P_{inj} - P_{entry}$

h^-: *y*-coordinate of the highest point on the left hand side of a steady-state plume boundary, corrected for distortion

V^-: Volume of the left hand side of a steady-state plume boundary

h^+: *y*-coordinate of the highest point on the right hand side of a steady-state plume boundary, corrected for distortion

V^+: Volume of the rigth hand side of a steady-state plume boundary

$h_{average}$: Average value of the highest *y*-coordinate on plume boundary

$V_{average}$:	Average steady-state plume volume
RZI:	Relative Zone of Influence of IAS well
Obs. Air velocity:	Velocity of the air front estimated from recorded images of sparging experiments
Pres. Grad.:	Pressure gradient driving air front
Calc. Air velocity:	Velocity of the air front estimated from Darcy's law using pressure gradient values
Bo:	Bond number
Ca_{obs}:	Capillary number based on observed velocities
Ca_{calc}:	Capillary number based on calculated velocities
Bo/Ca_{Obs}:	*Bo/Ca* ratio based on observed velocities
Bo/Ca_{Calc}:	*Bo/Ca* ratio based on calculated velocities
Re_{obs}:	Reynolds number based on observed velocities
Re_{calc}:	Reynolds number based on calculated velocities
Sat. factor:	Saturation index assigned to sparging plumes that quantifies level of saturation within boundaries of plumes.

Additional headings included in Table E-2

B-through V^-:	Volume of left hand side plume *at breakthrough*
Steady-State V^-:	Volume of left hand side plume *at steady-state*
B-through V^+:	Volume of right hand side plume *at breakthrough*
Steady-State V^+:	Volume of rigjt hand side plume *at steady-state*
B-through $V_{average}$:	Average volume of plume at breakthrough
Steady-State $V_{average}$:	Average volume of plume at steady-state
B-through RZI :	Relative Zone of Influence at breakthrough
Steady-State RZI :	Relative Zone of Influence at steady-state

Test Name	Injector	Pore fluid	Target g-level	Actual ω [rpm]	Actual g-level	P_{inj} [KPa]	h_s [cm]	h_{LL} [cm]	σ [KPa]	u [KPa]	σ' [KPa]	P_{entry} [KPa]	ΔP [KPa]
LL01i1	MPI #1	IL	1	----	1.0	11.75	21.0	19.0	4.61	1.58	3.0	1.7	10.0
LL10i1	MPI #1	IL	10	89.3	10.7	21.94	21.0	19.9	49.15	17.67	31.5	17.8	4.1
LL20i1	MPI #1	IL	20	121.7	19.8	32.84	20.5	19.5	89.11	32.16	56.9	32.3	0.5
LL30i1	MPI #1	IL	30	145.9	28.4	48.13	20.8	19.3	129.94	45.75	84.2	45.9	2.2
LL40i1	MPI #1	IL	40	172.8	39.9	67.78	20.8	19.2	182.28	63.85	118.4	64.0	3.8
LL50i1	MPI #1	IL	50	185.6	46.0	74.83	21.3	18.8	215.33	72.12	143.2	72.3	2.6
LL60i1	MPI #1	IL	60	209.8	58.8	82.22	20.8	16.7	268.69	81.86	186.8	82.0	0.2
LL70i1	MPI #1	IL	70	225.4	67.9	101.47	21.2	17.4	316.10	98.45	217.7	98.6	2.9
LL80i1	MPI #1	IL	80	244.1	79.6	119.10	19.5	17.5	340.99	116.12	224.9	116.3	2.8
LL90i1	MPI #1	IL	90	250.0	83.5	127.63	20.0	17.8	366.85	123.89	243.0	124.0	3.6
LL100i1	MPI #1	IL	100	272.1	98.9	148.76	20.2	17.6	438.92	145.12	293.8	145.3	3.5
LL110i1	MPI #1	IL	110	288.6	111.2	160.36	20.5	17.0	501.10	157.68	343.4	157.8	2.5
LL130i1	MPI #1	IL	130	318.8	135.7	210.13	19.3	18.5	575.67	209.39	366.3	209.5	0.6
LL150i1	MPI #1	IL	150	337.5	152.1	235.88	19.5	18.3	651.87	232.14	419.7	232.3	3.6

Table 0-1 Summary of characteristics of air sparging experiments conducted under a constant injection pressure

Test Name	Injector	Pore fluid	Target g-level	Actual ω [rpm]	Actual g-level	P_{inj} [KPa]	h_s [cm]	h_{LL} [cm]	σ [KPa]	u [KPa]	σ' [KPa]	P_{entry} [KPa]	ΔP [KPa]
2LL1i1	MPI #1	IL	1	----	1.0	12.71	21.0	17.0	4.61	1.42	3.2	1.6	11.1
2LL10i1	MPI #1	IL	10	91.2	11.1	17.72	22.8	18.1	55.65	16.77	38.9	16.9	0.8
2LL20i1	MPI #1	IL	20	119.0	18.9	29.79	23.0	18.3	95.59	28.86	66.7	29.0	0.8
3LL20i1	MPI #1	IL	20	118.1	18.6	31.59	22.0	20.0	90.05	31.07	59.0	31.2	0.4
2LL30i1	MPI #1	IL	30	145.3	28.2	49.85	22.2	20.7	137.55	48.67	88.9	48.8	1.0
2LL40i1	MPI #1	IL	40	167.1	37.3	64.52	22.0	20.0	180.28	62.19	118.1	62.3	2.2
2LL50i1	MPI #1	IL	50	190.7	48.6	88.61	21.7	21.4	231.60	86.67	144.9	86.8	1.8
2LL60i1	MPI #1	IL	60	207.0	57.2	98.23	21.8	20.0	274.14	95.44	178.7	95.6	2.6
2LL70i1	MPI #1	IL	70	225.3	67.8	120.91	21.9	21.1	326.25	119.28	207.0	119.4	1.5
2LL80i1	MPI #1	IL	80	241.9	78.2	136.27	22.2	20.7	381.24	134.89	246.4	135.0	1.2
2LL90i1	MPI #1	IL	90	256.6	87.9	148.01	22.2	19.9	428.99	145.92	283.1	146.1	1.9
2LL100i1	MPI #1	IL	100	271.9	98.7	171.51	21.2	20.6	459.97	169.60	290.4	169.8	1.8
LL1i2	MPI #2	IL	1	----	1.0	9.24	22.1	19.2	4.86	1.60	3.3	1.8	7.5
LL10i2	MPI #2	IL	10	90.4	10.9	19.17	21.5	20.5	51.56	18.66	32.9	18.8	0.4
LL20i2	MPI #2	IL	20	119.0	18.9	29.90	19.2	18.5	79.79	29.18	50.6	29.3	0.6
LL30i2	MPI #2	IL	30	145.8	28.4	46.42	22.4	19.5	139.75	46.16	93.6	46.3	0.1
LL40i2	MPI #2	IL	40	168.9	38.1	68.18	22.5	21.2	188.37	67.35	121.0	67.5	0.7
LL50i2	MPI #2	IL	50	189.7	48.1	89.00	22.1	21.4	233.40	85.76	147.6	85.9	3.1
LL60i2	MPI #2	IL	60	208.3	57.9	104.09	22.3	21.5	283.96	103.89	180.1	104.0	0.1
LL70i2	MPI #2	IL	70	225.2	67.7	114.04	22.0	19.5	327.44	110.13	217.3	110.3	3.8
LL80i2	MPI #2	IL	80	241.6	78.0	132.25	22.0	19.8	376.87	128.71	248.2	128.9	3.4
LL90i2	MPI #2	IL	90	256.8	88.1	153.21	22.4	20.7	433.53	152.02	281.5	152.2	1.0

Table E-1 (ctd.) *Summary of characteristics of air sparging experiments conducted at constant injection pressure*

Test Name	Injector	Pore fluid	Target g-level	Actual ω [rpm]	Actual g-level	P_{inj} [KPa]	h_s [cm]	h_{LL} [cm]	σ [KPa]	u [KPa]	σ' [KPa]	P_{entry} [KPa]	ΔP [KPa]
2LL20i2	MPI #2	IL	20	118.2	18.7	32.92	21.7	19.5	88.98	30.34	58.6	30.5	2.4
2LL30i2	MPI #2	IL	30	143.8	27.6	49.96	21.7	19.8	131.69	45.60	86.1	45.7	4.2
2LL40i2	MPI #2	IL	40	165.5	36.6	65.72	21.7	19.5	174.43	59.48	115.0	59.6	6.1
2LL50i2	MPI #2	IL	50	187.8	47.1	83.41	21.7	19.7	224.61	77.38	147.2	77.5	5.9
2LL60i2	MPI #2	IL	60	207.6	57.6	100.83	21.5	19.9	271.94	95.51	176.4	95.7	5.2
2LL70i2	MPI #2	IL	70	223.7	66.8	112.07	21.5	19.3	315.75	107.56	208.2	107.7	4.4
2LL80i2	MPI #2	IL	80	240.6	77.3	134.45	22.0	20.6	373.76	132.80	241.0	133.0	1.5
2LL90i2	MPI #2	IL	90	255.8	87.4	154.10	21.5	20.5	412.87	149.38	263.5	149.5	4.6
2LL100i2	MPI #2	IL	100	271.3	98.3	169.78	21.8	20.4	470.91	167.22	303.7	167.4	2.4
LL01i3	MPI #3	IL	1	----	1.0	10.27	21.0	17.0	4.61	1.42	3.2	1.6	8.7
LL20i3	MPI #3	IL	20	118.4	18.7	34.70	21.7	20.9	89.28	32.63	56.6	32.8	1.9
LL30i3	MPI #3	IL	30	147.2	28.9	54.50	22.5	22.0	143.08	53.09	90.0	53.2	1.3
LL40i3	MPI #3	IL	40	171.8	39.4	73.45	22.7	22.1	196.63	72.64	124.0	72.8	0.7
LL50i3	MPI #3	IL	50	189.5	48.0	84.04	22.7	20.5	239.23	81.98	157.3	82.1	1.9
LL60i3	MPI #3	IL	60	209.6	58.7	100.90	22.7	20.5	292.68	100.30	192.4	100.4	0.5
LL80i3	MPI #3	IL	80	241.8	78.1	130.33	22.7	19.8	389.51	128.92	260.6	129.1	1.3
LL90i3	MPI #3	IL	90	256.3	87.7	142.46	23.0	19.2	443.41	140.46	302.9	140.6	1.9
LL100i3	MPI #3	IL	100	270.9	98.0	159.94	22.8	19.3	491.06	157.73	333.3	157.9	2.1

Table E-1 (ctd.) *Summary of characteristics of air sparging experiments conducted at constant injection pressure*

Test Name	Injector	Pore fluid	Target g-level	Actual ω [rpm]	Actual g-level	P_{inj} [KPa]	h_s [cm]	h_{LL} [cm]	σ [KPa]	u [KPa]	σ' [KPa]	P_{entry} [KPa]	ΔP [KPa]
2LL20i3	MPI #3	IL	20	119.3	19.0	32.88	22.0	20.3	91.89	32.18	59.7	32.3	0.6
2LL30i3	MPI #3	IL	30	144.6	27.9	48.29	21.9	20.0	134.39	46.57	87.8	46.7	1.6
2LL40i3	MPI #3	IL	40	167.3	37.4	65.54	22.1	20.3	181.54	63.28	118.3	63.4	2.1
2LL50i3	MPI #3	IL	50	189.0	47.7	81.57	21.8	20.0	228.54	79.56	149.0	79.7	1.9
2LL60i3	MPI #3	IL	60	206.4	56.9	97.14	21.8	20.2	272.55	95.83	176.7	96.0	1.2
2LL70i3	MPI #3	IL	70	224.0	67.0	112.90	22.0	19.7	323.96	110.08	213.9	110.2	2.7
2LL80i3	MPI #3	IL	80	241.6	78.0	133.70	22.3	20.2	382.01	131.31	250.7	131.5	2.2
2LL90i3	MPI #3	IL	90	256.3	87.7	148.60	22.2	19.9	427.98	145.58	282.4	145.7	2.9
2LL100i3	MPI #3	IL	100	270.9	98.0	168.21	21.7	20.2	467.36	165.09	302.3	165.2	3.0
LL1i4	SPI #1	IL	1	----	1.0	11.58	21.0	19.0	4.61	1.58	3.0	1.7	9.8
LL10i4	SPI #1	IL	10	87.4	10.2	20.20	21.0	18.8	47.08	15.99	31.1	16.1	4.1
LL20i4	SPI #1	IL	20	118.8	18.8	31.00	21.7	19.2	89.88	30.18	59.7	30.3	0.7
LL30i4	SPI #1	IL	30	145.2	28.2	51.81	22.0	21.3	136.12	50.01	86.1	50.2	1.6
LL40i4	SPI #1	IL	40	168.1	37.7	65.67	22.1	20.2	183.28	63.57	119.7	63.7	2.0
LL50i4	SPI #1	IL	50	191.9	49.2	89.08	21.8	21.0	235.60	86.12	149.5	86.3	2.8
LL60i4	SPI #1	IL	60	207.2	57.3	98.50	22.1	20.0	278.45	95.62	182.8	95.8	2.7
LL70i4	SPI #1	IL	70	224.6	67.4	111.63	22.6	19.6	334.58	110.11	224.5	110.3	1.4
LL80i4	SPI #1	IL	80	240.8	77.4	135.48	22.2	20.6	377.78	133.02	244.8	133.2	2.3
LL90i4	SPI #1	IL	90	257.0	88.2	150.34	21.9	20.2	424.51	148.58	275.9	148.7	1.6
LL100i4	SPI #1	IL	100	275.0	101.0	181.08	22.0	21.3	488.28	179.39	308.9	179.5	1.5

Table E-1 (ctd.) *Summary of characteristics of air sparging experiments conducted at constant injection pressure*

Test Name	Injector	Pore fluid	Target g-level	Actual ω [rpm]	Actual g-level	P_{inj} [KPa]	h_s [cm]	h_{LL} [cm]	σ [KPa]	u [KPa]	σ' [KPa]	P_{entry} [KPa]	ΔP [KPa]
LL20i5	SPI #2	IL	20	118.8	18.8	32.29	22.8	19.8	94.44	31.12	63.3	31.3	1.0
LL30i5	SPI #2	IL	30	144.7	28.0	49.09	22.2	20.3	136.42	47.33	89.1	47.5	1.6
LL40i5	SPI #2	IL	40	167.5	37.5	65.22	22.6	20.1	186.09	62.80	123.3	63.0	2.3
LL50i5	SPI #2	IL	50	188.1	47.3	82.59	22.0	20.2	228.44	79.59	148.8	79.7	2.8
LL60i5	SPI #2	IL	60	206.2	56.8	99.51	22.2	20.2	277.02	95.65	181.4	95.8	3.7
LL70i5	SPI #2	IL	70	224.8	67.5	116.41	22.4	20.2	332.21	113.68	218.5	113.8	2.6
LL80i5	SPI #2	IL	80	240.6	77.3	134.11	22.2	20.3	377.16	130.87	246.3	131.0	3.1
LL90i5	SPI #2	IL	90	255.7	87.3	150.53	22.2	20.0	425.98	145.63	280.4	145.8	4.8
LL100i5	SPI #2	IL	100	271.9	98.7	168.37	22.2	20.0	481.67	164.66	317.0	164.8	3.6
LL1i6	SPI #3	IL	1	----	1.0	9.38	22.4	20.2	4.92	1.68	3.2	1.8	7.5
LL10i6	SPI #3	IL	10	77.0	7.9	16.36	22.7	20.2	39.50	13.34	26.2	13.5	2.9
LL20i6	SPI #3	IL	20	117.3	18.4	32.59	22.8	20.1	92.07	30.80	61.3	30.9	1.6
LL30i6	SPI #3	IL	30	143.8	27.6	48.82	22.4	20.2	135.94	46.52	89.4	46.7	2.2
LL40i6	SPI #3	IL	40	167.6	37.5	65.74	22.5	20.2	185.48	63.19	122.3	63.3	2.4
LL50i6	SPI #3	IL	50	188.1	47.3	82.87	22.6	20.3	234.67	79.99	154.7	80.1	2.7
LL60i6	SPI #3	IL	60	208.0	57.8	99.52	22.4	20.2	284.42	97.33	187.1	97.5	2.0
LL70i6	SPI #3	IL	70	225.1	67.7	118.13	22.7	20.5	337.56	115.68	221.9	115.8	2.3
LL80i6	SPI #3	IL	80	240.4	77.2	133.75	22.8	20.3	386.71	130.65	256.1	130.8	2.9
LL90i6	SPI #3	IL	90	258.0	88.9	151.95	22.9	20.4	447.36	151.22	296.1	151.4	0.6
LL100i6	SPI #3	IL	100	271.8	98.7	168.51	22.9	20.3	496.49	167.01	329.5	167.2	1.4

Table E-1 (ctd.) *Summary of characteristics of air sparging experiments conducted at constant injection pressure*

Test Name	Injector	Pore fluid	Target g-level	Actual ω [rpm]	Actual g-level	P_{inj} [KPa]	h_s [cm]	h_{LL} [cm]	σ [KPa]	u [KPa]	σ' [KPa]	P_{entry} [KPa]	ΔP [KPa]
LL20i7	MPI #4	IL	20	119.0	18.9	31.65	22.6	19.5	93.92	30.75	63.2	30.9	0.7
LL30i7	MPI #4	IL	30	145.3	28.2	47.90	22.8	19.7	141.27	46.32	95.0	46.5	1.4
LL40i7	MPI #4	IL	40	166.6	37.1	61.87	22.3	19.7	181.65	60.89	120.8	61.0	0.8
LL50i7	MPI #4	IL	50	188.1	47.3	80.48	22.4	19.7	232.60	77.62	155.0	77.8	2.7
LL60i7	MPI #4	IL	60	205.2	56.2	96.71	22.4	19.7	276.81	92.38	184.4	92.5	4.2
LL70i7	MPI #4	IL	70	224.0	67.0	113.95	22.0	19.8	323.96	110.64	213.3	110.8	3.2
LL80i7	MPI #4	IL	80	239.1	76.4	128.72	22.4	19.6	375.82	124.79	251.0	124.9	3.8
LL90i7	MPI #4	IL	90	255.2	87.0	147.15	22.0	19.7	420.50	142.88	277.6	143.0	4.1
LL100i7	MPI #4	IL	100	270.0	97.4	159.90	22.4	19.3	479.24	156.69	322.6	156.8	3.1
GLY05i1	MPI #1	Gly.	5	62.3	5.2	22.13	21.8	19.7	24.83	12.62	12.2	12.9	9.2
GLY10i1	MPI #1	Gly.	10	79.6	8.5	25.53	22.8	21.4	42.40	22.38	20.0	22.7	2.8
GLY20i1	MPI #1	Gly.	20	118.3	18.7	51.75	22.4	21.8	92.00	50.36	41.6	50.7	1.1
GLY30i1	MPI #1	Gly.	30	146.3	28.6	78.22	21.8	21.0	136.94	74.20	62.7	74.5	3.7
GLY40i1	MPI #1	Gly.	40	168.4	37.9	93.92	22.6	19.6	188.09	91.76	96.3	92.1	1.9
GLY45i1	MPI #1	Gly.	45	179.2	42.9	104.29	22.7	19.3	213.93	102.31	111.6	102.6	1.7
GLY50i1	MPI #1	Gly.	50	191.6	49.0	124.73	22.7	20.4	244.57	123.63	120.9	123.9	0.8
GLY60i1	MPI #1	Gly.	60	210.0	58.9	153.51	22.9	21.0	296.38	152.88	143.5	153.2	0.3
GLY70i1	MPI #1	Gly.	70	229.2	70.2	189.37	22.6	21.3	348.43	184.72	163.7	185.0	4.3
GLY80i1	MPI #1	Gly.	80	246.5	81.2	212.90	23.0	21.0	410.15	210.65	199.5	211.0	1.9
GLY90i1	MPI #1	Gly.	90	263.7	92.9	247.68	22.3	21.5	455.10	246.81	208.3	247.1	0.6

Table E-1 (ctd.) *Summary of characteristics of air sparging experiments conducted at constant injection pressure*

Test Name	poro-sity	h^-	V^-	h^+	V^+	$h_{average}$	$V_{average}$	RZI
		[cm]	[cm^3]	[cm]	[cm^3]	[cm]	[cm^3]	[%]
LL01i1	0.447	15.83	4241.70	15.88	4668.70	15.86	4455.20	35.58
LL10i1	0.447	13.82	1291.70	14.12	741.50	13.97	1016.60	11.87
LL20i1	0.434	13.32	283.80	13.72	61.80	13.52	172.80	2.23
LL30i1	0.442	14.07	576.60	14.26	274.70	14.17	425.65	4.77
LL40i1	0.442	13.82	572.50	14.22	184.40	14.02	378.45	4.37
LL50i1	0.455	13.37	326.10	13.92	100.50	13.65	213.30	2.67
LL60i1	0.442	13.52	304.90	13.96	76.10	13.74	190.50	2.34
LL70i1	0.452	14.07	241.20	14.12	67.50	14.10	154.35	1.75
LL80i1	0.405	14.17	231.80	14.01	105.90	14.09	168.85	1.92
LL90i1	0.420	14.62	202.50	14.37	84.50	14.50	143.50	1.50
LL100i1	0.425	14.17	230.20	14.17	68.50	14.17	149.35	1.67
LL110i1	0.434	13.96	209.00	13.96	55.20	13.96	132.10	1.55
LL130i1	0.399	14.37	153.20	14.72	64.00	14.55	108.60	1.12
LL150i1	0.405	15.03	181.30	15.40	59.80	15.22	120.55	1.09

Table E-1 (ctd.) *Summary of characteristics of air sparging experiments conducted at constant injection pressure*

Test Name	poro-sity	h^-	V^-	h^+	V^+	$h_{average}$	$V_{average}$	RZI
		[cm]	[cm^3]	[cm]	[cm^3]	[cm]	[cm^3]	[%]
2LL20i1	0.414	14.53	287.00	14.78	14.78	14.66	150.89	1.53
3LL20i1	0.388	16.35	714.50	16.46	16.46	16.41	365.48	2.64
2LL30i1	0.393	16.73	461.70	16.90	16.90	16.82	239.30	1.60
2LL40i1	0.388	15.60	378.10	16.25	16.25	15.93	197.17	1.55
2LL50i1	0.379	17.28	410.50	17.06	17.06	17.17	213.78	1.34
2LL60i1	0.382	16.29	316.80	16.63	16.63	16.46	166.71	1.19
2LL70i1	0.385	17.17	422.00	17.23	17.23	17.20	219.61	1.37
2LL80i1	0.393	16.84	346.70	17.00	17.00	16.92	181.85	1.19
2LL90i1	0.393	16.14	287.80	16.40	16.40	16.27	152.10	1.12
2LL100i1	0.365	16.67	283.60	16.99	17.00	16.83	150.30	1.00
LL1i2	0.391	16.23	4469.76	15.98	4359.38	16.11	4414.57	33.64
LL10i2	0.373	14.14	559.64	14.54	487.16	14.34	523.40	5.65
LL20i2	0.298	14.90	264.40	15.10	141.80	15.00	203.10	1.92
LL30i2	0.399	15.10	292.60	15.30	177.20	15.20	234.90	2.13
LL40i2	0.401	15.80	443.10	16.10	255.30	15.95	349.20	2.74
LL50i2	0.391	15.80	428.10	15.50	220.70	15.65	324.40	2.69
LL60i2	0.396	16.00	425.60	16.00	183.60	16.00	304.60	2.37
LL70i2	0.388	15.90	405.60	16.30	204.10	16.10	304.85	2.33
LL80i2	0.388	15.60	335.00	15.70	154.00	15.65	244.50	2.03
LL90i2	0.399	14.70	283.30	15.00	170.30	14.85	226.80	2.20

Table E-1 (ctd.) *Summary of characteristics of air sparging experiments conducted at constant injection pressure*

Test Name	poro-sity	h^-	V^-	h^+	V^+	$h_{average}$	$V_{average}$	RZI
		[cm]	[cm^3]	[cm]	[cm^3]	[cm]	[cm^3]	[%]
2LL30i2	0.379	15.88	439.90	16.14	217.30	16.01	328.60	2.55
2LL40i2	0.379	16.57	456.20	16.90	224.30	16.73	340.25	2.31
2LL50i2	0.379	16.84	338.20	17.06	131.00	16.95	234.60	1.53
2LL60i2	0.373	16.78	330.50	16.67	135.40	16.73	232.95	1.58
2LL70i2	0.373	15.97	267.20	16.19	91.40	16.08	179.30	1.37
2LL80i2	0.388	16.84	233.60	17.00	92.60	16.92	163.10	1.07
2LL90i2	0.373	16.95	272.80	17.00	72.10	16.97	172.45	1.12
2LL100i2	0.382	14.77	134.50	15.00	61.10	14.89	97.80	0.94
LL01i3	0.359	15.09	4218.10	15.88	3555.90	15.48	3887.00	33.34
LL20i3	0.379	16.95	593.00	17.23	328.20	17.09	460.60	2.94
LL30i3	0.401	17.50	620.80	17.56	280.60	17.53	450.70	2.66
LL40i3	0.407	17.39	470.10	17.29	217.90	17.34	344.00	2.10
LL50i3	0.407	16.78	409.30	17.29	155.60	17.03	282.45	1.82
LL60i3	0.407	16.40	321.00	17.11	85.20	16.76	203.10	1.37
LL80i3	0.407	15.97	307.10	16.35	124.10	16.16	215.60	1.63
LL90i3	0.414	15.45	194.20	15.66	76.70	15.55	135.45	1.15
LL100i3	0.409	15.56	240.40	15.66	85.00	15.61	162.70	1.36

Table E-1 (ctd.) *Summary of characteristics of air sparging experiments conducted at constant injection pressure*

Test Name	poro-sity	h^-	V^-	h^+	V^+	$h_{average}$	$V_{average}$	RZI
		[cm]	[cm^3]	[cm]	[cm^3]	[cm]	[cm^3]	[%]
2LL30i3	0.385	16.29	516.80	16.73	215.60	16.51	366.20	2.59
2LL40i3	0.391	16.78	481.70	16.90	200.90	16.84	341.30	2.28
2LL50i3	0.382	16.52	418.00	16.57	170.90	16.55	294.45	2.07
2LL60i3	0.382	16.73	374.30	16.90	128.10	16.81	251.20	1.68
2LL70i3	0.388	15.97	304.90	16.29	134.00	16.13	219.45	1.66
2LL80i3	0.396	16.57	360.30	17.06	123.50	16.81	241.90	1.62
2LL90i3	0.393	16.25	317.90	16.73	145.30	16.49	231.60	1.64
2LL100i3	0.379	16.57	332.70	16.78	106.30	16.68	219.50	1.51
LL1i4	0.330	14.01	2849.00	14.88	2856.50	14.45	2852.75	30.13
LL10i4	0.330	16.35	584.79	16.38	521.06	16.37	552.93	4.02
LL20i4	0.351	15.56	402.90	15.82	237.50	15.69	320.20	2.64
LL30i4	0.360	17.17	406.10	17.29	220.20	17.23	313.15	1.95
LL40i4	0.363	16.63	379.10	16.84	158.20	16.74	268.65	1.82
LL50i4	0.354	17.50	363.20	17.56	114.50	17.53	238.85	1.41
LL60i4	0.363	16.52	293.60	16.40	102.70	16.46	198.15	1.41
LL70i4	0.377	16.08	287.80	16.35	128.20	16.21	208.00	1.55
LL80i4	0.366	16.08	272.50	16.25	140.00	16.17	206.25	1.55
LL90i4	0.357	16.46	200.00	16.46	47.60	16.46	123.80	0.88
LL100i4	0.360	17.00	173.60	17.11	49.60	17.06	111.60	0.72

Table E-1 (ctd.) *Summary of characteristics of air sparging experiments conducted at constant injection pressure*

Test Name	poro-sity	h^-	V^-	h^+	V^+	$h_{average}$	$V_{average}$	RZI
		[cm]	[cm^3]	[cm]	[cm^3]	[cm]	[cm^3]	[%]
LL30i5	0.393	16.40	300.20	16.84	140.40	16.62	220.30	1.53
LL40i5	0.404	16.29	269.60	16.63	85.40	16.46	177.50	1.27
LL50i5	0.388	16.19	220.90	16.57	61.50	16.38	141.20	1.02
LL60i5	0.393	16.46	198.70	16.78	74.20	16.62	136.45	0.95
LL70i5	0.399	16.46	225.70	16.67	77.10	16.57	151.40	1.06
LL80i5	0.393	16.40	222.10	16.67	69.80	16.54	145.95	1.03
LL90i5	0.393	16.40	208.30	16.67	69.70	16.54	139.00	0.98
LL100i5	0.393	16.52	237.90	16.63	55.40	16.57	146.65	1.03
LL1i6	0.399	15.39	3853.80	15.50	3158.50	15.44	3506.15	30.30
LL10i6	0.407	16.14	493.70	16.40	337.00	16.27	415.35	3.07
LL20i6	0.409	16.19	332.10	16.67	117.10	16.43	224.60	1.61
LL30i6	0.399	15.60	247.70	17.29	107.30	16.44	177.50	1.27
LL40i6	0.401	16.29	177.40	16.57	83.00	16.43	130.20	0.93
LL50i6	0.404	16.25	158.30	16.46	62.60	16.35	110.45	0.80
LL60i6	0.399	16.19	169.20	16.52	46.50	16.36	107.85	0.78
LL70i6	0.407	16.19	180.50	16.63	29.90	16.41	105.20	0.76
LL80i6	0.409	16.35	132.60	16.29	40.70	16.32	86.65	0.63
LL90i6	0.412	16.46	117.50	16.35	26.20	16.40	71.85	0.52
LL100i6	0.412	16.35	135.80	16.46	23.60	16.40	79.70	0.57

Table E-1 (ctd.) *Summary of characteristics of air sparging experiments conducted at constant injection pressure*

Test Name	poro-sity	h^-	V^-	h^+	V^+	$h_{average}$	$V_{average}$	RZI
		[cm]	[cm^3]	[cm]	[cm^3]	[cm]	[cm^3]	[%]
LL30i7	0.409	16.14	401.90	16.40	178.40	16.27	290.15	2.14
LL40i7	0.396	16.19	495.70	16.63	201.70	16.41	348.70	2.51
LL50i7	0.399	16.29	433.50	16.63	228.20	16.46	330.85	2.36
LL60i7	0.399	16.40	412.80	16.84	131.20	16.62	272.00	1.89
LL70i7	0.388	16.08	349.10	16.96	125.20	16.52	237.15	1.68
LL80i7	0.399	16.19	363.20	16.63	115.20	16.41	239.20	1.72
LL90i7	0.388	16.25	343.20	16.57	104.60	16.41	223.90	1.61
LL100i7	0.399	15.87	301.20	16.35	108.70	16.11	204.95	1.56
GLY05i1	0.477	13.92	1373.60	14.01	770.60	13.97	1072.10	12.52
GLY10i1	0.500	14.98	802.20	15.66	538.50	15.32	670.35	5.94
GLY20i1	0.491	16.67	303.80	16.67	276.10	16.67	289.95	1.99
GLY30i1	0.477	17.39	329.30	17.56	394.70	17.47	362.00	2.16
GLY40i1	0.496	15.77	397.20	16.19	227.70	15.98	312.45	2.44
GLY45i1	0.498	15.51	400.30	15.82	239.00	15.66	319.65	2.65
GLY50i1	0.498	16.78	147.90	17.29	321.20	17.03	234.55	1.51
GLY60i1	0.502	15.51	132.50	15.93	207.80	15.72	170.15	1.39
GLY70i1	0.496	16.95	277.20	16.95	260.60	16.95	268.90	1.76
GLY80i1	0.504	16.63	216.90	17.11	126.60	16.87	171.75	1.14
GLY90i1	0.489	17.34	277.50	17.39	126.80	17.36	202.15	1.23

Table E-1 (ctd.) *Summary of characteristics of air sparging experiments conducted at constant injection pressure*

Test Name	Obs. Air velocity	Pres. Grad.	Calc. Air velocity	Bo	Ca_{obs}	Ca_{calc}	Bo/Ca_{Obs}	Bo/Ca_{Calc}	Re_{obs}	Re_{calc}	Sat. factor
	[m/s]	[-]	[m/s]	[-]	[-]	[-]	[-]	[-]	[-]	[-]	
LL01i1	0.093	7.3	0.044	0.18	0.06	0.03	3.20	6.72	3.56	1.69	2
LL10i1	0.099	13.7	0.084	1.89	0.06	0.05	32.15	38.05	3.77	3.18	2
LL20i1	0.070	21.5	0.131	3.51	0.04	0.08	84.97	45.02	2.65	5.00	2
LL30i1	0.352	32.4	0.197	5.05	0.21	0.12	24.09	43.00	13.42	7.52	1
LL40i1	0.367	46.3	0.282	7.08	0.22	0.17	32.42	42.19	13.99	10.75	1
LL50i1	0.147	52.4	0.320	8.17	0.09	0.19	93.18	42.96	5.62	12.18	1
LL60i1	0.426	66.1	0.403	10.44	0.25	0.24	41.20	43.54	16.23	15.36	1
LL70i1	0.334	78.0	0.476	12.05	0.20	0.28	60.61	42.56	12.73	18.13	1
LL80i1	0.443	91.2	0.556	14.14	0.26	0.33	53.61	42.73	16.88	21.18	1
LL90i1	0.598	95.9	0.585	14.83	0.36	0.35	41.71	42.61	22.76	22.28	1
LL100i1	0.440	113.4	0.691	17.57	0.26	0.41	67.09	42.69	16.76	26.34	1
LL110i1	0.383	127.2	0.776	19.76	0.23	0.46	86.67	42.80	14.60	29.56	1
LL130i1	0.617	151.7	0.926	24.11	0.37	0.55	65.72	43.78	23.49	35.26	1
LL150i1	0.387	172.5	1.053	27.02	0.23	0.63	117.45	43.15	14.73	40.10	1

Table E-1 (ctd.) *Summary of characteristics of air sparging experiments conducted at constant injection pressure*

Test Name	Obs. Air velocity	Pres. Grad.	Calc. Air velocity	Bo	Ca_{obs}	Ca_{calc}	Bo/Ca_{Obs}	Bo/Ca_{Calc}	Re_{obs}	Re_{calc}	Sat. factor
	[m/s]	[-]	[m/s]	[-]	[-]	[-]	[-]	[-]	[-]	[-]	
2LL20i1	0.081	20.9	0.128	3.36	0.05	0.08	70.05	44.26	3.07	4.86	2
3LL20i1	0.195	20.0	0.122	3.31	0.12	0.07	28.49	45.47	7.44	4.66	1
2LL30i1	0.061	31.0	0.189	5.01	0.04	0.11	137.55	44.56	2.33	7.20	1
2LL40i1	0.059	42.0	0.256	6.62	0.04	0.15	188.38	43.47	2.25	9.76	1
2LL50i1	0.090	53.8	0.328	8.63	0.05	0.20	161.11	44.20	3.43	12.50	1
2LL60i1	0.153	64.4	0.393	10.17	0.09	0.23	111.59	43.46	5.83	14.98	1
2LL70i1	0.123	74.9	0.457	12.04	0.07	0.27	165.22	44.29	4.67	17.41	1
2LL80i1	0.159	86.4	0.527	13.88	0.09	0.31	147.11	44.28	6.04	20.08	1
2LL90i1	0.148	98.2	0.599	15.62	0.09	0.36	177.39	43.84	5.64	22.81	1
2LL100i1	0.149	109.6	0.668	17.54	0.09	0.40	197.44	44.10	5.69	25.46	1
LL1i2	0.053	5.4	0.033	0.18	0.03	0.02	5.68	8.99	2.00	1.26	2
LL10i2	0.050	11.4	0.070	1.94	0.03	0.04	65.69	46.75	1.89	2.66	2
LL20i2	0.041	20.7	0.126	3.36	0.02	0.08	136.39	44.64	1.58	4.82	2
LL30i2	0.051	30.8	0.188	5.04	0.03	0.11	166.85	45.10	1.94	7.16	1
LL40i2	0.089	41.6	0.254	6.77	0.05	0.15	127.38	44.84	3.40	9.66	1
LL50i2	0.109	54.0	0.330	8.54	0.06	0.20	132.12	43.55	4.14	12.55	1
LL60i2	0.089	63.0	0.384	10.29	0.05	0.23	195.04	45.00	3.38	14.64	1
LL70i2	0.135	77.2	0.471	12.03	0.08	0.28	149.79	42.97	5.14	17.93	1
LL80i2	0.142	88.1	0.537	13.85	0.08	0.32	164.25	43.31	5.40	20.47	1
LL90i2	0.153	97.3	0.593	15.65	0.09	0.35	171.97	44.32	5.82	22.60	1

Table E-1 (ctd.) *Summary of characteristics of air sparging experiments conducted at constant injection pressure*

Test Name	Obs. Air velocity	Pres. Grad.	Calc. Air velocity	Bo	Ca_{obs}	Ca_{calc}	Bo/Ca_{Obs}	Bo/Ca_{Calc}	Re_{obs}	Re_{calc}	Sat. factor
	[m/s]	[-]	[m/s]	[-]	[-]	[-]	[-]	[-]	[-]	[-]	
2LL30i2	0.045	32.7	0.199	4.91	0.03	0.12	184.45	41.38	1.70	7.59	1
2LL40i2	0.173	44.0	0.269	6.50	0.10	0.16	63.02	40.65	6.60	10.23	1
2LL50i2	0.063	55.5	0.339	8.37	0.04	0.20	222.86	41.53	2.40	12.90	1
2LL60i2	0.096	66.6	0.406	10.22	0.06	0.24	178.63	42.33	3.66	15.47	1
2LL70i2	0.148	76.7	0.468	11.87	0.09	0.28	135.27	42.65	5.62	17.82	1
2LL80i2	0.360	85.7	0.523	13.73	0.21	0.31	64.10	44.16	13.72	19.91	1
2LL90i2	0.123	98.9	0.603	15.52	0.07	0.36	211.94	43.25	4.69	22.98	1
2LL100i2	0.166	109.7	0.669	17.46	0.10	0.40	176.90	43.88	6.32	25.48	1
LL01i3	0.073	7.2	0.044	0.18	0.04	0.03	4.11	6.78	2.77	1.68	2
LL20i3	0.032	21.0	0.128	3.33	0.02	0.08	177.45	43.60	1.20	4.88	2
LL30i3	0.051	31.7	0.193	5.14	0.03	0.11	171.08	44.71	1.92	7.36	1
LL40i3	0.115	42.8	0.261	7.00	0.07	0.16	102.34	45.05	4.38	9.95	1
LL50i3	0.131	53.5	0.326	8.52	0.08	0.19	109.55	43.89	4.98	12.43	1
LL60i3	0.185	64.4	0.393	10.42	0.11	0.23	94.53	44.58	7.06	14.97	1
LL80i3	0.158	86.8	0.530	13.87	0.09	0.32	147.73	44.03	6.01	20.17	1
LL90i3	0.290	98.3	0.600	15.58	0.17	0.36	90.26	43.67	11.06	22.85	1
LL100i3	0.156	109.9	0.670	17.41	0.09	0.40	188.06	43.66	5.93	25.53	1

Table E-1 (ctd.) *Summary of characteristics of air sparging experiments conducted at constant injection pressure*

Test Name	Obs. Air velocity	Pres. Grad.	Calc. Air velocity	Bo	Ca_{obs}	Ca_{calc}	Bo/Ca_{Obs}	Bo/Ca_{Calc}	Re_{obs}	Re_{calc}	Sat. factor
	[m/s]	[-]	[m/s]	[-]	[-]	[-]	[-]	[-]	[-]	[-]	
2LL30i3	0.066	31.2	0.190	4.96	0.04	0.11	126.13	43.84	2.52	7.24	1
2LL40i3	0.067	42.0	0.256	6.64	0.04	0.15	166.32	43.61	2.56	9.75	1
2LL50i3	0.079	53.3	0.325	8.47	0.05	0.19	180.52	43.77	3.01	12.40	1
2LL60i3	0.100	63.0	0.384	10.11	0.06	0.23	169.19	44.20	3.82	14.64	1
2LL70i3	0.132	75.5	0.461	11.90	0.08	0.27	151.68	43.44	5.02	17.54	1
2LL80i3	0.125	87.1	0.531	13.85	0.07	0.32	186.49	43.80	4.75	20.24	1
2LL90i3	0.185	98.6	0.601	15.58	0.11	0.36	141.89	43.57	7.03	22.90	1
2LL100i3	0.197	109.8	0.670	17.41	0.12	0.40	148.46	43.67	7.51	25.52	1
LL1i4	0.073	7.2	0.044	0.18	0.04	0.03	4.12	6.82	2.76	1.67	2
LL10i4	0.076	13.4	0.082	1.81	0.05	0.05	39.92	37.20	2.91	3.12	2
LL20i4	0.057	20.6	0.126	3.35	0.03	0.07	98.21	44.75	2.18	4.79	1
LL30i4	0.090	31.2	0.190	5.00	0.05	0.11	93.82	44.18	3.41	7.25	1
LL40i4	0.074	42.3	0.258	6.70	0.04	0.15	152.26	43.69	2.82	9.82	1
LL50i4	0.069	55.2	0.337	8.74	0.04	0.20	211.58	43.59	2.64	12.83	1
LL60i4	0.090	64.6	0.394	10.19	0.05	0.23	191.26	43.43	3.41	15.02	1
LL70i4	0.106	75.1	0.458	11.97	0.06	0.27	189.93	43.93	4.03	17.44	1
LL80i4	0.157	86.4	0.527	13.76	0.09	0.31	146.98	43.89	5.99	20.07	1
LL90i4	0.135	98.1	0.598	15.67	0.08	0.36	195.22	44.03	5.14	22.79	1
LL100i4	0.203	111.5	0.680	17.94	0.12	0.40	148.32	44.33	7.74	25.92	1

Table E-1 (ctd.) *Summary of characteristics of air sparging experiments conducted at constant injection pressure*

Test Name	Obs. Air velocity	Pres. Grad.	Calc. Air velocity	Bo	Ca_{obs}	Ca_{calc}	Bo/Ca_{Obs}	Bo/Ca_{Calc}	Re_{obs}	Re_{calc}	Sat. factor
	[m/s]	[-]	[m/s]	[-]	[-]	[-]	[-]	[-]	[-]	[-]	
LL30i5	0.055	31.2	0.190	4.97	0.03	0.11	153.07	43.91	2.08	7.24	1
LL40i5	0.064	42.2	0.257	6.66	0.04	0.15	174.71	43.44	2.44	9.81	1
LL50i5	0.098	53.4	0.326	8.39	0.06	0.19	144.55	43.29	3.72	12.41	1
LL60i5	0.099	64.6	0.394	10.09	0.06	0.23	170.81	43.04	3.78	15.00	1
LL70i5	0.085	75.7	0.462	11.99	0.05	0.27	236.58	43.63	3.24	17.59	1
LL80i5	0.089	86.9	0.530	13.73	0.05	0.32	258.82	43.55	3.40	20.19	1
LL90i5	0.125	99.3	0.606	15.51	0.07	0.36	208.26	43.04	4.77	23.07	1
LL100i5	0.133	111.2	0.678	17.54	0.08	0.40	222.26	43.47	5.05	25.84	1
LL1i6	0.079	5.2	0.032	0.18	0.05	0.02	3.80	9.45	2.99	1.20	2
LL10i6	0.010	9.8	0.060	1.41	0.01	0.04	236.41	39.62	0.38	2.27	2
LL20i6	0.033	20.6	0.126	3.26	0.02	0.07	165.75	43.67	1.26	4.79	1
LL30i6	0.036	31.2	0.190	4.91	0.02	0.11	232.26	43.36	1.35	7.24	1
LL40i6	0.054	42.3	0.258	6.66	0.03	0.15	207.41	43.39	2.06	9.83	1
LL50i6	0.055	53.3	0.325	8.39	0.03	0.19	255.57	43.38	2.10	12.39	1
LL60i6	0.074	64.6	0.394	10.26	0.04	0.23	232.80	43.79	2.82	15.01	1
LL70i6	0.076	75.6	0.461	12.02	0.05	0.27	266.19	43.82	2.89	17.56	1
LL80i6	0.096	86.7	0.529	13.71	0.06	0.31	241.29	43.60	3.64	20.14	1
LL90i6	0.086	98.0	0.598	15.79	0.05	0.36	309.33	44.38	3.27	22.78	1
LL100i6	0.098	109.4	0.668	17.53	0.06	0.40	300.88	44.13	3.73	25.43	1

Table E-1 (ctd.) *Summary of characteristics of air sparging experiments conducted at constant injection pressure*

Test Name	Obs. Air velocity	Pres. Grad.	Calc. Air velocity	Bo	Ca_{obs}	Ca_{calc}	Bo/Ca_{Obs}	Bo/Ca_{Calc}	Re_{obs}	Re_{calc}	Sat. factor
	[m/s]	[-]	[m/s]	[-]	[-]	[-]	[-]	[-]	[-]	[-]	
LL30i7	0.067	31.5	0.192	5.01	0.04	0.11	125.94	43.87	2.55	7.31	1
LL40i7	0.098	40.9	0.250	6.58	0.06	0.15	112.61	44.34	3.74	9.51	1
LL50i7	0.085	53.5	0.327	8.39	0.05	0.19	165.23	43.21	3.25	12.44	1
LL60i7	0.140	64.5	0.394	9.99	0.08	0.23	120.13	42.66	5.32	14.99	1
LL70i7	0.151	75.8	0.462	11.90	0.09	0.28	132.68	43.28	5.74	17.61	1
LL80i7	0.167	86.7	0.529	13.56	0.10	0.31	136.58	43.10	6.36	20.15	1
LL90i7	0.176	98.7	0.602	15.45	0.10	0.36	147.81	43.13	6.69	22.94	1
LL100i7	0.209	109.8	0.670	17.30	0.12	0.40	139.32	43.38	7.95	25.52	1
GLY05i1	0.007	9.1	0.003	0.65	0.07	0.03	8.99	24.16	0.01	0.53	2
GLY10i1	0.005	9.6	0.003	1.06	0.05	0.03	19.68	37.27	0.01	0.64	2
GLY20i1	0.016	20.1	0.006	2.34	0.16	0.06	14.81	39.42	0.03	0.74	2
GLY30i1	0.010	32.3	0.010	3.59	0.10	0.10	35.41	37.60	0.02	0.86	1
GLY40i1	0.016	42.2	0.013	4.75	0.16	0.12	29.49	38.16	0.03	0.97	1
GLY45i1	0.023	47.8	0.014	5.38	0.23	0.14	23.55	38.15	0.04	1.09	1
GLY50i1	0.030	53.8	0.016	6.15	0.30	0.16	20.83	38.69	0.05	0.00	1
GLY60i1	0.021	64.4	0.019	7.39	0.21	0.19	35.43	38.88	0.03	0.05	1
GLY70i1	0.036	78.4	0.024	8.80	0.35	0.23	25.14	38.03	0.06	0.11	1
GLY80i1	0.035	89.7	0.027	10.18	0.34	0.26	29.51	38.46	0.06	0.21	1
GLY90i1	0.027	101.8	0.031	11.65	0.26	0.30	44.34	38.78	0.04	0.31	1

Table E-1 (ctd.) *Summary of characteristics of air sparging experiments conducted at constant injection pressure*

Test Name	Injector	Fluid	Flow Rate	Target g-level	Actual ω	Actual g-level	P_{inj}	h_s	h_{LL}	σ	u	σ'	P_{entry}	ΔP
			[cm^3/s]		[rpm]		[KPa]	[cm]	[cm]	[KPa]	[KPa]	[KPa]	[KPa]	[KPa]
LLsl2i1	MPI #1	IL	0.26	1	----	1.0	8.27	15.8	14.9	3.47	1.24	2.2	1.4	6.9
LLslwi1	MPI #1	IL	0.66	1	----	1.0	8.34	15.8	14.9	3.47	1.24	2.2	1.4	7.0
LLmd3i1	MPI #1	IL	1.05	1	----	1.0	7.45	15.78	14.85	3.47	1.24	2.2	1.4	6.1
LLmedi1	MPI #1	IL	1.58	1	----	1.0	9.03	15.6	14.7	3.43	1.23	2.2	1.4	7.7
LLmd2i1	MPI #1	IL	2.11	1	----	1.0	10.96	15.8	14.9	3.47	1.24	2.2	1.4	9.6
LLfasi1	MPI #1	IL	2.63	1	----	1.0	9.31	15.9	14.7	3.49	1.23	2.3	1.4	7.9
LL3slwi1	MPI #1	IL	0.67	3	46.7	2.9	8.83	15.8	14.75	10.11	3.58	6.5	3.7	5.1
LL6slwi1	MPI #1	IL	0.67	6	71.0	6.7	12.27	15.7	14.8	23.23	8.31	14.9	8.5	3.8
LL9slwi1	MPI #1	IL	0.67	9	88.2	10.4	19.86	15.8	14.6	36.07	12.65	23.4	12.8	7.1
LL12slwi1	MPI #1	IL	0.67	12	96.7	12.5	23.10	15.9	14.8	43.63	15.41	28.2	15.6	7.5
LL15slwi1	MPI #1	IL	0.67	15	113.2	17.1	32.34	15.6	14.8	58.67	21.12	37.5	21.3	11.1
LL30slwi1	MPI #1	IL	0.67	30	153.0	31.3	47.64	15.7	14.7	107.86	38.32	69.5	38.5	9.2
LL70slwi1	MPI #1	IL	0.67	70	231.2	71.4	94.39	15.9	14.9	249.43	88.70	160.7	88.8	5.5
LL100slwi1	MPI #1	IL	0.67	100	275.5	101.4	133.76	15.8	14.8	351.95	125.10	226.8	125.2	8.5
LL30md2i1	MPI #1	IL	1.29	30	153.0	31.3	46.54	15.8	14.8	108.55	38.58	70.0	38.7	7.8
LL70md2i1	MPI #1	IL	1.29	70	232.3	72.1	93.50	15.5	14.8	245.48	88.94	156.5	89.1	4.4
LL100md2i1	MPI #1	IL	1.29	100	274.9	100.9	133.07	15.8	14.7	350.42	123.71	226.7	123.9	9.2
LLsl2i2	MPI #2	IL	0.26	1	----	1.0	8.89	15.7	14.8	3.45	1.23	2.2	1.4	7.5
LLslwi2	MPI #2	IL	0.66	1	----	1.0	8.83	15.8	14.4	3.47	1.20	2.3	1.4	7.5
LLmd3i2	MPI #2	IL	1.05	1	----	1.0	8.34	15.9	14.6	3.49	1.22	2.3	1.4	7.0
LLmedi2	MPI #2	IL	1.58	1	----	1.0	8.27	15.8	14.9	3.47	1.24	2.2	1.4	6.9
LLmd2i2	MPI #2	IL	2.11	1	----	1.0	8.69	15.6	14.7	3.43	1.23	2.2	1.4	7.3
LLfasi2	MPI #2	IL	2.63	1	----	1.0	8.83	15.8	14.7	3.47	1.23	2.2	1.4	7.4

Table E-2 Summary of characteristics of air sparging experiments conducted under constant flow rates of injection

Test Name	Injector	Fluid	Flow Rate	Target g-level	Actual ω	Actual g-level	P_{inj}	h_s	h_{LL}	σ	u	σ'	P_{entry}	ΔP
			[cm^3/s]		[rpm]		[KPa]	[cm]	[cm]	[KPa]	[KPa]	[KPa]	[KPa]	[KPa]
LLmedi3	MPI #3	IL	1.58	1	----	1.0	8.62	15.9	14.8	3.49	1.23	2.3	1.4	7.2
LLmd2i3	MPI #3	IL	2.11	1	----	1.0	9.03	15.6	14.7	3.43	1.23	2.2	1.4	7.7
LL20gslwi3	MPI #3	IL	0.67	20	127.5	21.7	28.75	15.8	14.78	75.38	26.76	48.6	26.9	1.8
LL30gslwi3	MPI #3	IL	0.67	30	157.0	32.9	41.58	15.7	14.7	113.57	40.35	73.2	40.5	1.1
LL70gslwi3	MPI #3	IL	0.67	70	235.2	73.9	93.98	15.8	14.9	256.51	91.79	164.7	91.9	2.0
LL100gslwi3	MPI #3	IL	0.67	100	275.0	101.0	135.69	15.8	14.8	350.67	124.65	226.0	124.8	10.9
LL30gmd3i3	MPI #3	IL	1.05	30	153.8	31.6	42.40	15.7	14.9	108.99	39.25	69.7	39.4	3.0
LL70gmd3i3	MPI #3	IL	1.05	70	234.9	73.7	96.74	15.8	14.9	255.86	91.56	164.3	91.7	5.0
LL100gmd3i3	MPI #3	IL	1.05	100	279.7	104.5		15.9	14.9	365.06	129.81	235.2		
LL20gmd2i3	MPI #3	IL	1.29	20	125.7	21.1	36.06	15.8	14.7	73.27	25.87	47.4	26.0	10.0
LL30gmd2i3	MPI #3	IL	1.29	30	153.0	31.3	47.78	15.7	14.8	107.86	38.58	69.3	38.7	9.0
LLsl2i4	SPI #1	IL	0.26	1	----	1.0	8.34	16.8	15.9	3.69	1.33	2.4	1.5	6.9
LLslwi4	SPI #1	IL	0.66	1	----	1.0	8.55	16.8	15.9	3.69	1.33	2.4	1.5	7.1
LLmd3i4	SPI #1	IL	1.05	1	----	1.0	8.83	16.6	15.6	3.65	1.30	2.3	1.5	7.4
LLmedi4	SPI #1	IL	1.58	1	----	1.0	8.76	16.7	15.8	3.67	1.32	2.4	1.5	7.3
LLmd2i4	SPI #1	IL	2.11	1	----	1.0	8.55	16.8	15.8	3.69	1.32	2.4	1.5	7.1
LLfasi4	SPI #1	IL	2.63	1	----	1.0	8.69	16.8	15.8	3.69	1.32	2.4	1.5	7.2

Table E-2 (ctd.) *Summary of characteristics of air sparging experiments conducted under constant flow rates of injection*

Test Name	Injector	Fluid	Flow Rate [cm^3/s]	Target g-level	Actual ω [rpm]	Actual g-level	P_{inj} [KPa]	h_s [cm]	h_{LL} [cm]	σ [KPa]	u [KPa]	σ' [KPa]	P_{entry} [KPa]	ΔP [KPa]
LLmedi5	SPI #2	IL	1.58	1	----	1.0	9.52	15.78	14.8	3.47	1.23	2.2	1.4	8.1
LLmd2i5	SPI #2	IL	2.11	1	----	1.0	8.21	15.8	14.9	3.47	1.24	2.2	1.4	6.8
LLfasi5	SPI #2	IL	2.63	1	----	1.0	10.27	15.68	14.7	3.45	1.23	2.2	1.4	8.9
LLsl2i6	SPI #3	IL	0.26	1	----	1.0	8.48	15.8	14.7	3.47	1.23	2.2	1.4	7.1
LLslwi6	SPI #3	IL	0.66	1	----	1.0	9.17	15.65	14.8	3.44	1.23	2.2	1.4	7.8
LLmd3i6	SPI #3	IL	1.05	1	----	1.0	9.38	15.75	14.6	3.46	1.22	2.2	1.4	8.0
LLmedi6	SPI #3	IL	1.58	1	----	1.0	8.89	15.8	14.9	3.47	1.24	2.2	1.4	7.5
LLmd2i6	SPI #3	IL	2.11	1	----	1.0	8.89	15.9	14.8	3.49	1.23	2.3	1.4	7.5
LLfasi6	SPI #3	IL	2.63	1	----	1.0	10.76	15.8	14.7	3.47	1.23	2.2	1.4	9.4
LL1gBDi1s	MPI #1	IL	0.67	1	----	1.0	8.55	19.8	17.7	4.35	1.48	2.9	1.6	6.9
LL3gBDi1s	MPI #1	IL	0.67	3	44.2	2.6	11.58	19.8	17.5	11.35	3.81	7.5	4.0	7.6
LL6gBDi1s	MPI #1	IL	0.67	6	67.6	6.1	9.58	19.8	17.9	26.55	9.11	17.4	9.3	0.3
LL12gBDi1s	MPI #1	IL	0.67	12	93.2	11.6	20.89	19.8	17.2	50.47	16.64	33.8	16.8	4.1
LL20gBDi1s	MPI #1	IL	0.67	20	118.8	18.8	36.20	19.8	17.1	82.01	26.88	55.1	27.0	9.2
LL1gBDi1f	MPI #1	IL	1.29	1	----	1.0	8.89	19.8	17.7	4.35	1.48	2.9	1.6	7.3
LL3gBDi1f	MPI #1	IL	1.29	3	46.0	2.8	11.72	19.8	17.7	12.30	4.17	8.1	4.3	7.4
LL1gBDi3s	MPI #3	IL	0.67	1	----	1.0	9.10	19.8	18.1	4.35	1.51	2.8	1.7	7.4
LL3gBDi3s	MPI #3	IL	0.67	3	48.3	3.1	12.27	19.8	18.1	13.56	4.70	8.9	4.9	7.4
LL12gBDi3s	MPI #3	IL	0.67	12	94.5	11.9	22.00	19.8	18.1	51.89	18.00	33.9	18.2	3.8
LL1gBDi3f	MPI #3	IL	1.29	1	----	1.0	8.62	19.8	18.1	4.35	1.51	2.8	1.7	7.0
LL3gBDi3f	MPI #3	IL	1.29	3	48.5	3.1	11.93	19.8	18.1	13.67	4.74	8.9	4.9	7.0

Table E-2 (ctd.) *Summary of characteristics of air sparging experiments conducted under constant flow rates of injection*

Test Name	h^-	B-through V^-	Steady-State V^-	h+	B-through V^+	Steady-State V^+	$h_{average}$	B-through $V_{average}$	Steady-State $V_{average}$	B-through RZI	Steady-State RZI
	[cm]	[cm^3]	[cm^3]	[cm]	[cm^3]	[cm^3]	[cm]	[cm^3]	[cm^3]	[%]	[%]
LLsl2i1	14.31	276.11	585.40	14.32	389.38	679.28	14.32	332.75	632.34	3.61	7.4224
LLslwi1	15.09	354.16	777.99	14.92	249.59	866.45	15.01	301.88	822.22	2.84	9.2672
LLmd3i1	14.22	491.14	907.80	13.96	604.64	663.70	14.09	547.89	785.75	6.23	9.8018
LLmedi1	14.07	576.06	1298.42	14.42	362.36	642.44	14.25	469.21	970.43	5.17	10.1324
LLmd2i1	14.72	449.04	1320.46	14.22	527.98	1273.19	14.47	488.51	1296.83	5.13	14.6944
LLfasi1	13.82	558.30	1779.60	13.52	656.87	942.51	13.67	607.59	1361.06	7.57	14.5090
LL3slwi1	14.83	617.14	617.14	14.81	592.53	592.53	14.82	604.84	604.84	5.91	5.9148
LL6slwi1	14.26	543.12	543.12	14.01	553.81	553.81	14.14	548.47	548.47	6.18	6.1818
LL9slwi1	14.97	427.98	427.98	14.92	362.27	362.27	14.95	395.13	395.13	3.77	3.7679
LL12slwi1	14.64	343.07	343.07	14.54	304.58	304.58	14.59	323.83	323.83	3.32	3.3189
LL15slwi1	14.32	192.70	192.70	14.36	218.31	218.31	14.36	205.51	205.51	2.21	2.2091
LL30slwi1	13.92	189.49	189.49	13.92	209.80	209.80	13.92	199.65	199.65	2.36	2.3561
LL70slwi1	14.32	119.79	119.79	14.48	91.94	91.94	14.40	105.87	105.87	1.13	1.1285
LL100slwi1	14.51	74.78	74.78	14.53	73.60	73.60	14.52	74.19	74.19	0.77	0.7714
LL30md2i1	14.83	185.26	185.26	14.87	220.26	220.26	14.85	202.76	202.76	1.97	1.9708
LL70md2i1	13.84	99.18	99.18	13.91	87.32	87.32	13.88	93.25	93.25	1.11	1.1112
LL100md2i1	14.07	77.63	77.63	14.07	82.94	82.94	14.07	80.29	80.29	0.92	0.9175
LLsl2i2	13.47	634.42	1168.60	13.42	216.34	638.25	13.45	425.38	903.43	5.57	9.3262
LLslwi2	14.36	293.77	917.29	14.07	464.89	645.67	14.22	379.33	781.48	4.20	7.5199
LLmd3i2	13.32	645.85	1300.41	13.28	516.12	805.32	13.30	580.99	1052.87	7.86	10.5504
LLmedi2	14.01	747.14	1641.69	13.92	763.24	995.35	13.97	755.19	1318.52	8.83	14.8296
LLmd2i2	13.42	953.67	1337.60	13.47	754.29	1087.48	13.45	853.98	1212.54	11.18	13.4371
LLfasi2	14.31	1196.86	1800.05	13.72	842.07	866.31	14.02	1019.47	1333.18	11.79	13.4415

Table E-2 (ctd.) *Summary of characteristics of air sparging experiments conducted under constant flow rates of injection*

Test Name	h^-	B-through V^-	Steady-State V^-	h^+	B-through V^+	Steady-State V^+	$h_{average}$	B-through $V_{average}$	Steady-State $V_{average}$	B-through RZI	Steady-State RZI
	[cm]	[cm^3]	[cm^3]	[cm]	[cm^3]	[cm^3]	[cm]	[cm^3]	[cm^3]	[%]	[%]
LLmedi3	14.26	774.28	1188.79	14.01	542.96	696.09	14.14	658.62	942.44	7.42	9.4343
LLmd2i3	14.26	860.33	1467.70	13.92	653.06	1016.08	14.09	756.70	1241.89	8.61	13.2387
LL20gslwi3	15.13	181.70	181.70	15.13	228.16	228.16	15.13	204.93	204.93	1.88	1.8834
LL30gslwi3	14.98	174.86	174.86	14.92	164.77	164.77	14.95	169.82	169.82	1.62	1.6177
LL70gslwi3	14.31	111.90	111.90	14.30	126.05	126.05	14.31	118.98	118.98	1.29	1.2937
LL100gslwi3	14.31	96.82	96.82	14.31	91.97	91.97	14.31	94.40	94.40	1.03	1.0254
LL30gmd3i3	16.14	342.76	342.76	16.14	89.49	89.49	16.14	216.13	216.13	1.64	1.6362
LL70gmd3i3	14.92	149.06	149.06	14.97	150.47	150.47	14.95	149.77	149.77	1.43	1.4281
LL100gmd3i3	14.95	111.86	111.86	14.97	95.19	95.19	14.96	103.53	103.53	0.98	0.9842
LL20gmd2i3	13.94	202.59	202.59	13.94	172.88	172.88	13.94	187.74	187.74	2.21	2.2060
LL30gmd2i3	14.97	174.48	174.48	14.97	159.50	159.50	14.97	166.99	166.99	1.58	1.5844
LLsl2i4	13.28	263.80	413.01	14.30	332.26	592.24	13.79	298.03	502.63	3.62	5.5936
LLslwi4	11.45	286.37	887.18	11.22	353.03	569.08	11.34	319.70	728.13	6.99	9.3266
LLmd3i4	12.50	347.09	754.78	12.69	502.16	919.83	12.60	424.63	837.31	6.76	9.3675
LLmedi4	12.26	409.25	602.42	12.60	480.75	559.16	12.43	445.00	580.79	7.38	7.7266
LLmd2i4	13.42	415.97	934.08	12.97	660.26	991.79	13.20	538.12	962.94	7.46	8.6085
LLfasi4	13.82	785.73	1558.52	13.23	590.26	1203.55	13.53	688.00	1381.04	8.85	11.2195

Table E-2 (ctd.) *Summary of characteristics of air sparging experiments conducted under constant flow rates of injection*

Test Name	h^-	B-through V^-	Steady-State V^-	h^+	B-through V^+	Steady-State V^+	$h_{average}$	B-through $V_{average}$	Steady-State $V_{average}$	B-through RZI	Steady-State RZI
	[cm]	[cm^3]	[cm^3]	[cm]	[cm^3]	[cm^3]	[cm]	[cm^3]	[cm^3]	[%]	[%]
LLmedi5	12.69	503.50	1640.54	12.55	536.35	690.34	12.62	519.93	1165.44	8.23	10.4189
LLmd2i5	13.47	629.54	934.15	13.30	598.16	771.93	13.39	613.85	853.04	8.15	8.7789
LLfasi5	13.82	1159.70	1203.10	13.72	503.50	942.09	13.77	831.60	1072.60	10.14	10.8586
LLsl2i6	14.01	462.97	1065.98	13.13	157.58	291.02	13.57	310.28	678.50	3.95	5.6183
LLslwi6	14.86	824.34	1851.68	15.37	302.61	385.27	15.12	563.48	1118.48	5.19	8.8153
LLmd3i6	14.78	657.20	975.73	14.72	459.52	569.93	14.75	558.36	772.83	5.54	5.9443
LLmedi6	14.31	407.25	1704.76	14.22	564.72	506.95	14.27	485.99	1105.86	5.33	9.0182
LLmd2i6	14.77	1101.35	1266.61	14.87	189.66	262.41	14.82	645.51	764.51	6.31	7.5833
LLfasi6	13.37	813.14	1591.21	13.28	410.62	397.97	13.33	611.88	994.59	8.23	9.1770
LL1gBDi1s	13.42	459.24	459.24	13.47	347.59	347.59	13.45	403.42	403.42	5.28	5.2835
LL3gBDi1s	13.87	278.08	278.08	13.77	255.23	255.23	13.82	266.66	266.66	3.22	3.2157
LL6gBDi1s	15.97	59.38	59.38	15.93	57.22	57.22	15.95	58.30	58.30	0.46	0.4573
LL12gBDi1s	15.87	66.31	66.31	15.71	55.07	55.07	15.79	60.69	60.69	0.49	0.4907
LL20gBDi1s	14.62	46.13	46.13	14.78	31.57	31.57	14.70	38.85	38.85	0.39	0.3893
LL1gBDi1f	14.26	480.70	480.70	14.31	482.51	482.51	14.29	481.61	481.61	5.26	5.2590
LL3gBDi1f	13.96	222.53	222.53	14.07	229.09	229.09	14.02	225.81	225.81	2.61	2.6110
LL1gBDi3s	14.17	380.94	380.94	14.22	332.81	332.81	14.20	356.88	356.88	3.97	3.9716
LL3gBDi3s	14.22	140.69	140.69	14.31	173.93	173.93	14.27	157.31	157.31	1.73	1.7250
LL12gBDi3s	15.50	60.21	60.21	15.50	47.57	47.57	15.50	53.89	53.89	0.46	0.4606
LL1gBDi3f	14.31	518.61	518.61	14.26	441.27	441.27	14.29	479.94	479.94	5.24	5.2408
LL3gBDi3f	14.62	165.32	165.32	14.67	213.34	213.34	14.65	189.33	189.33	1.92	1.9187

Table E-2 (ctd.) *Summary of characteristics of air sparging experiments conducted under constant flow rates of injection*

Test Name	Pressure gradient	Calculated Air velocity	Bo	Ca_{obs}	Ca_{calc}	Bo/Ca_{Calc}	Bo/Ca_{Obs}	Re_{obs}	Re_{calc}	Sat. factor
	[-]	[m/s]	[-]	[-]	[-]	[-]	[-]	[-]	[-]	
LLsl2i1	6.69	0.041	0.18	0.006	0.024	7.31	28.54	0.40	1.56	2
LLslwi1	6.76	0.041	0.18	0.008	0.025	7.24	21.46	0.53	1.57	2
LLmd3i1	5.95	0.036	0.18	0.010	0.022	8.23	18.07	0.63	1.38	2
LLmedi1	7.53	0.046	0.18	0.011	0.027	6.50	16.48	0.69	1.75	2
LLmd2i1	9.19	0.056	0.18	0.013	0.033	5.32	14.00	0.81	2.14	2
LLfasi1	7.79	0.048	0.18	0.022	0.028	6.28	8.14	1.40	1.81	2
LL3slwi1	7.30	0.045	0.52	0.009	0.027	19.52	55.78	0.59	1.70	1
LL6slwi1	10.50	0.064	1.20	0.010	0.038	31.38	118.03	0.65	2.44	1
LL9slwi1	17.90	0.109	1.85	0.013	0.065	28.41	147.28	0.80	4.16	1
LL12slwi1	20.64	0.126	2.22	0.012	0.075	29.61	178.82	0.79	4.80	1
LL15slwi1	29.30	0.179	3.04	0.025	0.106	28.59	123.89	1.57	6.81	1
LL30slwi1	43.99	0.268	5.55	0.030	0.160	34.78	184.46	1.93	10.22	2
LL70slwi1	86.75	0.529	12.68	0.040	0.315	40.28	314.08	2.59	20.16	2
LL100slwi1	124.33	0.758	18.01	0.060	0.451	39.91	302.45	3.81	28.89	2
LL30md2i1	42.61	0.260	5.55	0.051	0.155	35.91	108.85	3.27	9.90	2
LL70md2i1	86.60	0.528	12.80	0.067	0.314	40.73	189.86	4.32	20.12	2
LL100md2i1	124.66	0.760	17.93	0.094	0.452	39.62	190.25	6.03	28.97	2
LLsl2i2	7.33	0.045	0.18	0.006	0.027	6.67	27.90	0.41	1.70	2
LLslwi2	7.54	0.046	0.18	0.008	0.027	6.49	20.94	0.54	1.75	2
LLmd3i2	6.94	0.042	0.18	0.010	0.025	7.05	18.61	0.61	1.61	2
LLmedi2	6.69	0.041	0.18	0.011	0.024	7.31	16.30	0.70	1.56	2
LLmd2i2	7.20	0.044	0.18	0.013	0.026	6.79	13.17	0.86	1.67	2
LLfasi2	7.33	0.045	0.18	0.020	0.027	6.67	9.01	1.26	1.70	2

Table E-2 (ctd.) *Summary of characteristics of air sparging experiments conducted under constant flow rates of injection*

Test Name	Pressure gradient	Calculated Air velocity	Bo	Ca_{obs}	Ca_{calc}	Bo/Ca_{Calc}	Bo/Ca_{Obs}	Re_{obs}	Re_{calc}	Sat. factor
	[-]	[m/s]	[-]	[-]	[-]	[-]	[-]	[-]	[-]	
LLmd3i3	6.88	0.042	0.18	0.010	0.025	7.12	17.31	0.66	1.60	2
LLmedi3	7.08	0.043	0.18	0.011	0.026	6.92	15.82	0.72	1.64	2
LLmd2i3	7.53	0.046	0.18	0.015	0.027	6.50	11.78	0.97	1.75	2
LL20gslwi3	25.98	0.158	3.86	0.032	0.094	40.90	118.67	2.08	6.04	2
LL30gslwi3	38.26	0.233	5.85	0.032	0.139	42.11	184.22	2.03	8.89	1
LL70gslwi3	86.37	0.527	13.12	0.078	0.313	41.87	167.65	5.01	20.07	1
LL100gslwi3	126.13	0.769	17.94	0.078	0.458	39.19	229.24	5.01	29.31	2
LL30gmd3i3	38.42	0.234	5.61	0.055	0.139	40.24	101.60	3.54	8.93	1
LL70gmd3i3	88.93	0.542	13.09	0.085	0.323	40.56	153.78	5.45	20.67	2
LL100gmd3i3	NA	NA	18.56	0.123	0.000	NA	150.55	7.89	0.00	1
LL20gmd2i3	33.05	0.202	3.75	0.038	0.120	31.25	99.07	2.42	7.68	1
LL30gmd2i3	43.77	0.267	5.55	0.042	0.159	34.96	131.56	2.70	10.17	1
LLsl2i4	6.20	0.038	0.18	0.005	0.022	7.90	33.06	0.34	1.44	2
LLslwi4	6.38	0.039	0.18	0.006	0.023	7.68	28.43	0.40	1.48	2
LLmd3i4	6.78	0.041	0.18	0.009	0.025	7.22	19.44	0.59	1.58	2
LLmedi4	6.61	0.040	0.18	0.012	0.024	7.40	14.52	0.78	1.54	2
LLmd2i4	6.43	0.039	0.18	0.045	0.023	7.61	3.92	2.90	1.49	2
LLfasi4	6.55	0.040	0.18	0.014	0.024	7.47	12.27	0.93	1.52	2

Table E-2 (ctd.) *Summary of characteristics of air sparging experiments conducted under constant flow rates of injection*

Test Name	Pressure gradient	Calculated Air velocity	Bo	Ca_{obs}	Ca_{calc}	Bo/Ca_{Calc}	Bo/Ca_{Obs}	Re_{obs}	Re_{calc}	Sat. factor
	[-]	[m/s]	[-]	[-]	[-]	[-]	[-]	[-]	[-]	
LLmedi5	7.91	0.048	0.18	0.022	0.029	6.18	8.21	1.39	1.84	2
LLmd2i5	6.63	0.040	0.18	0.031	0.024	7.38	5.79	1.96	1.54	2
LLfasi5	8.70	0.053	0.18	0.031	0.032	5.62	5.76	1.98	2.02	2
LLsl2i6	7.01	0.043	0.18	0.012	0.025	6.98	14.69	0.77	1.63	2
LLslwi6	7.59	0.046	0.18	0.011	0.028	6.45	16.03	0.71	1.76	2
LLmd3i6	7.93	0.048	0.18	0.016	0.029	6.18	11.00	1.03	1.84	2
LLmedi6	7.27	0.044	0.18	0.022	0.026	6.73	8.16	1.39	1.69	2
LLmd2i6	7.33	0.045	0.18	0.028	0.027	6.67	6.31	1.80	1.70	2
LLfasi6	9.16	0.056	0.18	0.038	0.033	5.34	4.64	2.45	2.13	2
LL1gBDi1s	5.53	0.498	2.50	0.028	0.297	8.42	89.59	0.29	0.55	1
LL3gBDi1s	7.96	0.717	6.52	0.064	0.427	15.27	101.92	0.66	0.79	1
LL6gBDi1s	6.23	0.561	15.25	0.071	0.334	45.66	215.48	0.72	0.62	1
LL12gBDi1s	15.48	1.395	28.98	0.131	0.830	34.91	221.57	1.34	1.53	1
LL20gBDi1s	27.75	2.500	47.09	0.139	1.488	31.65	338.45	1.43	2.74	1
LL1gBDi1f	5.79	0.522	2.50	0.039	0.311	8.04	64.74	0.40	0.57	1
LL3gBDi1f	7.95	0.717	7.06	0.062	0.426	16.56	113.13	0.64	0.79	1
LL1gBDi3s	5.78	0.521	2.50	0.021	0.310	8.06	116.23	0.22	0.57	1
LL3gBDi3s	8.14	0.734	7.78	0.042	0.436	17.83	187.43	0.43	0.80	1
LL12gBDi3s	15.38	1.386	29.79	0.103	0.825	36.13	288.70	1.06	1.52	1
LL1gBDi3f	5.42	0.488	2.50	0.022	0.291	8.60	113.22	0.23	0.54	1
LL3gBDi3f	7.89	0.710	7.85	0.057	0.423	18.56	137.58	0.58	0.78	1

Table E-2 (ctd.) *Summary of characteristics of air sparging experiments conducted under constant flow rates of injection*

APPENDIX F

AIR SPARGING PROGRAM

```
DECLARE FUNCTION Pentry (Z)
DECLARE FUNCTION Phydro (Z)
COMMON SHARED dx, dz, jmax, rhoWater, g, Pcap, n
'-----------------------------------------------------------------------
' Specify input and output files

OPEN "data1c.dat" FOR OUTPUT AS #1
OPEN "data2c.dat" FOR OUTPUT AS #2
OPEN "data3c.dat" FOR OUTPUT AS #3
OPEN "data4c.dat" FOR OUTPUT AS #4
OPEN "data5c.dat" FOR OUTPUT AS #5
OPEN "data6c.dat" FOR OUTPUT AS #6
OPEN "data7c.dat" FOR OUTPUT AS #7
OPEN "data8c.dat" FOR OUTPUT AS #8
OPEN "data9c.dat" FOR OUTPUT AS #9
OPEN "data10c.dat" FOR OUTPUT AS #10
OPEN "data11c.dat" FOR OUTPUT AS #11

'-----------------------------------------------------------------------
' INPUT PARAMETERS

' gravitational acceleration
n = 1

' Grid size
dx = .0062                          ' m
dz = .0062                          ' m
area = dx * dz                      ' m^2

' angle: angle over which the wedge will be estimated, in radians.
' for example, for a wedge angle of pi/16, use angle = 16
angle = 4

' Number of mesh elements in xy and z directions
imax = 25
jmax = 25
groundLevel = 50

' jmax is the number of elements above the injector, to the water table
```

```
' ground is the number of elements above the injector, to the ground level

pmax = imax + 1
qmax = jmax + 1

' the model assumes the soil is initially fully saturated so jmax*dz is the
' height of the phreatic surface

q = .0000026                        ' m^3/s
flowRate = q/n                      ' m^3/s

'-------------------------------------------------------------------
' PORE FLUID PROPERTIES
rhoWater = 850                      ' kg/m^3
rhoAir = 1.2                        ' kg/m^3
deltaRho = rhoWater - rhoAir        ' kg/m^3

muWater = .01785                    ' kg/m.s
muAir = .0000181                    ' kg/m.s

surfTens = .03                      ' N/m

'-------------------------------------------------------------------
' SOIL PROPERTIES

pi = 3.14159                        ' rad

permeability = 1.31E-08             'm2
porosity = .4
Gs = 2.24
D10 = .0008                          ' m

'-------------------------------------------------------------------

' AIR CONSTANTS

Patm = 101000                       ' kg/m.s^2 - Standard atmospheric pressure
Pcap = ((4 * surfTens) / D10)       ' kg/m.s^2

g = n * 9.81                        ' m/s^2
R = 287                             ' j/kg-K - Universal Gas Const. at SAT
T = 288                             ' degK (degC + 273 = degK)
bulkModulus = 142000                ' kg/m.s^2 B - Bulk modulus of air
molWeightAir = .0288                ' kg/mol

'-------------------------------------------------------------------
```

```
' Step size and maximum number of steps

'INPUT "Time step, dt"; dt

dt = .0001                          's
tmax = 23000                        's

'-------------------------------------------------------------------
hydCond = (permeability * rhoWater * 9.81) / (porosity * muWater)

headWaterTable = jmax * dz
distBoundX = 1
distBoundZ = 1

'-------------------------------------------------------------------

' Dimensionalize arrays
DIM volX(pmax, qmax)
DIM volZ(pmax, qmax)
DIM volXZ(pmax, qmax)
DIM tempVolXZ(pmax, qmax)
DIM volPores(pmax, qmax)
DIM headZ(pmax, qmax)
DIM headX(pmax, qmax)
DIM flowLengthZ(pmax, qmax)
DIM flowLengthX(pmax, qmax)
DIM velocityX(pmax, qmax)
DIM velocityZ(pmax, qmax)
DIM marker(pmax, qmax)
DIM volAir(pmax, qmax)
DIM volWater(pmax, qmax)
DIM tempAir(pmax, qmax)
DIM tempWater(pmax, qmax)
DIM tempMark(pmax, qmax)
DIM tempXZ(pmax, qmax)
DIM gradientX(pmax, qmax)
DIM gradientZ(pmax, qmax)
DIM flowX(pmax, qmax)
DIM flowZ(pmax, qmax)
DIM topFront(pmax)
DIM airWidthX(pmax, qmax)
DIM airLevelZ(pmax, qmax)
DIM actualWidthX(pmax, qmax)
DIM actualLevelZ(pmax, qmax)
DIM interface(pmax, qmax)
'-------------------------------------------------------------------
```

```
' Initialize arrays
  FOR i = 1 TO imax
     FOR j = 1 TO jmax
        IF i = 1 THEN
          volPores(i, j) = (pi / (2 * angle)) * porosity * dx ^ 2 * dz * i ^ 2
        ELSE
          volPores(i, j) = (pi / (2 * angle)) * porosity * dx ^ 2 * dz * (i ^ 2 - (i - 1) ^ 2)
        END IF

     NEXT j, i

  FOR i = 0 TO imax
     FOR j = 0 TO jmax + 1
           volWater(i, j) = volPores(i, j)
           volAir(i, j) = 0
           marker(i, j) = 0
     NEXT j
  NEXT i

  CLS


'================================================================='===
================================================================
' During the first step air is injected into the system at the
' injection point.  During this step the injection pressure is set to a
' fraction of the pressure that would cause critical gradient conditions
' and hence an instability situation.

Pcritical = Gs * rhoWater * g * jmax * dz
deltaPressure = Pcritical - Pentry(1)
Pinj = Pentry(1)
pAirCP = Pinj

' assume that a given number of cells is filled with air (dummy cells), which
' will prevent from getting huge pressure variations.  Keep track of the air
' in the dummy cells in later iterations.  redFlag is a marker that turns
' off after the first iteration' the ideal gas law. greenFlag is a marker
' that helps recognize when breakthrough has occurred.

volAir(1, 1) = volPores(1, 1)
plumeVolume = volAir(1, 1)
marker(1, 1) = 1
greenFlag = 0
redFlag = 0
```

```
whiteFlag = 0


10  FOR iteration = 1 TO tmax

   ' pinkFlag is a marker that turns on every time a cell with a gradient
   ' that is too low is encountered in a run.  If the gradient is indeed
   ' too low then the flow rate is increased at the end of the iteration.
   ' pinkFlag needs to be reset at the end of each iteration.
   pinkFlag = 0

   ' There are two parts to the pressure iteration.  At the beginning of the
   ' program, the injection pressure is constant.  Constant pressure
   ' conditions are maintained until the number of moles coming into the
   ' system under constant flow rate conditions has stabilized, and pressures
   ' have decreased to the level of the constant pressure condition.

   ' Under constant pressure conditions,

15    pAirCP = pAirCP
      molesCP = (pAirCP + Patm) * plumeVolume / (R * T)

   ' Under constant flow rate conditions,

20    airIn = flowRate * dt
25    molesIn = (rhoAir * airIn) / molWeightAir

30    volInject = volInject + airIn
40    massInject = rhoAir * volInject
50    molesInject = massInject / molWeightAir

      pAirCFR = ((molesInject * R * T) / plumeVolume) - Patm

     deltaMoles = molesCP - molesInject
     IF iteration = 1 AND deltaMoles < 0 THEN
          PRINT "Decrease time step"
          GOTO 1610
     END IF

      time = iteration * dt
      slope = -1 * (pAirCFR - tempPAirCFR) / (time - tempTime)

      IF iteration <= 5 THEN GOTO 55


      IF (slope > 3000 AND switch = 0) THEN
```

```
55      whiteFlag = 0

        pAir = pAirCP
        tempPAirCFR = pAirCFR
        tempTime = time
        tempSlope = slope

        volInject = (molesCP * molWeightAir) / rhoAir
        GOTO 210

    ELSE
        whiteFlag = 1
        switch = 1

        ' if first time switching from constant pressure to constant
        ' flow rate then skip the guessVolume loop

        '  IF switch = 0 THEN
        '    guessVolume = plumeVolume
        '    switch = 1
        '    GOTO 190
        '  END IF

    END IF

  ' Assume a number of cells that will be occupied by air at the end of
  ' the time step, to initialize the solving process for the pressure.
  ' The assumed number of cells is chosen as a percentage of the cells
  ' already occupied by air.

  guessVolume = plumeVolume + .01 * plumeVolume


    ' Calculate air pressure for assumed injection conditions
    ' according to the ideal gas law (IGL)

190   pAirCFR = ((molesInject * R * T) / guessVolume) - Patm

        pAir = pAirCFR

        ' If the pressure is too high, and it's only due to a
        ' low guess of the estimated plume size, then guess a higher
        ' volume of invasion

        IF redFlag = 0 THEN
          IF pAir >= (groundLevel * Gs * rhoWater * g * dz) THEN
```

```
          ' Use the volume required to maintain stable conditions
            stableVol = (molesInject * R * T) / (groundLevel * Gs * rhoWater * g * dz)
            guessVolume = stableVol
            GOTO 190
          END IF

        END IF

200     IF pAir < 0 THEN

        ' If the pressure is too low, and it's only due to a
        ' high guess of the estimated plume size, then guess a lower
        ' volume of invasion

          IF redFlag = 0 THEN
            guessVolume = guessVolume - .001 * guessVolume
            GOTO 190
          END IF


      END IF

210   FOR i = 1 TO imax
220       FOR j = 1 TO jmax


        ' For cells that are half full or more of air in the vertical
        ' direction, flow in the x and z-directions will be calculated.
        ' For cells with less than half of the "vertical pores" full of
        ' air, only flow calculations in the z-direction will be performed.

        ' Determine what is the height of air in the cell.  Assume the full
        ' width of the cell contains air.

       IF marker(i, j) = 1 THEN

'-------------------------------------------------------------------------
'                       FLOW IN THE Z-DIRECTION
'-------------------------------------------------------------------------

        IF i = 1 THEN
          airLevelZ(i, j + 1) = volAir(i, j + 1) / ((pi / (2 * angle)) * porosity * dx ^ 2 * i ^ 2)
        ELSE
          airLevelZ(i, j + 1) = volAir(i, j + 1) / ((pi / (2 * angle)) * porosity * dx ^ 2 * (i ^ 2 - (i
- 1) ^ 2))
```

```
        END IF

        IF volAir(i, j + 1) = volPores(i, j + 1) THEN GOTO 380

270       IF pAir >= Pentry((j + 1) + airLevelZ(i, j + 1) / dz) THEN

            ' Flow in the z-direction
280           headZ(i, j + 1) = (pAir / (rhoWater * 9.81)) + ((j + 1) + airLevelZ(i, j + 1) / dz)
* dz
            headWaterZ = (Phydro((j + 1) + airLevelZ(i, j + 1) / dz) / (rhoWater * 9.81)) + ((j
+ 1) + airLevelZ(i, j + 1) / dz) * dz
290           flowLengthZ(i, j + 1) = distBoundZ * jmax * dz - ((j + 1) + airLevelZ(i, j + 1) /
dz) * dz

              IF (flowLengthZ(i, j + 1) = 0 AND greenFlag = 1) THEN
                  PRINT "Breakthrough at time (secs):", iteration * dt
                  GOTO 1550
              END IF

300           gradientZ(i, j + 1) = (headWaterZ - headZ(i, j + 1)) / flowLengthZ(i, j + 1)
310           velocityZ(i, j + 1) = -hydCond * gradientZ(i, j + 1)

            IF i = 1 THEN
              flowZ(i, j + 1) = velocityZ(i, j + 1) * (pi / (2 * angle)) * dx ^ 2 * i ^ 2
            ELSE
              flowZ(i, j + 1) = velocityZ(i, j + 1) * (pi / (2 * angle)) * dx ^ 2 * (i ^ 2 - (i - 1) ^
2)
            END IF

            IF (-1 * gradientZ(i, j + 1) > 0 AND -1 * gradientZ(i, j + 1) < .005) THEN
              IF pinkFlag = 0 THEN
                 pinkFlag = 1
                 BEEP
                 PRINT "Increase flow rate, gradient too low"
                 PRINT "Current flow rate, q ="; flowRate
                 INPUT "New q, m3/sec"; flowRate
              END IF
            END IF

            ' The maximum volume OF WATER that can be pushed out
            ' of cell (i, j+1) in the z- direction under the current air
            ' pressure is:
330           volZ(i, j + 1) = flowZ(i, j + 1) * dt

            ' volZ(i,j) cannot exceed the maximum volume that can flow
            ' out under stable conditions, for the chosen dt.  Need to
```

```
        ' determine what that volume is first, and then compare it to
        ' volZ

      ' If entry pressure conditions are not verified, no flow occurs
      ' in the z-direction

      ELSE
         volZ(i, j + 1) = 0
      END IF


'-------------------------------------------------------------------
'                  FLOW IN THE X-DIRECTION
'-------------------------------------------------------------------

      ' Determine what is the width of air in the cell.  Assume the full
      ' height of the cell contains air.

380      airWidthX(i + 1, j) = (SQR(i ^ 2 + volAir(i + 1, j) / ((pi / (2 * angle)) * porosity * dx
^ 2 * dz)) - i) * dx

       IF volAir(i + 1, j) = volPores(i + 1, j) THEN GOTO 395


390      IF pAir >= Pentry((j + (j + 1)) / 2) THEN

          ' Flow in the x-direction
           headX(i + 1, j) = (pAir / (rhoWater * 9.81)) + ((j + (j + 1)) / 2) * dz
           headBoundaryX = (Phydro((j + (j + 1)) / 2) / (rhoWater * 9.81)) + ((j + (j + 1)) /
2) * dz
           flowLengthX(i + 1, j) = distBoundX * imax * dx - ((i + 1) + airWidthX(i + 1, j) /
dx) * dx
          ' flowLengthX(i + 1, j) = distBoundX * imax * dx
           gradientX(i + 1, j) = (headBoundaryX - headX(i + 1, j)) / flowLengthX(i + 1, j)
           velocityX(i + 1, j) = -hydCond * gradientX(i + 1, j)

           flowX(i + 1, j) = velocityX(i + 1, j) * (pi / angle) * i * dx * dz


          ' The maximum volume OF WATER that can be pushed out
          ' of this cell in the X-direction under the current air
          ' pressure is:
           volX(i + 1, j) = flowX(i + 1, j) * dt

       ' If entry pressure conditions are not verified, no flow occurs
       ' in the x-direction
```

```
        ELSE
            volX(i + 1, j) = 0
        END IF

    IF (pAir < Pentry((j + 1) + airLevelZ(i, j + 1) / dz) AND pAir < Pentry((j + (j + 1)) / 2))
THEN
        IF redFlag = 0 THEN
           PRINT "Not enough pressure for breakthrough"
           guessVolume = guessVolume - .1 * guessVolume
           GOTO 190
           GOTO 1545
        END IF
      END IF


'-------------------------------------------------------------------
'                VOLUME BALANCE IN ALL DIRECTIONS
'-------------------------------------------------------------------


     ' For each cell (i,j) where air pressure is being applied, determine
     ' the volume of water that flows out of the surrounding cells

     ' Vertical flow

395     IF volAir(i, j + 1) = volPores(i, j + 1) THEN GOTO 396

       IF volZ(i, j + 1) > volPores(i, j + 1) THEN
        PRINT "Gradient too high -z"
        GOTO 1550
       ELSEIF volZ(i, j + 1) >= volWater(i, j + 1) THEN
           volWater(i, j + 1) = 0
           volAir(i, j + 1) = volPores(i, j + 1)
       ELSE
           volWater(i, j + 1) = volWater(i, j + 1) - volZ(i, j + 1)
           volAir(i, j + 1) = volPores(i, j + 1) - volWater(i, j + 1)

       END IF

396     IF i = 1 THEN
           actualLevelZ(i, j + 1) = volAir(i, j + 1) / ((pi / (2 * angle)) * porosity * dx ^ 2 * i ^
2)
       ELSE
           actualLevelZ(i, j + 1) = volAir(i, j + 1) / ((pi / (2 * angle)) * porosity * dx ^ 2 * (i ^
2 - (i - 1) ^ 2))
```

```
        END IF


       'Horizontal flow

        IF volAir(i + 1, j) = volPores(i + 1, j) THEN GOTO 397

        IF volX(i + 1, j) > volPores(i + 1, j) THEN
         PRINT "Gradient too high -x"
         GOTO 1550
        ELSEIF volX(i + 1, j) >= volWater(i + 1, j) THEN
            volWater(i + 1, j) = 0
            volAir(i + 1, j) = volPores(i + 1, j)
        ELSE
            volWater(i + 1, j) = volWater(i + 1, j) - volX(i + 1, j)
            volAir(i + 1, j) = volPores(i + 1, j) - volWater(i + 1, j)
        END IF

397     actualWidthX(i + 1, j) = (SQR(i ^ 2 + volAir(i + 1, j) / ((pi / (2 * angle)) * porosity *
dx ^ 2 * dz)) - i) * dx


       ' CROSS FLOW

        IF volAir(i + 1, j + 1) = volPores(i + 1, j + 1) THEN GOTO 1280
       IF (volAir(i + 1, j) = volPores(i + 1, j) OR volAir(i, j + 1) = volPores(i, j + 1)) THEN
GOTO 1280


        IF pAir > Pentry(((j + 1) + actualLevelZ(i, j + 1) / dz) / 2) THEN
            volXZ(i + 1, j + 1) = porosity * (pi / (2 * angle)) * ((i + actualWidthX(i + 1, j) / dx)
^ 2 - i ^ 2) * dx ^ 2 * actualLevelZ(i, j + 1)

            IF volXZ(i + 1, j + 1) > volPores(i + 1, j + 1) THEN
                PRINT "Gradient too high -XZ"
                GOTO 1550
            ELSE
                deltaXZ = volXZ(i + 1, j + 1) - tempVolXZ(i + 1, j + 1)
                volWater(i + 1, j + 1) = volWater(i + 1, j + 1) - deltaXZ
                volAir(i + 1, j + 1) = volPores(i + 1, j + 1) - volWater(i + 1, j + 1)
                tempVolXZ(i + 1, j + 1) = volXZ(i + 1, j + 1)
            END IF

        ELSE
            volXZ(i + 1, j + 1) = volXZ(i + 1, j + 1)
        END IF
```

```
      ' End of marker(i,j) = 1 if-statement

1280     END IF

1290     IF volAir(i, j + 1) = volPores(i, j + 1) THEN marker(i, j + 1) = 1
         IF volAir(i + 1, j) = volPores(i + 1, j) THEN marker(i + 1, j) = 1
         IF volAir(i + 1, j + 1) = volPores(i + 1, j + 1) THEN marker(i + 1, j + 1) = 1

1299     NEXT j, i


      lmax = imax
      mmax = jmax

      FOR l = 1 TO lmax
       rightFront = 0
       topFront(l) = 0

        FOR m = 1 TO mmax
          IF volAir(l, m) > 0 THEN
            IF l = 1 THEN
              IF m = 1 THEN
                topFront(l) = volAir(l, m) / (porosity * dx ^ 2 * (pi / (2 * angle)) * l ^ 2)
              ELSE
                topFront(l) = m + (volAir(l, m) / (porosity * dx ^ 2 * (pi / (2 * angle)) * l ^ 2))
              END IF
            ELSE
              IF m = 1 THEN
                topFront(l) = volAir(l, m) / (porosity * dx ^ 2 * (pi / (2 * angle)) * (l ^ 2 - (l -
1) ^ 2))
              ELSE
                topFront(l) = m + (volAir(l, m) / (porosity * dx ^ 2 * (pi / (2 * angle)) * (l ^ 2 -
(l - 1) ^ 2)))
              END IF
            END IF
          END IF
        NEXT m

        IF topFront(l) = 0 THEN
          IF l = 1 THEN
            righFront = l
          ELSE
            rightFront = l - 1
          END IF
```

```
        GOTO 1305
        END IF

      NEXT l


1305      totalVol = 0

1320    FOR i = 1 TO imax
1330      FOR j = 1 TO jmax
1340        IF volAir(i, j) > 0 THEN
            totalVol = totalVol + volAir(i, j)
1380        END IF
1390    NEXT j, i


1400    plumeVolume = totalVol

        IF whiteFlag = 0 THEN GOTO 1530

        epsilon = guessVolume - plumeVolume
'       PRINT "epsilon", epsilon
'       LINE INPUT "yo:", a$
'       IF (a$ = "q") THEN END


1420    IF ABS(epsilon) < .01 * plumeVolume THEN

1425      IF pAir >= (groundLevel * Gs * rhoWater * g * dz) THEN
            PRINT "Soil fractured"
            GOTO 1550
          END IF

          redFlag = 1

1430      PRINT "Volumes match!"
            ' need to save the last stage of the plume at which
            ' pressures and volumes matched
            FOR i = 1 TO imax
              FOR j = 1 TO jmax
                tempAir(i, j) = volAir(i, j)
                tempWater(i, j) = volWater(i, j)
                tempXZ(i, j) = tempVolXZ(i, j)
                tempMark(i, j) = marker(i, j)
```

```
            NEXT j, i

            tempPlumeVol = plumeVolume

            tempFlag = 1
            greenFlag = 1

1450    ELSE
1460        PRINT "Volumes don't match..."

1465          IF tempFlag = 0 THEN
              FOR i = 1 TO imax
               FOR j = 1 TO jmax
                  marker(i, j) = 0
                  volAir(i, j) = 0
                  tempVolXZ(i, j) = 0
                  volWater(i, j) = volPores(i, j)
              NEXT j, i

                  volAir(1, 1) = volPores(1, 1)
                  marker(1, 1) = 1

                  iteratePlume = plumeVolume
                  plumeVolume = initVolume

                  GOTO 1470

            ELSE
              FOR i = 1 TO imax
               FOR j = 1 TO jmax
                  marker(i, j) = tempMark(i, j)
                  volAir(i, j) = tempAir(i, j)
                  volWater(i, j) = tempWater(i, j)
                  tempVolXZ(i, j) = tempXZ(i, j)

              NEXT j, i

              iteratePlume = plumeVolume
              plumeVolume = tempPlumeVol

            END IF


1470        guessVolume = (guessVolume + iteratePlume) / 2

1480        GOTO 190
```

```
1490   END IF


1530   PRINT iteration, rightFront


1543  abacus = abacus + 1
    IF blackflag = 0 THEN
1544        WRITE #11, "n", "time", "Volume", "pAirCP", "pAirCFR", "pAir", "molesCP",
"molesCFR"
      blackflag = 1
    END IF

    IF abacus = 25 THEN
      WRITE #11, n, iteration * dt, plumeVolume, pAirCP, pAirCFR, pAir, molesCP,
molesInject
      abacus = 0
    END IF

1545  NEXT iteration

1550  WRITE #1, "i", "j", "n", "angle", "dt", "q", "k", "volume", "dummy", "pAir", "it. #",
"dx", "dz", "sat.", "marker(i,j)", "Pentry(i+1)", "Pentry(j+1)", "aLevZ(i,j+1)", "headX(i+1, j)",
"headZ(i, j+1)", "LengthX", "LengthZ", "iX(i+1,j)", "iZ(i,j+1)", "volX(i+1,j)", "vZ(i,j+1)",
"actZ(i,j+1)", "actX(i+1,j)", "vAir(i,j+1)", "vAir(i+1,j)", "vWat(i,j+1)", "vWat(i+1,j)",
"vXZ(i+1,j+1)", "vPor(i+1,j)", "vPor(i,j+1)", "vPor(i+1,j+1)"

1551  FOR i = 1 TO imax

1560   FOR j = 1 TO jmax

1570      WRITE #1, i, j, n, angle, dt, flowRate, permeability, plumeVolume - initVolume,
dummy, pAir, iteration, i * dx, j * dz, (volAir(i, j) / volPores(i, j)) * 100, marker(i, j),
Pentry((j + (j + 1)) / 2), Pentry((j + 1) + airLevelZ(i, j + 1) / dz), airLevelZ(i, j + 1), headX(i +
1, j), headZ(i, j + 1), flowLengthX(i + 1, j), flowLengthZ(i, j + 1), gradientX(i + 1, j),
gradientZ(i, j + 1), volX(i + 1, j), volZ(i, j + 1), actualLevelZ(i, j + 1), actualWidthX(i + 1, j),
volAir(i, j + 1), volAir(i + 1, j), volWater(i, j + 1), volWater(i + 1, j), volXZ(i + 1, j + 1),
volPores(i + 1, j), volPores(i, j + 1), volPores(i + 1, j + 1)
1580  NEXT j, i

1600  BEEP

1610  END

      'LINE INPUT "yo:", a$
```

```
      'IF (a$ = "q") THEN END

FUNCTION Pentry (Z)
      Pentry = Phydro(Z) + Pcap
END FUNCTION

FUNCTION Phydro (Z)
     Phydro = rhoWater * g * dz * (jmax - Z)
END FUNCTION
```

APPENDIX G

MODEL EQUATIONS

G.1.CELL VOLUMES

Calculations of the available volume of voids at every mesh element *(i,j)* were performed at the beginning of program execution, as will be outlined in this section. For an wedge angle α specified as one of the input parameters, Figure G-1 illustrates the volume of voids calculated.

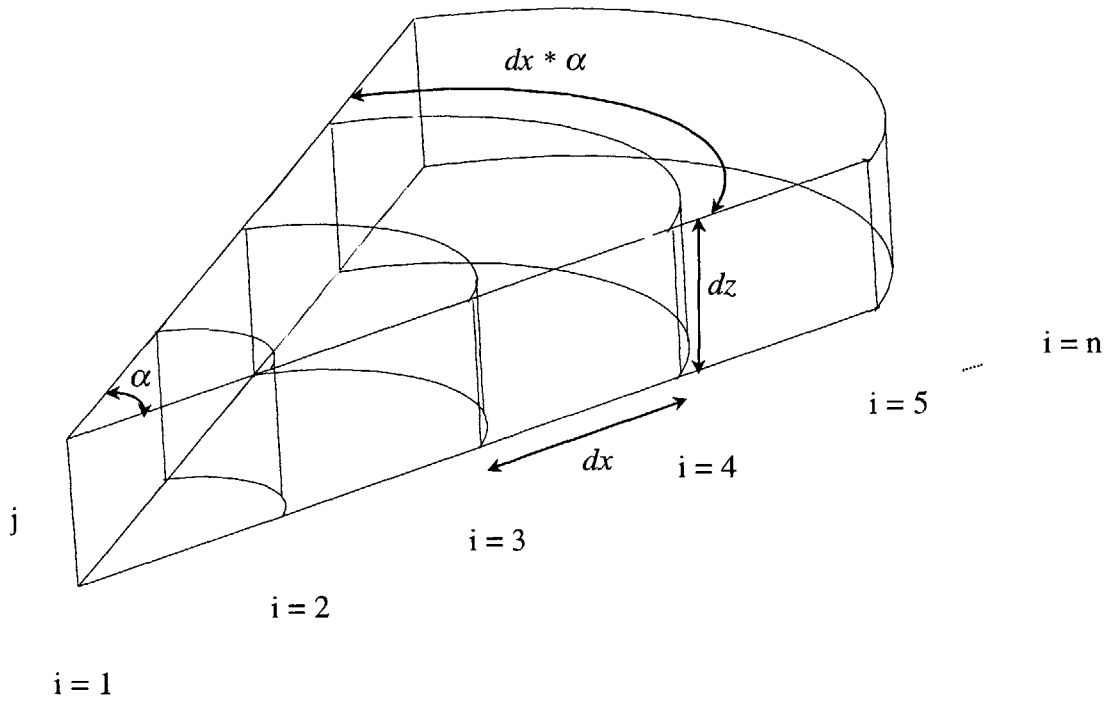

Figure G-1 *Schematic of one row of elements used in calculations of volume of voids available for flow*

The axis of the injection well runs along column *i = 1* on Figure G-1.

The volume of available voids for a given cell *(i,j)*, *volCell(i,j)*, is calculated according to the set of G-1, in which the porosity of the porous medium is represented by the symbol η:

$$If\ i = 1: \qquad volCell(i,j) = \eta.\frac{\alpha}{2}.dx^2.dz.i^2$$

$$If\ i \neq 1: \qquad volCell(i,j) = \eta.\frac{\alpha}{2}.dx^2.dz.\left[i^2 - (i-1)^2\right]$$

Equation G-3

G.2.FLOW IN THE X-DIRECTION

G.2.1. Area of Flow

For flow in the *x*-direction, the cross sectional area of a cell element across which pore fluid flow takes place is shown, shaded in gray, in Figure G-2. This area is used in calculations of the average flow of pore fluid out of an element during a given time step.

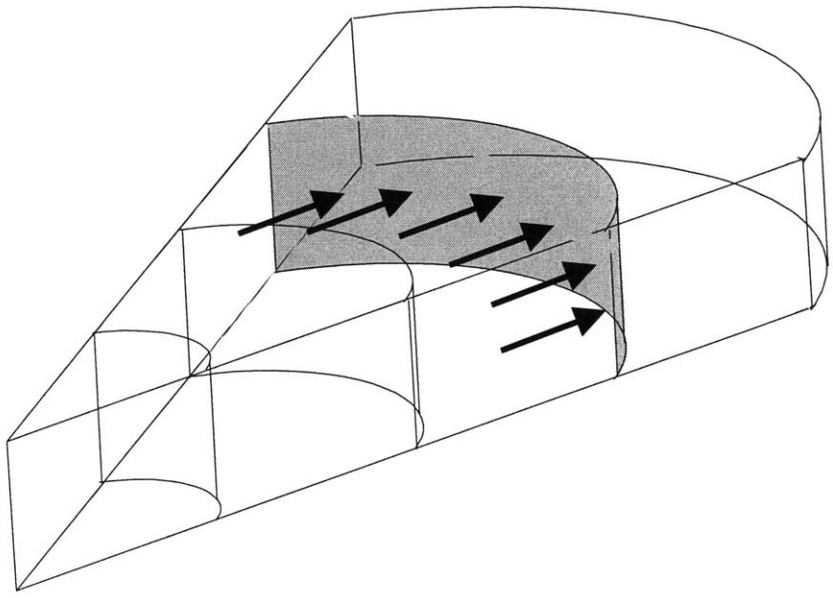

Figure G-2 Schematic of cross sectional area of pore fluid outflow in the x-direction

The magnitude of the area of flow for an element *(i,j)*, $Aflow_x(i,j)$ is given by equation G-2 as follows:

$$Aflow_x(i,j) = \alpha.(i+1).dx.dz \qquad \text{Equation G-4}$$

G.2.2. Width of Fluid in Cell

During program execution, as flow is taking place, the advancement of the air front through the mesh is tracked by determining the width and the height of air in a given cell at successive time steps. These two dimensions are calculated from the knowledge of the volume of pore fluid that has flown out of a cell under a given gradient. This volume of fluid outflow becomes the available volume for the air to flow in, and it is a known quantity. The *width* and *height* of air in a given cell however, need to be determined for each step, since the geometry of the mesh elements varies with position. Figure G-3 illustrates the dimensions in question.

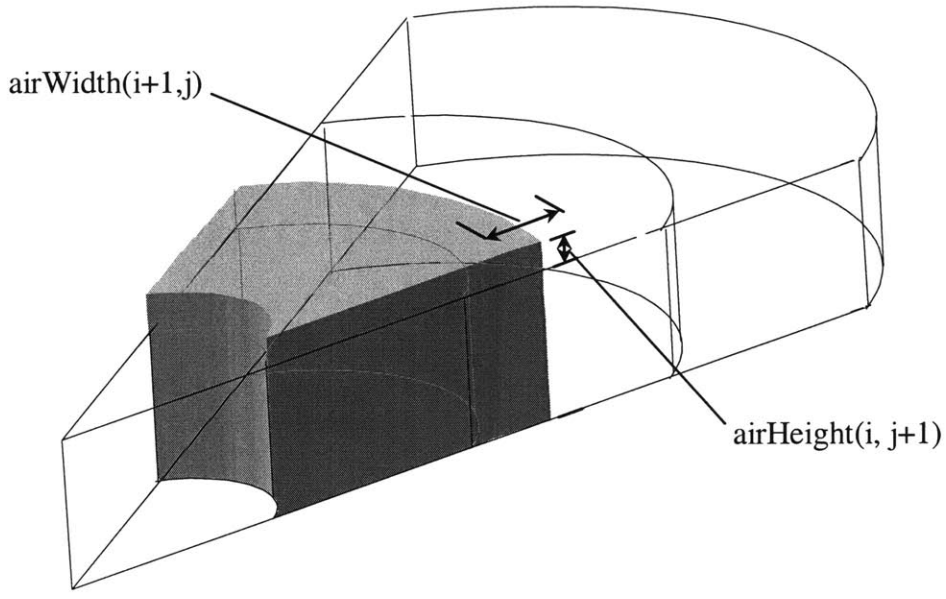

Figure G-3 Volume of air propagating into adjacent cells

If the width of air in a cell, *airWidth(i+1, j)* is designated by *w*, then the following equation must be solved to find *w*, once the volume available for air flow in the adjacent cell, *airVolume(i+1, j)*, has been determined:

$$airVolume(i+1,j) = \eta.\frac{\alpha}{2}.dx^2.dz.\left((i+w)^2 - i^2\right) \qquad \text{Equation G-5}$$

Equation G-3 is a quadratic equation for *w*, for which the positive root is given by:

$$w = \sqrt{i^2 + \frac{airVolume(i+1,j)}{\eta.\frac{\alpha}{2}.dx^2.dz}} - i \qquad \text{Equation G-6}$$

G.3.FLOW IN THE Z-DIRECTION

G.3.1. Area of flow

Similarly to what was described in section G.2.1., for flow in the *z*-direction, the cross sectional area through which pore fluid flows is shown shaded in gray on figure G-4. The dimension of the area of flow in the *z*-direction, $Aflow_z(i,j)$ is calculated according to Equation G-5 as follows:

$$If\ i = 1 \qquad Aflow_z(i,j) = \frac{\alpha}{2}.dx^2.i^2$$

$$If\ i \neq 1 \qquad Aflow_z(i,j) = \frac{\alpha}{2}.dx^2.\left[i^2 - (i-1)^2\right] \qquad \text{Equation G-7}$$

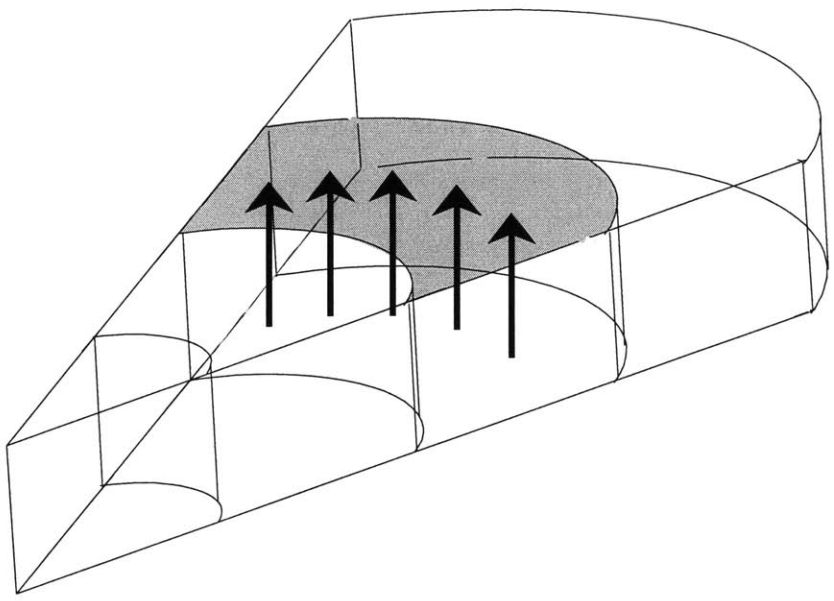

Figure G-4 Schematic of cross sectional area of pore fluid outflow in the z-direction

G.3.2. Height of Air in Cell

Figure G-3 also illustrates the dimension referred to as *airHeight(i, j+1)*, which needs to be determined at each step, for every element of the mesh, in order to account for air propagation across the mesh. This parameter is designated as h, and can be calculated from the known value of the volume of air that can flow into cell *(i, j+1)*, namely *airVolume(i, j+1)* according to Equation G-6:

$$If\ i = 1 \qquad h = \frac{airVolume(i, j+1)}{\eta . \frac{\alpha}{2} . dx^2 . i^2}$$

Equation G-8

$$If\ i \neq 1 \qquad h = \frac{airVolume(i, j+1)}{\eta . \frac{\alpha}{2} . dx^2 . \left[i^2 - (i-1)^2 \right]}$$